The Pennsylvania State University

The Graduate School

College of Earth and Mineral Sciences

INTERPRETING PORE PRESSURE IN MARINE MUDSTONES WITH PORE PRESSURE PENTROMETERS, IN SITU DATA, AND LABORATORY MEASUREMENTS

A Thesis in

Energy and Geo-Environmental Engineering

by

Hui Long

Submitted in Partial Fulfillment
of the Requirements
for the Degree of

Doctor of Philosophy

December, 2007

The thesis of Hui Long was reviewed and approved* by the following:

Peter B. Flemings
Professor of Geosciences
Thesis Co-Adviser
Co-Chair of Committee

Derek Elsworth
Professor of Energy and Geo-Environmental Engineering
Thesis Co-Adviser
Co-Chair of Committee

Abraham S. Grader
Professor of Petroleum and Gas Engineering

Chris J. Marone
Professor of Geosciences

Demian M. Saffer
Associate Professor of Geosciences

John T. Germaine
Special Member
Senior Research Associate of Civil and Environmental Engineering, MIT

Yaw D. Yeboah
Professor of Energy and Geo-Environmental Engineering
Head of the Department of Energy and Mineral Engineering

*Signatures are on file in the Graduate School.

Abstract

Pore fluid pressure plays an important role in deformation and mass transfer in the Earth's crust. However, it is extremely challenging to directly measure pore fluid pressures in low-permeability mudstones. We developed a new pressure penetrometer, the Temperature-Two-Pressure (T2P) probe, which allows the pore fluid pressure to be accurately inferred from partial dissipation records. We used the strain path method to simulate pore pressure generation and dissipation due to penetration of penetrometers with various geometries. Our theoretical analyses suggest that one of the key controls on soil behavior is the undrained rigidity index. The step geometry of the T2P enables that the pore fluid pressure and hydraulic diffusivity of the penetrated sediment to be estimated independently within a very short monitoring time by comparing the dissipated pressures at the tip and shaft pressure ports. The measured data suggested the proposed approach can provide reliable and rapid estimates of pore fluid pressure from partial dissipation records. However, this approach requires high quality dissipation data and accurate soil model. Modeling results show that the tip pressure dissipation of a tapered probe initially follows that of its needle probe, starts to depart from its needle probe when the pressure front coming from its overlying shaft reaches the tip pressure port, and converges to the pressure dissipation of its overlying shaft when the narrow pressure pulse caused by its needle probe decays away. During the transition, it forms a "bench" on the tip pressure dissipation curve. We related the excess pore pressure ratio on the "bench" to a single parameter, the undrained rigidity index. This allows the in situ pressure to be estimated from partial dissipation data without knowing detailed soil properties. In addition, we proposed a new extrapolation approach, inverse square root of time extrapolation, based on the model results. It can provide pore fluid pressure with desirable accuracy for soft marine sediments with low undrained rigidity index. On the other hand, we conducted extensive uniaxial consolidation tests on whole core

samples to obtain the consolidation properties of the sediments, and use them to predict pore fluid pressure from porosity profiles. The results suggest that the compression index linearly decreases with in situ void ratio. This implies that a local virgin compression curve cannot validly be extrapolated over a large range in effective stress. This effect is particularly important at shallow depth where void ratio decreases rapidly. The relationship of compressibility index versus void ratio can be obtained from a single consolidation test by compressing the soil over a large range in effective stress. A virgin compression curve can then be constructed based on this relationship to predict pore fluid pressure. In the Ursa Basin, this new approach successfully predicted pressures interpreted from the penetrometer measurements within the non-deformed sediments. The mass transport deposits appear to be more compacted than the non-deformed sediments. The virgin compression curve based on the assumption of uniaxial strain under-predicts the in situ pressure in the mass transport deposits.

This thesis comprises a series of six papers either published or in-review. In chronological order these papers are:

Long, H., P.B. Flemings, J.T. Germaine, and D.M. Saffer (in review) Consolidation characteristics, effective stress and pore fluid pressure of Ursa sediments, Gulf of Mexico, *Earth and Planetary Science Letter*.

Long, H., Flemings, P.B., Germaine, J.T., and Elsworth, D. (in review), Analysis and Interpretation of Pore Pressure Measurement by a New Penetrometer: Temperature-Two-Pressure (T2P) Probe, *Journal of Geophysical Research*.

Long, H., P. B. Flemings, J. T. Germaine, and D. M. Saffer (in review), Consolidation characteristics of sediments from IODP Expedition 308, Ursa Basin, Gulf of Mexico, *in. Proceeding of the integrated ocean drilling program, Science Results, vol, 308*.

Long, H., P. B. Flemings, J. T. Germaine, B. Dugan, D. Ferrell, and Expedition 308 Scientists (in

review), Penetrometer Measurements of In Situ Temperature and Pressure on IODP Expedition 308, *in. Proceeding of the integrated ocean drilling program, Science Results, vol, 308*.

Long, H., P.B. Flemings, J. Germaine, B. Dugan, D. Sawyer, and Shipboard Scientific Party, IODP Expedition 308 (2007), In Situ Pore Pressure at IODP Site U1324, Ursa Basin, Gulf of Mexico, *Proceedings of the Offshore Technology Conference, Houston, Texas*, *OTC Paper #18772*.

Long, H., P. B. Flemings, and J. T. Germaine (2007), Interpreting in situ pressure and hydraulic properties with borehole penetrometers in ocean drilling: DVTPP and Piezoprobe deployments at southern Hydrate Ridge, offshore Oregon, *J. Geophys. Res.*, *112*, B04101, doi:04110.01029/02005JB004165.

Table of Contents

List of Figures

List of Tables

Acknowledgments

I would like to especially thank Professor Peter Flemings, my thesis adviser, for his guidance and insights, both technical and philosophical. His enthusiasm and strong motivation to explore demanding questions has greatly shaped and broadened my perspective of research. I would like to thank Professor Derek Elsworth, my thesis co-adviser, for the valuable contributions he provided throughout my work.

Many other faculty members and colleagues have influenced my academic adventures. I thank Drs. John Germaine, Demian Saffer, Chris Marone and Abraham Grader for serving as my committee members and for their insightful inputs and advice to my work. My appreciation also extends to all my friends and colleagues in Basin Research Group for their support, insights and encouragement. Heather Nelson and Christie Rosenhoover provided support and assistance without which many things would not have been completed.

I wish to thank my parents and my wife for their support and understanding over this long journey.

This work is as a result of partial support from the National Science Foundation under Grants 0447235 and 0351085, and U. S. Science Support Program. Additional funding has been provided by GeoFluids Consortium, The Pennsylvania State University.

Chapter 1: Interpreting In-Situ Pressure and Hydraulic Properties with Borehole Penetrometers in Ocean Drilling: DVTPP and Piezoprobe Deployments at southern Hydrate Ridge, Offshore Oregon

Abstract

Two borehole penetrometers, Fugro-McClelland's Piezoprobe and the Ocean Drilling Program's (ODP) DVTPP, were deployed 50 meters below seafloor at Site 1244 on ODP Leg 204 to measure formation pressure at southern Hydrate Ridge, offshore Oregon. The Piezoprobe pressure reaches 90% of dissipation 14 times sooner than the DVTPP. The observed and modeled pore pressure response illustrate how penetrometer geometry impacts our ability to interpret in situ properties, and demonstrate under what conditions these tools can be effectively used. Because of its narrow tip, the Piezoprobe disturbs a narrower interval around the borehole than the DVTPP does. This generates a narrower pressure spike that dissipates much faster than the DVTPP. As consolidation proceeds, pressure dissipation of the Piezoprobe is retarded and forms a 'bench' on the dissipation curve. Due to its distinct two-radius geometry, it is possible to apply a consistent method to estimate in situ pressure from partial dissipation record based on the 'bench' feature. At 50 meters below sea floor at Site 1244, pore pressure is interpreted to be hydrostatic and the sediment's coefficient of consolidation is interpreted to lie between 6.92 to 7.8×10^{-7} m^2/s, which is in approximate agreement with laboratory measurements.

1.1 Introduction

Direct measurement of pore pressure and hydrologic properties will strengthen our understanding of fundamental geological processes. We continue to debate the relationship between pore pressure and faulting in accretionary prisms [*Davis, et al.*, 1983; *Dahlen, et al.*, 1984; *Saffer and Bekins*, 2002]. Pore pressure is thought to have a role in the earthquake cycle [*Sibson*, 1981]. In hydrate systems, pore pressure may control how free gas is trapped and migrates [*Hyndman and Davis*, 1992; *Holbrook et al.*, 2002; *Flemings, et al.*, 2003]. Pore pressure is known to have an effect on the potential for submarine landslides [*Dillon, et al.*, 2000; *Dugan and Flemings*, 2000; 2002].

Despite its importance, we are only beginning to learn how to directly measure pressure in low permeability sediments. In the Ocean Drilling Program, two techniques have been used. Permanent borehole installations (CORKs, ACORKs) have isolated parts of the formation to monitor pressure [*Davis*, 1992; *Davis and Becker*, 1994; *Becker, et al.*, 1997] and penetrometers have been developed [*Davis*, 1997; *Taylor, et al.*, 2000].

Penetrometers induce a pressure pulse as they are inserted into sediments, and subsequently this pressure decays. The induced pore pressure and its subsequent dissipation are constrained by the strength of the sediment and its consolidation coefficient. The initial excess pore pressure after penetration can be used to estimate the shear modulus of the sediments if conditions are undrained [*Randolph and wroth*, 1979a]. The pressure dissipation is used to infer in situ pore pressure and the coefficient of consolidation [*Randolph and Wroth*, 1979a; *Gupta and Davidson*, 1986], which can be used to infer permeability.

Free fall probes sample pore pressure within a few meters of the seafloor, including the Puppi [*Schultheiss and McPhail*, 1986; *Fang, et al.*, 1993; *Urgeles, et al.*, 2000] and a tethered probe [*Davis, et al.*, 1991]. A second class of penetration tools was developed for use in boreholes, such as the Davis-Villinger Temperature/Pressure Probe (DVTPP) [*Moore, et al.*, 2001; *Tréhu, et al.*, 2003], and a tapered Piezoprobe [*Ostermeier, et al.*, 2001; *Whittle, et al.*, 2001].

The goal of this experiment was to evaluate the relative behavior of the Piezoprobe and the DVTPP by deploying them both at one location. For both tools, we first characterized the pressure responses during deployment. We then simulated the pressure response for these two tools using soil parameters derived from laboratory testing of core samples collected from Site 1244. We then linked observations of the pressure dissipations with our modeling results to infer in situ pressure and the coefficient of consolidation and we compared our field-predicted consolidation coefficients with our laboratory-derived ones. More broadly, ODP Leg 204 was dedicated to understanding the factors controlling the distribution and concentration of gas hydrates in an accretionary [*Tréhu, et al.*, 2003]. Recent work has suggests that overpressured pore fluids may drive fluid flow and the formation and distribution of gas hydrates [*Gorman, et al.*, 2002; *Flemings, et al.*, 2003]. Thus, understanding in situ pressure is critical to understand hydrate system behavior and this effort begins with a better understanding of penetrometer behavior in marine soils.

The results illustrate how penetrometer geometry plays a critical role in our ability to interpret in situ properties, and they demonstrate under what conditions these tools can be effectively used. There have been a variety of industry applications of the Piezoprobe [*Varney*, 1998; *Sutabutr*, 1999; *Ostermeier, et al.*, 2001; *Whittle, et al.*, 2001]. Although the DVTPP has been deployed multiple times, to our knowledge this is the first published analysis of results of the DVTPP that combines theory and observation. Our presentation parallels work that couples theory and measurement in a land-based Piezoprobe example [*Sutabutr*, 1999; *Whittle, et al*, 2001].

1.2 Instruments

The DVTPP was previously deployed on ODP Leg 190 [*Moore, et al.*, 2001]. The Piezoprobe was developed by Fugro-McClelland Marine Geosciences Inc. and is deployed by industry [*Ostermeier, et al.*, 2001; *Whittle, et al*, 2001; *Dugan and Flemings*, 2002; *Orange, et al.*, 2003]. The DVTPP and the Piezoprobe differ in their geometry (Figure 1.1). The Piezoprobe has a needle probe that is 175 mm long including the short, tapered tip. An 18 degree taper connects the needle probe to a larger diameter shaft. A porous element above the tip allows communication of pore fluid with the pressure transducer. The cone-shaped DVTPP is more than twice as long as the Piezoprobe and the maximum diameter is 1.5 times that of the shaft of the Piezoprobe. The pressure port is located farther from the probe tip than it is on the Piezoprobe (Figure 1.1).

1.3 Geological Setting

Hydrate Ridge is a 25-km-long and 15-km-wide ridge in the Cascadia accretionary complex, Offshore Oregon (Figure 1.2). ODP Site 1244 is located in 895 meters of water, approximately 3 km northeast of the southern summit of Hydrate Ridge (Figure 1.2B). 3-D seismic data image the bottom simulating reflector (BSR) occurs at approximately 125 meters below sea floor (mbsf) [*Tréhu, et al.*, 2003]. The gas hydrate stability zone lies above the BSR, while beneath the BSR, free gas is stable if present in sufficient concentration.

The goal of this experiment was to evaluate the relative behavior of the Piezoprobe and the DVTPP by deploying them at an identical location. Site 1244 was selected for these deployments because it lay within a known hydrate-bearing zone where a BSR was present. In addition, it was the first location cored and the Piezoprobe could only be kept on the ship for a limited amount of time. A depth of approximately 50 mbsf was chosen because this is a depth

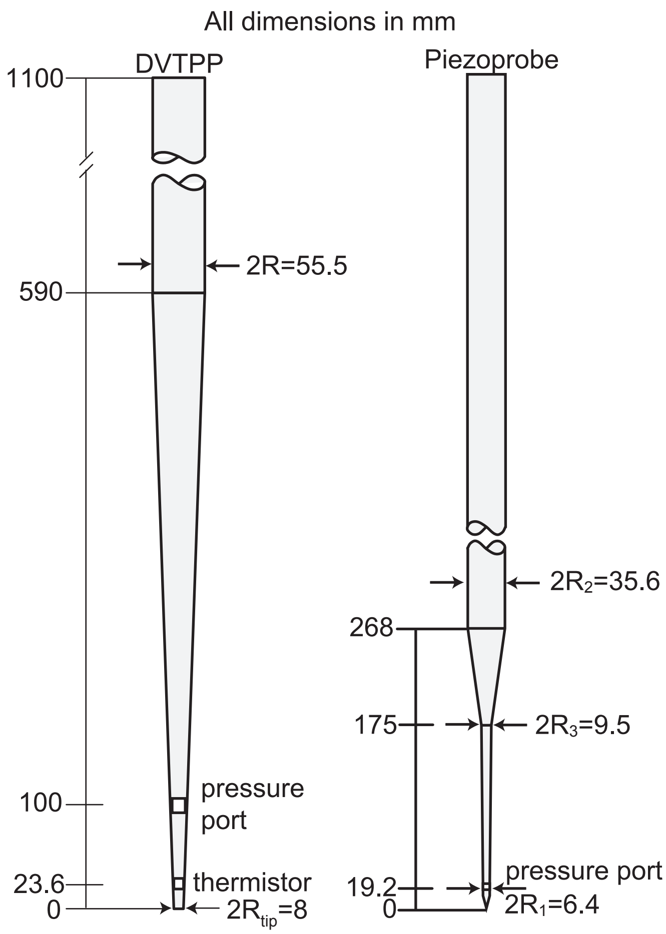

Figure 1.1: The DVTPP and Piezoprobe pore pressure penetrometers have very different geometries. The DVTPP (left) has a long, tapered tip that extends beyond the constant diameter shaft. Its tip tapers continuously from 8 to 55.5 mm in diameter. The pressure port is located 100 mm above the tip. The Piezoprobe (right) has a tapered extension piece 268 mm long which fits onto the end of a standard 35.6 mm diameter cone rod. The tip of the probe is 175 mm long and it has a 9.5 mm diameter at the top and a 6.4 mm diameter near the tip. Pore pressures are measured through a porous filter element located 19.2 mm above the tip, where the probe has a 6.4 mm.

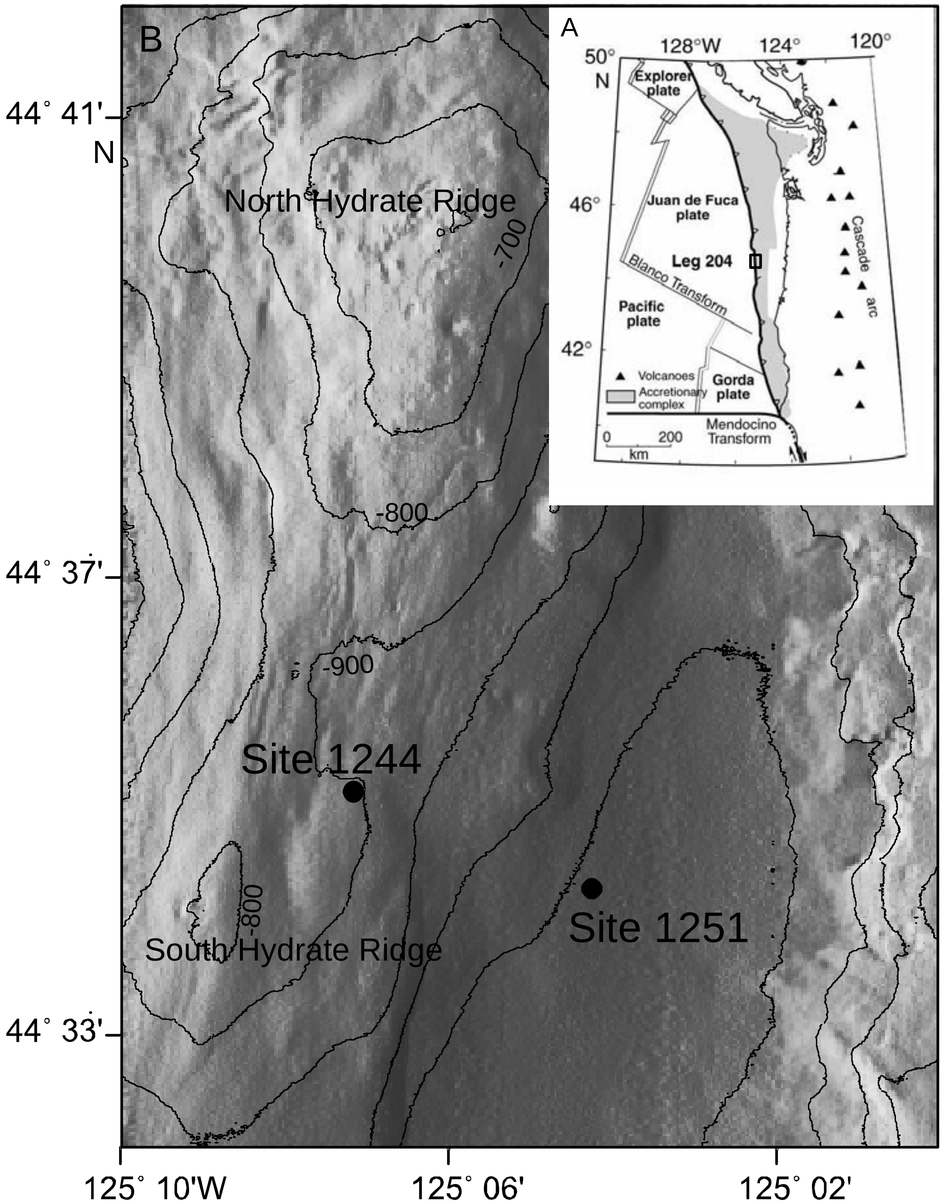

Figure 1.2: Bathymetric map of Hydrate Ridge. Contour interval is 100 m. Site 1244 is located in 895 meters of water, ~3 km northeast of the southern summit of Hydrate Ridge. Inset map shows location of Hydrate Ridge.

where there is little possibility that the drill string will become trapped by hole closure. Later DVTPP deployments on ODP Leg 204 were much deeper. One DVTPP measurement was made at 52.6 mbsf in Hole 1244E. A Piezoprobe measurement was made in Hole 1244C at 53.5 mbsf. This was as close to an equivalent depth as possible because penetrometer measurements can only be made after a piston-core is taken and the exact depth of this point cannot be controlled. Holes 1244C and E are 40 meters apart.

Both measurements were made in dark greenish gray clay that contains 70% clay [*Tréhu, et al.*, 2003; *Gracia, et al.*, 2006]. Porosity is approximately 61% at the level of the DVTPP and the Piezoprobe (Figure 1.3C). Immediately below the level of these deployments there is an abrupt increase in porosity of 4 porosity units. This abrupt change is also reflected on the resistivity and bulk density data (Figure 1.3A, 1.3B). Shipboard bulk density measurements were integrated to calculate the vertical hydrostatic effective stress (σ'_{vh}) at Site 1244 (Figure 1.3D). σ'_{vh} at the Piezoprobe deployment depth is 0.340 MPa whereas it is 0.334 MPa at the DVTPP deployment depth, (Figure 1.3D). The site parameters are summarized in Table 1.1.

1.4 Field Measurement

The deployments of the DVTPP and the Piezoprobe are described in detail in Appendix 1.A and Tables 1.2 and 1.3. Both tools were lowered on a wireline to the bottom of the hole. They were then pushed into the formation with the weight of the drill string. The tools record the pressure pulse induced by their insertion and the subsequent dissipation of this pressure disturbance. Initially, the DVTPP generated a greater pressure pulse than the Piezoprobe (Figure 4). As discussed in Appendix 1.A, this initial DVTPP pressure pulse records the moment that the tip of the DVTPP touched the formation and the pressure pulse is generated only by the weight of the tool. We focus on the dissipation phase of the DVTPP deployment, which starts from the

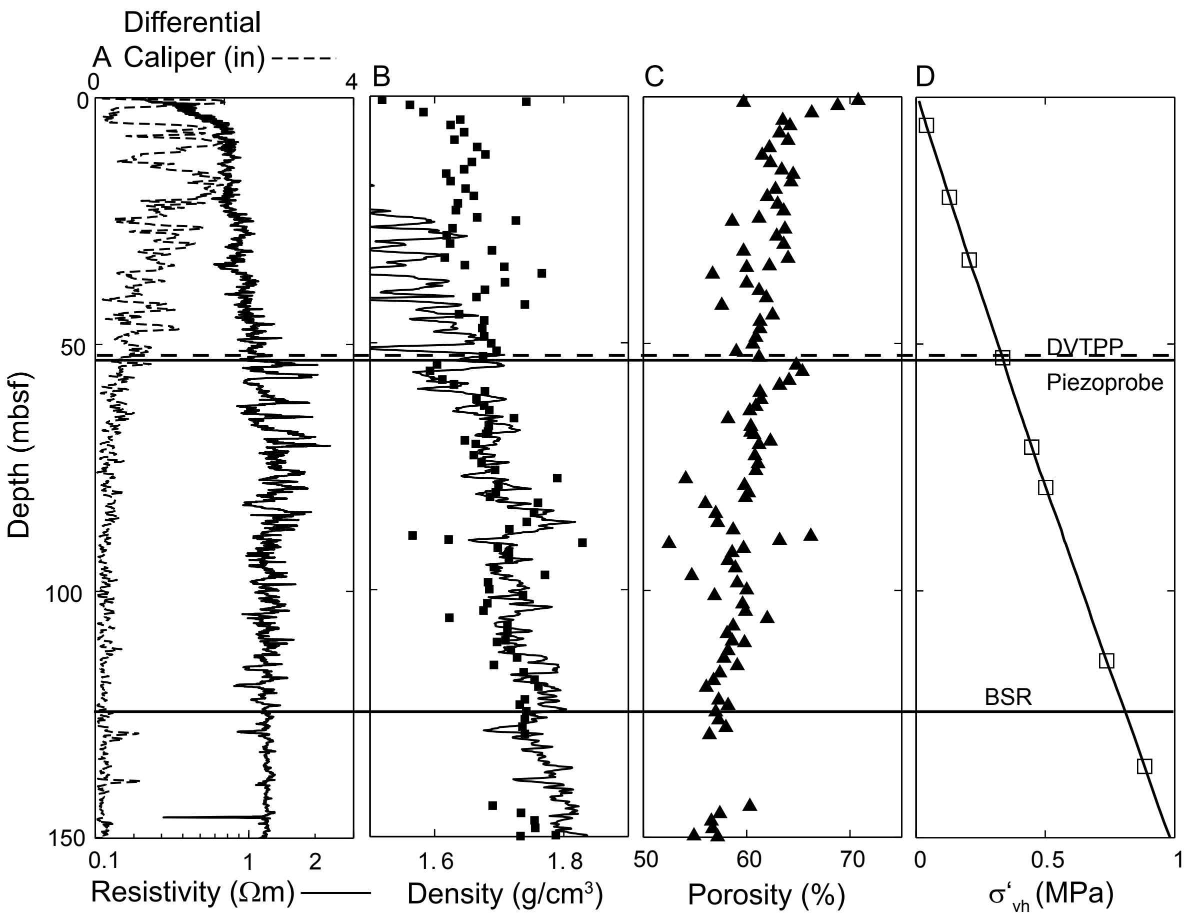

Figure 1.3: Core and log data from ODP Site 1244. The horizontal dashed line and horizontal solid line show where the DVTPP and the Piezoprobe were deployed at approximately 52 meters below sea floor (mbsf). A) Logging While Drilling (LWD) deep resistivity (solid line) and caliper log (dashed line) from Hole 1244D. B) LWD bulk density from Hole 1244D (solid line) and core derived Moisture and Density (MAD) bulk density from Hole 1244C (squares). C) Porosity from Hole 1244C is based on shipboard MAD measurements. D) Hydrostatic effective stress (σ'_{vh}) is determined by integrating MAD bulk density measured in Hole 1244C and assuming a seawater density of 1.024 g/cm3. σ'_{vh} is the total overburden stress less the hydrostatic pressure ($\sigma'_{vh} = \sigma_v - u_h$). The squares show where geotechnical samples were taken. Laboratory analysis of these samples provided parameters for modeling presented in the text (Appendix 1.B). BSR= bottom simulating reflector.

Table 1.1: Site Parameters[a]

	Site, hole	Depth (mbsf)	Water Depth (meters)	Overburden Stress, σ_v (MPa)	Hydrostatic Pressure, u_h (MPa)	Hydrostatic Effective Stress, σ'_{vh} (MPa)
Piezoprobe (7/14/02)	1244C	53.5	895.1	9.869	9.529	0.340
DVTPP (8/19/02)	1244E	52.6	893.3	9.836	9.502	0.334

[a] calculations assume seawater density of 1.024 g/cm^3

Table 1.2: DVTPP Deployment Log

Event #	Time GMT	Time (minutes since deployment)	Event Description
1	20:28:05	48.42	Stop at seafloor, turn pump off
2	28:33:20	53.67	Lower tool with coring winch, turn pump on
3	20:33:58	54.3	Stop lowering
4	20:34:19	54.65	Turn pump off, lower tool slowly on coring winch
5	20:35:59	56.32	Tool latches into CDS; stop winch
6	20:46:26	66.77	Lower drill string
7	20:47:10	67.5	DVTPP tip touches bottom of hole
8	20:49:30	69.83	CDS closed; tool starts to be pushed into formation
9	20:50:33	70.88	Stop lowering drill string; begin raising drill string
10	20:50:54	71.23	Stop raising drill string
11	21:20:52	101.2	Start raising coring line
12	21:22:00	102.33	Pull tool free, hold for 1 minute
13	21:23:42	104.03	Raise tool with coring winch, turn pump on
14	21:24:29	104.82	Stop at seafloor, turn pump off and hold for 5 minutes
15	21:29:38	109.97	Raise tool to ship; turn pump on

Table 1.3: Piezoprobe Deployment Log[a]

Event #	Time GMT	Time (minutes since deployment)	Event Description
1	7:32:34	0.565	Sitting in pipe--tip in water
2	8:09:22	37.365	Setting bit 7 meters from bottom
3	8:16:27	44.449	Lowering
4	8:22:11	50.182	Taking hydrostatic pressure
5	8:26:23	54.365	Pulled up 1.3 meters off of landing ring, now ~8 feet off bottom
6	8:27:13	55.215	Lowering bit down to 3.5 meters off bottom
7	8:36:35	64.582	Stopped pumping
8	8:38:22	66.365	Tagging bottom
9	8:39:31	67.515	Pushing
10	9:26:30	114.498	End of test - pulling
11	9:28:20	116.332	Coming to surface
12	9:45:42	133.699	At top of pipe

[a] After Dugan and Flemings, [2003a]

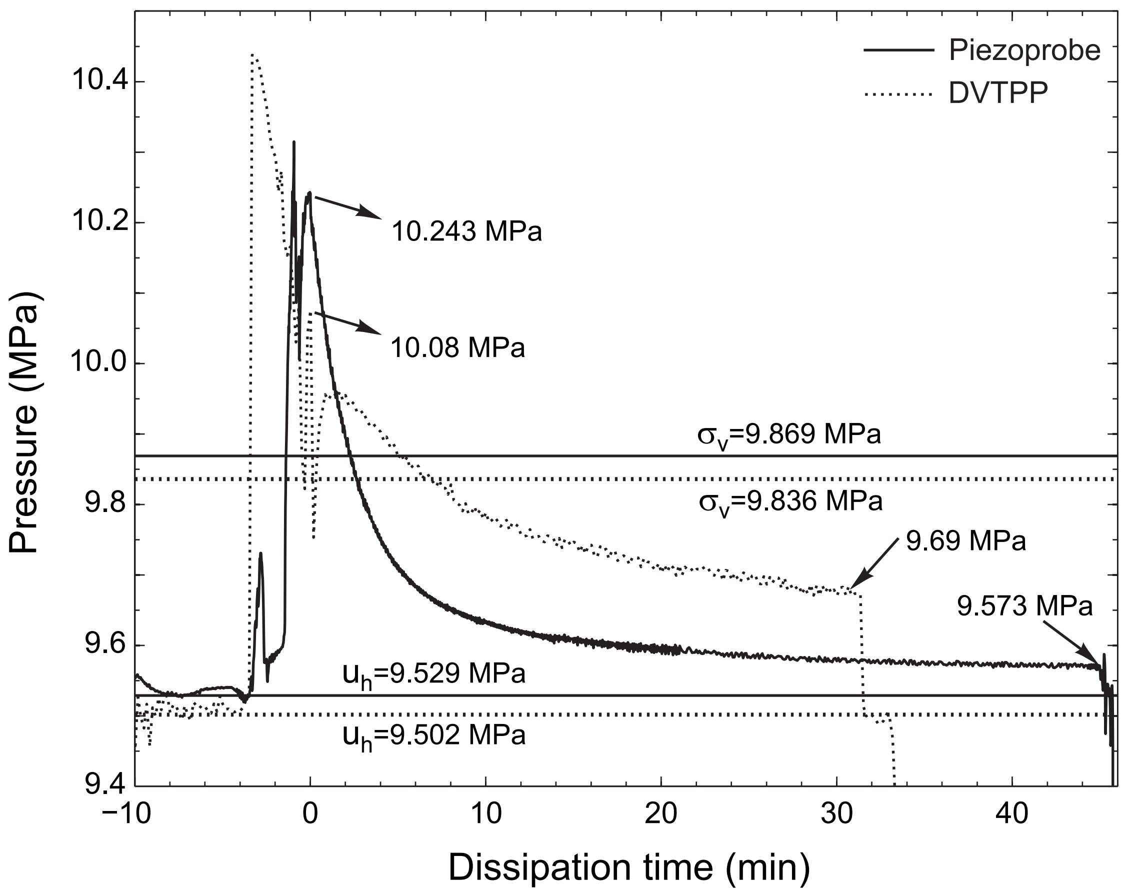

Figure 1.4: Corrected pressure records for DVTPP (dashed line) and Piezoprobe (solid line). The second pressure peak was selected as the initial pressure for both tools and the Dissipation Time is set to zero at this point. Hydrostatic pressure (u_h) and overburden stress (σ_v) are shown at the deployment depth of each tool (dotted = DVTPP, solid = Piezoprobe). They differ slightly for the two deployments because the Piezoprobe was deployed at a slightly deeper depth than the DVTPP. Appendix 1.A describes how these data were corrected.

halt of the insertion (marked as 10.08 MPa) to the record prior to the pullout (Figure 1.4). We focus on the Piezoprobe deployment between the peak pressure of 10.243 MPa to a final pressure of 9.573 MPa, which records the dissipation phase (Figure 1.4).

We initially assume that the in situ pressure is hydrostatic (u_h). The excess pore pressure ratio $\frac{u-u_h}{u_i-u_h}$ measures the fractional dissipation that has occurred with time (Figure 1.5A). By the end of the deployment, the Piezoprobe pressure dissipated significantly more relative to its peak pressure than the DVTPP pressure did (Figure 1.5A). At the end of the test, the DVTPP pressure drops more rapidly with time than the Piezoprobe pressure. The normalized excess pore pressure ratio ($\lambda^*=\frac{u-u_h}{\sigma'_{vh}}$) is the magnitude of the pore pressure relative to the vertical hydrostatic effective stress. The Piezoprobe has an initial excess pore pressure 2.05 times the hydrostatic vertical effective stress whereas the DVTPP has an initial excess pore pressure 1.75 times the hydrostatic vertical effective stress (Figure 1.5B).

1.5 Theoretical Analysis of Pore Pressure Response due to Probe Penetration

1.5.1 Methodology

Theoretical models that describe the response of the soil to penetration include one dimensional idealization of the problem as a spherical or cylindrical cavity expansion in a saturated elastic-perfectly-plastic medium [*Ladanyi*, 1963; *Randolph and Wroth*, 1979a] or models that treat the penetrometer as a moving dislocation in an elastic medium [*Elsworth*, 1991; 1998]. More elaborate and computationally demanding numerical simulations use finite element methods [*Kiousis, et al.*, 1988; *Yu, et al.*, 2000]. Significant advances have been achieved by modeling penetration in saturated low permeability sediments using the Strain Path Method (SPM; [*Baligh*, 1985]). This technique has achieved a good match between the modeled and the

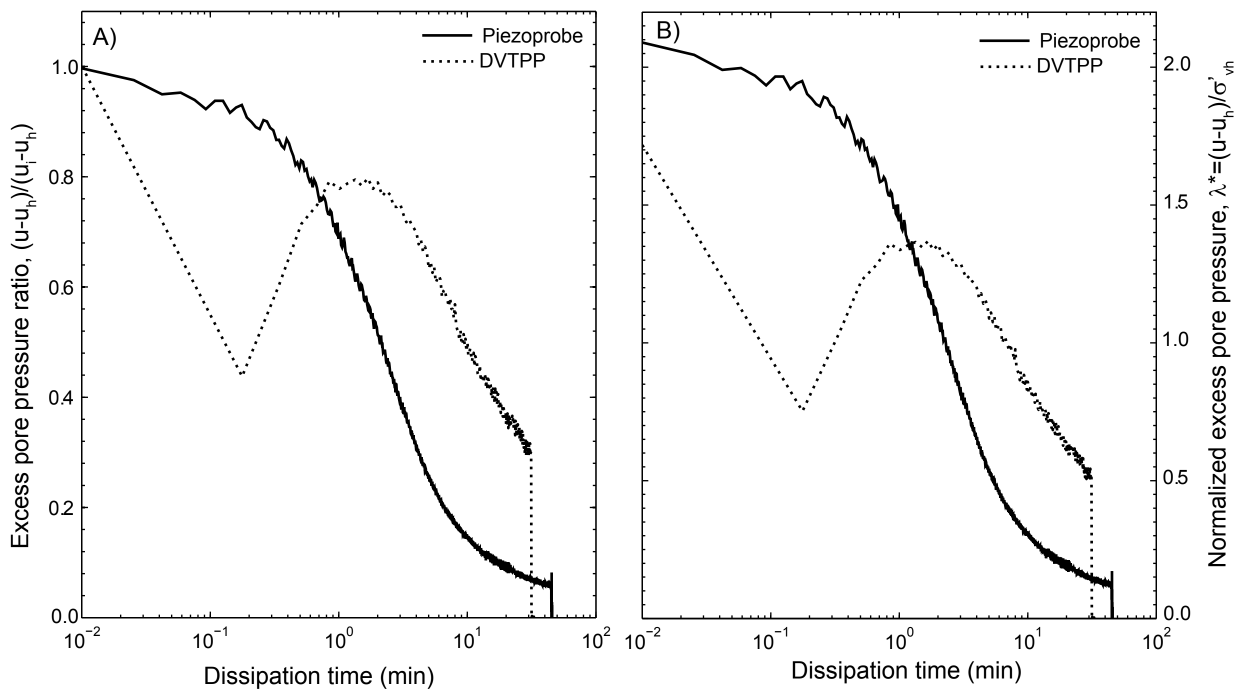

Figure 1.5: Comparison of DVTPP pressure dissipation (dotted line) and Piezoprobe pressure dissipation (solid line). A) Excess pore pressure ratio. Here, u_i is the peak pore pressure upon insertion, and u_h is the hydrostatic pressure at penetration depth. The Piezoprobe has dissipated 94% of its induced pressure while the DVTPP has dissipated only 70% of its induced pressure at the end of deployment. B) Normalized excess pore pressure. The DVTPP has an initial excess pore pressure 1.75 times the hydrostatic vertical effective stress (σ'_{vh}) and dissipates to $0.5\sigma'_{vh}$. The Piezoprobe has an insertion pres¬sure of $2.05\sigma'_{vh}$ and declines to $0.12\sigma'_{vh}$.

observed dissipation curves and between the modeled coefficient of consolidation and the coefficient of consolidation derived from lab tests [*Levadoux and Baligh*, 1980; *Baligh and Levadoux*, 1986c; *Aubeny*, 1992; *Kurup, et al.*, 1994; *Whittle, et al.*, 2001].

We adopt the frame work of the Strain Path Method (SPM) [*Baligh*, 1985; 1986a; 1986b]. In the SPM, it is postulated that soil deformation during undrained penetration in saturated cohesive soil can be reduced to an inviscid and incompressible flow problem where soil particles flow along streamlines around a rigid penetrometer. *Baligh* [1975; 1985] demonstrated that this approach correctly predicted the strain field around a penetrometer. Application of the SPM greatly simplifies the analysis because we do not need to consider constitutive relations for the soil to calculate the strain during penetration. We apply the SPM within a cylindrical coordinate system in the following manner (Figure 1.6).

1. Determine the streamlines for the soil particles as they move around the penetrometer.
2. Calculate the incremental strain along the streamline at each node in the system.
3. Integrate the incremental strains along streamlines to determine the strain path of each soil element.
4. Determine the deviatoric stresses (S_{ij}) and shear induced pore (Δu_s) pressure by combining the strain path with a total stress soil model.
5. Determine the penetration-induced pore pressure (Δu), which is the sum of the pore pressure change (Δu_{oct}) due to the change in octahedral normal total stress ($\Delta\sigma_{oct}=(\Delta\sigma_{rr}+\Delta\sigma_{\theta\theta}+\Delta\sigma_{zz})/3)$, and the shear induced pore pressure (Δu_s).
6. Model the subsequent pressure dissipation as uncoupled-isotropic, linear consolidation.

1.5.2 Streamline for DVTPP and Piezoprobe Penetration

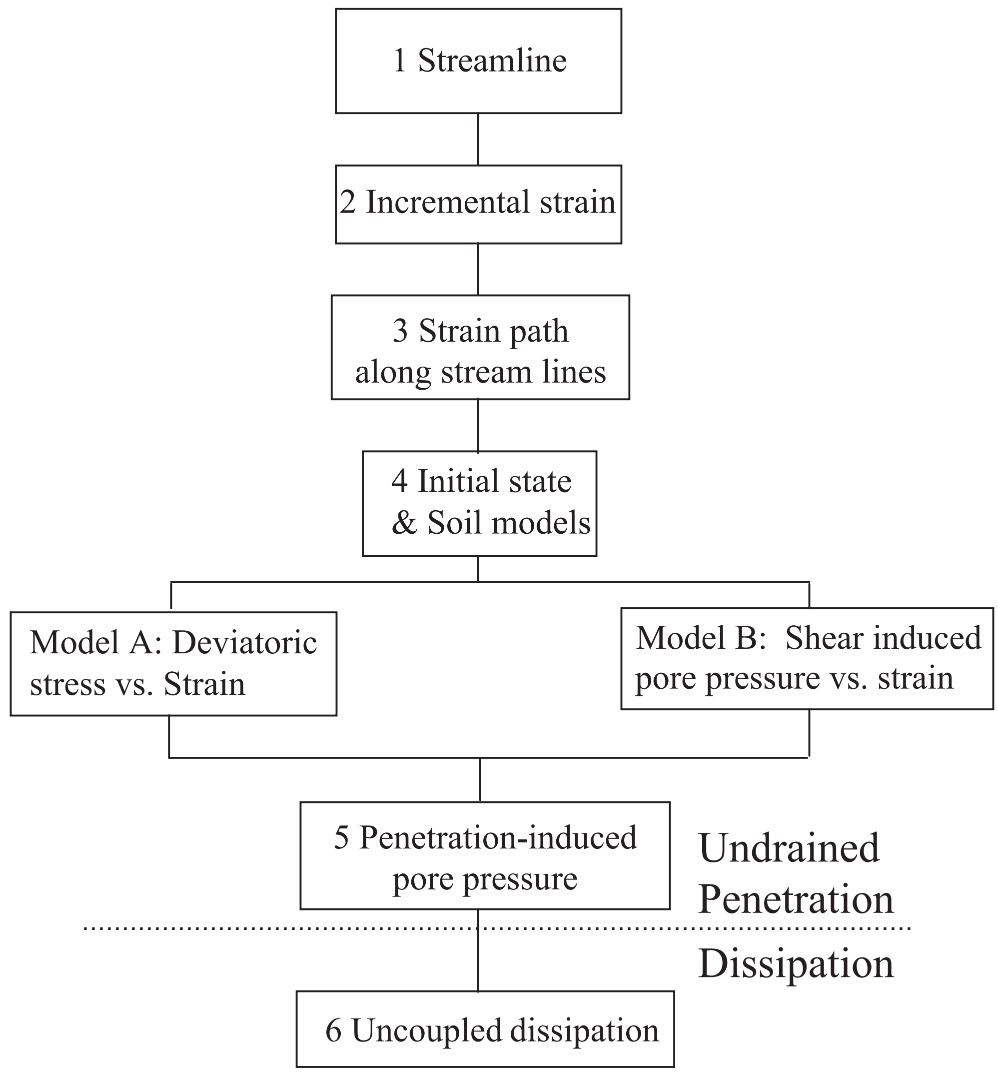

Figure 1.6: Analysis steps used in this application of the Strain Path Method (SPM). This approach is used to predict the penetration-induced pore pressure and its subsequent dissipation.

Using an arrangement of line sources and sinks in conjunction with a uniform flow, we develop approximate solutions for the axially symmetric, incompressible and irrotational flow around the closed surface of the penetrometer [*Kaufmann*, 1963; *Levadoux and Baligh*, 1980]. We choose a discrete number of body points to represent the probe geometry (Figure 1.7). The probe is exposed to a flow that far away from the probe is uniform, with a direction parallel to the axis of symmetry of the probe. The technique is to establish a series of line sources and sinks along the axis of symmetry. The strengths of the line sources and sinks are adjusted so that when combined with the uniform flow, one can form a stream surface with a shape approximating the probe geometry. Any number of sources and sinks could be used depends on the desired degree of accuracy.

For convenience, we choose a series of line sources and sinks with equal length for both the DVTPP and the Piezoprobe (Figure 1.7). The conical tip of the DVTPP was analyzed using 100 line sources and sinks (Figure 1.7A). The tapered extension piece of the Piezoprobe was modeled using 45 line sources and sinks (Figure 1.7B). In both tools, we modeled 1.5 meters of the constant diameter shaft above the taper. The strengths of the line sources and sinks are solved by satisfying a constant value of the stream function at the body points.

1.5.3 Soil Displacements and Octahedral Shear Strains

A soil particle that is initially in front of the probe is first displaced downward and then as it passes the probe tip it moves upward (Figure 1.8A). The process is repeated as the soil particle passes the transition from the taper to the constant diameter shaft. The upward movement after passage of the probe tip is only significant for soil elements that are very close to probe surface (compare location A with location E, Figure 1.8). The ultimate vertical displacement decreases with increasing distance from the probe. Soil particles initially located

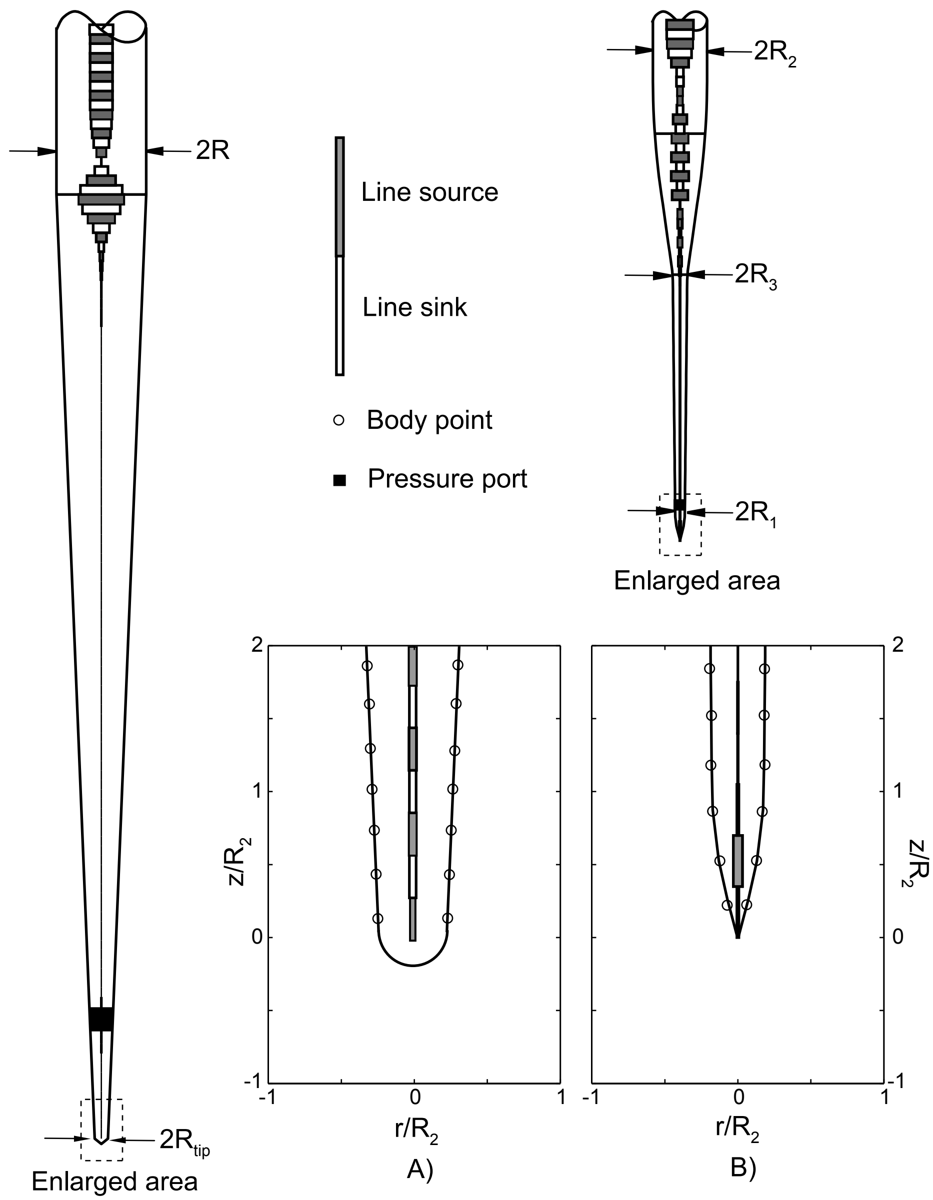

Figure 1.7: Source-sink combinations used to simulate inviscid flow around A) the DVTPP and B) the Piezoprobe. Sources/sinks are located along the centerline of probe. The line weights represent their relative strengths. The small circles on the probe surface represent the body points selected to simulate probe geometry.

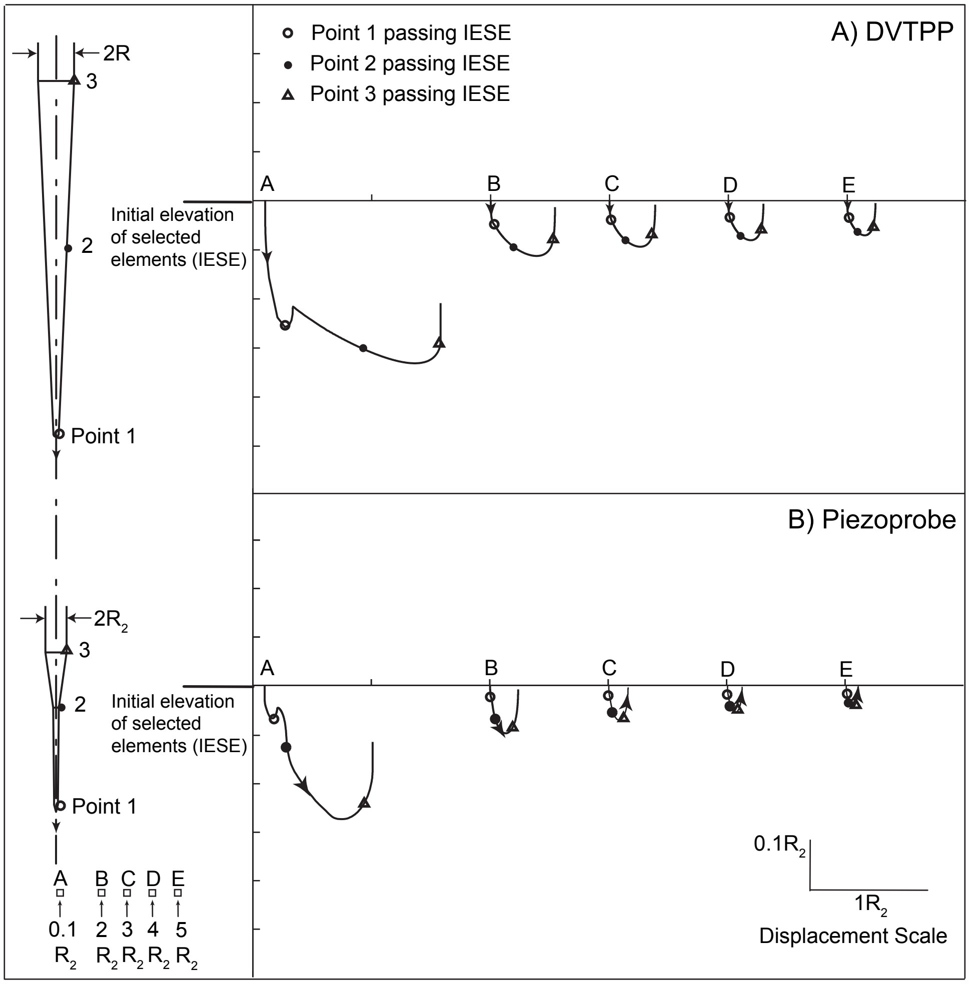

Figure 1.8: Modeled soil deformation paths during penetration. The selected soil elements (A, B, C, D, and E, lower left) are initially located far ahead of the probe tip. The small squares shows the initial radial distance from selected soil elements to the centerline of the probe. As the penetration proceeds, three selected locations on the probe surface (Point 1, Point 2, and Point 3) will sequentially pass by the soil elements. Deformations at the corresponding time are illustrated on the right hand side.

far from the probe centerline tend to return to their initial elevation, which is in agreement with laboratory experiments conducted by *Randolph, et al*. [1979b]. All soil particles are monotonically pushed outward and the ultimate radial displacement decreases with the distance from the probe.

The strain induced by probe penetration is characterized by three deviatoric strain components: $E_1 = \varepsilon_{zz}$, $E_2 = 1/\sqrt{3}(\varepsilon_{rr} - \varepsilon_{\theta\theta})$, and $E_3 = 2/\sqrt{3}\varepsilon_{rz}$. We computed these strain components by integrating the incremental strain as the soil particles move along the stream lines. The octahedral strain, $E = 1/\sqrt{2}(E_1^2 + E_2^2 + E_3^2)^{1/2}$, provides a good indication of the magnitude of shear during penetration [*Prévost*, 1978]. Octahedral strain at equivalent distances from the probe surface is greater for the DVTPP than the Piezoprobe (Figure 1.9). Very large strains (E>10%) are located within a thin annular zone similar in radius to the probe itself.

1.5.4 Penetration-induced pore pressures

The penetration-induced pore pressure, Δu_i, is the sum of two components: Δu_{oct} is the change in pore pressure resulting from changes in octahedral normal total stress ($\Delta\sigma_{oct}$), and Δu_s, is the shear induced pore pressure. We determine the deviatoric stresses and the shear induced pore pressure from the strain path using a total stress soil model, MIT-T1, developed by *Levadoux and Baligh* [1980] for this purpose. $\Delta\sigma_{oct}$ is obtained by integrating the equilibrium equations along the radial direction. MIT-T1 describes the complicated strain paths of various soil elements (including large strain and reversal of strains), initial and stress-induced anisotropy, as well as strain-softening of saturated clays under undrained loading conditions. Initial excess pore pressure predictions presented here are based on parameters derived from laboratory tests on re-sedimented normally consolidated Hydrate Ridge soils (Appendix 1.B).

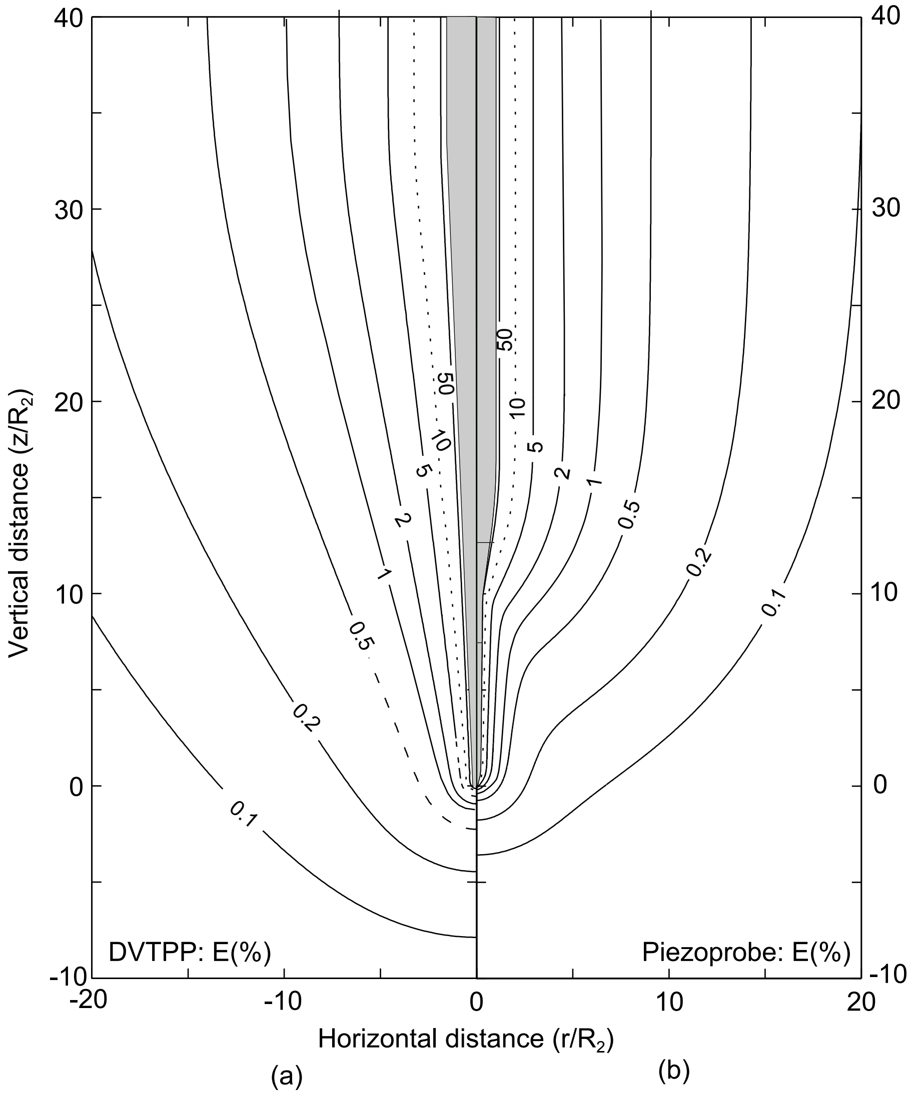

Figure 1.9: Octahedral shear strain (E) around the DVTPP (left) and the Piezoprobe (right). The zone of high shear strains, E>10%, is confined to a thin annular zone similar in radius to the probe itself. There is much greater shear strain around the DVTPP tip than the Piezoprobe tip at equivalent radial distances. The shapes of the small strain contours (E<0.1%) show no significant similarity to probe geometry. The coordinates *(r, z)* are normalized by the radius of the shaft of the Piezoprobe (R_2) .

The normalized initial excess pore pressures ($\Delta u_i/\sigma'_{v0}$) generated by the DVTPP and the Piezoprobe are distinct (Figure 1.10). The shapes of the pressure contours are clearly confined by the geometry of the probe near the probe surface, and their sizes are proportional to the probe diameter. Excess pore pressure is generated further in front of the DVTPP than the Piezoprobe (Figure 1.10, 1.11).

The excess pore pressure variation along probe surface closely follows the probe geometry (Figure 1.11). The highest pressures (approximately 2.7 σ'_{v0}) are encountered at the tip for both the DVTPP and the Piezoprobe. High pressures are also generated along the tapered part of the probes. Behind the probe tip and the taper-shaft transition, the excess pore pressure drops rapidly. This pressure drop is due to the sharp decreases in the total stresses after the cone face.

1.5.5 Dissipation

The dissipation of the excess pore pressures induced by penetrometer penetration is modeled as uncoupled, isotropic, linear consolidation. We used a total stress soil model as opposed to an effective stress soil model, to simulate the pore pressure induced by penetration. As a result, it is not possible to model this dissipation as a coupled process as *Whittle et al*. [2001] did. Our analyses were conducted using the ABAQUS™ finite element code with a fine mesh (4000 nodes) to provide a sufficient resolution commensurate with the high-pressure gradients within the vicinity of the probe. We assume no flow normal to the probe surface, no vertical flow on the top, and the excess pore pressure at the far field boundary is fixed at zero. The initial pore pressure field is the pore pressure field induced by either the DVTPP or the Piezoprobe (Figure 1.10).

The solution is expressed in dimensionless coordinates where the dimensionless time factor T is given by

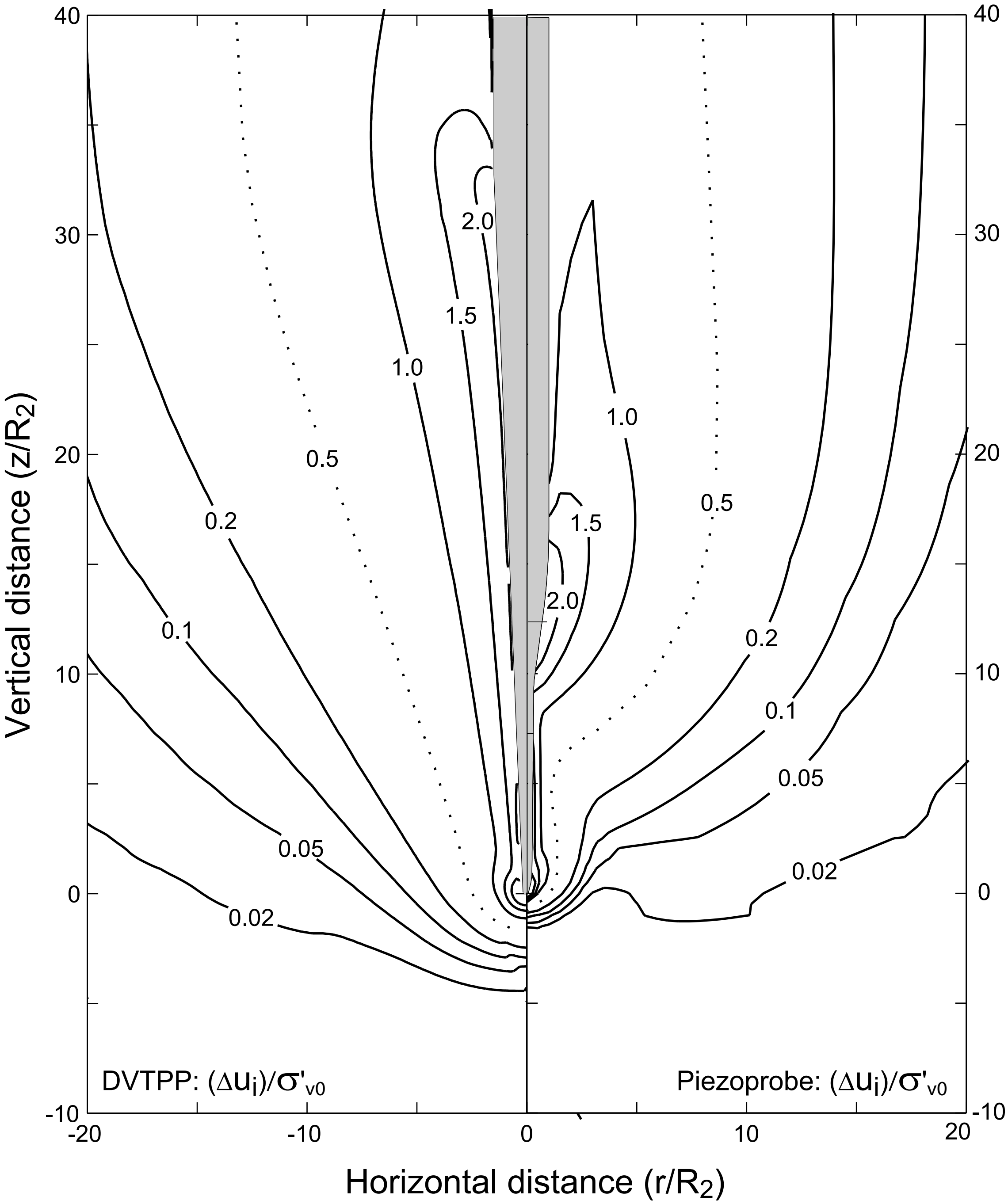

Figure 1.10: Penetration-induced pore pressures for the DVTPP (left) and the Piezoprobe (right). The DVTPP generates much larger pressures at equivalent radial distances from the tip. The initial excess pore pressure due to penetration, Δu_i, is normalized by the vertical effective stress (σ'_{v0}) prior to penetration.

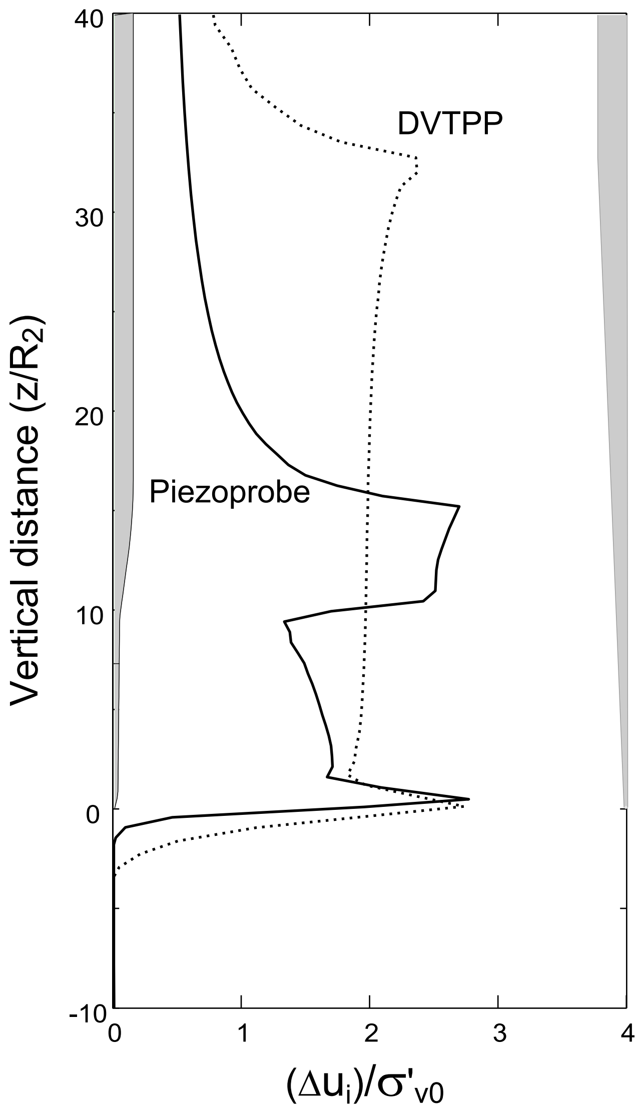

Figure 1.11: Initial excess pore pressure along the surface of the DVTPP and Piezoprobe. The Piezoprobe has peaks in pore pressure at the tip and at the tip-shaft transition. In contrast the DVTPP has a broad zone of elevated pressure associated with its tapered geometry (right). Here, Δu_i is normalized by the vertical effective stress (σ'_{v0}) prior to penetration.

$$T = \frac{ct}{R_2^{\ 2}} \tag{1.1}$$

where t is the time after penetration, and R_2 is the shaft radius of the Pizeoprobe. We display the excess pore pressure, $\Delta u_i/\sigma'_{v0}$, and excess pore pressure ratio, $\Delta u/\Delta u_i$, with the dimensionless time in log scale (Figure 1.12).

For both tools, the induced pressure at the pressure ports is approximately twice the vertical effective stress (Figure 1.12A). Initially, the pore pressure dissipation follows a similar path. However, the Piezoprobe pressure (#1) declines more rapidly than the DVTPP pressure (#3) (Figure 1.12). The time to achieve 90% dissipation, T_{90}, for the DVTPP is approximately 14 times that for the Piezoprobe (Figure 1.12B). As consolidation proceeds, the dissipation of the Piezoprobe pressure is retarded: no significant pressure dissipation over a long period of time, which results in a flat spot or 'bench' between T = 10 and T = 100 (Figure 1.12B). The excess pore pressure has dissipated approximately 94% percent at the bench. This feature can be used to estimate in situ pore pressure from partial pressure dissipation, if the pressure dissipation has reached the bench at the end of the monitoring.

The nature of the dissipation curve for the Piezoprobe can be understood by breaking the geometry of the Piezoprobe into two parts (Figure 1.12, inset): 1) a constant diameter thin probe (R=3.2 mm); and 2) the upper tapered shoulder that includes the 18 degree taper and the constant diameter shaft (R=17.8 mm). We used the SPM to simulate the pressure response to these individual components and examined the resulting dissipation. The constant diameter thin probe (#4) generates the same pressure dissipation as the Piezoprobe (#1) for time factors, T<5 (Figure 1.12, #4-dashed line). Thereafter, the Piezoprobe pressure dissipation stalls (Line #1), whereas the constant diameter thin probe pressure continues to decline (Line #4) (Figure 1.12). The upper tapered shoulder of the Piezoprobe (Line #2) generates a small increase in pore

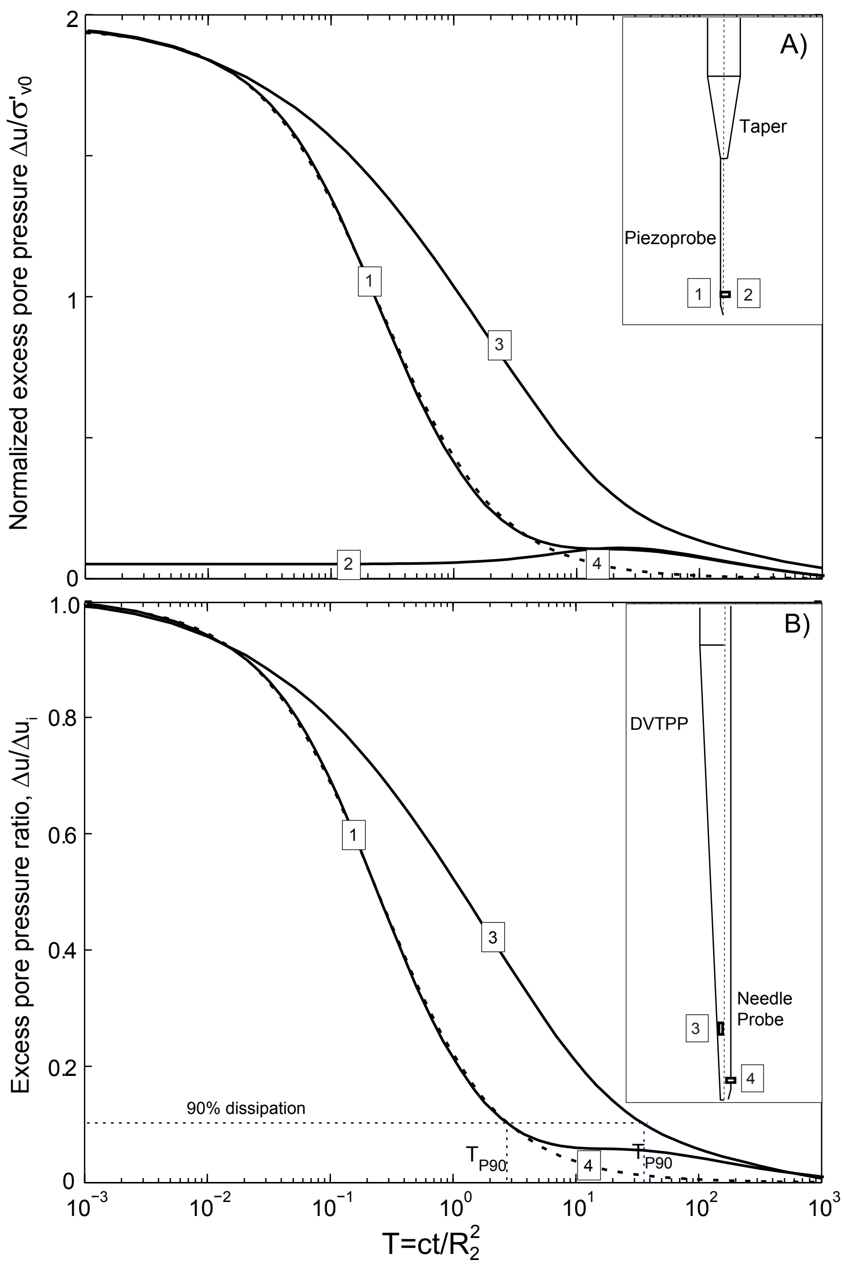

Figure 1.12: Modeled pressure dissipation for the Piezoprobe (#1, solid line) and the DVTPP (#3, solid line) penetrometers. A) Normalized excess pore pressure vs. dimensionless time. B) Excess pore pressure ratio vs. dimensionless time. The geometry of the Piezoprobe is shown in the top inset and the geometry of the DVTPP is shown in the bottom inset. Also shown is the dissipation response to a constant diameter thin probe (R=3.2 mm) (Line #4, dotted line) measured at location 1 (Fig. 1.12A, inset) and the dissipation response to just the upper tapered shoulder and the overlying shaft at location 2 (Fig. 1.12A, inset) (Line #2, solid line). Dissipation time is normalized by the coefficient of consolidation and the radius of the shaft of the Piezoprobe.

pressure ($\Delta u_{i}/\sigma'_{v0}$=0.07). There is a very slight increase in pressure with time at T>1, which reaches a maximum at T=22.5 before further dissipation occurs (Figure 1.12). The excess pore pressure dissipation predicted for the Piezoprobe (Line #1) are identical to that for the tapered shoulder (Line #2) for time factors, T>15. This result indicates that the long-term dissipation of the Piezoprobe converges to the dissipation behavior of its upper tapered shoulder. Similar behavior was described by *Whittle et al*. [2001]. We emphasize that the pressure response of the Piezoprobe is not simply the sum of those induced by its needle shaft and its upper tapered shoulder due to the elastic-plastic nature of the soil.

1.6 Interpretation

1.6.1 In Situ Pore Pressure

In ocean drilling, the time available for downhole tool measurements is precious, expensive, and limited. In this environment, we will almost always be faced with interpreting in situ properties from partial dissipation records. We use the dissipation curves derived in this study to estimate the in situ pressure. The Piezoprobe pressure is nearly constant over the last 5 minutes of the test (Figure 1.4) and we interpret that the pressure at this time lies on the 'bench' and thus has dissipated to 94% of the induced pressure (e.g. Figure 1.12). The in situ pressure is,

$$u_0 = u_i - (u_i - u_l)/0.94\,, \tag{1.2}$$

where u_i is the peak pressure, u_l is the last recorded pressure. The estimated in situ pressure (u_0) is 9.527 MPa, which is extremely close to the inferred hydrostatic pressure (9.529 MPa) (Fig. 1.12). It is not possible to interpret u_0 for the DVTPP because there is no characteristic step present in the dissipation curve that would record the stage of dissipation.

For the DVTPP and the Piezoprobe, we also applied a more formal technique where we varied in situ pore pressure and the coefficient of consolidation and then compared the resultant curve with the modeled dissipation curves. The error analysis suggested a best fit (u_0=9.28 MPa; c=6x10^{-7} m^2/s) for the DVTPP whereas we found a best fit u_0=9.522 MPa, slightly less than hydrostatic pressure, and c=6.6x10^{-7} m^2/s for the Piezoprobe. The difference between the predicted u_0 for the Piezoprobe using this statistical approach and that using the 'bench' is only 1 percent of the hydrostatic effective stress. The u_0 for the DVTPP measurement is significantly less than the hydrostatic pressure (9.502 MPa), and is unreasonable. We infer that not enough of the dissipation history of the DVTPP is recorded to make a reasonable estimate of in situ pore pressure.

We compare the above approach with a 1/t extrapolation, as suggested by *Davis et al*. [1991] and *Fang et al*. [1993]. This technique extrapolates the data on a reverse time scale to estimate the in situ pore pressure from partial dissipation records (Figure 1.13). Application of this technique for the Piezoprobe results in a u_0 value of 9.553 MPa or an overpressure ratio of 0.07 ($\lambda^* = \dfrac{u_0 - u_h}{\sigma_v - u_h}$) (Figure 1.13). This value is larger than that estimated from the bench feature espoused above, most likely because we are extrapolating the late time data on the retarded dissipation feature (bench). For the DVTPP, this approach yields a u_0 value of 9.622 MPa or λ^*=0.36, far greater than the u_0 value measured by the Piezoprobe (Figure 1.13). We conclude that, within the restricted monitoring time, the 1/t extrapolation over estimates the in situ pressure for low permeability sediments.

1.6.2 Coefficient of Consolidation

The rate of pressure dissipation is conditioned by the coefficient of consolidation (c), which can be estimated by matching the observed pressure dissipation with the modeled result (Figure 1.14). We found the best fit with a coefficient of consolidation of 7.8x10^{-7} m^2/s for the DVTPP and 6.92x10^{-7} m^2/s for the Piezoprobe. These values are slightly greater than values

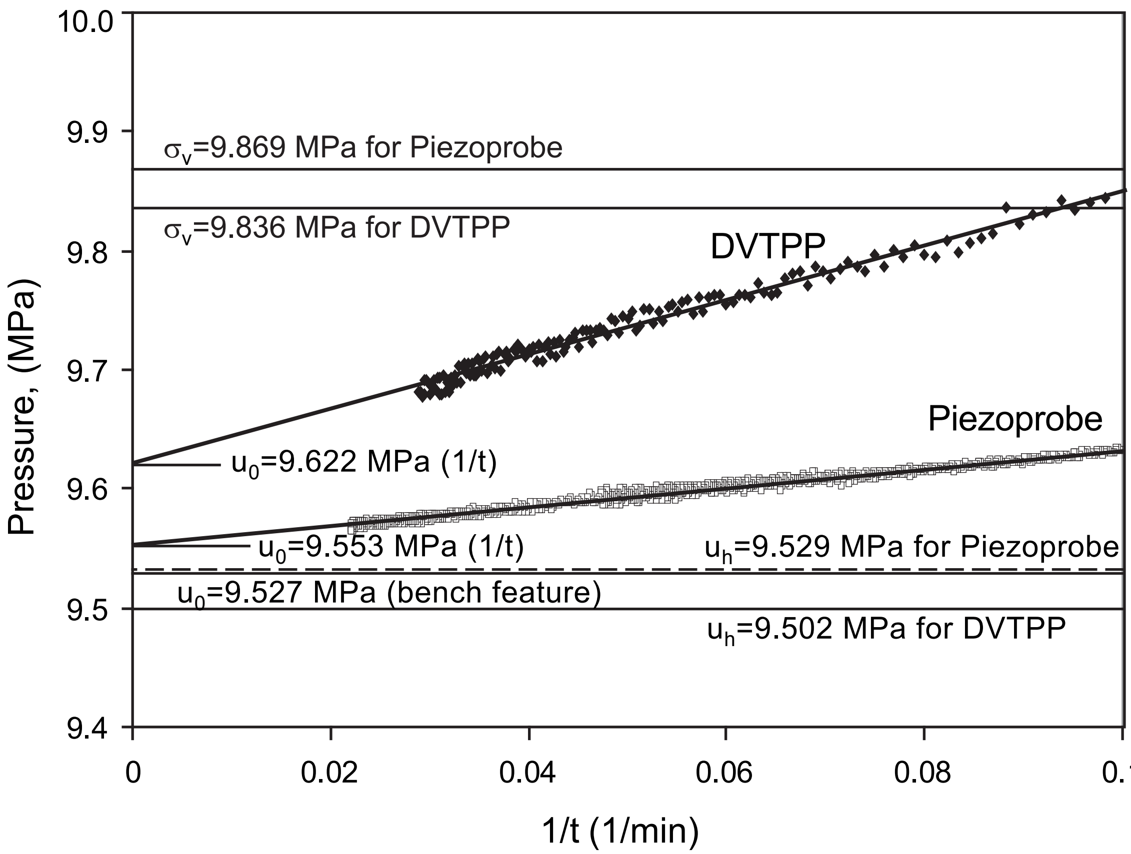

Figure 1.13: The predicted in situ pore pressure from the DVTPP and the Piezoprobe data from an inverse time (1/t) approach and from using the "bench" predicted from the modeled dissipation of the Piezoprobe ("bench feature"). The "bench" feature yields an estimate of 9.527 MPa based on the Piezoprobe data. The in situ pore pressures estimated using 1/t technique are shown for comparison. The in situ pressure extrapolated from the DVTPP data is much higher than that extrapolated from the Piezoprobe data. Hydrostatic pressure (u_h) and overburden stress (σ_v) at the depth of the DVTPP and Piezoprobe deployments are shown for reference.

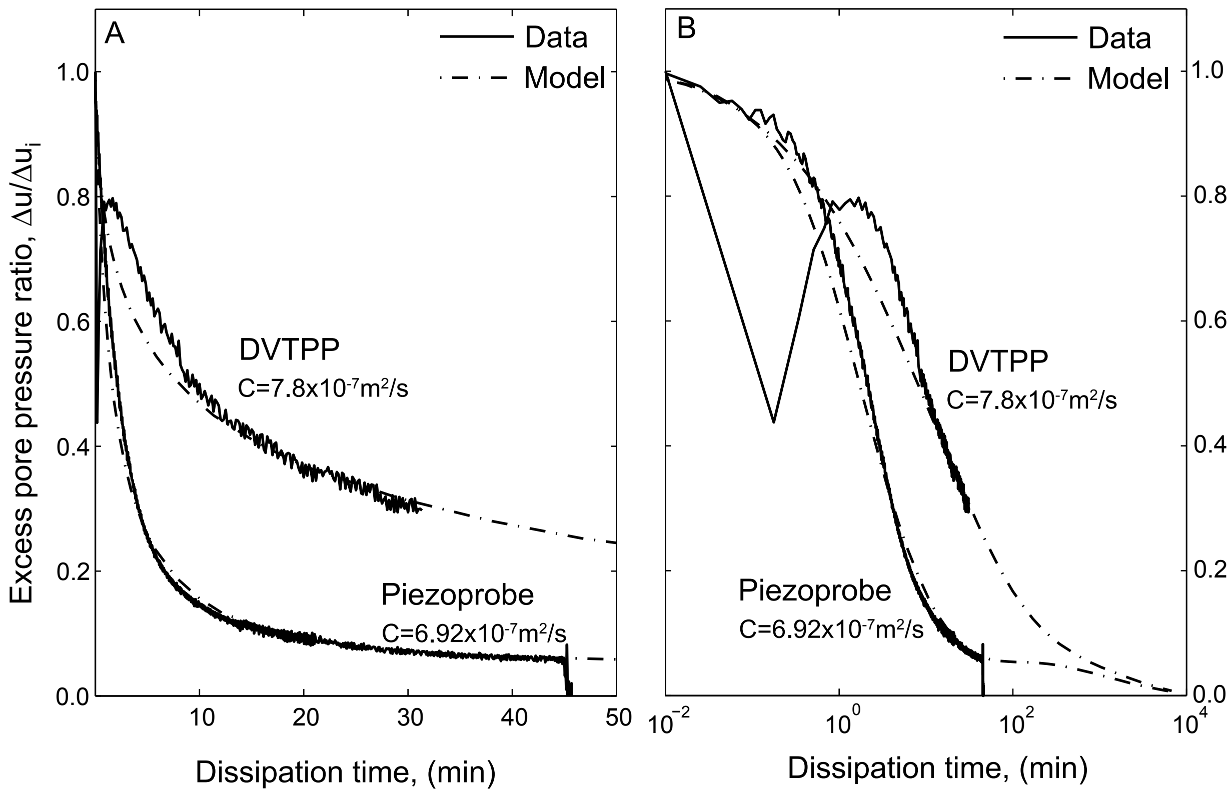

Figure 1.14: Predicted and measured excess pore pressure ratio vs. time for A) linear time and B) log time. For the Piezoprobe, we assume the in situ pressure is equal to the pore pressure estimated using the “bench” behavior. For DVTPP, the in situ pressure is calculated by assuming the same overpressure ratio as inferred at the Piezoprobe location. Based on the best fit between the model prediction and the observed data we find a coefficient of consolidation of 6.92×10^{-7} m^2/s for the Piezoprobe data and 7.8×10^{-7} m^2/s for the DVTPP data.

measured on whole round samples taken from Site 1244 which ranged from 1.5×10^{-7} to 5.8×10^{-7} m^2/s [*Tan*, 2004]. Previous work has also suggested that penetrometer experiments record slightly larger consolidation coefficients than those measured in the laboratory [*Baligh and Levadoux*, 1986c; *Tavenas, et al.*, 1986; *Sills, et al.*, 1988; *Schaid, et al.*, 1997]. This could be due to permeability anisotropy: pressure dissipation around the Piezoprobe is largely controlled by horizontal permeability whereas only vertical permeability is measured in the laboratory. Scale effect may also contribute, where larger permeabilities are found when larger volumes are examined.

1.6.3 Error Analysis: The Impact of Different Soil Types

We infer that the late stage Piezoprobe data, where the pressures do not decline as rapidly as previously, lie on the 'bench' predicted from our Strain Path Model (SPM) results: at this point, 94% of the induced pressure has dissipated (e.g. Figure 1.12). SPM soil parameters were derived from geotechnical experiments on cores from Site 1244, which was the same location that we deployed the Piezoprobe and the DVTPP (Appendix 1.B). We explore how different soil types impact our model results by comparing simulations from the Hydrate Ridge soil with those for the Drammen Clay [*Prévost*, 1978] and the Boston Blue Clay [*Sutabutr*, 1999] (Figure 1.15). These simulations are used to predict in situ pressure (u_o) and the consolidation coefficient (c_v) at Hydrate Ridge (Table 1.4). The Hydrate Ridge Clay and the Drammen Clay produce very similar predicted pressures and consolidation coefficients. This is not surprising because the 'bench' is at a similar position (Figure 1.15). In contrast, the Boston Blue Clay predicts a lower in situ pressure (Table 1.4). This is because the 'bench' in the BBC data is higher than either the Drammen Clay or the Hydrate Ridge Clay (Figure 1.15). All three models will predict in situ pressure with a range of error of about 5% of the hydrostatic effective stress, and the coefficient

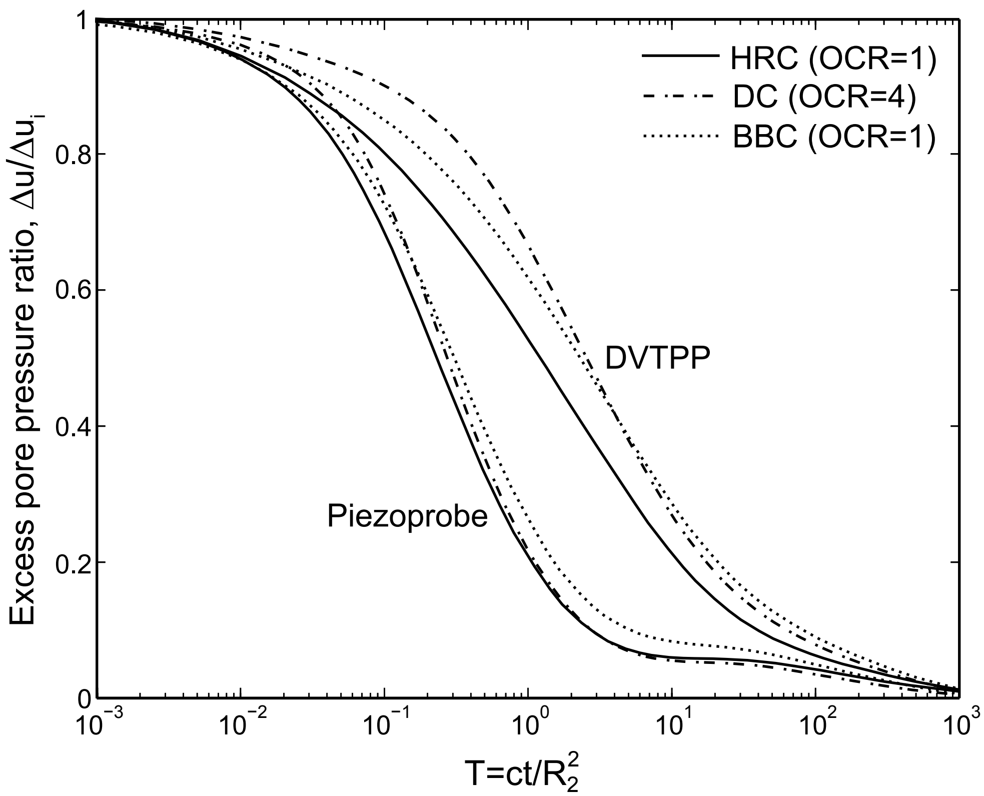

Figure 1.15: Pressure dissipation of the DVTPP and the Piezoprobe for penetration in different soils. HRC = uniaxially normally consolidated resedimented Hydrate Ridge Clay (also illustrated in Figure 1.12 and 1.14). DC=uniaxially over-consolidated (K_o) Drammen Clay [Prévost, 1978]. BBC = uniaxially normally consolidated (K_o) Boston Blue Clay [Levadoux and Baligh, 1980]. (OCR= Over Consolidation Ratio).

Table 1.4: Potential errors due to soil properties[a]

	Piezoprobe u_0 (MPa)	DVTPP u_0 (MPa)	Piezoprobe c_v (m^2/s)	DVTPP c_v (m^2/s)	Overpressure ratio λ^*
HRC (OCR=1)	9.527	9.5	6.92×10^{-7}	7.8×10^{-7}	-0.006
DC (OCR=4)	9.527	9.5	7.6×10^{-7}	1.4×10^{-6}	-0.006
BBC (OCR=1)	9.512	9.485	9.8×10^{-7}	1.2×10^{-6}	-0.05

[a] For piezoprobe, in situ pore pressure is estimated using the bench behavior. For DVTPP, in situ pore pressure is calculated by assuming same overpressure ratio as the Piezoprobe location.

of consolidation within a factor of two. Future work will examine what soil properties control the magnitude of residual pressure on the ‘bench’.

1.7 Discussion

The physical processes that underlie the interpretation of pressure penetrometer data are similar, yet distinct, from those that underlie the interpretation of temperature penetrometer data. In both cases, in situ state (pressure or temperature) and the diffusion coefficient are interpreted from partial dissipation through the diffusion equation. Furthermore, at least for the 50 meter depth in this study, the thermal diffusivity and the hydraulic diffusivity are similar. However, in the case of temperature, it is generally assumed that only the penetrometer, and not the sediment bounding the penetrometer, is heated by friction [*Bullard*, 1954; *Von Herzen*, 1959; *Hyndman*, 1979; *Lister*, 1979; *Villinger and Davis*, 1987]. As a result, very high thermal gradients are imposed around the penetrometer and rapid temperature decay results. In contrast, the installation of the penetrometer results in the deformation of the soil a large distance from the penetrometer, which induces a pressure increase a large distance from the penetrometer (Figure 1.10). As a result, the pressure gradients around the penetrometer are relatively small and the rate of pressure decay is slow. This fundamental difference is why temperatures decay much more rapidly than pressures (e.g. Figure 1.A1C).

Our results suggest that the pore pressure is hydrostatic at 50 mbsf at Site 1244 approximately 3 km northeast of the southern Hydrate Ridge summit. This result is congruent with uniaxial consolidation estimates of pre-consolidation stresses on Northern Hydrate Ridge that suggested that within the first 70 meters, in material similar to the mudstone studied here, the pore pressure lies between λ^*=0-0.44 [*Brown*, 1995b]. The range results from a minimum and maximum estimate of the pre-consolidation stress. Uniaxial consolidation experiments on southern Hydrate Ridge [*Weinberger*, 2005] were performed at ODP Site 1251, 5.5 km east of the southern Hydrate Ridge summit. Void ratio vs. effective stress relationships from the consolidation studies suggest under-consolidation of sediments within the upper 140 meters, and an overpressure ratio λ^* =0.9 [*Weinberger*, 2005]. Although relatively near each other, ODP Site 1251 and ODP Site 1244 are in very different geologic settings (Figure 1.12). Sediments at Site 1251 are younger than those penetrated at Site 1244 and they were rapidly deposited in an evolving basin that flanked southern Hydrate Ridge. The sedimentation rate is 160 cm/k.y. in the upper 140 mbsf at Site 1251, in contrast, is only 27 cm/k.y. in the upper 80 mbsf at Site 1244 [*Tréhu, et al.*, 2003]. We interpret that the overpressures present at Site 1251 are driven by the much higher sedimentation rate.

Based on our analysis, the Piezoprobe will achieve 90% dissipation 14 times sooner than the DVTPP (Figure 1.16). Coefficients of consolidation for sediments penetrated in the Ocean Drilling Program range from 4×10^{-8} to 2×10^{-6} m^2/s (Table 1.5) [*Dugan and Flemings*, 2003b; *Tan*, 2004; *Saffer and Mckiernan*, 2005]. For this range of properties it will take from 6 minutes to 5 hours to achieve 90% dissipation with the Piezoprobe. In contrast, 1.5 hours to 3 days are required for the DVTPP (Figure 1.16). In general, Ocean Drilling deployments will be on the order of hours. Thus the Piezoprobe geometry provides an exciting option for the measurement of pore pressure in low permeability sediments. The rapid dissipation of the Piezoprobe relative to the DVTPP results from its narrow tip, which generates a narrower pressure increase around the probe. The resulting very high pressure gradients dissipate much faster than the DVTPP. Furthermore, because of the Piezoprobe's distinct two-radius geometry, it is possible to apply a consistent method to extrapolate in situ pressure based on the 'bench' feature on the dissipation profile. In contrast, the cone-shaped DVTPP has no characteristic pressure decline curve that

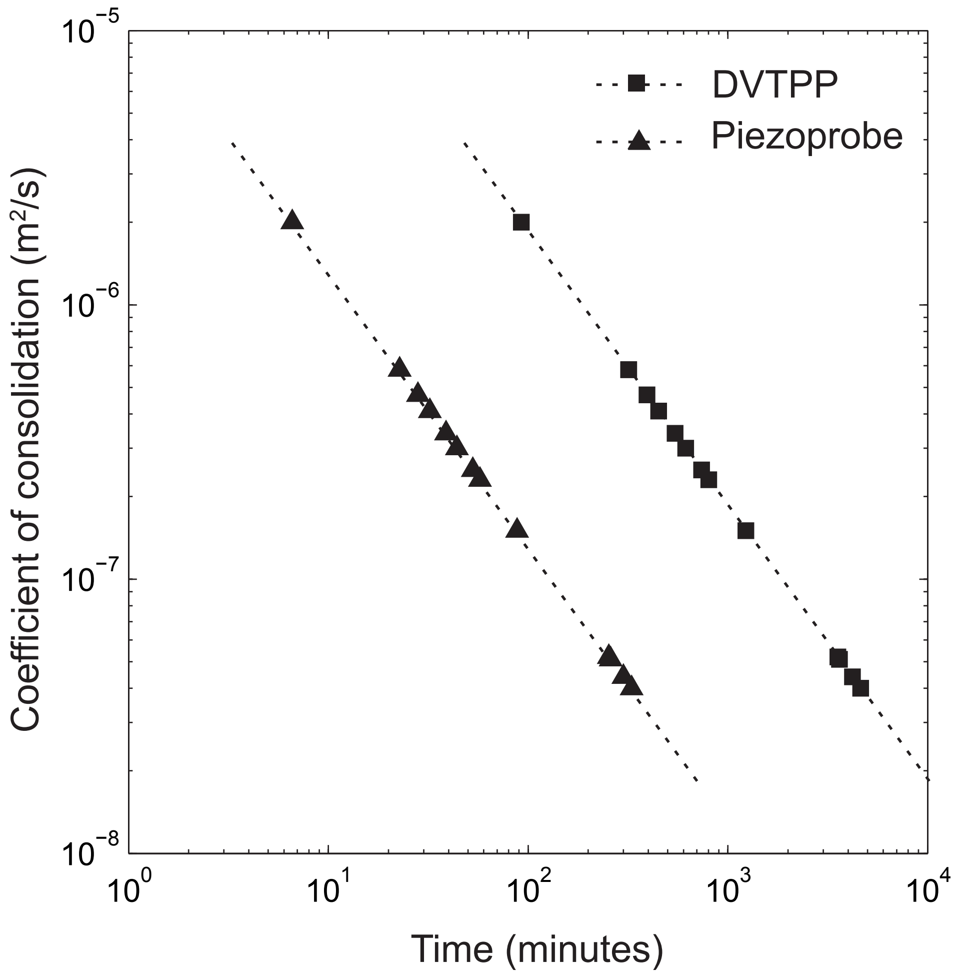

Figure 1.16: Time to dissipate 90% of the induced pressure as a function of coefficient of consolidation for the DVTPP (squares) and the Piezoprobe (triangles). The Piezoprobe reaches 90% dissipation 14 times sooner than the DVTPP. Coefficients of consolidation for sediments penetrated in the Ocean Drilling Program range from 4×10^{-8} to 2×10^{-6} m^2/s (Table 5). The initial excess pore pressure distribution is assumed to be that modeled for Hydrate Ridge soil in this study.

Table 1.5: Porosity, coefficient of consolidation and permeability for sediments encountered in Ocean Drilling[a]

Sample	Depth (mbsf)	Porosity (%)	c_v (m^2/s)	k (m^2)	Location	Source
1073-8H	63.75	52	4.1×10^{-7}	1.9×10^{-17}	New Jersey margin, ODP Leg 174	*Dugan et al*. [2003b]
1073-71X	644.7	48.5	2.0×10^{-6}	5.1×10^{-17}		
1244B-1H	6.94	61	5.8×10^{-7}	1.5×10^{-16}	Hydrate Ridge, ODP Leg 204	*Tan*, [2004]
1244B-3H	21.65	60.5	2.5×10^{-7}	9.8×10^{-17}		
1244B-4H	34.27	62.8	3.4×10^{-7}	9.3×10^{-17}		
1244B-6H	52.89	62.5	2.3×10^{-7}	1.4×10^{-16}		
1244C-8H	71.48	60.8	3.0×10^{-7}	7.5×10^{-17}		
1244C-9H	80.11	60.2	4.7×10^{-7}	1.3×10^{-16}		
1244C-13H	115.56	58.8	5.8×10^{-7}	1.0×10^{-16}		
1244C-17H	136.51	56.6	1.5×10^{-7}	5.0×10^{-17}		
1254-16R	366.7	59	4.4×10^{-8}	1.0×10^{-17}	Costa Rica, ODP Leg 205	*Saffer and McKiernan*, [2005]
1255-2R	134.9	57	5.1×10^{-8}	1.5×10^{-17}		
1255-3R	146.5	53	4.0×10^{-8}	2.6×10^{-18}		
1255-4R	152.4	---	5.2×10^{-8}	3.2×10^{-18}		

[a] Permeability of samples from New Jersey margin, ODP Leg 174 is measured by flow-through test. c_v is calculated using the volume compressibility at in situ hydrostatic vertical effective stress.

would allow the interpretation of partial dissipation. Extrapolation of these results is tentative because the initial pressure distribution is controlled by the soil properties and we have not fully explored a range of soil types. Further analysis of other soil types must be completed to generalize these results.

Our modeled results do not match the pressure data well for the first 10 minutes of dissipation of the DVTPP and the first 3 minutes of dissipation for the Piezoprobe (Figure 1.14). Three factors may contribute to this mismatch. First, the initial penetration may not be entirely undrained and there may be disturbance when the drill string is raised to decouple it from the tool. Significant disturbance due to decoupling the drill string was observed for the DVTPP (see Appendix 1.A). Future design should focus on how to minimize these effects. Second, our model may not capture all of the physical processes of penetration. We have determined the strain paths of soil elements by assuming steady penetration in an incompressible, inviscid, fluid. An inviscid fluid cannot permanently resist any shearing stresses, however, while in the case of plastic material like clay, small stresses of definite magnitude are required to produce deformation. We have assumed a rate-independent soil behavior to determine the distribution of the initial excess pore pressure. However, *Lacasse* [1979] proposes that a 10^n increase in strain rate increases the undrained shear strength (S_u) by an amount $n\beta S_u$. Typical values of β range from 3 to 20%. Finally, it is possible that a high system compliance and thus a slower probe response, may contribute to this early stage mismatch.

1.8 Conclusion

We used two pressure penetrometers, Fugro-McClelland's Piezoprobe and the ODP's DVTPP, to measure in situ pore pressure and coefficient of consolidation approximately 50 mbsf at southern Hydrate Ridge, offshore Oregon. We modeled both the penetration and subsequent dissipation to assemble type dissipation curves for these instruments. We used the type-curves to extrapolate in situ pressure and the coefficient of consolidation. We found that these shallow marine sediments have hydrostatic pressures and a coefficient of consolidation of 6.92 to 7.8×10^{-7} m^2/s.

Comparison of the DVTPP and the Piezoprobe provide general insights for the deployment of penetrometers in ocean drilling boreholes. For typical marine mudstones encountered by the Ocean Drilling Program, the DVTPP cannot be used to interpret in situ pressure within the 0.5 to 1.0 hour typically available on a drill ship. The DVTPP is relatively thick, and it has a cone-shaped geometry that results in a monotonic pressure decline. As a result dissipation times are long and there is no distinct feature in the dissipation curve that records a degree of partial dissipation. The Piezoprobe's narrow tip allows very rapid initial dissipation and the abrupt transition to its wider diameter shaft results in a characteristic dissipation profile with a step or 'bench' that records a known degree of dissipation. This feature can be used to estimate in situ pore pressure from partial pressure dissipation.

Appendix 1.A: DVTPP and Piezoprobe Deployments

We used core line depth, core line tension, hook load, bit depth and pump strokes to determine the series of events that occurred during penetrometer deployment (Table 1.2 and 1.3).

1.A.1 DVTPP

The DVTPP was lowered down the drill pipe on the coring wireline (Figure 1.A1A). As it was lowered, sea water was pumped continuously. At Pt. 1 (Figure 1.A1A, B) the tool was stopped at the seafloor and the pumps were turned off. After 5 minutes, the pumps were turned on and the tool was further lowered on the wireline (Pt. 2, Figure 1.A1A). At Pt. 5, the colleted delivery system (CDS) landed into the bottom hole assembly (BHA), which is recorded by a

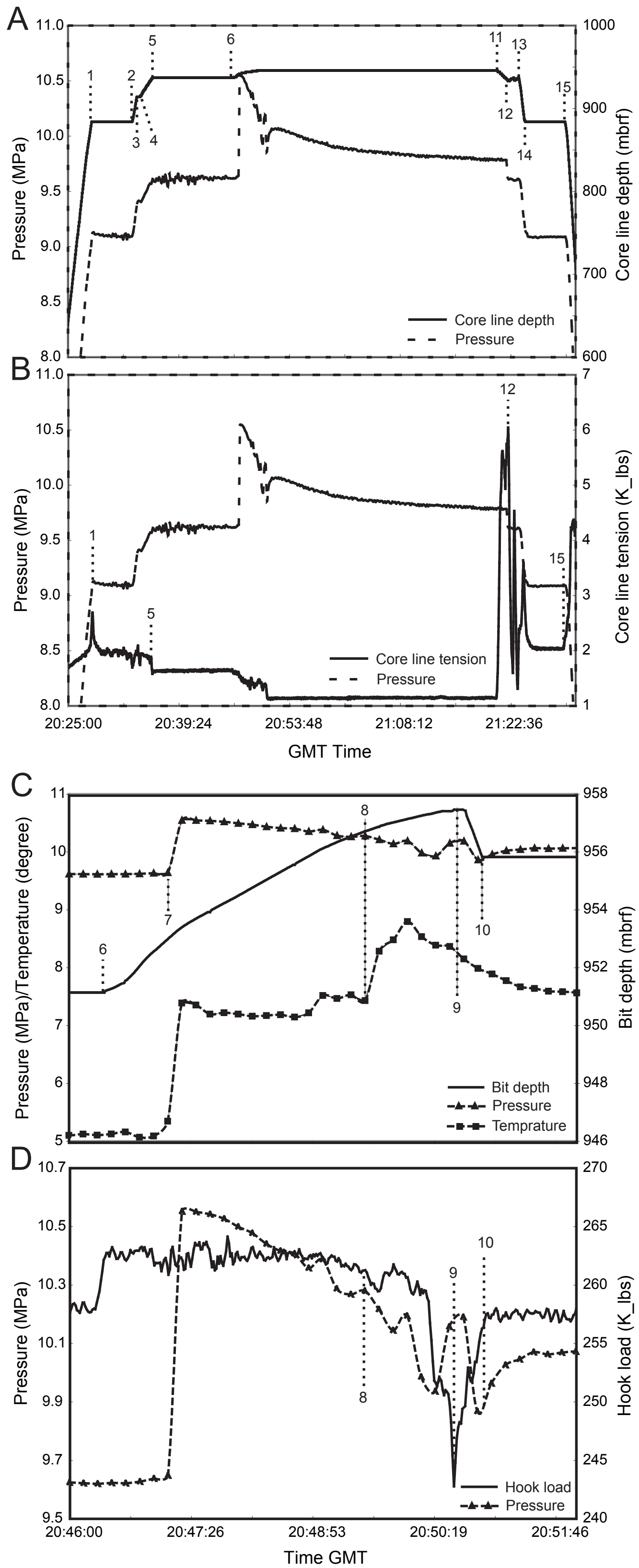

Figure 1.A1: Summary of DVTPP deployment. The deployment events are identified by numbers and are explained in Table 1.2. A) Pressure record and core line depth. B) Pressure record and core line tension. C) Pressure, temperature and bit depth. D) Pressure record and hook load. See

drop in core line tension (Figure 1.A1B). At this point, the bit was 6.3 meters above the bottom of the hole, and the tip of the DVTPP extended 4.4 meters ahead of the bit: the CDS was extended. At Pt. 6, the drill string started to lower (Figure 1.A1C). At Pt. 7, the DVTPP tip touched the bottom of the hole, which is recorded by an abrupt increase in pressure and temperature (Figure 1.A1C). The drill string continued to lower and as it did so the CDS closed (much like an accordion). At Pt. 8, the CDS was completely closed and the drill string began pushing the DVTPP into the formation (Figure 1.A1C, D). This is recorded by an increase in temperature and by a slight oscillation in the pressure response (Figure 1.A1C). As the tool is pushed further into the formation, the hookload decreases by 20,000 lbs (Figure 1.A1D). At Pt. 9 (or perhaps slightly sooner), the tool has fully penetrated into the formation and the drill bit is now pushing directly against the bottom of the formation. The drill string is then raised. At Pt. 10, the drill string is stopped after having been raised 1.64 meters above the bottom of the hole (Figure 1.A1C). After 30 minutes in place, the DVTPP is removed by pulling on the coring wireline. Release of the tool is recorded by a brief increase in temperature that is coincident with a decrease in tension on the coring wireline as the tool breaks free (Pt. 12 Figure 1.A1B). The tool is then held in place briefly 1 minute before it is raised with the coring line to the seafloor (Pt. 14 Figure 1.A1) and held for 5 minutes. Then the tool is raised to the surface (Pt. 15 Figure 1.A1).

We interpret that from Pt. 5 to Pt. 6 and from Pt. 12 to Pt. 13, the tip of the tool is just above the bottom of the hole and is measuring the hydrostatic pressure within the borehole. This pressure, 9.612 MPa, corresponds to a column of water reaching to the sea surface with a density of 1.036 g/cm^3. We interpret that this unreasonably high fluid density is because the tool is not perfectly calibrated. For this reason, we applied a static shift of the data of 0.108 MPa to match an average seawater density of 1.024 g/cm^3. The figures in the text have had this shift applied. We also note that the time used in the DVTPP deployment (GMT) is that recorded by the DVTPP. The core line depth, core line tension, hook load and bit depth data were shifted 20 seconds in time to correctly match the DVTPP data.

1.A.2 Piezoprobe

For the Piezoprobe deployment, core line depth and core line tension were not recorded. The deployment events are defined by *Dugan and Flemings* [2003a]. The Piezoprobe was stopped at the seafloor after 33 minutes of deployment (Pt. 2 Figure 1.A2). Thereafter it was lowered to the bottom of the hole at 53.5 mbsf (Pt. 3 to Pt. 4, Figure 1.A2). It was pushed into the formation (Pt. 9, Figure 1.A2) over 40 seconds, and generated a peak pressure of 10.356 MPa. After that, pressure sharply dropped to 10.05 MPa. This is most likely due to a pull after the first insertion. Then pressure built up to 10.284 MPa in 36 seconds due to further insertion. The dissipation lasted 45 minutes. Pressure declined to 9.614 MPa before pullout, which is 0.085 MPa greater than estimated u_h (Figure 1.A2). The pressure at the bottom of the hole, before and after insertion is 9.57 MPa (Pt. 7 and Pt. 10, Figure 1.A2). This is 0.041 MPa greater than the predicted hydrostatic (u_h) pressure assuming a fluid density of 1.024 g/cm^3. This could be due to poor tool calibration or a borehole fluid density greater than 1.024 g/cm^3. We applied a static shift of the data of 0.041 MPa to match the estimated hydrostatic pressures at the base of the hole.

Appendix 1.B: Parameters for Total Stress Soil Model (MIT-T1)

To develop soil parameters for the total stress approach, K_0-consolidated undrained triaxial compression and extension tests were performed on intact and resedimented specimens [*Tan, et al.*, 2006]. The test involves two stages: first the specimen is consolidated one-dimensionally until the desired stress state is reached; second, the specimen is sheared without

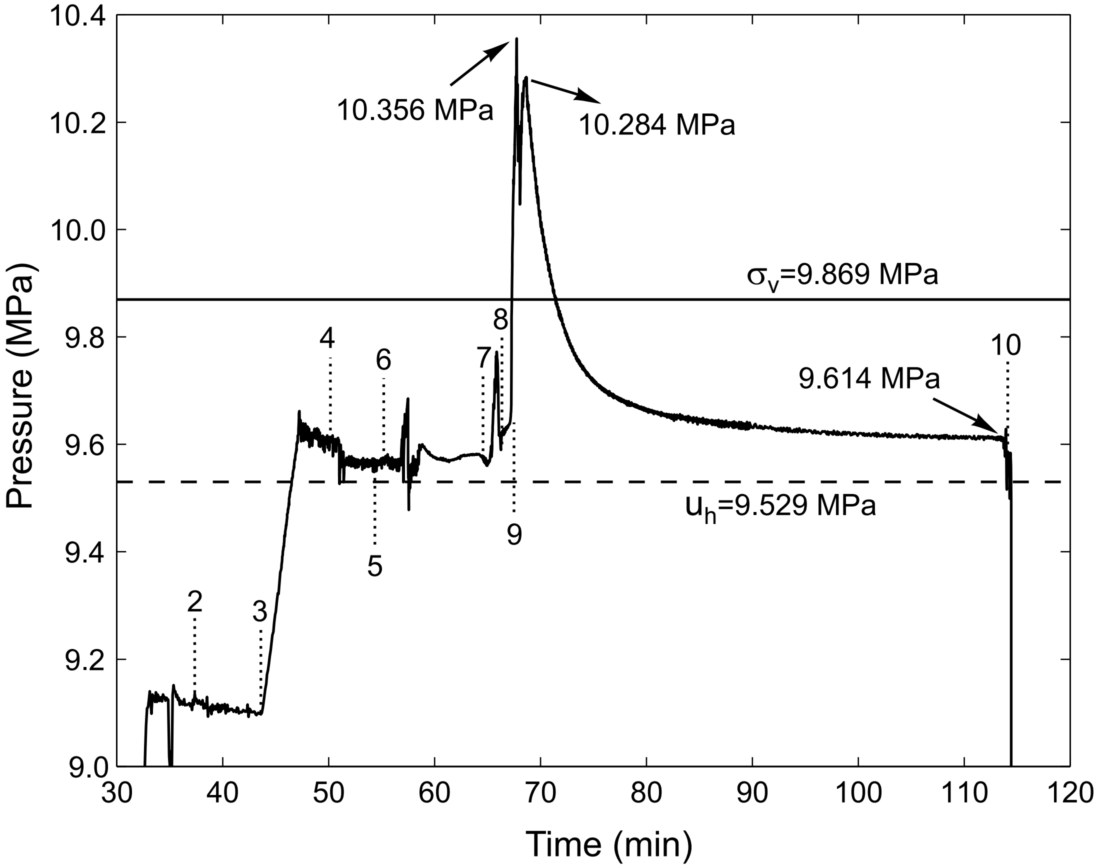

Figure 1.A2: Pressure records for the Piezoprobe deployment. The deployment events are identified by numbers and are explained in Table 1.3. See Appendix 1.A for discussion.

drainage. *Tan* [2004] and *Tan et al.* [2006] showed that resedimented specimens exhibit similar behavior to intact specimens, especially during undrained shearing. Because we did not have enough sample for triaxial testing at the depth the penetrometers were deployed and because sample disturbance during piston coring affected the strength of the samples, we determined stress-strain relations and the shear induced pressure versus strain relations from the test results on the resedimented specimens. The preparation procedure of the resedimented specimens is described by *Tan* [2004] and *Tan et al.* [2006]. The sample material was acquired from multiple depths at Site 1244 and represented material of similar composition to the soil present at the depth the penetrometers were deployed. Definitions and derivations of the soil parameters are presented by *Levadoux and Baligh* [1980].

1.B.1 Parameters for Stress-strain Relationships

1. The dimensionless elastic shear modulus, G/σ'_{v0}, is equal to 144.44.
2. The initial yield surfaces are presented in Table 1.B1.
3. The experimental constant, A_m, is equal to 25, which controls the reduction in plastic modulus, H_m', during the process of plastic flow. The limiting (minimum) plastic modulus ($H_m'^{l}$) is equal to 10% of its initial value ($H_m'^{0}$).
4. Post-peak strain softening is controlled by A_p, a constant that controls the rate of decrease in radius of the failure surface when the soil has reached the failure state. All yield surfaces remain tangent to the failure surface at the current stress point and decrease in size by the same relative amount. A_p is equal to 1.2 for the resedimented Hydrate Ridge soil. The initial radius of failure surface ($k_o^{(p)}/\sigma'_{v0}$) is equal to 0.6485 and the limiting (minimum) radius of failure surface ($k_l^{(p)}/\sigma'_{v0}$) is equal to 0.3.

Table 1.B1. Soil parameters to describe the stress-strain relation for normally-consolidated resedimented Hydrate Ridge Soil (K_0=0.486)

Yield surface number m	Center location $\alpha_1^{(m)}/\sigma'_{v0}$	Radius $k^{(m)}/\sigma'_{v0}$	Elasto-Plastic modulus $H^{(m)}/\sigma'_{v0}$
1	0.4945	0.0563	214.8533
2	0.5065	0.0765	149.0533
3	0.4766	0.1201	117.8960
4	0.4441	0.1668	91.1027
5	0.4168	0.2093	67.2560
6	0.3829	0.2564	47.8947
7	0.3559	0.3006	37.9893
8	0.3427	0.3206	23.1120
9	0.2706	0.4022	13.6453
10	0.2507	0.4367	5.3929
11	0.1671	0.5274	1.4904
12	0.0671	0.6294	1.1504
13	0.0484	0.6484	0.0000

Table 1.B2. Soil parameters to describe shear-induced pressure versus strain relation for normally-consolidated resedimented Hydrate Ridge Soil (K_0=0.486)[a]

Sphere number n	Center location $\beta_1^{(n)}/\sigma'_{v0}$	Radius $\rho^{(n)}/\sigma'_{v0}$	Rate of pore pressure generation $I^{(n)}/\sigma'_{v0}$
1	0.000000	0.000000	56.6870
2	-0.000235	0.000258	28.0920
3	-0.000220	0.000290	21.5160
4	-0.002292	0.002409	14.6560
5	-0.004967	0.005259	9.5551
6	-0.003333	0.009690	7.0988
7	-0.003796	0.014383	5.2304
8	-0.004313	0.019649	3.5092
9	-0.003555	0.027770	2.3292
10	-0.002045	0.036154	1.5845
11	-0.002474	0.046007	1.0883
12	0.003542	0.053590	0.5452
13	0.008883	0.071117	0.1044
14	0.011069	0.088931	0.0010

[a]Maximum normalized shear-induced pore pressure $\frac{(\Delta u_s)_{\max}}{\sigma'_{v0}} = 0.54$.

1.B.2 Parameters for Shear-induced Pore Pressure versus Strain Relation

Table 1.B2 presents the model parameters that predict the shear-induced pore pressure for general strain paths. The maximum shear-induced pore pressure can be obtained from results of cyclic undrained triaxial tests. It is assumed to be 54% of the initial vertical effective stress for the Hydrate Ridge clay.

Nomenclature

A_m constant that controls the rate of decrease in plastic modulus

A_p constant that controls the rate of decrease in radius of the yield surfaces

c coefficient of consolidation L^2T^{-1}

E octahedral shear strain

E_1, E_2, E_3 triaxial, cylindrical expansion and direct simple shear strain component

G elastic shear modulus $ML^{-1}T^{-2}$

$H^{(m)}$ elastic-plastic modulus $ML^{-1}T^{-2}$

$H_m'^{0}$ initial plastic modulus $ML^{-1}T^{-2}$

$H_m'^{l}$ limiting (minimum) plastic modulus $ML^{-1}T^{-2}$

$I^{(n)}$ slope of shear induced pressure vs. octahedral shear strain curve $ML^{-1}T^{-2}$

$k^{(m)}$ initial radius of yield surfaces $ML^{-1}T^{-2}$

$k_0^{(p)}$ initial radius of failure surface $ML^{-1}T^{-2}$

$k_l^{(p)}$ limiting (minimum) radius of failure surface $ML^{-1}T^{-2}$

K_0 earth pressure coefficient at rest

R radius of the DVTPP shaft L

R_1, R_2 tip and shaft radii respectively for Piezoprobe L

r, z radial and vertical coordinates for strain path models of probe penetration L

S_{ij} deviatoric shear stress components in axisymmetric problems $ML^{-1}T^{-2}$

T dimensionless time factor

T_{90} dimensionless time to achieve 90% dissipation

t time after penetration is halted T

u_0 in situ pressure $ML^{-1}T^{-2}$

u_h hydrostatic pressure $ML^{-1}T^{-2}$

u_i peak pore pressure $ML^{-1}T^{-2}$

u_l last-recorded pore pressure $ML^{-1}T^{-2}$

$\alpha_1^{(m)}$ center location of initial yield surfaces $ML^{-1}T^{-2}$

$\beta_1^{(n)}$ center location of spheres that define shear induced pressure generation $ML^{-1}T^{-2}$

ε_{ij} components of stain tensor

λ^* overpressure ratio

$\rho^{(n)}$ radius of spheres that define shear induced pressure generation $ML^{-1}T^{-2}$

σ_{ij} components of total stress tensor $ML^{-1}T^{-2}$

σ_v overburden stress $ML^{-1}T^{-2}$

σ'_{v0} in situ vertical effective stress before penetration $ML^{-1}T^{-2}$

σ'_{vh} hydrostatic vertical effective stress $ML^{-1}T^{-2}$

$\Delta\sigma_{ij}$ change in components of total stress tensor (in cylindrical coordinate system: i=r, θ and z; j=r, θ and z) $ML^{-1}T^{-2}$

Δu excess pore pressure $ML^{-1}T^{-2}$

Δu_i initial excess pore pressure induced by steady penetration $ML^{-1}T^{-2}$

Δu_{oct} pore pressure change due to change in octahedral normal stress $ML^{-1}T^{-2}$

Δu_s shear-induced excess pore pressure $ML^{-1}T^{-2}$

$\Delta\sigma_{oct}$ change in octahedral normal stress $ML^{-1}T^{-2}$

Acknowledgements

We thank the participants of ODP Leg 204 that made the deployment of the DVTPP and Piezoprobe possible. We thank D. Elsworth, and A. Whittle for many fruitful discussions. The Associate Editor and two anonymous reviewers provided very helpful reviews. Frank Rack went to extraordinary efforts to acquire funding for deployment of the Piezoprobe. This work was supported by the National Science Foundation under grant OCE 0351085 and grant EAR 0447235. In addition, the Penn State GeoFluids Consortium and the NSF-sponsored U.S. Science Support Program (USSSP) supported this research. This research results from samples and/or data provided by the Ocean Drilling Program (ODP). ODP is sponsored by the US National Science Foundation and participation counties under management of Joint Oceanographic Institutions (JOI), Inc.

References:

Aubeny, C. P. (1992), Rational interpretation of in-situ tests in cohesive soils, PhD thesis, 433 pp, Massachusetts Institute of Technology, Cambridge, MA.

Baligh, M. M. (1975), Theory of deep static cone penetration resistance, Research Report, 133 pp, Massachusetts Institute of Technology, Cambridge, MA.

Baligh, M. M. (1985), Strain path method, *Journal of Geotechnical Engineering, ASCE*, *111*, 1108-1136.

Baligh, M. M. (1986), Undrained deep penetration: I. Shear stresses, *Geotechnique*, *36*, 471-485.

Baligh, M. M. (1986), Undrained deep penetration: II. Pore pressures, *Geotechnique*, *36*, 487-501.

Baligh, M. M., and J. N. Levadoux (1986), Consolidation after undrained piezocone penetration II: interpretation, *Journal of Geotechnical Engineering, ASCE*, *112*, 447-461.

Becker, K., et al. (1997), The Cork Experiment in Hole 949C: Long-Term Observations of Pressure and Temperature in the Barbados Accretionary Prism, paper presented at Proceedings of the Ocean Drilling Program Scientific Results 156.

Brown, K. M. (1995), 17. The Variation of the Hydraulic Conductivity Structure of an Overpres¬sured Thrust Zone with Effective Stress, paper presented at Proceedings of the Ocean Drilling Program, Ocean Drilling Program, College Station.

Bullard, E. C. (1954), The flow of heat through the floor of the Atlantic Ocean, *Proc. R. Soc. London, Ser. A*, *222*, 408-429.

Dahlen, F. A., et al. (1984), Mechanics of fold-and-thrust belts and accretionary wedges; cohesive Coulomb theory, *J. Geophys. Res.*, *89*, 10087-10101.

Davis, D., et al. (1983), Mechanics of fold-and-thrust belts and accretionarywedges, *J. Geophys. Res.*, *88*, 1153-1172.

Davis, E. E., and K. Becker (1994), Formation temperatures and pressures in a sedimented rift hydrothermal system; 10 months of CORK observations, holes 857D and 858G, paper presented at Proceedings of the Ocean Drilling Program, Scientific Results 139.

Davis, E. E., H. Villinger, R. D. Macdonald, R. D. Meldrum and J. Grigel (1997), A robust rapid-response probe for measuring bottom-hole temperatures in deep-ocean boreholes, *Marine Geophys. Res.*, *19*, 267-281.

Davis, E. E., K. Becker, T. Pettigrew, B. Caron, and R. Macdonald (1992), CORK: A hydrologic seal and downhole observatory for deep-sea boreholes, paper presented at Proceedings of the Ocean Drilling Program, Initial Reports, eds. 139, Ocean Drilling Program, College Station.

Davis, E. E., et al. (1991), Pore pressures and permeabilities measured in marine sediments with a tethered probe, *J. Geophys. Res.*, *96*, 5975-5984.

Dillon, W. P., et al. (2000), Seafloor collapse and methane venting associated with gas hydrate on the Blake Ridge: causes and implications to seafloor stability and methane release, in Geophysical Monograph, C.K. Paull and W.P. Dillon, eds. 124, 211-233 pp.

Dugan, B., and P.B. Flemings (2003), Measuring pore pressure in marine sediments with penetrometers: comparison of the piezoprobe and DVTP-P tools in ODP Leg 204, in *Research Papers of the Link Foundation Fellows*, edited, pp. 179-199.

Dugan, B., and P. B. Flemings (2000), Overpressure and fluid flow in the New Jersey Continental Slope: implications for slope failure and cold seeps, *Science*, *289*, 288-291.

Dugan, B., and P. B. Flemings (2002), Fluid flow and stability of the US continental slope offshore New Jersey from the Pleistocene to the present, *Geofluids*, *2*, 137-146.

Dugan, B., P.B. Flemings, D.L. Olgaard and M.J. Gooch (2003), Consolidation, effective stress, and fluid pressure of sediments from ODP Site 1073, US mid-Atlantic continental slope, *Earth and Planetary Science Letters*, *215*, 13-26.

Elsworth, D. (1991), Dislocation analysis of penetration in saturated porous media, *Journal of Engineering Mechanics*, *117*, 391-408.

Elsworth, D. (1998), Indentation of a sharp piezometer in a poroelastic medium, *Int. J. Solids Structures*, *35*, 4895-4904.

Fang, W. W., et al. (1993), Analysis and application of in situ pore pressure measurements in marine sediments, *J. Geophys. Res.*, *98*, 7921-7938.

Flemings, P. B., et al. (2003), Critical pressure and multiphase flow in Blake Ridge gas hydrates, *Geology*, *31*, 1057-1060.

Gorman, A. R., et al. (2002), Migration of methan gas through the hudrate stability zone in a low-flux hydrate province, *Geology*, *30*, 327-330.

Gracia, E., et al. (2006), Data report: Grain-size and bulk and clay mineralogy of sediments from the summit and flanks of southern Hydrate Ridge, Sites 1244-1250, ODP Leg 204, in *Proceedings of the Ocean Drilling Program, Scientific Results*, edited by A. M. Trehu, et al., ODP.

Gupta, R. C., and J. L. Davidson (1986), Piezoprobe Determined Coefficient of Consolidation, *Soil and Foundations*, *26*, 12-22.

Holbrook, W. S., et al. (2002), Escape of methane gas through sediment waves in a large methane hydrate province, *Geology*, *30*, 467-470.

Hyndman, R. D., and E. E. Davis (1992), A mechanism for the formation of methane hydrate and seafloor bottom-simulating reflectors by vertical fluid expulsion, *Journal of Geophysical Research*, *97*, 7025-7041.

Hyndman, R. D., et al. (1979), The measurement of marine geothermal heat flow by a multipenetration probe with digital acoustic telemetry and in situ thermal conductivity, *Mar. Geophys. Res.*, *4*, 181-205.

Kaufmann, W. (1963), *Fluid mechanics*, McGraw-Hill Book Company Inc., New York.

Kiousis, P. D., et al. (1988), A large strain theory and its application in the analysis of the cone penetration mechanism, *Int. J. Numer. Anal. Meth. Geomech.*, *12*, 45–60.

Kurup, P. U., et al. (1994), Calibration chamber studies of piezocone test in cohesive soils, *Journal of Geotechnical Engineering*, *120*, 81-107.

Lacasse, S. (1979), Effect of load duration on undrained behavior of clay and sand, Literature Survey, NGI Internal Report 40007-1, 72 pp.

Ladanyi, B. (1963), Expansion of a cavity in a saturated clay medium, *Journal of the Soil Mechanics and Foundation Engineering Division, ASCE*, *89*, 127-161.

Levadoux, J. N., and M. M. Baligh (1980), Pore pressures during cone penetration in clays, Research Report, 310 pp, Massachusetts Institute of Technology, Cambridge, MA.

Lister, C. R. B. (1979), The pulse-probe method of conductivity measurement, *Geophys. J. R. Astron. Soc.*, *57*, 451-461.

Moore, G. F., et al. (2001), Sturctural setting of the Leg 190 Muroto Transect, Texas A&M University, Ocean Drilling Program, College Station, Tx.

Orange, D. L., et al. (2003), Measurements and modeling of the shallow pore pressure regime at the Sigsbee Escarpment; Successful prediction of overpressure and ground-truthing with borehold measurements, *The Leading Edge*, *22*, 906-913.

Ostermeier, R. M., et al. (2001), Trends in Shallow Sediment Pore Pressures - Deepwater Gulf of Mexico, paper presented at Society of Petroleum Engineers, SPE/IADC 67772.

Prévost, J. H. (1978), Anisotropic undrained stress-strain behavior of clays, *Journal of Geotechnical Engineering Division*, *104*, 1075-1090.

Randolph, M. F., and C. P. Wroth (1979a), An analytical solution for the consolidation around a driven pile, *Int. J. Numer. Anal. Meth. Geomech.*, *3*, 217-229.

Randolph, M. F., J.S. Steenfelt, and C.P. Wroth (1979b), The effect of pile type of design parameters for driven piles, paper presented at 7th European Conference on Soil Mechanics and Foundation Engineering, Brighton, England.

Saffer, D. M., and A. W. McKiernan (2005), Permeability of underthrust sediments at the Costa Rican subduction zone: Scale dependence and implications for dewatering, *Geophysical Research Letters*, *32*, L02302.

Saffer, D. M., and B.A. Bekins (2002), Hydrologic Controls on the Morphology and Mechanics of Accretionary Wedges, *Geology*, *30*, 271-274.

Schaid, F., et al. (1997), Prediction of the coefficient of consolidation from piezocone tests, *Can. Geotch. J.*, *34*.

Schultheiss, P. J., and S. D. McPhail (1986), Direct indication of pore water advection from pore-pressure measurements in Madeira abyssal plain sediments, *Nature*, *320*, 348-350.

Sibson, R. H. (1981), Fluid flow accompanying faulting: Field evidence and models, in

Simpson, D.W., Richards, P.G., eds, Earthquake prediction: An international review. AGU Maurice Ewing Series 4: 593-603.

Sills, G. C., et al. (1988), Piezocone measurements with four pore pressure positions, In Penetration Testing in the U.K., Thomas Telford, London, 967-974.

Sutabutr, T. (1999), Analysis and interpretation of tapered Piezoprobe and application to offshore pile disign, PhD thesis, MIT, Cambridge, MA.

Tan, B. (2004), Geotechnical characterization of sediments from Hydrate Ridge, Cascadia Continental Margin, MS thesis, 264 pp, Massachusetts Institute of Technology, Cambridge, MA.

Tan, B., et al. (2006), Data report: Consolidation and strength characteristics of sediments from ODP Site 1244, Hydrate Ridge, Cascadia continental margin, in *Proceedings of the Ocean Drilling Program, Scientific Results*, edited by A. M. Trehu, et al., ODP.

Tavenas, F., et al. (1986), In situ measurement of permeability in soft clays, Proceedings, American Society of Civil Engineering, Blackburger, VA, ASCE, New York, pp. 1034-1048.

Taylor, B., et al. (2000), *Proc. ODP, Init. Repts. 180*, College Station TX (Ocean Drilling Program).

Tréhu, A. M., et al. (2003), *Proc. ODP, Init. Repts., 204 [CD-ROM]*, Available from: Ocean Drilling Program, Texas A&M University, College Station TX 77845-9547, USA.

Urgeles, R., et al. (2000), Fluid flow from pore pressure measurements off La Palma, Canary Islands, *Journal of Volcanology and Geothermal Research*, *101*, 253-271.

Varney, A. (1998), A performance comparison between a novel Piezoprobe and the piezocone in Boston Blue Clay, MS thesis, MIT, Cambridge, MA.

Villinger, H., and E. E. Davis (1987), A new reduction algorithm for marine heat flow measurements, *J. Geophys. Res.*, *92*, 1557-1563.

Von Herzen, R. P., and A. E. Maxwell (1959), The measurement of thermal conductivity of deep-sea sediments by a needle probe method, *J. Geophys. Res.*, *64*, 1557-1563.

Weinberger, J. L. (2005), Investigations of the structural and hydrologic context of gas hydrate deposits on Hydrate Ridge, Oregon. PhD thesis, University of California, San Diego.

Whittle, A. J., et al. (2001), Prediction and interpretation of pore pressure dissipation for a tapered piezoprobe, *Geotechnique*, *51*, 601-617.

Yu, H. S., et al. (2000), Analysis of steady cone penetration in clay, *Journal of geotechnical and geoenvironmental engineering*, *126*, 594-605.

Chapter 2: In Situ Pore Pressure at IODP Site U1324, Ursa Basin, Gulf of Mexico

Abstract

We measured pore pressures with two pore pressure penetrometers at IODP Site U1324 in Pleistocene sediments of the Ursa Basin, Gulf of Mexico, directly offshore from the Mississippi Delta. Between the seafloor and 300 meters below the seafloor (mbsf), overpressures reach 80% of the hydrostatic effective stress ($\lambda^* = 0.8 = (u_0 - u_h) / (\sigma_v - u_h)$). In this interval, only low permeability mudstones are present. Beneath 300 mbsf, λ^* is approximately 0.2 and the sediments are composed of interbedded mudstone, siltstone, and very fine sandstone. We interpret that the lower relative pressures beneath 300 mbsf are caused by the higher permeability of these sediments. Penetrometer deployments ranged from 30 minutes to 90 minutes, which was not enough time for the measured pressure to dissipate to the in-situ pressure. To estimate the in-situ pressure, we used two inverse time extrapolation techniques: $1/\sqrt{t}$, and $1/t$. We use a theoretical soil model to show that the $1/\sqrt{t}$ extrapolation provides a desirable accuracy in much shorter amount of time than the $1/t$ extrapolation.

2.1 Introduction

Overpressures, pore pressures in excess of hydrostatic pressure, have been observed in sedimentary basins around the world [*Fertl, et al.*, 1994a]. Knowledge of the distribution of overpressure is critical to explore, drill, and produce hydrocarbons [*Fertl*, 1976; *Flemings, et al.*, 2002a]. Overpressures drive pore water flow [*Harrison and Summa*, 1991], impact large-scale structural development [*Rubey and Hubbert*, 1959], and affect the state of stress [*Zoback and Healy*, 1984].

In young, cool, sedimentary basins, overpressures are generated in low permeability mudstones due to their inability to drain as they are loaded by sedimentation or deformation. Although the pressure is generated within the mudstone, it is most often measured in permeable formations adjacent to the mudstone [*Flemings, et al.*, 2002]. Recently, the petroleum industry has extended geotechnical techniques to measure pore pressure within mudstones through the use of pore pressure penetrometers in the borehole to depths of many hundred of meters [*Ostermeier, et al.*, 2001; *Ostermeier, et al*, 2002; *Orange, et al.*, 2003]. This exciting technique provides direct measurements of pore pressure in low permeability rocks and in some locations it has documented very high pore pressures immediately beneath the seafloor [*Ostermeier, et al*, 2002].

When the penetrometer is pushed into the formation below the bottom of the hole (BOH), a pressure disturbance is created. The time that it takes to dissipate this pressure depends on the probe diameter and the hydraulic diffusivity of the sediment. In ocean drilling, the time available for downhole tool measurements is expensive and limited. In this environment, in-situ properties must be interpreted from partial dissipation records. If detailed soil properties are available, the in-situ pressure and diffusivity of the sediment can be inferred from modeling of soil behavior for different penetrometer geometries [*Levadoux and Baligh*, 1980; *Baligh*, 1985; *Levadoux and Baligh*, 1986; *Whittle, et al.*, 2001; *Long, et al.*, 2007]. However, in many cases soil properties are not available, or there are insufficient resources to pursue soil modeling. In these cases, in-situ pressure is inferred from a simple extrapolation approach.

We deployed two types of pore pressure penetrometers in the Gulf of Mexico deepwater during Integrated Ocean Drilling Program (IODP) Expedition 308: the Temperature-Two-Pressure (T2P) probe and the Davis-Villinger Temperature Pressure Probe (DVTPP) (Figure 2.1). The DVTPP was deployed previously during ODP Legs 190, 201, and 204 [*Moore, et al.*,

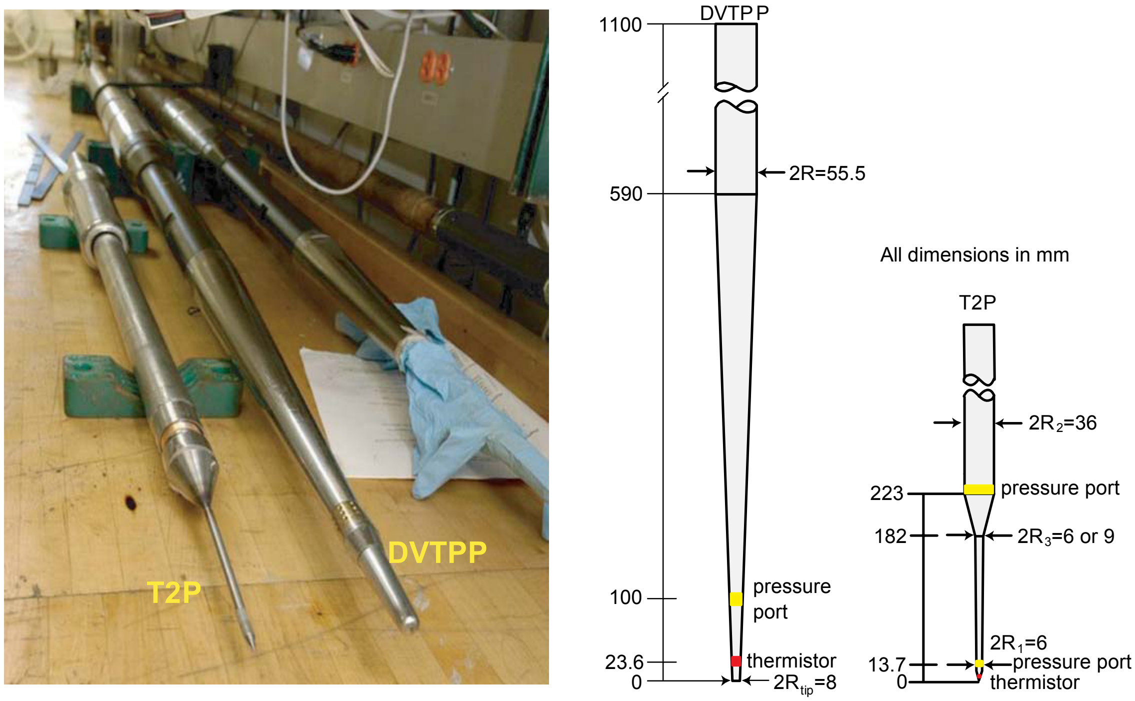

Figure 2.1: The DVTPP and T2P pore pressure penetrometers have very different geometries. The DVTPP has a long, tapered tip that extends beyond the constant diameter shaft. Its tip tapers continuously from 8 to 55.5 mm in diameter. The pressure port is located 100 mm above the tip. The T2P has a tapered extension piece 223 mm long which fits onto the end of a standard 36 mm diameter cone rod. Its modular design allows the use of multiple tip geometries and it measures pore pressure at its narrow tip and at the larger diameter shaft behind the narrow tip.

2001; *D'Hondt, et al.*, 2003; *Trehu, et al.*, 2003]. The T2P is a new tool under development as a cooperative effort between Penn State University, MIT, and IODP-TAMU [*Flemings, et al.*, 2005; *Flemings, et al.*, 2006]. The diameter of the DVTPP is large and as a result it takes a very long time for the induced pressure to dissipate to in-situ conditions in marine mudstones [*Long, et al.*, 2007]. The T2P has a much narrower diameter and dissipates toward the in-situ pressure at a more rapid rate than the DVTPP [*Flemings, et al.*, 2005; *Flemings, et al.*, 2006; *Long, et al.*, 2007].

We present the DVTPP and the T2P deployments in the Ursa Basin, deepwater Gulf of Mexico at Site U1324 during IODP Expedition 308. We use a theoretical soil model to show that an inverse square root of time ($1/\sqrt{t}$) extrapolation provides a desirable accuracy in a much shorter amount of time than an inverse time ($1/t$) extrapolation. We illustrate the results of both extrapolation techniques to infer in-situ pore pressure at Site U1324. We document the presence of significant overpressures immediately beneath the seafloor at Site U1324.

2.2 Geological Setting

The Mars-Ursa salt-withdrawal basin (hereafter referred to as "Ursa Basin") is located 210 km south-southeast of New Orleans, Louisiana (USA), on the northeastern Gulf of Mexico continental slope (Figure 2.2, inset). Late Pleistocene deposition from the ancestral Mississippi River is recorded by a southward bulge in the 500 and 1000 m bathymetric contours. The Mars Ridge, a prominent north-south–trending bathymetric high, bounds the study area to the west (Figure 2.2).

Late Pleistocene shelf, shelf-margin, and turbidite deposits sourced from the Mississippi River are termed the Eastern Depositional Complex [*Winker and Booth*, 2000]. *Sawyer et al.* [2007] describe these strata within the Ursa Basin. They are divided into the sand-prone Blue

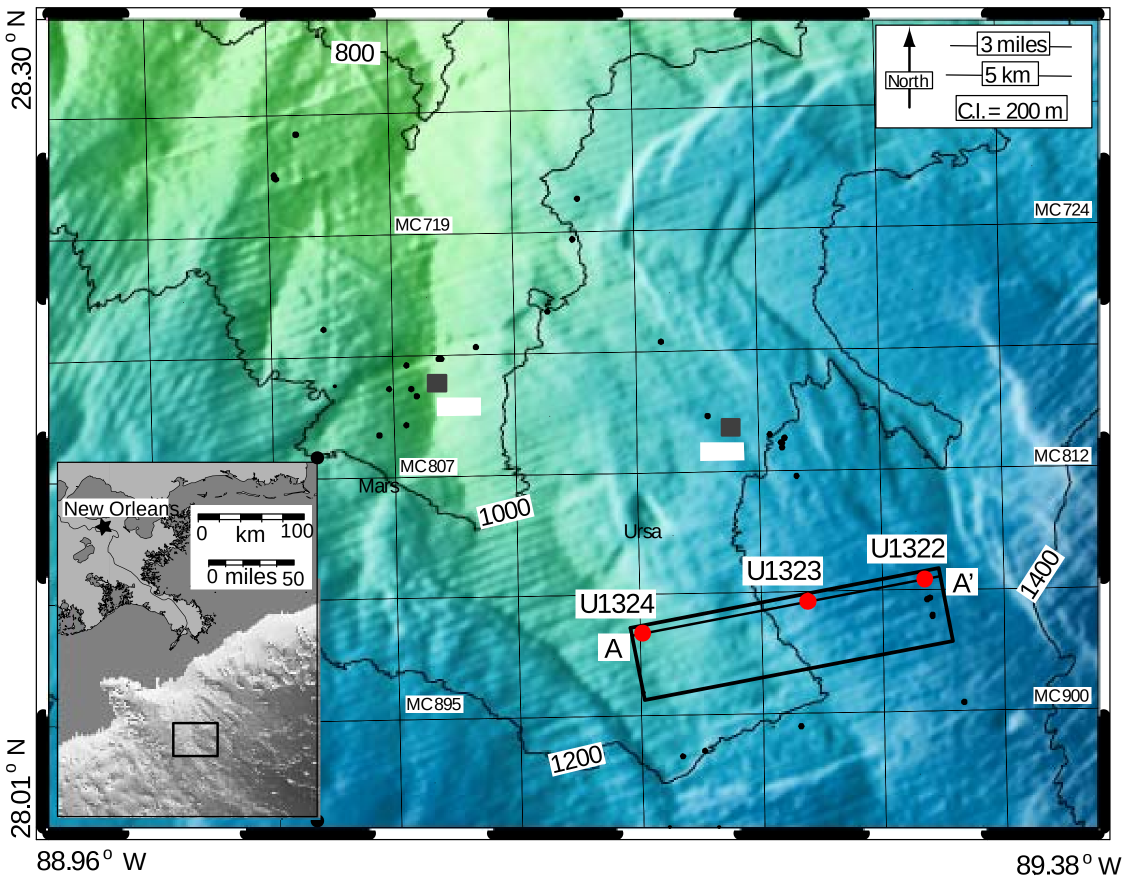

Figure 2.2: The Ursa region is located 210 km SE of New Orleans, Louisiana, USA (inset map). The IODP drilling transect is located in Mississippi Canyon protraction area in 1000-1300 meters of water. IODP Expedition 308 Sites are delineated with red circles. Cross section A-A' is illustrated in Figure 2.3. The Morgus-North 3-D seismic survey (black rectangle), Ursa and Mars tension-leg platforms (gray rectangles), and other industry wells (black dots) are shown.

Unit, which is overlain by mud-prone leveed-channel deposition (Figure 2.3). The Blue Unit is a sand-dominated turbidite unit that was deposited in a broad topographic low that extended 200 km to the east and west and 100 km to the north and south [*Sawyer, et al.*, 2007]. The leveed-channel systems contain a channel and its bounding levees. The Ursa Canyon channel-levee system immediately overlies the Blue Unit, whereas the Southwest Pass Canyon channel-levee system is younger and lies west of the Ursa Canyon (Figure 2.3). Mudstones that overlie the Southwest Pass Canyon record deposition from leveed channels that lay further to the west, outside of the study area (Figure 2.2). Multiple Mass Transport Deposits (MTDs) are present in the leveed-channel deposits. The ultimate geometry of the Blue Unit and the overlying leveed-channel deposition is that of a wedge: the Blue Unit is approximately horizontal and the leveed-channel deposits thin to the east.

During IODP Expedition 308, we drilled to just above the Blue Unit at three locations within this sedimentary wedge: Sites U1322, U1323, and U1324 (Figure 2.3). We describe only the results from Site U1324. At Site U1324, we encountered hemipelagic silty claystone to a depth of 358 meters below seafloor (mbsf). Beneath this we encountered hemipelagic silty claystone interbedded with beds of silt and very-fine sand (Figure 2.4). The silts and very-fine sands are interpreted to record levee deposition proximal to the Southwest Canyon, which lies to the west.

At Site 1324, porosity declines from 80% to 55% within the first 50 mbsf (Figure 2.4). Between 50 mbsf and 550 mbsf, the mudstone porosity gradually declines to 42%. Between 550 mbsf and the bottom of the hole (620 mbsf), porosity declines from 42% to 37%. Resistivity generally increases as porosity decreases. However, in the silts and very fine sandstones,

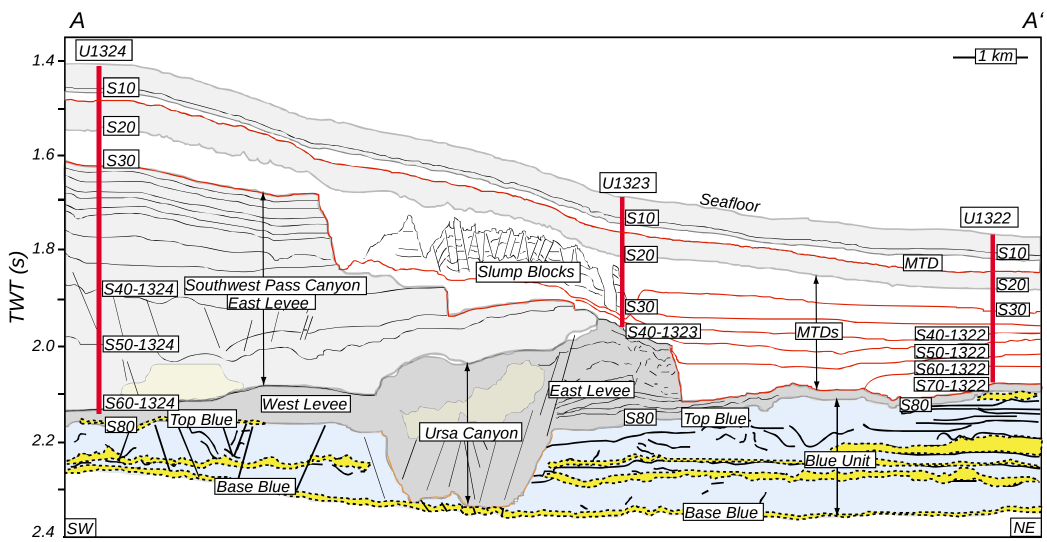

Figure 2.3: (A) East-West seismic cross section A-A' (located in Figure 2.2). (B) Interpreted cross section A-A'. Light and dark gray represent mud-rich levee, rotated channel-margin slides, and hemipelagic drape; yellow represents sand-rich channel fill. The Blue Unit (light blue) is composed of sand and mud. Mass transport deposits have occurred in the mud-rich levee deposits above the Blue Unit. Detachment surfaces are colored red.

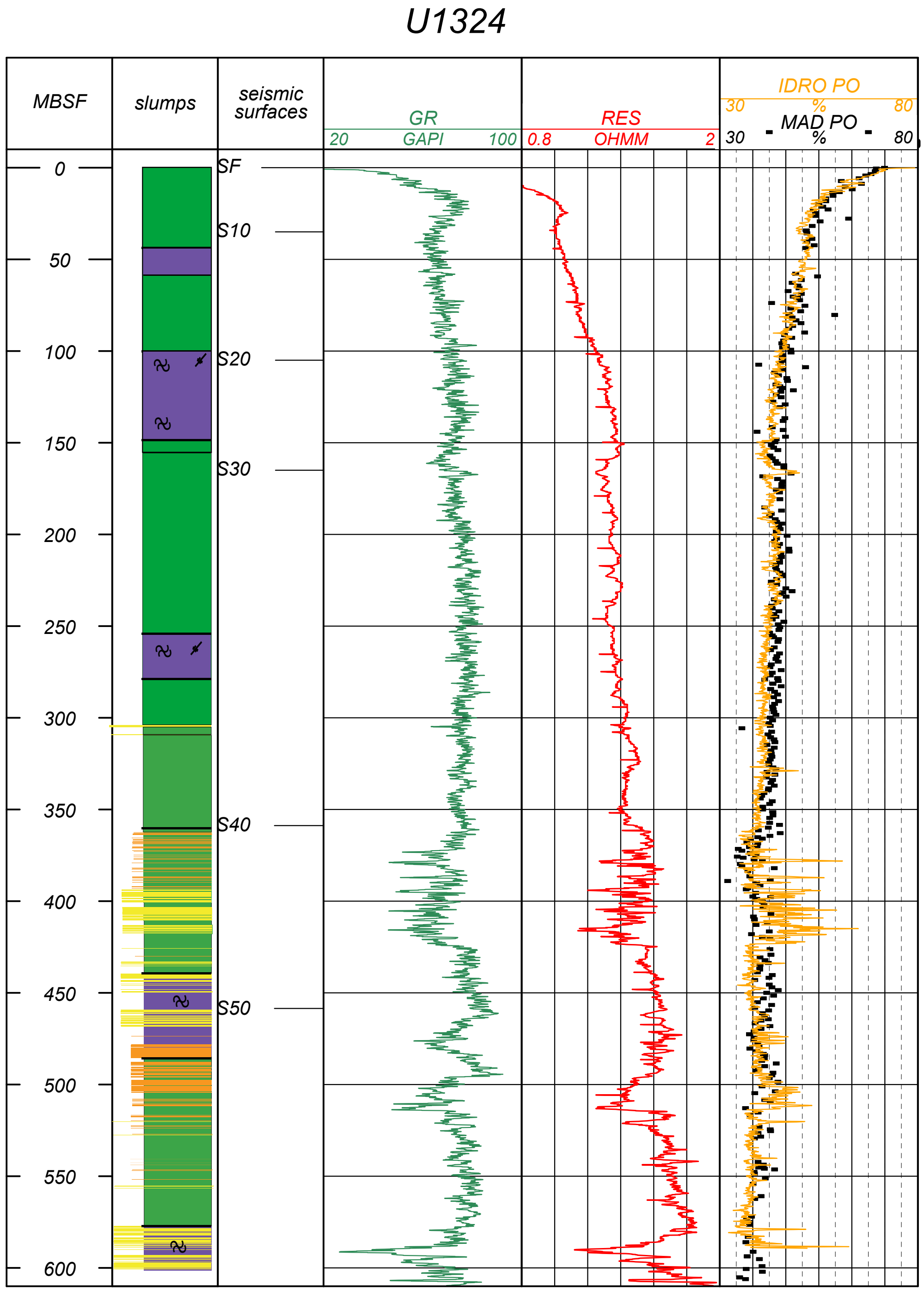

Figure 2.4: IODP Site U1324. A) Depth in meters below sea floor (mbsf). B) Lithologic section. Mass Transport Complexes are delineated in purple. C) Seismic surfaces (see Figure 2.3) are delineated with the letter ‘S’. D) Gamma Ray (GR) log. E) Resistivity log (RES) log. F) Porosity log interpreted from shipboard moisture and density (MAD) measurements (solid symbols). Porosity interpreted from logging while drilling (LWD) bulk density log assuming a grain density of 2.74 g/cc.

resistivity is lower, either due to borehole washout, lower toruosity in the pore structure, or higher salinity in the coarse material.

2.3 Instrument Calibration

The DVTPP measures pore pressure with a force-sensitive quartz crystal whose output period changes with applied load. Calibration factors of the pressure transducers are stored in the CPU of the pressure interface module (PIM) mounted to the logger. The T2P measures pore pressure with steel pressure transducers. The force on the sensing element due to the pressure results in a deformation of the sensing element and thus a change in the resistance of the element. Detailed pressure calibrations of the DVTPP and the T2P are presented in Long et al. [in preparation].

2.4 Pressure Data at IODP Site U1324

Pore Pressure measurements on IODP Expedition 308 were extremely challenging. We completed 13 DVTPP deployments and 12 T2P deployments at Site U1324. Figure 2.5A illustrates one ideal deployment for both the DVTPP and the T2P, which we term a Type I deployment (Table 2.1). The recorded pressure is at a maximum during insertion and subsequently pressure declines with time. The T2P measures the shaft pressure in addition to the tip pressure (Figure 2.1). At the end of the deployment, the shaft pressure of the T2P is much greater than that of the tip pressure. This is because the shaft has a much larger diameter. As a result, it disturbs a greater region around the penetrometer and this takes a greater amount of time to subside to the in-situ pressure. A detailed comparison of the DVTPP and the T2P geometries and their consequent behavior during insertion and dissipation is presented by *Long* et al. [2007].

Table 2.1. DVTPP and T2P deployments at Site U1324 during IODP Expedition 308.

Deployment #	Hole	Date (GMT)	Depth (mbsf)	Depth (mbsl)	Decay time (min)	Type	u_L (MPa)	u_0- $1/t$ (MPa)	u_0- $1/\sqrt{t}$ (MPa)	λ^*- $1/t$	λ^*- $1/\sqrt{t}$	Δu_i (MPa)	± 5% Error Bar (MPa)
DVTP-P10	U1324B	25-Jun-05	560.4	1617.2	32	IIA	19.97	18.50	16.67	0.46	0.09	5.64	0.282
DVTP-P12	U1324B	25-Jun-05	608.2	1665.0	61	IIA	18.90	18.49	17.80	0.33	0.20	5.60	0.280
DVTP-P13	U1324C	27-Jun-05	250	1305.7	90	I	14.70	14.31	13.87	0.60	0.38	2.19	0.110
T2P_6	U1324B	21-Jun-05	89.3	1146.1	25	Tip:III; Shaft:I	12.20	12.12	12.02	1.01	0.85	0.69	0.035
T2P_7	U1324B	21-Jun-05	117.8	1174.6	31	Tip:III; Shaft:I	12.96	12.74	12.49	1.12	0.83	1.23	0.062
T2P_8	U1324B	22-Jun-05	136.3	1193.1	30	Tip:III; Shaft:IIA	13.26	13.00	12.70	1.02	0.73	1.69	0.085
T2P_12	U1324C	26-Jun-05	50	1105.7	60	Tip:I; Shaft:I	11.33; 11.53	11.32; 11.42	11.30; 11.31	0.68; 0.99	0.61; 0.64	0.21; 0.61	0.011; 0.031
T2P_13	U1324C	26-Jun-05	100	1155.7	60	Tip:IIA; Shaft:I	12.04; 12.39	12.03; 12.21	12.02; 12.01	0.57; 0.86	0.59; 0.60	0.39; 1.04	0.020; 0.052
T2P_14	U1324C	26-Jun-05	150	1205.7	60	Tip:IIB; Shaft:IIA	13.18	13.07	12.93	0.85	0.72	2.03	0.102
T2P_15	U1324C	27-Jun-05	200	1255.7	60	Tip:IIA; Shaft:I	14.16; 14.51	14.00; 14.18	13.81; 13.84	0.88; 1.00	0.76; 0.78	0.90; 2.00	0.045; 0.100
T2P_16	U1324C	27-Jun-05	300	1355.7	90	Tip:I; Shaft:I	14.44; 15.31	14.27; 14.68	14.21; 13.96	0.27; 0.44	0.24; 0.14	2.69; 3.54	0.135; 0.177

Notes: 'Deployment #' correlates to the deployment number presented in Flemings et al. [2005]. Table 2.1 includes only the deployments that are used to estimate in-situ pressures at Site U1324 in this publication. GMT = Greenwich Mean Time. mbsf = meter below seafloor; mbsl = meter below sea level. Type I = type pressure dissipation (Figure 3a); Type IIA = pressure drops rapidly due to tool dislodgement (Figure 3b), after rebounds to certain level, pressure decays towards formation pressure; Type IIB = pressure drops rapidly due to tool dislodgement and then builds up to formation pressure (Figure 3b). The penetration-induced pressure, Δu_i, is calculated by assuming the in-situ pressure is equal to the $1/\sqrt{t}$ extrapolation.

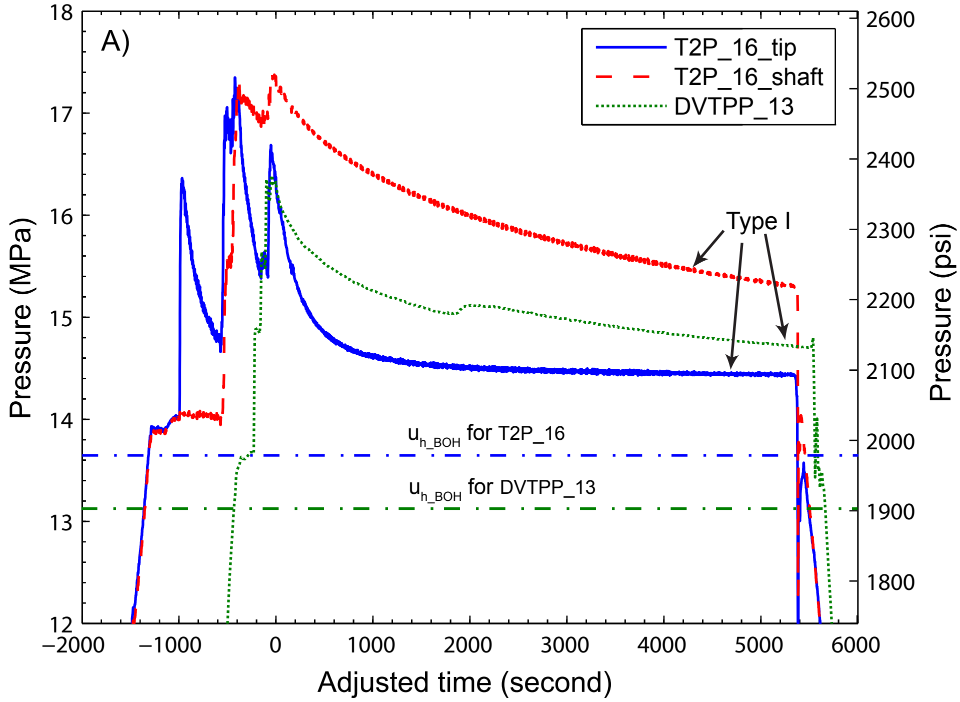

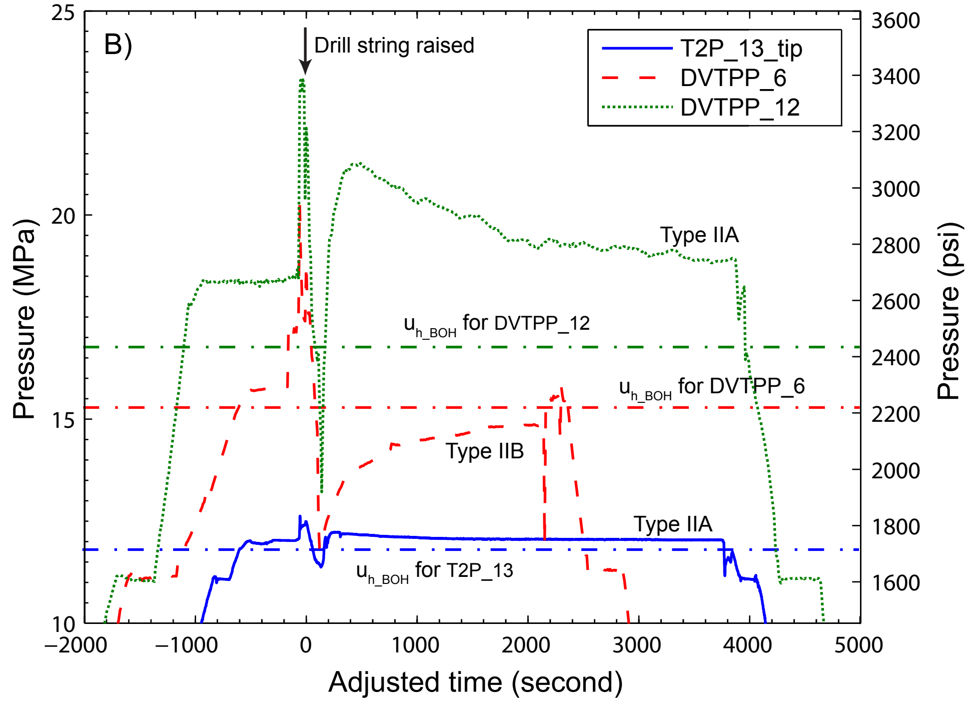

Figure 2.5: Pressure records for the DVTPP and the T2P. Zero time is marked at the start of the dissipation phase of the deployment. Time is plotted in seconds. Hydrostatic pressure at the bottom of the hole (BOH) is calculated assuming a seawater density of 1.024 g/cc. A) Type I deployments with type pressure dissipation curves. B) Type II deployments: pressure drops rapidly due to tool dislodgement, after rebounds to certain level, pressure decays towards formation pressure (Type IIA); pressure drops rapidly due to tool dislodgement and then

Figure 2.5B presents deployments for both the DVTPP and the T2P that were slightly dislodged when the drill string was raised subsequent to penetration to decouple itself from the penetrometer through the colleted delivery system (Type IIA and IIB). In this situation, the measured pressure drops abruptly when the bit is raised. Analysis of the temperature record in both tools and the accelerometer record in the DVTPP suggests that this abrupt drop in pressure coincides with a frictional heating pulse and tool movement [*Flemings, et al.*, 2005; *Long, et al.*, in preparation]. In Type II deployment, the pressure either decays towards the formation pressure after it rebounds to a certain level (Type IIA, Table 2.1) or keeps building up during the dissipation phase (Type IIB, Table 2.1) (Figure 2.5B).

2.5 Extrapolation of Pressure Decays

To interpret in-situ pressure (u_0) from penetrometer data that record only partial dissipation data, an inverse time approach is commonly used ($1/t$, where t = dissipation time) [*Davis, et al.*, 1991; *Fang and Langseth*, 1993; *Urgeles, et al.*, 2000]. In this technique, the data are plotted on an inverse time scale and a linear extrapolation is made based on the gradient of the last part of the data available (e.g. Figure 2.7). Unfortunately, there is no theoretical foundation to this approach that we have encountered. Laboratory calibration chamber tests by Lim et al. [2006] suggest that $1/t$ extrapolation provides very accurate estimate of in-situ pressure. However, *Lim et al*. [2006] only use examples where the measured pressure has already dissipated by more than 90% relative to the initial pressure disturbance. *Whittle et al*. [2001] and *Long et al*. [2007] suggest that the $1/t$ extrapolation overestimates the in-situ pressure for low permeability sediments during typical penetrometer deployments. In our deployments, we estimate that, on average, the T2P tip dissipated approximately 90%, whereas the T2P shaft

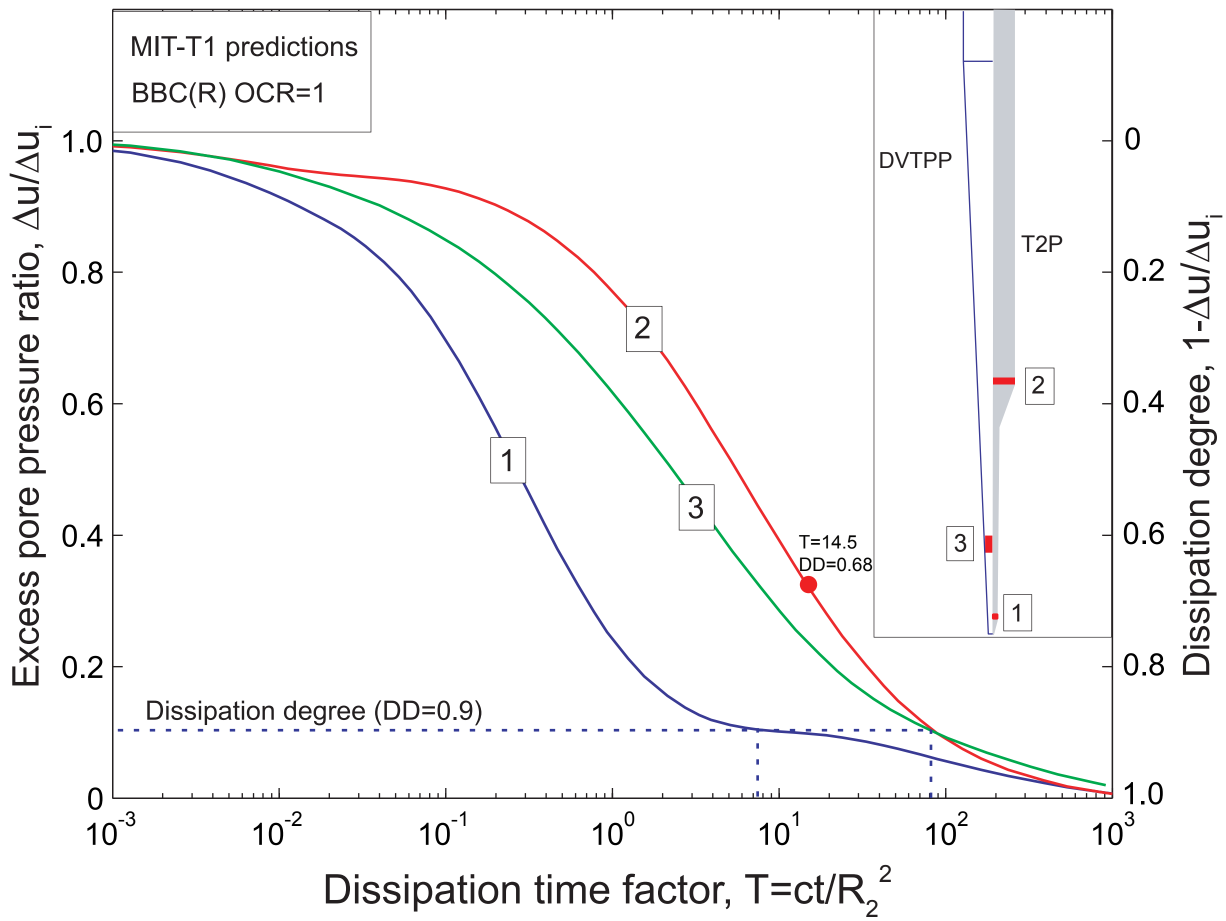

Figure 2.6: Modeled pressure dissipation for the T2P (tip #1; shaft #2) and the DVTPP (#3). Excess pore pressure ratio is plotted in log time. Dissipation time factor is normalized by the diffusivity and the radius of the shaft of the T2P. The geometries and locations of pressure ports of the T2P and the DVTPP are shown in the inset figure.

dissipated approximately 70% and the DVTPP had dissipated approximately 75%. We explore two different extrapolation approaches under these conditions.

Figure 2.6 presents the type dissipation curves of the DVTPP and the T2P that are obtained using the Strain Path Method (SPM) [*Baligh*, 1985; *Levadoux and Baligh*, 1986; *Long, et al.*, 2007], using model parameters corresponding to properties of resedimented Boston Blue Clay (BBC(R), OCR=1 [*Levadoux and Baligh*, 1980]). The most obvious result is that the narrow diameter T2P tip (#1) dissipates its pressure more rapidly than either the T2P shaft (#2) or the DVTPP (#3). In fact the T2P tip reaches 90% dissipation at least an order of magnitude quicker than either the T2P shaft or the DVTPP.

We use this theoretical model to test two inverse time extrapolation techniques: $1/\sqrt{t}$ and $1/t$. We use both the $1/\sqrt{t}$ and the $1/t$ extrapolation techniques on the T2P shaft pressure for a time factor (T) of 14.5, which corresponds to a dissipation degree of 68% (Figure 2.6 and 2.7). The $1/t$ extrapolation yields a positive error that is 18% of the installation pressure $\left(\delta u_0/\Delta u_i = 0.18\right)$ whereas the $1/\sqrt{t}$ error is only 1% of the installation pressure (Figure 2.7).

We next vary the dissipation time (T) and estimate the error ($\delta u_0/\Delta u_i$) for both extrapolation approaches (Figure 2.8B). The error of the $1/t$ extrapolation is consistently larger than that of the $1/\sqrt{t}$ extrapolation for both the DVTPP and the T2P when the dissipation degree is less than 80%. After 80% dissipation, the two approaches yield errors of similar magnitude. The $1/\sqrt{t}$ extrapolation may underpredict the in-situ pressure at higher dissipation degrees (>70%), while the $1/t$ extrapolation almost always overpredicts the in-situ value. The error for the

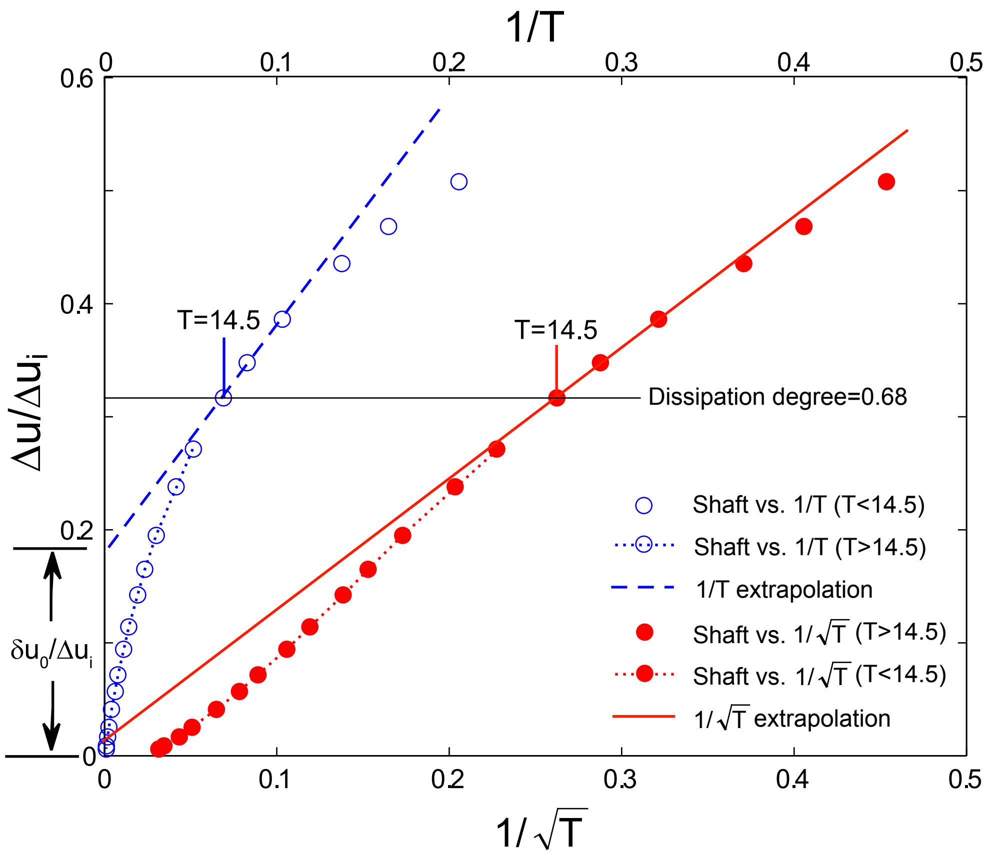

Figure 2.7: Estimating in-situ pressure from incomplete dissipation record using $1/\sqrt{t}$ and 1/t extrapolation. The excess pore pressure ratio prediction of the shaft of T2P (Figure 2.6) is plotted with $1/\sqrt{T}$ and 1/T respectively. Linear extrapolations are conducted on data with the dissipation time T =14.5 (hollow and solid circles with no lines). The circles with dashed line represent the modeled dissipation curve for T >14.5.

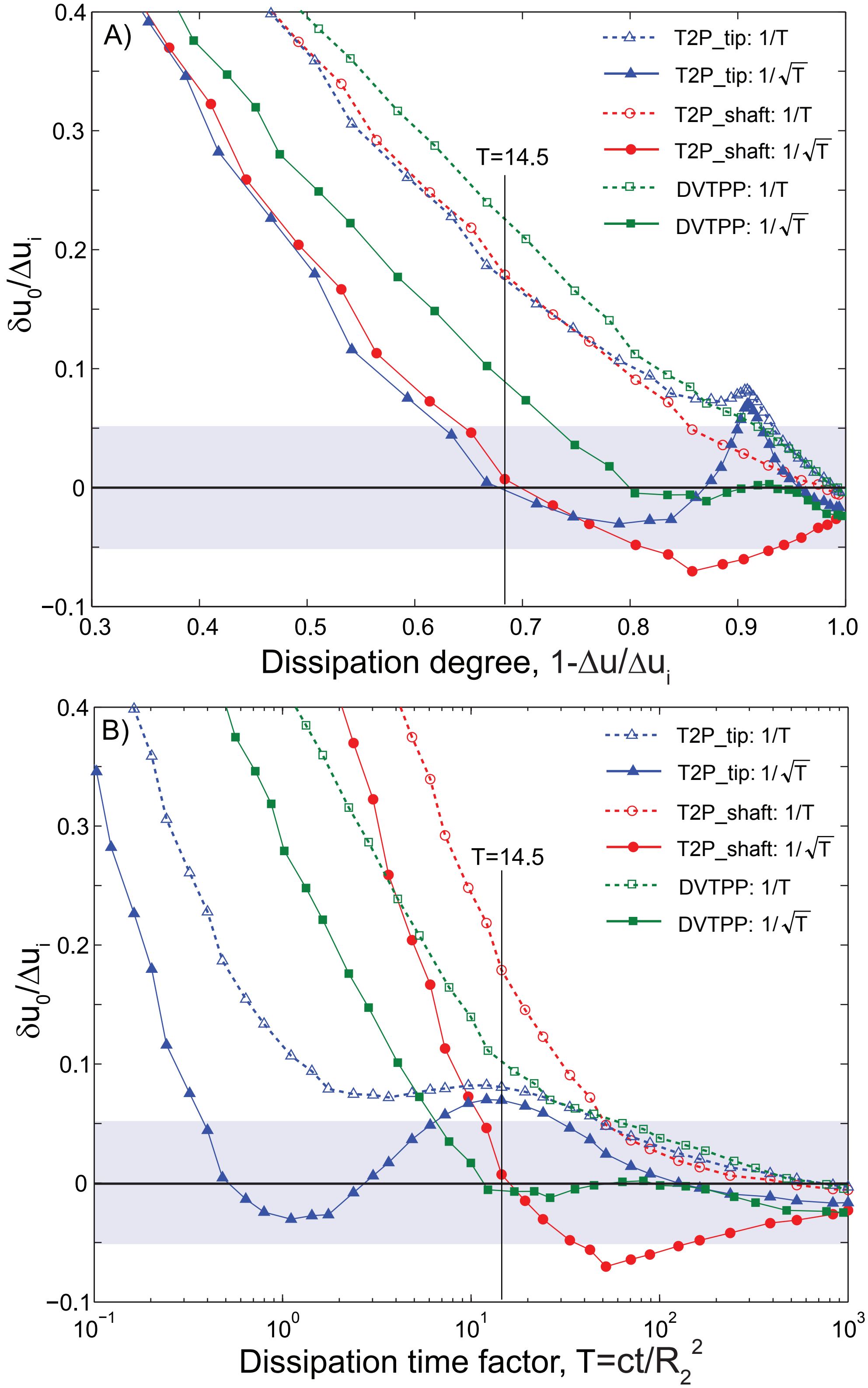

Figure 2.8: Theoretical prediction of errors in estimating u_0 by $1/\sqrt{t}$ and 1/t extrapolation. The colored band marks an error window of ±5% of the installation pressure (Δu_i). A) Errors as a function of dissipation degree. B) Error as a function of dissipation time factor (T).

tip of the T2P reaches a local maximum around 90% dissipation for both approaches, which reflects the dissipation retardation described by Whittle, et al. [2001] and Long et al. [2007].

Figure 2.8C illustrates the error as a function of the dissipation time factor, *T*. To achieve an error of 5% of the installation pressure ($\Delta u_i = u_i - u_0$), the $1/\sqrt{t}$ extrapolation needs much less deployment time than the $1/t$ extrapolation.

2.6 Pore Pressure at IODP Site U1324

Figure 2.9 presents overpressure vs. depth for Type I and Type IIA deployments at IODP Site U1324 in three fashions. First, we illustrate the last recorded overpressure recorded by either the DVTPP or the T2P at the end of the deployment (Figure 2.9A). Second, we present the estimated in-situ overpressure using the $1/t$ extrapolation (Figure 2.9B). Third, we present the estimated in-situ pressures using the $1/\sqrt{t}$ extrapolation method (Figure 2.9C). We use the overpressure ratio (λ^*) to characterize the relationship between the pore pressure and the overburden stress. When $\lambda^* = 0$, the overpressure equals zero and hence the pore pressure equals the hydrostatic pressure. When $\lambda^* = 1$, the pore pressure equals the overburden stress and the measured pore pressures lie on the zero effective stress line (solid line, Figure 2.9).

The last recorded shaft pore pressures from the T2P between the seafloor and 300 mbsf all equal or exceed the zero effective stress line (σ'_v=0, Figure 2.9A). This clearly shows that pressures had not dissipated to the in-situ pressure. The last recorded pressures beneath 300 mbsf are significantly less than the zero effective stress line (Figure 2.9A).

Figure 2.9B presents the estimated in-situ pressures by the $1/t$ extrapolation. The $1/t$ extrapolation predicts consistently higher in-situ pressure at the shaft of T2P than that at the tip, which indicates the ending dissipation time factor is less than 50 (Figure 2.8B). Some shaft

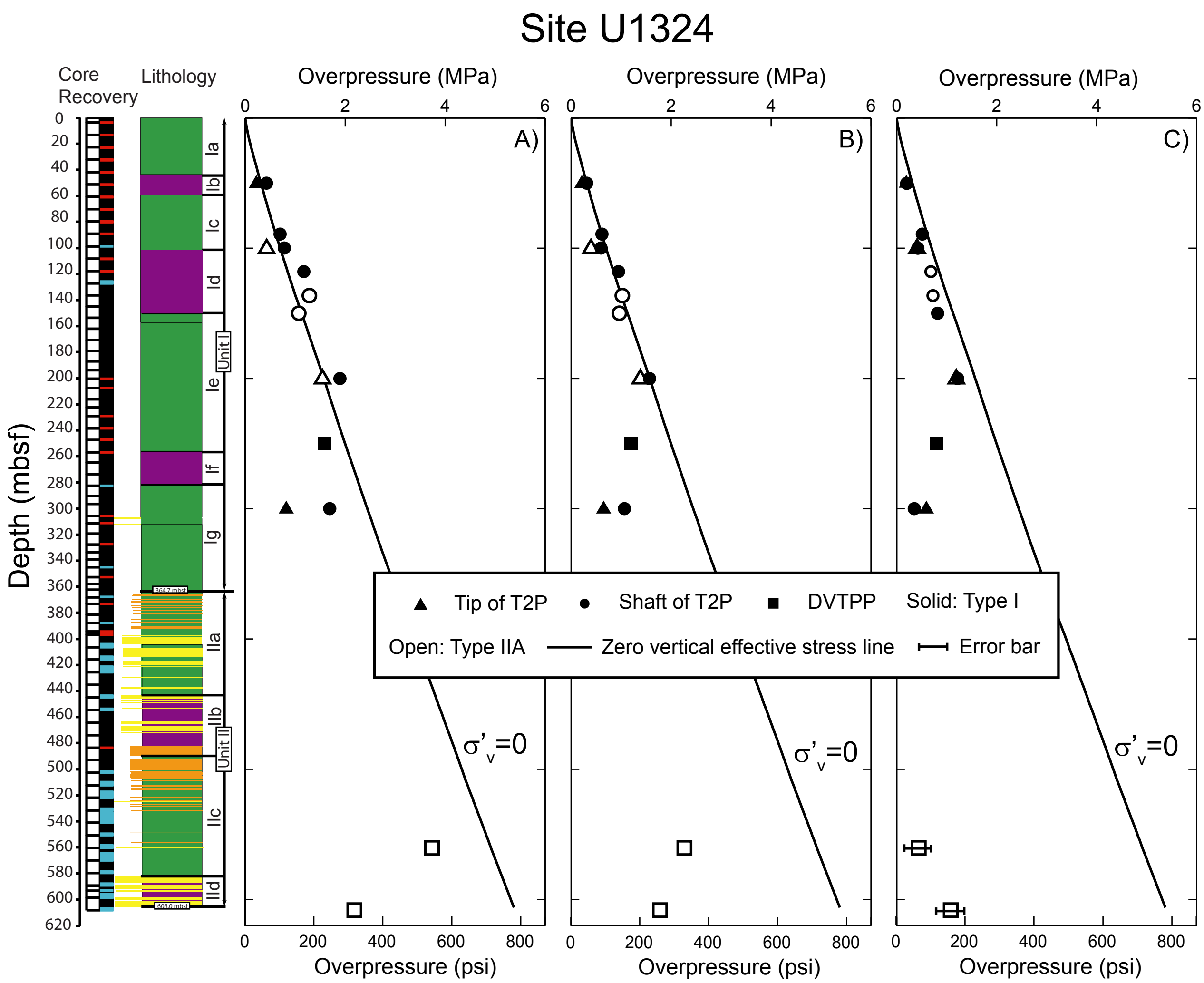

Figure 2.9: Pore pressure measurements at IODP Site U1324. Pressure data are presented in the sense of overpressure (pressure above the hydrostatic pressure). The zero vertical effective stress line is interpreted from shipboard moisture and density (MAD) measurements. A) Last recorded overpresure of the DVTPP and the T2P deployments. B) Overpressure estimated by 1/t extrapolation. C) Overpressure estimated by $1/\sqrt{t}$ extrapolation. Error bars are illustrated only for deep deployments (see Table 2.1 for others).

pressures are still equal to or even higher than the overburden stress. This is in good agreement with the theoretical error prediction that the $1/t$ extrapolation overpredicts in-situ pressure by more than $0.05\Delta u_i$ with an ending dissipation time factor less than 50 (Figure 2.8B).

Figure 2.9C presents the estimated in-situ pressures by the $1/\sqrt{t}$ extrapolation for Site U1324. The 90-minute T2P deployment (#16, Table 2.1) has a lower pressure at the tip than that at the shaft, and tip pressures are in the middle of the shaft pressures predicted by $1/t$ and $1/\sqrt{t}$ extrapolations (Table 2.1). These suggest that this deployment ended at $T\approx15$, and the shaft pressure by $1/\sqrt{t}$ extrapolation should be very close to the in-situ pressure (Figure 2.8B). For the three 60-minute T2P deployments (#12, #13 and #15, Table 2.1), the tip pressure is very close to the pressure measured at the shaft and the tip pressure estimated by $1/t$ extrapolation. These suggest that these deployments ended at $T\approx10$. The in-situ pressure should be approximately $0.07\Delta u_i$ lower than the $1/\sqrt{t}$ prediction. With the special design of a step geometry and two pressure ports, the T2P allows to locate where the last-recorded pressures lie on the dissipation curve and how much error the extrapolations may have (Figure 2.8). Thus, the T2P can achieve a more accurate pressure measurement within a restricted deployment time.

Both extrapolation approaches predict significant overpressure in the sediments above ~300 mbsf that correspond to the hemipelagic silty claystone (Figure 2.4). The overpressure ratio is up to 0.8 (Table 2.1). The sediments below 300 mbsf have smaller overpressure ratios, even though the overpressures of the two deeper DVTPPs predicted by either approach may not be accurate as the quality of these two deployments is poor. The deepest deployment was subject to tool movements during the dissipation phase, and the other one has an unusual dissipation record [*Long, et al.*, in preparation].

Sediments encountered beneath 360 mbsf are composed of silty claystone interbedded with beds of silt and very-fine sand (Figure 2.4). We interpret that the interbedded silt and sand results in a significantly larger effective permeability. The higher permeability has allowed the section beneath 360 mbsf to drain relatively rapidly and this results in values of $\lambda^* = \sim 0.2$.

2.7 Conclusions

Pressure penetrometer measurements at Site U1324 in the Ursa Basin in the deepwater Gulf of Mexico did not reach the in-situ pressure at the end of the deployment. Theoretical error analysis on two in-situ pressure interpretation approaches suggests that the $1/\sqrt{t}$ extrapolation requires much less decay time to achieve a desirable accuracy than the $1/t$ extrapolation.

Significant overpressures are interpreted in shallow sediments at the Ursa Basin. The overpressures are up to 80% of the difference between hydrostatic and overburden stress above 300 meters below the seafloor. The sediments below 300 mbsf have significantly lower overpressures ($\lambda^* = \sim 0.2$). We interpret that the lower overpressure ratio results from the fact that the deeper sediments have a significantly higher permeability.

Nomenclature

c diffusivity L^2T^{-1}

R radius of the DVTPP shaft L

R_1, R_2 tip and shaft radii respectively for T2P L

T dissipation time factor

t dissipation time T

u pressure recorded by penetrometers $ML^{-1}T^{-2}$

u_0 in-situ pressure $ML^{-1}T^{-2}$

u_h hydrostatic pressure $ML^{-1}T^{-2}$

u_i pore pressure at the end of penetration $ML^{-1}T^{-2}$

u_L last-recorded pore pressure $ML^{-1}T^{-2}$

λ^* overpressure ratio

σ_v overburden stress $ML^{-1}T^{-2}$

σ'_v vertical effective stress $ML^{-1}T^{-2}$

Δu excess pore pressure ($\Delta u=u-u_0$) $ML^{-1}T^{-2}$

Δu_i installation pressure ($\Delta u_i=u_i-u_0$) $ML^{-1}T^{-2}$

δu_0 error in the estimated in-situ pore pressure $ML^{-1}T^{-2}$

Acknowledgements

We thank the participants of IODP Expedition 308. This work was supported by the National Science Foundation under grant 6284184 and the Geofluids Consortium, Penn State University. This research used data provided by the Integrated Ocean Drilling Program (ODP). IODP is sponsored by the US National Science Foundation and participating countries under management of Joint Oceanographic Institutions (JOI), Inc.

References

Baligh, M. M. (1985), Strain path method, *Journal of Geotechnical Engineering, ASCE*, *111*, 1108-1136.

D'Hondt, S. L., et al. (2003), *Proc. ODP, Init. Repts., 201 [CD-ROM]*, Available from: Ocean Drilling Program, Texas A&M University, College Station TX 77845-9547, USA.

Davis, E. E., et al. (1991), Pore pressures and permeabilities measured in marine sediments with a tethered probe, *Journal of Geophysical Research*, *96*, 5975-5984.

Fang, W. W., and M. G. Langseth (1993), Analysis and application of in situ pressure measurements in marine sediments, *Journal of Geophysical Research*, *98*, 7921-7938.

Fertl, W. H. (1976), *Abnormal Formation Pressures: Implications to Exploration, Drilling, and Production of Oil and Gas Resources*, 382 pp., Elsevier, Amsterdam.

Fertl, W. H., et al. (1994), Studies in abnormal pressures, 454.

Flemings, P. B., B. B. Stump, T. Finkbeiner, M. Zoback (2002), Flow Focusing in Overpressured Sandstones: Theory, Observations, and Applications, *American Journal of Science*, *302*, 827-855.

Flemings, P. B., et al. (2005), Overpressure and fluid flow processes in the deepwater Gulf of Mexico: slope stability, seeps, and shallow-water flow, paper presented at in IODP Prel. Rept, Integrated Ocean Drilling Program, College Station, TX.

Flemings, P. B., Germaine, J., Long, H., Dugan, B., Sawyer, D., Behrmann, J.H., John, C., Shipboard Scientific Party, IODP Expedition 308 (2006), Measuring Temperature and Pressure with the Temperature Two Pressure (T2P) Probe in the Ursa Basin, Gulf of Mexico: Development of a New Pressure and Temperature Probe for the IODP, *Proceedings of the Offshore Technology Conference*, *OTC Paper #17957.*

Harrison, W. J., and L. L. Summa (1991), Paleohydrology of the Gulf of Mexico Basin, *American Journal of Science*, *291*, 109-176.

Levadoux, J.-N., and M. M. Baligh (1986), Consolidation after undrained piezocone penetration; I, Prediction, *Journal of Geotechnical Engineering*, *112*, 707-126.

Levadoux, J. N., and M. M. Baligh (1980), Pore pressures during cone penetration in clays, Research Report, 310 pp, Massachusetts Institute of Technology, Cambridge, MA.

Lim, B. S., et al. (2006), Status of Consolidation from Incomplete Piezocone Dissipation Tests. In: Site and Geomaterial Characterization (GSP 149), *Proceedings of Sessions of GeoShanghai*.

Long, H., et al. (2007), Interpreting in situ pressure and hydraulic properties with borehole penetrometers in ocean drilling: DVTPP and Piezoprobe deployments at southern Hydrate Ridge, offshore Oregon, *Journal of Geophysical Research*, *112*.

Long, H., et al. (in preparation), In Situ Pressure and Temperature Measurements on IODP Expedition 308, *Proceedings of the Integrated Ocean Drilling Program*.

Moore, G. F., et al. (2001), *Proceedings of the Ocean Drilling Program, Initial Reports [CD-ROM]*, Ocean Drilling Program, Texas A&M University, College Station TX 77845-9547, USA.

Orange, D. L., D. Saffer, P. Jeanjean, Z. Al-Khafaji, G. Riley, G. Humphrey (2003), Measurements and Modeling of the Shallow Pore Pressure Regime at the Sigsbee Escarpment: Successful Prediction of Overpressure and Ground-Truthing with Borehole Measurements, paper presented at Offshore Technology Conference.

Ostermeier, R. M., et al. (2001), Trends in Shallow Sediment Pore Pressures - Deepwater Gulf of Mexico, *Society of Petroleum Engineers*, *SPE/IADC 67772*.

Ostermeier, R. M., Pelletier, J.H., Winker, C.D., Nicholson, J.W., Cowan, C.K. (2002), Dealing with Shallow-Water Flow in the Deepwater Gulf of Mexico, *The Leading Edge*, 660-668.

Rubey, W. W., and M. K. Hubbert (1959), Role of fluid pressure in mechanics of overthrust faulting, Part 2. Overthrust belt in geosynclinal area of western Wyoming in light of fluid-pressure hypothesis, *Geol. Soc. Am. Bull.*, *70*, 167–205.

Sawyer, D. E., et al. (2007), Seismic Geomorphology, Lithology, and Evolution of the Late Pleistocene Mars-Ursa Turbidite Region, Mississippi Canyon Area, Northern Gulf of Mexico, *American Association of Petroleum Geologists Bulletin*, *91*, 215-234.

Trehu, A. M., et al. (2003), Proceedings of the Ocean Drilling Program Initial Reports, Leg 204, [CD ROM], Texas A&M University, College Station, TX.

Urgeles, R., et al. (2000), Fluid flow from pore pressure measurements off La Palma, Canary Islands, *Journal of Volcanology and Geothermal Research*, *101*, 253-271.

Whittle, A. J., et al. (2001), Prediction and interpretation of pore pressure dissipation for a tapered piezoprobe, *Geotechnique*, *51*, 601-617.

Winker, C. D., and J. R. Booth (2000), Sedimentary Dynamics of the Salt-Dominated Continental Slope, Gulf of Mexico: Integration of Observations from the Seafloor, Near-Surface, and Deep Subsurface, paper presented at GCSSEPM Foundation 20th Annual Research Conference, December, 2000.

Zoback, M. D., and J. H. Healy (1984), Friction, faulting, and in-situ stress, *Annales Geophysicae*, *2*, 689-698.

Chapter 3: Analysis and Interpretation of Pore Pressure Measurements by a New Penetrometer: Temperature-Two-Pressure (T2P) Probe

Abstract

We developed a new pressure penetrometer, the Temperature-Two-Pressure (T2P) probe to directly measure the in situ pressure in low-permeability marine sediments. We deployed the T2P probe in Ursa Basin, Gulf of Mexico during integrated ocean drilling program (IODP) Expedition 308. Our theoretical analyses of the tapered T2P probe suggest that the in situ pressure and hydraulic diffusivity of the penetrated sediment can be estimated independently within a short monitoring time by comparing the dissipated pressures at the tip and shaft pressure ports. Measured data suggested the proposed approach can achieve reliable and very rapid pore pressure measurement. This approach requires high quality dissipation data and an accurate soil model. We related the excess pore pressure ratio on the "bench" of the tip pressure to a single parameter, the undrained rigidity index. This allows the in situ pore pressure to be accurately estimated from partial dissipation data without knowing detailed soil properties. The measured data suggested that the "bench" approach can provide reliable and rapid estimates of in situ pressure from partial dissipation records. We compared the prediction of an idealized elastic perfectly plastic (EPP) soil model with that of an advanced soil model, MIT-T1. With specially defined shear modulus and undrained shear strength, the EPP prediction is similar to that of the MIT-T1 model.

3.1 Introduction

Pore pressure penetrometers induce a pressure pulse as they are inserted into sediments and subsequently the elevated pore pressure dissipates towards the in situ pressure. In situ pressure, hydraulic diffusivity and/or permeability of the penetrated sediments can be inferred from the pressure dissipation profile [*Baligh and Levadoux*, 1986; *Gupta and Davidson*, 1986; *Whittle, et al.*, 2001]. The petroleum industry, the Ocean Drilling Program (ODP) and its successor, the Integrated Ocean Drilling Program (IODP), have extended this geotechnical technique to sub-seafloor depths of many hundred of meters [*Moore, et al.*, 2001; *Ostermeier, et al.*, 2001; *Tréhu, et al.*, 2003; *Long, et al.*, 2007a].

Tremendous advances have been made in understanding the theoretical response to pile installation and penetrometer penetration. Early approaches modeled penetration as a spherical or cylindrical cavity expansion in saturated elastic-perfectly-plastic (EPP) material [*Ladanyi*, 1963; *Randolph and Wroth*, 1979]. Subsequently, *Baligh* [1985] introduced the strain path method (SPM) to account for the complex deformation history of the soil during probe penetration. The SPM assumes that during deep undrained penetration, soil strains are independent of its shearing resistance. This method has been applied to a range of penetrometer problems [*Levadoux and Baligh*, 1986; *The and Houlsby*, 1991; *Whittle, et al.*, 2001; *Long, et al*, 2007a]. A growing field of research uses finite element methods to model the soil deformation and pressure response induced by penetration [*Kiousis, et al.*, 1988; *Mabsout and Tassoulas*, 1996; *Yu, et al.*, 2000; *Abu-Farsakh, et al.*, 2003; *Huang, et al.*, 2004].

An immediate practical problem is to understand how to interpret in situ pressure and permeability from partial pressure dissipation of tapered probe geometries. In ocean drilling, low-permeability sediments are generally encountered and the time required to achieve full dissipation can exceed 24 hours for a single deployment. In situ properties must be interpreted from partial dissipation records even with a tapered probe that was designed to cut the monitoring time [*Whittle, et al.*, 2001; *Flemings, et al*, 2006b; *Long, et al.*, 2007a]. The most common approach is to use an inverse time extrapolation to take the last part of the acquired data and project the in situ pressure [*Davis, et al.*, 1991; *Fang, et al.*, 1993; *Whittle, et al.*, 2001; *Lim, et al.*, 2006; *Long, et al.*, 2007b]. Unfortunately, there is no theoretical basis for these extrapolation approaches. *Whittle et al*., [2001] and *Long et al*., [2007b] used theoretical models based on the SPM to predict the accuracy of these extrapolation approaches: they showed that the accuracy of the prediction depends on how much pressure has dissipated relative to its initial value.

Based on SPM analysis of Boston Blue Clay (BBC), *Whittle et al*., [2001] suggested that measuring pore pressure at two probe diameters in a single tapered penetrometer could provide rapid and accurate approach to predicting in situ pressure. To explore this behavior, we designed, built and deployed a new pentrometer, the Temperature-Two-Pressure (T2P) probe [*Flemings, et al*, 2006b; *Long, et al.*, 2007b; *Long*, *et al.*, in review] (Figure 3.1). We present a T2P deployment made in the Ursa Basin, Gulf of Mexico on IODP Expedition 308. Here, we use the SPM with two total stress soil models to simulate the pore pressure generation and dissipation of the T2P. We summarize basic insights that can be derived from an elastic-perfectly plastic (EPP) soil model and we compare these results to a more advanced soil model, MIT-T1 [*Levadoux and Baligh*, 1980]. We emphasize that one of the key controls on soil behavior is the undrained rigidity index. We then discuss different approaches to interpreting the in situ pressure from partial dissipation data.

3.2 The T2P Probe

The T2P was designed to meet very specific goals. The primary objectives were to provide pore pressure measurements at two locations on one device corresponding to different penetrometer diameters and to provide a measurement of in situ temperature. Given the fact that this would require a tapered geometry, it was desirable to reduce the smaller diameter as much as practical and create a sharp contrast between the two diameters. A step-geometry was preferable to a continuous taper based on prior research concerning interpretation of the measurements [*Whittle, et al.*, 2001; *Long, et al.*, 2007a]. An extensive set of numerical analyses were performed to guide the decision making process. Parameters of primary concern were the diameter of the tip, the shaft to tip diameter ratio, the length of the tip, and the transition angle between the two diameters. The parametric study was complimented with a stress analysis of the instrument and connections. The final geometry is discussed below.

The T2P geometry is relatively compact (Figure 3.1). The tip extension tapers from 9 to 6mm in diameter. The taper increases the bending resistance of the tip in the event of small eccentric loads. The tip extension terminates with a 30 degree sharp point. A miniature thermistor is epoxied in the center of the tip cone to provide maximum coupling with the formation. A 5 mm 40μm stainless steel filter resides directly behind the cone base. A short transition section, having a 40 degree angle, expands the probe geometry to the shaft diameter of 36 mm. A second porous element is a 20 mm 40 μm stainless steel filter that resides directly above the taper. The shaft is a thick walled tube that extends 959 mm to the third and final taper. This taper is 50 deg and increases the diameter of the probe to 105 mm. This section is 1500mm long and contains the remote data acquisition system. The probe then simply attaches to the existing Colleted Delivery System.

Connectivity of the various elements posed a significant design challenge. The two miniature pressure transducers are screwed into the transducer block situated in the drive shaft just above the second porous element. These transducers are set off center to allow space for the stainless steel conduit encasing the thermistor electric wires. The upper porous element is

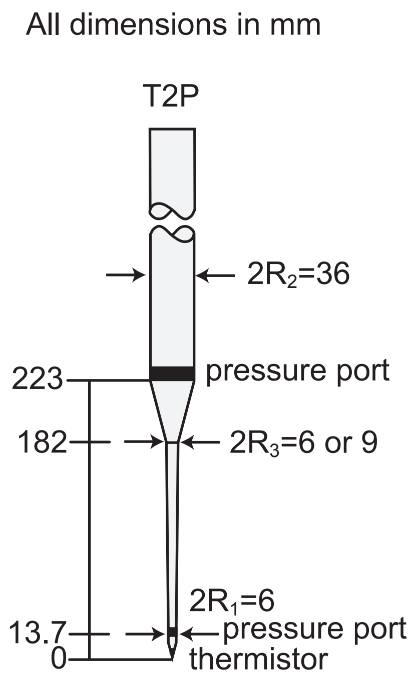

Figure 3.1: T2P pore pressure penetrometer a tapered extension piece 223 mm long which fits onto the end of a standard 36 mm diameter cone rod. Its modular design allows the use of multiple tip geometries and it measures pore pressure at its narrow tip and at the larger diameter shaft behind its needle probe.

hydraulically connected to one transducer with an angled borehole. The tip porous element is hydraulically connected through an annular passage between the hole bored through the length of the tip extension and the conduit encasing the thermistor wires. This annulus is connected to the transducer via an offset hole located behind the upper porous element. The annulus is plugged at the top of the transducer block. The two transducers and thermistor wires pass through the drive shaft and connect to the base of the data acquisition housing by means of a high pressure connector.

3.3 Geological Settings and Field Measurements

3.3.1 Geological Settings

The T2P was deployed on IODP Expedition 308 in the summer of 2005 to investigate the overpressure and fluid flow on the Gulf of Mexico continental slope [*Flemings, et al.*, 2006a]. Ursa Basin lies in ~1000 m of water (Figure 3.2A). The Mississippi Canyon Blue Unit is a late Pleistocene, sand-dominated, “ponded fan” that was deposited in a broad topographic low that extended in an east-west direction for as much as 200 km and a north-south direction for as much as 100 km [*Sawyer, et al.*, 2007; *Winker and Booth*, 2000] (Figure 3.2C). Seismic reflection profiles and drilling show that the Blue Unit is overlain by a leveed-channel assemblage that is mud dominated and thickens to the west (Figures 3.2B and 3.2C). Site U1322 and Site U1324 were cored and penetrometer measurements were made.

3.3.2 Field Measurements

Figure 3.3A presents a time history of the T2P deployment at 300 mbsf at Site U1324. The tool was deployed down the borehole using the coring wireline. When the colleted delivery system (CDS) was finally latched in the bottom hole assembly (BHA), the temperature and tip pressure records increased (Point 1, Figure 3.3A) while the shaft pressure did not increase. This

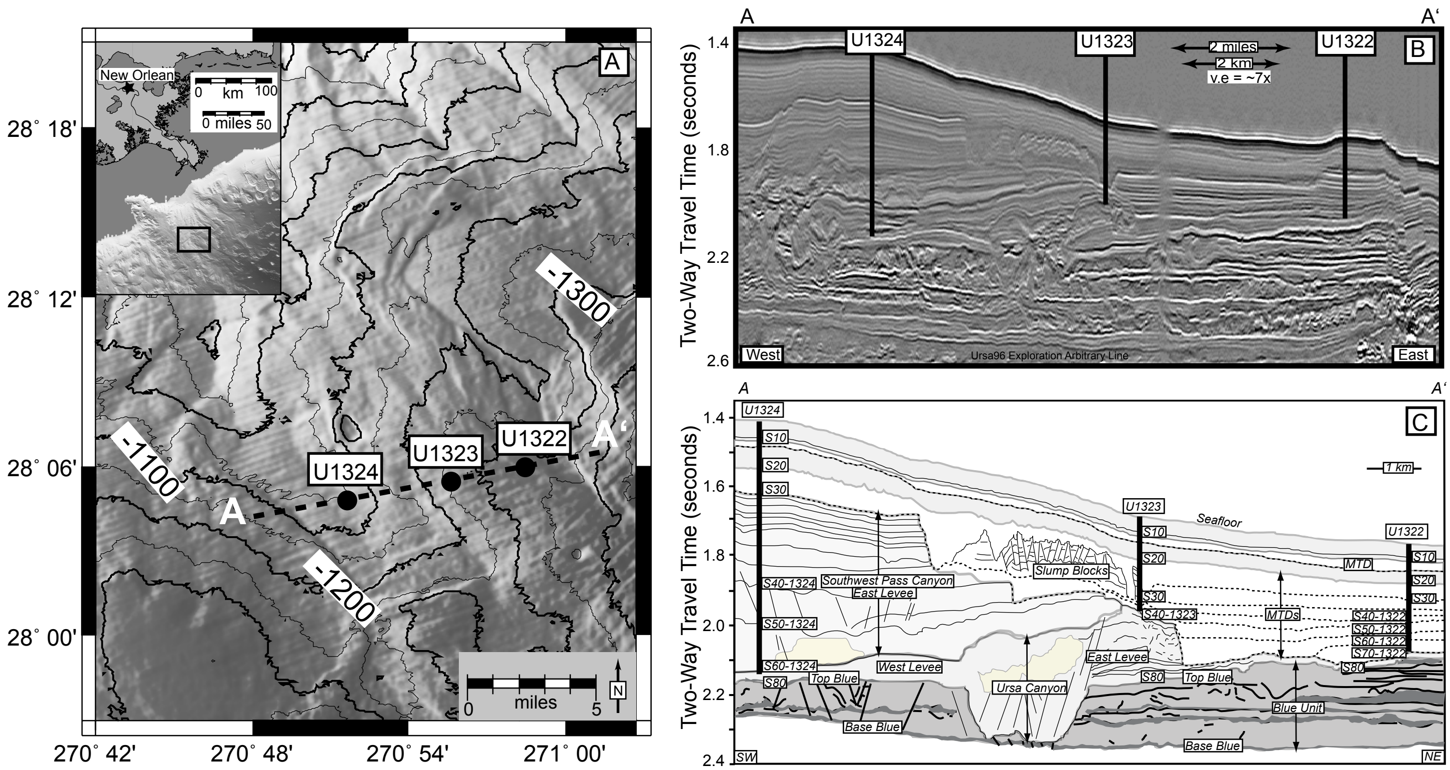

Figure 3.2: Geological setting. A) IODP Expedition 308 Site locations, and bathymetry contours. The Ursa Basin is located 210 km SE of New Orleans, Louisiana, USA (inset map). Three drilled Sites are delineated with black dots. Contour interval is 100 m. (B) East-West seismic cross section A-A’ (located in Figure 3.2A). (C) Interpreted cross section A-A’. The Blue Unit is composed of sand and mud. The darkest gray represents sand-rich channel fill. Mass transport deposits have occurred in the mud-rich levee deposits above the Blue Unit. Detachment surfaces are dotted lines.

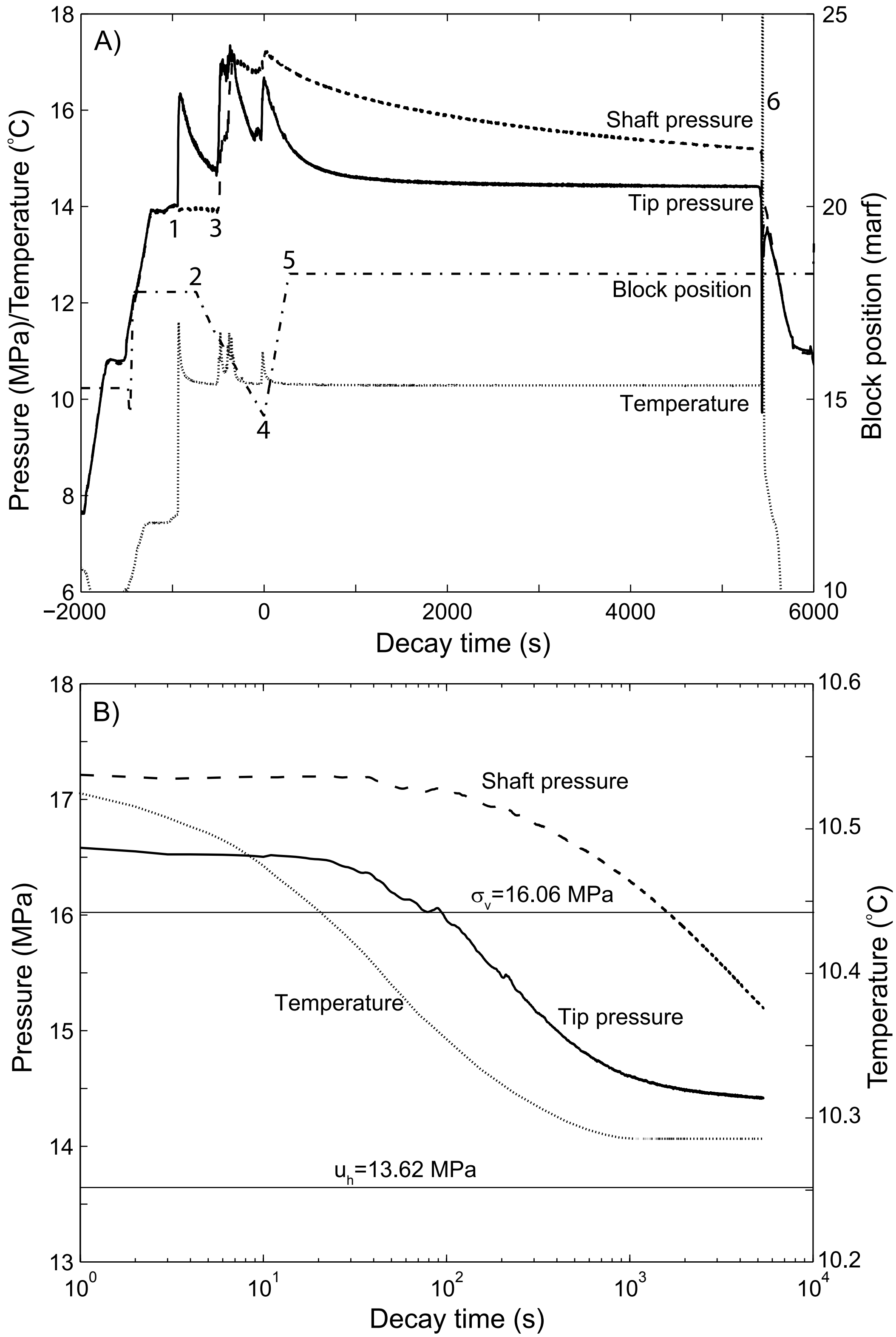

Figure 3.3: Penetration and dissipation phase of T2P deployment #16. Zero time is marked at the start of the dissipation phase of the deployment. Time is plotted in seconds. The traveling block is attached to the top end of the drill string above the rig floor. Its position was recorded in meter above rig floor (marf), which illustrates movements of the drill bit during tool deployment.

suggests the tip of the tool entering the formation while positioning the CDS. The drill bit was lowered down to install the tool (Point 2, Figure 3.3A). Once the CDS was fully retracted, the T2P was pushed into the formation at a controlled rate. Both temperature and pressure records increased (Point 3, Figure 3.3A) and varied during penetration. These variations were due to variations in the properties of the surrounding sediments. Penetration continued to Point 4 (Figure 3.3A), when the drill string was immediately lifted to engage the decoupling action of the CDS. The pressure and temperature sensors recorded 90-minute continuous dissipation curves. The tool was pulled out the formation via the wireline at Point 6 (Figure 3.3A).

At the end of the 90-minute recording period, the final temperature of 10.29 $^{\circ}$C was equilibrated with the formation (Figure 3.3). The situation is far less obvious for the pressures (Figures 3.3B). The tip pressure dissipated at a faster rate than the shaft at the early stage of the dissipation. At the end of the test, the shaft pressure drops more rapidly with time than the tip pressure. The end shaft pressure (15.20 MPa) was significantly higher than the end tip pressure (14.42 MPa), and both of them are higher than the hydrostatic pressure (u_h) at the deployment depth.

3.4 Analysis of Probe Penetration

3.4.1 Methodology

We use the SPM [*Baligh*, 1985] to explore the pore pressure response of T2P penetration in different soil types. The general approach has been previously presented for Fugro-McClelland's piezoprobe geometry, which is extremely close to that of the T2P [*Whittle, et al.*, 2001; *Long, et al.*, 2007a]. In the SPM, the flow pattern and strain history of each soil element are obtained by assuming inviscid and incompressible fluid flow around a stationary rigid penetrometer. Once the strain field is determined, we then apply the EPP soil model and the

MIT-T1 soil model to the strain path of each soil element to compute the stress changes due to penetration.

The pore pressure generated during penetration (Δu_i) is the sum of the pore pressure change that results from change in the octahedral normal total stress ($\Delta\sigma_{oct}$=$\Delta\sigma_{ij}/3$), and the shear-induced pore pressure (Δu_s) [*Levadoux and Baligh*, 1980; *Long, et al*, 2007a]:

$$\Delta u_i = \Delta u_{oct} + \Delta u_s = \Delta\sigma_{oct} + \Delta u_s \,. \tag{3.1}$$

The contribution to Δu_i from the Δu_s term is relatively small for soft cohesive clays and excess pore pressure changes are primarily due to changes in the octahedral normal total stress [*Randolph and Wroth*, 1979; *Teh and Houlsby*, 1991]. For simplicity and convenience, we neglect the shear-induced pore pressure in the EPP soil model. Later, we include the shear-induced pore pressure in the MIT-T1 soil model to show that this is a reasonable approximation.

The governing equation for the dissipation of the induced pore pressure is the uncoupled, linear consolidation equation derived from conservation of mass into and out of an element of porous material [*Lambe and Whitman*, 1969]

$$\frac{\partial \Delta u}{\partial t} = c\nabla^2 \Delta u \,, \tag{3.2}$$

where c is the hydraulic diffusivity of the sediments. We solve the consolidation equation using the ABAQUS^{TM} finite element code [*Long, et al.*, 2007a]. The solution is presented in dimensionless form where T, the time factor is

$$T = \frac{ct}{R_2^2} \,, \tag{3.3}$$

where R_2 is the radius of the T2P shaft.

3.4.2 Predictions from the EPP Soil Model

In the EPP soil model, the soil behaves elastically until shear stress exceeds the undrained shear strength (S_u), whereupon it deforms plastically (Figure 3.4A). The failure zone around the probe is bounded by the elastic-plastic boundary. The extent of the failure zone is related to the strain to failure (ε_f) or the undrained rigidity index, $I_r=G/S_u=1/\varepsilon_f$ (Figure 3.4A) [*Ladanyi*, 1963; *Randolph and Wroth*, 1979]. Excess pore pressures develop within the failure zone (Figure 3.5). With a lower value of ε_f (higher I_r), the failure zone extends further out, and a larger initial excess pore pressure field is generated (Figure 3.5). The extent of the failure zone controls the rate of dissipation. Thus lower values of ε_f (higher I_r) result in longer times for excess pore pressure to decay away (solid lines, Figure 3.6A).

As shown by *Whittle et al*., [2001] and *Long et al*., [2007a], we compare the pressure dissipation at the tip of the T2P to those generated by its needle probe and its overlying tapered shaft at the tip pressure port (inset figure, Figure 3.6B). If the strain to failure is small (I_r=640), insertion of the shaft alone results in an immediate increase in pore pressure at the tip location; the pore pressure remains constant in the early stage, then rises slightly with time to a peak pressure and finally dissipates (dashed line #2A, Figure 3.6B). If the strain to failure is large (I_r=176), the tip does not feel the installation of the shaft; instead the pore pressure rises with time to a peak pressure and then dissipates (dashed line #2B, Figure 3.6B). If only the needle probe is inserted, the initial pore pressure generated by the insertion progressively dissipates (dotted lines, Figure 3.6B).

The tip pressure dissipation of the T2P (solid lines, Figure 3.6B) initially follows that of the single needle probe (dotted lines, Figure 3.6B). This illustrates that the tip pressure dissipation in the early stage is largely decoupled from the effect of the penetration of the overlying tapered shaft. In later time, the tip pressure departs from the dissipation caused by the

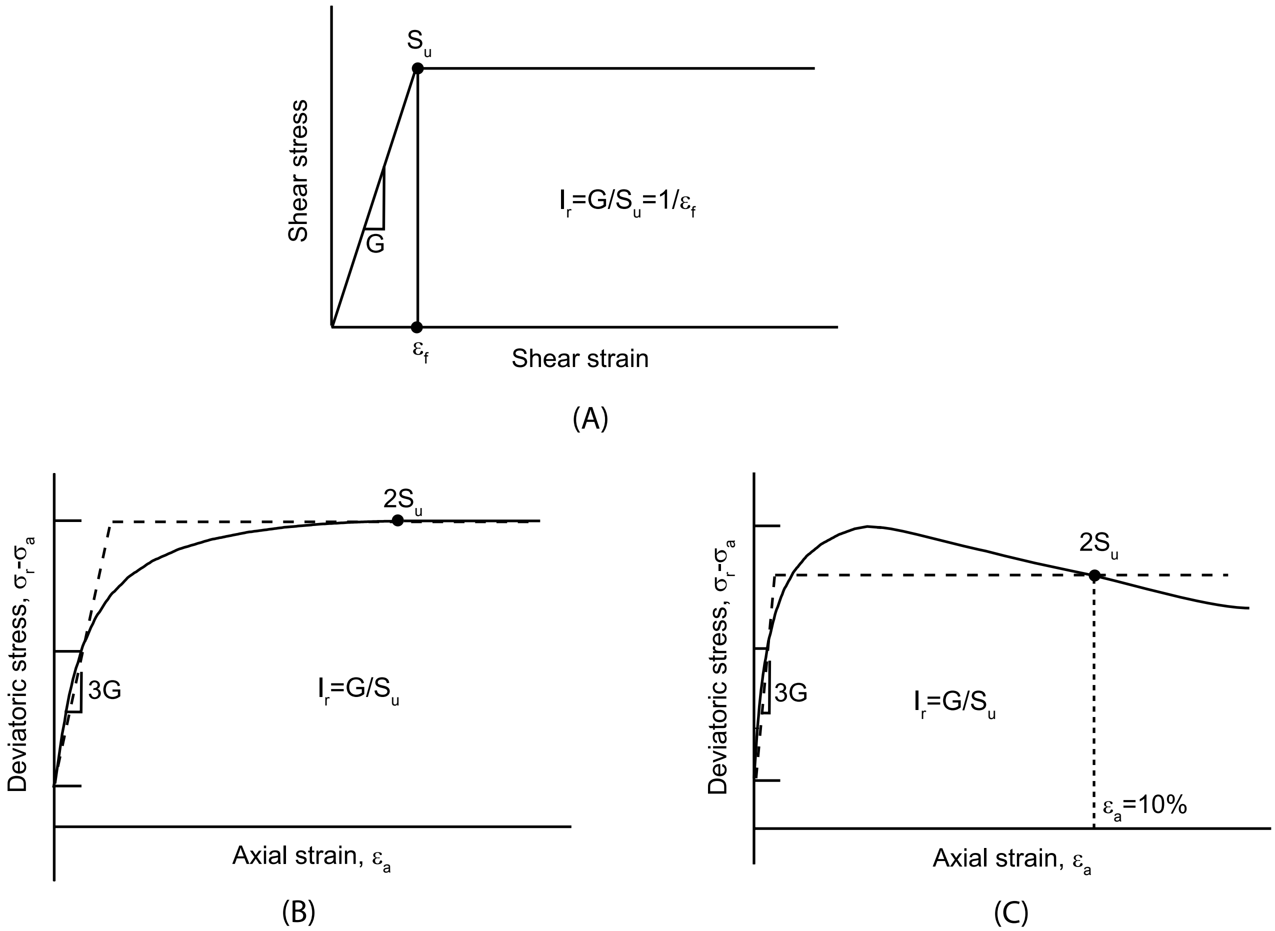

Figure 3.4: A) In an elastic-perfectly plastic (EPP) rheology, the shear stress increases linearly to the undrained failure strength (S_u), which occurs at a failure strain of ε_f. B) Solid line illustrates a typical strain-hardening response. We approximate this in an EPP model as follows. S_u is equal to the undrained peak shear strength and G is equal to the secant shear modulus evaluated at half way between the initial shear stress and the peak failure stress. C) Solid line illustrates a typical strain-softening response. We approximate this in an EPP model as follows. S_u is equal to the shear stress at 10% of axial strain and G is equal to the secant shear modulus evaluated at half way between the initial shear stress and the peak failure stress.

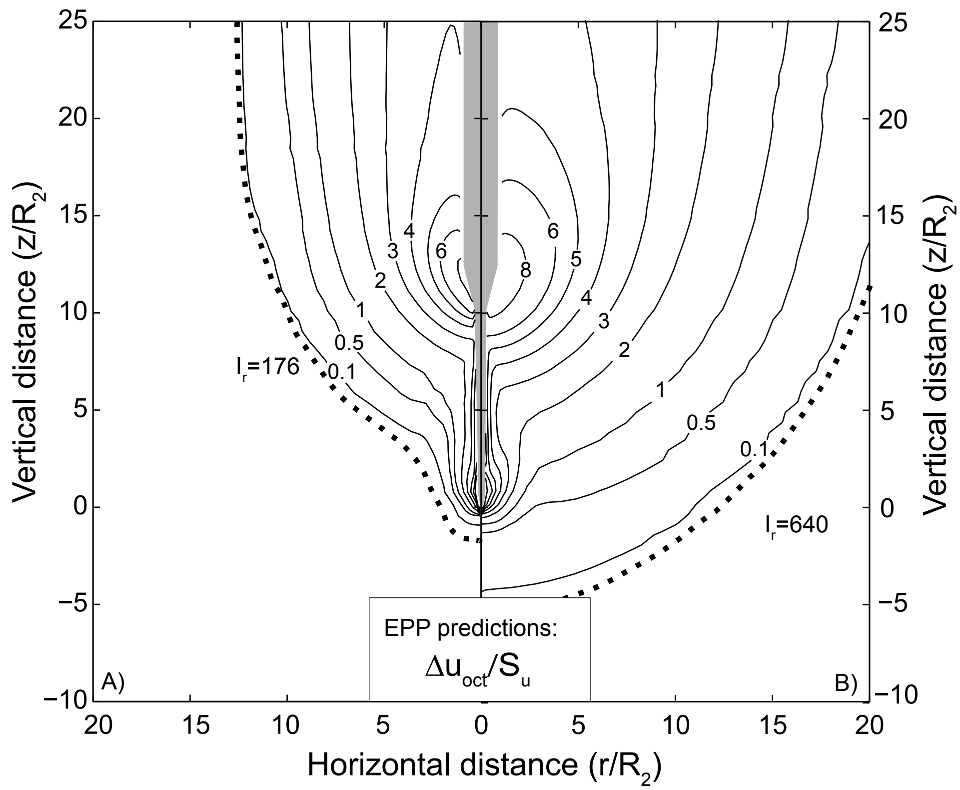

Figure 3.5: Initial excess pore pressure fields around the T2P predicted by EPP model. Left: Pressure field predicted for an I_r of 176. Right: pore pressure field predicted for an I_r =640. The dashed line marks the boundary of the failure zone. Shear-induced pore pressure is not included in this analysis (see text).

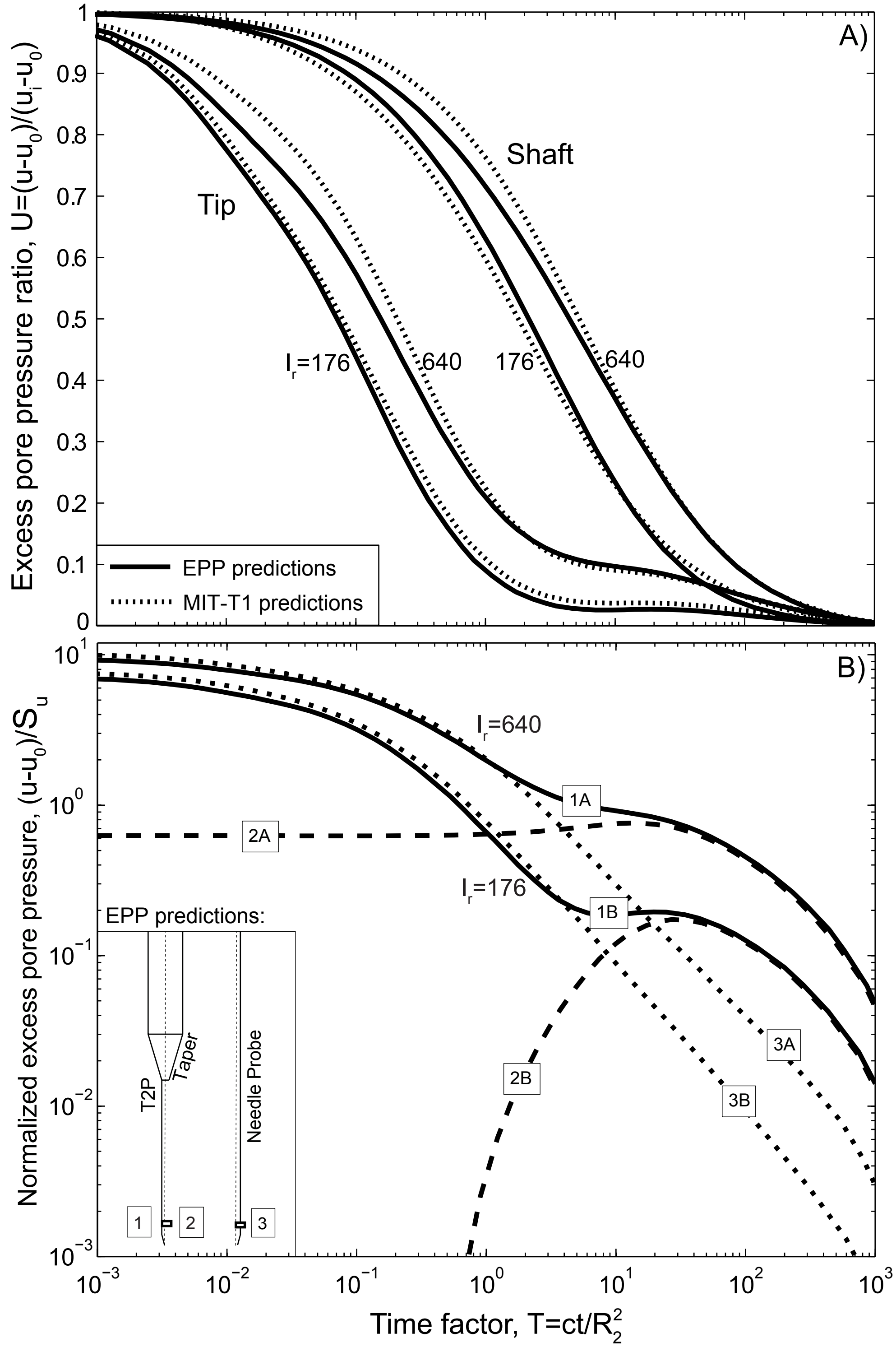

Figure 3.6: Pore pressure dissipation for soils with different I_r. A) Excess pore pressure ratio (U) plotted against time factor T. Solid lines represent the EPP model predictions and dotted lines represent the MIT-T1 predictions. B) Normalized excess pore pressure plotted against time factor T for EPP model predictions. Line #1A and Line #1B (solid line) record the dissipation response at tip of the T2P for I_r =176 and 640, respectively. Line #2A and Line #2B (dashed line) record the dissipation response of the overlying tapered shaft at location 2 (inset figure) for I_r = 176 and 640, respectively. Line #3A and #3B (dotted line) is the dissipation response of a constant diameter needle probe (R=3.2 mm), for I_r = 176 an d640, respectively. Dissipation at the tip of the tapered probe clearly follows the dissipation response of only the tip geometry in early time.

needle probe and follows the pressure caused by the overlying shaft (note how solid lines shift from dotted to dashed lines as time progresses, Figure 3.6B). The transition between pressure dissipation that is controlled by the needle probe to the dissipation driven by installation of the overlying shaft forms a “bench” on the tip dissipation curve (Figure 3.6A).

As illustrated in Figure 3.5, decreasing the strain to failure (increasing I_r) results in a larger volume around the probe where there is pore pressure generated during insertion. As shown in Figure 3.6A, the larger zone of influence of the probe results in a slower dissipation. *Teh and Houlsby*, [1991] proposed to normalize this behavior through a different time factor,

$$T^* = \frac{ct}{R_2^2\sqrt{I_r}}. \qquad (3.4)$$

This approach collapses the dissipation curves for I_r values ranging from 25 to 1000 (Figure 3.7).

The effect of decreasing the strain to failure is to install progressively higher pore pressures at the tip due to the overlying shaft. This results in a “bench” that increases with decreasing strain to failure (Figure 3.7). We take the excess pore pressure ratio at $T^*=0.5$ as a characteristic value (U_B) where the pressure pulse caused by the needle probe decays more than 99%. The EPP predictions indicate that values of U_B approximately linearly increase with I_r (open circles, Figure 3.8).

3.4.3 Predictions from the MIT-T1 Soil Model

We conducted a series of K_0-consolidated undrained (CK_0U) compression and extension tests on the intact whole core samples taken from IODP Expedition 308. An example of the measured stress-strain curve and shear-induced pore pressure for the compression test is illustrated in Figure 3.9. For the normally consolidated Ursa Clay (OCR=1), the initial shear stress under K_0-consolidation (no lateral strain) is 0.2 times the vertical effective stress (Figure 3.9A). Plastic deformation occurs at the very beginning of the deformation. The stress-strain

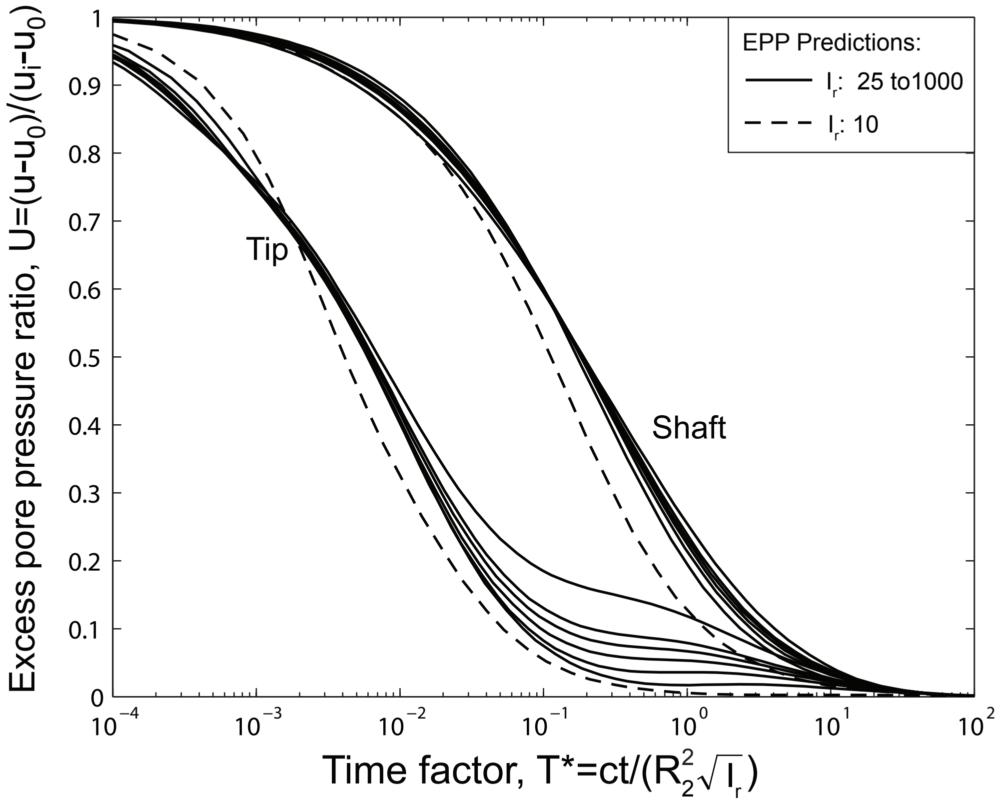

Figure 3.7: Excess pore pressure ratio plotted against time factor T^* for EPP model for increasing values of I_r.

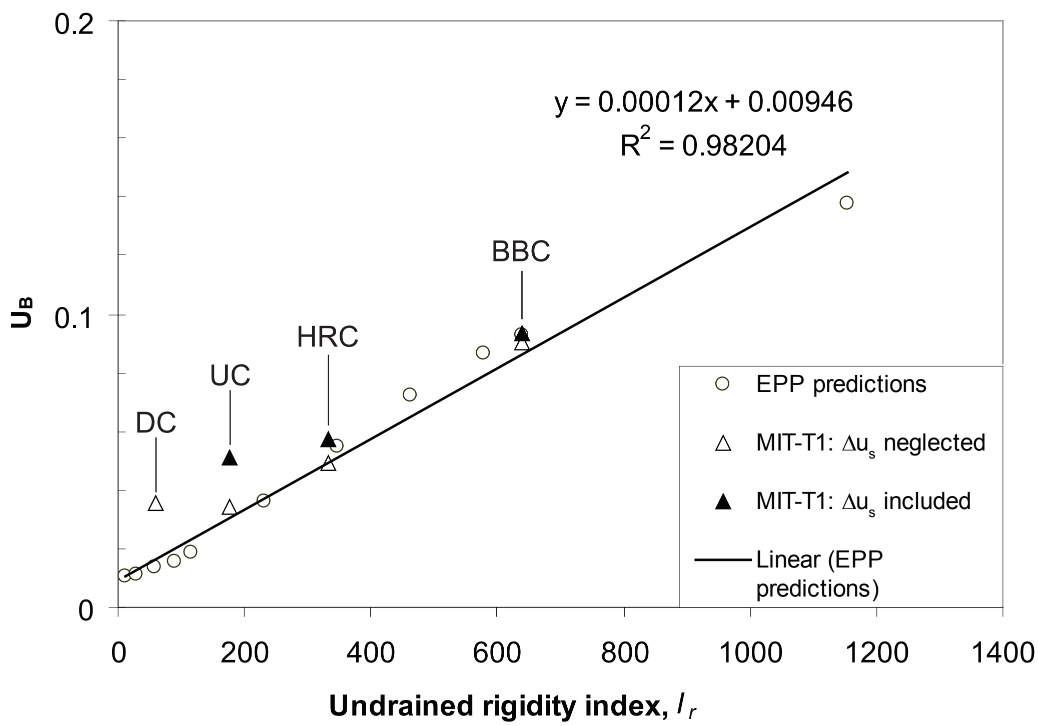

Figure 3.8: Prediction of the excess pore pressure ratio on the "bench" (U_B). The open circles represent the EPP predictions (excess pore pressure ratio was taken at T^*=0.5, Figure 3.7). Three normally consolidated clays and one overconsolidated clay are analyzed using MIT-T1 soil model (triangles): 1) the resedimented Boston Blue Clay (BBC(R), OCR=1, after Levadoux and Baligh, [1980]), 2) the resedimented Hydrate Ridge Clay (HRC(R), OCR=1, after Long et al., [2007a]), and 3) the Ursa Clay (UC, OCR=1), and 4) the Drammen Clay (DC, OCR=4, after Prévost, [1978]). OCR= overconsolidation ratio. Ir is determined based on stress-strain curves derived from experiment on the soil as described in Figure 3.4. No shear-induced pore pressure data and model are available for the DC.

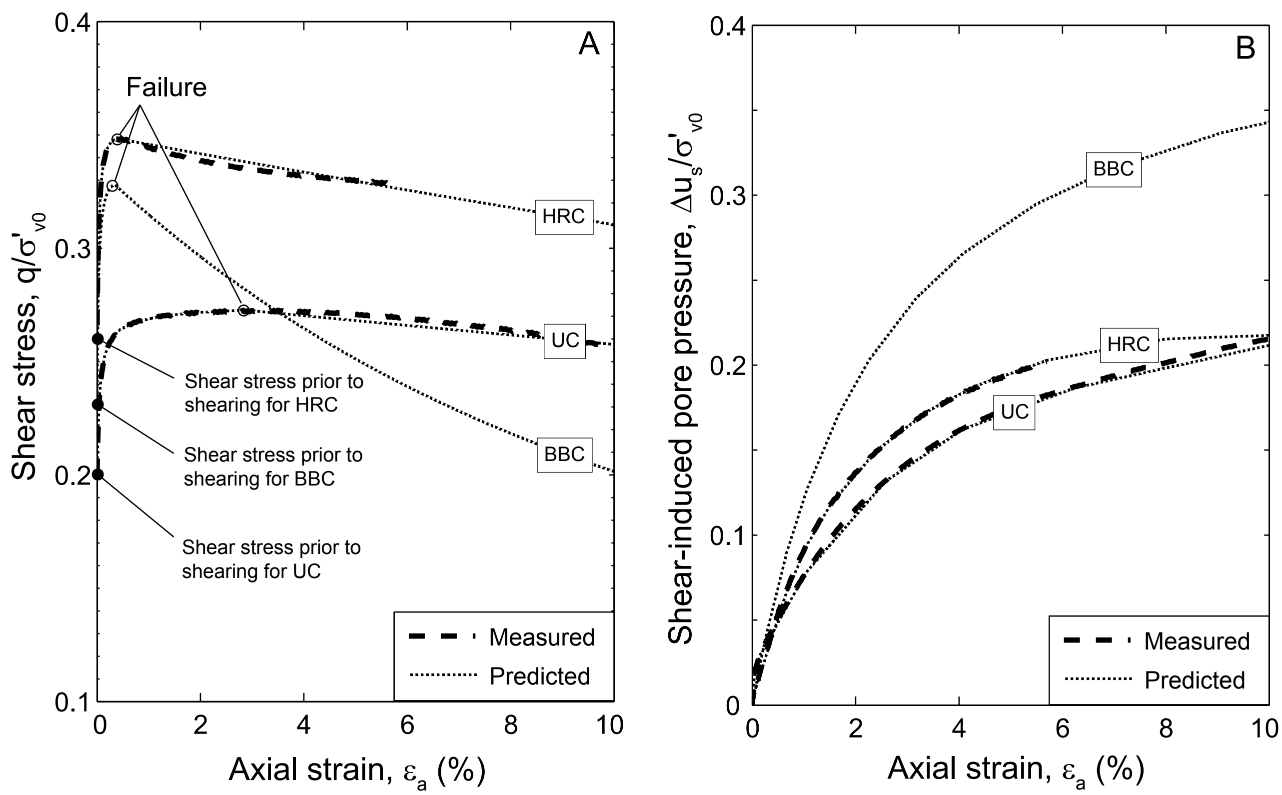

Figure 3.9: Data and predictions of K_0-consolidated undrained compression test. The dashed lines represent experimental data and the dotted lines represent predictions of the MIT-T1 model. A) The stress-strain curve derived from compression test. The tested Ursa clay was from whole core sample U1324D-2H-2WR, 72 mbsf. B) The shear-induced pore pressure for compression test.

curve prior to failure (the peak undrained shear strength) is nonlinear, and the post-failure deformation shows slight strain softening. During the undrained compression shearing, the shear-induced pore pressure nonlinearly increases with the axial strain (Figure 3.9B).

We built a full MIT-T1 soil model (Δu_s is included) for the Ursa Clay (UC) based on our best quality tests. The MIT-T1 model describes the exact stress-strain curve and the anisotropic properties of a real soil (Figure 3.9A). In the MIT-T1 model, Δu_s is modeled independently from the stress-strain curve as a function of the shear strain [*Levadoux and Baligh*, 1980]. The detailed input parameters of the MIT-T1 soil model are presented in Appendix 3.A.

We also plotted the undrained shearing behavior of the HRC and the BBC for comparison (Figure 3.9). The UC has much higher strain to failure (2.87%) than either the HRC (0.39%) or the BBC (0.33%) (Figure 3.9A). The UC also has less strain softening.

The MIT-T1 soil model predicts similar pressure dissipation behavior to those predicted by the EPP soil model (Figure 3.10). The tip pressure initially dissipates rapidly. As consolidation proceeds, the pressure decay is retarded and forms a “bench” on the dissipation curve. The UC has the highest value of strain to failure, and the pressure dissipation at both the tip and the shaft pressure ports are the fastest.

3.4.4 Comparing EPP and MIT-T1

We question whether a simplified stress-strain curve (Figure 3.4A) is sufficient to describe the initial excess pore pressure due to probe penetration and its subsequent dissipation. To answer that, it is essential to choose a proper way to define the input parameters for the EPP soil model: the shear modulus (G) and the undrained shear strength (S_u). Both are characterized by the undrained rigidity (I_r).

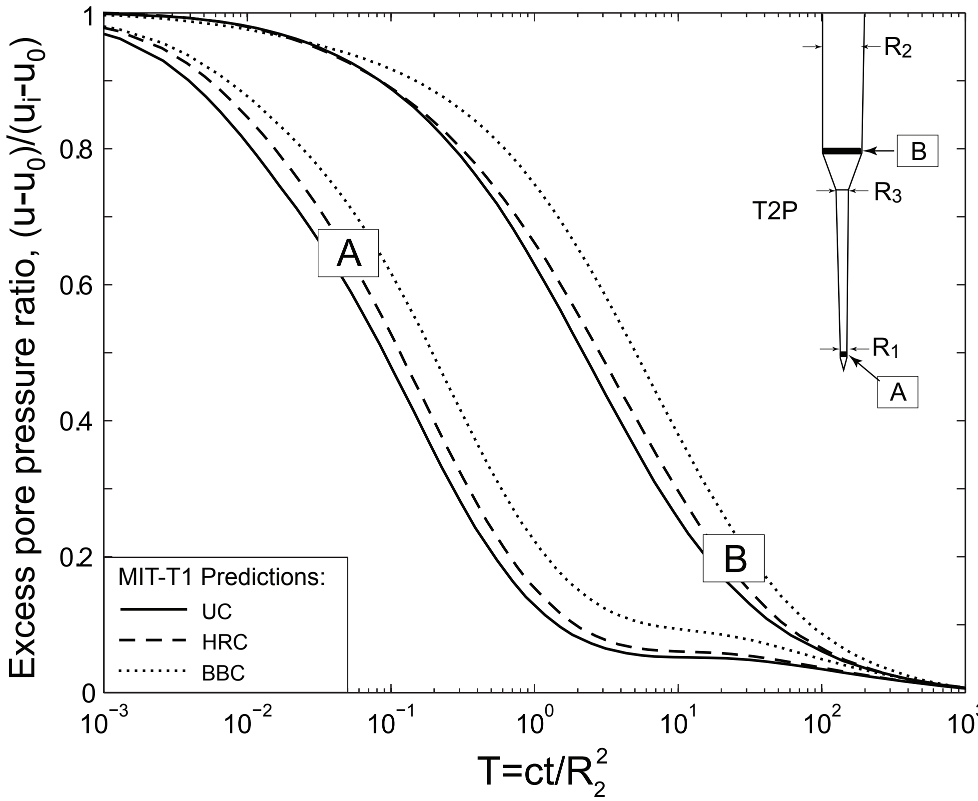

Figure 3.10: T2P pressure dissipation predicted at the tip (A) and Shaft (B) by full MIT-T1 soil model (Δu_S is included) for three soil types: UC = Ursa Clay (solid line); HRC = Hydrate Ridge Clay (dashed line), BBC = Boston Blue Clay (dotted line).

To obtain a characteristic I_r for a real soil, we use a similar approach to that proposed by [*Marsland and Randolph*, 1977] to define equivalent values of the G and S_u. We derive values of G and S_u using the stress-strain curve from a K_0-consolidated undrained compression (CK_0UC) test. For strain hardening material, S_u is equal to the peak shear strength and G is equal to the secant shear modulus evaluated at half way from the initial (in situ) shear stress to the peak shear strength (Figure 3.4B). For strain softening material, S_u will lie somewhere between the peak and ultimate values. In this study, we take the shear stress at 10% of axial strain as the value of S_u. G is equal to the secant shear modulus evaluated at half way from the initial (in situ) shear stress to the peak shear strength (Figure 3.4C).

With this definition of I_r, the UC has an I_r of 176 and the BBC has an I_r of 640. The initial excess pore pressure fields (Δu_{oct}) predicted by the MIT-T1 model are shown in Figure 3.11. The essential difference from the EPP predictions (Figure 3.5) is that the MIT-T1 model predicts significant excess pore pressure outside of the failure zone (Figure 3.11). This is because, in a MIT-T1 soil model, plastic deformation occurs at the very beginning of the deformation. Change in the mean total stresses is not equal to zero even through the volume strain is zero for an undrained penetration. In addition, the initial pressure fields are significantly different in the zone far above the tapered shaft due to the strain softening effect described by the MIT-T1 model (Figure 3.5 vs. 3.11). However, in an average sense, the EPP model predicts similar initial excess pore pressure fields to the MIT-T1 model. The value of I_r provides a good constraint on the extent of the zone where significant excess pore pressures develop. The dissipation curves predicted from the EPP model are close to those from the MIT-T1 model particularly for the long term dissipation (Figure 3.6A).

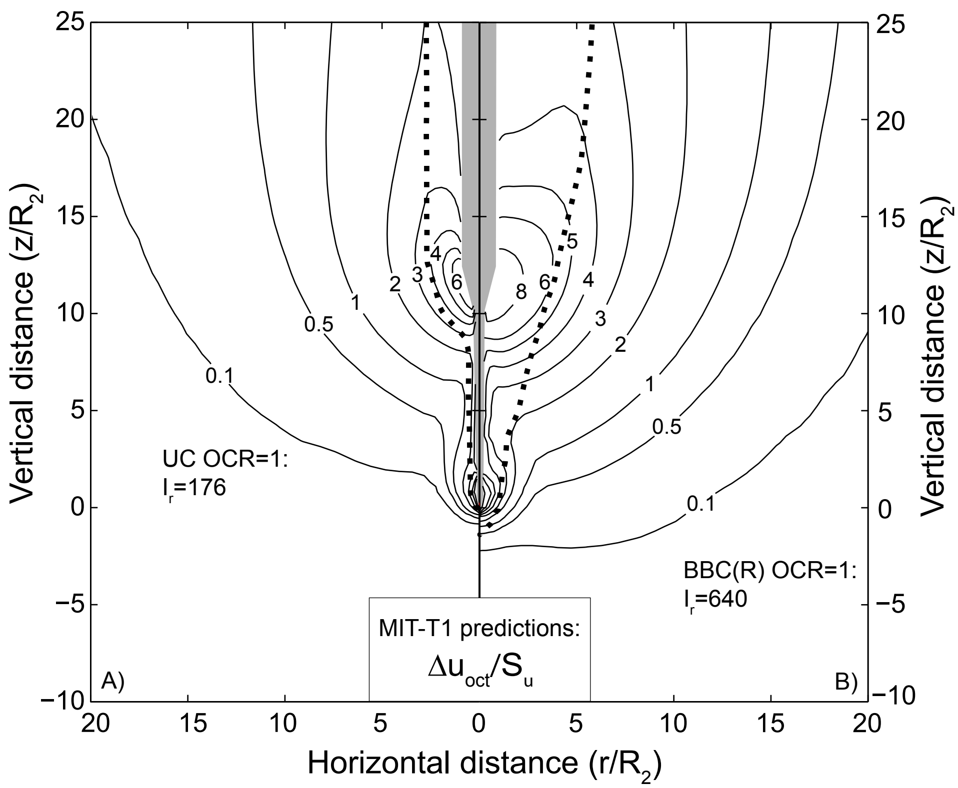

Figure 3.11: Initial excess pore pressure fields around the T2P predicted by the MIT-T1 model (Δu_S is neglected) for the Ursa Clay (UC) (left) and the Boston Blue Clay (BBC), right. The stress strain behavior for these soils is described in Figure 3.9. Inside the dashed line, failure has occurred and shear stress has exceeded the peak shear strength illustrated in Figure 3.9A. I_r values for the Ursa Clay and the Boston Blue Clay are calculated according to the method illustrated in Figure 3.4.

The dissipation curves predicted by the MIT-T1 model (Δu_s neglected) for different soils cannot be generally unified with time factor T^* (Figure 3.12) whereas they fall into a narrow band around the unified EPP dissipation curve. The time factors T^* at 50% of dissipation for the analyzed soils are shown in Table 3.1.

The MIT-T1 model predicts similar U_B to that of the EPP model at a given I_r for normally consolidated clays whereas the overconsolidated DC does not fall on the trendline of the EPP predictions (Figure 3.8). More soils may need to be analyzed to confirm this behavior.

3.4.5 Effect of Shear-Induced Pore Pressure

The relative contribution of the shear-induced pore pressure (Δu_s) depends on the strain path (deformation mode) and the type of the soil. It is relatively small for probe penetration in soft cohesive clays [*Teh and Houlsby*, 1991]. We use the MIT-T1 soil model to examine the effect of Δu_s on the excess pore pressure dissipation for different soils. Δu_s affects the time to reach 50% dissipation (T_{50}) by less than twenty percent for the three analyzed soils (Table 3.2). This is a small effect in the sense of hydraulic diffusivity measurements. The influence of Δu_s on T_{50} decreases with the increase of I_r, and it either delays (high I_r) or hastens (low I_r) the time to reach 50% dissipation by excluding Δu_s. This can be explained by the relative magnitude and dissipation rate of the Δu_{oct} and Δu_s. Generally, for soil with higher I_r, Δu_{oct} has greater magnitude, is distributed in a broader zone (Figure 3.11), and decays at a slower rate.

The value of U_B is elevated with the contribution of Δu_s. The influence of Δu_s on the value of U_B also decreases with the increase of I_r. For sediments with high I_r, Δu_s has negligible effect (Table 3.2 and Figure 3.8).

3.5 Interpretation of Partial Pressure Records

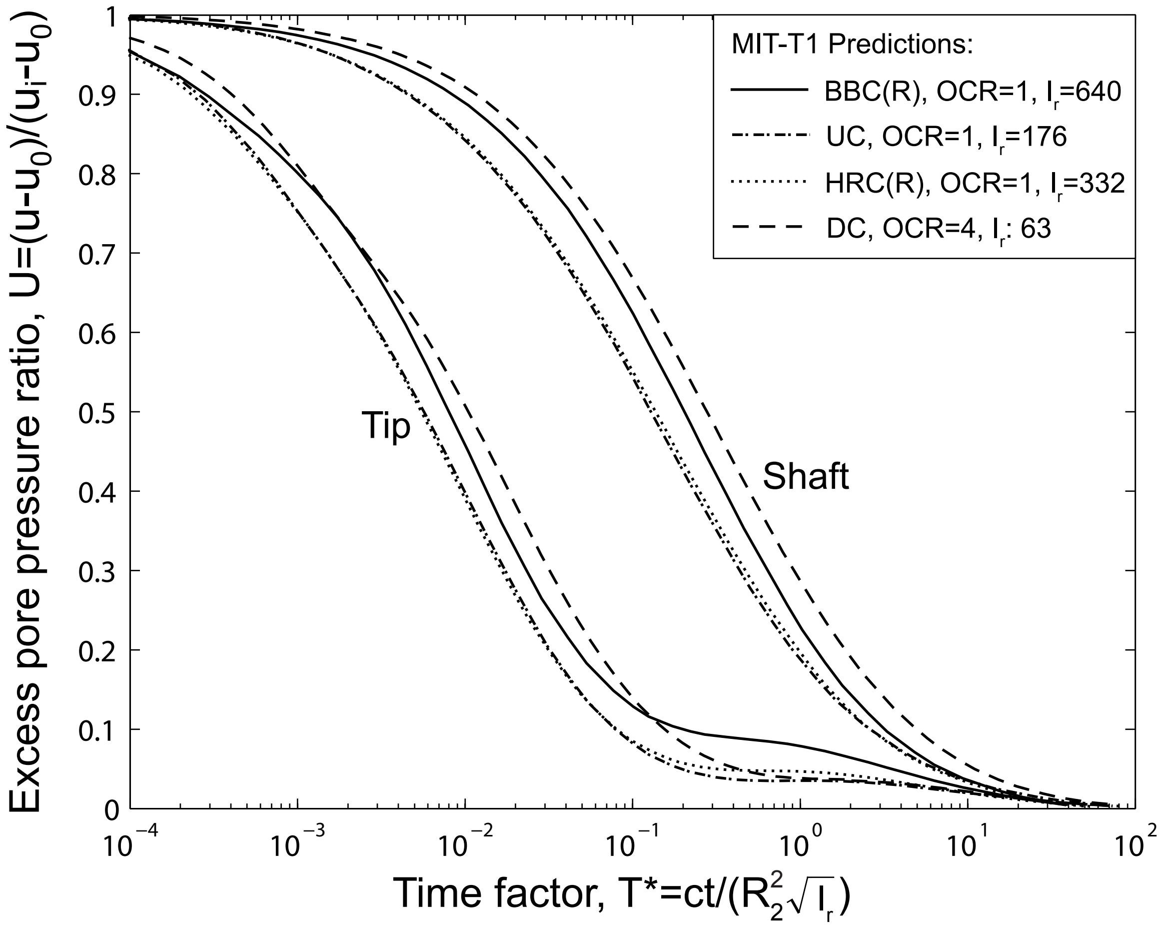

Figure 3.12: Pressure dissipation predicted by the MIT-T1 model (Δu_S is neglected). Excess pore pressure ratio (*U*) is plotted against modified time factor *T**. BBC=Boston Blue Clay, UC=Ursa Clay, HRC=Hydrate Ridge Clay, DC= Drammen Clay. OCR= overconsolidation ratio. I_r values are calculated according to the method illustrated in Figure 3.4.

Table 3.1. Modified Time Factor at 50% of Dissipation

	I_r	T^*_{50} (Tip)	T^*_{50} (Shaft)
EPP predictions	25-1000	0.007-0.008	0.17-0.20
BBC(R), OCR=1	640	0.008	0.211
HRC(R), OCR=1	332	0.006	0.142
DC, OCR=4	63	0.011	0.282
UC, OCR=1	176	0.006	0.132

Table 3.2. Effect of the Shear-Induced Pore Pressure Based on MIT-T1 Predictions

	I_r	U_B ($\Delta u_{oct}+\Delta u_s$)	U_B (Δu_{oct})	T_{50} ($\Delta u_{oct}+\Delta u_s$)	T_{50} (Δu_{oct})
BBC(R), OCR=1	640	0.093	0.091	0.195[1] 5.103[2]	0.210 5.331
HRC(R), OCR=1	332	0.058	0.049	0.116 2.842	0.103 2.587
UC, OCR=1	176	0.051	0.034	0.089 2.180	0.078 1.757

[1] for tip pressure port; [2] for shaft pressure port.

Certain types of inverse time extrapolation are commonly used to interpret in situ pressure from penetrometer data that record only partial dissipation [*Davis, et al.*, 1991; *Fang, et al.*, 1993; *Whittle, et al.*, 2001; *Lim, et al.*, 2006; *Long, et al.*, 2007b]. Unfortunately, there is no theoretical foundation to these approaches. Based on SPM analysis on the BBC, *Whittle et al.*, [2001] proposed a two-point matching method to estimate the in situ pore pressure from partial dissipation records of a tapered penetrometer with two pressure ports. *Long et al.*, [2007a] proposed to estimate the in situ pore pressure using the "bench" feature on the tip pressure dissipation curve of a tapered penetrometer. Analyses of our model results suggest that the concurrent pressure dissipation state can be determined by comparing the dissipated pressures at the tip and shaft pressure ports. This allows the in situ pore pressure to be estimated within a very short monitoring time. We will use the full MIT-T1 prediction for the Ursa clay (with Δu_s included) and one of our best T2P deployments to evaluate the capability of the four techniques.

3.5.1 The New Approach

Figure 3.13A is a different display of the full MIT-T1 model prediction for the UC (solid lines, Figure 3.10). We compute the dissipated pressure at the tip and the shaft pressure ports, and plot the concurrent excess pore pressure ratios against the ratio of the dissipated pressures at the tip and shaft. Our results suggest that the concurrent pressure dissipation state of the tip and shaft pressures can be determined by this ratio (Figure 3.13A). Figure 3.6 suggests that the pressure dissipations at the tip and the shaft pressure ports of the T2P are primarily controlled by the radius of the probe at the pressure ports. For a single diameter probe, pressure dissipation is only a function of its radius provided that the penetrated sediment is the same. This approach is essentially determining the dissipation state by comparing the decay rates of two constant diameter probes.

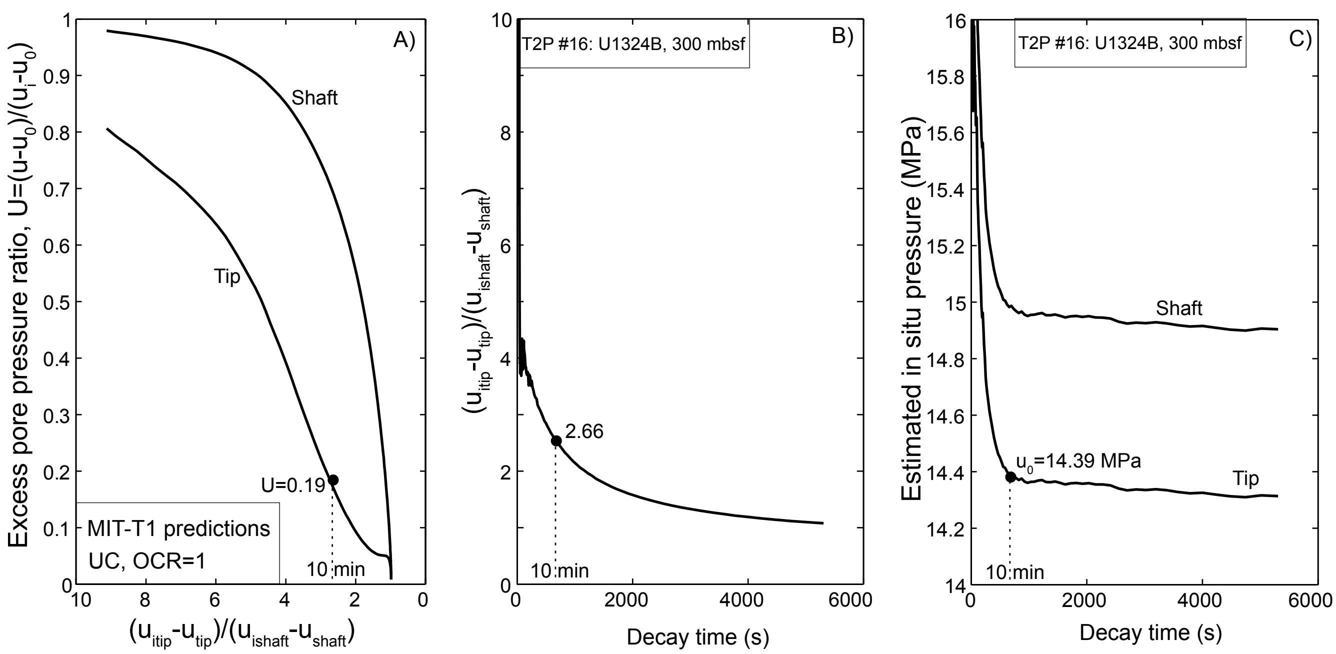

Figure 3.13: Estimating in situ pressure from the ratio of dissipated pressures at the tip and shaft pressure ports. A) Excess Pore Pressure (*U*) vs. the ratio of the total dissipation at the tip and the shaft. These results are derived directly from the full MIT-T1 model for the Ursa Clay (Figure 3.10, solid line). As time increases, the excess pore pressure declines and the fractional dissipation becomes equal at the tip and shaft. B) The ratio of total dissipation at the tip and shaft vs. time for T2P deployment 16. C) Estimated in situ pressure calculated from Equation 3.5.

For T2P deployment 16, we calculated the dissipated pressures at the tip and the shaft pressure ports and used the ratio of them to find out the excess pore pressure ratio at any given time from the model prediction (Figure 3.13A). We then estimate the in situ pressure (u_0) using the following relationship:

$$u_0 = u_i - \left(\frac{u_i - u}{1-U}\right) = u_i\left(\frac{-U}{1-U}\right) + \frac{u}{1-U}, \tag{3.5}$$

where u_i is the initial pore pressure, u is the current pressure and U is the excess pore pressure ratio at the current time.

The estimated u_0 from the dissipation state of the tip and the shaft pressures are stabilized approximately 10 minutes after penetration (Figures 3.13B). The estimations from the tip pressure are slightly lower than its last recorded value (Figure 3.3) and appear to be reasonable values. The u_0 estimated from the shaft pressure is unreliable as it is even higher than the last recorded tip pressure (Figure 3.3). We interpret the error in the estimated u_0 at early time (<10 minutes) and at the shaft pressure port is mainly because the tool did not record correct initial pressures.

It is very difficult to accurately measure the initial pore pressure due to: 1) inherent soil variability causing the recorded value at the beginning of dissipation to be different from the relevant (average) value u_i (Figure 3.3) [*Levadoux and Baligh*, 1986]; and 2) high system compliance or low permeability of the clay causing a time lag in the measurements [*Cauble*, 1996].

Rearranging Equation 3.5, the error in the estimated in situ pressure (δu_0) can be expressed as a function of the error in the recorded initial pore pressure (δu_i)

$$\delta u_0 = \delta u_i\left(\frac{-U}{1-U}\right). \tag{3.6}$$

δu_i will be magnified where U is greater than 0.5 (early stage dissipation) and result in bigger δu_0. Instead, δu_i will be minimized where U is less than 0.5 (late stage dissipation) and result in smaller δu_0. Overall, δu_0 given by Equation 3.6 decreases from a larger value rapidly in the early dissipation stage and then decreases at slower rates at much lower values in the late time (Figure 3.13B). The shaft pressure decayed much less than the tip pressure relative to their initial values within the monitoring time, and thus had greater U than the tip pressure and provided less accurate estimate of u_0. In addition, δu_i will result in errors in the calculation of the ratio of the dissipated pressure at the tip and the shaft pressure ports, and thus in the estimated values of U. This effect is also more significant at the early stage pressure dissipation (Equation 3.5).

The hydraulic diffusivity of the formation can be estimated independently from the in situ pressure by comparing the measured and modeled ratios of the dissipated pressures at the tip and shaft (Figure 3.14A). The best fit gives a value of $4\text{x}10^{-7}$ m^2/s (Figure 3.14A). Take this value and the in situ pressure estimated from the tip pressure at 90 minutes after penetration (14.31 MPa, Table 3.3), we normalized the recorded pressure data and plotted them together with the predicted dissipation curves. We found difficulty in achieving a good match for the pressure dissipations in the early dissipation stage (Figure 3.14B). We interpret that is due to the error in the initial pressure (δu_i) recorded by the T2P. The δu_i can significantly change the shape of the early part of the dissipation curve whereas its influence on the later part of the dissipation curve is insignificant (Figure 3.15).

This approach determines the dissipation state by comparing the pressure decays of two constant diameter probes. It could be extended to a constant diameter probe for which the dissipation state can be determined by comparing the dissipated pressures at different decay times (Figure 3.16A). We calculated the dissipated pressures at two different times with (t_2=$2t_1$),

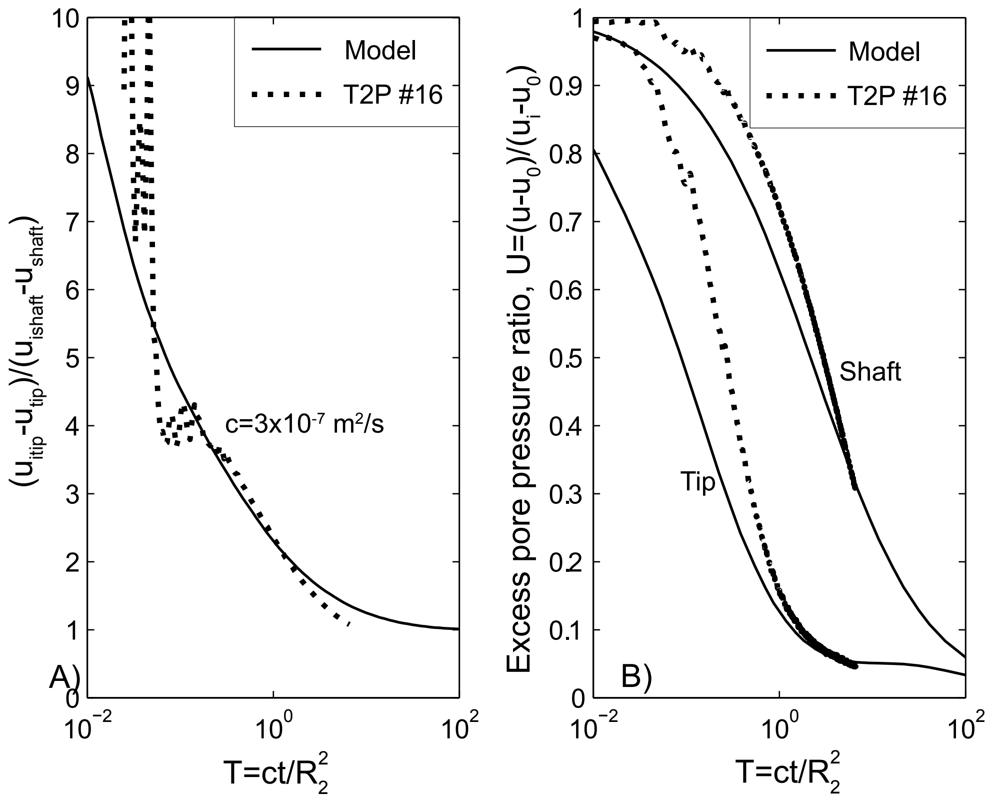

Figure 3.14: Interpretation of hydraulic diffusivity. The solid lines represent modeled behavior by full MIT-T1 soil model for the Ursa Clay (Figure 3.10, solid line). The dotted lines represent the measured data. A) Determining the hydraulic diffusivity by curve matching. B) Comparison of predicted and measured dissipation behavior.

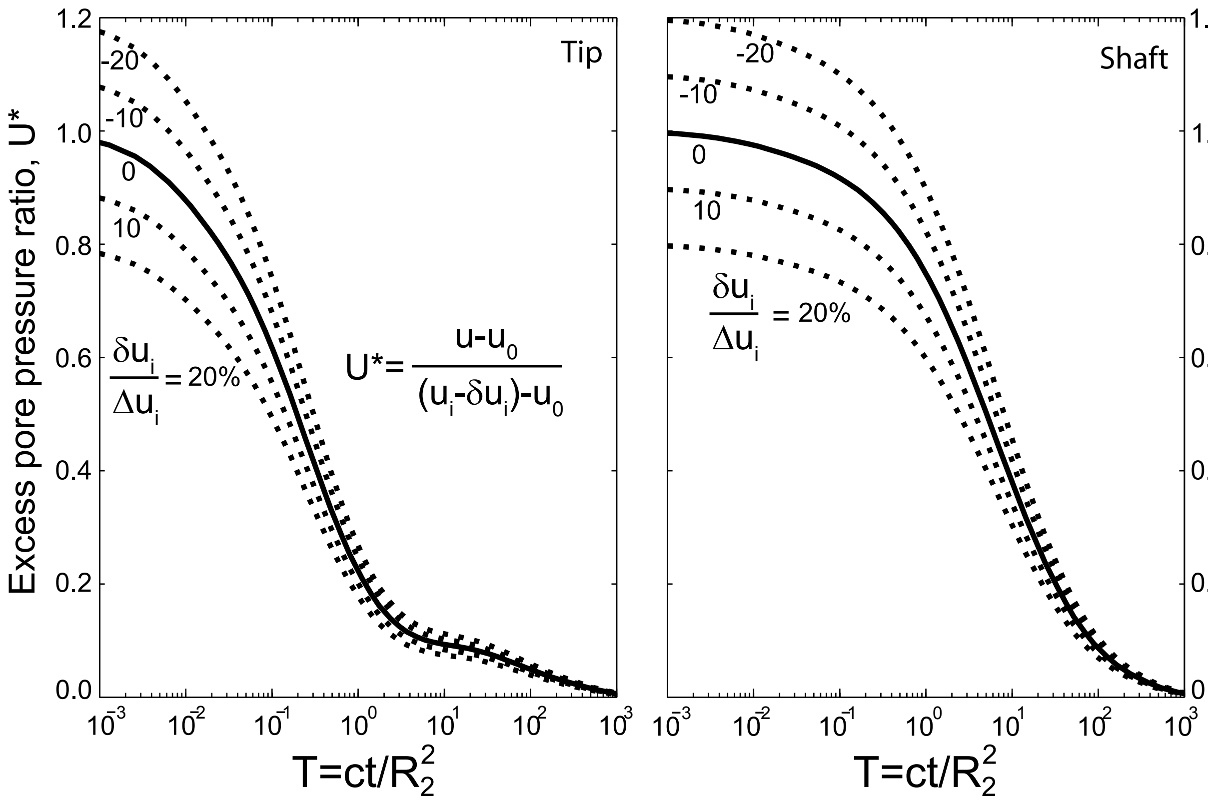

Figure 3.15: Effect of the error in the initial excess pore pressure on the dissipation curve. The solid lines represent modeled behavior by full MIT-T1 soil model for the Boston Blue Clay (Figure 3.10, dotted line). "Apparent" dissipation curves (dotted lines) are given for $\delta u_i/\Delta u_i$ =20, 10, -10 and -20%.

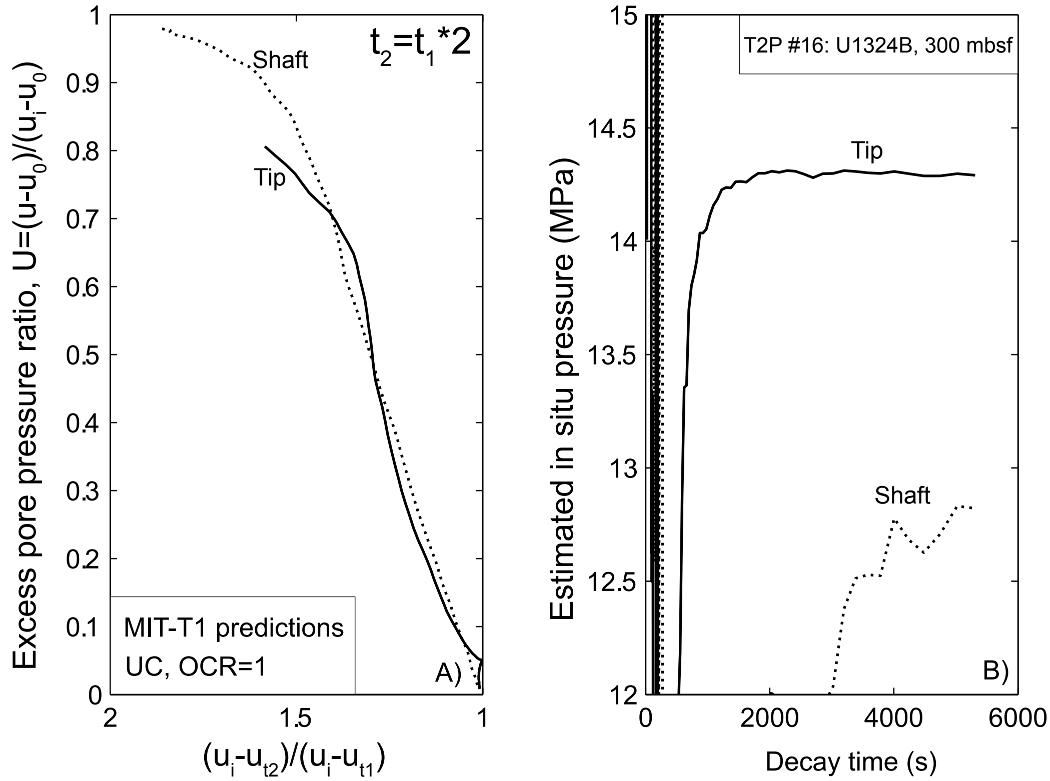

Figure 3.16: Estimating in situ pressure from the ratio of dissipated pressures at two different times (t_2=2t_1). A) Excess Pore Pressure (U) vs. the ratio of the total dissipation at time t_2 and time t_1. These results are derived directly from the full MIT-T1 model for the Ursa Clay (Figure 3.10, solid line). B) Estimated in situ pressure calculated from Equation 3.5.

Table 3.3. Estimated in situ pressure from T2P #16, U1324B 300 mbsf

	New approach	Bench (model)	Bench (I_r)	1/t	$1/\sqrt{t}$	σ'_{vh} (MPa)
Overpressure	0.77[1] 0.69[3]	0.84[2] 0.69[3]	0.87[2] 0.72[3]	0.76[4] 0.90[5]	72[4] 0.23[5]	2.44

[1] estimation from tip pressure at 10 minutes after penetration,
[2] estimation from tip pressure at 20 minutes after penetration,
[3] estimation from tip pressure at 90 minutes after penetration,
[4] estimation from tip pressure using extrapolation approaches,
[5] estimation from shaft pressure using extrapolation approaches.

used the ratio of them to find out the excess pore pressure ratio for the tip and shaft pressures from the model prediction (Figure 3. 16A), and then estimate the in situ pressure using Equation 3.5. The estimated u_0 from the dissipation state of the tip is stabilized approximately 20 minutes after penetration (Figures 3.16B) or twice as long as the two diameter approach. The estimate u_0 is 14.29 MPa at 90 minutes after penetration. The u_0 estimated from the shaft pressure is unreliable as it is even lower than hydrostatic pressure.

3.5.2 The "Bench" Approach

Comparison of Figure 3.17A and Figure 3.6B indicates that the tip pressure was going towards the dissipation of the overlying tapered shaft at the end of the deployment. This suggests that the last recorded tip pressure lies on the "bench". The full MIT-T1 model predicts U_B is 0.05 for T2P penetration in the Ursa clay. We take the last recorded tip pressure as the characterized value on the "bench". The in situ pressure is estimated using a similar relationship to Equation 3.5 as 14.31 MPa.

In many cases there are insufficient resources to pursue soil modeling. In situ pressure can be inferred from the predicted relationship in Figure 3.8 provided I_r is known. The Ursa clay has an I_r of 176. The estimated U_B is 0.031 and the in situ pressure is 14.35 MPa (Table 3.3).

Accuracy of this approach is also subject to the error in the recorded u_i, whereas, the effect is limited because U_B is less than 0.2 for most of the soils (Figure 3.8 and Equation 3.5). In addition, it is impossible to locate a pressure point on the field data that exactly matches the time where U_B is determined. We assume the tip pressure reached the "bench" at 20 and 90 minutes after the penetration. They provide very similar in situ pressure estimations (Table 3.3).

3.5.3 Two-Point Matching Approach

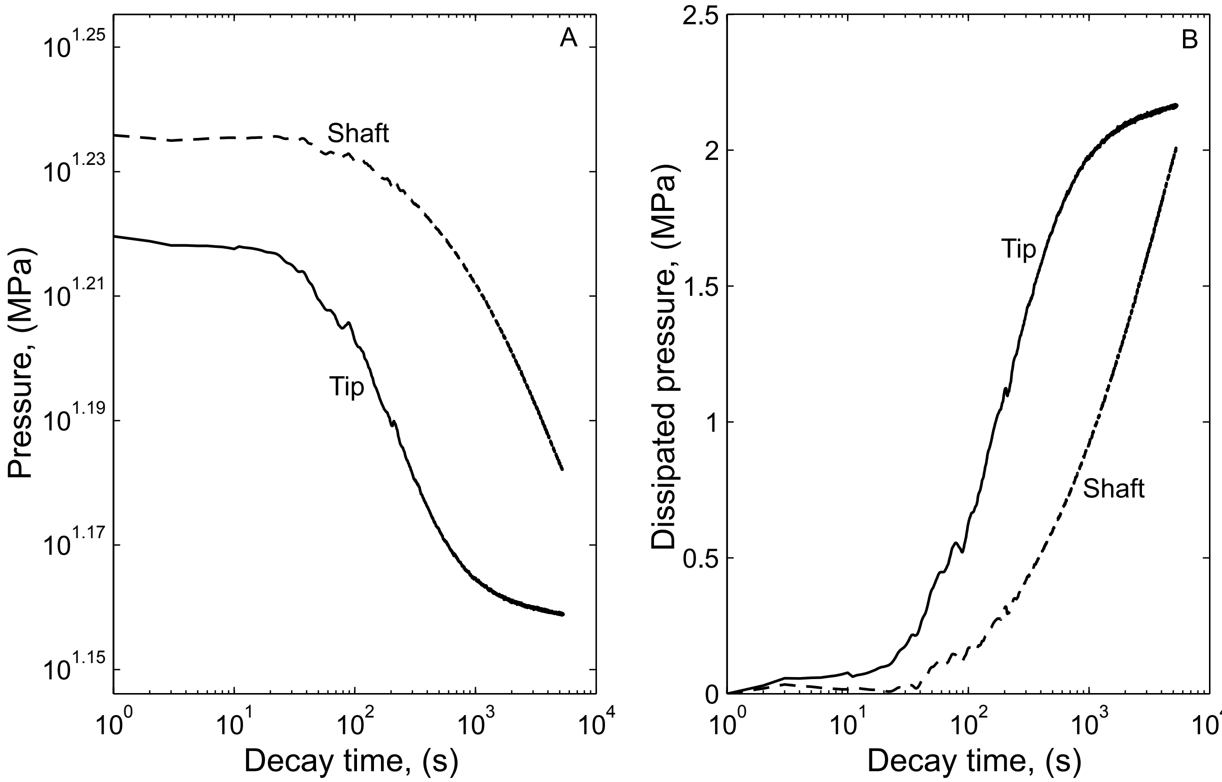

Figure 3.17: Dissipation phase of T2P deployment #16. A) A log-log plot of the dissipation phase. B) Dissipated pressure plotted against the log of time.

Whittle et al., [*2001*] proposed a two-point matching method to estimate the in situ pressure from partial dissipation records of a tapered penetrometer with two pressure ports. One can define a characteristic intersection point where the dissipated pore pressures are identical for the tip and shaft pressures of the T2P. This intersection point corresponds to a reference point on the predicted dissipation curve at the tip. Provided the intersection point is observed, in situ pressure can be estimated using a relationship similar to Equation 3.5.

For T2P deployment 16, we plot the dissipated pressures at the tip and shaft respectively against the log of time (Figure 3.17B). The two curves did not intersect yet at the end of the deployment. Thus the two-point matching approach cannot be applied to estimating the in situ pressure for this deployment.

3.5.4 Empirical Extrapolation

If soil properties are not available, in situ pressure may be inferred from some type of inverse time extrapolation approaches. We use the full MIT-T1 predictions for the UC, vary the dissipation time factor (T) and estimate the error ($\delta u_0/\Delta u_i$) for two extrapolation approaches: $1/t$ and $1/\sqrt{t}$ (Figure 3.18). With dissipation degree less than 80%, the error of the $1/t$ extrapolation is larger than that of the $1/\sqrt{t}$ extrapolation for both pressure ports. After 80% dissipation, the two approaches yields errors of similar magnitude (Figure 3.18A). The $1/\sqrt{t}$ extrapolation underpredicts the in situ pressure at more than 70% dissipation, while the $1/t$ extrapolation overpredicts the in situ value (Figure 3.18A). The error for the tip of the T2P reaches a local maximum at 95% dissipation for both approaches. This reflects the retardation of dissipation at the tip due to the influence of the overlying tapered shaft of the T2P. We also illustrate the error as a function of the dissipation time factor, T (Figure 3.18B). To achieve an

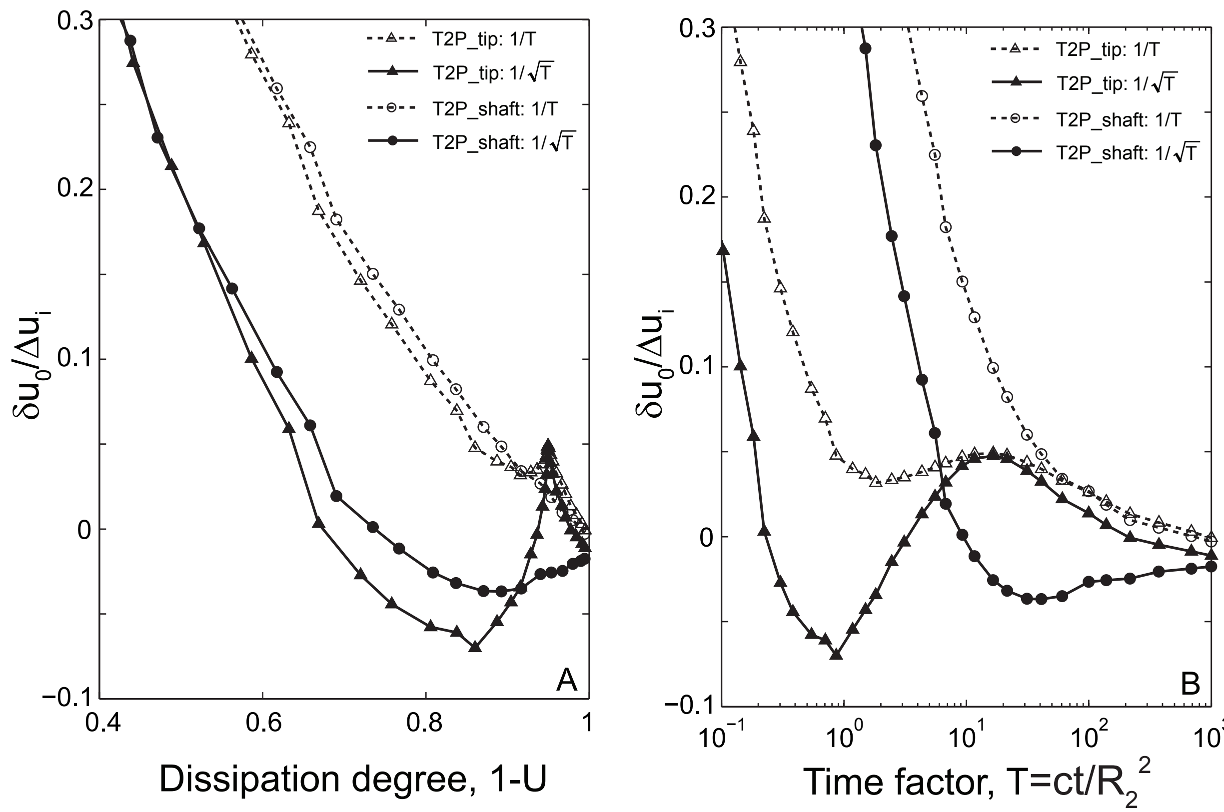

Figure 3.18: Theoretical prediction of errors in estimating u_0 by $1/t$ and $1/\sqrt{t}$ extrapolations. Full MIT-T1 predictions for the Ursa clay are used (Figure 3.8). A) Errors as a function of dissipation degree. B) Error as a function of dissipation time factor (T).

error of 5% of the installation pressure, the $1/\sqrt{t}$ extrapolation needs much less monitoring time than the $1/t$ extrapolation.

Figure 3.19 plots the pressure data beyond 625 seconds for T2P Deployment #16. We used the pressure data recorded in the last 5-minute before the tool was pullout to project the in situ pressure. The $1/t$ extrapolation provides an in situ pressure of 14.38 MPa at the tip and 14.52 MPa at the shaft (Figure 3.19A). The $1/\sqrt{t}$ extrapolation gives 14.34 MPa at the tip and 13.85 MPa at the shaft (Figure 3.19B).

For this 90-minute T2P deployment, all approaches predict similar in situ pressure at the tip of T2P (Table 3.3). The overpressure is approximately 28% of the difference between the overburden stress and hydrostatic pressure at 300 mbsf at Site U1324.

3.6 Discussion

We proposed a new approach that uses the ratio of dissipated pressures at the tip and shaft of a tapered probe to estimate in situ pressure from partial dissipation records. This approach determines the dissipation state by comparing the decay rates of two constant diameter probes. It could be used with a constant diameter probe for which the dissipation state can be determined by comparing the dissipated pressures at different decay times. However, it takes twice as long as the two diameter approach for the in situ pressure estimates to be stabilized. Error in the recorded initial pore pressure could significantly affect its accuracy particularly when the excess pore pressure ratio is greater than 0.5. Relationships showed in Figure 3.13A cannot be satisfactorily unified using the time factor T^*. This implies that exact dissipation curves are necessary to apply this approach.

In contrast, the "bench" feature provides a reliable and robust way to estimate the in situ pressure from partial dissipation data. Time needed to reach the "bench" is generally short, and

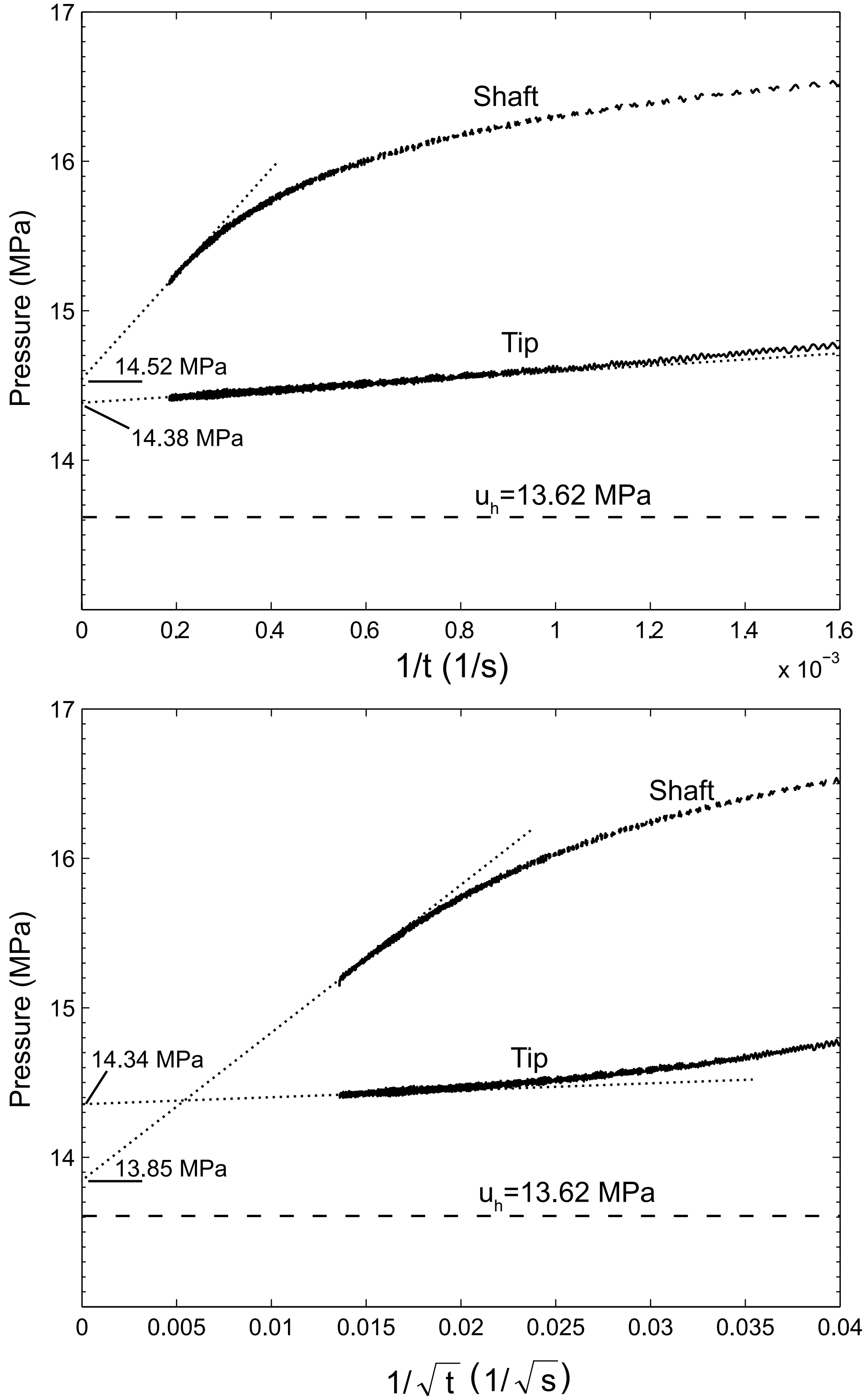

Figure 3.19: Estimating in situ pressure by 1/*t* and $1/\sqrt{t}$ extrapolations. A) Pressure dissipation plotted on inverse time (1/*t*). A trend line is fit linearly to the last 5-minute dissipation data and projected to infinite time. B) Pressure dissipation plotted on inverse square root of time ($1/\sqrt{t}$). A trend line is fit linearly to the last 5-minute dissipation data and projected to infinite time.

the excess pore pressure ratio on the "bench" (U_B) can be estimated from a single parameter, undrained rigidity index (I_r). I_r can be determined from the stress-stain curves of a CK_0UC test using the proposed definition. In practice, I_r may be estimated from routine soil parameters. *Keaveny and Mitchell*, [1986] proposed an empirical relationship to estimate I_r from the plastic index and OCR. One should notice that in their approach I_r is the ratio of shear modulus at 50% to failure over the peak undrained shear strength. For strain softening material, the value of I_r must be adjusted to account for the different shear strength definitions before use it to estimate U_B. The error in u_i has limited effect on the "bench" approach as the tip pressure dissipates more than 80% on the "bench" for most materials. Our analyses show that a low vertical hydraulic diffusivity will delay the occurrence of the "bench" but the value of U_B does not change much with increased anisotropic hydraulic diffusivity ratio (Figure 3.20).

The two-point matching approach generally needs longer monitoring time than the "bench" approach. The EPP model predicts that the time needed to reach the intersection point increases with I_r (open circles, Figure 3.21). The MIT-T1 predictions (open triangles, Figure 3.21) do not fall on the trend of the EPP predictions. And the shear-induced pore pressure may significantly alter the intersection time for certain soils (solid triangles, Figure 3.21). In addition, Error in u_i and layering of lithology and permeability in the sedimentary basin (e.g. turbidite sediments) can significantly alter the occurrence of the intersection point.

For sediments with low I_r value, the $1/t$ extrapolation and $1/\sqrt{t}$ extrapolation of the tip pressure can provide good in situ pressure prediction. It makes the T2P an exciting option for the measurement of pore pressure in low-permeability marine sediments.

3.7 Conclusion

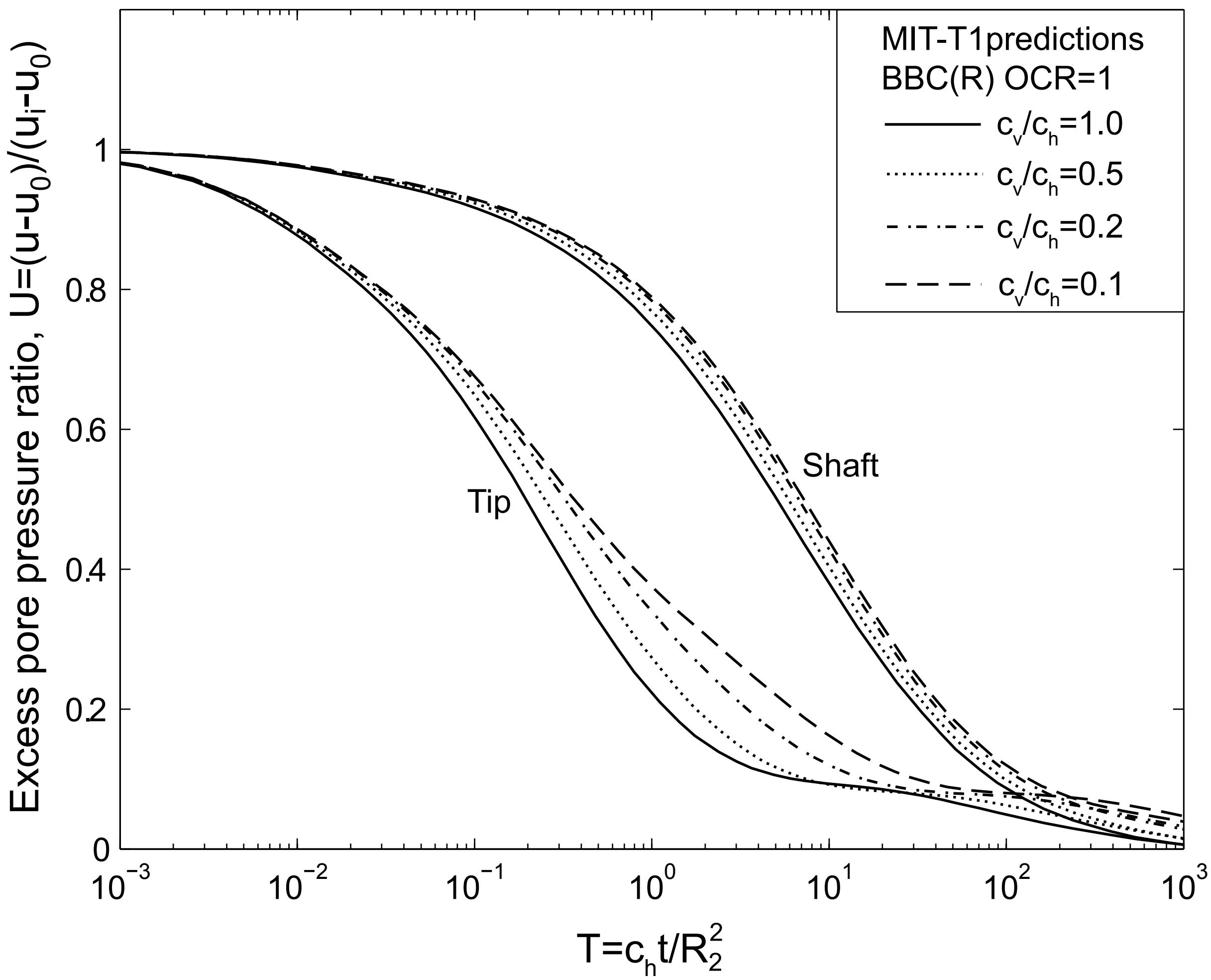

Figure 3.20: Effect of anisotropic hydraulic diffusivity on pressure dissipations.

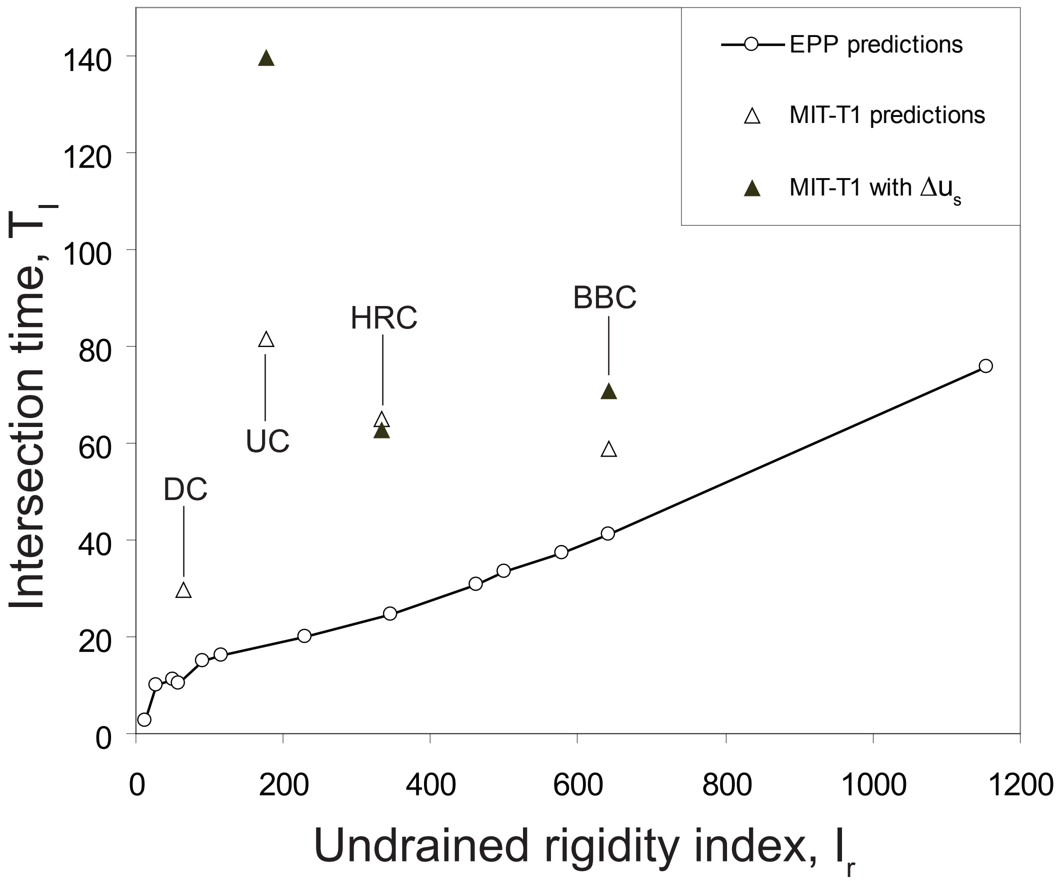

Figure 3.21: Prediction of the intersection time for the two-point matching approach. T_1 defines the time factor (T) when the dissipated pore pressures are identical for the tip and shaft pressures of the T2P. No shear-induced pore pressure data and model are available for the DC.

This paper presents a theoretical and experimental evaluation of the performance of a new pressure penetrometer, T2P. Theoretical analyses are based on strain path method using an idealized EPP soil model and an advanced soil model, MIT-T1. We show that the undrained rigidity index of the soil controls the magnitude and distribution of the installation pressure, and thus its subsequent dissipation. The predictions show that the in situ pressure and the hydraulic diffusivity can be independently estimated within a short monitoring time by comparing the dissipated pressures at the tip and the shaft pressure ports of the T2P. We relate the excess pore pressure ratio on the "bench" of the tip pressure to a single parameter, undrained rigidity index. This allows the in situ pressure to be accurately estimated from partial dissipation data once the pressure decay has reached the "bench". The measured data suggested that the proposed approach and the "bench" approach can provide reliable and rapid estimates of in situ pressure from partial dissipation records.

Appendix 3.A: Parameters for the MIT-T1 Soil Model of Ursa Clay

To develop input parameters for the MIT-T1 soil model, K_0-consolidated undrained triaxial compression and extension tests were performed on intact whole core samples taken from Ursa Basin. The test involves two stages: first the specimen is consolidated one-dimensionally until the desired stress state is reached; second, the specimen is sheared without drainage. Definitions and derivations of the soil parameters are presented by *Levadoux and Baligh* [1980].

3.A.1 Parameters for Stress-Strain Relationships

1. The dimensionless elastic shear modulus, G/σ'_{v0}, is equal to 79.4.
2. The initial yield surfaces are presented in Table 3.A1.

3. The experimental constant (A_m) controls the reduction of the plastic modulus (H_m') due to cyclic shearing. For the Ursa Clay, A_m is assumed to be 25, and the limiting (minimum) plastic modulus ($H_m'^{l}$) is assumed to be 10% of its initial value ($H_m'^{0}$).
4. Post-failure strain softening is controlled by A_p, a constant that controls the rate of decrease in radius of the failure surface when the soil has reached the failure state. All yield surfaces remain tangent to the failure surface at the current stress point and decrease in size by the same relative amount. A_p is equal to 0.8 for the Ursa Clay. The initial radius of failure surface ($k_o^{(p)}/\sigma'_{v0}$) is equal to 0.5128 and the limiting (minimum) radius of failure surface ($k_l^{(p)}/\sigma'_{v0}$) is equal to 0.24.

3.A.2 Parameters for Shear-Induced Pore Pressure Versus Strain Relation

Table 3.A2 presents the model parameters that predict the shear-induced pore pressure for general strain paths. The maximum shear-induced pore pressure can be obtained from results of cyclic undrained triaxial tests. For Ursa Clay, it is assumed to be 54% of the initial vertical effective stress.

Table 3.A1. MIT-T1 Input Parameters to Describe the Stress-Strain Curve for Normally-Consolidated Ursa Clay (K_0=0.6)

Yield surface number m	Center location $\alpha_1^{(m)}/\sigma'_{v0}$	Radius $k^{(m)}/\sigma'_{v0}$	Elasto-Plastic modulus $H^{(m)}/\sigma'_{v0}$
1	0.4018	0.0121	134.1867
2	0.3927	0.0253	117.9467
3	0.3855	0.0422	110.6933
4	0.3910	0.0490	85.9200
5	0.3759	0.0813	56.0400
6	0.3594	0.1123	36.4400
7	0.3239	0.1595	19.3067
8	0.2652	0.2385	13.5467
9	0.2587	0.2472	8.1467
10	0.2002	0.3169	4.6533
11	0.1490	0.3744	3.0933
12	0.1296	0.3981	1.6533
13	0.0728	0.4620	0.6667
14	0.0302	0.5103	0.2800
15	0.0316	0.5118	0.1600
16	0.0327	0.5128	0.0000

Table 3.A2. MIT-T1 Input Parameters to Describe the Shear-Induced Pore Pressure versus Strain Relation for Normally-Consolidated Ursa Clay (K_0=0.6)[a]

Sphere number n	Center location $\beta_1^{(n)}/\sigma'_{v0}$	Radius $\rho^{(n)}/\sigma'_{v0}$	Rate of pore pressure generation $I^{(n)}/\sigma'_{v0}$
1	0.000000	0.000000	59.6160
2	0.000000	0.000051	46.4780
3	0.000003	0.000214	31.5900
4	-0.000004	0.000416	16.7980
5	-0.000005	0.000703	10.1240
6	-0.004025	0.005435	5.4620
7	-0.004311	0.014680	3.4850
8	-0.000192	0.026036	2.0435
9	-0.001477	0.042207	1.1270
10	0.002476	0.059727	0.6686
11	0.029877	0.094382	0.3343
12	0.057293	0.132707	0.0000

[a]Maximum normalized shear-induced pore pressure $\frac{(\Delta u_s)_{\max}}{\sigma'_{v0}} = 0.54$.

Nomenclature

A_m constant that controls the rate of decrease in plastic modulus

A_p constant that controls the rate of decrease in radius of the yield surfaces

c hydraulic diffusivity L^2T^{-1}

G elastic shear modulus $ML^{-1}T^{-2}$

$H^{(m)}$ elastic-plastic modulus $ML^{-1}T^{-2}$

$H_m{}'^{0}$ initial plastic modulus $ML^{-1}T^{-2}$

$H_m{}'^{l}$ limiting (minimum) plastic modulus $ML^{-1}T^{-2}$

$I^{(n)}$ slope of shear induced pressure vs. octahedral shear strain curve $ML^{-1}T^{-2}$

K_0 earth pressure coefficient at rest

$k^{(m)}$ initial radius of yield surfaces $ML^{-1}T^{-2}$

$k_0^{(p)}$ initial radius of failure surface $ML^{-1}T^{-2}$

$k_l^{(p)}$ limiting (minimum) radius of failure surface $ML^{-1}T^{-2}$

I_r undrained rigidity index

q shear stress $ML^{-1}T^{-2}$

R_1, R_2 tip and shaft radii respectively for Piezoprobe L

r, z radial and vertical coordinates of probe penetration L

S_u undrained shear strength $ML^{-1}T^{-2}$

T time factor

T_I time factor at the intersection point

T^* modified time factor

T_{50} time factor for 50% pressure dissipation

T^*_{50} modified time factor for 50% pressure dissipation

t time after penetration is halted T

U excess pore pressure ratio

U^* apparent excess pore pressure ratio

U_B excess pore pressure ratio on the "bench"

u curent pore pressure $ML^{-1}T^{-2}$

u_0 in situ pressure $ML^{-1}T^{-2}$

u_B tip pressure on the "bench" $ML^{-1}T^{-2}$

u_i peak pore pressure $ML^{-1}T^{-2}$

$\alpha_1^{(m)}$ center location of initial yield surfaces $ML^{-1}T^{-2}$

$\beta_1^{(n)}$ center location of spheres that define shear induced pressure generation $ML^{-1}T^{-2}$

ε_a axial strain

ε_f strain to failure

$\rho^{(n)}$ radius of spheres that define shear induced pressure generation $ML^{-1}T^{-2}$

σ'_{v0} vertical consolidation stress $ML^{-1}T^{-2}$

δu_0 error in the estimated in situ pressure $ML^{-1}T^{-2}$

δu_i error recorded initial pore pressure $ML^{-1}T^{-2}$

Δu excess pore pressure $ML^{-1}T^{-2}$

Δu_i initial excess pore pressure induced by steady penetration $ML^{-1}T^{-2}$

Δu_{oct} pore pressure change due to change in octahedral normal stress $ML^{-1}T^{-2}$

Δu_s shear-induced excess pore pressure $ML^{-1}T^{-2}$

$\Delta\sigma_{ij}$ change in components of total stress tensor (cylindrical coordinate system, i, j=r, θ and z) $ML^{-1}T^{-2}$

$\Delta\sigma_{oct}$ change in octahedral normal stress $ML^{-1}T^{-2}$

Acknowledgements

This research used samples and/or data provided by the Integrated Ocean Drilling Program (IODP). Funding for this research was provided by the National Science Foundation under NSF Grants 0447235 and 0351085. The Penn State GeoFluids Consortium supported this research. We thank the participants of IODP Expedition 308 that made the deployment of the T2P possible.

References

Abu-Farsakh, M., Tumay, M., and Voyiadjis, G. (2003), Numerical Parametric Study of Piezocone Penetration Test in Clays, *International Journal of Geomechanics, ASCE*, *3*, 170-181.

Baligh, M. M. (1985), Strain path method, *Journal of Geotechnical Engineering, ASCE*, *111*, 1108-1136.

Baligh, M. M., and J. N. Levadoux (1986), Consolidation after undrained piezocone penetration II: interpretation, *Journal of Geotechnical Engineering, ASCE*, *112*, 447-461.

Cauble, F. D. (1996), An experimental investigation of the behavior of a model suction caisson in a cohesive soil, PhD thesis, 627 pp, Massachusetts Institute of Technology, Cambridge, MA.

Davis, E. E., R. D. Macdonald, H. Villinger, R. H. Bennett, and H. Li (1991), Pore pressures and permeabilities measured in marine sediments with a tethered probe, *J. Geophys. Res.*, *96*, 5975-5984.

Fang, W. W., M. G. Langseth and P. J. Schultheiss (1993), Analysis and application of in situ pore pressure measurements in marine sediments, *J. Geophys. Res.*, *98*, 7921-7938.

Flemings, P. B., Behrmann, J., John, C., and Shipboard Scientists IODP Expedition 308 (2006a), Proceedings of the Integrated Ocean Drilling Program, DOI: doi:10.2204/iodp.proc.308.2006.

Flemings, P. B., Germaine, J., Long, H., Dugan, B., Sawyer, D., Behrmann, J.H., John, C., Shipboard Scientific Party, IODP Expedition 308 (2006b), Measuring Temperature and Pressure with the Temperature Two Pressure (T2P) Probe in the Ursa Basin, Gulf of Mexico: Development of a New Pressure and Temperature Probe for the IODP, *Proceedings of the Offshore Technology Conference, Houston, Texas, May 1-4, 2006, OTC Paper #17957*.

Gupta, R. C., and J.L. Davidson (1986), Piezoprobe Determined Coefficient of Consolidation, *Soil and Foundations*, *26*, 12-22.

Huang, W., D. Shenga, S.W. Sloana and H.S. Yu (2004), Finite element analysis of cone penetration in cohesionless soil, *Computers and Geotechnics*, *31*, 517-528.

Keaveney, J., and Mitchell, J.K., (1986), Strength of fine grained soils using the piezocone, paper presented at Use of In-Situ Tests in Geotechnical Engineering (GSP 6), ASCE, Reston, VA, 668-685.

Kiousis, P. D., G.Z. Voyiadjis and M.T. Tumay (1988), A large strain theory and its application in the analysis of the cone penetration mechanism, *Int. J. Numer. Anal. Meth. Geomech.*, *12*, 45–60.

Ladanyi, B. (1963), Expansion of a cavity in a saturated clay medium, *Journal of the Soil Mechanics and Foundation Engineering Division, ASCE*, *89*, 127-161.

Lambe, T. W., and R.V. Whitman (1969), *Soil Mechanics*, 553 pp., John Wiley, New York.

Levadoux, J. N., and M.M. Baligh (1980), Pore pressures during cone penetration in clays, Research Report, 310 pp, Massachusetts Institute of Technology, Cambridge, MA.

Levadoux, J. N., and M.M. Baligh (1986), Consolidation after undrained piezocone penetration. I: prediction, *Journal of Geotechnical Engineering*, *112*, 707-725.

Lim, B. S., M.T. Tumay, and D.D. Seo (2006), Status of Consolidation from Incomplete Piezocone Dissipation Tests, *In: Site and Geomaterial Characterization (GSP 149), Proceedings of Sessions of GeoShanghai. Shanghai, China.*

Long, H., P. B. Flemings, and J. T. Germaine (2007a), Interpreting in situ pressure and hydraulic properties with borehole penetrometers in ocean drilling: DVTPP and Piezoprobe deployments at southern Hydrate Ridge, offshore Oregon, *J. Geophys. Res.*, *112*, B04101, doi:04110.01029/02005JB004165.

Long, H., P. B. Flemings, J. T. Germaine, B. Dugan, D. Ferrell, and Expedition 308 Scientists (in review), Penetrometer Measurements of In Situ Temperature and Pressure on IODP Expedition 308, *in. Proceeding of the integrated ocean drilling program, vol, 308*.

Long, H., P.B. Flemings, J. Germaine, B. Dugan, D. Sawyer, and Shipboard Scientific Party, IODP Expedition 308 (2007b), In Situ Pore Pressure at IODP Site U1324, Ursa Basin, Gulf of Mexico, *Proceedings of the Offshore Technology Conference, Houston, Texas*, *OTC Paper #18772*.

Mabsout, M. E., and Tassoulas, J.L. (1996), An Eulerean finite model for penetration in layered soil, *International Journal for Numerical and Analytical Methods*, *20*, 865-886.

Marsland, A., and Randolph, M.F. (1977), Comparisons of the results from pressuremeter tests and large in situ plate tests in London Clay, *Geotechnique*, *27*, 217-243.

Moore, G. F., Taira, A., Klaus, A., et al. (2001), Proc. ODP, Init. Repts., v. 190 [CD-ROM]. Available from: Ocean Drilling Program, Texas A&M University, College Station TX 77845-9547, USA.

Ostermeier, R. M., Pelletier, J.H., Winker, C.D. and Nicholson, J.W. (2001), Trends in Shallow Sediment Pore Pressures - Deepwater Gulf of Mexico, paper presented at Society of Petroleum Engineers, SPE/IADC 67772.

Prévost, J. H. (1978), Anisotropic undrained stress-strain behavior of clays, *Journal of Geotechnical Engineering Division*, *104*, 1075-1090.

Randolph, M. F., and C.P. Wroth (1979), An analytical solution for the consolidation around a driven pile, *Int. J. Numer. Anal. Meth. Geomech.*, *3*, 217-229.

Sawyer, D. E., et al. (2007), Seismic Geomorphology, Lithology, and Evolution of the Late Pleistocene Mars-Ursa Turbidite Region, Mississippi Canyon Area, Northern Gulf of Mexico, *American Association of Petroleum Geologists Bulletin*, *91*, 215-234.

Teh, C. I., and Houlsby, G.T. (1991), An analytical study of the cone penetration test in clay, *Geotechnique*, *41*, 17-34.

Tréhu, A. M., Bohrmann, G., Rack, F.R., Torres, M.E., et al., (2003), *Proc. ODP, Init. Repts., v. 204 [CD-ROM]*, Available from: Ocean Drilling Program, Texas A&M University, College Station TX 77845-9547, USA.

Whittle, A. J., T. Sutabutr, J. T. Germaine and A. Varney (2001), Prediction and interpretation of pore pressure dissipation for a tapered piezoprobe, *Geotechnique*, *51*, 601-617.

Winker, C. D., and J. R. Booth (2000), Sedimentary dynamics of the salt-dominated continental slope, Gulf of Mexico; integration of observations from the seafloor, near-surface, and deep subsurface, in *GCSSEPM Foundation 20th Annual Research Conference, Deep-Water Reservoirs of the World*, edited, pp. 1059-1086.

Yu, H. S., L. R., Herrmann and R. W., Boulanger (2000), Analysis of steady cone penetration in clay, *Journal of geotechnical and geoenvironmental engineering*, *126*, 594-605.

Chapter 4: Consolidation Characteristics, Effective Stress and Pore Fluid Pressure of Ursa Sediments, Gulf of Mexico

Abstract

We conducted extensive uniaxial consolidation tests on whole core samples to obtain the consolidation properties of the Ursa mudstones. The results suggest that the compression index linearly decreases with in situ void ratio. This implies that a locally-defined virgin compression curve cannot validly be extrapolated over a large range in effective stress. This effect is particularly important at shallow depth where void ratio decreases rapidly. We have shown that the relationship of compressibility index versus void ratio can be obtained from a single consolidation test by compressing the soil over a large range in effective stress. A virgin compression curve can then be constructed based on this relationship to predict pore fluid pressure. In the Ursa Basin, this new approach successfully predicted pressures interpreted from the penetrometer measurements within the non-deformed sediments. The mass transport deposits appear to be more compacted than the non-deformed sediments. The virgin compression curve based on the assumption of uniaxial strain underpredicts the in situ pressure in the mass transport deposits.

4.1 Introduction

Overpressures (pressures in excess of hydrostatic pressure) are present in sedimentary basins of many ages around the world [*Fertl, et al.*, 1994]. Overpressures drive pore water circulation [*Harrison and Summa*, 1991], impact large-scale structural development [*Rubey and Hubbert*, 1959], and influence slope stability [*Dugan and Flemings*, 2002]. Knowledge of the distribution of overpressures is critical to explore, drill, and produce hydrocarbons [*Fertl, et al.*, 1994; *Flemings, et al.*, 2002; *Ostermeier, et al*, 2002].

Inverse models predict pore fluid pressure from compaction state. Pressures are predicted from a range of data including porosity (or void ratio), bulk density, resistivity, and sonic velocity [*Athy*, 1930; *Rubey and Hubbert*, 1959; *Wallace*, 1965; *Hottman and Johnson*, 1965; *Eaton*, 1975; *Dugan, et al.*, 2003; *Saffer*, 2003]. All of these approaches rely fundamentally on a relationship between pore space and effective stress.

A common geological approach is to assume an exponential relationship between porosity (ϕ) and vertical effective stress (σ'_v) [*Rubey and Hubbert*, 1959]

$$\phi = \phi_0 e^{-\beta\sigma'_v}, \qquad (4.1)$$

where ϕ_0 is the porosity at zero effective stress and β is an empirically derived compressibility constant. ϕ_0 and β are calibrated in zones where the vertical effective stress and porosity are known. In zones where pressure is unknown, it is predicted by rearranging Equation 4.1 as follows:

$$P = \sigma_v - \frac{1}{\beta}\ln\left(\frac{\phi_0}{\phi}\right), \qquad (4.2)$$

where σ_v is the total overburden stress due to the overlying sediments. This approach has been applied by a range of authors [*Hart, et al.*, 1995; *Dugan and Flemings*, 2000; *Lahann*, 2002; *Flemings and Lupa*, 2004].

The geotechnical community relies on a different relationship between pore space and effective stress: void ratio ($e=\phi/1-\phi$) is proportional to the log of vertical effective stress ($\log(\sigma'_v)$):

$$e = e_0 - C_c \log(\sigma'_v), \qquad (4.3)$$

where C_c is the compression index and e_0 is a reference void ratio at an effective stress of unity. e_0 and C_c can be obtained from a field-based compression curve where void ratio and vertical effective stress are known [*Dugan, et al.*, 2003; *Saffer*, 2003]. Alternatively, uniaxial laboratory consolidation tests can be used to determine these parameters [*Saffer*, 2003]. Equation 4.3 can be rearranged to predict pore fluid pressure as follows:

$$P = \sigma_v - 10^{(\frac{e_0 - e}{C_c})} . \qquad (4.4)$$

Pore fluid pressure can also be obtained from experimentally derived preconsolidation pressures [*Brown*, 1995; *Saffer, et al.*, 2000; *Stump and Flemings*, 2002; *Dugan, et al.*, 2003]. In this approach, there is a boundary between largely elastic versus largely plastic deformation that is imaged by the change in slope on stress-strain curve during uniaxial consolidation. This boundary is interpreted to be the maximimum effective stress that the sediment has undergone [*Casagrande*, 1936]. To predict pore pressure, this approach assumes that the sediment is normally consolidated, which means that the present effective stress in the sediment is the maximum effective stress the sediment has ever experienced.

Equations 4.1 and 4.3 cannot capture the relationship between pore space and effective stress over a large range of effective stresses. For example, neither Equation 4.1 nor Equation 4.3 can capture the rapid change in pore space with effective stress near the sea floor. A common result is that when ϕ_0 is derived from porosity and effective stress data extending to a few kilometers, the value generated for ϕ_0 (40-48%) is lower than the actual porosity at the seafloor [*Rubey and Hubbert*, 1959; *Hart, et al.*, 1995; *Flemings and Lupa*, 2004]. For this reason, it is common to ignore the very shallow section in pore pressure prediction. At the opposite end of the spectrum, if Equation 4.3 is based on relatively shallow sediments, it can predict negative pore space at higher effective stresses.

We are particularly interested in understanding the inter-relationships between pore pressure, effective stress, and pore space near the seafloor where effective stresses are low. High overpressures near the seafloor may cause slope instability and drilling problems [*Dugan and Flemings*, 2002; *Ostermeier, et al.*, 2002]. In addition, there are very low stress regimes at deeper depths.

Expedition 308 targeted the Ursa Basin because it is located at the epicenter of late Pleistocene Mississippi River deposition, which provides an exciting opportunity to study how compaction and overpressure are coupled near the seafloor. We drilled, logged, cored and made in situ measurements in a region of very rapid sedimentation (Figure 4.1). We took many whole core samples for shore-based consolidation tests to characterize the pore fluid pressure and effective stress.

In this paper, we report on results of uniaxial consolidation tests on samples from IODP Expedition 308. We show that Equation 4.1 and 4.3 cannot be used directly to predict the pore space reduction with increase of effective stresses at shallow depth. We show, however, that if C_c increases linearly with effective stress the field behavior can be captured and can be used to predict pore fluid pressure over a large range in effective stress. We also show that the preconsolidation stress determined from consolidation tests is subject to considerable uncertainty when sample disturbance is severe.

4.2 Overview

4.2.1 Geological Setting

The Mars-Ursa salt-withdrawal basin (the "Ursa Basin") is located 210 km south-southeast of New Orleans, Louisiana (USA), on the northeastern Gulf of Mexico continental slope (inset map in Figure 4.1A). Late Pleistocene deposition from the ancestral Mississippi

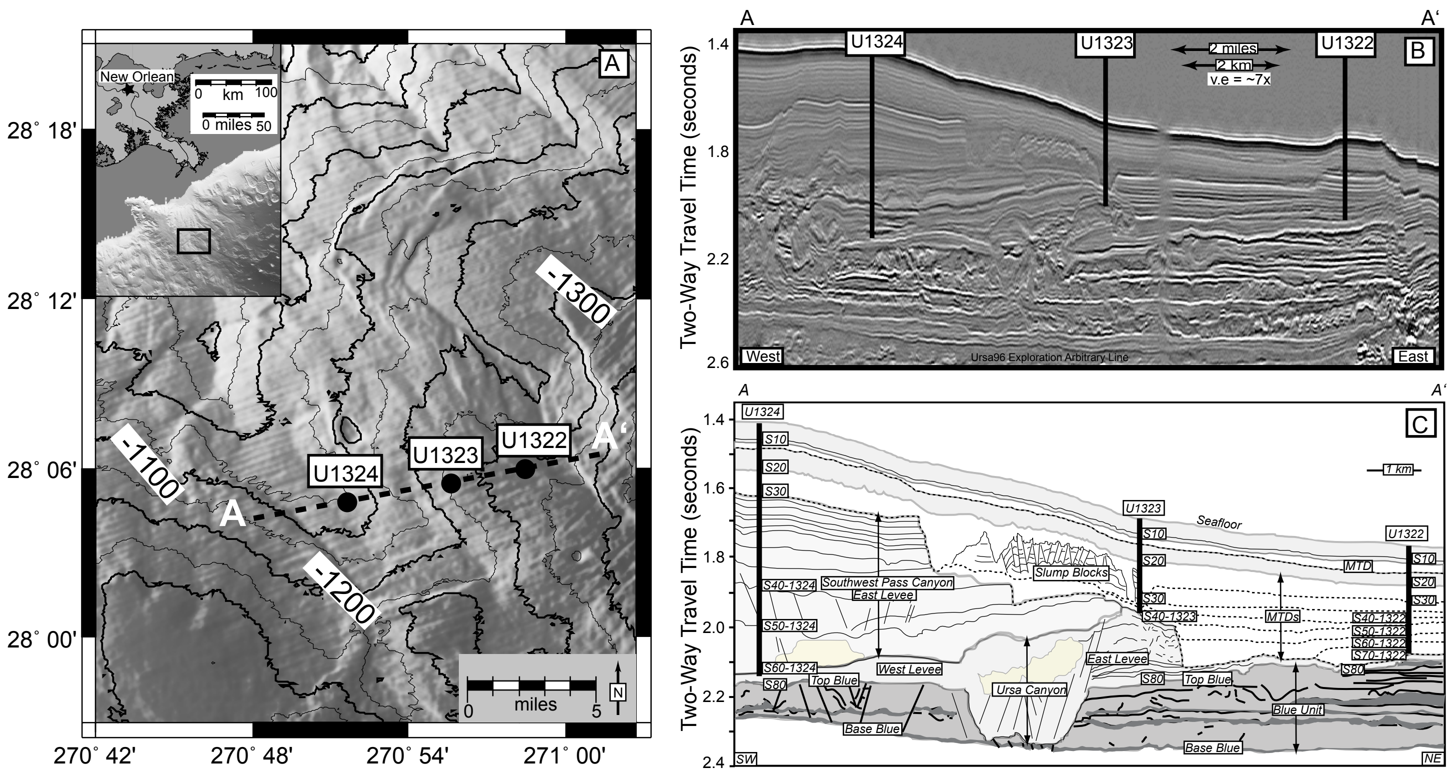

Figure 4.1: A) IODP Expedition 308 Site locations, and bathymetry contours. The Ursa Basin is located 210 km SE of New Orleans, Louisiana, USA (inset map). Three drilled Sites are delineated with black dots. Contour interval is 100 m. (B) East-West seismic cross section A-A' (Flemings, 2006). (C) Interpreted cross section A-A' (Flemings, 2006). The Blue Unit is composed of sand and mud. The darkest gray represents sand-rich channel fill. Mass transport deposits have occurred in the mud-rich levee deposits above the Blue Unit. Detachment surfaces are dotted lines.

River is recorded by a southward bulge in the 500 and 1000 m bathymetric contours. The Mars Ridge, a prominent north-south–trending bathymetric high, bounds the study area to the west (Figure 4.1A).

Late Pleistocene shelf, shelf-margin, and turbidite deposits sourced from the Mississippi River are termed the Eastern Depositional Complex [*Winker and Booth*, 2000]. Eastern Depositional Complex strata in the Ursa Basin accumulated outboard of the shelf break during Marine Isotope Stages (MIS) 2–4 in response to late Wisconsinan continental glaciation [*Flemings, et al.*, 2006; *Winker and Booth*, 2000; *Winker and Shipp*, 2002]. In the Ursa Basin, these strata are divided into the Blue Unit, which is overlain by mud-prone leveed-channel deposition (Figure 4.1C). The Blue Unit is a sand-dominated turbidite unit that was deposited in a broad topographic low that extended 200 km to the east and west and 100 km to the north and south [*Sawyer, et al.*, 2007a]. The overlying leveed-channel systems contain a channel and bounding levees. The Ursa Canyon channel-levee system immediately overlies the Blue Unit, whereas the Southwest Pass Canyon channel-levee system is younger and lies west of the Ursa Canyon (Figure 4.1C). Mudstones that overlie the Southwest Pass Canyon record deposition from leveed channels that lay further to the west, outside of the study area (Figure 4.1A). Multiple Mass Transport Deposits (MTDs) are present in the leveed-channel deposits (Figure 4.1C) [*Sawyer, et al.*, 2007b].

During IODP Expedition 308, we drilled to just above the Blue Unit at three locations within this sedimentary wedge: Sites U1322, U1323, and U1324 (Figure 4.1). We cored and made in situ pressure measurements at Sites U1322 and U1324. At Site 1324, we encountered silty claystone to a depth of 370 meters below seafloor (mbsf) as indicated by the high gamma ray signature (Figure 4.2). Beneath this we encountered silty claystone interbedded with beds of

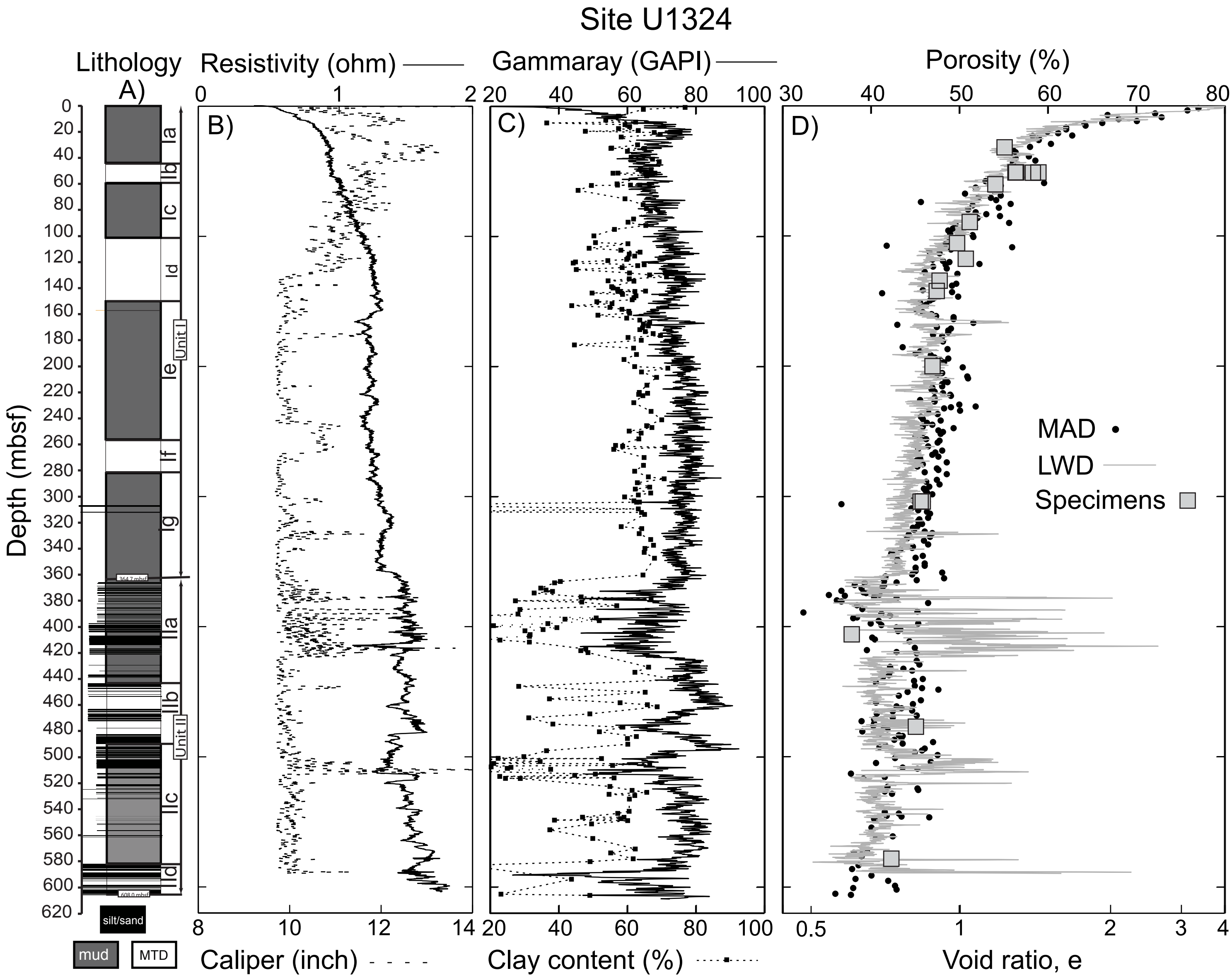

Figure 4.2: Core, log data and interpretations from IODP Site U1324. A) Logging-while-drilling (LWD) deep resistivity (A40B) and caliper log from Hole U1324A. B) Gamma ray log data from Hole U1324A and clay content measurements on samples from Hole U1324B (Jacoby, in preparation). C) Initial porosity of the tested specimens, shipboard moisture and density (MAD) measurements and LWD porosity are shown.

silt and very-fine sand. The silts and very-fine sands are interpreted to record levee deposition proximal Southwest Pass Canyon. At Site 1322, we encountered only silty claystone (Figure 4.3). At Site 1322, deformed bedding records the presence of MTDs that comprise approximately 60% of the stratigraphic section (white bedding, Figure 4.3). At Site 1324, there are fewer MTDs present (Figure 4.2).

4.2.2 Porosity

We present porosity data obtained from three sources (Figures 4.2 and 4.3): 1) shipboard moisture and density (MAD) measurements; 2) bulk density measured during logging while drilling (LWD); and 3) porosity measured on the whole core specimens used for consolidation tests. MAD measurements measure the grain density, bulk density and porosity using the shipboard technique “C” [*Blum*, 1997], in which dry volume is measured by gas pycnometry and the pore volume is calculated by assuming a pore fluid density equal to seawater (1.024 g/cc). LWD measures only the bulk density; we assumed a pore fluid density of 1.024 g/cc, and took the grain densities interpolated from MAD grain density to calculate the porosity. The frequency of the MAD data is about 1.5 m as opposed to 0.15 m for the LWD data. Therefore, one abnormal MAD measurement can have a large influence. To minimize the impact of unusual lithologies and measurement errors, we threw the extreme low (<2.6 g/cc) and high (>2.8 g/cc) MAD grain density measurements, and then averaged them over a moving window of ten samples, representing about 15 m of section. Porosity of the tested specimen is determined from the wet volume of the specimen (measured in the consolidation ring) and the grain density that is interpolated from the averaged MAD grain density profile. This approach accounts for the unsaturated pore space due to expansion.

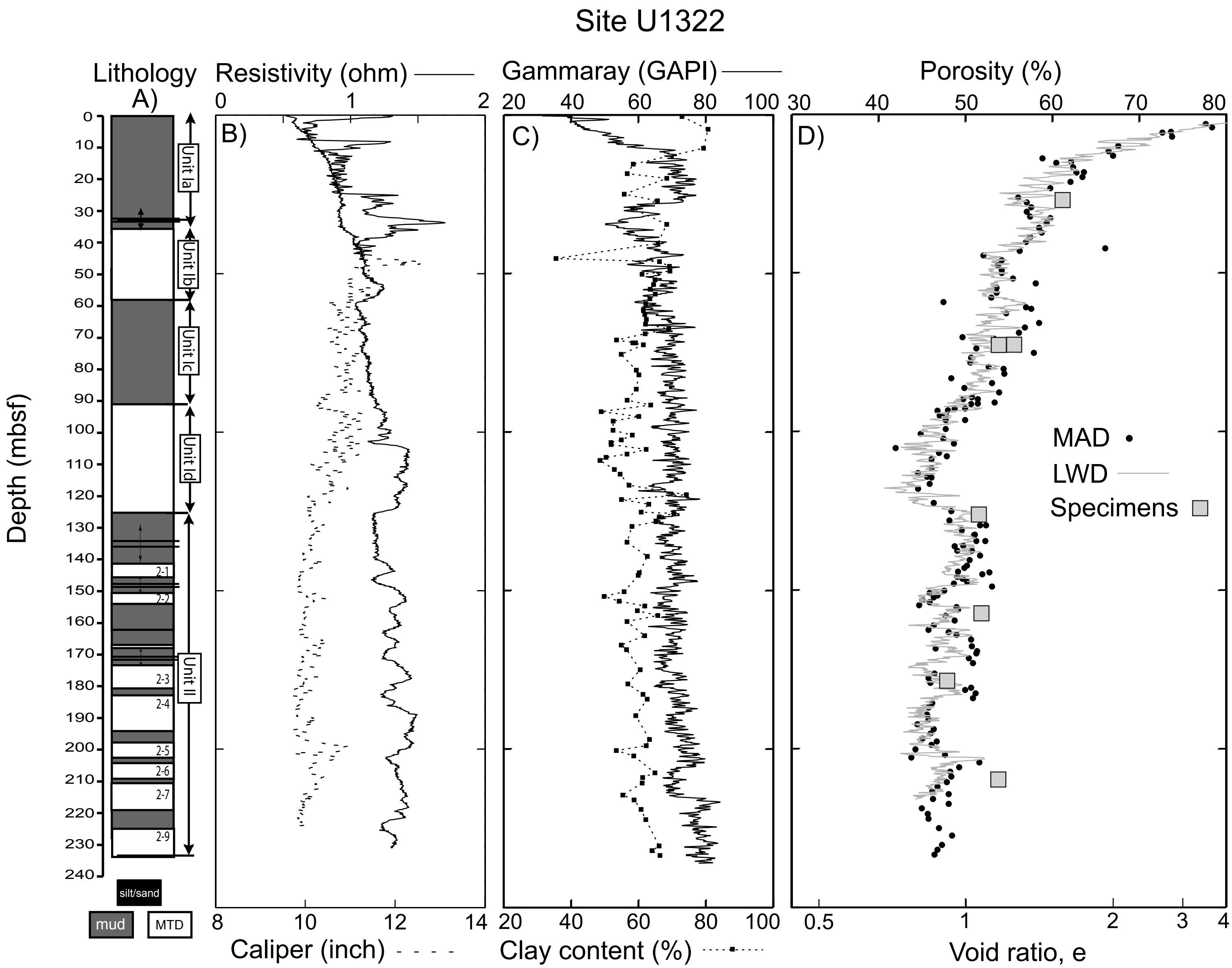

Figure 4.3: Core, log data and interpretations from IODP Site U1322. A) Logging-while-drilling (LWD) deep resistivity (A40B) and caliper log from Hole U1322A. B) Gamma ray log data from Hole U1322A and clay content measurements on samples from Hole U1322B (Jacoby, in preparation). C) Initial porosity of the tested specimens, shipboard moisture and density (MAD) measurements and LWD porosity are shown.

LWD porosity is generally slightly less than the MAD porosity (Figure 4.2C). It is possible that, during MAD measurements, oven drying during water content determinations in smectitic clays may remove some of the interlayer water [*Brown and Ransom*, 1996]. This results in higher estimates of void ratio than those would be calculated from LWD bulk density. The porosities measured on the tested specimens are generally consistent with the MAD measurements, although two of them are significantly higher than the MAD porosities (Figure 4.3D). These high values are measured on specimens with low saturation (<90%). We interpret that the unsaturated pore space was created by expansion occurred during core recovery, or preparation of the specimens (e.g. sub-sampling and trimming) due to the decreased effective stresses present after core recovery [*Moore and Tobin*, 1997].

4.2.2.1 Porosity Profiles at Site U1324 and Site U1322

At Site U1324, porosity declines from 80% to 54% within the first 50 mbsf (Figure 4.2D). Between 50 mbsf and 520 mbsf, the mudstone porosity gradually declines from 54% to 40%. Finally, between 520 mbsf and the bottom of the hole (612 mbsf), porosity declines from 42% to 37%. In the sand and silt rich zones beneath 300mbsf, the caliper log has high values, indicating borehole enlargement (Figure 4.2B). High porosities are measured with the LWD in these intervals and we interpret that the LWD density values are partially recording the open borehole (Figure 4.2B).

At Site U1322, the porosity decreases from 80% to 54% within the first 50 mbsf and between 50 and 120 mbsf, the porosity gradually declines to 44% (Figure 4.3D). Beneath this, the porosity is approximately constant. At Site U1322, the entire section is composed of mudstones (Figure 4.3A and 4.3C), so there are no variations due to lithology.

4.2.2.2 Mass Transport Deposits (MTDs) and Porosity Behavior

MTDs are present at both sites, although Site U1322 has many more than Site U1324 (white bedding, Figures 4.2A and 4.3A). MTDs have lower porosities than the non-deformed sediments above and below them and sharp porosity increases are generally observed beneath the MTDs. The best example of a MTD is illustrated at Site U1322 between 90 and 125 mbsf (Figure 4.3D). *Sawyer, et al.*, [2007b] and *Dugan et al*. [2007] describe these MTDs in detail. *Dugan et al*. [2007] interpreted that the decreased porosity results from consolidation associated with shear deformation due to slumping. At Site U1322, from 125 mbsf to the bottom of the hole, there are shifts of about 5 porosity units at frequent intervals. Where porosity is lower and resistivity is higher, MTDs are present (white bedding, Figure 4.3).

4.3 Experimental Analyses

4.3.1 Sample Descriptions

We conducted constant rate of strain consolidation (CRSC) test on 7 samples from Site U1322 and 17 samples from Site U1324 in two laboratories at the Massachusetts Institute of Technology (MIT) and at Penn State (PSU) (Table 4.1). All tested samples are silty clays that contain 50 to 70% clay-sized particles (less than 2 microns) except U1324C-7H-1WR (405 mbsf) which is clayey silt with 32% clay (Table 4.1) [*Sawyer, et al.*, in preparation]. The clay compositions are very similar in the different samples. Smectite makes up more than 80% of the clay fraction [*Dugan*, 2007].

During coring, retrieval of the core sample from the ground, storage, and installation of the specimen in the testing device, the soil undergoes changes in stress and deformation. These changes are referred to as sample disturbance. The sample disturbance affects the quality of the consolidation tests. Cores with higher silt/sand fraction likely have more internal voids, cracks, and generally poor quality. This is particularly significant in the lower section at Site U1324 where encountered silty clays interbedded with beds of silt and very-fine sand. *Nelson, et al.*, [in preparation] report the radiography and CatScan images of the whole core samples. The amount of deformation caused by shear stress at the interface of the core barrel and the sediment during insertion is evidenced at the edge of the core. Visual observations on the split cores show that the deformation increases significantly with depth within each individual core [*Flemings, et al.*, 2006].

4.3.2 Uniaxial Consolidation Experiments

In CRSC tests, specimens were laterally confined with a steel ring. Samples were saturated with de-aired water and backpressured to 300-425 kPa for 24 hours prior to testing to drive any gases present into solution. We applied a constant rate of strain (0.15-0.6% per hour) using a computer-controlled load frame, with the specimen base undrained and the specimen top open to the backpressure. In all cases the excess pore pressure generated at the base of the specimen was within 15% of the applied axial stress at the maximum loading point. We continuously monitored sample height, axial load, and basal pore pressure. *Long et al*., [in review-a] described the detailed experimental procedures and data.

The stress strain behavior for two experiments is illustrated with an e-log (σ'_v) plot (Figure 4.4). The initial branch of the curve (recompression) has a relatively flat slope until the vertical effective stress exceeds the preconsolidation pressure (P'_c), the maximum vertical effective stress the specimen experienced. Deformation then follows a virgin compression curve with a steeper slope. The slope of the virgin compression portion defines the compression index (C_c, Equation 4.3). To be consistent, we determined the values of C_c from data with the vertical effective stress ranges from 1.5 to 2.5 times the hydrostatic vertical effective stress (Table 4.1).

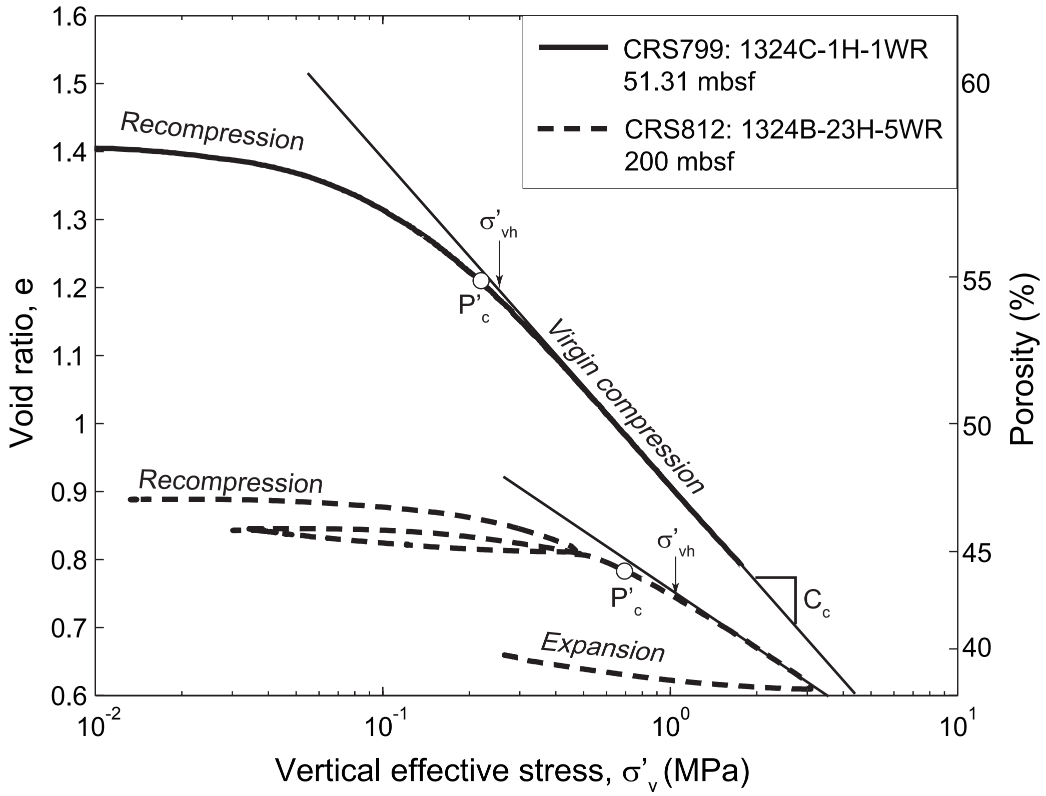

Figure 4.4: Examples of consolidation test results. σ'_{vh} is calculated from the LWD bulk density profile and an assumed seawater density of 1.024 g/cc. Preconsolidation pressures (P'_c, open circle) are derived using work-stress method (Becker, et al., 1987).

Table 4.1. Sample Summary and Consolidation Properties

Test #	Sample[1]	Depth (mbsf)	Clay[2] content (%)	σ'_{vh}[3]	e_s[4]	C_c[5]	P'_c[6]
CRS796_mit	1322D-2H-2WR	72.78	58.6	0.485	1.250	0.478	0.280
CRS797_mit	1324C-1H-1WR	51.27	66.8	0.328	1.437	0.491	0.160
CRS798_mit	1322D-2H-2WR	72.83	58.6	0.485	1.164	0.408	0.200
CRS799_mit	1324C-1H-1WR	51.31	66.8	0.328	1.401	0.464	0.224
CRS800_mit	1324B-4H-7WR	31.86	58.6	0.187	1.230	0.366	0.180
CRS801_mit	1324B-16H-5WR	142.13	--	1.080	0.904	0.278	0.435
CRS802_mit	1324B-7H-7WR	60.31	49.6	0.395	1.178	0.423	0.283
CRS803_mit	1324B-15H-5WR	134.20	62	1.009	0.916	0.278	0.422
CRS807_mit	1324C-2H-4WR	105.48	50.8	0.758	0.991	0.325	0.448
CRS808_mit	1322B-15H-1WR	126.28	70.4	0.942	1.060	0.320	0.516
CRS810_mit	1322B-18H-6WR	157.42	65.6	1.208	1.074	0.300	0.480
CRS812_mit	1324B-23H-5WR	200.00	62.2	1.599	0.886	0.278	0.700
CRS813_mit	1324B-10H-7WR	89.22	60.3	0.622	1.050	0.320	0.400
CRS815_mit	1322B-4H-3WR	27.21	65.5	0.153	1.571	0.501	0.135
CRS824_mit	1322B-25H-6WR	209.81	--	1.670	1.160	0.347	0.450
CRS825_mit	1322B-21H-3WR	178.70	--	1.395	0.917	0.259	0.580
CRS001_psu	1324C-6H-3WR	304.02	63.6	2.541	0.840	0.304	1.124
CRS002_psu	1324C-6H-3WR	303.94	62.8	2.541	0.849	0.280	1.020
CRS003_psu	1324C-1H-1WR	51.21	55.9	0.328	1.297	0.407	0.197
CRS004_psu	1324C-1H-1WR	51.14	57.4	0.327	1.292	0.435	0.232
CRS005_psu	1324B-13H-7WR	117.40	59.9	0.861	1.031	0.376	0.500
CRS006_psu	1324B-70X-6WR	578.13	61.8	5.138	0.734	0.253	1.829
CRS007_psu	1324B-60X-2WR	476.86	58.7	4.162	0.823	0.275	1.050
CRS008_psu	1324C-7H-1WR	405.81	31.7	3.497	0.609	0.153	1.502

Notes: [1] numbering of sites, holes, cores, and sections follows the standard IODP procedure. [2] Clay content measurements can be found in IODP data report [*Sawyer, et al.*, in preparation]. [3] σ'_{vh} is calculated using LWD bulk density data and a seawater density of 1.024 g/cc. [4] e_s is the void ratio measured on the tested specimens. e_s is calculated from water content using the grain densities interpreted from MAD grain density data. [5] C_c is determined over a range in vertical effective stress from 1.5 to 2.5 times σ'_{vh}. [6] P'_c is determined using the work-stress method [*Becker, et al.*, 1987].

The transition from recompression to virgin compression behavior provides estimate of preconsolidation pressure (P'_c) [*Casagrande*, 1936; *Becker, et al.*, 1987]. We used the work-stress method [*Becker, et al.*, 1987] to determine the P'_c from the CRSC tests. This approach assumes linear behavior between the strain energy density and the effective stress for consolidation dominated by elastic deformation and for virgin consolidation. The intersection of the two straight lines provides an estimate of the P'_c (Figure 4.5).

4.3.3 Compression Index with Void Ratio

The compression behavior of the Ursa silty clays is similar at Sites U1322 and U1324 (Figure 4.6). Values of C_c range from 0.501 at high void ratios to 0.253 at low void ratios. We plotted C_c with the mean void ratio over the effective stress range where C_c is determined to reflect the specimen condition the most. A striking result of our experiments is that the compression index declines with the void ratio (Figure 4.6).

There are two possible interpretations of the decline in C_c with in situ void ratio: either the observation is real and reflects the change in sample stiffness with decreasing void ratio, or the observation is an effect of sample disturbance and the more compacted samples undergo more disturbances during coring. If C_c decreases with void ratio, then the true virgin compression curve should have a concave up profile in the e-log (σ'_v) space instead of being a straight line. This has been observed by other researchers C_c [*Nishida*, 1956; *Hough*, 1957; *Sowers*, 1970; *Azzous, et al.*, 1976]. The alternate interpretation is that the sample disturbance is greater in the deeper samples that have a lower void ratio. In this case, the C_c is lower for the more disturbed samples because the rearrangement of the soil's structure produced by disturbance reduces the value of C_c [*Schmertmann*, 1955; *Wood*, 1990; *Santagata and Germaine*, 2002].

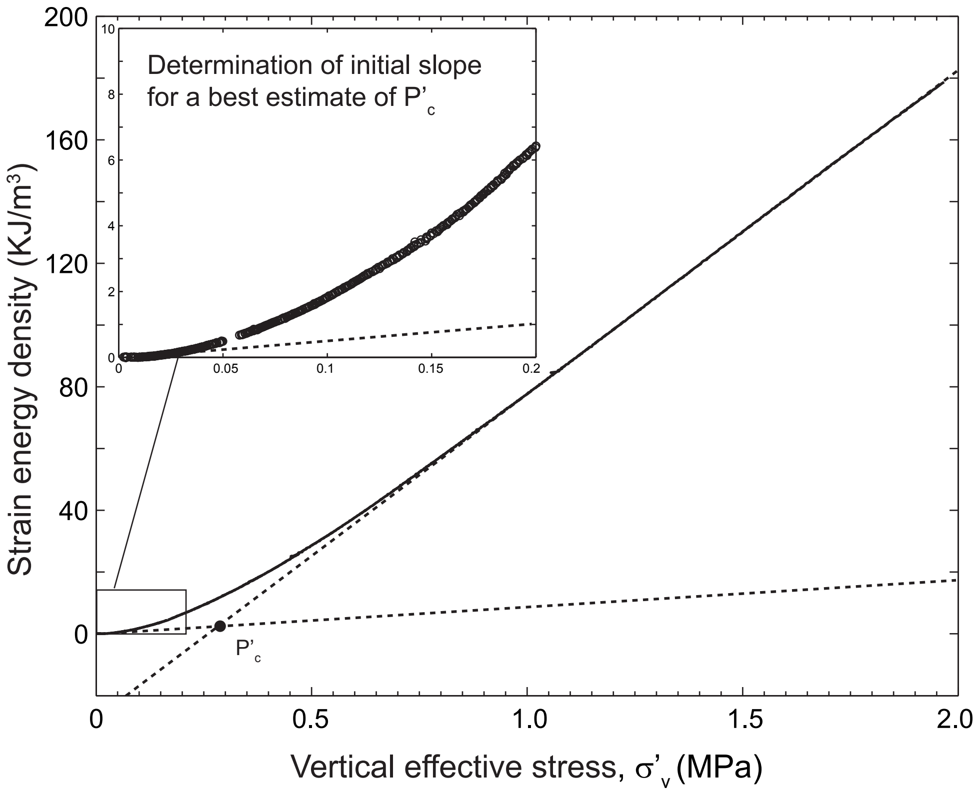

Figure 4.5: Example of derivation of preconsolidation pressure using work-stress method (Becker, et al., 1987).

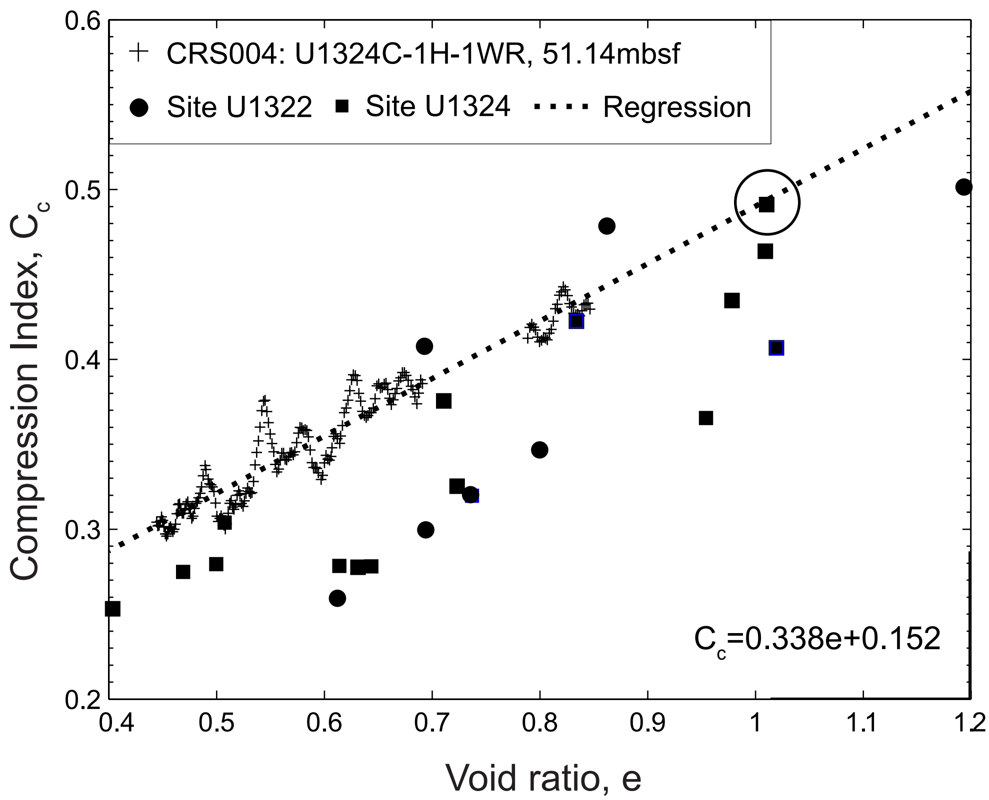

Figure 4.6: Compression indices for Ursa mudstones. The values of C_c for individual consolidation tests are determined over a stress range of 1.5 to 2.5 times the hydrostatic vertical effective stress at the corresponding depth. They are plotted with the mean void ratio over the stress range. Data within the rectangles in Figure 4.7 were used to calculate the C_c values for test CRS004. C_c was computed over a data interval with a load increment ratio of 1.1.

We compressed one of our shallow samples to a vertical effective stress of 20 MPa to determine the behavior of C_c through a large change in effective stress. The compression curve in the e-log (σ'_v) space is concave upwards (Figures 4.7) and C_c varies approximately linearly with void ratio ('+' symbols Figure 4.6). A linear regression of these data is illustrated with the dotted line (Figure 4.6), where

$$C_c = 0.338e + 0.152\,. \qquad (4.5)$$

The slope of the plot C_c against void ratio is similar for both the single compression test and the individual tests on all the samples (Figure 4.6, dotted line vs. square and circle symbols). However, at a given void ratio, approximately half of the individual measurements give significantly lower C_c than those of the single test (Figures 4.6), and 70% of these measurements were conducted on the specimens from the lower sections of a whole core. Whereas, 75% of the measurements that match the single test well were conducted on specimens from the upper sections of a whole core. In addition, most of the measurements that match the single test were conducted on specimens from shallow depth (above 100 mbsf). These by the large reflect our observations on the quality of the whole core samples. We interpret that the lower C_c measurements are mainly because the core samples from Ursa were deformed by the coring.

4.4 Virgin Compression Behavior

A virgin compression curve can be obtained for any material with C_c linearly decreasing with void ratio by integrating Equation 4.6:

$$\frac{de}{d\log(\sigma'_v)} = C_c = Ae + B\,. \qquad (4.6)$$

The solution to Equation 4.6 is:

$$e = -\frac{B}{A} + (e_0 + \frac{B}{A})\sigma_v'^{-\frac{A}{\ln(10)}}\,, \qquad (4.7)$$

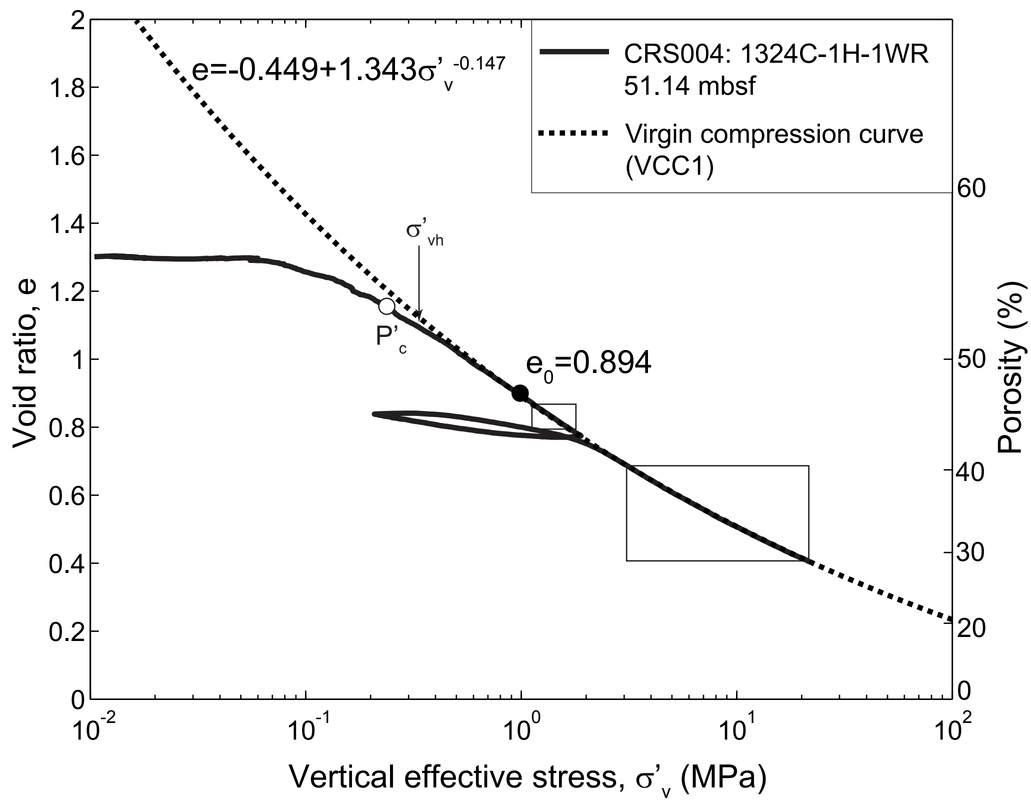

Figure 4.7: Consolidation test result for specimen from U1324C-1H-1WR, 51.14 mbsf. The dotted line is the reconstructed virgin compression curve using Equations 4.5 and 4.7. Preconsolidation pressure (*P'_c*, open circle) is derived using work-stress method (Becker, et al., 1987). σ'_{vh} is calculated from the LWD bulk density and an assumed seawater density of 1.024 g/cc.

where e_0 is a reference void ratio at an effective stress of unity. The value of e_0 depends on the units chosen for the measurement of stress. For the Ursa mudstones, A = 0.338 and B = 0.152 (Equation 4.5), and consequently, e_0=0.894 at 1 MPa when units of MPa are used. The virgin compression curve (VCC1) is illustrated in Figure 4.7.

The parameter A describes how much the soil strengthens with decreasing void ratio. Decreasing the value of A increases the strengthening behavior. For example, if A is reduced to 60% of its original value, the void ratios at effective stresses less than 1 MPa are reduced significantly whereas the void ratios below 1MPa are increased (Figure 4.8A, dotted line with '0.6*A*'). The opposite behavior is generated if A is increased (Figure 4.8A, dotted line with '1.4*A*').

We compare the compression curve derived with a void ratio dependent C_c with three other compression curves (Figure 4.8B). First, we take one of the compression curves derived from our CRSC tests (CRS797 in Table 1, the circled square in Figure 4.6) and plot its behavior (VCC2 in Figure 4.8B). Its prediction matches VCC1 closely at void ratios around 1 where the compression index was determined, whereas it predicts significantly different void ratio for a given effective stresses at a much lower or higher effective stress.

Alternatively, when there are no experimental data to constrain the compression curve, a common approach is to establish a virgin compression curve based on observation of void ratio or porosity with depth and assuming the pore pressure is hydrostatic [*Hart, et al.*, 1995; *Saffer*, 2003]. We use this approach on the mudstones from the Ursa Basin by applying Equation 4.1 (VCC3) and Equation 4.3 (VCC4) on the LWD porosity for the upper 43.9-meters at Site U1324 (Figure 4.8B).

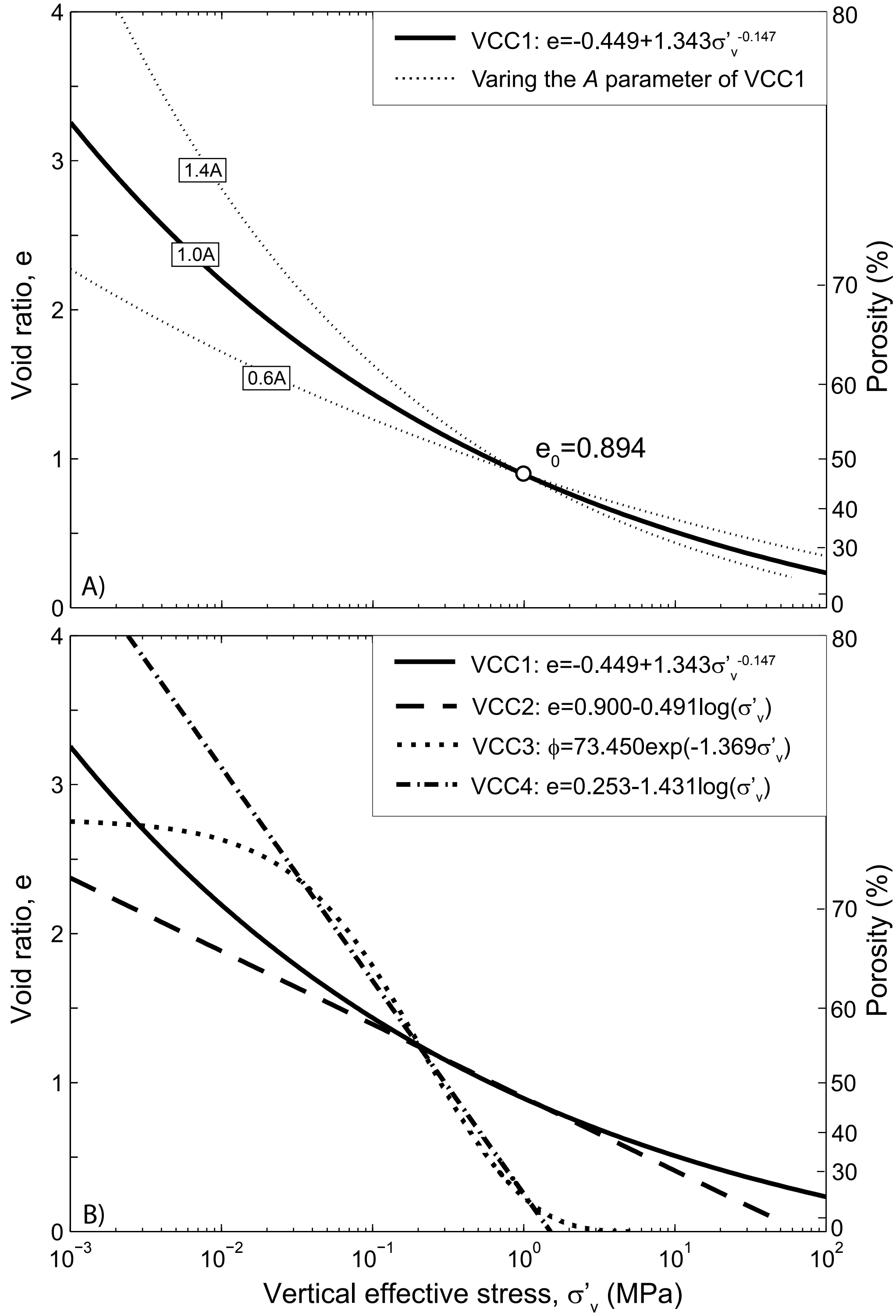

Figure 4.8: Comparison of virgin compression curves established by various approaches.

VCC3 and VCC4 predict similar pore space reduction with effective stress over the range in effective stress from 0.03 to 1.2 MPa (Figure 4.8B). However, outside of this range the two curves show very different behavior. VCC3 predicts nearly zero porosity (and hence nearly zero void ratio) at an effective stress of 3 MPa, which corresponds to a depth of approximately 400 mbsf if the sediments were hydrostatically pressured in the Ursa basin. VCC4 predicts zero void ratio (porosity) at an effective stress of only 1.5 MPa. At low effective stresses, VCC3 converges on a void ratio of about 2.75 ($\phi = 0.73$) whereas VCC4 has a linear void ratio vs. log effective stress behavior. Finally, VCC4 provides a much greater compression index (1.431) than the experimental values, which lie between 0.5 and 0.25 (Figure 4.6). The experimental values of C_c are all derived at void ratios less than 1.2 (Figure 4.6), which corresponds to the lowest void ratio that was used to derive VCC4. We interpret that value of C_c inferred from the porosity depth data of the shallow sediments (above 43.9 mbsf) is much larger than the experimental data because of the strengthening that occurs during compression: the C_c decreases rapidly within the first 50 mbsf as the void ratio rapidly reduces from 4 to 1. We note also other two factors may contribute: 1) sample disturbance can reduce the lab-derived C_c by a certain amount, and 2) the field-derived C_c can be either over- or under-estimated if the sediments are overpressured.

In summary, we suggest that an appropriate void ratio-stress relationship is one where void ratio is proportional to the log of effective stress and where the constant of proportionality changes as a function of void ratio. This results in the ability to capture the rapid change in void ratio with effective stress that is observed at low effective stresses and allows a prediction of reasonable porosities at higher effective stresses.

4.5 Pore Pressure Prediction

4.5.1 Pore Pressure from Porosity

We use the virgin compression curves (VCC1 and VCC4) to predict pore pressure within mudstones in the Ursa Basin. We apply these void ratio-effective stress relationships only on the clay-rich sediments. At Site U1324, we used the gamma ray log to separate sand/silt and mud/clay, and the caliper log to eliminate the data with poor quality due to borehole effects. Silt and sand layers beneath 300 mbsf are filtered by removing data where LWD gamma ray values are less than 73GAPI. Between 280 to 525 mbsf, sediments with caliper log greater than 10 inches are removed. Beneath 525 mbsf, sediments with caliper log greater than 10.1 inches are removed. After these data are removed, the LWD porosity is smoothed with a low pass Chebyshev Type II filter (first order, stopband ripple of 1, cutoff frequency of 0.01) to eliminate noise due to minor borehole effects or lithologic changes.

The pore fluid pressure for VCC4 can be predicted from void ratio using Equation 4.4. For VCC1, pore fluid pressure can be predicted from void ratio by rearranging Equation 4.7

$$P = \sigma_v - \left(\frac{e + \frac{B}{A}}{e_0 + \frac{B}{A}} \right)^{-\frac{\ln(10)}{A}} . \tag{4.8}$$

For each of these approaches, overpressure (P^*) is then calculated from

$$P^* = P - P_h , \tag{4.9}$$

where P_h is the hydrostatic pressure. The results are illustrated in Figures 4.9 and 4.10.

Comparing to VCC4, VCC1 accounts for the C_c change due to change in the soil condition, and predicts reasonable porosity over larger effective stress range (Figures 4.9B). We subtracted the porosity-depth profile predicted by VCC1 for sediments with hydrostatic pressure from the LWD porosity profile. The positive offsets indicate the sediments are less compacted or overpressured (Figure 4.9C). At Site U1324, VCC1 predicts slight overpressure in sediments

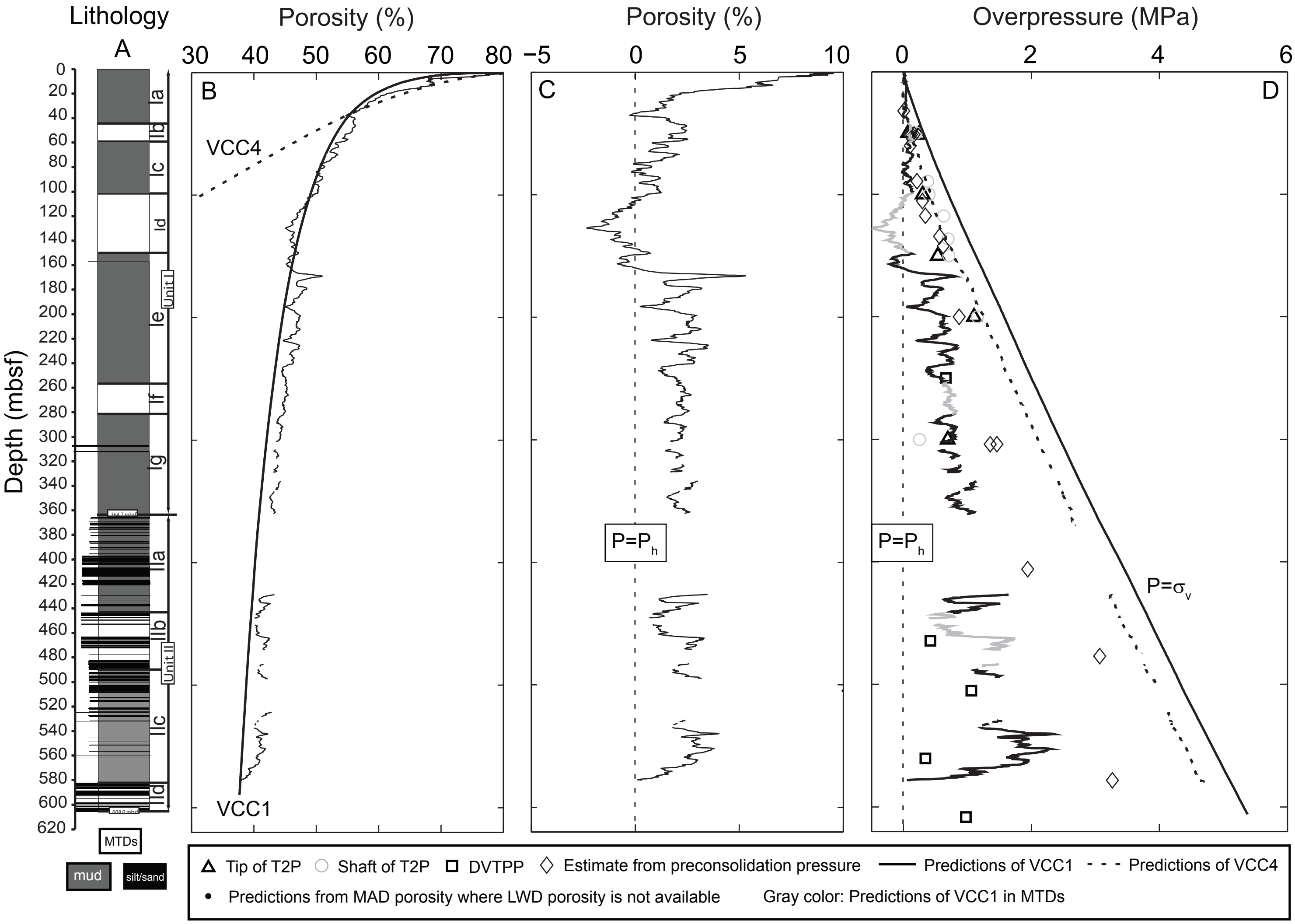

Figure 4.9: Overpressure predictions and measurements at Site U1324. The pressure measurements made by the Temperature-Two-Pressure (T2P) probe and the Davis-Villinger Temperature Pressure Probe (DVTPP) were extrapolated to in situ pressure using inverse square root of time approach (Long, et al., in review-b).

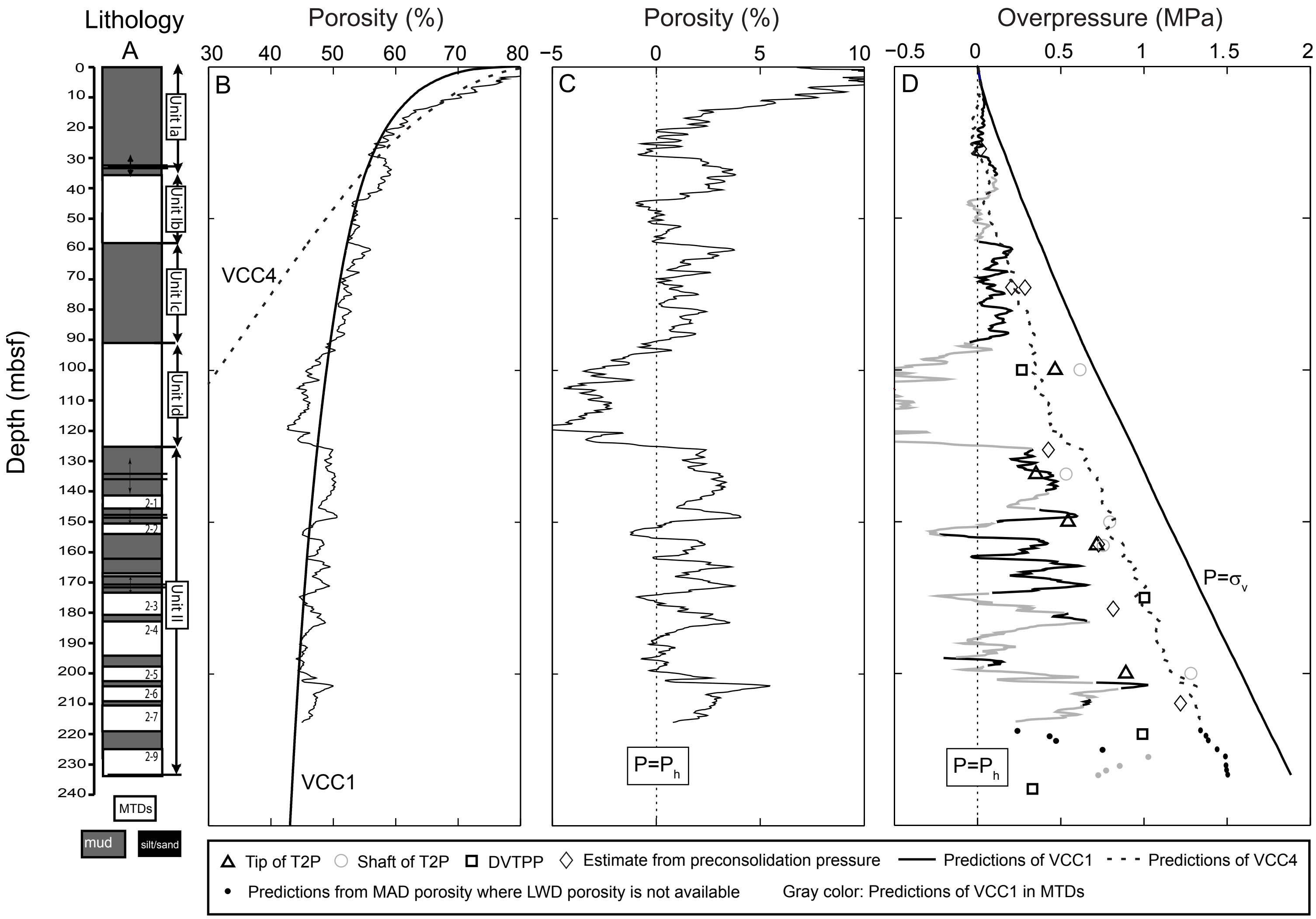

Figure 4.10: Overpressure predictions and measurements at Site U1322. The pressure measurements made by the Temperature-Two-Pressure (T2P) probe and the Davis-Villinger Temperature Pressure Probe (DVTPP) were extrapolated to in situ pressure using inverse square root of time approach (Long, et al., in review-b).

above 100 mbsf, sub-hydrostatic pressure in the major MTD (100-150 mbsf), and slightly increasing overpressure with depth beneath 160 mbsf (Figure 4.9D). VCC4 predicts zero void ratio (porosity) at ~200 mbsf for hydrostatically pressured Ursa mudstones. Beneath the section where it is established, VCC4 predicts significantly higher overpressure than VCC1. We interpret that VCC4 cannot be applied over large range in effective stress (depth) because of the strengthening that occurs during compression. At Site U1322, VCC1 predicts overpressure in the non-deformed sediments. And it consistently predicts significantly lower pressure within the MTDs (Figures 4.10).

At both sites, VCC1 predicts similar overpressure to the penetrometer measurements in the non-deformed sediments. The VCC1 prediction suggests that the sediments from seafloor to ~15 mbsf are overpressured. It is almost impossible for VCC4 to catch the pressure feature in such a shallow depth. All the pore space based models presented in this paper assume there is no lateral strain during the compression. Therefore, they cannot describe the pore space reduction due to shearing (e.g. the MTDs).

4.5.2 Overpressure from Preconsolidation pressure

If the soil is normally consolidated, then the overpressure can be estimated from the preconsolidation pressure:

$$P^* = \sigma'_{vh} - P'_c, \qquad (4.10)$$

where σ'_{vh} is the hydrostatic vertical effective stress. At both Site U1322 and Site U1324, the estimated overpressures are in good agreement with directly measured overpressure above 200 mbsf (Figures 4.9D and 4.10D). It is somewhat surprising that the preconsolidation pressures within the mass transport deposits (e.g. 100-150 mbsf at Site U1324, Figure 4.9) are producing reasonable values for in situ pressure. This suggests the shear deformation associated with formation of the MTD does not significantly affect the P'_c value. Below 200 mbsf, the P'_c values are relatively low and as a result they predict significantly higher overpressure than the penetrometer measurements (Figure 4.9D). We interpret that this may be because the deeper samples are more highly disturbed as sample disturbance often lowers the value of the preconsolidation pressure [*Jamiolkowski, et al.*, 1985].

4.6 Discussion

Values of the compression index relate to the type of soil, in situ condition, and mechanical structure of soil [*Mikasa*, 1964]. It was generally correlated with liquid limit [*Skempton*, 1944; *Terzaghi and Peck*, 1948; *Cozzolino*, 1961], which reflects type of soil; or correlated with void ratio [*Nishida*, 1956; *Hough*, 1957; *Sowers*, 1970], which reflects the in situ condition. In this study, the soils are very similar in composition. We related the compression index to the in situ void ratio and ignored the influence of soil structure.

A main observation is that the compression index linearly decreases with in situ void ratio. The relationship of C_c vs. e can be obtained from a single consolidation test by compressing the soil over a large stress range. A virgin compression curve can then be constructed based on the relationship of C_c vs. e. This extends the previous geotechnical observations, and has a significant impact on pore fluid pressure prediction in shallow sediments. It is also useful for forward fluid flow modeling through successfully describing the mudstone compression over large range in effective stress. In the Ursa Basin, we have shown that our pressure prediction based on the new approach successfully predict pressures interpreted from the penetrometer measurements. This approach can be applied for general applications in a similar way to the Equations 4.1 and 4.3: parameters A, B and e_0 can be calibrated in zones where the vertical effective stress and porosity are known by applying a nonlinear least-square regression of Equation 4.7.

Analysis of this new model shows that a locally defined virgin compression curve cannot validly be extrapolated over large range in effective stress. This effect is particularly important at very shallow depth where void ratio decreases rapidly. At a deeper depth, void ratio change is less so is the change in compression index. The virgin compression curve may be treated as a straight line. Many researchers achieved good pressure predictions at deep depth with a simple compressibility relationship [*Hart, et al.*, 1995; *Screaton, et al.*, 2002; *Saffer*, 2003; *Flemings and Lupa*, 2004].

The preconsolidation pressures matched penetrometer measurements in both deformed and non-deformed sediments to a depth of 200 mbsf. We infer that cores were so disturbed in the deeper section that we could not get good preconsolidation pressure from a consolidation test.

In the Ursa Basin, the ubiquitous presence of mass transport deposits has a significant effect on the porosity profile. The mass transport deposits appear to be more compacted than the non-deformed sediments. It suggests that extra shearing can reduce the porosity of the sediments with the vertical effective stress kept the same. As a result, the virgin compression curve based on the assumption of uniaxial strain will under-predict the in situ pressure in the mass transport deposits.

4.7 Conclusion

We conducted extensive CRSC tests on whole core samples to obtain the consolidation properties of the Ursa mudstones. The results suggest that the compression index linearly decreases with in situ void ratio. This implies that a local virgin compression curve cannot validly be extrapolated over large range in effective stress. This effect is particularly important at shallow depth where void ratio decreases rapidly. We have shown that the relationship of C_c vs. e can be obtained from a single consolidation test by compressing the soil over a large range in effective stress. A virgin compression curve can then be constructed based on the relationship of C_c vs. e to predict pore fluid pressure. In the Ursa Basin, this new approach successfully predicted pressures interpreted from the penetrometer measurements.

Nomenclature

Variable	Definition	Dimensions
A	slope of C_c vs. e relationship	Dimensionless
B	compression index at zero void ratio	Dimensionless
Cc	compression index	Dimensionless
Ce	expansion index	Dimensionless
P	pore fluid pressure	M/LT^2
P_h	hydrostatic pressure	M/LT^2
P'_c	preconsolidation pressure	M/LT^2
P^*	overpressure	M/LT^2
e	void ratio	Dimensionless
e_0	void ratio at an effective stress of unity	Dimensionless
e_s	void ratio measured on tested specimens	Dimensionless
β	empirical constant	LT^2/M
ϕ	porosity	Dimensionless
ϕ_0	porosity at zero effective stress	Dimensionless
σ_v	vertical total stress	M/LT^2
σ'_v	vertical effective stress	M/LT^2
σ'_{vh}	hydrostatic vertical effective stress	M/LT^2

Acknowledgements

This research used samples and data provided by the Integrated Ocean Drilling Program (IODP). Funding for this research was provided by the U.S. Science Support Program for IODP that is administered by Joint Oceanographic Institutions. In addition, the NSF Grants 0447235 and 0351085 supported this research.

References

Athy, L. F. (1930), Density, Porosity, and Compaction of Sedimentary Rocks, *American Association of Petroleum Geologist Bulletin*, *14*, 1-24.

Azzous, A. S., Krizek, R.J., and Corotis, R.B. (1976), Regression analysis of soil compressibility, *Soil and Foundations*, *16*, 19-29.

Becker, D. E., J.H.A. Crooks, K. Been and M.G. Jefferies (1987), Work as a criterion for determing in situ and yield stresses in clays, *Can. Geotch. J.*, *24*, 549-564.

Blum, P. (1997), Physical properties handbook: a guide to the shipboard measurement of physical properties of deep-sea cores, edited, ODP Tech. Note, 26 [Online]. Available from World Wide Web: <http://www-odp.tamu.edu/publications/tnotes/tn26/INDEX.HTM>.

Brown, K. M. (1995), 17. The Variation of the Hydraulic Conductivity Structure of an Overpres¬sured Thrust Zone with Effective Stress, paper presented at Proceedings of the Ocean Drilling Program, Ocean Drilling Program, College Station.

Brown, K., and Ransom, B., (1996), Porosity corrections for smectite-rich sediments: Impact on studies of compaction, fluid generation and tectonic history, *Geology*, 24.

Casagrande, A. (1936), The determination of the pre-consolidation load and its practical significance, *1st International Conference on Soil Mechanics*, 60-64.

Cozzolino, V. M. (1961), Statistical forecasting of compression index, *Proc., 5th Int. Conf. on Soil Mechanics and Foundation Engineering*, Paris, Vol. 1, 51–53.

Dugan, B. (2007), Personal communication.

Dugan, B., et al. (2007), Physical Properties of Mass Transport Complexes in the Ursa Region, Northern Gulf of Mexico (IODP Expedition 308) Determined from Log, Core, and

Seismic Data, *Proceedings of the Offshore Technology Conference*, Houston, Texas, April 30-May 3, 2007, OTC Paper #18704.

Dugan, B., and P. B. Flemings (2000), Overpressure and Fluid Flow in the New Jersey Continental Slope: Implications for Slope Failure and Cold Seeps, *Science*, *289*, 288-291.

Dugan, B., and P. B. Flemings (2002), Fluid flow and stability of the US continental slope offshore New Jersey from the Pleistocene to the present, *Geofluids*, *2*, 137-146.

Dugan, B., P.B. Flemings, D.L. Olgaard and M.J. Gooch (2003), Consolidation, effective stress, and fluid pressure of sediments from ODP Site 1073, US mid-Atlantic continental slope, *Earth and Planetary Science Letters*, *215*, 13-26.

Eaton, B. A. (1975), The equation for geopressure prediction from well logs, paper presented at Society of Petroleum Engineers.

Fertl, W. H., et al. (1994), Studies in abormal pressures, 454.

Flemings, P. B., Behrmann, J., John, C., and Shipboard Scientists IODP Expedition 308 (2006), Proceedings of the Integrated Ocean Drilling Program, DOI: doi:10.2204/iodp.proc.308.2006.

Flemings, P. B., and J. Lupa (2004), Pressure Prediction in the Bullwinkle Basin through Petrophysics and Flow Modeling (Green Canyon 65, Gulf of Mexico), *Marine and Petroleum Geology*, *21*, 1311-1322.

Flemings, P. B., Stump, B.B., Finkbeiner, T., and Zoback, M. (2002), Flow focusing in overpressured sandstones: theory, observations, and applications, *Am. J. Sci.*, *302*, 827–855.

Harrison, W. J., and L. L. Summa (1991), Paleohydrology of the Gulf of Mexico Basin, *American Journal of Science*, *291*, 109-176.

Hart, B. S., et al. (1995), Porosity and pressure: role of compaction disequilibrium in the development of geopressures in a Gulf Coast Pleistocene basin, *Geology*, *23*, 45-48.

Hottman, C. E., and R. K. Johnson (1965), Estimation of formation pressures from log-derived shale properties, *Journal of Petroleum Technology*, *17*, 717-722.

Hough, B. K. (1957), *Basic soil engineering*, 114-115 pp., The Ronald Press Company, New York.

Jamiolkowski, M., et al. (1985), New developments in field and laboratory testing of soils, paper presented at Proc., 11 th int. Conf. on Soil Mechanics and Foundation Engineering, San Francisco,1, 57-153.

Lahann, R. (2002), Impact of Smectite Diagenesis on Compaction Modeling and Compaction Equilibrium, in *Pressure regimes in sedimentary basins and their prediction*, edited by A. R. Huffman and G. L. Bowers, pp. 61-72.

Long, H., P. B. Flemings, J. T. Germaine, and D. M. Saffer (in review-a), Consolidation characteristics of sediments from IODP Expedition 308, Ursa Basin, Gulf of Mexico, *in. Proceeding of the integrated ocean drilling program, vol, 308*.

Long, H., P. B. Flemings, J. T. Germaine, B. Dugan, D. Ferrell, and Expedition 308 Scientists (in review-b), Penetrometer Measurements of In Situ Temperature and Pressure on IODP Expedition 308, *in. Proceeding of the integrated ocean drilling program, vol, 308*.

Mikasa, M. (1964), Chart for classification of engineering properties of soils and its significance, *Tsuchi-to-Kiso*, 12(4), 17–24

Moore, J. C. and H.J. Tobin (1997), Estimated fluid pressures of the Barbados accretionary prism and adjacent sediments, in *Proceedings of the Ocean Drilling Program, Scientific Results, ed. C.M. Miller, 156,* 229-238.

Nelson, H., J. Germaine, H. Long, and P.B. Flemings (in preparation), X-ray radiography and C.T. scan of whole cores from IODP Expedition 308, *in. Proceeding of the integrated ocean drilling program, vol, 308*.

Nishida, Y. (1956), A brief note on compression index of soils, *Journal of soil mechanics and foundations division, ASCE*, *82*, 1027-1021-1027-1014.

Ostermeier, R. M., Pelletier, J.H., Winker, C.D., Nicholson, J.W., Cowan, C.K. (2002), Dealing with Shallow-Water Flow in the Deepwater Gulf of Mexico, *The Leading Edge*, 660-668.

Rubey, W. W., and M. K. Hubbert (1959), Role of fluid pressure in mechanics of overthrust faulting, Part 2. Overthrust belt in geosynclinal area of western Wyoming in light of fluid-pressure hypothesis, *Geol. Soc. Am. Bull.*, *70*, 167–205.

Saffer, D. M. (2003), Pore pressure development and progressive dewatering in underthrust sediments at the Costa Rican subduction margin: Comparison with northern barbados and Nankai, *J. Geophys. Res.*, *108*, 2261, doi:2210.1029/2002JB001787.

Saffer, D. M., Silver, E.A., Fisher, A. T., Tobin, H, Moran, K (2000), Inferred pore pressures at the Costa Rica subduction zone: implications for dewatering processes, *Earth and Planetary Science Letters*, *177*, 193-207.

Santagata, M. C., and J.T. Germaine (2002), Sampling disturbance effects in normally consolidated clays, *Journal of geotechnical and geoenvironmental engineering*, *128*, 997-1006.

Sawyer, D. E., et al. (2007a), Seismic Geomorphology, Lithology, and Evolution of the Late Pleistocene Mars-Ursa Turbidite Region, Mississippi Canyon Area, Northern Gulf of Mexico, *American Association of Petroleum Geologists Bulletin*, *91*, 215-234.

Sawyer, D., et al. (2007b), Lateral Variations in Core, Log, and Seismic Attributes of a Mass Transport Complex in the Ursa Region, IODP Expedition 308, Northern Gulf of Mexico, paper presented at 2007 Offshore Technology Conference, Houston, TX, April 30-May 3, 2007.

Sawyer, D., Flemings, P.B., and Germain, J.T. (in preparation), Particle size distribution analysis, IODP Leg 308 Sites 1322 and 1324 in the Ursa Region on the continental slope of the Northern Gulf of Mexico, *in Proceeding of the integrated ocean drilling program, vol, 308*.

Schmertmann, J. H. (1955), The undisturbed consolidation behavior of clay, *Trans. ASCE*, *120*, 1201-1233.

Screaton, E., D. Saffer, P. Henry and S. Hunze (2002), Porosity loss within the underthrust sediments of the Nankai accretionary complex: Implication for overpressures, *Geology*, *30*, 19-22.

Skempton, A. W. (1944), Notes on the compressibility of clays, *Q. J. Geological Soc. London*, 100, 119–135

Sowers, G. B. (1970), *Introductory soil mechanics and foundations*, 386 pp., Collier-Macmillan Limited, London.

Stump, B.B., and P.B. Flemings (2002), Consolidation State, Permeability, and Stress Ratio as Determined from Uniaxial Strain Experiments on Mud Samples from the Eugene Island 330 Area, Offshore Louisiana, in Pressure regimes in sedimentary basins and their prediction, eds. A.R. Huffman and G.L. Bowers, v. 76, p. 131-144.

Terzaghi, K. and R.B. Peck (1948), Soil Mechanics in Engineering Practice, New York, p. 556.

Wallace, W. E. (1965), Abnormal surface pressure measurements from conductivity or resistivity logs, *Oil & Gas Journal*, *63*, 102-106.

Winker, C. D., and J. R. Booth (2000), Sedimentary dynamics of the salt-dominated continental slope, Gulf of Mexico; integration of observations from the seafloor, near-surface, and deep subsurface, in *GCSSEPM Foundation 20th Annual Research Conference, Deep-Water Reservoirs of the World*, edited, pp. 1059-1086.

Winker, C. D., and R. C. Shipp (2002), Sequence Stratigraphic Framework for Prediction of Shallow Water Flow in the Greater Mars-Ursa Area, Mississippi Canyon Area, Gulf of Mexico Continental Slope, paper presented at 22nd Annual GCSSEPM Foundation Bob F. Perkins Research Conference, abs.

Wood, D. M. (1990), *Soil behavior and critical state soil mechanics*, 462 pp., Cambridge University Press.

Appendix A: Data Report: Penetrometer Measurements Of In Situ Temperature and Pressure on IODP Expedition 308

Abstract

We conducted temperature and pore pressure measurements with the DVTPP and the T2P penetremeters during IODP Expedition 308. At Ursa Basin, 18 measurements are used to determine that the geothermal gradient at Site U1324 is bilinear. The temperature gradient is 18.6 $^{\circ}$C/km in Lithostratigraphic Unit I and 16.7 $^{\circ}$C/km in Lithostratigraphic Unit II. Based on nine measurements at Site 1322, the geothermal gradient is 21.9 $^{\circ}$C/km. At Brazos Trinity IV Basin, the geothermal gradient at Site U1320 is 23.1 $^{\circ}$C /km. In Ursa Basin, significant overpressures are observed in the sediments above ~200 mbsf at Sites U1322 and U1324. The overpressure ratio is ~ 0.7 in these locations. At Site U1324, pore pressure decreases with increasing depth between 200 and 300 mbsf. Below 300 mbsf and within Lithostratigraphic Unit II, overpressure is approximately constant (~1 MPa). Lithostratigraphic Unit II is composed of silty claystone interbedded with beds of silt and very-fine sand. At Brazos Trinity IV Basin, only two penetrometer deployments were made and the data are inconclusive.

A.1 Introduction

The objective of this report is to present in situ pressure and temperature data measured by downhole pressure penetrometers during IODP Expedition 308 [*Flemings, et al.*, 2006a]. Pressure and temperature data are critical for constraining fluid flow, heat flow and hydraulic and thermal diffusivity. In addition, temperature affects sediment diagenesis and microbial activity. IODP Expedition 308 is dedicated to the study of overpressure and fluid flow on the Gulf of Mexico continental slope. Knowledge of the stress regime is critical for evaluating submarine slope stability. The in situ pressure is closely related to the in situ stress regime. Recently, it has been hypothesized that overpressure, pore pressures in excess of hydrostatic pressure, can weaken the strength of sediments and thus cause slope instability near the seafloor [*Davis, et al.*, 1983; *Dugan and Flemings*, 2002]. Overpressure and the shallow water flow frequently causes operational problems during drilling [*Ostermeier, et al.*, 2001].

During IODP Expedition 308, three sites were drilled at the Brazos Trinity IV Basin and three sites were drilled in the Ursa Basin (Figures A.1, A.2 and A.3). To document the in situ pore pressure and temperature, we deployed two types of pressure penetrometers during IODP Expedition 308: the Temperature/Dual Pressure (T2P) probe and the Davis-Villinger Temperature Pressure Probe (DVTPP) (Figure A.4). The DVTPP was deployed previously during ODP Legs 190, 201, and 204 [*D'Hondt*, 2003; *Long*, 2007a; *Moore*, 2001; *Tréhu*, 2003]. The T2P is a new tool under development as a cooperative effort between Penn State University, MIT, and IODP-TAMU [*Flemings*, 2005, 2006c].

A.2 Method

The DVTPP and T2P probe interface with the Colleted Delivery System (CDS). The CDS is lowered by wireline and engages with the Bottom Hole Assembly (BHA). Once the CDS is engaged in the BHA, the drill string is used to push the probe into the formation. The drill string is then raised 3–4 m and the CDS telescopes to decouple the probe from the drill string. The probe remains in the formation to measure pressure and temperature for 30–90 min. The wireline pulls the CDS to its extended position and then pulls the penetrometer out of the formation. A detailed description of the deployment procedure is presented in Appendix A.A. The data are downloaded from the data acquisition unit when the tool is retrieved.

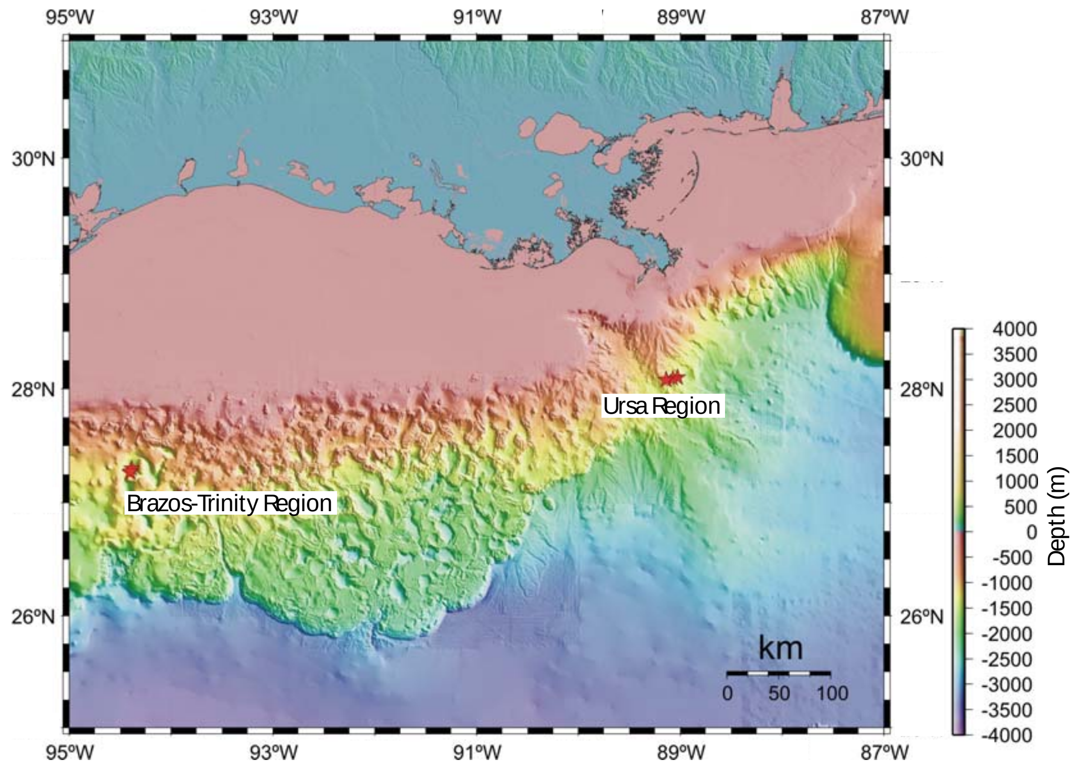

Figure A.1: Base map of study areas (after Flemings et al., (2006a)).

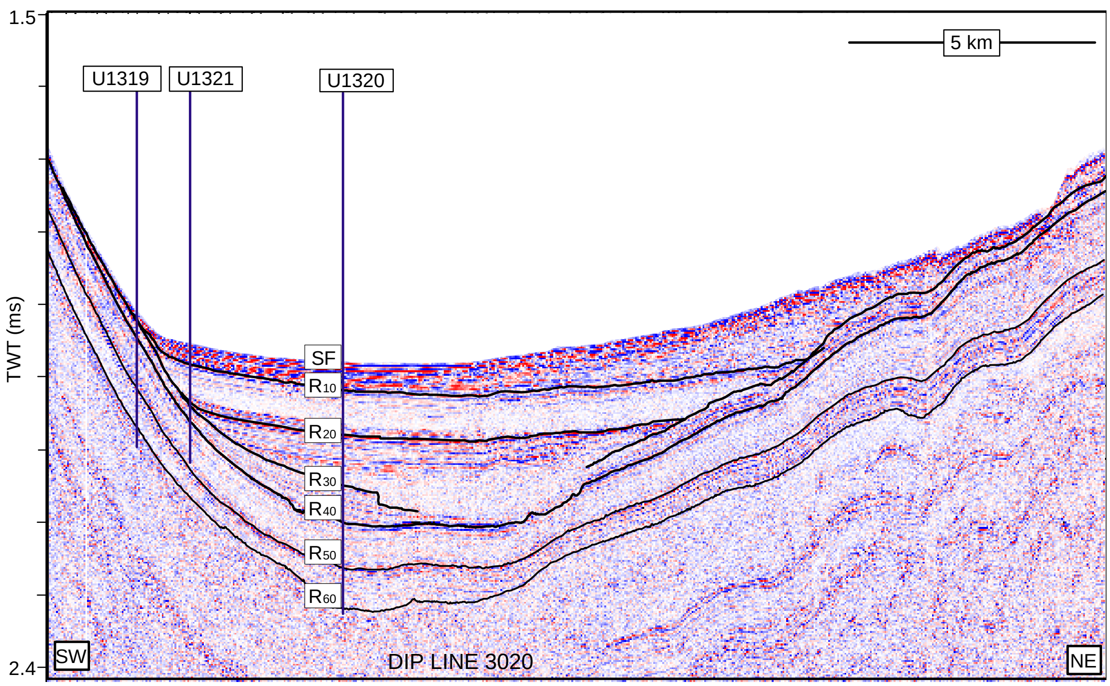

Figure A.2: Seismic cross section of Brazos Trinity IV Basin showing the location of Sites U1319, U1320, and U1321 (Flemings et al., 2006a).

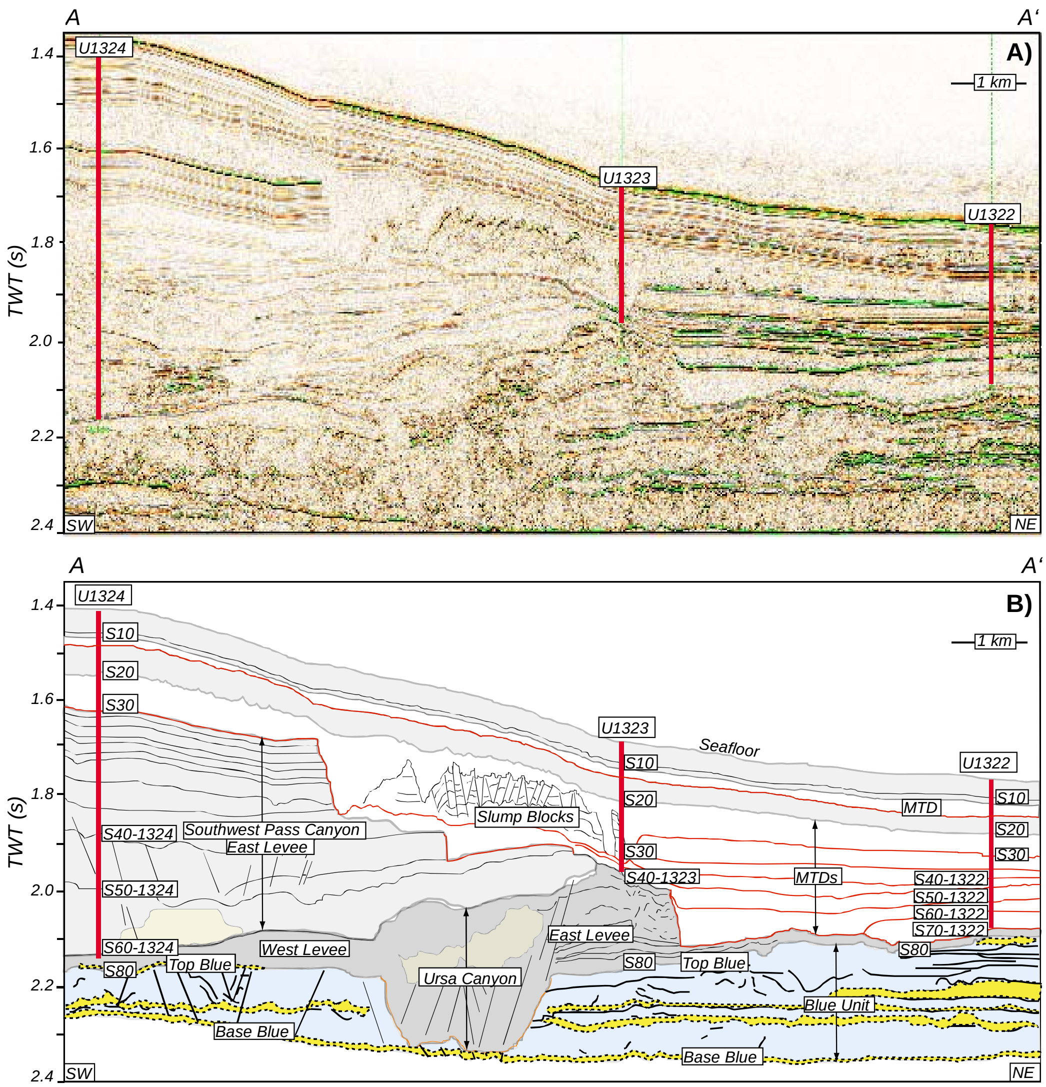

Figure A.3: Seismic and interpreted cross section of Ursa Basin and location of Sites U1322, U1323 and U1324 (Sawyer et al., 2007). A) East-West seismic cross section A-A'. (B) Interpreted cross section A-A'. Light and dark gray represent mud-rich levee, rotated channel-margin slides, and hemipelagic drape; yellow represents sand-rich channel fill. The Blue Unit (light blue) is composed of sand and mud. Mass transport deposits have occurred in the mud-rich levee deposits above the Blue Unit. Detachment surfaces are colored red.

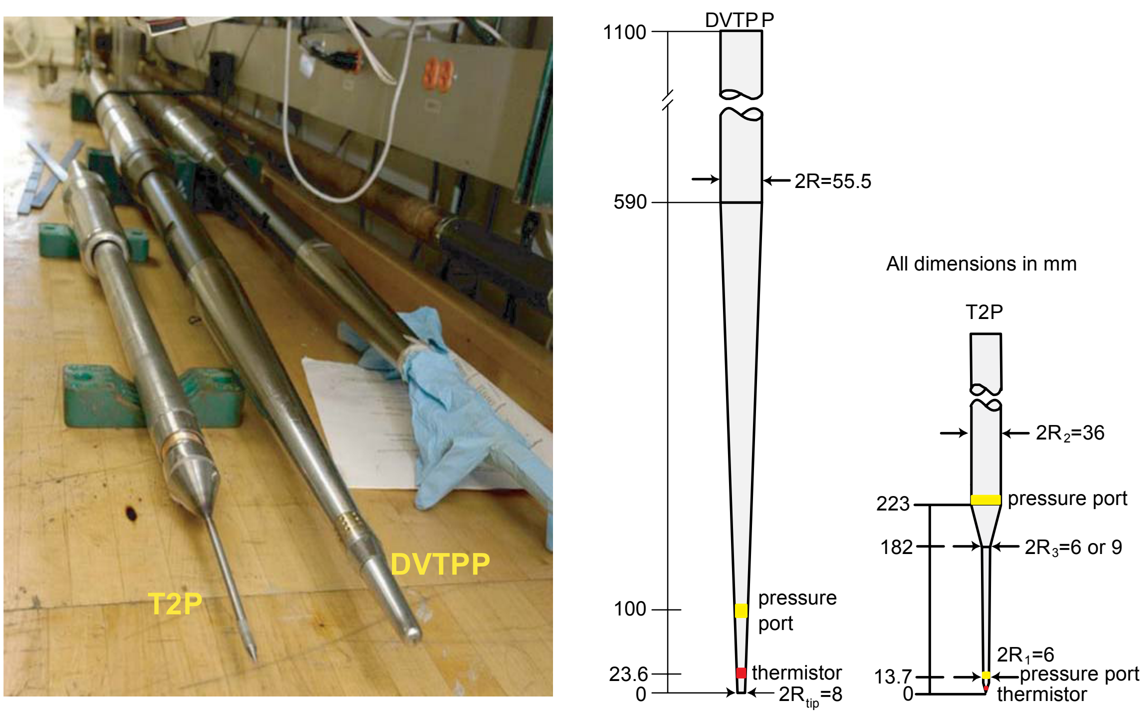

Figure A.4: The DVTPP and T2P pressure penetrometers. The DVTPP has a long, tapered tip that extends beyond the constant diameter shaft. Its tip tapers continuously from 8 to 55.5 mm in diameter. The pressure port is located 100 mm above the tip. The T2P has a tapered extension piece 223 mm long which fits onto the end of a standard 36 mm diameter cone rod. Its modular design allows the use of multiple tip geometries and it measures pore pressure at its narrow tip and at the larger diameter shaft behind the narrow tip.

When the penetrometers penetrate the formation, the temperature (due to friction on the tool) and pressure (due to deformation of the soil) are raised relative to their in situ values. Subsequently, the tools are left in order to dissipate toward the equilibrium values (Figure A.5). Temperature decay can be used to infer the formation temperature and thermal conductivity [*Davis*, 1997; *Villinger*, 1987]. Decay of the penetration-induced pore pressure can be used to infer the formation pressure, the hydraulic diffusivity and the permeability [*Baligh*, 1986c; *Gupta*, 1986; *Long*, 2007a; *Whittle*, 2001].

The rates of the pressure and temperature decay are functions of the probe diameter and the hydraulic/thermal diffusivity of the sediment [*Long*, 2007a; *Villinger*, 1987]. The pressure decay is much slower than the temperature decay in low-permeability mudstones [*Long*, 2007a]. Due to the restricted time available for deployment, we must interpret in situ pressure from partial dissipation records. If detailed soil properties are available, the in situ pressure and hydraulic diffusivity of the sediment can be inferred from modeling of soil behavior for different penetrometer geometries. However, in many cases soil properties are not available, or there are insufficient resources to pursue soil modeling. In these cases, in situ pressure is inferred from simple extrapolation approaches such as inverse time ($1/t$) extrapolation [*Davis*, 1991; *Lim*, 2006; *Long*, 2007b; *Whittle*, 2001] and inverse square root of time ($1/\sqrt{t}$) extrapolation [*Long*, 2007b].

A.3 Overview

U1319, U1320 and U1321, were drilled at Brazos Trinity IV Basin (Figure A.1 and A.2). Site U1319 and Site U1320 were cored and penetrometer measurements were made. U1322, U1323 and U1324, were drilled in the Ursa Basin (Figure A.1 and A.3). Site U1322 and Site U1324 were cored and penetrometer measurements were made.

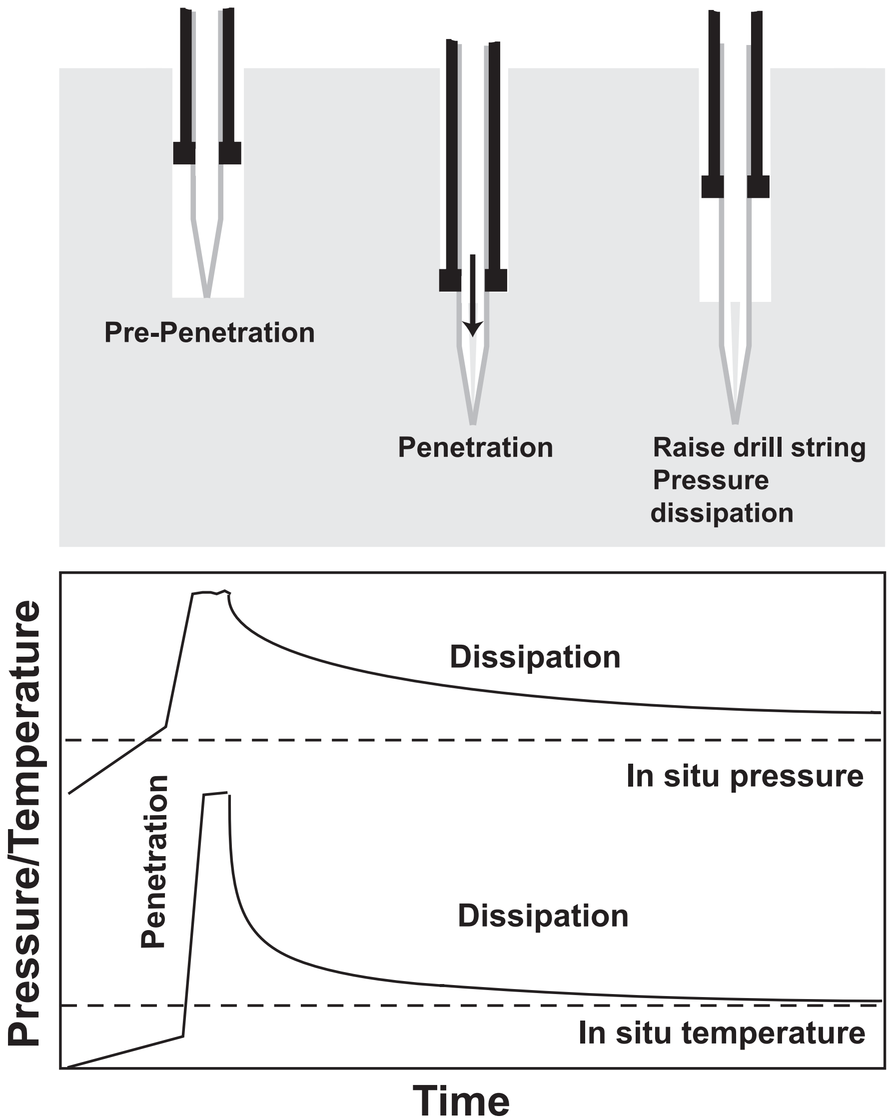

Figure A.5: Illustration of the procedure for probe penetration. The drill string pushes the probe into the formation. After penetration, the drill string is raised and the CDS telescopes to decouple the drill string from the tool. The probe stays in the formation to monitor the temperature and pressure. For a good measurement, there is an abrupt increase in pressure and temperature during penetration and then there is a slow dissipation of pressure and temperature when the tool stays in the formation.

We present the temperature and pressure data from the penetrometer deployments at the four sites in this report. In the main text, we present our best estimate of the in situ temperature and pressure. In Appendix A.A, we describe how the DVTPP was calibrated and present a detailed description of each deployment. In Appendix A.B, we describe how the T2P was calibrated, and we describe each deployment. In Appendix A.C, we present a discussion of the pressure state within the drill-pipe based on the DVTPP pressure measurements.

The temperature and pressure data are in Microsoft Excel format. These data have been recalibrated and consequently are different and improved relative to the data presented in IODP proceeding 308 [*Flemings, et al.*, 2006a]. The raw data can be found online in the Supplementary material [*Flemings*, 2006b]. The penetrometer data are integrated with the rig instrumentation system data ("Truview data") in order to better understand and assess the quality of each measurement.

A.4 Summary of Deployments

Twenty DVTPP deployments and twenty eight T2P deployments were completed during IODP Expedition 308 (Table A.1). The Deployment number (Table A.1) reflects the deployment sequence of each tool on Expedition 308 [*Flemings*, 2005]. Deployments are subdivided into three types: Type I, Type II and Type III (Table A.1 and Figure A.6).

Figure A.7A illustrates an ideal penetrometer deployment for the DVTPP and the T2P (Type I, Table A.1). The tip pressure is at a maximum during insertion and subsequently pressure declines with time. At the end of the deployment, the shaft pressure of the T2P is much greater than that of the tip pressure. This is because the shaft has a much larger diameter. As a result it disturbs a greater region around the penetrometer and this takes a greater amount of time to

Table A1. Summary of the DVTPP and T2P deployments during IODP Expedition 308.

Deployment #	Hole	File name	Depth (mbsf)	Depth (mbsl)	Truview data	Decay time (min)	Type	Date	Tool	Remarks
DVTP-P1	U1320A	1320a24	203.4	1673.4	LF	42	III	9-Jun-05	9367; 88587; 0226-3	Hydraulic leak; tool vibrating during decay
DVTP-P2	U1320A	1320a33	289.9	1759.9	LF	13	III	9-Jun-05	9367; 88587; 0226-3	Hydraulic leak; tool vibrating during decay
DVTP-P3	U1324B	1324b27	229.1	1285.9		50	III	22-Jun-05	9367; 88587; 0226-3	Hydraulic leak; tool vibrating during decay
DVTP-P4	U1324B	1324b45	362.4	1419.2	not match	47	III	23-Jun-05	9367; 88587; 0226-3	Hydraulic leak; good T
DVTP-P5	U1324B		387.9	1444.7	NA	10	III	23-Jun-05		Failed; no data recorded
DVTP-P6	U1324B	1324b59	464.3	1521.1	not match	34	IIB	24-Jun-05	9368; 88579; 0226-2	Pullout/void; good T
DVTP-P7	U1324B	1324b62	493.1	1549.9	not match	31	III	24-Jun-05	9368; 88579; 0226-2	Dilatant soil?, good T
DVTP-P8	U1324B	1324b64	521.9	1578.7	HF	41	III	24-Jun-05	9368; 88579; 0226-2	Weird pressure; tool movements during decay
DVTP-P9	U1324B		541.1	1597.9		30	III	25-Jun-05		Programing error; no data recorded
DVTP-P10	U1324B	1324b68	560.4	1617.2	HF	32	IIA	25-Jun-05	9367; 88587; 0226-3	Good T; unusual decay curve
DVTP-P11	U1324B	1324b72	589.2	1646.0	HF	45	III	25-Jun-05	9367; 88587; 0226-3	Unreliable data
DVTP-P12	U1324B	1324b74	608.2	1665.0	HF	61	IIA	25-Jun-05	9367; 88587; 0226-3	Pullout/void; tool vibrating during decay
DVTP-P13	U1324C	1324c05	250	1305.7	HF	90	I	27-Jun-05	9367; 88587; 0226-3	Tool vibrating during decay
DVTP-P14	U1324C	1324c07	405	1460.7	HF	94	III	27-Jun-05	9367; 88587; 0226-3	Pullout/void; communation with borehole
DVTP-P15	U1324C	1324c08	505	1560.7	HF	93	IIB	28-Jun-05	9367; 88587; 0226-3	Pullout/void; communation with borehole?; further tool insertion during decay
DVTP-P16	U1322B	1322b19	166.7	1486.2	HF	92	III	29-Jun-05	9367; 88587; 0226-3	Pullout/void; communation with borehole
DVTP-P17	U1322C	1322c02	100	1418.9	LF	91	IIA	1-Jul-05	9368; 88579; 0226-2	Pullout/void; good T
DVTP-P18	U1322C	1322c03	220	1538.9	HF	62	IIB	1-Jul-05	9368; 88579; 0226-2	Pullout/void; good T
DVTP-P19	U1322C	1322c04	238	1556.9	HF	93	IIA	1-Jul-05	9368; 88579; 0226-2	Pullout/void; good T

DVTP-P20	U1322D	1322d04	175	1493.9	HF	60	I	2-Jul-05	9368; 88579; 0226-2	Type pressure/temperature decay
T2P_1	U1319A	t2p_1						7-Jun-05	Sn4; S50-73; Z59-72; 0509-3; straight	pressure test in water column
T2P_2	U1319A	t2p_2	80.5	1510.1	LF	35	Tip:I; Shaft:I	7-Jun-05	Sn4; S50-73; Z59-72; 0509-3; straight	Tip broken; lost thermistor 3; insignificant pressure/temperature response due to pumping
T2P_3	U1320A	t2p_3	126.3	1596.3	LF	52	Tip:IIA; Shaft:III	8-Jun-05	Sn2; S50-75; S50-74; 0509-2; taper	Tip bent; shaft has no response; insignificant pressure/temperature response due to pumping
T2P_4	U1320A	t2p_4	213	1683.0	LF	25	Tip:I; Shaft:III	9-Jun-05	Sn4; S50-73; Z59-72; 0509-6; straight	installed by its own weight; slight pressure & temperature increase due to pumping
T2P_5	U1324B	t2p_5	51.3	1108.1	LF	34	Tip:IIA; Shaft:IIA	21-Jun-05	Sn2; S50-75; Y67-16; 0509-2; straight	Tip broken; lost thermistor 2; slight pressure increase due to pumping
T2P_6	U1324B	t2p_6	89.3	1146.1	LF	25	Tip:III; Shaft:I	21-Jun-05	Sn4; S50-73; Z59-72; 0509-6; taper	Further insertion due to pumping; internal leak at tip
T2P_7	U1324B	t2p_7	117.8	1174.6	LF	31	Tip:III; Shaft:I	21-Jun-05	Sn4; S50-73; Z59-72; 0509-6; taper	Further insertion due to pumping; internal leak at tip
T2P_8	U1324B	t2p_8	136.3	1193.1	LF	30	Tip:III; Shaft:IIA	22-Jun-05	Sn4; S50-73; Z59-72; 0509-6; taper	Shaft was not stable; internal leak at tip
T2P_9	U1324B	t2p_9	368	1424.8	LF	40	Tip:III; Shaft:III	23-Jun-05	Sn2; S50-75; S50-74; 0509-1; taper	Communication with borehole fluids
T2P_10	U1324B	t2p_10	394.5	1451.3		30	Tip:III; Shaft:III	23-Jun-05	Sn2; S50-75; S50-74; 0509-1; taper	Lost communication with sensors
T2P_11	U1324B	t2p_11	593.2	1650.0	bad data	15	Tip:III; Shaft:III	25-Jun-05	Sn4; S50-73; S50-74; 0509-6; taper	Tool test; weird T
T2P_12	U1324C	t2p_12	50	1105.7	LF	60	Tip:IIA; Shaft:IIA	26-Jun-05	Sn4; S50-73; S50-74; 0509-6; taper	Slight pressure increase due to pumping
T2P_13	U1324C	t2p_13	100	1155.7	LF	60	Tip:IIA; Shaft:I	26-Jun-05	Sn4; S50-73; S50-74; 0509-6; taper	Slight pressure pulses during decay

T2P_14	U1324C	t2p_14	150	1205.7	LF	60	Tip:IIB; Shaft:IIA	26-Jun-05	Sn4; S50-73; S50-74; 0509-6; taper	Pressure perturbations during decay
T2P_15	U1324C	t2p_15	200	1255.7	LF	60	Tip:IIA; Shaft:I	27-Jun-05	Sn4; S50-73; S50-74; 0509-6; taper	Shaft has typical decay
T2P_16	U1324C	t2p_16	300	1355.7	HF	90	Tip:I; Shaft:I	27-Jun-05	Sn2; Z59-72; S50-75; 0509-1; taper	Typical decay on both tip and shaft
T2P_17	U1322B	t2p_17	42	1361.5	HF	60	Tip:III; Shaft:III	28-Jun-05	Sn2; S50-74; S50-73; 0509-1; taper	Communication with borehole fluid
T2P_18								29-Jun-05		Bench test
T2P_19	U1322B	t2p_19	134.3	1453.8	HF	30	Tip:IIB; Shaft:IIB	29-Jun-05	Sn2; S50-74; S50-73; 0509-1; taper	Nearly constant pressure during decay
T2P_20	U1322B	t2p_20	157.8	1477.3	HF	60	Tip:IIB; Shaft:IIB	29-Jun-05	Sn2; S50-75; S50-73; 0509-1; taper	Nearly constant shaft pressure during decay
T2P_21	U1322C	t2p_21	50	1368.9		60	Tip:III; Shaft:III	30-Jun-05	Sn4; S50-72; S50-75; 0509-4; taper	Memory card was ajar; no data recorded
T2P_22	U1322C	t2p_22	75	1393.9		60	Tip:III; Shaft:III	30-Jun-05	Sn2; S50-74; S50-73; 0509-1; taper	Flooded the electronics; no data recorded
T2P_23	U1322C	t2p_23	150	1468.9	HF	60	Tip:IIB; Shaft:IIA	1-Jul-05	Sn4; S50-72; S50-75; 0509-4; taper	Truview data are only available for decay phase
T2P_24	U1322C	t2p_24	200	1518.9	HF	60	Tip:I; Shaft:I	1-Jul-05	Sn4; S50-72; S50-75; 0509-4; taper	Typical decay on both tip and shaft
T2P_25	U1322D	t2p_25	40	1358.9	N/A	60	Tip:III; Shaft:III	2-Jul-05	Sn4; S50-72; S50-75; 0509-4; taper	Communication with borehole fluid
T2P_26	U1322D	t2p_26	70	1388.9	LF	45	Tip:III; Shaft:III	2-Jul-05	Sn4; S50-72; S50-75; 0509-4; taper	Communication with borehole fluid
T2P_27	U1322D	t2p_27	100	1418.9	HF	45	Tip:IIB; Shaft:IIA	2-Jul-05	Sn4; S50-72; S50-75; 0509-4; taper	Pullout/void
T2P_28	U1322D	t2p_28	134	1452.9	HF	45	Tip:III; Shaft:III	2-Jul-05	Sn4; S50-72; S50-75; 0509-4; taper	Communication with borehole fluid; broken tip; bent drive tube

Notes: 1. LF = Low Frequecy data (1 minte period); HF = High Frequecy data (1 second period). 2. N/A = not available.
3. Sequence of elements in tool column follows logger, tip transducer, shaft transducer, thermistor, geometry. Shaft transducer and geometry are not applicable for DVTPP.

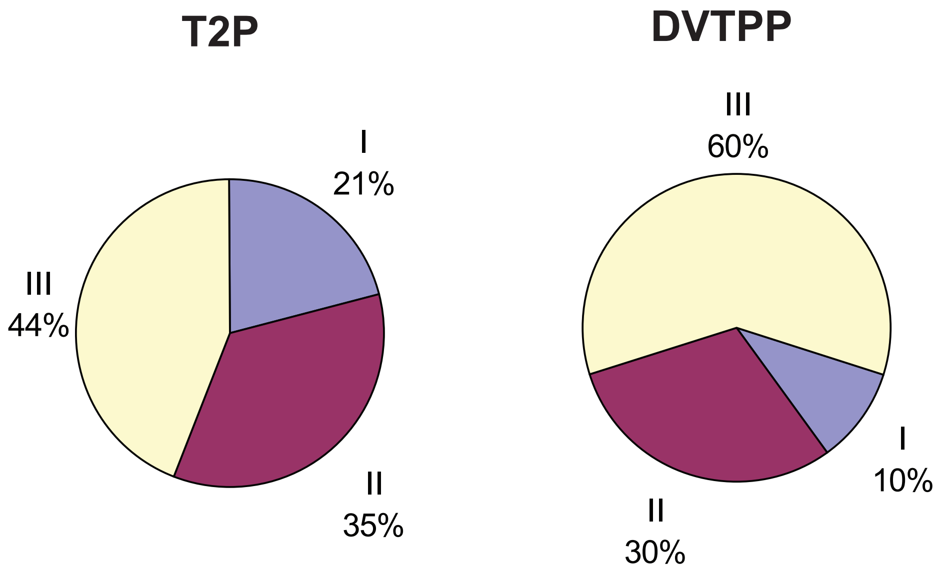

Figure A.6: Summary of the T2P and DVTPP deployments during IODP Expedition 308. Type I, II and III deployments are defined in Figure A.7. Type I and II deployments can give insight into in situ conditions. Type III deployments do not provide useful information of in situ conditions.

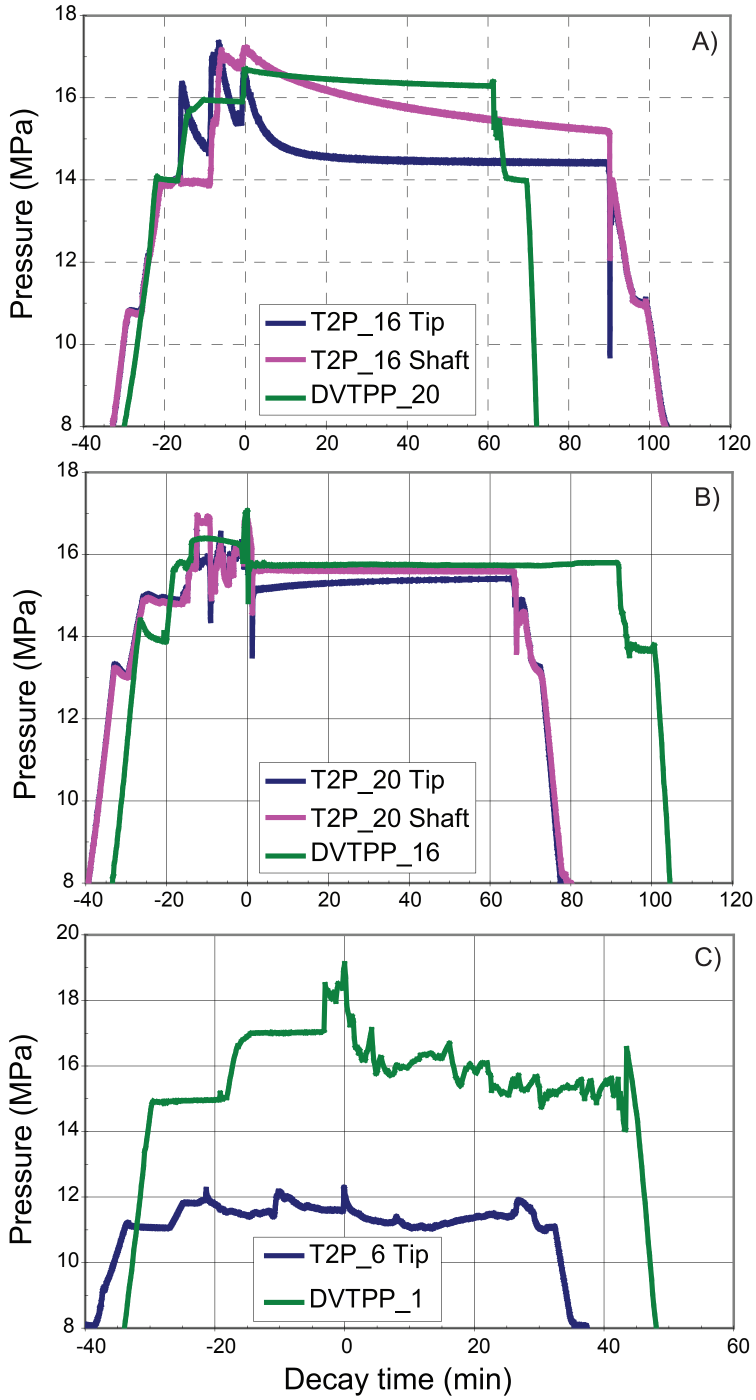

Figure A.7: Characteristic deployments of the DVTPP and T2P. A) Type I: typical pressure record for a penetration test with clear pressure buildup and clean pressure dissipation; B) Type II: pressure drops dramatically due to decoupling of the drill string from the tool. IIa) after the pressure drop, pressure decays towards in situ pressure; IIb) after the pressure drop, pressure builds up to in situ pressure; C) "Leak" deployments had abrupt and erratic changes in pressure during the dissipation phase. This is one example of a Type III deployment. Type III deployments include unsuccessful deployments due to hydraulic leaks, electronics failure, or tool damage and communication with borehole fluid.

subside to the in situ pressure. A detailed comparison of the DVTPP and the T2P geometries and their consequent behavior during insertion and dissipation is presented by Long et al., [*Long*].

Figure A.7B presents deployments for both the DVTPP and the T2P that were slightly dislodged when the drill string was raised subsequent to penetration to decouple itself from the penetrometer through the CDS (Type IIA and IIB). In this situation, the tool pressure drops abruptly when the bit was raised. Analysis of the temperature record in both tools and the accelerometer record in the DVTPP show that coincident with the abrupt drop in pressure, there was frictional heating and there was movement of the tool [*Flemings*, 2006d; *Long*, 2007b]. The pressure either decays toward the formation pressure after it rebounds to a certain level (Type IIA, Table A.1) or keeps building up during the dissipation phase (Type IIB, Table A.1) (Figure A.7B).

Type III includes all the unsuccessful deployments that fail to catch any useful information of the in situ conditions. Problems are three-fold. First, in early cases there was an internal hydraulic leak in the DVTPP and the tip pressure of the T2P. The leak resulted in abrupt and erratic drops in pressure during the dissipation phase (Figure A.7C). The internal hydraulic leak was repaired. Second, in the worst case the tool dislodgement could weaken the seal around the probe and create communications to the borehole fluid, which will ruin the pressure and temperature measurement (Appendix A.A and A.B). Third, the tool did not record any reliable data due to electronic and/or mechanical failure. The latter was especially true for the T2P as it is prone to bending due to its very narrow diameter tip.

In several deployments, the DVTPP was not fully decoupled from the BHA due to the friction in the CDS (Appendix A.A, DVTPP Deployment #1, 2, 3, 8, 12 and 13). In these cases, the tool moved during the dissipation phase. Frictional heating due to tool movement may have compromised the temperature measurement. Continuous movement of the tool may also have affected the pressure measurement. In several T2P deployments, circulation of the drilling fluid was resumed during the dissipation phase. In these cases, it is often possible to see a slight pressure increase and a slight temperature increase at the onset of circulation. (Appendix A.B, T2P Deployment #2, 3, 4, 5 and 12). In some cases, the onset of circulation resulted in further tool insertion (T2P Deployment # 6 and 7). The tool disturbance due to pumping fluid may affect the accuracy of the pressure and temperature measurements.

A.5 Data Extrapolation

During IODP Expedition 308, the T2P temperature equilibrated to the formation temperature (Appendix A.B). In contrast, the temperature measured with the DVTPP did not equilibrate to the in situ temperature (Appendix A.A). The reason for this is that the DVTPP has a significantly larger geometry. We use inverse time ($1/t$) extrapolation to estimate the in situ temperature for the DVTPP deployments [*Davis*, 1997; *Villinger*, 1987].

The pressure measured by both the T2P and the DVTPP did not reach the in situ pressure during the dissipation phase (Appendix A.A and A.B). In the absence of detailed soil properties, we use two empirical approaches to infer the in situ pressure from the partial dissipation records: $1/t$ extrapolation, and $1/\sqrt{t}$ extrapolation. Accuracy of the extrapolated in situ pressures depends on the tool that was used, pressure port, type of deployment, depth of deployment and the pressure decay time [*Long*, 2007b]. The error of a good deployment with long dissipation time (e.g. 90 minutes) should be within 0.1 MPa, whereas the error of a deep deployment with short decay time could be more than 0.5 MPa.

Table A.2 presents the interpreted in situ pressure and temperature for the T2P and the DVTPP deployments during IODP Expedition 308.

Table A2. In situ temperature and pressure results interpreted from the DVTPP and T2P deployments during IODP Expedition 308

Deployment#	**Hole**	**BOH (mbsf)**	**BOH (mbsl)**	**u_h (MPa)**	**σ_v (MPa)**	**Decay time (min)**	**u_{end} (MPa)**	**u_0-$1/t$ (MPa)**	**u_0-$1/\sqrt{t}$ (MPa)**	**T_{end} (°C)**	**$T_{1/t}$ (°C)**
DVTP-P1	U1320A	203.4	1673.4	16.81	18.43	42				9.22	9.10
DVTP-P2	U1320A	289.9	1759.9	17.68	20.09	13				11.08	10.90
DVTP-P3	U1324B	229.1	1285.9	12.92	14.72	50				9.49	9.47
DVTP-P4	U1324B	362.4	1419.2	14.26	17.26	47				11.68	11.63
DVTP-P6	U1324B	464.3	1521.1	15.28	19.27	34	14.80	15.07	15.69	12.96	12.82
DVTP-P7	U1324B	493.1	1549.9	15.57	19.83	31				13.40	13.25
DVTP-P8	U1324B	521.9	1578.7	15.86	20.39	41				13.81	13.67
DVTP-P10	U1324B	560.4	1617.2	16.25	21.15	32	19.97	18.41	16.58	14.54	14.42
DVTP-P12	U1324B	608.2	1665.0	16.73	22.11	61	18.80	18.39	17.69	16.09	15.70
DVTP-P13	U1324C	250	1305.7	13.12	15.11	90	14.61	14.22	13.78	10.00	9.79
DVTP-P15	U1324C	505	1560.7	15.68	20.06	93	16.84	16.74	16.74	12.31	13.50
DVTP-P17	U1322C	100	1418.9	14.25	14.95	91	14.64	14.58	14.52	7.04	6.99
DVTP-P18	U1322C	220	1538.9	15.46	17.20	62	16.28	16.35	16.45	9.84	9.75
DVTP-P19	U1322C	238	1556.9	15.64	17.55	93	16.47	16.23	15.97	10.03	10.03
DVTP-P20	U1322D	175	1493.9	15.01	16.35	60	16.28	16.16	16.01	8.45	8.43
T2P_2	U1319A	80.5	1510.1	15.17	15.71	35	15.71; 16.35	15.63; 16.25	15.54; 16.13	7.23	
T2P_3	U1320A	126.3	1596.3	16.04	17.04	52	16.27;	16.23;	16.17;	6.99	
T2P_4	U1320A	213	1683.0	16.91	18.61	25				8.99	
T2P_5	U1324B	51.3	1108.1	11.13	11.44	34	11.37; 11.65	11.37; 11.61	11.36; 11.54	5.78	
T2P_6	U1324B	89.3	1146.1	11.51	12.11	25	12.09	12.00	11.88	6.31	

T2P_7	U1324B	117.8	1174.6	11.80	12.63	31	12.90	12.68	12.42	7.00	
T2P_8	U1324B	136.3	1193.1	11.99	12.98	30	13.23	12.96	12.67	7.35	
T2P_12	U1324C	50	1105.7	11.11	11.42	60	11.21; 11.56	11.20; 11.44	11.18; 11.31	5.66	
T2P_13	U1324C	100	1155.7	11.61	12.30	60	11.93; 12.39	11.92; 12.21	11.91; 12.01	6.65	
T2P_14	U1324C	150	1205.7	12.11	13.24	60	12.69; 13.10	12.67; 12.97	12.65; 12.82	7.57	
T2P_15	U1324C	200	1255.7	12.61	14.18	60	14.09; 14.44	13.91; 14.12	13.72; 13.77	8.58	
T2P_16	U1324C	300	1355.7	13.62	16.06	90	14.42; 15.20	14.37; 14.58	14.31; 13.87	10.29	
T2P_19	U1322B	134.3	1453.8	14.60	15.60	30	15.08; 15.22	15.02; 15.19	14.95; 15.13	7.89	
T2P_20	U1322B	157.8	1477.3	14.84	16.04	60	15.41; 15.60	15.47; 15.60	15.55; 15.59	8.47	
T2P_23	U1322C	150	1468.9	14.76	15.89	60	15.29; 15.99	15.29; 15.78	15.30; 15.55	8.26	
T2P_24	U1322C	200	1518.9	15.26	16.83	60	16.34; 17.16	16.25; 16.86	16.15; 16.54	9.28	
T2P_27	U1322D	100	1418.9	14.25	14.95	45	14.69; 15.11	14.70; 14.99	14.72; 14.87	7.11	

Notes: 1. Only deployments used to interpret the in situ conditions are included in this table. 2. The temperature/dural pressure (T2P) probe has two pressure ports. The first row of columns 8-10 is the tip pressure of the T2P; the second row is the shaft pressure. 3. The T2P temperature reached equilibrium with the formation temperature at the end of the deployment. Thus, no extrapolation was applied.

A.6 Results: In situ temperature

A.6.1 Brazos Trinity IV Basin

Figure A.8 presents the in situ temperatures taken at Site U1319 and Site U1320. The geothermal gradient at Site U1320 is 23.1 $^{\circ}$C /km. The only measurement at Site U1319 suggests a higher geothermal gradient than that at Site U1320.

A.6.2 Ursa Basin

Figure A.9 presents the in situ temperatures taken at Site U1322 and Site U1324. The geothermal gradient at Site U1324 is bilinear. The thermal gradient is 18.6 $^{\circ}$C/km within the sediments above 360 mbsf, which corresponds to Lithostratigraphic Unit I which is predominantly composed of terrigenous clay and mud with a marked paucity of silt and sand [*Flemings, et al.*, 2006a]. The geothermal gradient is 16.7 $^{\circ}$C/km in Lithostratigraphic Unit II, which extends from 360 to 600.8 mbsf and includes interbedded silt and very fine sand with beds and laminae of mud and clay [*Flemings, et al.*, 2006a]. Sediments are predominantly clay and mud at Site U1322. The geothermal gradient is 21.9 $^{\circ}$C/km, which is significantly higher than that at Site U1324.

A.7 Results: In situ pressure

We present our pressure results with respect to the hydrostatic pressure and overburden stress. The hydrostatic pressure is calculated starting from the seafloor assuming a seawater density of 1.024 g/cc. Bulk density data from shipboard Moisture and Density measurements (MAD) were integrated to calculate the overburden stress. The static pressure due to the water column above seafloor was subtracted from the pressure results.

A.7.1 Brazos Trinity IV Basin

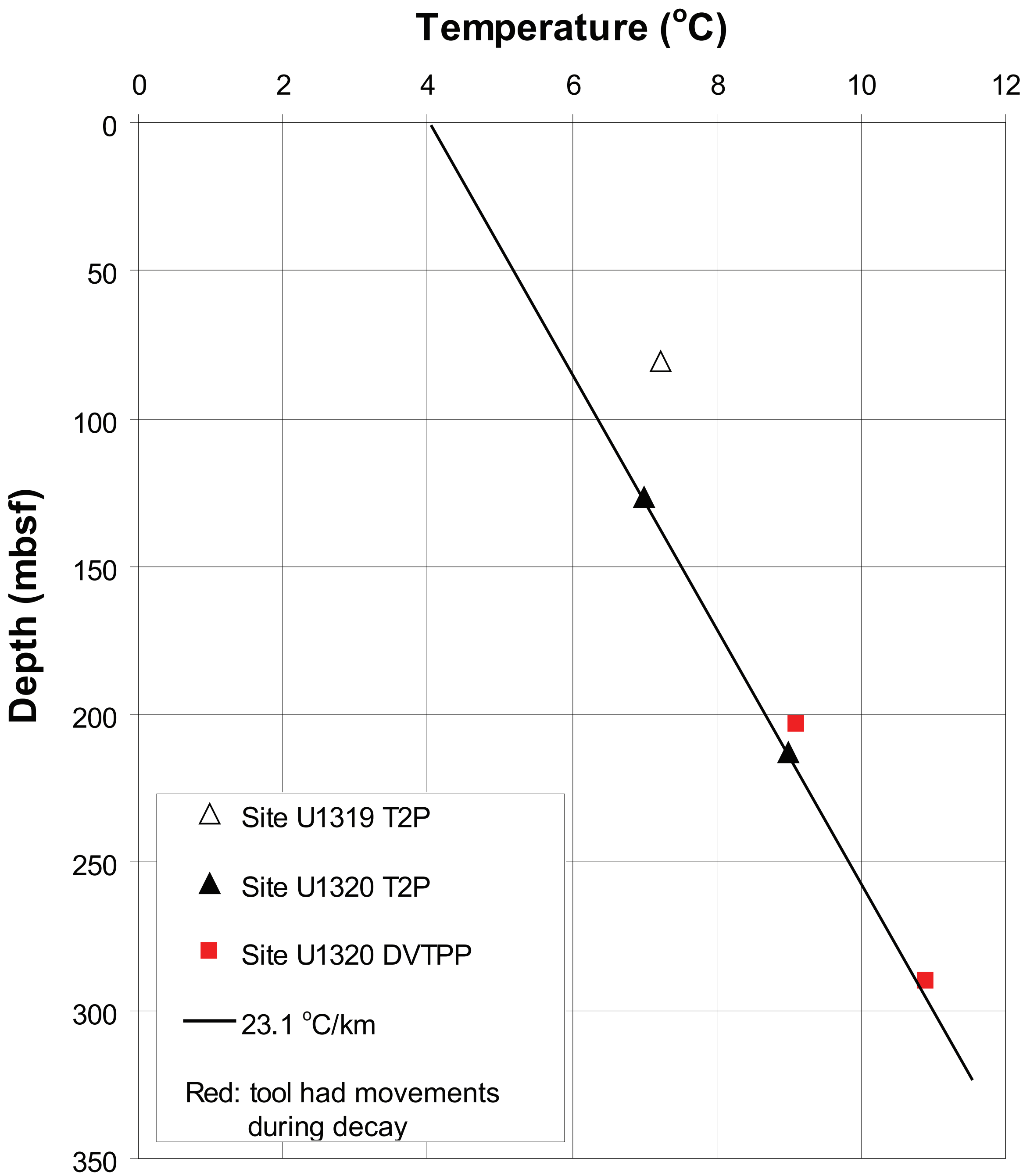

Figure A.8: In situ temperature in Brazos Trinity IV Basin at Site U1319 and Site U1320. T2P temperature reached equilibrium with the formation temperature at the end of the deployment (Table A.2, column 11). However the DVTPP temperature did not equilibrate with the formation temperature at the end of the deployment. In situ temperatures were estimated using 1/t extrapolation (Table A.2, column 12). Red symbols represent temperature measurements that were subjected to influence of tool movements during the dissipation phase.

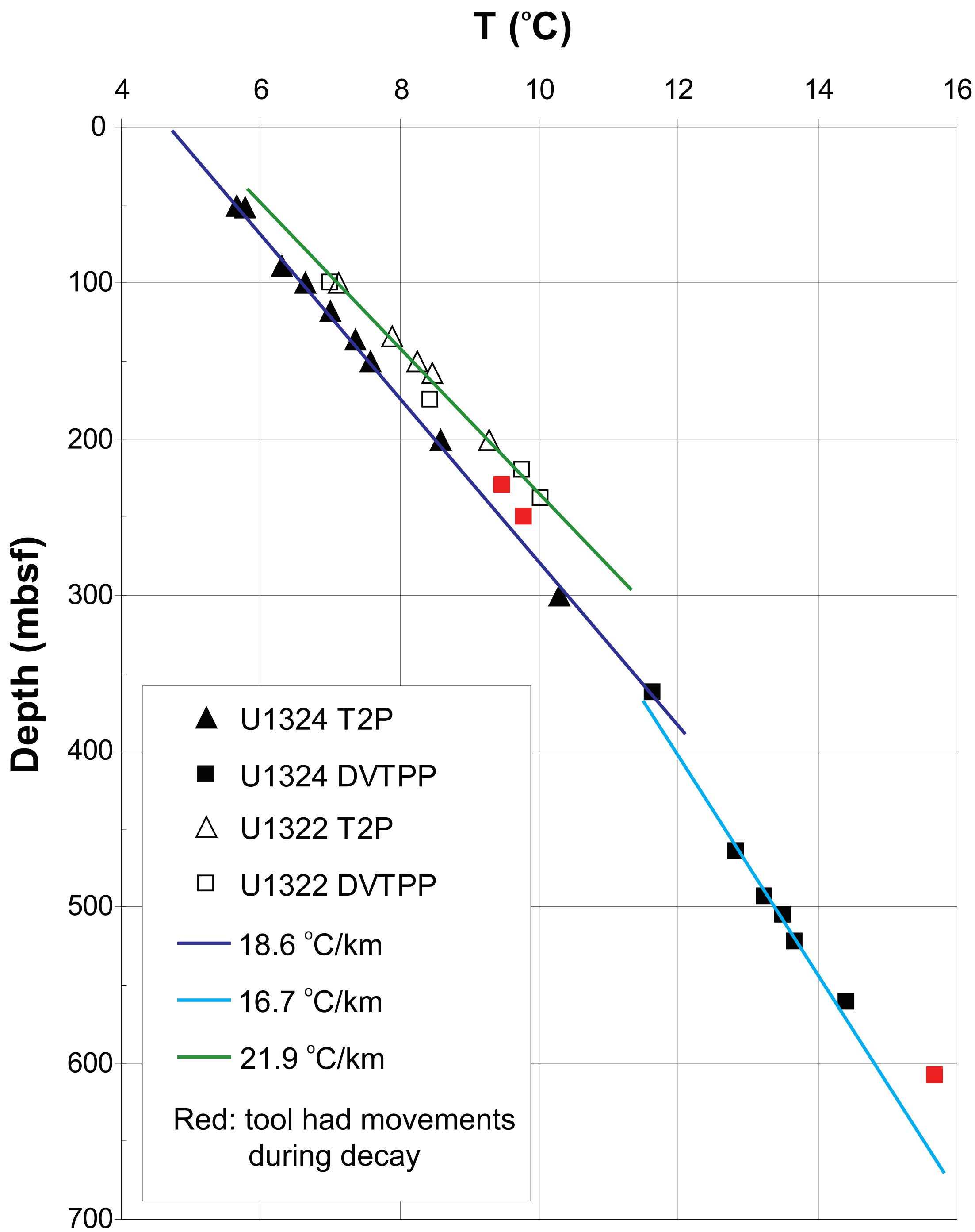

Figure A.9: Temperature data for Ursa Basin at Site U1322 and Site U1324. T2P temperature reached equilibrium with the formation temperature at the end of the deployment (Table A.2, column 11). However the DVTPP temperature did not equilibrate with the formation temperature at the end of the deployment. In situ temperatures were estimated using 1/t extrapolation (Table A.2, column 12). Red symbols represent temperature measurements that were subjected to influence of tool movements during the dissipation phase.

We have only one pressure measurement at Site U1319. The T2P penetration was completed at 80.5 mbsf. The last recorded pressure of the T2P tip equals the overburden stress whereas that of the shaft exceeds the overburden stress. This clearly shows that pressures had not dissipated to the in situ pressure (Figure A.10B). The pressure dissipation time was only 35 minutes for this deployment. The $1/\sqrt{t}$ extrapolation of the tip pressure should give a better estimation of in situ pressure [*Long*, 2007b]. The extrapolated in situ pressure by the $1/\sqrt{t}$ extrapolation suggests that the formation pressure at 80.5 mbsf 0.37 MPa higher than the hydrostatic pressure (Figure A.10D). The shaft pressure was still higher than the overburden stress after $1/t$ extrapolation and $1/\sqrt{t}$ extrapolation (Figure A.10C and A.10D).

We made two T2P and two DVTPP deployments at Site U1320 whereas only one deployment can be used to estimate the in situ pressure. The last recorded pressure was slightly greater than the hydrostatic pressure (Figure A.11B). The estimated in situ pressure by both $1/t$ extrapolation and $1/\sqrt{t}$ extrapolation suggests that formation pressure at 126.3 mbsf is close to hydrostatic pressure (Figure A.11C and A.11D).

A.7.2 Ursa Basin

Figure A.12 presents the pore pressure measurements at Site U1322. The last recorded pressures are scattered with some of them equal to or exceeding the overburden stress (σ_v) (Figure A.12B). This indicates that pressures had not dissipated to the in situ pressure at the end of deployment.

The $1/t$ extrapolation predicts consistently higher pressure at the shaft of T2P than that at the tip (Figure A.12C). Some shaft pressures are still equal to or even higher than the overburden stress (Figure A.12C). These indicate that $1/t$ extrapolation of the shaft pressure overestimates the in situ pressure which is in good agreement with the theoretical modeling presented by Long et al., [*2007*].

Long et al., [*2007*] showed that the $1/\sqrt{t}$ extrapolation more closely matches theoretical modeling results than the $1/t$ extrapolation does when pressure decays less than 80% of the penetration-induced pressure. Application of $1/\sqrt{t}$ extrapolation drives the shaft pressure closer to the tip pressure (Figure A.12D). The results make more physical sense because ultimately the shaft pressure and tip pressure converge at the in situ pressure. We believe the $1/\sqrt{t}$ extrapolation provides more accurate in situ pressure estimate than the $1/t$ extrapolation does for the shaft pressure of T2P and the DVTPP pressure.

Nevertheless, both extrapolation approaches predict significant overpressure and a similar trend. The overpressure ratio ($\lambda^* = {(u_0 - u_h)}/{(\sigma_v - u_h)}$) is up to 0.75. Overpressure starts to drop from ~200 mbsf. Sediments are predominantly clay and mud at Site U1322.

Figure A.13 presents the pore pressure measurements at Site U1324. Both extrapolation approaches predict significant overpressure in the sediments above ~200 mbsf (Figure A.13C and A.13D) that correspond to the hemipelagic silty claystone. Within this section, the magnitude and trend of the overpressure are similar to those at Site U1322 (Figure A.14). The sediments below 300 mbsf have less overpressure (Figure A.13). The overpressure seems to be constant within Lithostratigraphic Unit II in which sediments are composed of silty claystone interbedded with beds of silt and very-fine sand. The transition occurs at the section from 200 mbsf down to 300 mbsf.

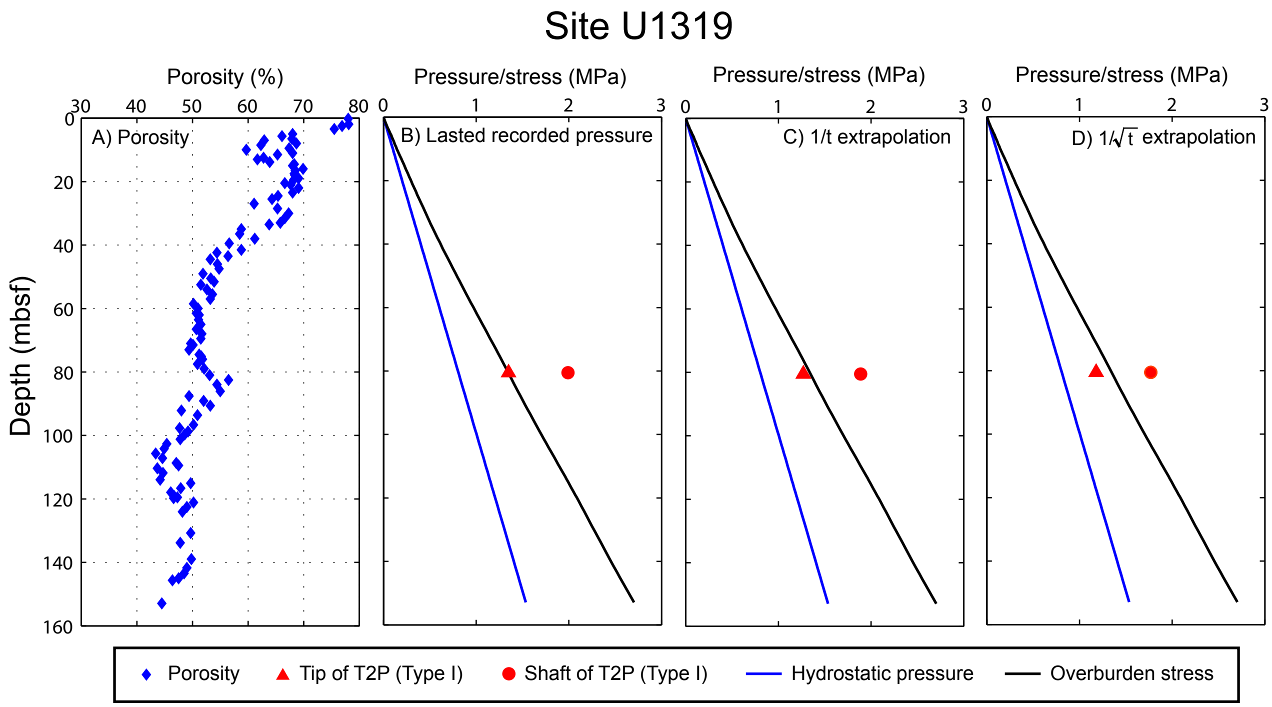

Figure A.10: Pore pressure measurements at Site U1319. The hydrostatic pressure is calculated starting from the seafloor assuming a seawater density of 1.024 g/cc. Bulk density data from shipboard Moisture and Density measurements (MAD) were integrated to calculate the overburden stress. The static pressure due to the water column above seafloor was subtracted from the pressure results. A) Porosity obtained from shipboard moisture and density (MAD) measurement. B) Last recorded pressure of the penetrometer (Table A.2, column 8). C) In situ pore pressure estimated by 1/t extrapolation (Table A.2, column 9). D) In situ pore pressure estimated by $1/\sqrt{t}$ extrapolation (Table A.2, column 10).

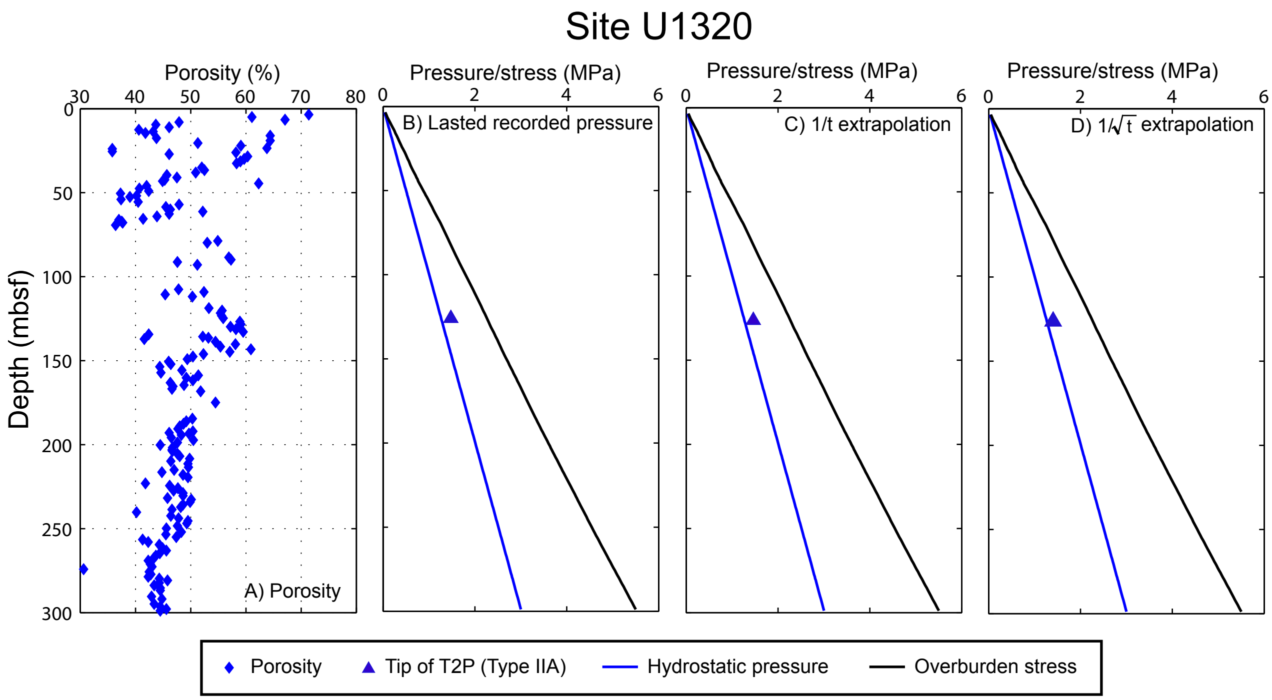

Figure A.11: Pore pressure measurements at Site U1320. The hydrostatic pressure is calculated starting from the seafloor assuming a seawater density of 1.024 g/cc. Bulk density data from shipboard Moisture and Density measurements (MAD) were integrated to calculate the overburden stress. The static pressure due to the water column above seafloor was subtracted from the pressure results. A) Porosity obtained from shipboard moisture and density (MAD) measurement. B) Last recorded pressure of the penetrometer (Table A.2, column 8). C) In situ pore pressure estimated by 1/t extrapolation (Table A.2, column 9). D) In situ pore pressure estimated by $1/\sqrt{t}$ extrapolation (Table A.2, column 10).

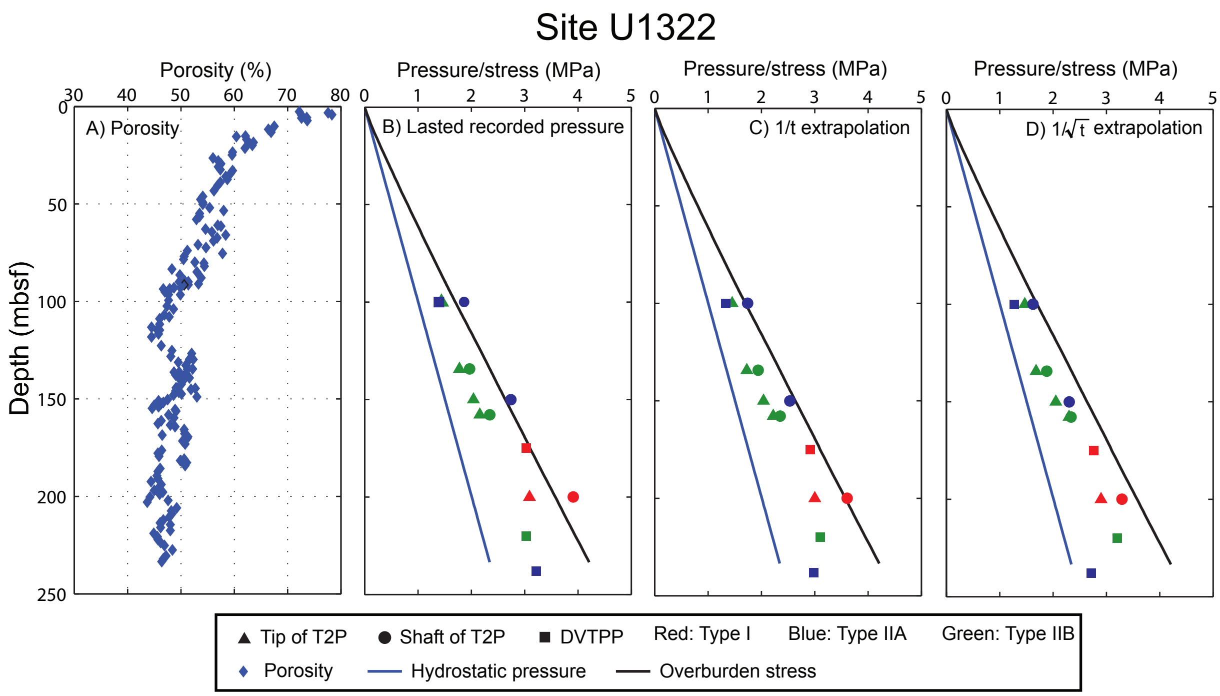

Figure A.12: Pore pressure measurements at Site U1322. The hydrostatic pressure is calculated starting from the seafloor assuming a seawater density of 1.024 g/cc. Bulk density data from shipboard Moisture and Density measurements (MAD) were integrated to calculate the overburden stress. The static pressure due to the water column above seafloor was subtracted from the pressure results. A) Porosity obtained from shipboard moisture and density (MAD) measurement. B) Last recorded pressure of the penetrometer (Table A.2, column 8). C) In situ pore pressure estimated by 1/t extrapolation (Table A.2, column 9). D) In situ pore pressure estimated by $1/\sqrt{t}$ extrapolation (Table A.2, column 10).

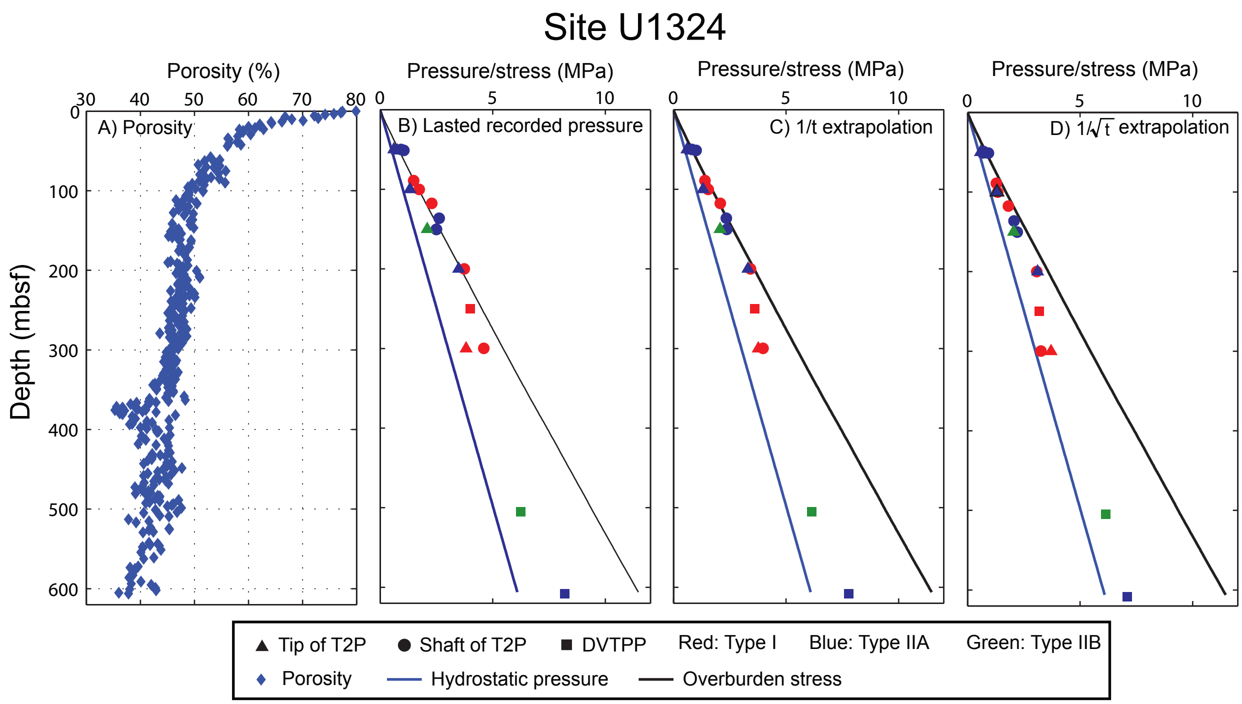

Figure A.13: Pore pressure measurements at Site U1324. The hydrostatic pressure is calculated starting from the seafloor assuming a seawater density of 1.024 g/cc. Bulk density data from shipboard Moisture and Density measurements (MAD) were integrated to calculate the overburden stress. The static pressure due to the water column above seafloor was subtracted from the pressure results. A) Porosity obtained from shipboard moisture and density (MAD) measurement. B) Last recorded pressure of the penetrometer (Table A.2, column 8). C) In situ pore pressure estimated by 1/t extrapolation (Table A.2, column 9). D) In situ pore pressure estimated by $1/\sqrt{t}$ extrapolation (Table A.2, column 10).

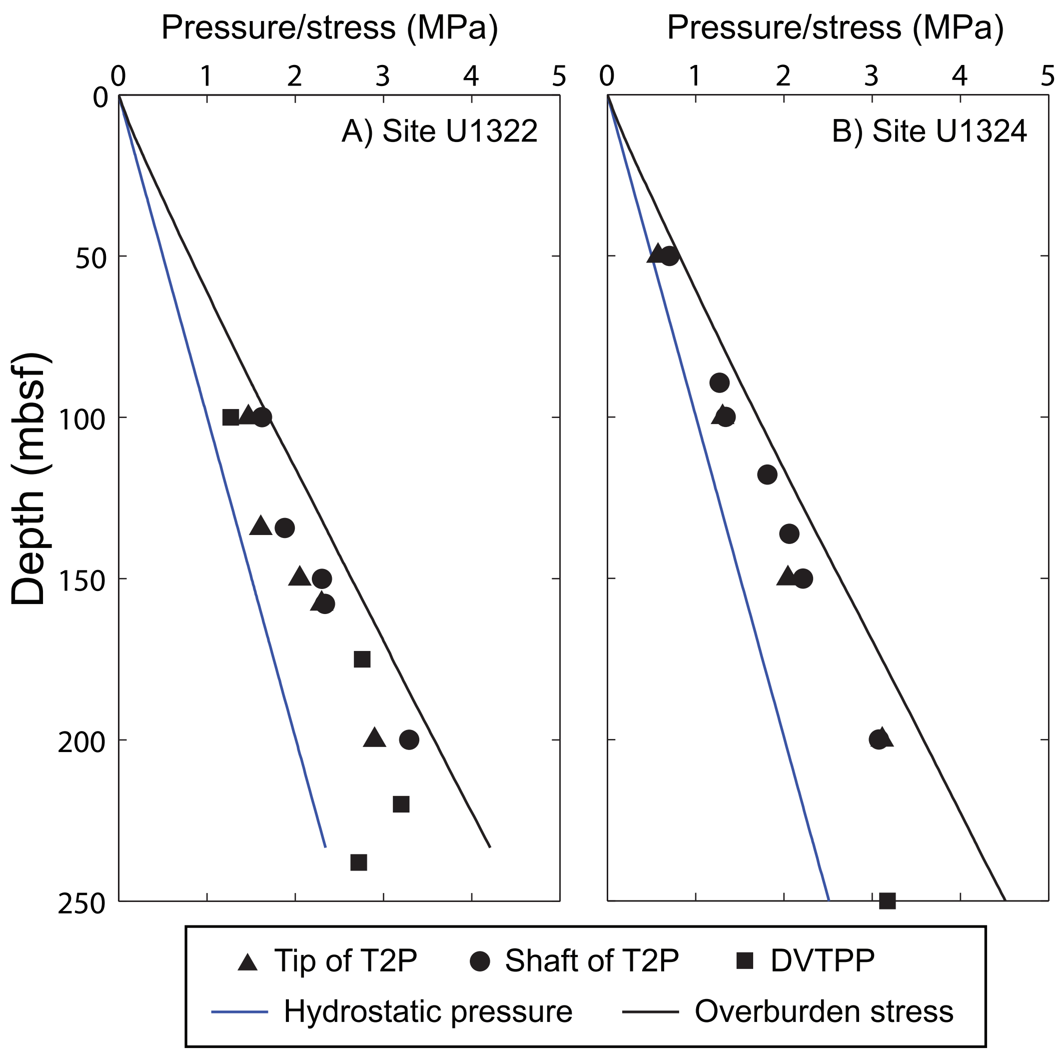

Figure A.14: In situ pressure estimates by $1/\sqrt{t}$ extrapolation in the upper 250 mbsf at Site U1322 and Site U1324. The hydrostatic pressure is calculated starting from the seafloor assuming a seawater density of 1.024 g/cc. Bulk density data from shipboard Moisture and Density measurements (MAD) were integrated to calculate the overburden stress. The static pressure due to the water column above seafloor was subtracted from the pressure results.

Acknowledgements

We thank the participants of IODP Expedition 308 that made the deployment of the T2P possible. We also thank Derryl Schroeder and Mike Meiring for their help and assistance on the post-cruise T2P pressure calibration. Kevin Grigar is thanked for helpful discussion on the geometry and operation of the CDS and the BHA.

This research used samples and/or data provided by the Integrated Ocean Drilling Program (IODP). Funding for this research was provided by the U.S. Science Support Program for IODP that is administered by Joint Oceanographic Institutions. In addition, the NSF Grants 0447235 and 0351085 supported this research.

Nomenclature

H_w	water depth at hole location L
P	fluid pressure $ML^{-1}T^{-2}$
T	temperature θ
t	time T
g	acceleration of gravity MT^{-2}
u_0	in situ pressure $ML^{-1}T^{-2}$
u_h	hydrostatic pressure $ML^{-1}T^{-2}$
u_{end}	final pressure $ML^{-1}T^{-2}$
z	target depth L
λ^*	overpressure ratio
ρ_c	density of fluid with drilling cuttings ML^{-3}
ρ_m	density of drilling mud ML^{-3}
ρ_w	density of seawater ML^{-3}
σ_v	overburden stress $ML^{-1}T^{-2}$

Appendix A.A Davis Villinger Temperature-Pressure Probe (DVTPP)

A.A.1 Overview

In Appendix A.A, we present the DVTPP deployments during Expedition 308. It includes five sections: 1) the instruments that were used; 2) temperature calibration; 3) pressure calibration; 4) an example DVTPP deployment shows the detailed deployment procedure and 5) detailed description of each DVTPP deployment.

A.A.2 Instruments

During Expedition 308, two data logger/pressure transducer/thermistor combinations were used: 1) logger 9368 - PXDCR 88579 - Thermistor 0226-2 (DVTPP2) and 2) logger 9367 - PXDCR 88587 - Thermistor 0226-3 (DVTPP3). In the published online data [*Flemings*, 2006b], PXDCR 79481 and Thermistor 0226-1 were listed together with logger 9367. However, this is not correct.

A.A.3 Temperature Calibration

Temperature calibrations were carried out on the data logger and the thermistor separately. The data logger response to resistance was determined using a highly stable resistance box which simulates the resistance variation of the thermistor over its full temperature range. The calibration coefficients of the data logger were provided by the USIO (Table A.A1a). Table A.A1b presents the commercial calibration of the thermistors. The Steinhart-Hart relationship is used to describe the temperature as a function of the thermistor resistance (Table A.A1a) [*Davis*, 1997].

During Expedition 308, the DVTPP temperature data were not always reduced correctly. For example, the temperature data of tool DVTPP3 was calibrated using the calibration coefficients of thermistor 0226-1 [*Flemings*, 2006b]. However, thermistor 0226-1 was not used in either of the DVTPP tools that were deployed during Expedition 308. This problem was also reported during Expedition 311 [*Tréhu*, 2007]. In a similar fashion for tool DVTPP2, the temperature calibrations of several deployments were done using coefficients of thermistor 0226-1 or 0226-3 instead of 0226-2 [*Flemings*, 2006b]. In this report, we recalculated the temperature for all deployments using the correct calibration coefficients provided by the USIO (Table A.A1).

A.A.4 Pressure Calibration

The calibration factors for all pressure transducers are illustrated in Table A.A2. The calibration factors of the pressure transducers are stored in the CPU of the pressure interface module mounted to the DVTPP logger. Two frequency (or period) output signals are sent from the pressure transducer. Pressure is measured with a force-sensitive quartz crystal whose output period changes with applied load. A second period output comes from a quartz crystal temperature sensor used for temperature compensation. The last calibration of the two transducers was made in 2002 by the manufacturer (Table A.A2).

In December 2006, the USIO performed a calibration verification of the DVTPP pressure transducers using a deadweight tester that was recently calibrated by the manufacturer. DVTPP2 recorded a pressure 7 psi greater than that measured by the deadweight tester. DVTPP3 recorded a pressure 4 psi greater than that measured by the deadweight tester. In this report, we subtracted the average atmosphere pressure recorded by the DVTPP from the pressure data. After the correction, the calibration offsets are excluded and the DVTPP pressure is comparable to the hydrostatic pressure calculated from an assumed seawater density of 1.024 g/cc in which the atmosphere pressure is not accounted.

A.A.5 DVTPP Deployment Procedure

Every DVTPP deployment is slightly different. We present DVTPP Deployment #20 to illustrate our approach to interpreting the deployment history. This deployment was at 175 mbsf at Hole U1322D. The operational sequence for this deployment is illustrated in Table A.A3, and a graphical representation of the pressure, temperature, coreline depth, block position , accelerometer, pump strokes, coreline tension and hook load, are illustrated in Figure A.A1. For reasons that we do not understand, some of the bit depth data had shifts during deployment. Instead, we use the traveling block position to constrain movements of the drill bit during tool deployment whenever it is available (Figure A.A1b). The traveling block is attached to the top end of the drill string above the rig floor. Its position was recorded in meters above rig floor (marf).

Prior to the deployment, the BHA was located 5.5 meters above the bottom of the hole (BOH). The DVTPP was connected to the colleted delivery system (CDS), and lowered down the borehole with the wireline (Figure A.A1a, Event #1). The DVTPP was stopped at the seafloor for 5 minutes to record the fluid pressure and temperature in the pipe (Figure A.A1a, Event #2). Fluid circulation was stopped during the tool stop to remove the effect of pump pressure on the measured pressure (Figure A.A1c). The pump flux is proportional to the pump stroke rate (1.654 gal/stroke) [*Graber*, 2002].

The CDS was then lowered by the wireline (Figure A.A1a, event #3). At this time, the CDS was fully extended and hanging inside the drill pipe. The BHA was moved downward to 7 meters above the BOH (Figure A.A1b, event #4). As the CDS approaches the BHA, it was decelerated and slowly lowered to latch into the BHA. This can be identified by a sharp decrease in coreline tension (Figure A.A1e, event #5). For this deployment, when the CDS was fully extended, it has a length of 21.84 meters including the DVTPP probe. When the CDS was fully retracted, the tip of the DVTPP extends 1.1 m below the BHA. This length can vary depending on how many spacers (92 cm long) are connected to the DVTPP. The CDS was retracted approximately 2 m when latched in (event #5).

Next, the BHA was lowered to further retract the CDS stoke (Figure A.A1b, event #6). The probe was pushed into the formation. This induced increase in pressure and temperature after the CDS was fully retracted. The operator stops the insertion when the hook load drops by ~ 15,000 pounds (Figure A.A1f, event #7). This indicates that the BHA reached the BOH or that the formation is too firm for further penetration. In this case, the probe was pushed approximately 1.1 m into the formation. Subsequently, the BHA was raised 2.4 meters, and the CDS was partially extended to decouple the DVTPP from the BHA (Figure A.A1b, event #8).

In this deployment, the tool was left in place for 60 minutes. The tool acceleration was recorded during the deployment (Figure A.A1d), which is a measure of tool movement during the dissipation phase. The tool was then recovered via wireline (Figure A.A1e, event #9) and stopped at the mudline for 5 minutes to register the fluid pressure in the pipe (Figure A.A1a, event #10).

A.A.6 DVTPP Deployments during IODP 308

A.A.6.1 DVTPP Deployment #1: Hole U1320A, 203.4 mbsf

Table A.A4 and Figure A.A2 present the sequence of the operations and the tool response to particular events for DVTPP Deployment #1. The fluid circulation was kept on for the entire deployment (Figure A.A2c). The tool was stopped at the seafloor for 10 minutes to record the fluid pressure in the pipe. When the probe was pushed into the formation, the temperature and pressure increased. After the pressure pulse due to penetration, the pressure decreased rapidly and erratically (Figure A.A2b). The last pressure reading was 1 MPa less than the hydrostatic pressure.

We interpreted that this was caused by an internal hydraulic leak in the DVTPP; when pressure reached a high value, fluid leaks into the pressure housing which causes a rapid decrease; the pressure then slowly increases and leakage once again occurs. Because of the internal leak, no in situ pressure can be ascertained. Unfortunately, this internal leak was not identified and fixed until DVTPP deployment #4. The temperature record appears reasonable. The last temperature reading was 10.2 $^{\circ}$C (Figure A.A2). However, the accelerometer recorded slight tool movement throughout the dissipation phase (Figure A.A2d). The tool movements resulted in a very slight oscillation (magnitude < 0.01 $^{\circ}$C, period ≈ 50 seconds) in the temperature record. This suggests that there was minor coupling (through the CDS) with the BHA. The frictional heat due to tool movement may affect the temperature measurement.

A.A.6.2 DVTPP Deployment #2: Hole U1320A, 289.9 mbsf

As the probe was pushed into the formation, the temperature and pressure increased (Table A.A5 and Figure A.A3b). The pressure then decreased rapidly to less than the hydrostatic pressure (Figure A.A3). Once again an internal leak is interpreted to be present. And no in situ pressure can be inferred from Deployment #2. The temperature record was reasonable and the last temperature reading was 11.08 $^{\circ}$C. The accelerometer recorded tool movements throughout the dissipation phase (Figure A.A3d). The frictional heat due to tool movement may affect the temperature measurement.

A.A.6.3 DVTPP Deployment #3: Hole U1324B, 229.1 mbsf

Table A.A6 and Figure A.A4 present the sequence of the operations and the tool response to particular events for DVTPP Deployment #3. The TruView data are missing for this deployment. Key deployment events are derived from the shipboard ‘DVTPP Downhole Tool Data Sheet’ [*Flemings*, 2006b] and the pressure and temperature data.

When the probe was pushed into the formation, the temperature and pressure increased. After the pressure pulse due to penetration, the pressure decreased rapidly and erratically (Figure A.A4). Because of the internal leak, no in situ pressure could be inferred from Deployment #3. The temperature record looks reasonable and the last temperature reading was 9.5 $^{\circ}$C. The accelerometer recorded tool movements throughout the dissipation phase (Figure A.A4). The tool movements resulted in a slight oscillation (magnitude ≈ 0.05 $^{\circ}$C, period ≈ 1 min) in the temperature record. This most likely was due to some coupling between the BHA and the tool. The frictional heat due to tool movement may affect the temperature measurement.

A.A.6.4 DVTPP Deployment #4: Hole U1324B, 362.4 mbsf

Table A.A7 and Figure A.A5 present the sequence of the operations and the tool response to particular events for DVTPP Deployment #4. The TruView data do not match this deployment. Key deployment events are derived from the shipboard ‘DVTPP Downhole Tool Data Sheet’ [*Flemings*, 2006b] and the pressure and temperature data.

As the pressure decay starts, the pressure decreases rapidly and erratically (Figure A.A5). This was the 4th consecutive deployment where erratic pressures were recorded. After this deployment the tool was inspected and an internal hydraulic leak was found and fixed. No in situ pressure could be inferred from Deployment #4 because of the leak. The temperature record was reasonable and the last reading was 11.68 $^{\circ}$C. The temperature record had a very slight oscillation (magnitude ≈ 0.01 $^{\circ}$C, period ≈ 1 min) during the dissipation phase whereas the accelerometer did not record significant tool acceleration. This indicates some minor coupling between the BHA and the tool.

A.A.6.5 DVTPP Deployment #5: Hole U1324B, 387.9 mbsf

No data were recorded.

A.A.6.6 DVTPP Deployment #6: Hole U1324B, 464.3 mbsf

Table A.A8 and Figure A.A6 present the sequence of the operations and the tool response to particular events for DVTPP Deployment #6. The TruView data do not match this deployment. Key deployment events are derived from the shipboard ‘DVTPP Downhole Tool Data Sheet’ [*Flemings*, 2006b] and the pressure and temperature data.

As the probe was pushed into the formation, the temperature and pressure increased (Table A.A8 and Figure A.A6). When the BHA was lifted to decouple the BHA through the CDS, the pressure decreased dramatically to sub-hydrostatic pressure (Figure A.A6). A pressure rebound then occurred. We interpret that the tool was pulled up with the BHA. This created a void around the probe tip. As the void was equilibrating with the formation, the pressure increased to 14.86 MPa at the end of this deployment. This deployment recorded a good temperature decay curve. The last temperature reading was 12.96 $^{\circ}$C.

A.A.6.7 DVTPP Deployment #7: Hole U1324B, 493.1 mbsf

Table A.A9 and Figure A.A7 present the sequence of the operations and the tool response to particular events for DVTPP Deployment #7. The TruView data do not match this deployment. Key deployment events are derived from the onboard ‘DVTPP Downhole Tool Data Sheet’ [*Flemings*, 2006b] and the pressure and temperature profiles.

As the probe was pushed into the formation, the temperature and pressure increased (Table A.A9 and Figure A.A7). After penetration, the pressure decreased to a value significantly below hydrostatic pressure, and then slowly rebounded to a final value of 12.72 MPa. The pressure data may be explained by either a slow tool pullout after penetration or penetration in a dilatant sediment. Core photos show the sediment at this location is clayey silt to silt. Probe penetration could generate an annular dilation zone around the probe, which could have significant negative excess pore pressure. The drop to sub-hydrostatic pressure may reflect this negative excess pore pressure migrating to the pressure port. The temperature record looks very good and the last temperature reading was 13.4 °C.

A.A.6.8 DVTPP Deployment #8: Hole U1324B, 521.9 mbsf

Table A.A10 and Figure A.A8 present the sequence of the operations and the tool response to particular events for DVTPP Deployment #8. The measured pore pressure was less than the hydrostatic pressure throughout the deployment and there was no record of penetration. As a result, during the next DVTPP deployment, a different DVTPP penetrometer (DVTPP3) was deployed and this tool (DVTPP2) was rebuilt.

The temperature record was reasonable (Figure A.A8). The last temperature reading was 13.84 °C. However, the 'DVTPP Downhole Tool Data Sheet' [*Flemings*, 2006b] documented a tool pullout operation at 5 min after the end of the penetration. At this time, the BHA moved upwards 4 meters (Figure A.A8b) and the hookload increased (Figure A.A8f). The BHA was then moved upward 2 meters, and lowered and raised again. All of this occurred during the dissipation phase. The raising and lowering of the BHA were recorded by increase and decrease in the hook load (Figure A.A8f) and the accelerometer record (Figure A.A8d). The thermistor did not record any significant temperature change during those operations. A second pullout occurred at 41 min after the penetration (Figure A.A8e). These observations suggest that the first "pullout" and the following bit movements were within the retraction/extension limit of the CDS and thus did not cause significant tool movement.

A.A.6.9 DVTPP Deployment #9: Hole U1324B, 541.1 mbsf

A programming error occurred during this deployment and no data were recorded.

A.A.6.10 DVTPP Deployment #10: Hole U1324B, 560.4 mbsf

Pressure and temperature both increased sharply during penetration (Table A.A11 and Figure A.A9). When the BHA was lifted to decouple the BHA, the pressure decreased rapidly by approximately 1 MPa, and then decayed to a value of 20 MPa while the tool was in the formation. The pressure decayed linearly with time, which was unusual. And the pressure did not fall back to the atmosphere pressure when the DVTPP was raised up to the rig floor. In situ pressure may not be inferred from this deployment. The temperature decreased to 15.69 $^{\circ}$C prior to pullout.

A.A.6.11 DVTPP Deployment #11: Hole U1324B, 589.2 mbsf

Table A.A12 and Figure A.A10 present the sequence of the operations and the tool response to particular events for DVTPP Deployment #11. The temperature and pressure sensors both recorded unreliable data during this deployment.

A.A.6.12 DVTPP Deployment #12: U1324B, 608.2 mbsf

Deployment #12 was completed at the base of the hole. Table A.A13 and Figure A.A11 present the sequence of the operations and the tool response to particular events for this deployment. The pressure increased during penetration and then had a quick decline that was followed by a rapid recovery. The bit movement and acceleration record suggest that the quick pressure drop was related to the decoupling of the tool from the drill string after the insertion, and the rapid recovery was due to re-set of the tool on its own weight (Figure A.A11b and A.A11f). The pressure then followed a dissipation profile to a final pressure of 18.9 MPa. The temperature record continuously decayed to a low value of 17.2 $^{\circ}$C and then slightly increased to

17.34 °C. The last temperature reading was 17.15 °C. The accelerometer recorded tool movements throughout the dissipation phase (Figure A.A11d). We interpret that there was coupling between the BHA and the tool. The oscillating pressure and the odd temperature record were caused by tool movements. The tool movements may affect the temperature and pressure measurement.

A.A.6.13 DVTPP Deployment #13: Hole U1324C, 250 mbsf

Similar to Deployment #12, this deployment also recorded tool movements during the dissipation phase (Table A.A14 and Figure A.A12d). No sharp pressure drop was recorded due to the raise of drill bit after insertion (Figure A.A12b). The temperature record had a slight increase during the dissipation phase and the last temperature reading was 11.01 °C. It may not reflect the formation temperature due to the influence of the tool movement. The pressure also recorded a slight increase during dissipation and then subsided to an end value of 14.7 MPa. This pressure increase may affect the estimate of the formation pressure.

A.A.6.14 DVTPP Deployment #14: Hole U1324C, 405 mbsf

The tool insertion generated a relatively small pressure pulse for this depth (Table A.A15 and Figure A.A13). The pressure dropped rapidly when the drill bit was lifted (Figure A.A13b). The pressure then rebounded to a final value of 15.82 MPa, which was very close to the recorded pressure at the BOH prior to the penetration. The temperature increased when the drill bit was lifted, and then decreased rapidly to a value close to the borehole fluid temperature. Near the end of the deployment, the temperature increased to a final value of 11.38 °C. The temperature increase was most likely due to tool movement which can be identified on the acceleration data (Figure A.A13d). We interpret that tool dislodgement weakened the seal around the probe and created communication with the borehole fluid. The sensors recorded the pressure and temperature of the borehole fluids instead of in situ conditions.

A.A.6.15 DVTPP Deployment #15: Hole U1324C, 505 mbsf

Similar to Deployment #14, the tool insertion generated a relatively small pressure pulse for this depth (Table A.A16 and Figure A.A14). The pressure decreased rapidly when the drill bit was lifted (Figure A.A14b). The pressure then rebounded to a nearly constant value. The temperature only had a slight decrease after penetration and then increased to a high value (higher than its penetration temperature) at the end of the deployment. We interpreted that the tool surface temperature was lower than the formation temperature during penetration. The tool temperature had to increase to equilibrate with the formation. The end temperature was 13.5 $^{\circ}$C.

A.A.6.16 DVTPP Deployment #16: Hole U1322B, 166.7 mbsf

Table A.A17 and Figure A.A15 present the sequence of the operations and the tool response to particular events for DVTPP Deployment #16. The temperature and pressure increased when the CDS latched in position (Figure A.A15e). It suggests that the tip went into the formation a little bit while the CDS latching in. When the drill bit was lowered down to insert the tool, it recorded a second temperature and pressure increase. Pressure decreased rapidly when the drill bit was lifted (Figure A.A15b). The pressure then quickly rebounded to a near-constant value that was very close to the recorded pressure at the BOH prior to penetration. There may be communication with the borehole fluid. The temperature dropped rapidly and then slowly increased to 9.06 $^{\circ}$C. The end temperature of 9.06 $^{\circ}$C was not representative of in situ conditions.

A.A.6.17 DVTPP Deployment #17: Hole U1322C, 100 mbsf

Table A.A18 and Figure A.A16 present the sequence of the operations and the tool response to particular events for DVTPP Deployment #17. The bit depth data had dramatic shift during this deployment and the block position data are not available. The pressure had a rapid decrease after the insertion spike and then slowly dissipated to a final value of 14.73 MPa. This dissipation curve may be extrapolated to estimate in situ pressure. The temperature record had good insertion spike and continuous decay curve. The last temperature reading was 7.04 $^{\circ}$C.

A.A.6.18 DVTPP Deployment #18: Hole U1322C, 220 mbsf

Table A.A19 and Figure A.A17 present the sequence of the operations and the tool response to particular events for DVTPP Deployment #18. The pressure increased during penetration and then decreased abruptly when the drill bit was lifted (Figure A.A17b). The pressure then rebounded slowly to a final value of 16.36 MPa. Modeling of the rebound curve may constrain the in situ pressure. The temperature record had good insertion spike and continuous decay curve. The temperature decayed to 9.11 $^{\circ}$C at the end of deployment.

A.A.6.19 DVTPP Deployment #19: Hole U1322C, 238 mbsf

Table A.A20 and Figure A.A18 present the sequence of the operations and the tool response to particular events for DVTPP Deployment #19. The pressure increased during penetration and decreased abruptly when the bit was picked up off the BOH (Figure A.A18b). Pressure then slowly dissipated to a final value of 16.55 MPa. Extrapolation of the pressure record may provide an estimate of the in situ pressure. The temperature record had good insertion spike and continuous decay curve. The temperature decayed to 10.03 $^{\circ}$C at the end of deployment.

A.A.6.20 DVTPP Deployment #20: Hole U1322D, 175 mbsf

Table A.A3 and Figure A.A1 present the sequence of the operations and the tool response to particular events for DVTPP Deployment #20. Both pressure and temperature profile had good insertion spikes and continuous decay curves. The pressure dissipated to 16.37 MPa and the temperature dissipated to 8.68 $^{\circ}$C at the end of the deployment. Extrapolation of the pressure record will provide estimate of the in situ condition.

Table A.A1. Temperature calibration of DVTPP. a) Calibration coefficients for data loggers and thermistors. Channel T1 is the logger channel used to measure the thermistor. Rt' = the resistance in ohms of the thermistor. b) Actual thermistor calibration data.

a)

Channel T1 calibration

The formula for counts to ohms:

Rt'= R1 * (k1 - x) / (k0 - (k1 - x))

x=T1counts

Logger 9367	
R1=	251680.977
k0=	65564.0623
k1=	65550.3036

Logger 9368	
R1=	249507.092
k0=	65534.6958
k1=	65533.6013

Thermistor calibration

The formula for ohms to Kelvin

(Steinhart & Hart):

1/T = A+B*Ln(Rt')+C*Ln(Rt')^3

°C = K - 273.15

Thermistor 0226-3	
A=	4.60148156E-04
B=	2.10947147E-04
C=	6.41209309E-08

Thermistor 0226-2	
A=	4.52826700E-04
B=	2.11217111E-04
C=	6.19876025E-08

b)

ºC vs. Ohms				
Serial #	**0.000ºC**	**50.000ºC**	**100.000ºC**	**150.000ºC**
0226-2	1666200	162749	27716	6963
0226-3	1602700	157535	26907	6781

Table A.A2. Pressure calibration of DVTPP, June 7, 2002.

Internal temperature sensor

$Temp = Y_1U + Y_2U^2 + Y_3U^3$

Temp = Temperature (°C)

U_0 = Temperature signal period (microseconds) at 25 °C

U = Temperature signal period - U_0 (microseconds)

PXDCR 88587 — Temperature Coefficients

U0	5 .833194	usec
Y1	-4036.649	°C/usec
Y2	-12666.34	°C/usec
Y3	0	

PXDCR 88579 — Temperature Coefficients

U0	5.878972	usec
Y1	-3969.749	°C/usec
Y2	-11880.87	°C/usec
Y3	0	

Pressure transducer

Equations are used to calibrate pressure tramsducer:

$P = C(1-T_0^2/T^2)(1-D(1-T_0^2/T^2))$

P = Pressure (psi)

T = Pressure signal period (microseconds)

U_0 = Temperature signal period (microseconds) at 25 °C

$C = C_1 + C_2U + C_3U^2$

$D = D_1 + D_2U$

$T_0 = T_1 + T_2U + T_3U^2 + T_4U^3 + T_5U^4$

PXDCR 88587 — Pressure Coefficients

C1	-68866.77	psia
C2	-694.2135	psia/usec
C3	255224.2	psia/usec^2
D1	0.029732	
D2	0	
T1	30.32667	psia
T2	1.025313	psia/usec
T3	62.84291	psia/usec^2
T4	0	
T5	0	

PXDCR 88579 — Pressure Coefficients

C1	-66259.12	psia
C2	-2504.110	psia/usec
C3	223122.2	psia/usec^2
D1	0.030630	
D2	0	
T1	30.23938	psia
T2	0.409012	psia/usec
T3	58.71868	psia/usec^2
T4	0	
T5	0	

Table A.A3. Event summary of DVTPP deployment #20, Hole U1322D, 175 mbsf, 02-July-2005.

Event #	Time (GMT)	Event description
1	18:37:10	Start lowering DVTPP downhole
2	18:59:53	Stop at mudline for 5 min
3	19:00:09	Start lowering probe
4	19:04:22	Moving BHA to 7 m off BOH
5	19:13	CDS lands in BHA
6	19:20:26	Lower bit down, start penetration of DVTPP into formation
7	19:21:31	End of penetration; bit on BOH
8	19:21:50	Raising BHA 2.4 m off BOH
9	20:22:19	Pulling probe out of formation and uphole with wireline
10	20:26:03	Stop at mudline for 5 min
11	20:31:21	Pulling DVTPP uphole with wireline

Table A.A4. Event summary of DVTPP deployment #1, Hole U1320A, 203.4 mbsf, 09-June-2005.

Event #	Time (GMT)	Event description
1	8:50	Start lowering DVTPP downhole
2	9:01	Stop at mudline for 10 min
3	9:12	Start lowering probe
4	9:12	Raising BHA 11 m off BOH
5	9:16	CDS lands in BHA
6	9:27	Lower bit down, start penetration of DVTPP into formation
7	9:31	End of penetration; bit on BOH
8	9:33	Raising BHA 4 m off BOH
9	10:13	Pulling probe out of formation and uphole with wireline

Table A.A5. Event summary of DVTPP deployment #2, Hole U1320A, 289.9 mbsf, 09-June-2005.

Event #	Time (GMT)	Event description
1	19:00	Start lowering DVTPP downhole
2	19:11	Stop at mudline for 5 min
3	19:17	Start lowering probe
4	19:17	Raising BHA 16 m off BOH
5	19:22	CDS lands in BHA
6	19:23	Lower bit down, start penetration of DVTPP into formation
7	19:26	End of penetration; bit on BOH
8	19:28	Raising BHA 6 m off BOH
9	19:39	Pulling probe out of formation and uphole with wireline
10	19:42	Stop at mudline for 5 min
11	19:48	Pulling DVTPP uphole with wireline

Table A.A6. Event summary of DVTPP deployment #3, Hole U1324B, 229.1 mbsf, 22-June-2005.

Event #	Time (GMT)	Event description
1	9:46	Start lowering DVTPP downhole
2	10:09	Stop at mudline for 2 min
3	10:11	Start lowering probe
4		Raising BHA x m off BOH
5		CDS lands in BHA
6	10:24	Lower bit down, start penetration of DVTPP into formation
7	10:28	End of penetration; bit on BOH
8		Raising BHA x m off BOH
9	11:18	Pulling probe out of formation and uphole with wireline
10	12:30	Stop at mudline for 2 min
11	12:32	Pulling DVTPP uphole with wireline

Table A.A7. Event summary of DVTPP deployment #4, Hole U1324B, 362.4 mbsf, 23-June-2005.

Event #	Time (GMT)	Event description
1	6:15	Start lowering DVTPP downhole
2	6:36	Stop at mudline for 5 min
3	6:41	Start lowering probe
4		Raising BHA x m off BOH
5	6:57	CDS lands in BHA
6	7:01	Lower bit down, start penetration of DVTPP into formation
7	7:04	End of penetration; bit on BOH
8		Raising BHA x m off BOH
9	7:51	Pulling probe out of formation and uphole with wireline
10	8:27	Stop at mudline for 5 min
11	8:32	Pulling DVTPP uphole slowly with wireline

Table A.A8. Event summary of DVTPP deployment #6, Hole U1324B, 464.3 mbsf, 24-June-2005.

Event #	Time (GMT)	Event description
1	2:20	Start lowering DVTPP downhole
2	2:30	Stop at mudline for 5 min
3	2:35	Start lowering probe
4		Raising BHA x m off BOH
5	2:47	CDS lands in BHA
6	2:53	Lower bit down, start penetration of DVTPP into formation
7	2:57	End of penetration; bit on BOH
8		Raising BHA x m off BOH
9	3:31	Pulling probe out of formation and uphole slowly with wireline
10	3:38	Stop at mudline for 5 min
11	3:43	Pulling DVTPP uphole slowly with wireline

Table A.A9. Event summary of DVTPP deployment #7, Hole U1324B, 493.1 mbsf, 24-June-2005.

Event #	Time (GMT)	Event description
1	7:35	Start lowering DVTPP downhole
2	7:43	Stop at mudline for 5 min
3	7:48	Start lowering probe
4		Raising BHA x m off BOH
5	7:55	CDS lands in BHA
6	7:57	Lower bit down, start penetration of DVTPP into formation
7	8:01	End of penetration; bit on BOH
8		Raising BHA x m off BOH
9	8:32	Pulling probe out of formation and uphole with wireline
10	8:39	Stop at mudline for 5 min
11	8:44	Pulling DVTPP uphole with wireline

Table A.A10. Event summary of DVTPP deployment #8, Hole U1324B, 521.9 mbsf, 24-June-2005.

Event #	Time (GMT)	Event description
1	18:46	Start lowering DVTPP downhole
2	18:57	Stop at mudline for 5 min
3	19:02	Start lowering probe
4	18:56	Raising BHA 17 m off BOH
5	19:12	CDS lands in BHA
6	19:14	Lower bit down, start penetration of DVTPP into formation
7	19:24	End of penetration; bit on BOH
8	19:30	Raising BHA 4 m off BOH
9	20:05	Pulling probe out of formation and uphole with wireline
10	20:13	Stop at mudline for 5 min
11	20:18	Pulling DVTPP uphole with wireline

Table A.A11. Event summary of DVTPP deployment #10, Hole U1324B, 560.4 mbsf, 25-June-2005.

Event #	Time (GMT)	Event description
1	7:20	Start lowering DVTPP downhole
2	7:31	Stop at mudline for 5 min
3	7:36	Start lowering probe
4	7:39	Raising BHA 16 m off BOH
5	7:42	CDS lands in BHA
6	7:42	Lower bit down, start penetration of DVTPP into formation
7	7:47	End of penetration; bit on BOH
8	7:48	Raising BHA 4 m off BOH
9	8:19	Pulling probe out of formation and uphole with wireline
10	8:27	Stop at mudline for 5 min
11	8:32	Pulling DVTPP uphole with wireline

Table A.A12. Event summary of DVTPP deployment #11, Hole U1324B, 589.2 mbsf, 25-June-2005.

Event #	**Time (GMT)**	**Event description**
1	14:02	Start lowering DVTPP downhole
2	14:11	Stop at mudline for 5 min
3	14:16	Start lowering probe
4	14:16	Raising BHA 23 m off BOH
5	14:23	CDS lands in BHA
6	14:23	Lower bit down, start penetration of DVTPP into formation
7	14:30	End of penetration; bit on BOH
8		Raising BHA x m off BOH
9	15:15	Pulling probe out of formation and uphole with wireline
10	15:22	Stop at mudline for 5 min
11	15:27	Pulling DVTPP uphole with wireline

Table A.A13. Event summary of DVTPP deployment #12, Hole U1324B, 608.2 mbsf, 25-June-2005.

Event #	**Time (GMT)**	**Event description**
1	22:48	Start lowering DVTPP downhole
2	23:05	Stop at mudline for 5 min
3	23:10	Start lowering probe
4	22:57	Raising BHA 17 m off BOH
5	23:18	CDS lands in BHA
6	23:29	Lower bit down, start penetration of DVTPP into formation
7	23:34:15	End of the first penetration; bit is 0.2 m off BOH
8	23:34:36	Raising BHA 4 m off BOH
9	23:35:51	lower bit down, start further penetration
10	23:35:52	End of penetration; bit on BOH
11	23:36	Raising BHA 3 m off BOH
12	0:37	Pulling probe out of formation and uphole with wireline
13	0:45	Stop at mudline for 5 min
14	0:50	Pulling DVTPP uphole with wireline

Table A.A14. Event summary of DVTPP deployment #13, Hole U1324C, 250 mbsf, 27-June-2005.

Event #	Time (GMT)	Event description
1	7:00	Start lowering DVTPP downhole
2	7:09	Stop at mudline for 5 min
3	7:14	Start lowering probe
4	7:16	Raising BHA 14.5 m off BOH
5	7:17	CDS lands in BHA
6	7:17	Lower bit down, start penetration of DVTPP into formation
7	7:22	End of first penetration; bit 0.15 m off BOH
8	7:24	Raising BHA 3.5 m off BOH
9	7:24	lower bit down, start further penetration
10	7:25	End of penetration; bit on BOH
11	8:55	Pulling probe out of formation and uphole with wireline
12	9:00	Stop at mudline for 5 min
13	9:04	Pulling DVTPP uphole with wireline

Table A.A15. Event summary of DVTPP deployment #14, Hole U1324C, 405 mbsf, 27-June-2005.

Event #	Time (GMT)	Event description
1	17:52	Start lowering DVTPP downhole
2	18:00	Stop at mudline for 5 min
3	18:05	Start lowering probe
4	17:56	moving BHA to 17 m off BOH
5	18:12	CDS lands in BHA
6	18:22	Lower bit down, start penetration of DVTPP into formation
7	18:26	End of penetration; bit on BOH
8	18:30	Raising BHA 8.5 m off BOH
9	20:00	Pulling probe out of formation and uphole with wireline
10	20:07	Stop at mudline for 5 min
11	20:12	Pulling DVTPP uphole with wireline

Table A.A16. Event summary of DVTPP deployment #15, Hole U1324C, 505 mbsf, 28-June-2005.

Event #	Time (GMT)	Event description
1	0:30	Start lowering DVTPP downhole
2	0:43	Stop at mudline for 5 min
3	0:48	Start lowering probe
4	0:57	CDS lands in BHA
5	1:06	Lower bit down, start penetration of DVTPP into formation
6	1:09	End of penetration; bit on BOH
7	1:12	Raising BHA 6.4 m off BOH
8	2:42	Pulling probe out of formation and uphole with wireline
9	2:49	Stop at mudline for 5 min
10	2:54	Pulling DVTPP uphole with wireline

Table A.A17. Event summary of DVTPP deployment #16, Hole U1322B, 166.7 mbsf, 29-June-2005.

Event #	Time (GMT)	Event description
1	22:42	Start lowering DVTPP downhole
2	22:57	Stop at mudline for 5 min
3	23:02	Start lowering probe
4	22:54	Raising BHA 8 m off BOH
5	23:10	CDS lands in BHA; tip touched the formation
6	23:20	Lower bit down, start penetration of DVTPP into formation
7	23:22	End of penetration; bit on BOH
8	23:23	Raising BHA 3 m off BOH
9	23:24	Moving BHA back to BOH
10	0:54	Pulling probe out of formation and uphole with wireline
11	0:58	Stop at mudline for 5 min
12	1:03	Pulling DVTPP uphole with wireline

Table A.A18. Event summary of DVTPP deployment #17: Hole U1322C, 100 mbsf, 01-July-2005.

Event #	Time (GMT)	Event description
1	1:52	Start lowering DVTPP downhole
2	2:11	Stop at mudline for 5 min
3	2:16	Start lowering probe
4		Moving BHA to x m off BOH
5	2:22	CDS lands in BHA
6	2:33	Lower bit down, start penetration of DVTPP into formation
7	2:34	End of penetration; bit on BOH
8	2:35	Raising BHA 4 m off BOH
9	4:05	Pulling probe out of formation and uphole with wireline
10	4:09	Stop at mudline for 5 min
11	4:14	Pulling DVTPP uphole with wireline

Table A.A19. Event summary of DVTPP deployment #18: Hole U1322C, 220 mbsf, 01-July-2005.

Event #	Time (GMT)	Event description
1	15:45	Start lowering DVTPP downhole
2	16:07	Stop at mudline for 5 min
3	16:12	Start lowering probe
4		Moving BHA to 16 m off BOH
5	16:16	CDS lands in BHA
6	16:17	Lower bit down, start penetration of DVTPP into formation
7	16:19	End of penetration; bit on BOH
8	16:19	Raising BHA 5 m off BOH
9	17:21	Pulling probe out of formation and uphole with wireline
10	17:28	Stop at mudline for 5 min
11	17:33	Pulling DVTPP uphole with wireline

Table A.A20. Event summary of DVTPP deployment #19: Hole U1322C, 238 mbsf, 01-July-2005.

Event #	Time (GMT)	Event description
1	19:01	Start lowering DVTPP downhole
2	19:23	Stop at mudline for 5 min
3	19:28	Start lowering probe
4	19:28	Moving BHA to 11 m off BOH
5	19:34	CDS lands in BHA
6	19:44	Lower bit down, start penetration of DVTPP into formation
7	19:45	End of penetration; bit on BOH
8	19:46	Raising BHA 2 m off BOH
9	19:48	Lower BHA back to BOH
10	19:50	Raising BHA 6 m off BOH
11	21:18	Pulling probe out of formation and uphole with wireline
12	21:24	Stop at mudline for 5 min
13	21:28	Pulling DVTPP uphole with wireline

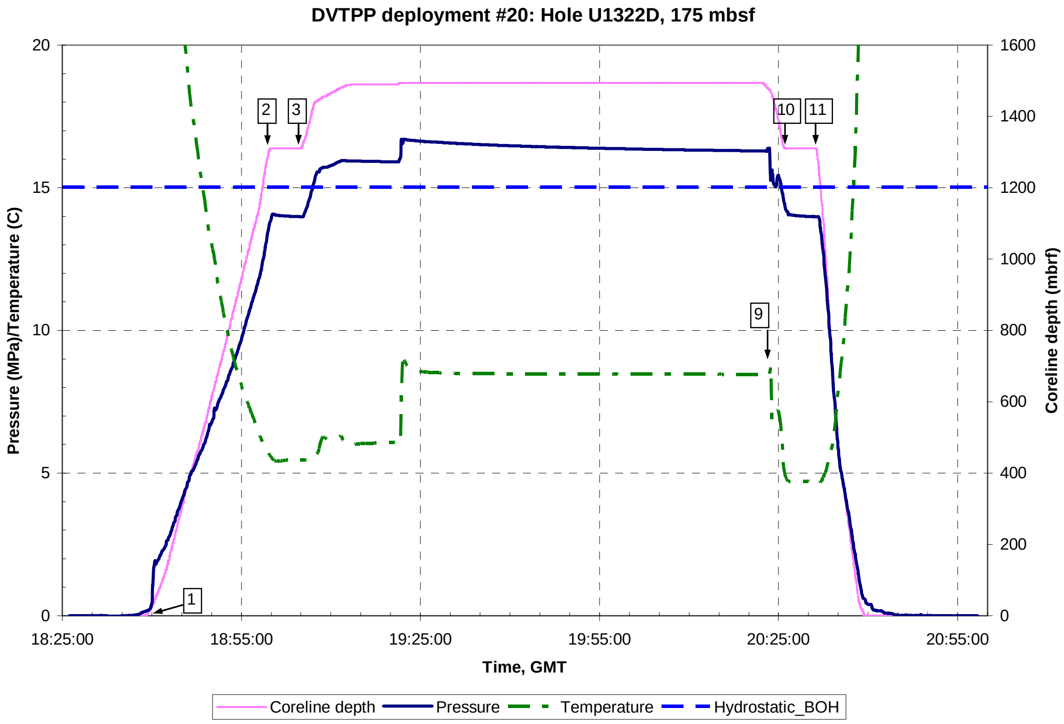

Figure A.A.1.a: Pressure, temperature and Truview data for DVTPP Deployment #20, Hole U1322D, 175 mbsf. GMT = Greenwich Mean Time, Hydrostatic_BOH is the hydrostatic pressure at the bottom of the hole.

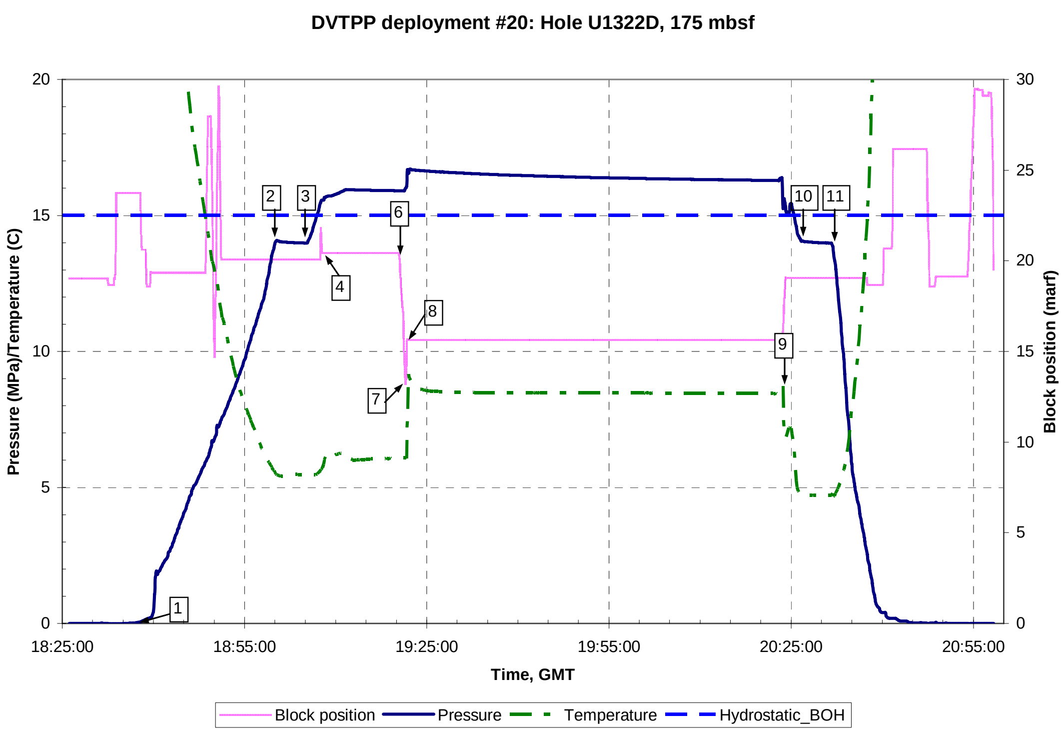

Figure A.A.1.b

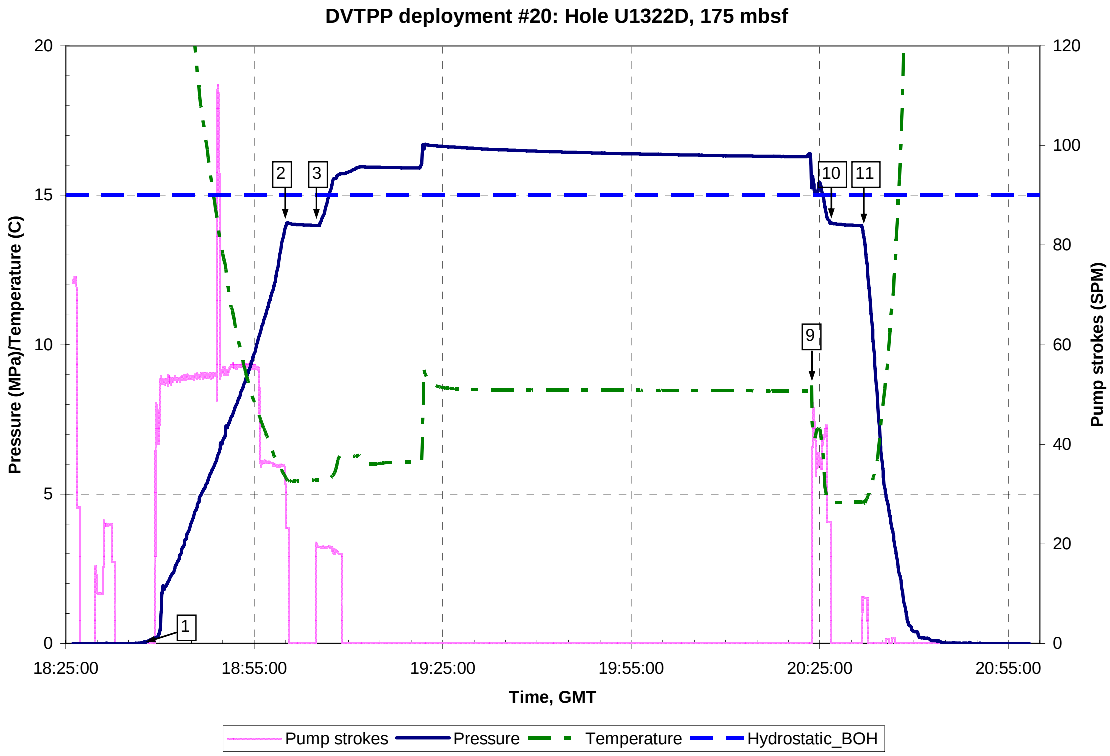

Figure A.A.1.c

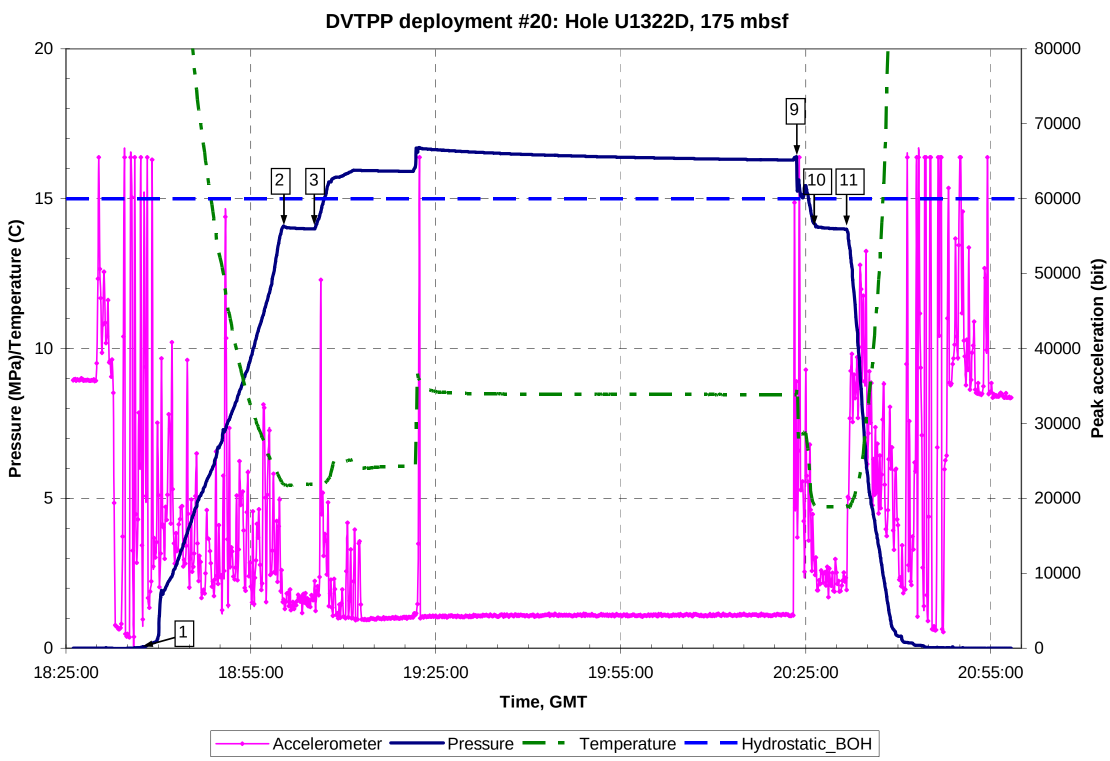

Figure A.A.1.d

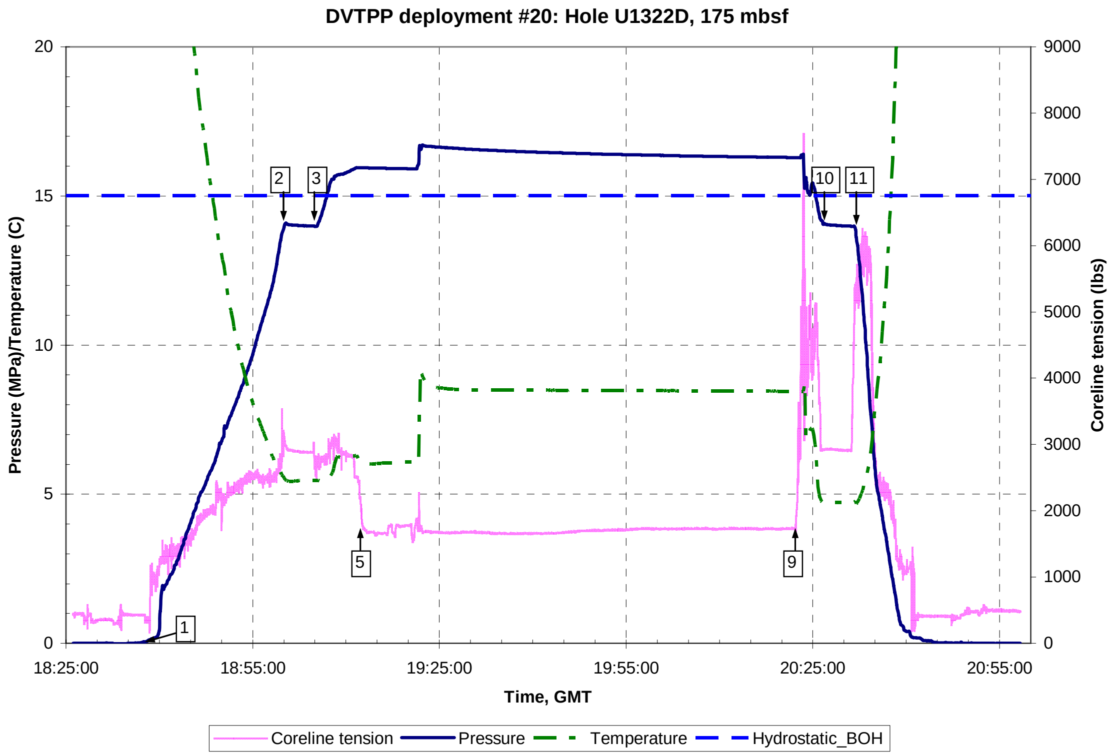

Figure A.A.1.e

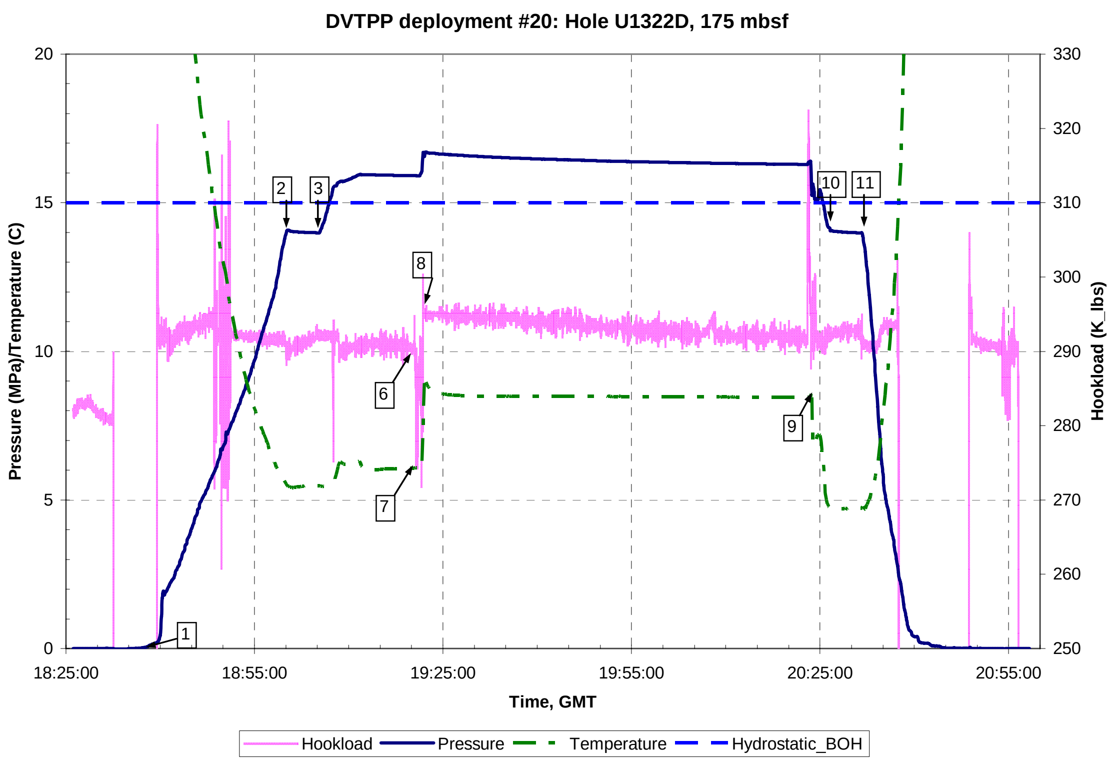

Figure A.A.1.f

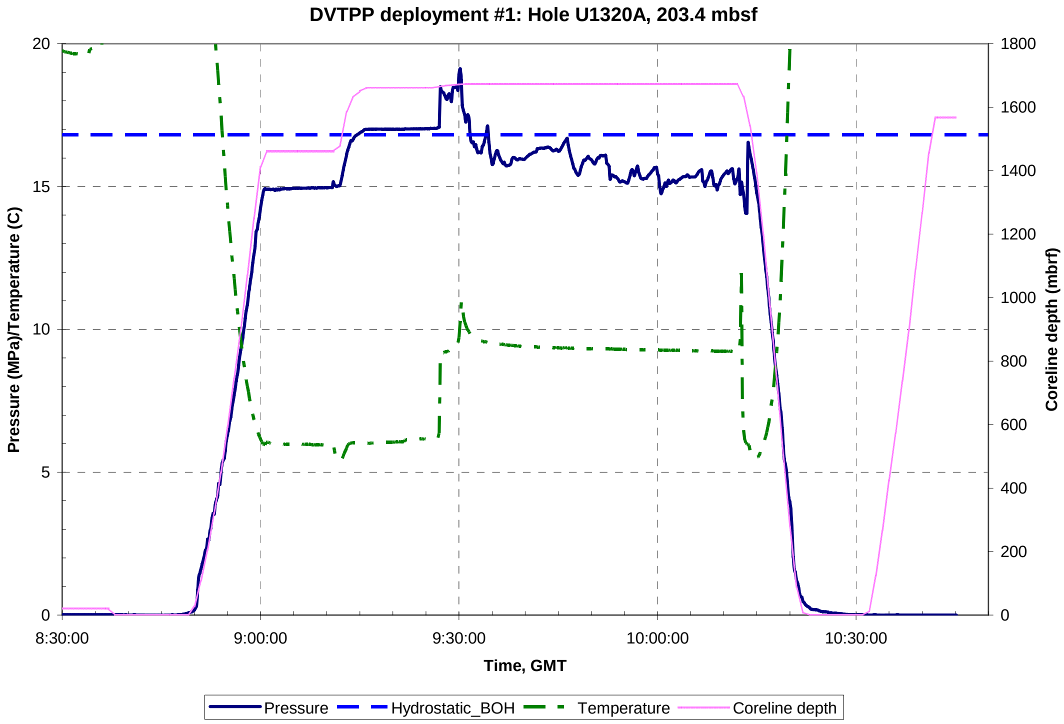

Figure A.A.2.a: Pressure, temperature and Truview data for DVTPP Deployment #1, Hole U1320A, 203.4 mbsf. GMT = Greenwich Mean Time, Hydrostatic_BOH is the hydrostatic pressure at the bottom of the hole.

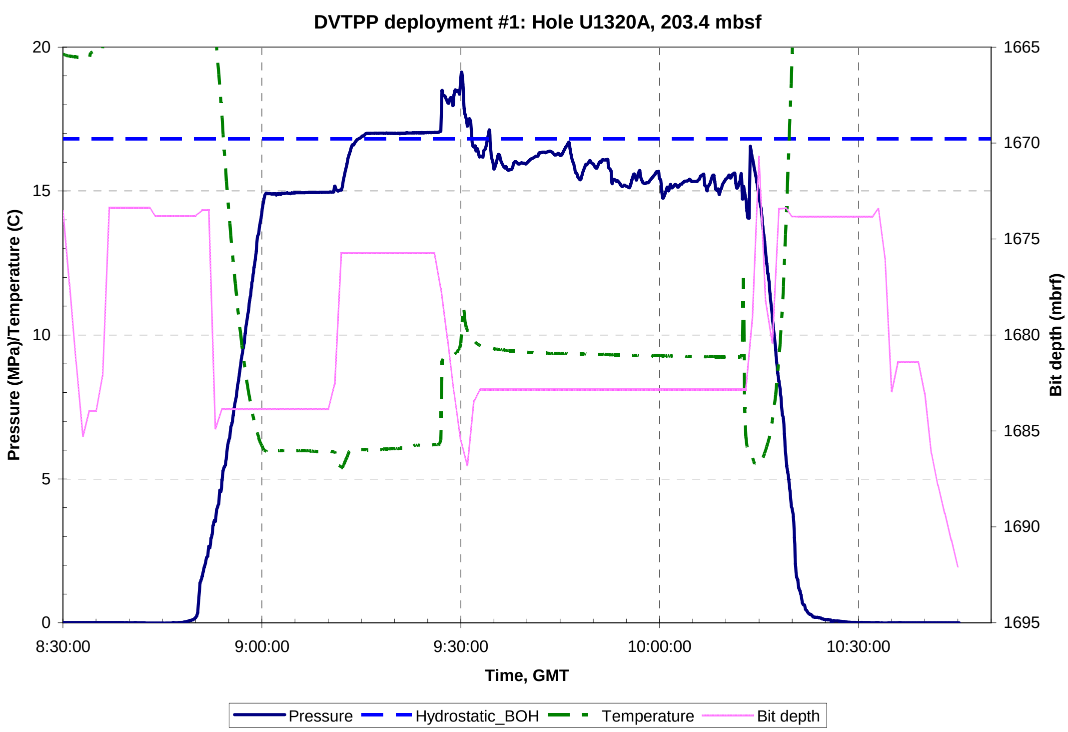

Figure A.A.2.b

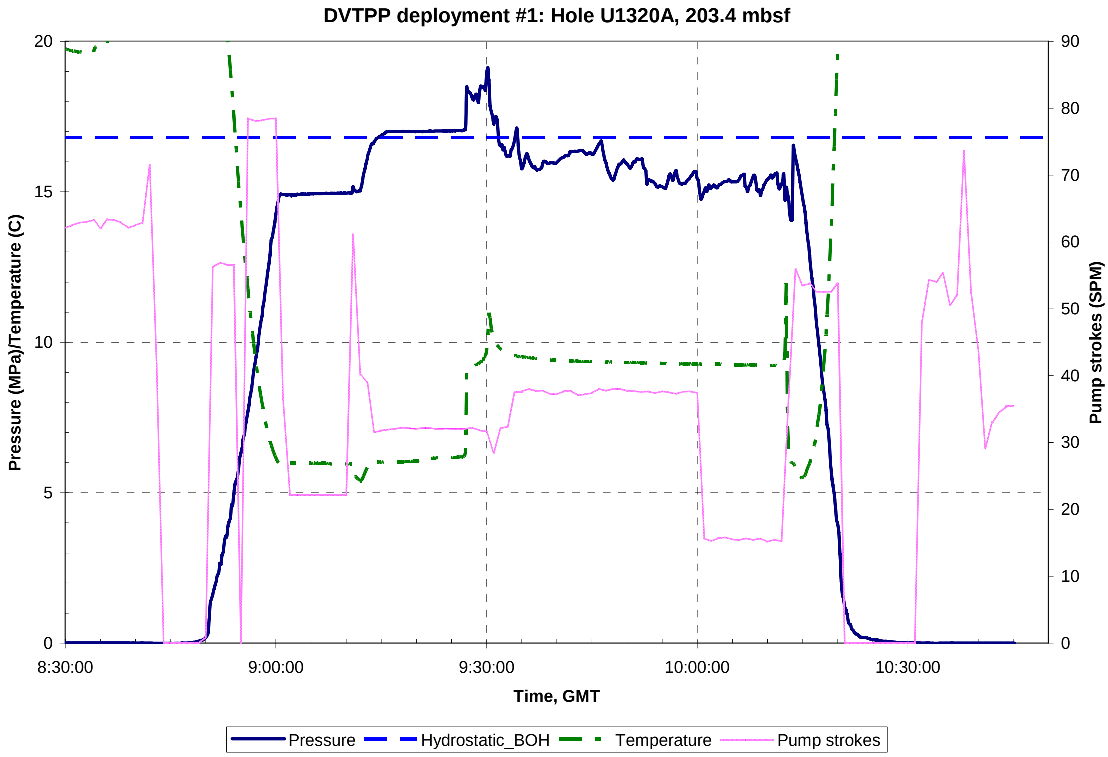

Figure A.A.2.c

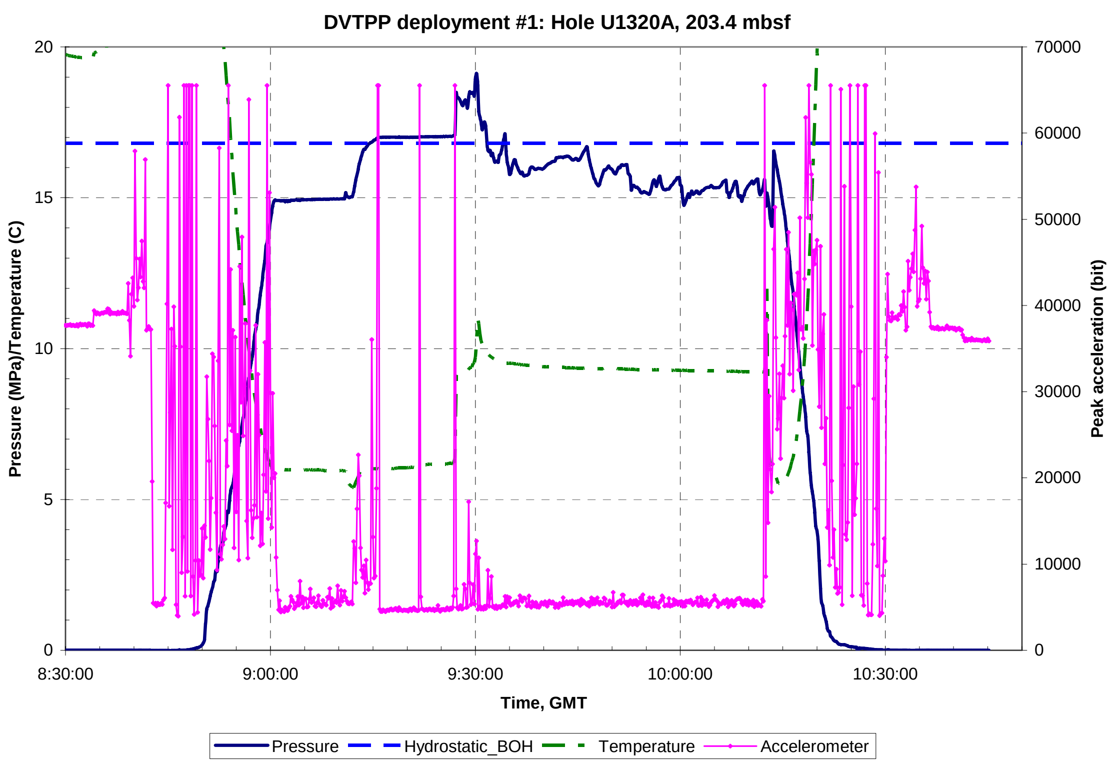

Figure A.A.2.d

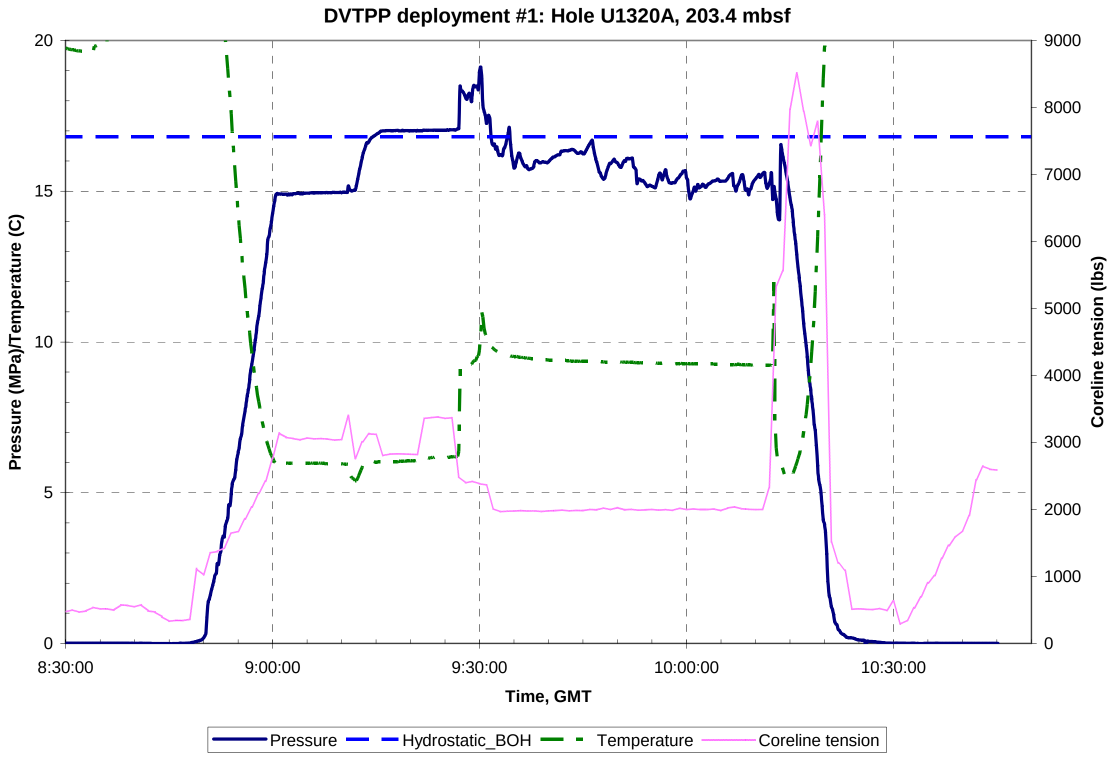

Figure A.A.2.e

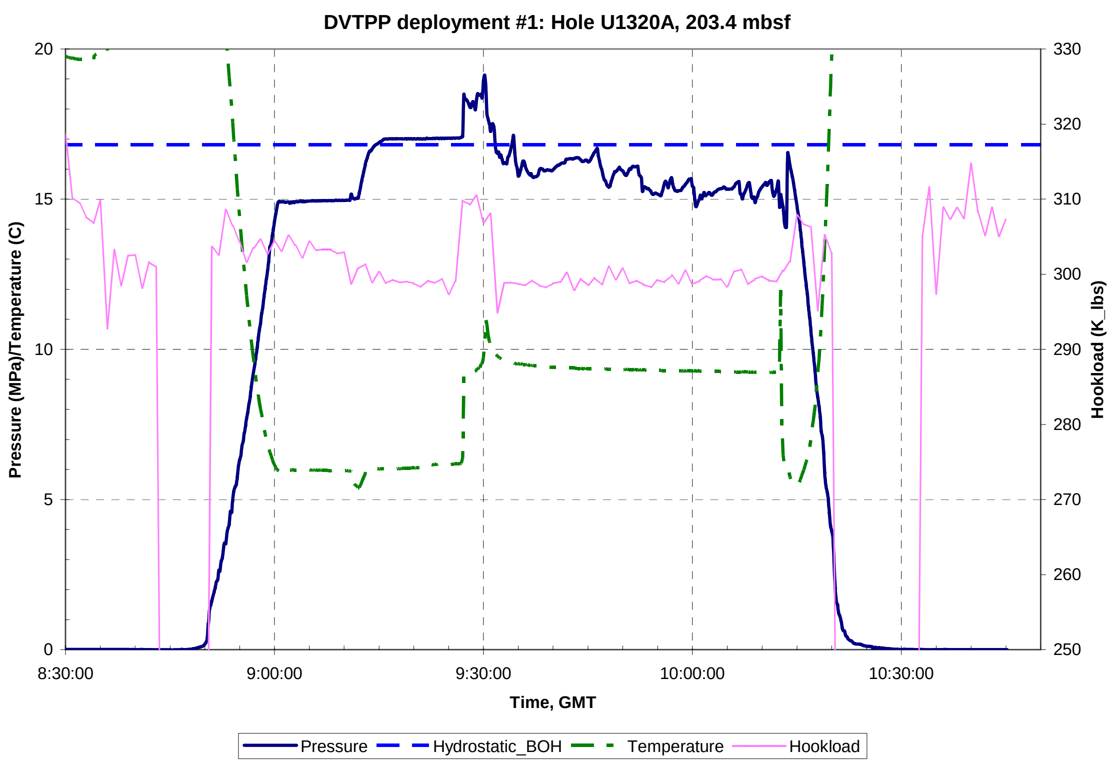

Figure A.A.2.f

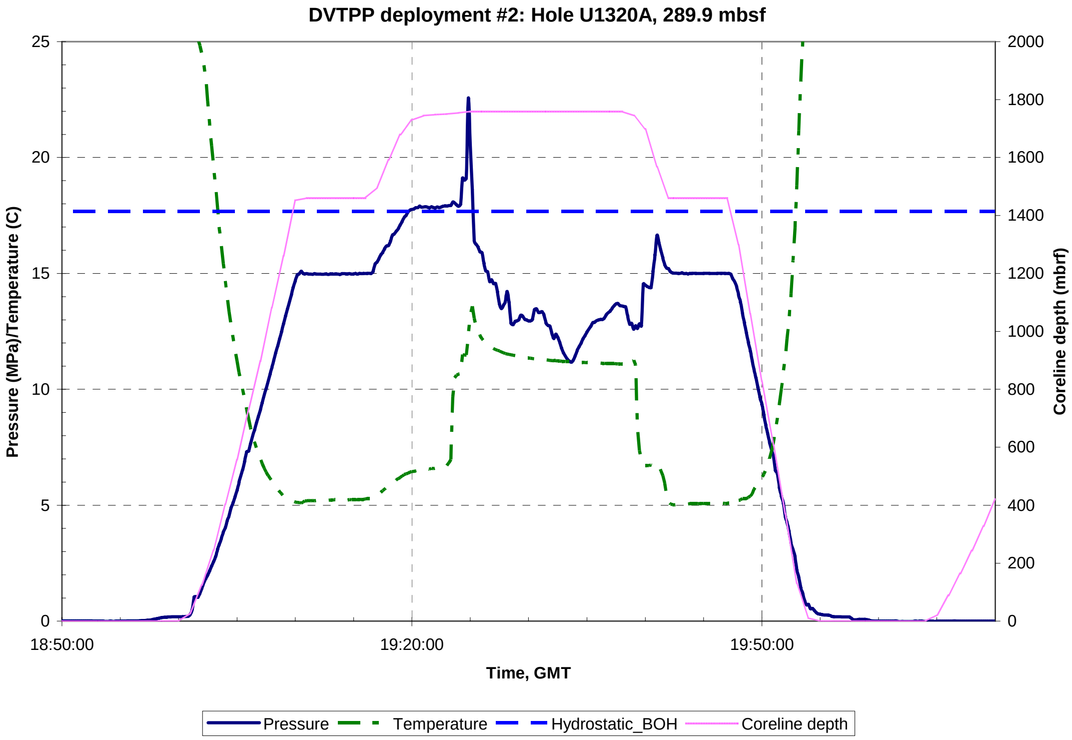

Figure A.A.3.a: Pressure, temperature and Truview data for DVTPP Deployment #2, Hole U1320A, 289.9 mbsf. GMT = Greenwich Mean Time, Hydrostatic_BOH is the hydrostatic pressure at the bottom of the hole.

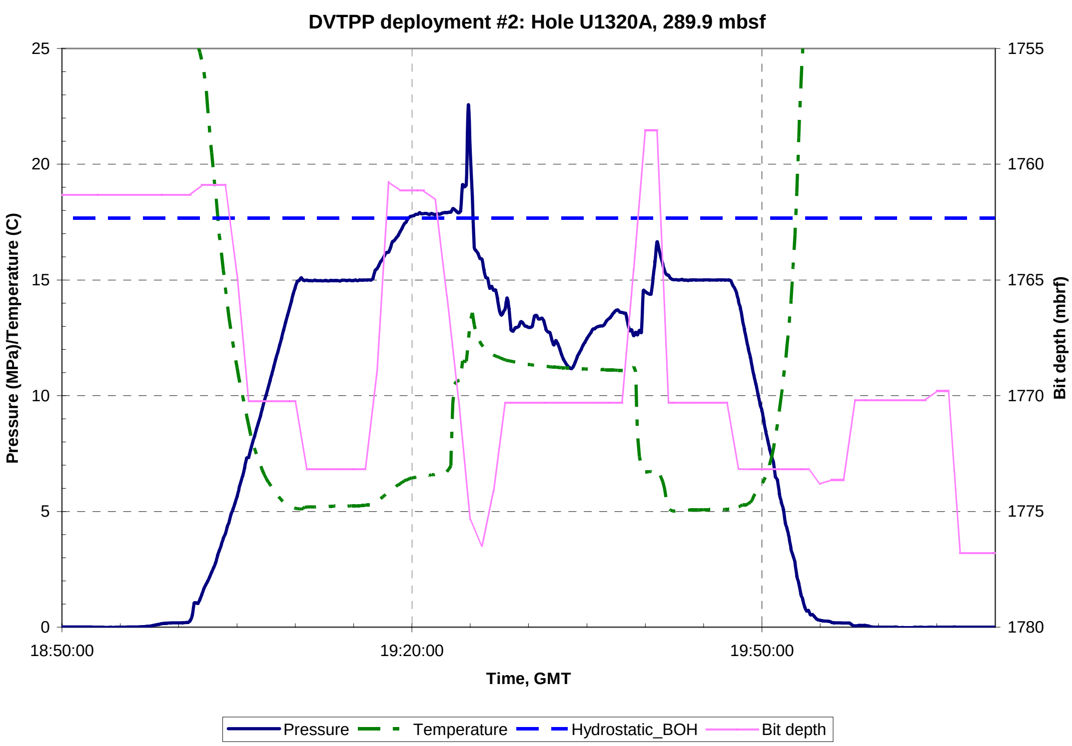

Figure A.A.3.b

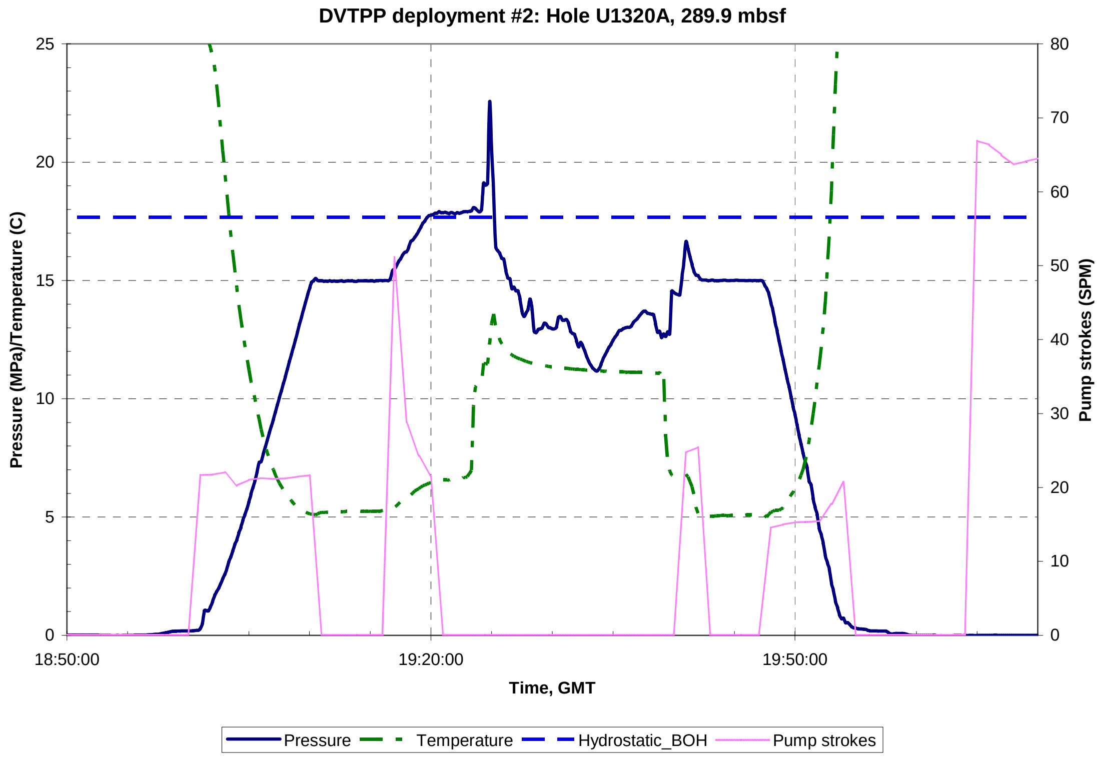

Figure A.A.3.c

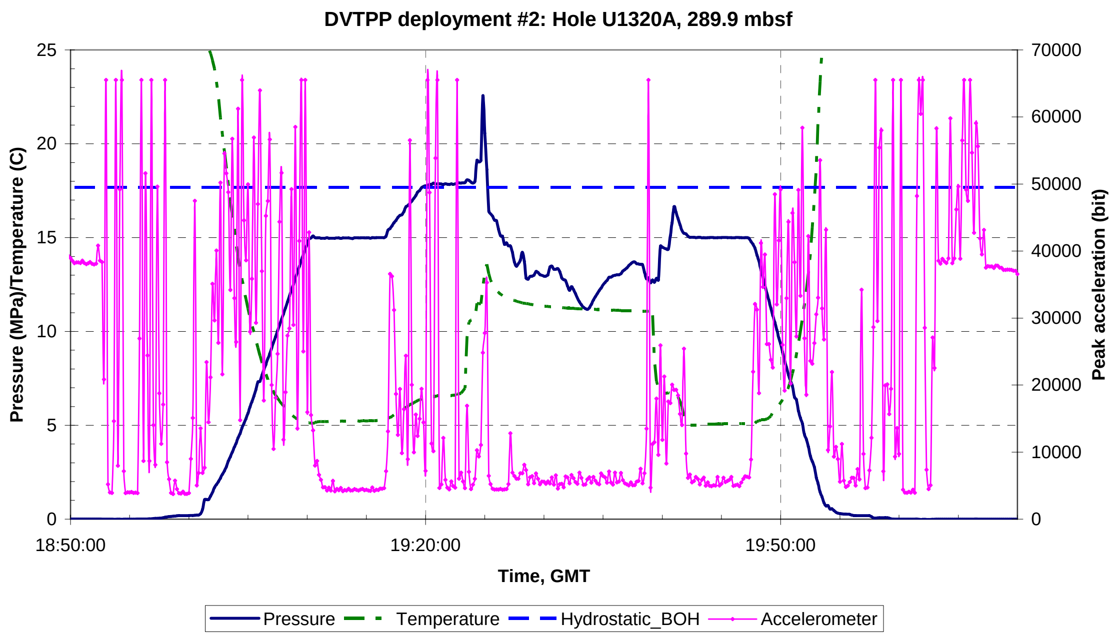

Figure A.A.3.d

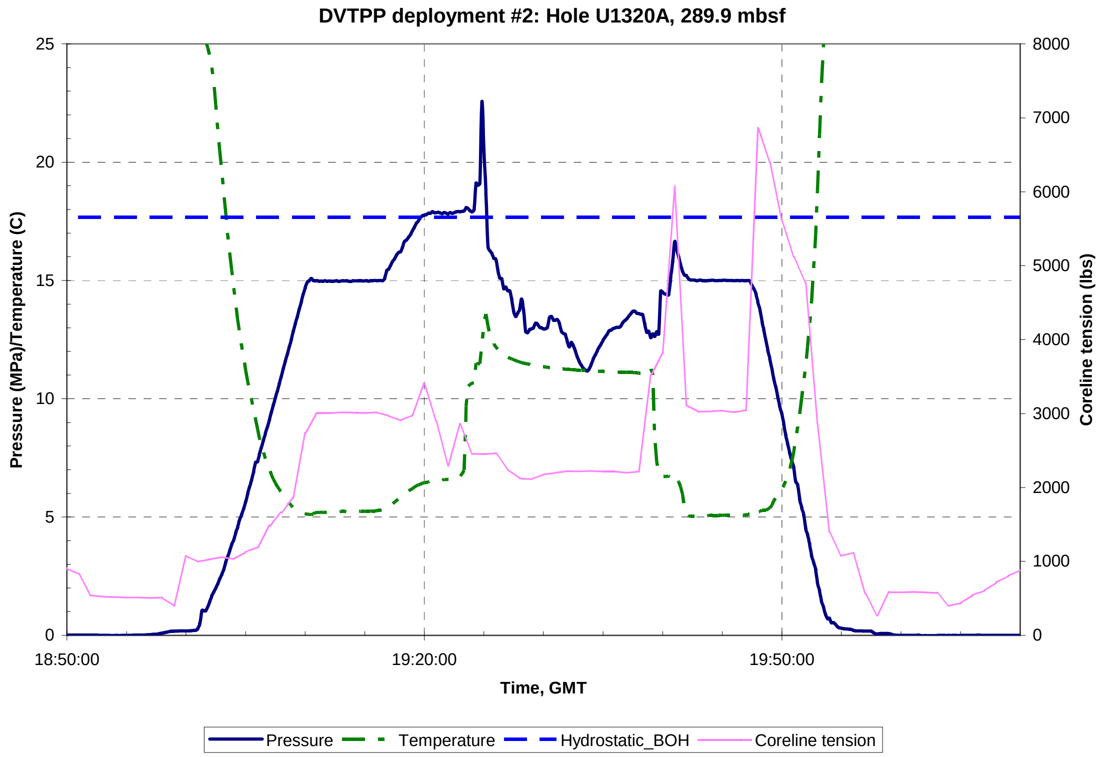

Figure A.A.3.e

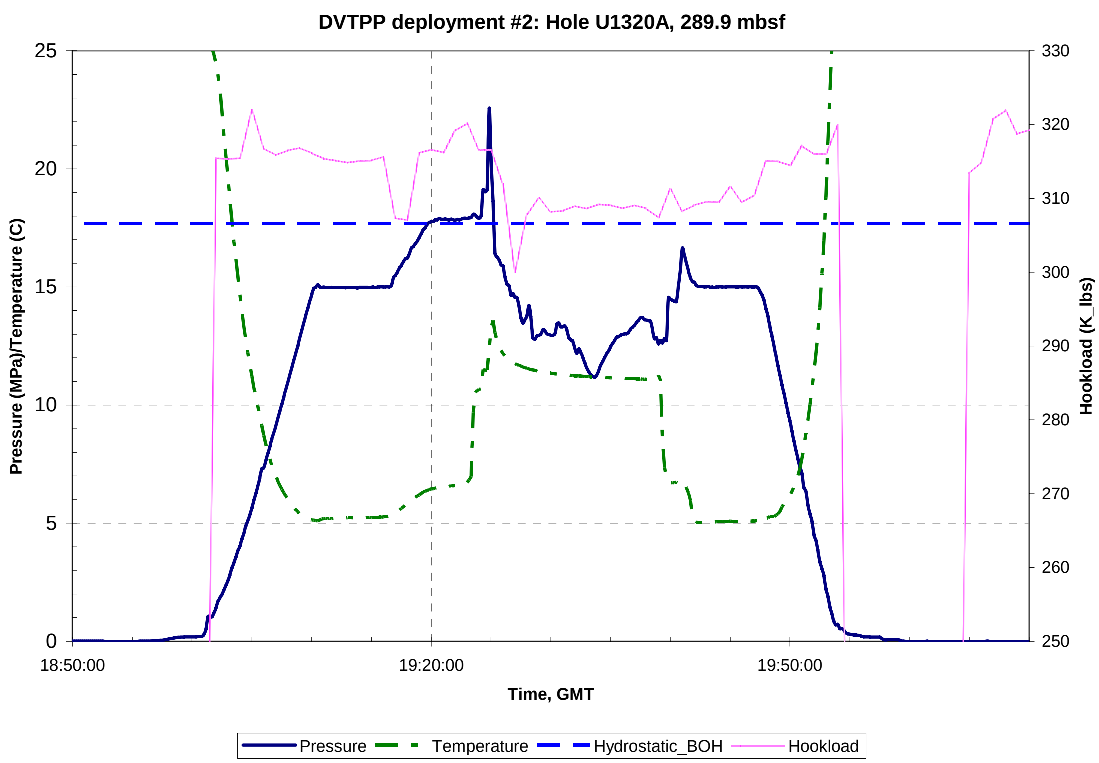

Figure A.A.3.f

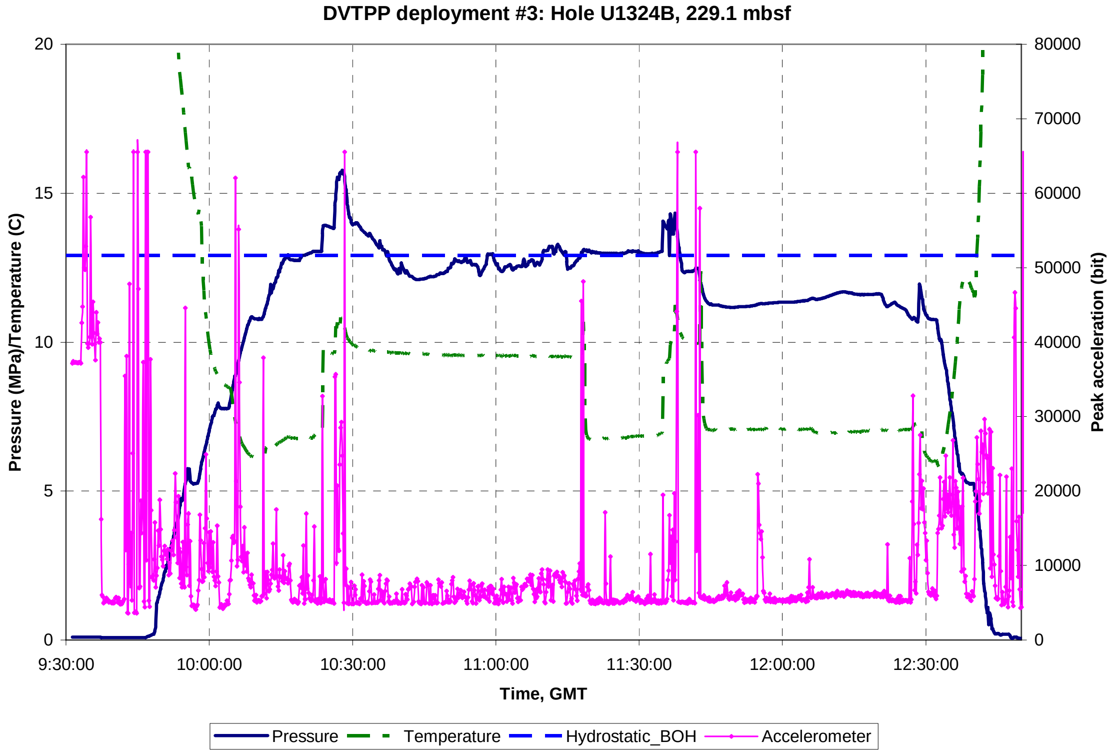

Figure A.A.4: Pressure, temperature and acceleration data for DVTPP Deployment #3, Hole U1324B, 229.1 mbsf. GMT = Greenwich Mean Time, Hydrostatic_BOH is the hydrostatic pressure at the bottom of the hole.

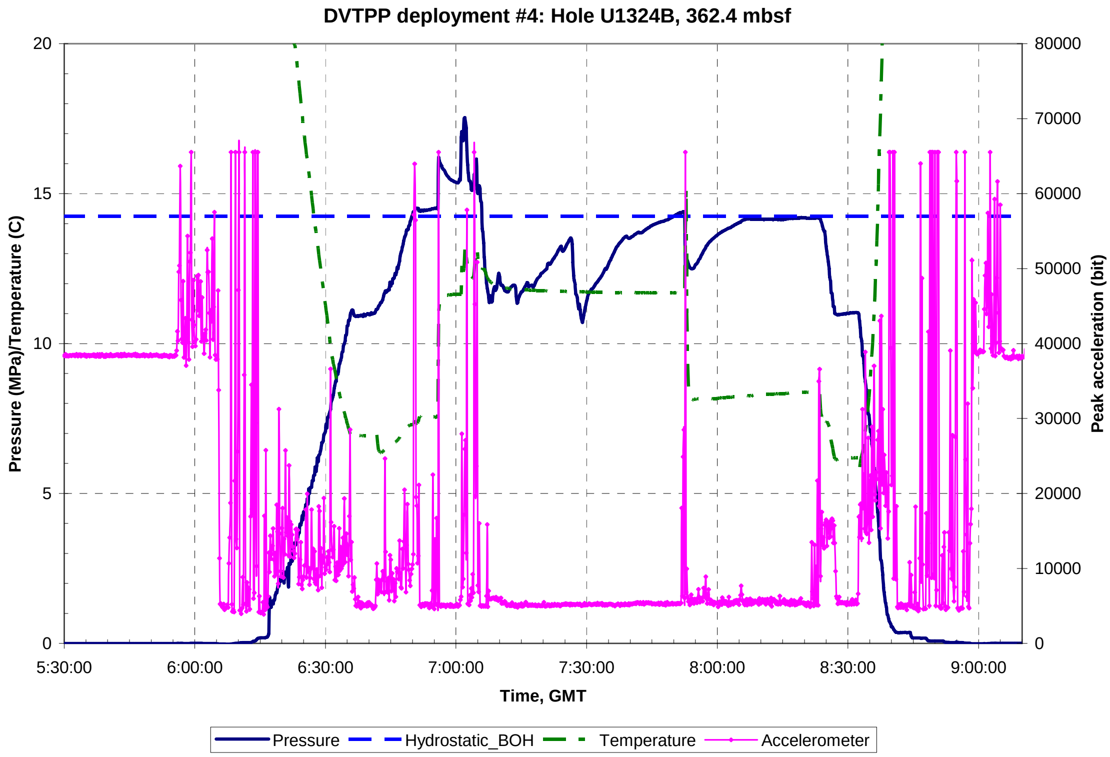

Figure A.A.5: Pressure, temperature and acceleration data for DVTPP Deployment #4, Hole U1324B, 362.4 mbsf. GMT = Greenwich Mean Time, Hydrostatic_BOH is the hydrostatic pressure at the bottom of the hole.

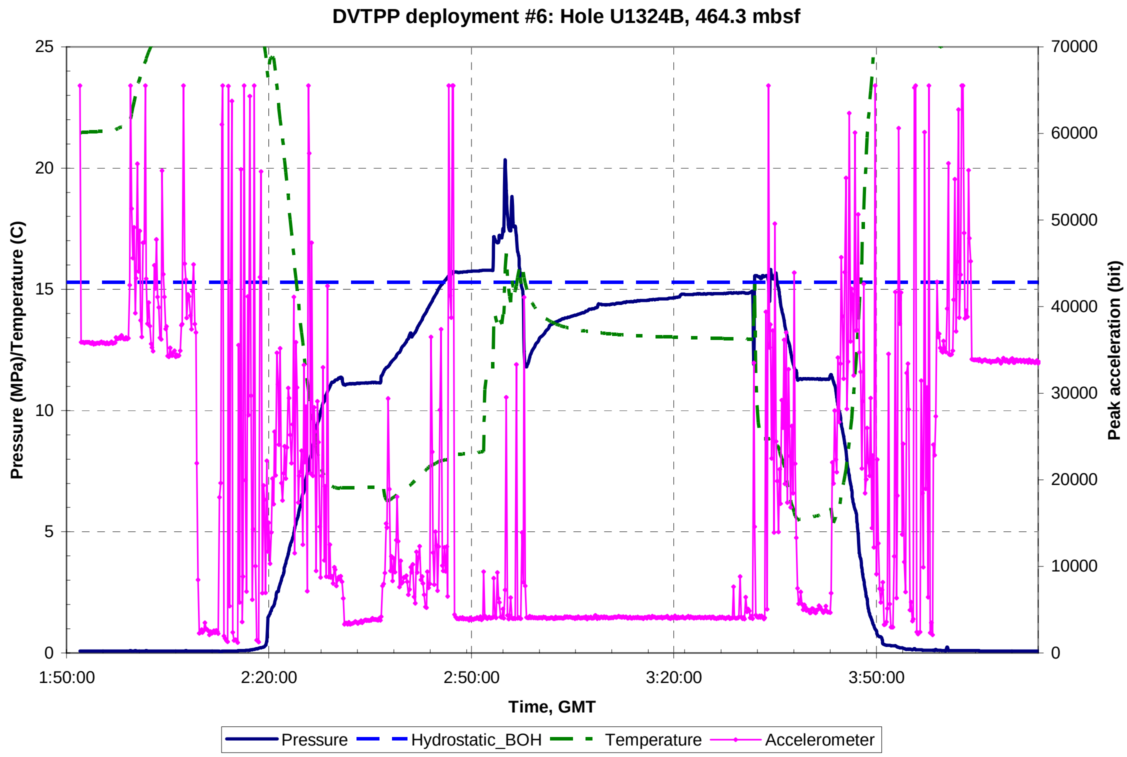

Figure A.A.6: Pressure, temperature and acceleration data for DVTPP Deployment #6, Hole U1324B, 464.3 mbsf. GMT = Greenwich Mean Time, Hydrostatic_BOH is the hydrostatic pressure at the bottom of the hole.

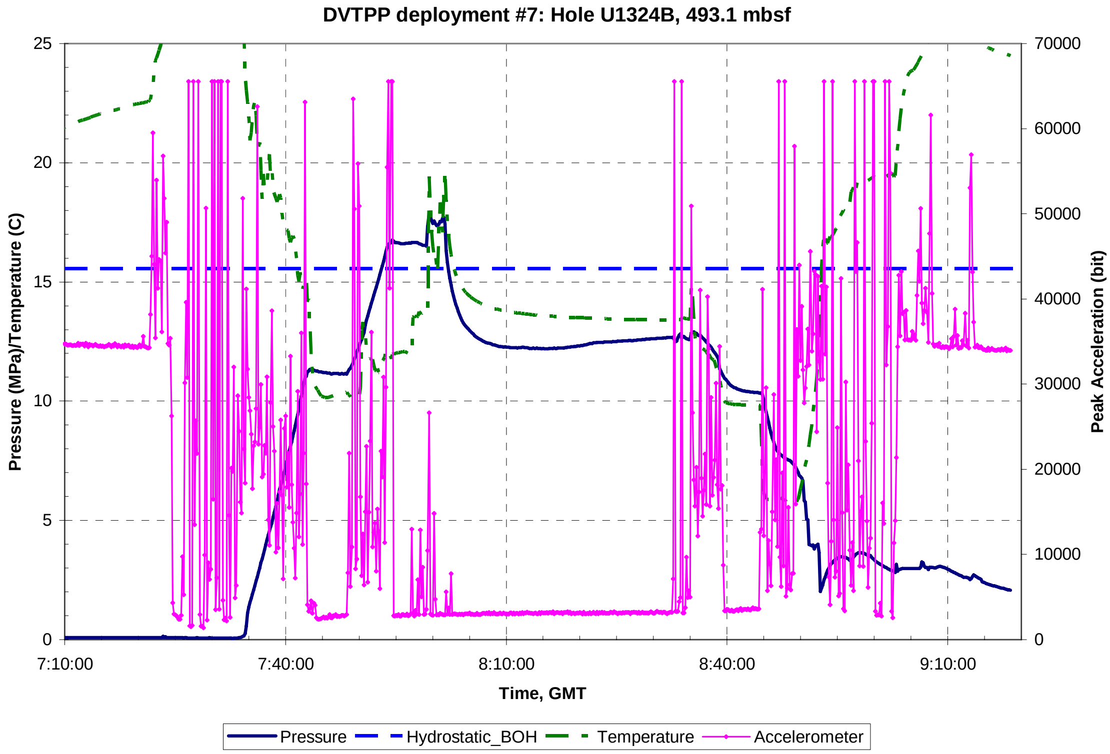

Figure A.A.7: Pressure, temperature and acceleration data for DVTPP Deployment #7, Hole U1324B, 493.1 mbsf. GMT = Greenwich Mean Time, Hydrostatic_BOH is the hydrostatic pressure at the bottom of the hole.

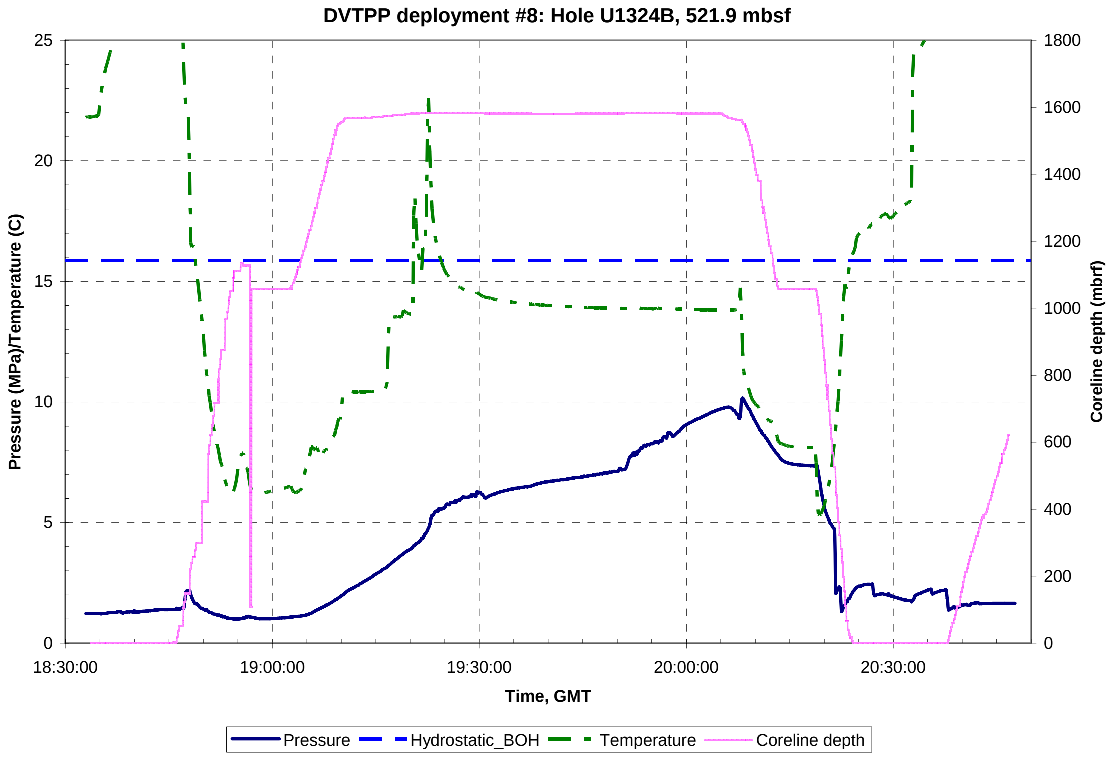

Figure A.A.8.a: Pressure, temperature and Truview data for DVTPP Deployment #8, Hole U1324B, 521.9 mbsf. GMT = Greenwich Mean Time, Hydrostatic_BOH is the hydrostatic pressure at the bottom of the hole.

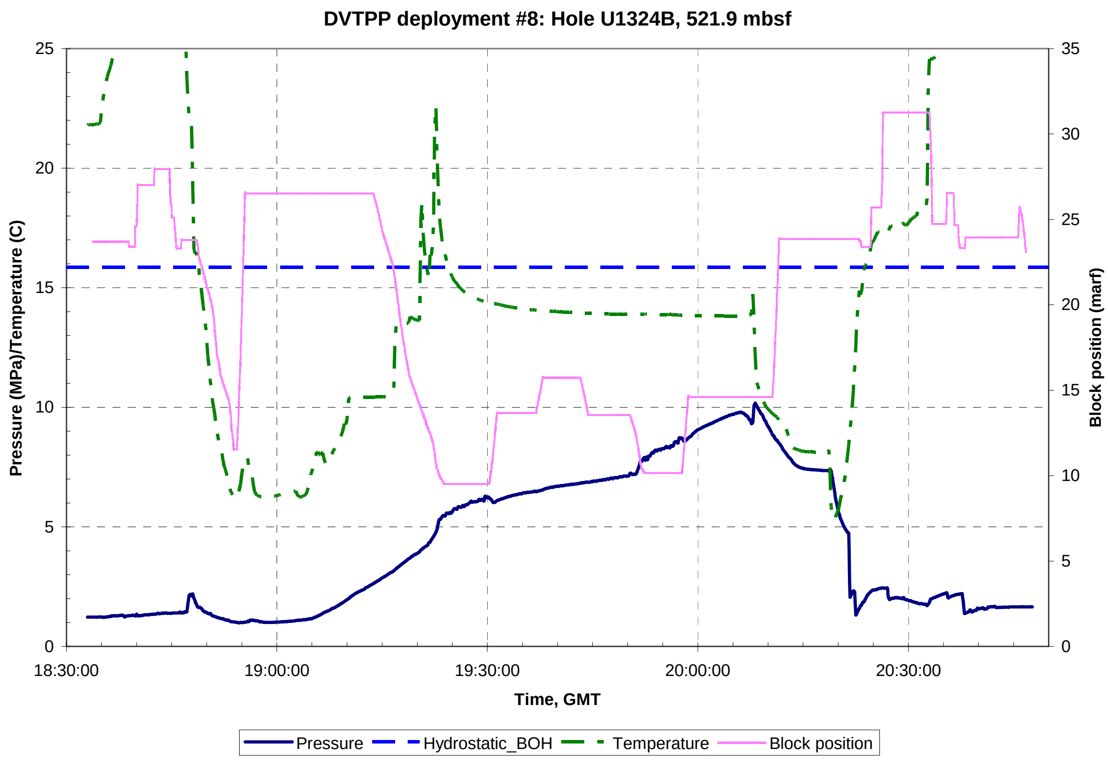

Figure A.A.8.b

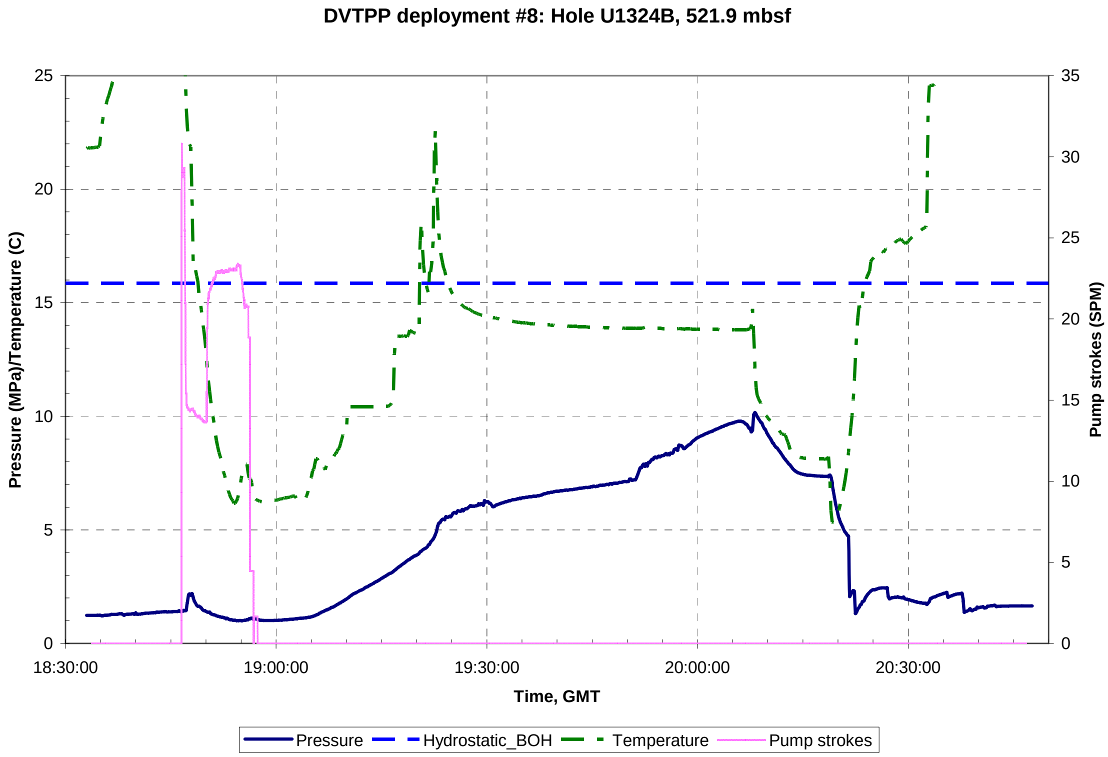

Figure A.A.8.c

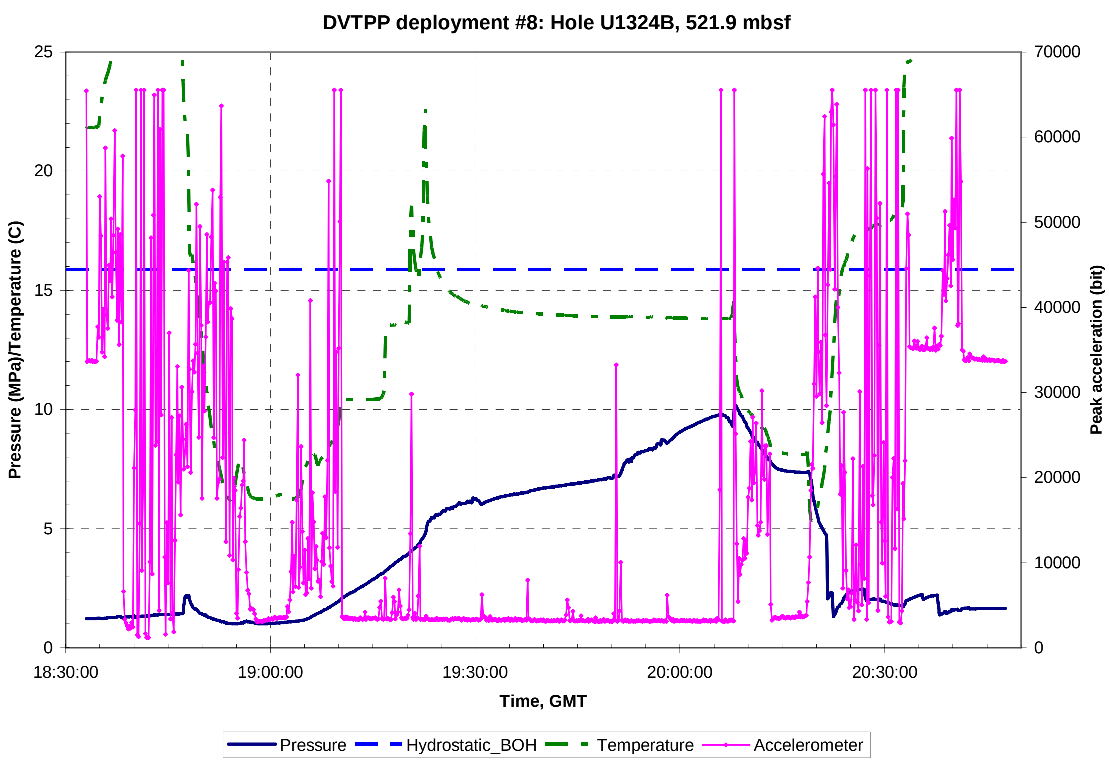

Figure A.A.8.d

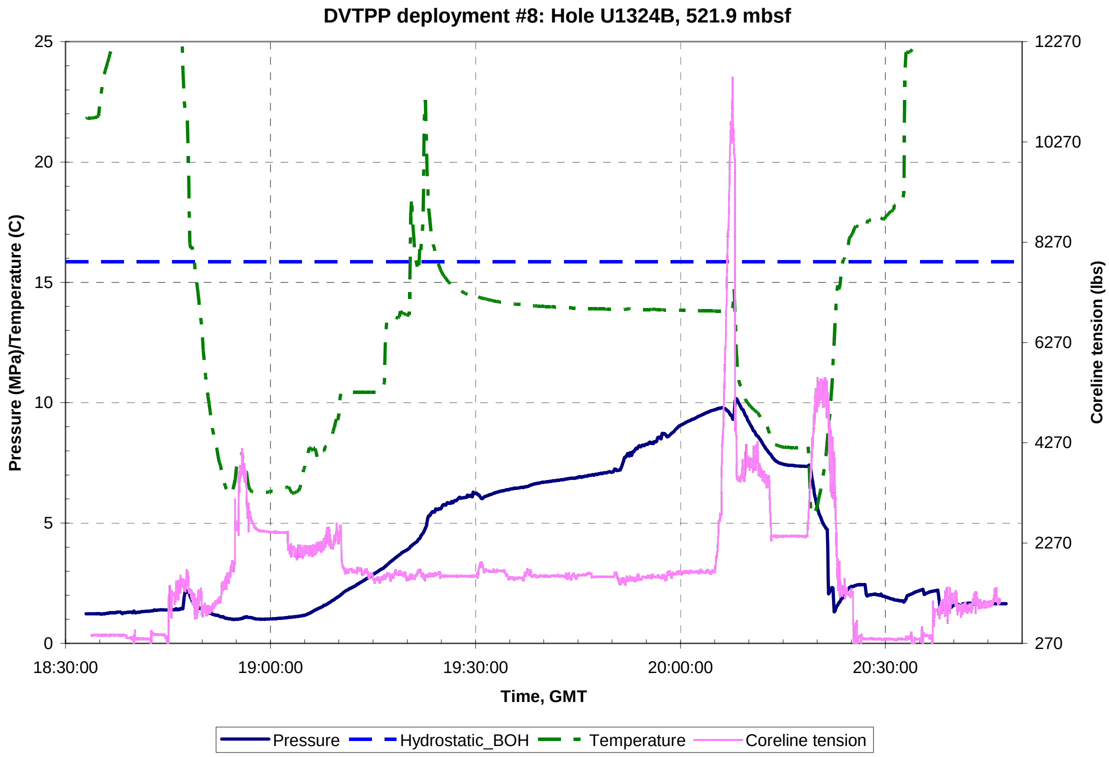

Figure A.A.8.e

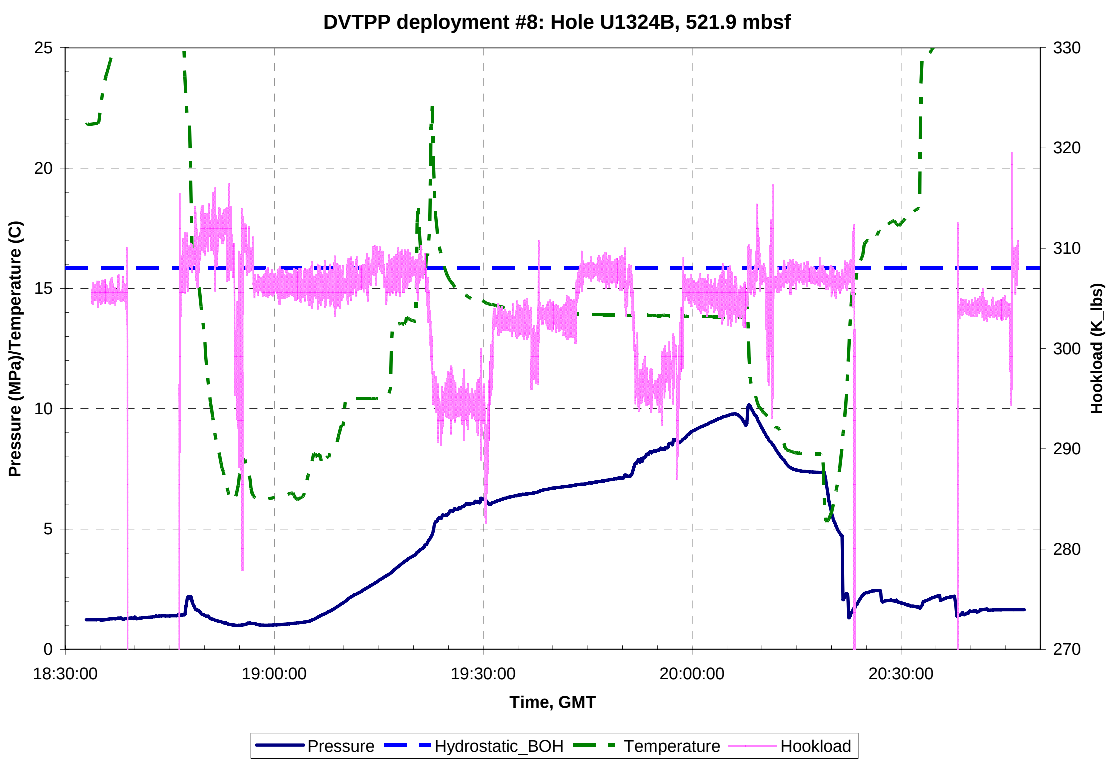

Figure A.A.8.f

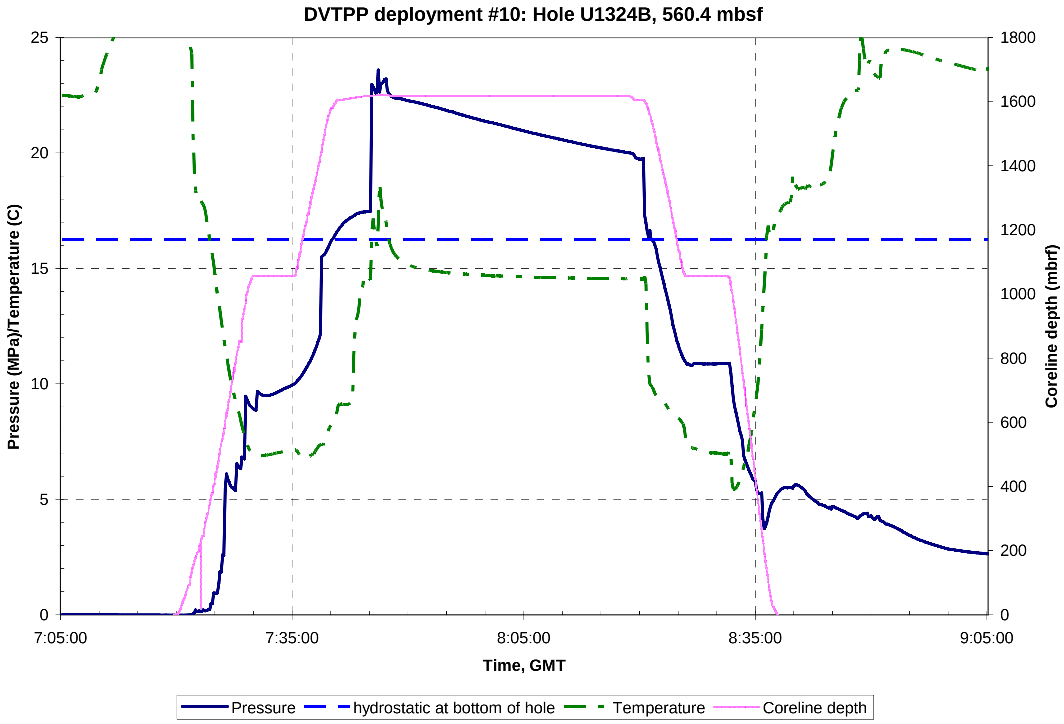

Figure A.A.9.a: Pressure, temperature and Truview data for DVTPP Deployment #10, Hole U1324B, 560.4 mbsf. GMT = Greenwich Mean Time, Hydrostatic_BOH is the hydrostatic pressure at the bottom of the hole.

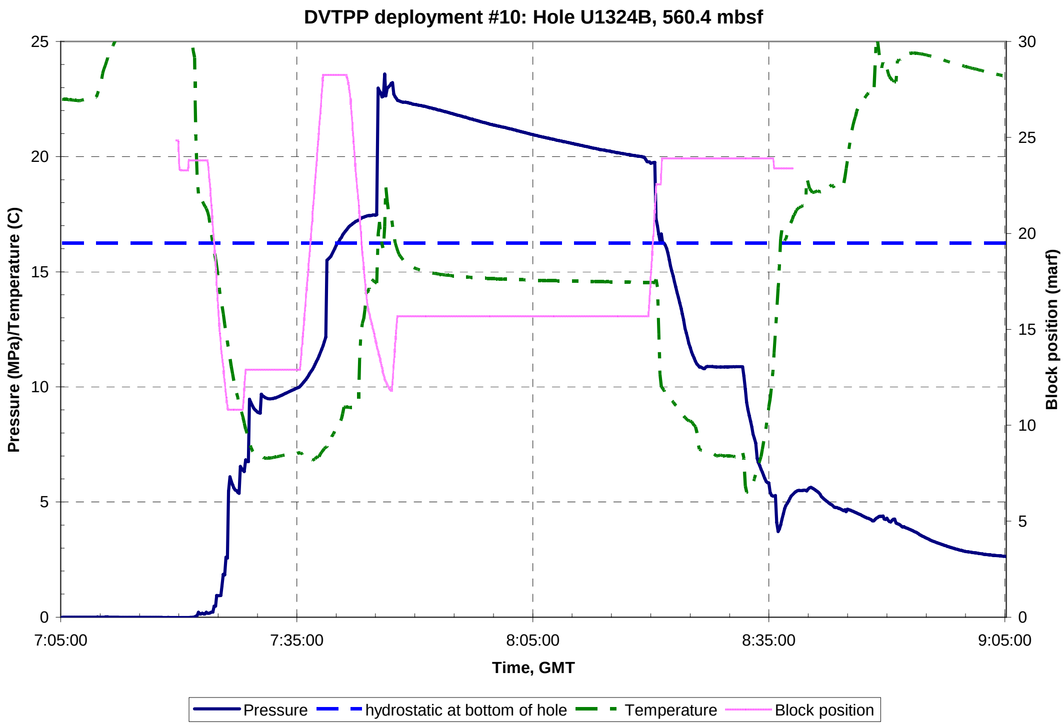

Figure A.A.9.b

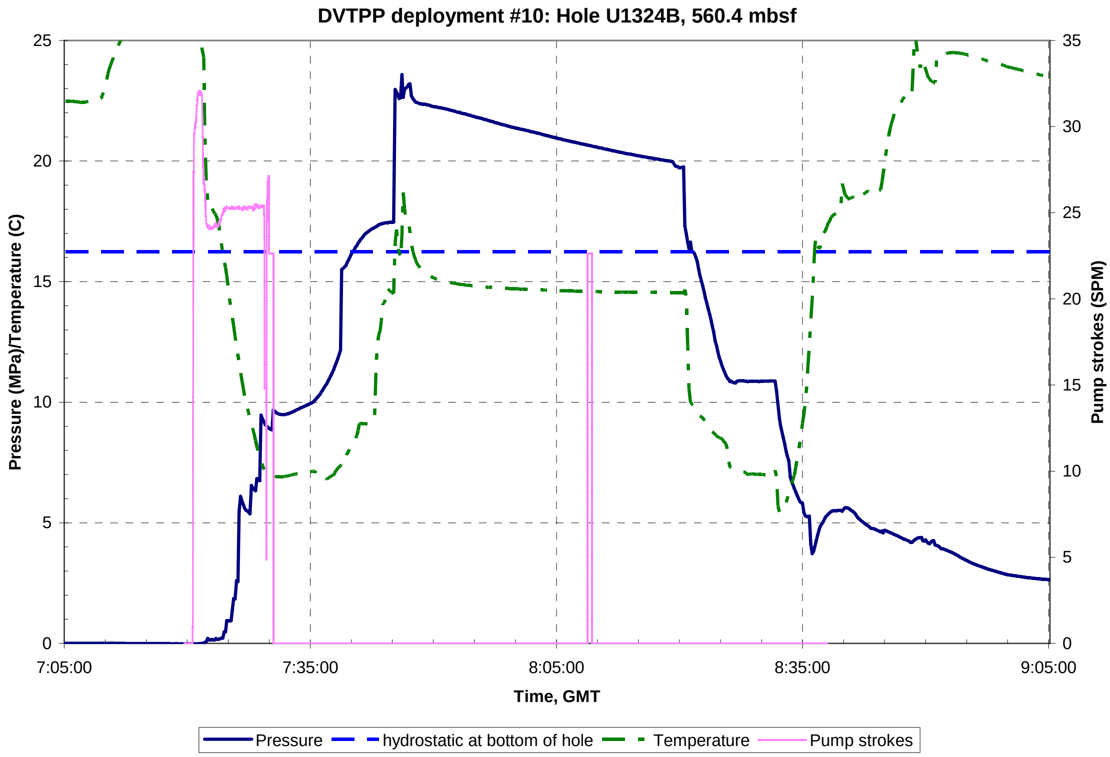

Figure A.A.9.c

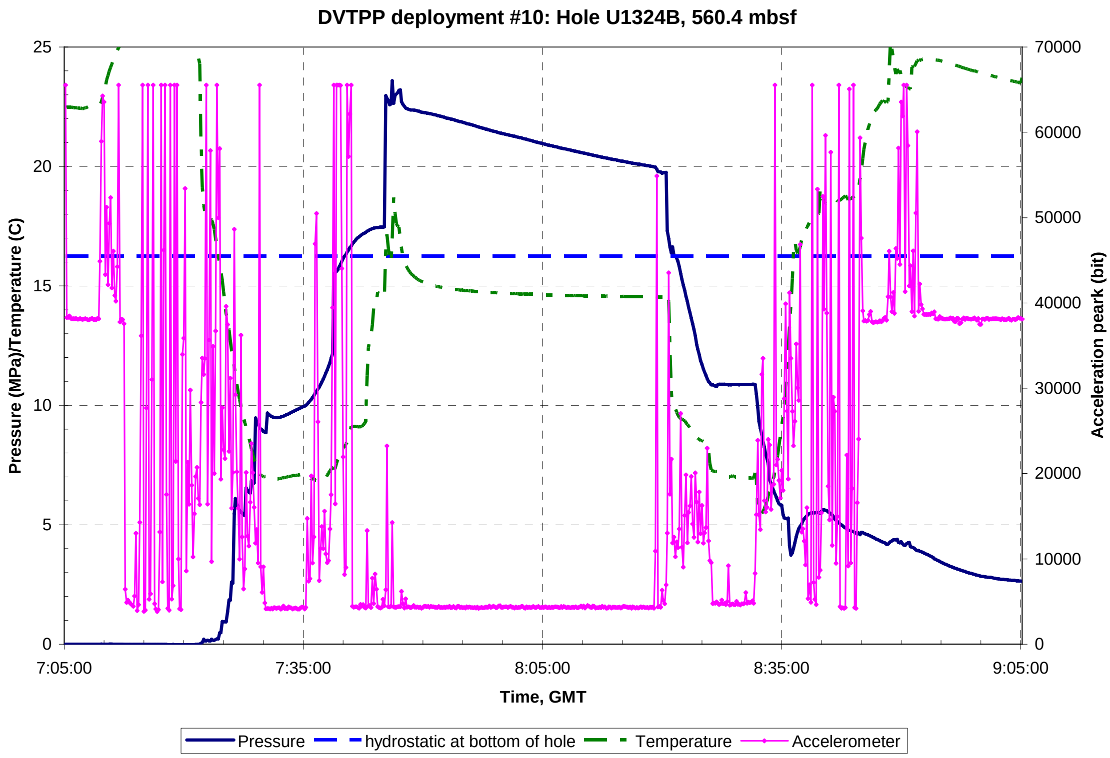

Figure A.A.9.d

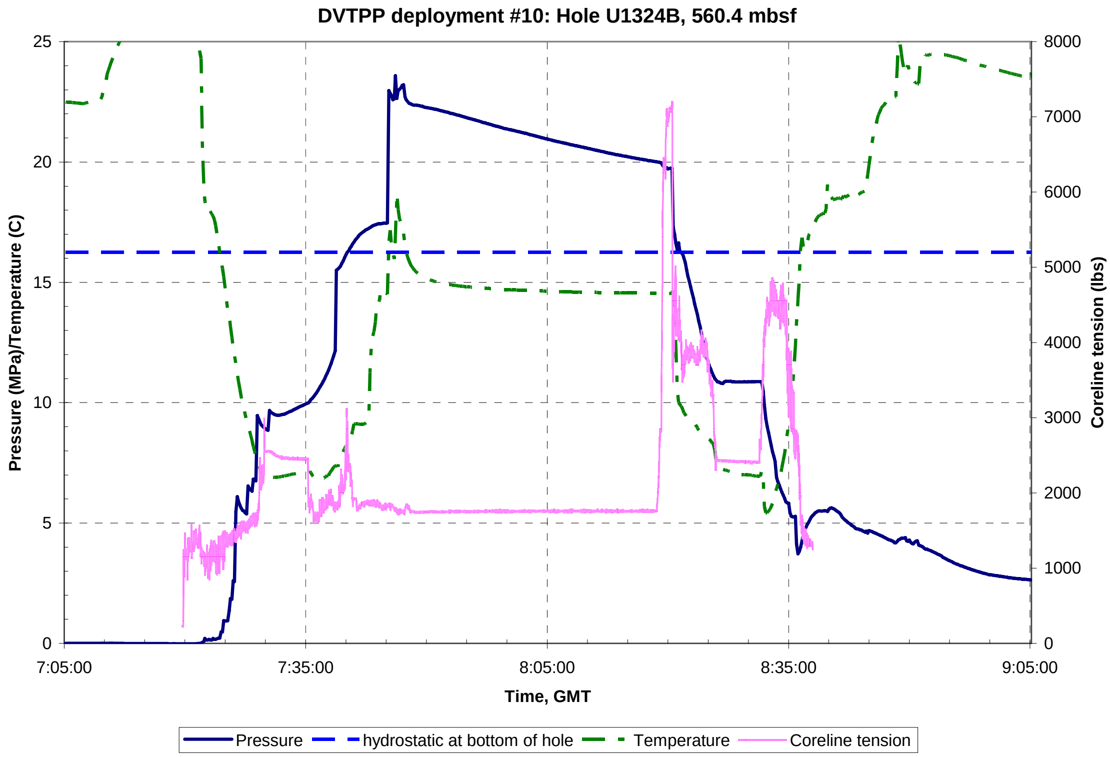

Figure A.A.9.e

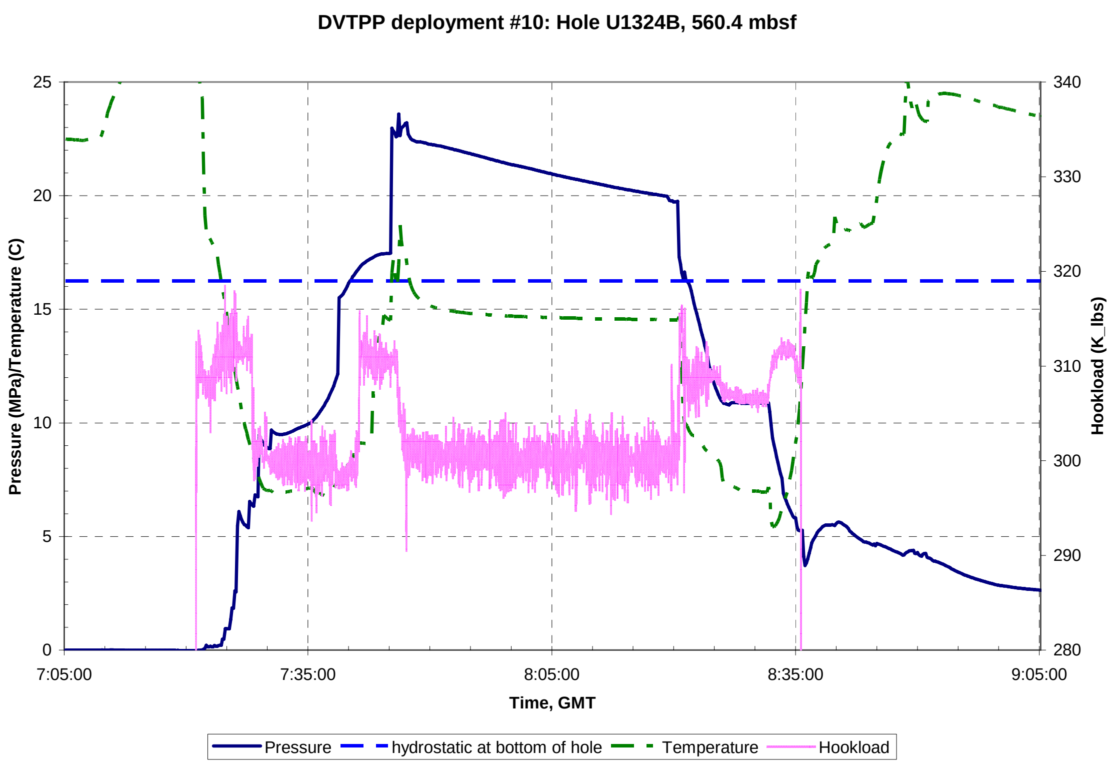

Figure A.A.9.f

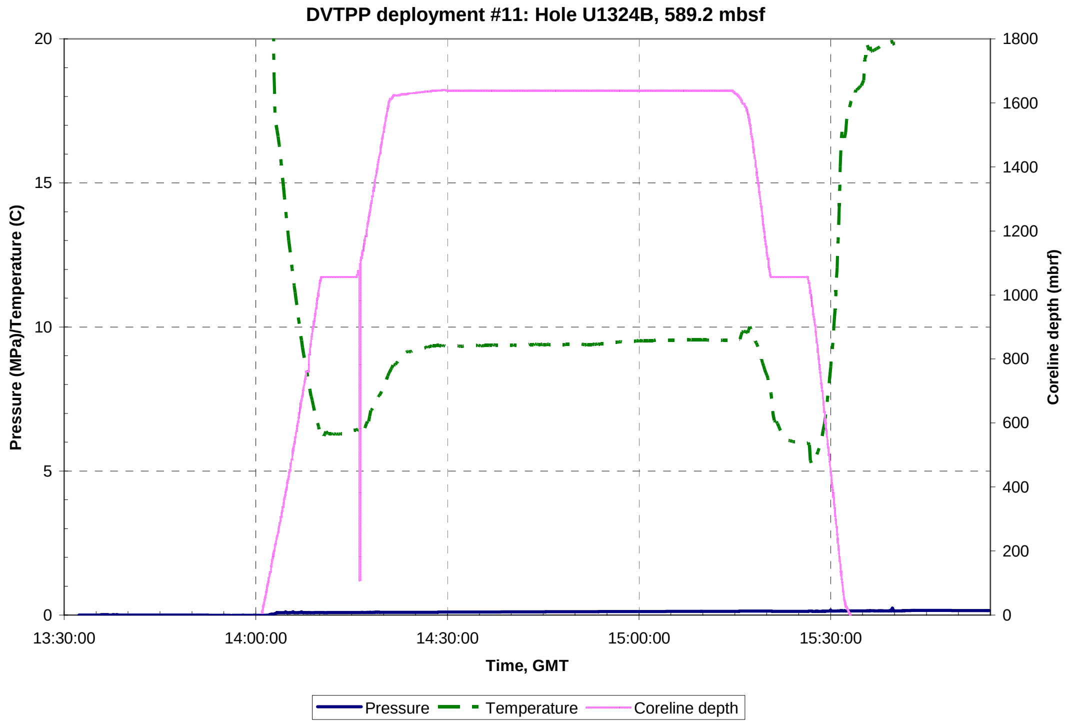

Figure A.A.10.a: Pressure, temperature and Truview data for DVTPP Deployment #11, Hole U1324B, 589.2 mbsf. GMT = Greenwich Mean Time, Hydrostatic_BOH is the hydrostatic pressure at the bottom of the hole.

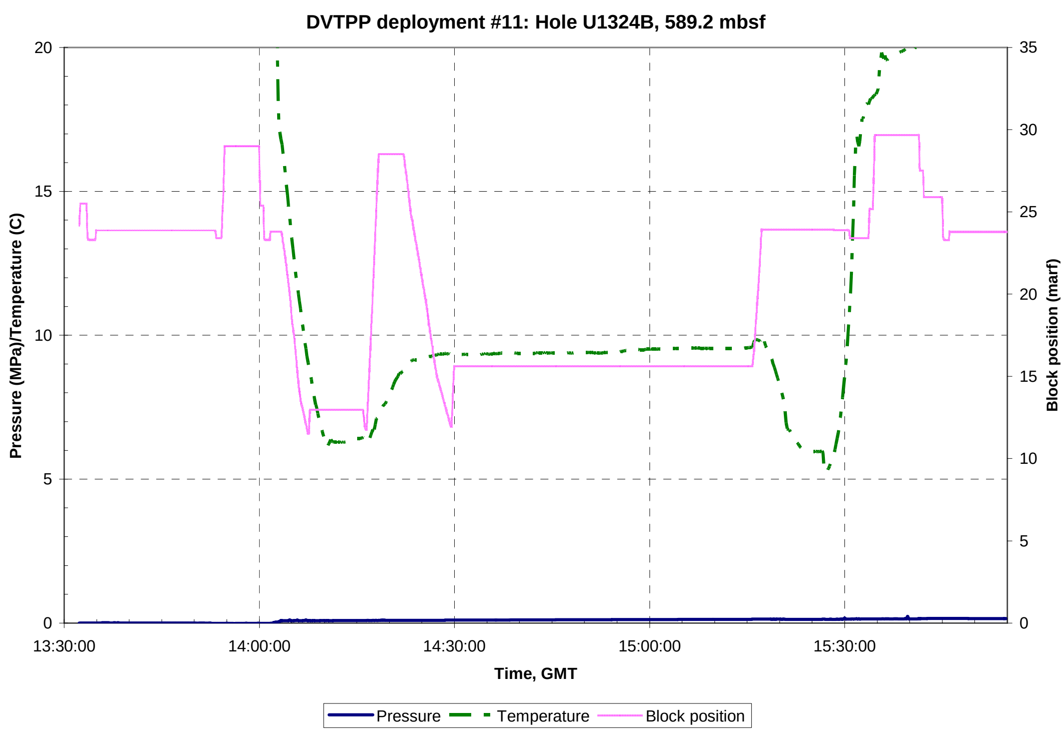

Figure A.A.10.b

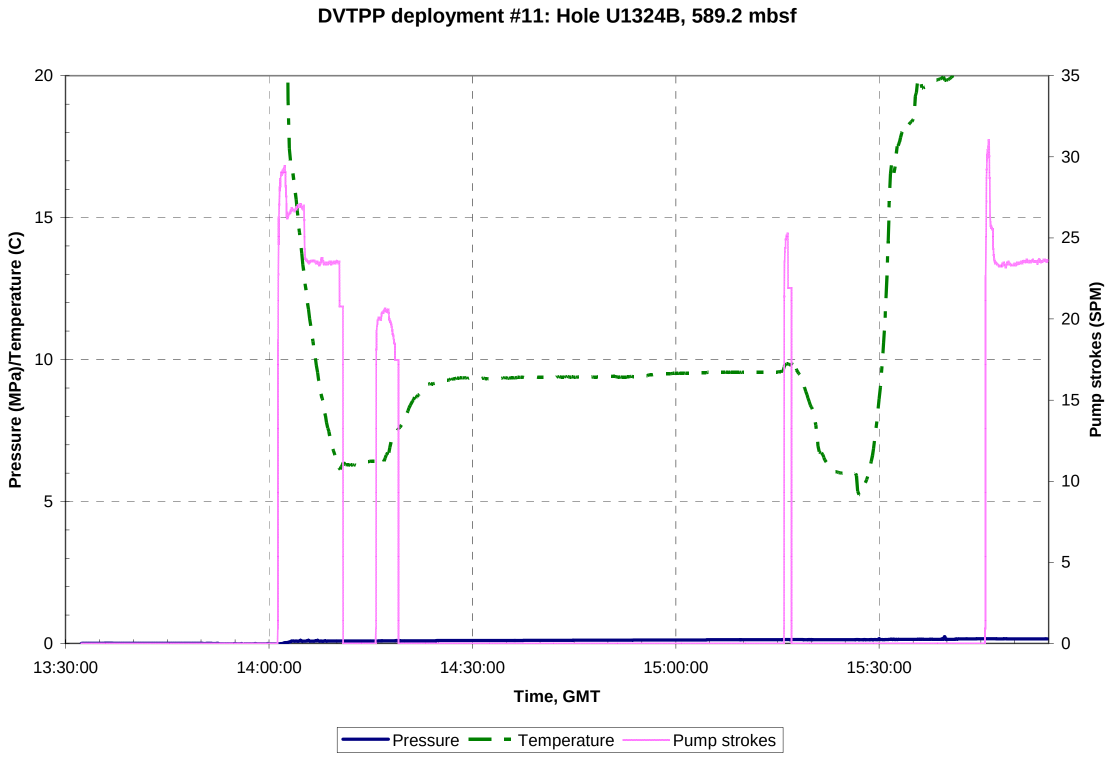

Figure A.A.10.c

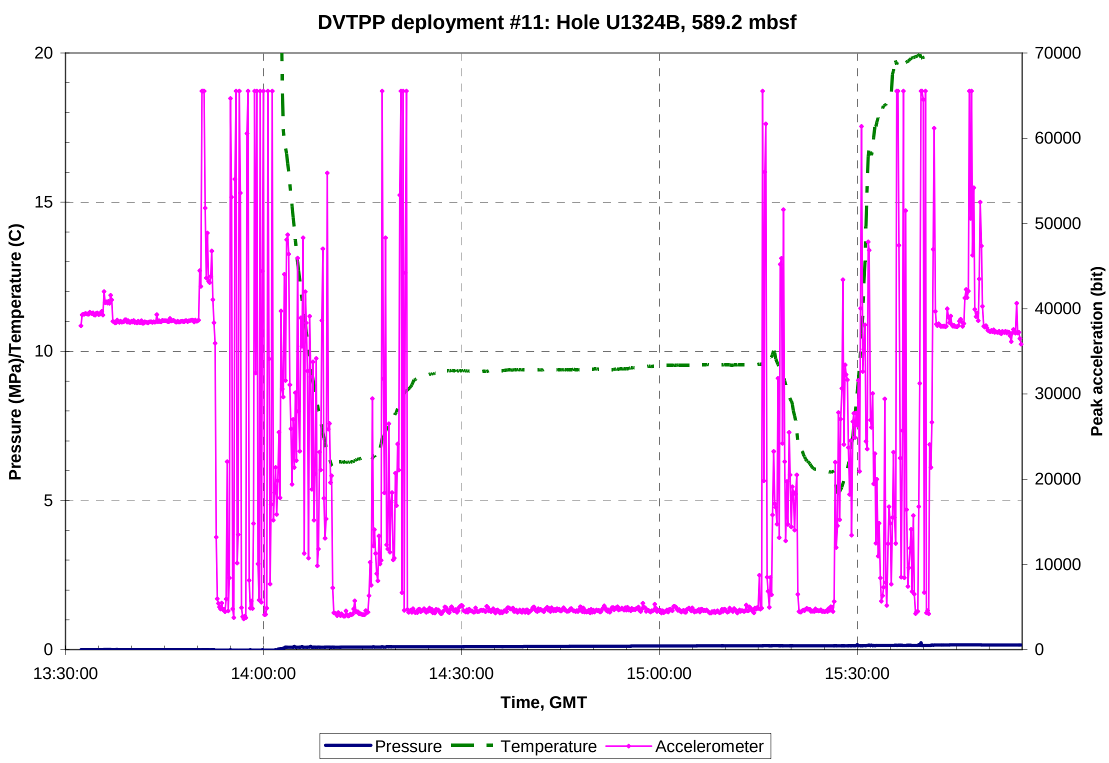

Figure A.A.10.d

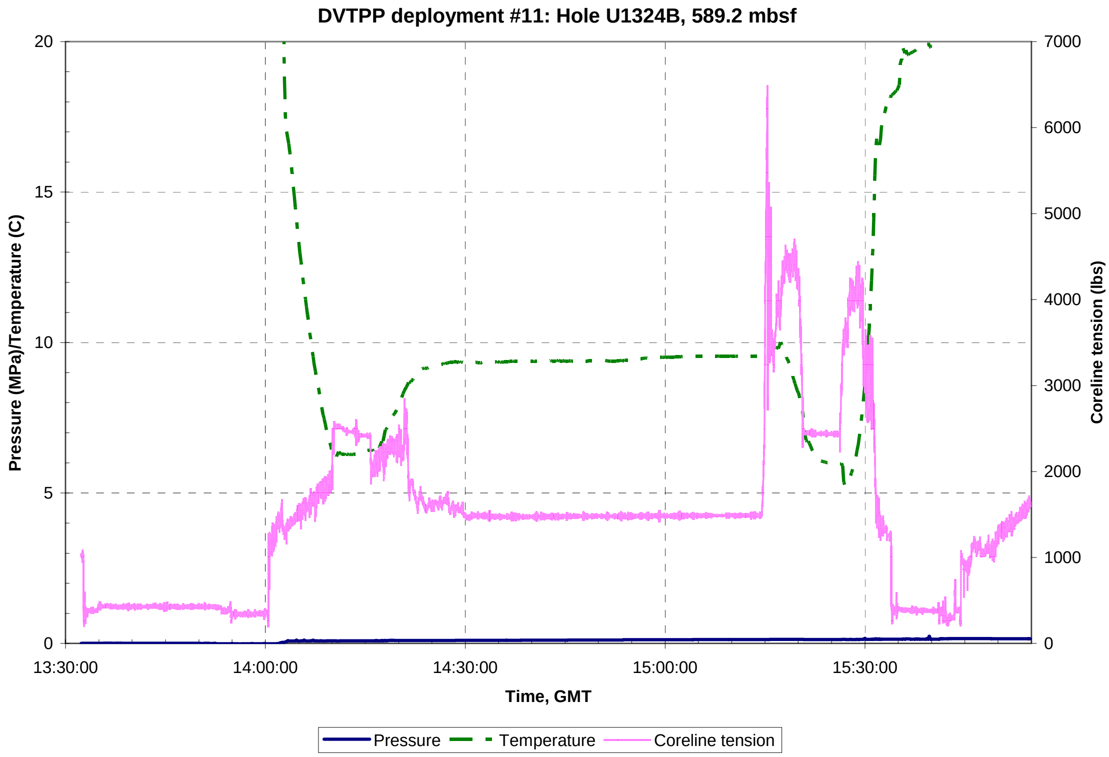

Figure A.A.10.e

Figure A.A.10.f

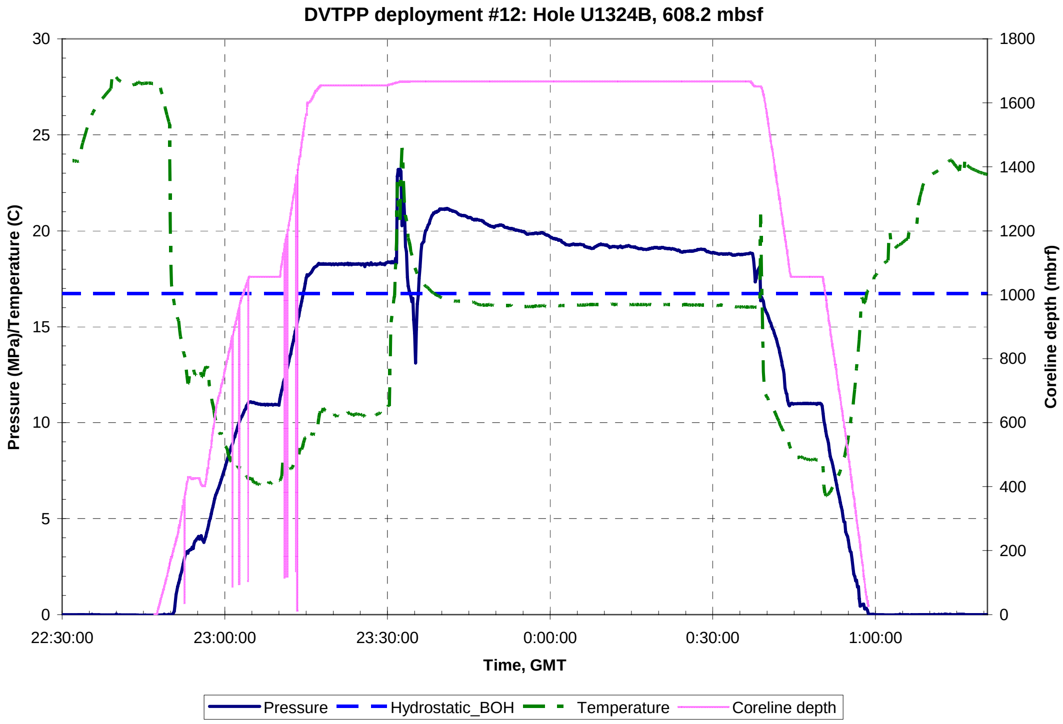

Figure A.A.11.a: Pressure, temperature and Truview data for DVTPP Deployment #12, Hole U1324B, 608.2 mbsf. GMT = Greenwich Mean Time, Hydrostatic_BOH is the hydrostatic pressure at the bottom of the hole.

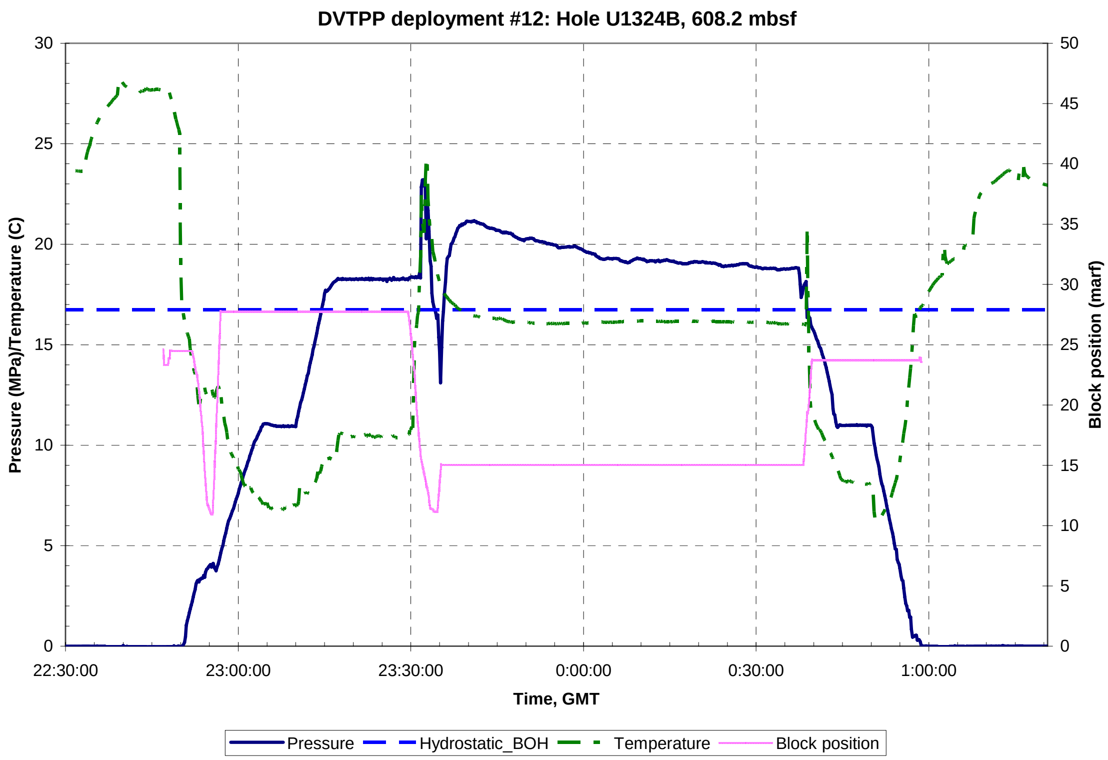

Figure A.A.11.b

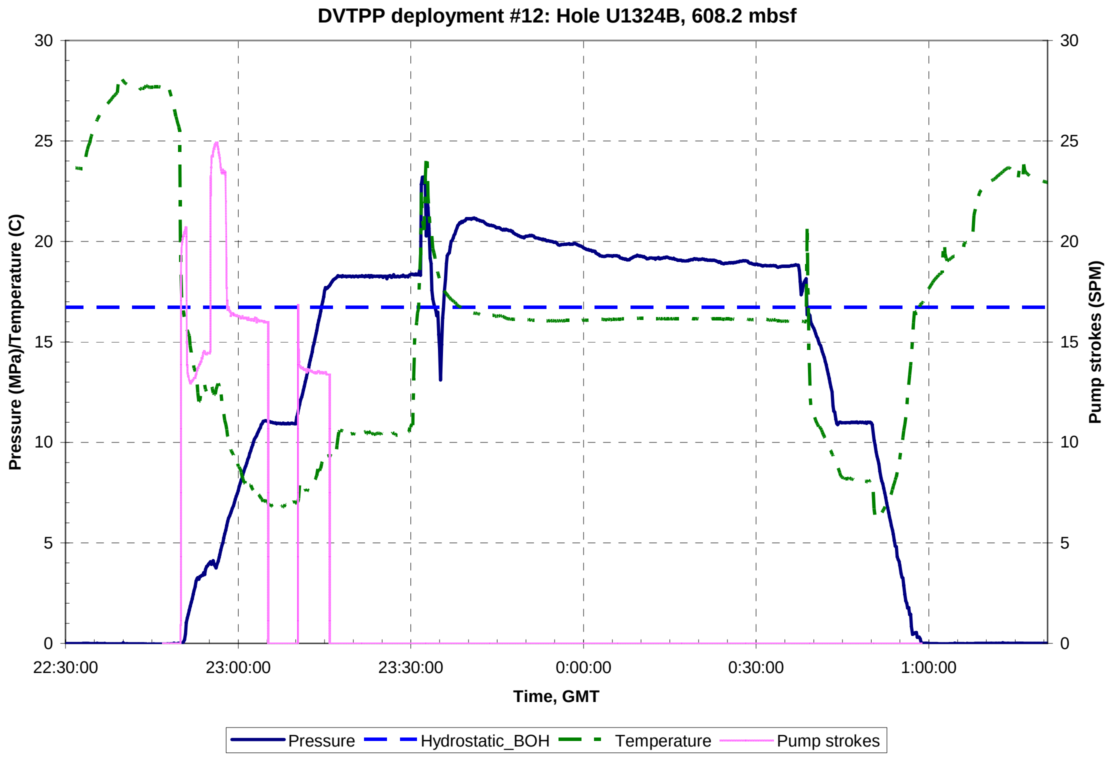

Figure A.A.11.c

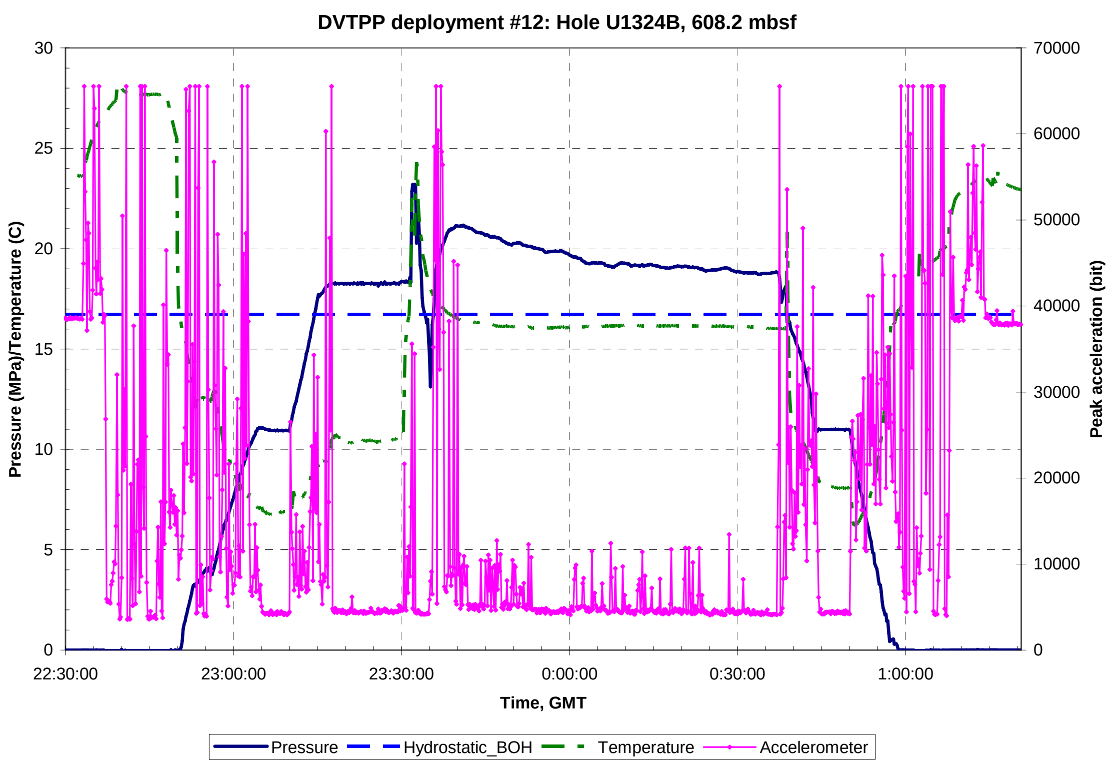

Figure A.A.11.d

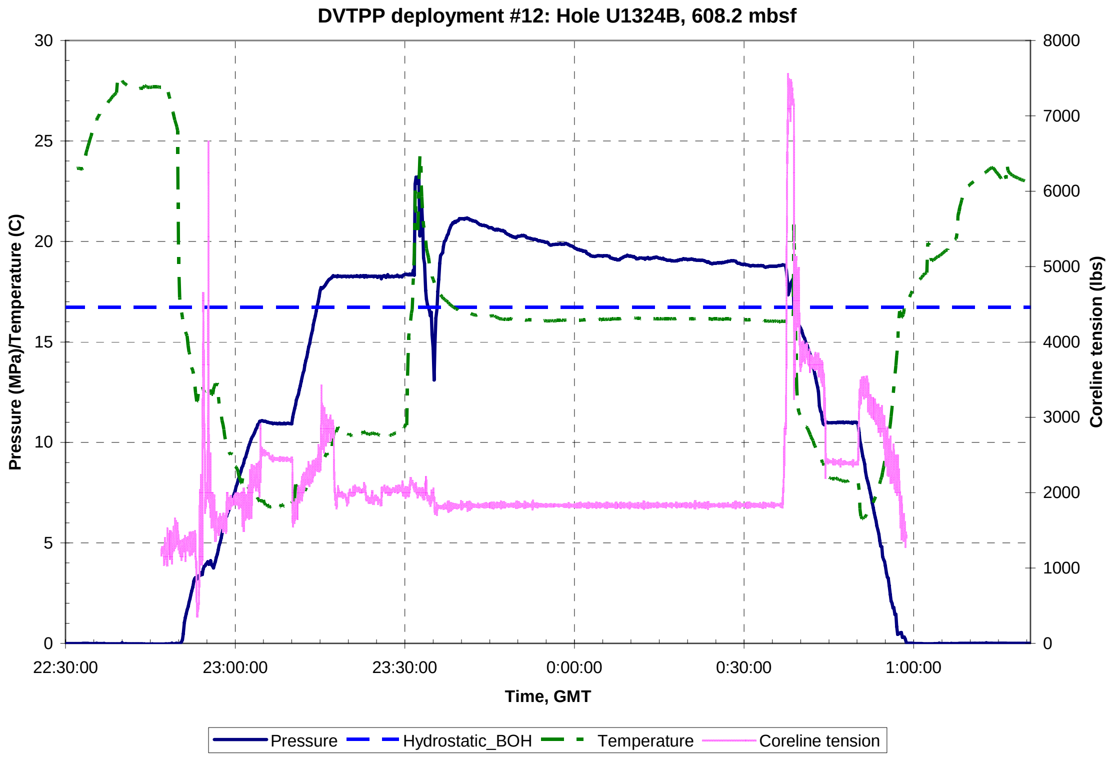

Figure A.A.11.e

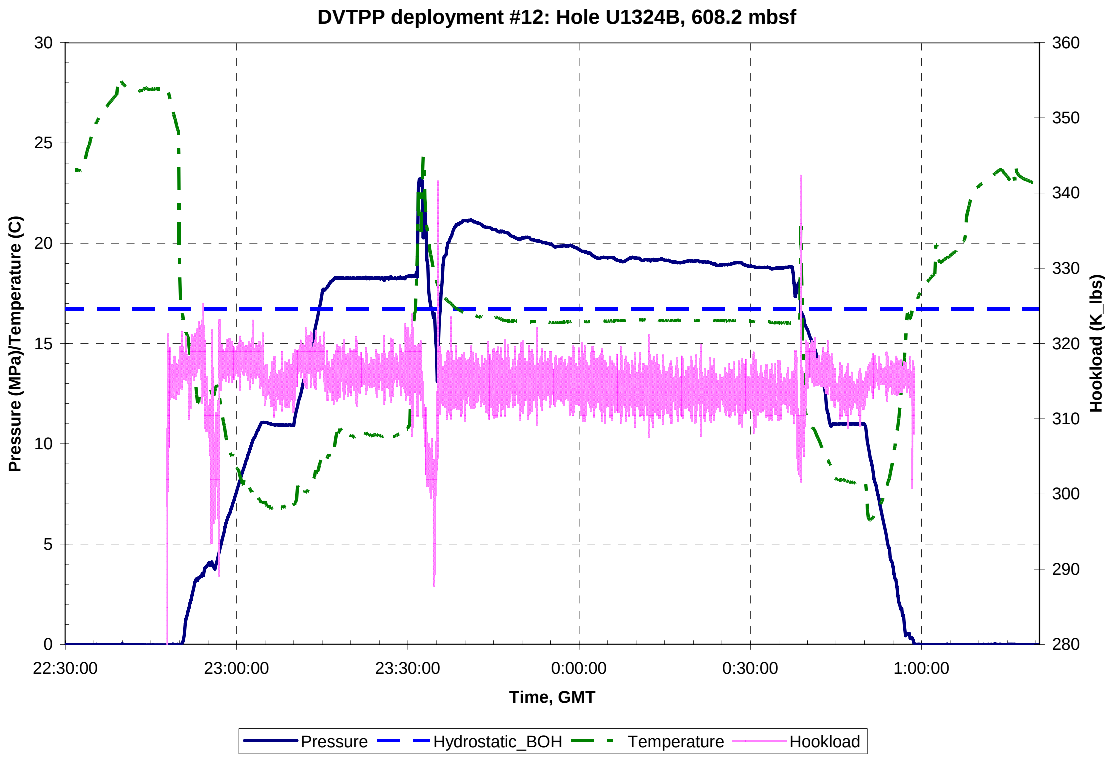

Figure A.A.11.f

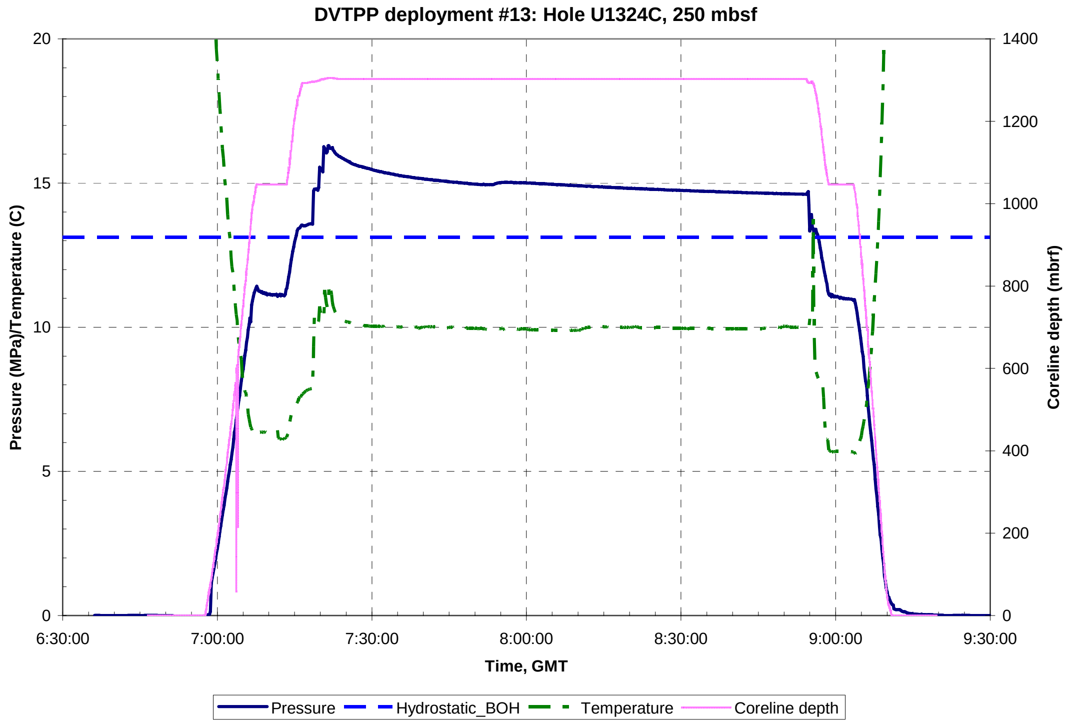

Figure A.A.12.a: Pressure, temperature and Truview data for DVTPP Deployment #13, Hole U1324C, 250 mbsf. GMT = Greenwich Mean Time, Hydrostatic_BOH is the hydrostatic pressure at the bottom of the hole.

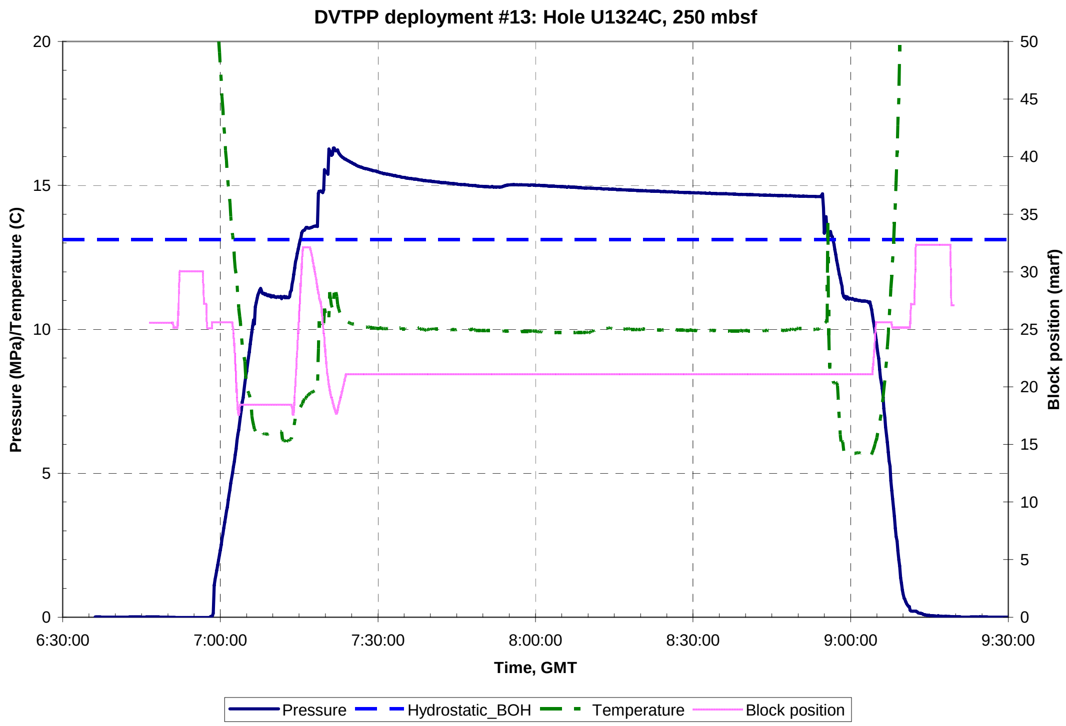

Figure A.A.12.b

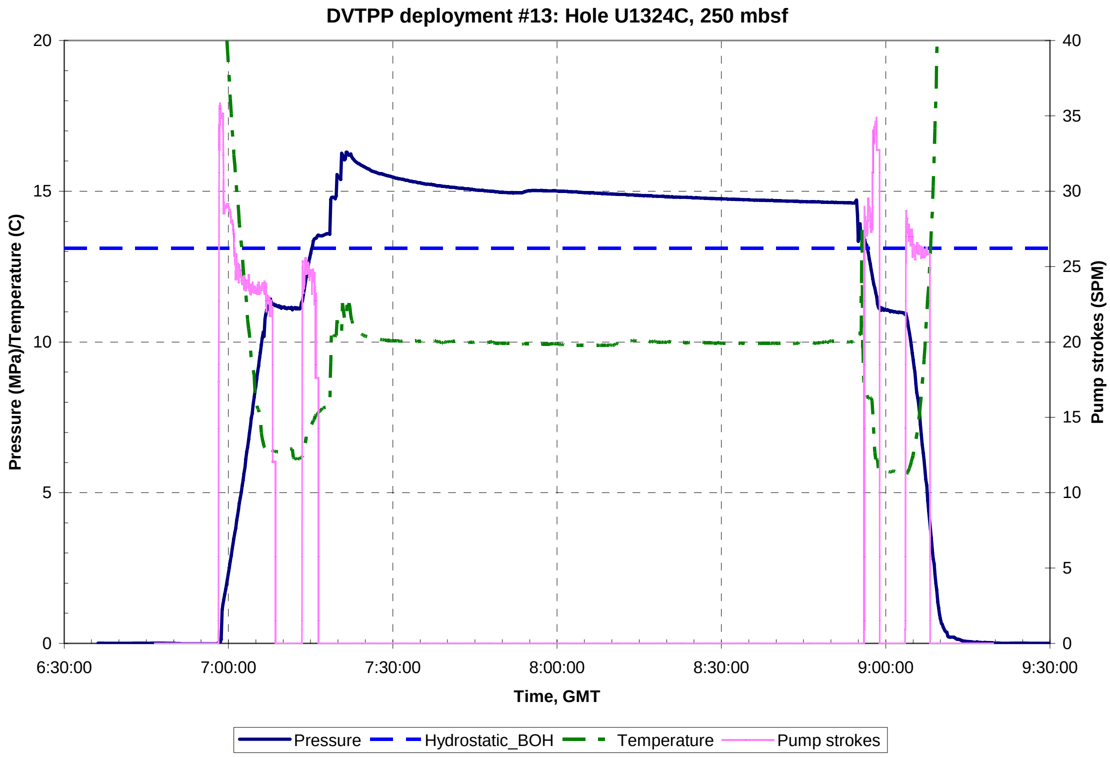

Figure A.A.12.c

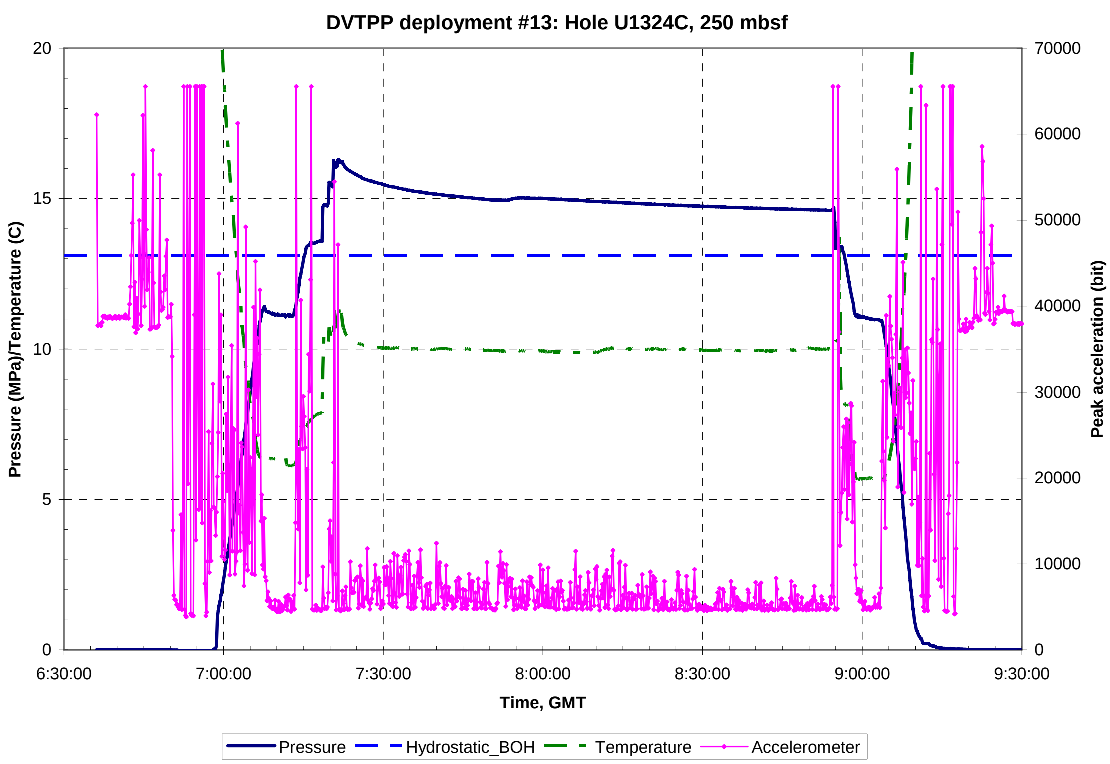

Figure A.A.12.d

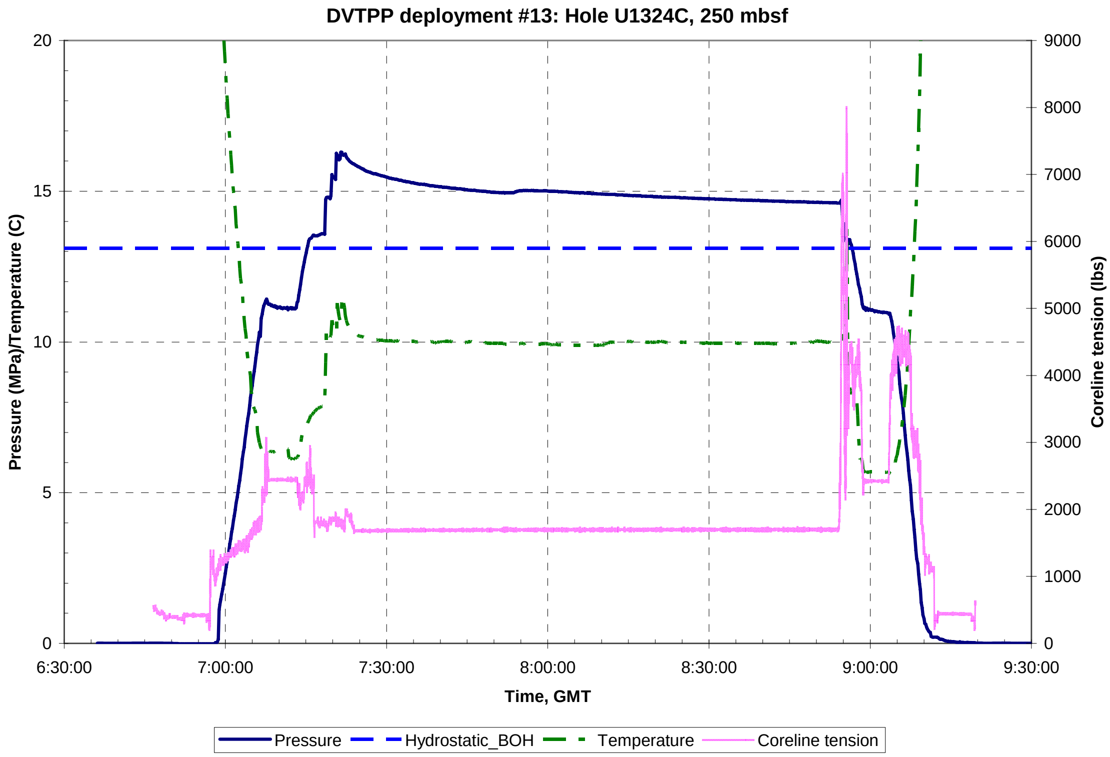

Figure A.A.12.e

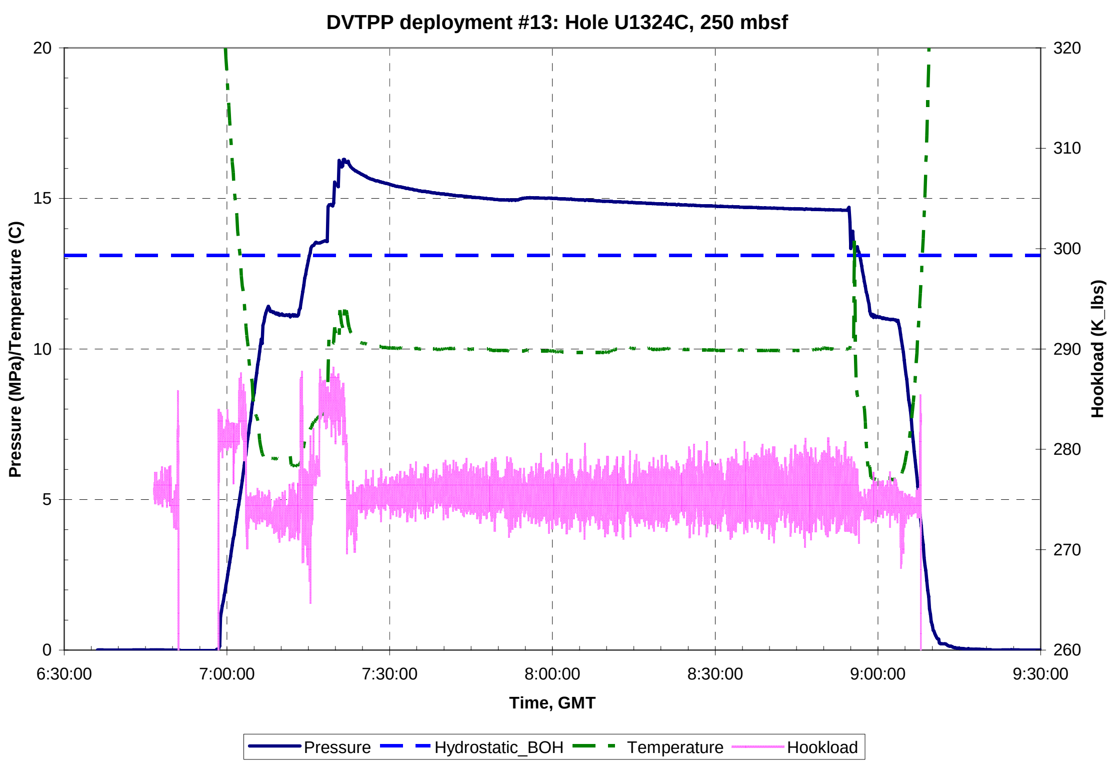

Figure A.A.12.f

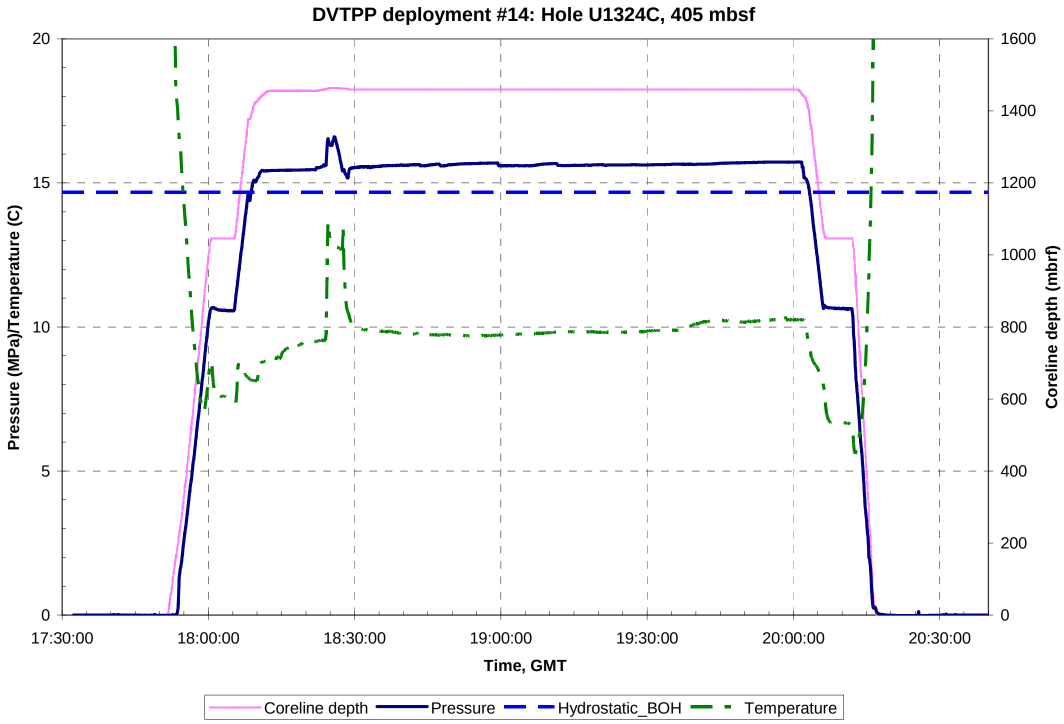

Figure A.A.13.a: Pressure, temperature and Truview data for DVTPP Deployment #14, Hole U1324C, 405 mbsf. GMT = Greenwich Mean Time, Hydrostatic_BOH is the hydrostatic pressure at the bottom of the hole.

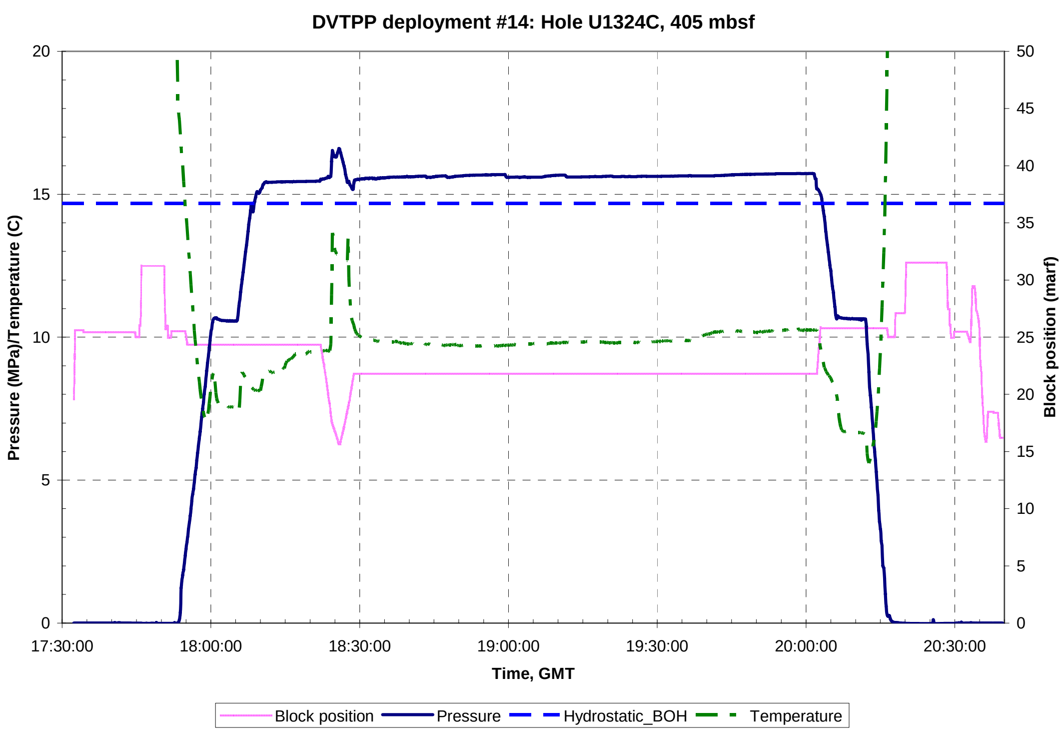

Figure A.A.13.b

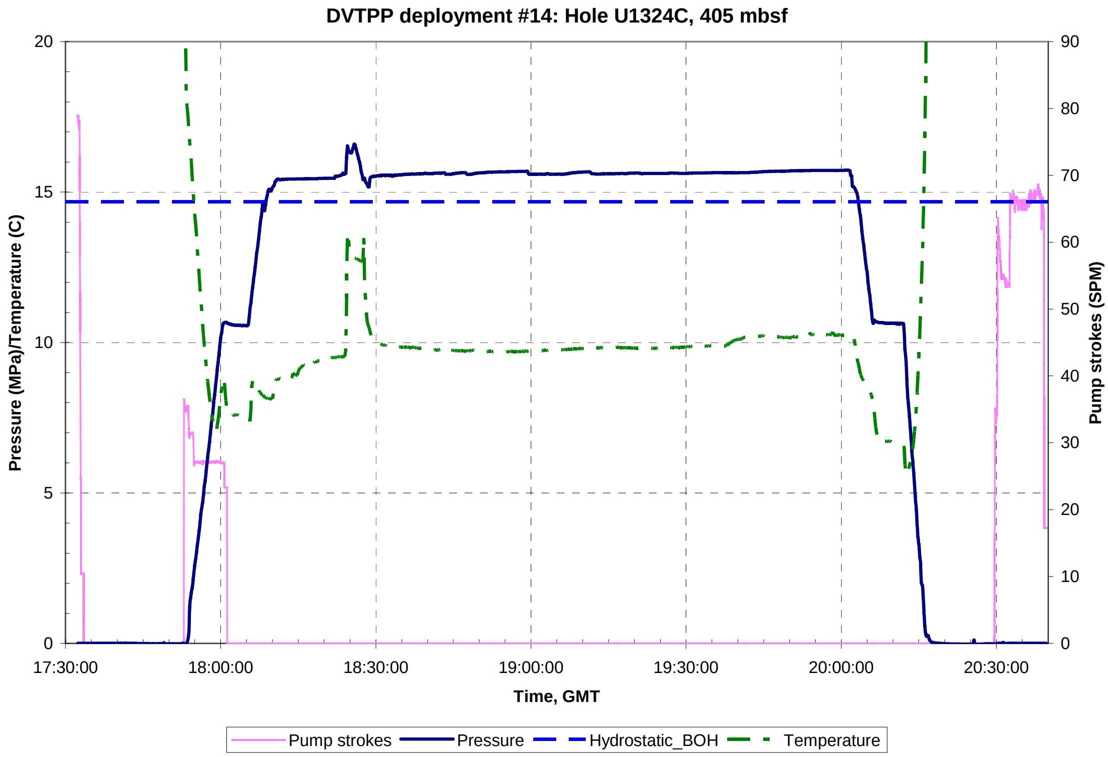

Figure A.A.13.c

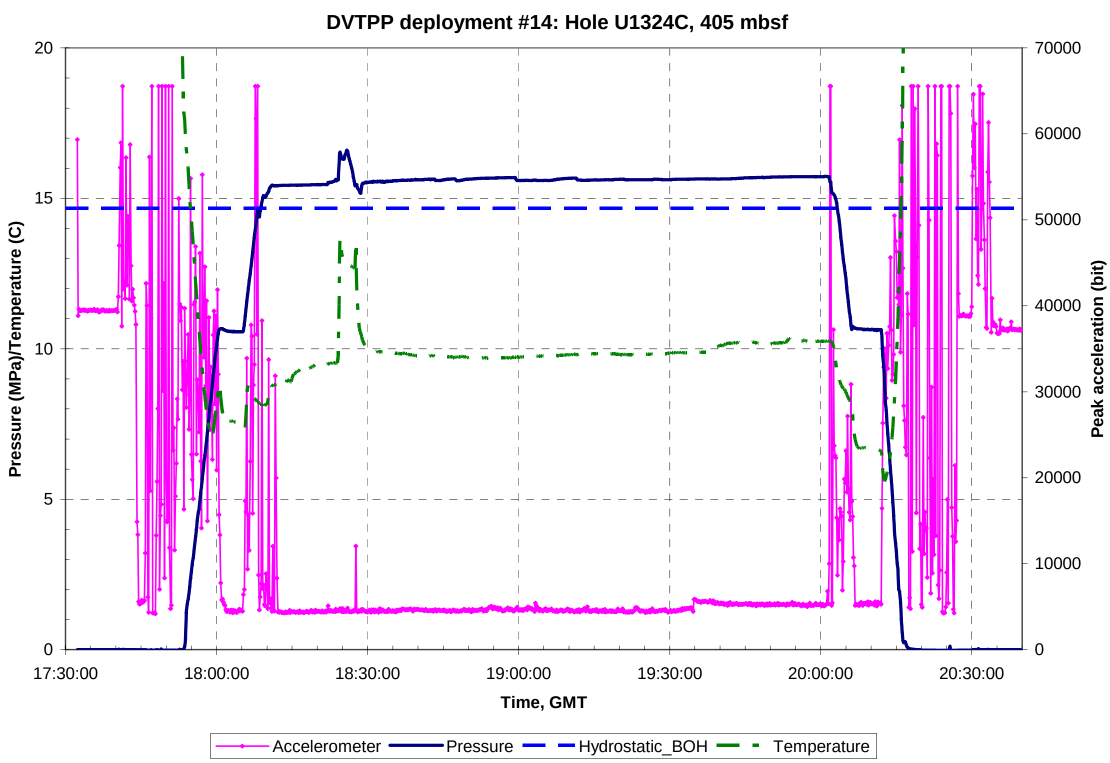

Figure A.A.13.d

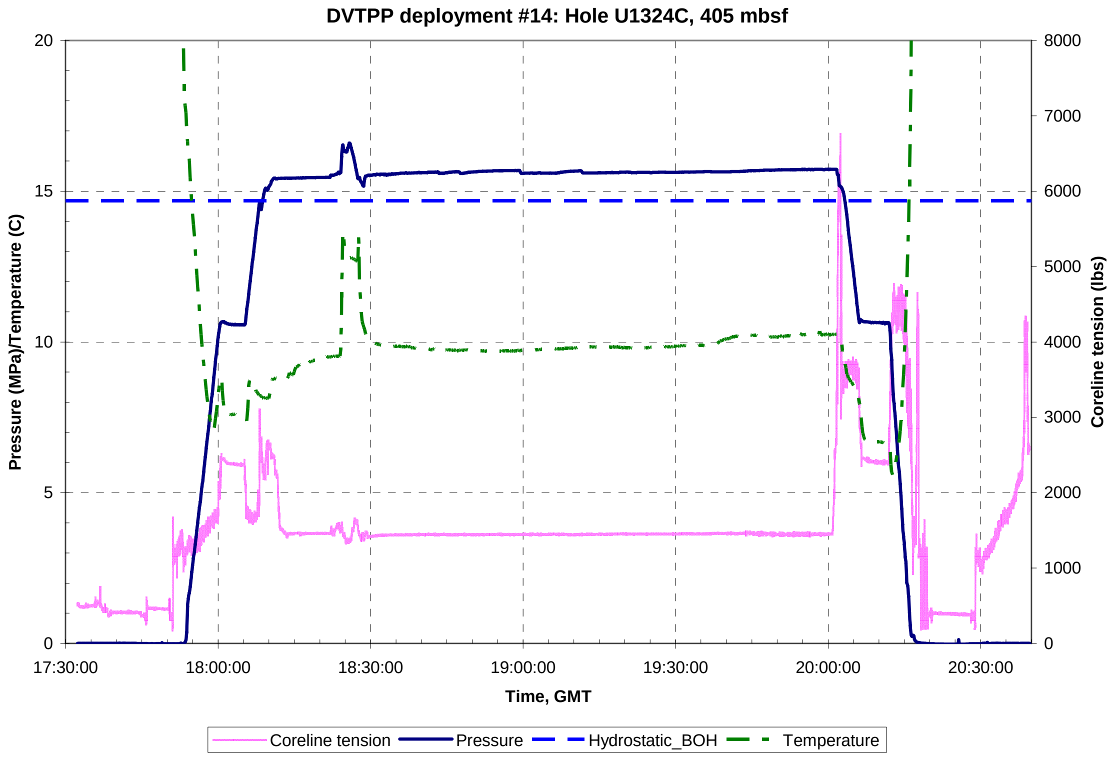

Figure A.A.13.e

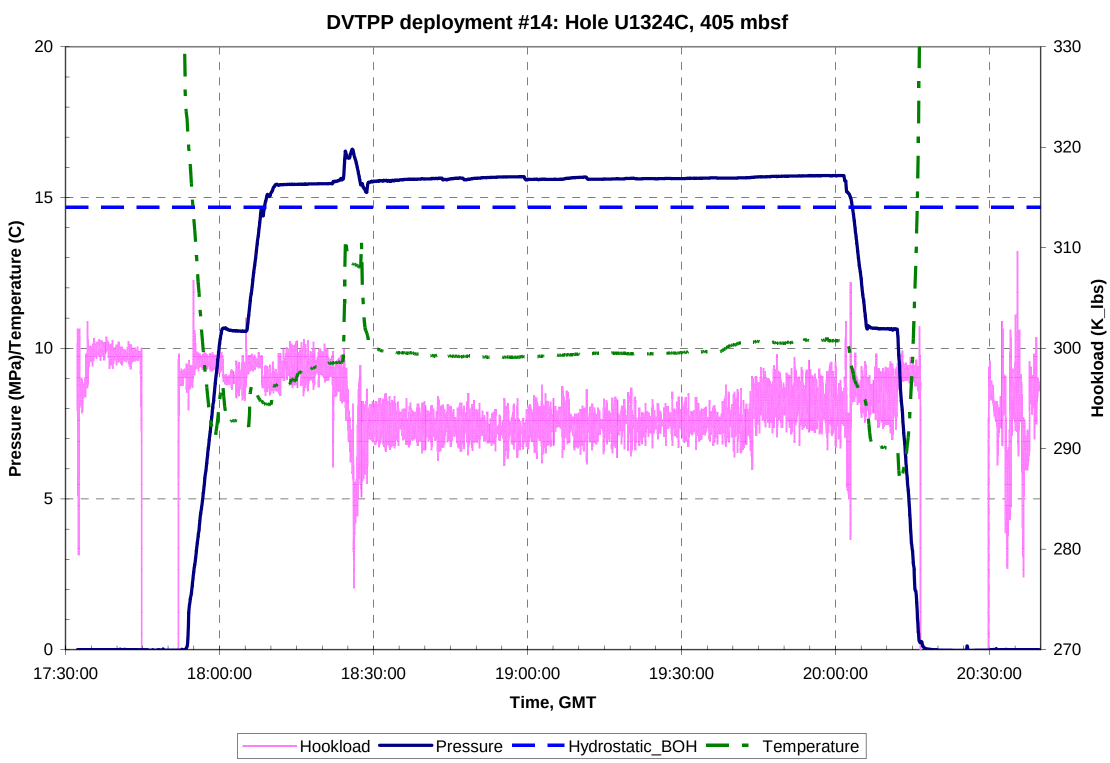

Figure A.A.13.f

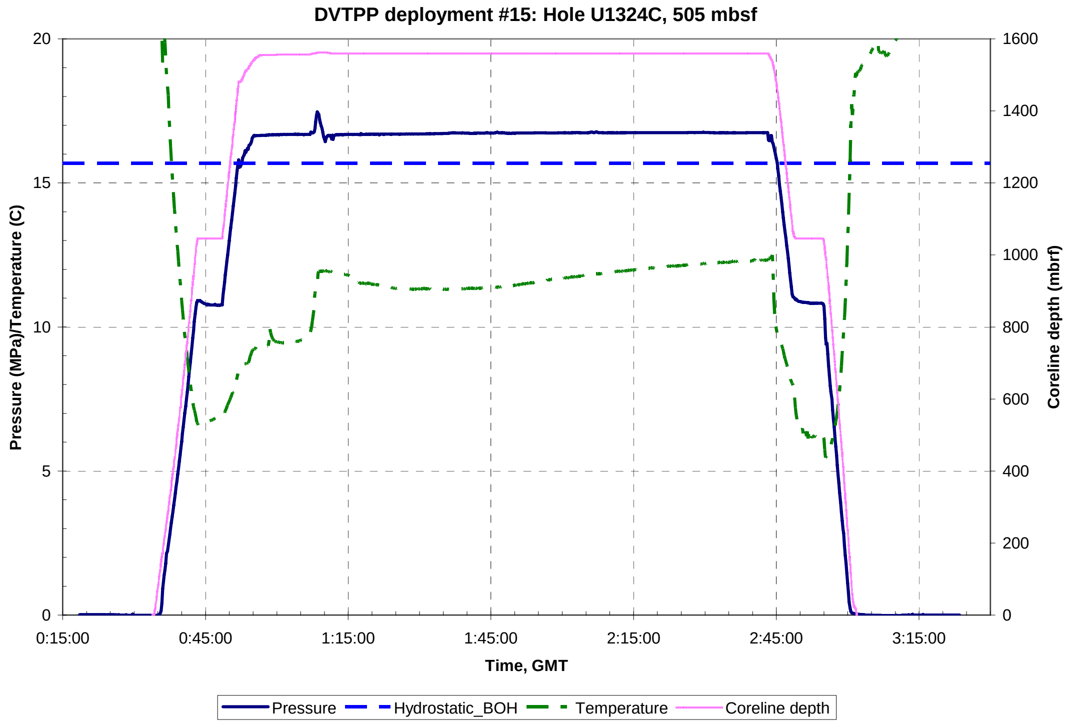

Figure A.A.14.a: Pressure, temperature and Truview data for DVTPP Deployment #15, Hole U1324C, 505 mbsf. GMT = Greenwich Mean Time, Hydrostatic_BOH is the hydrostatic pressure at the bottom of the hole.

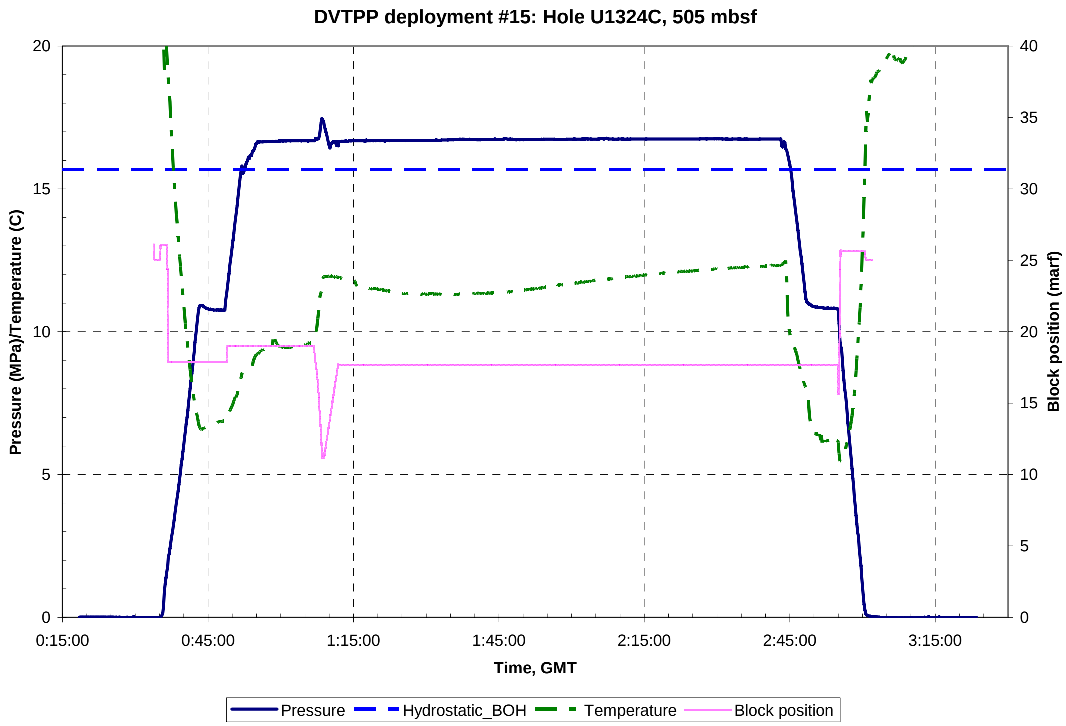

Figure A.A.14.b

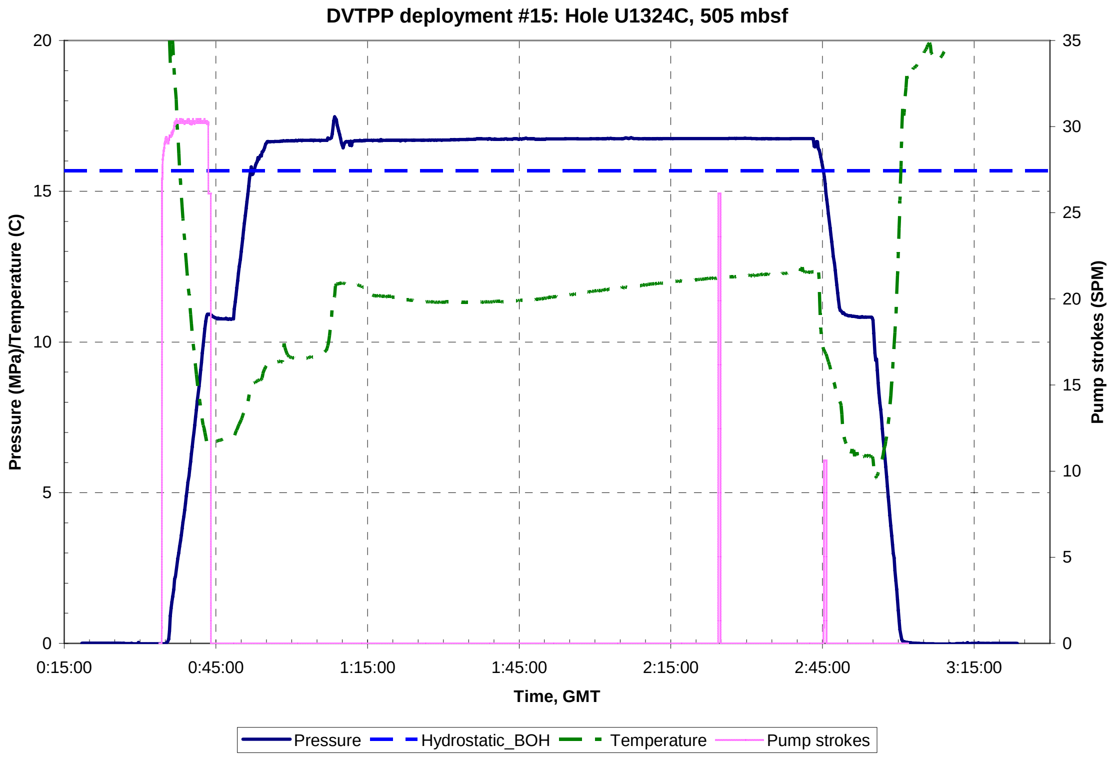

Figure A.A.14.c

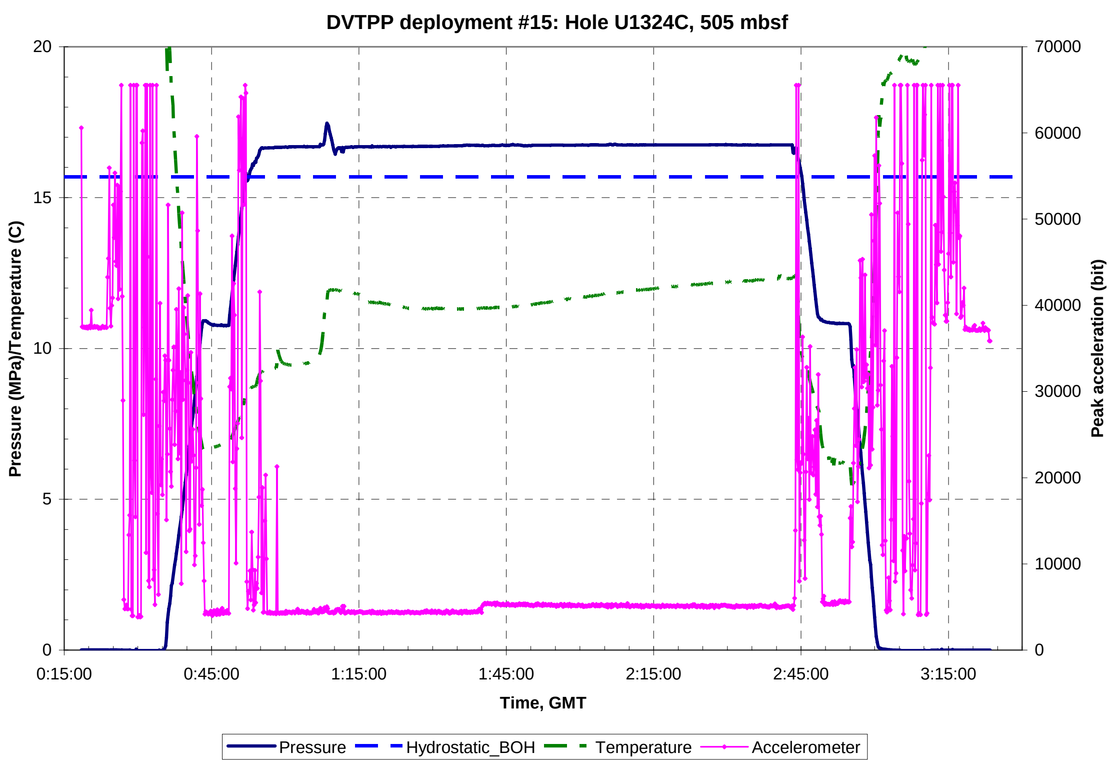

Figure A.A.14.d

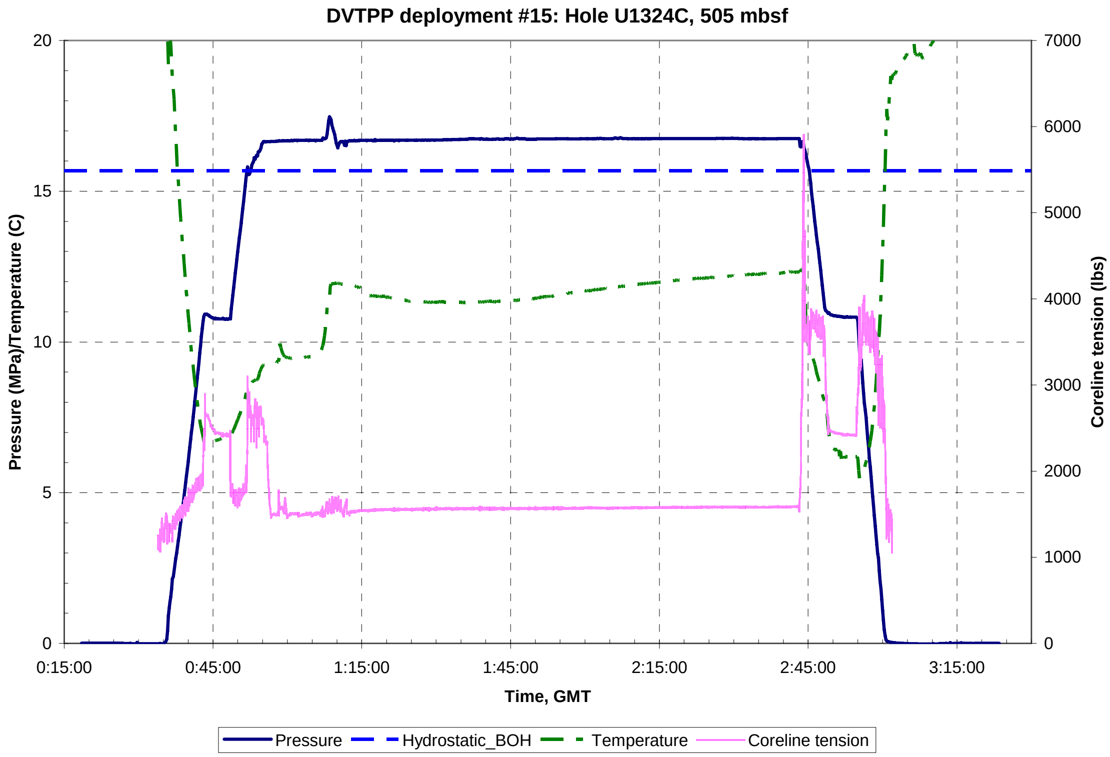

Figure A.A.14.e

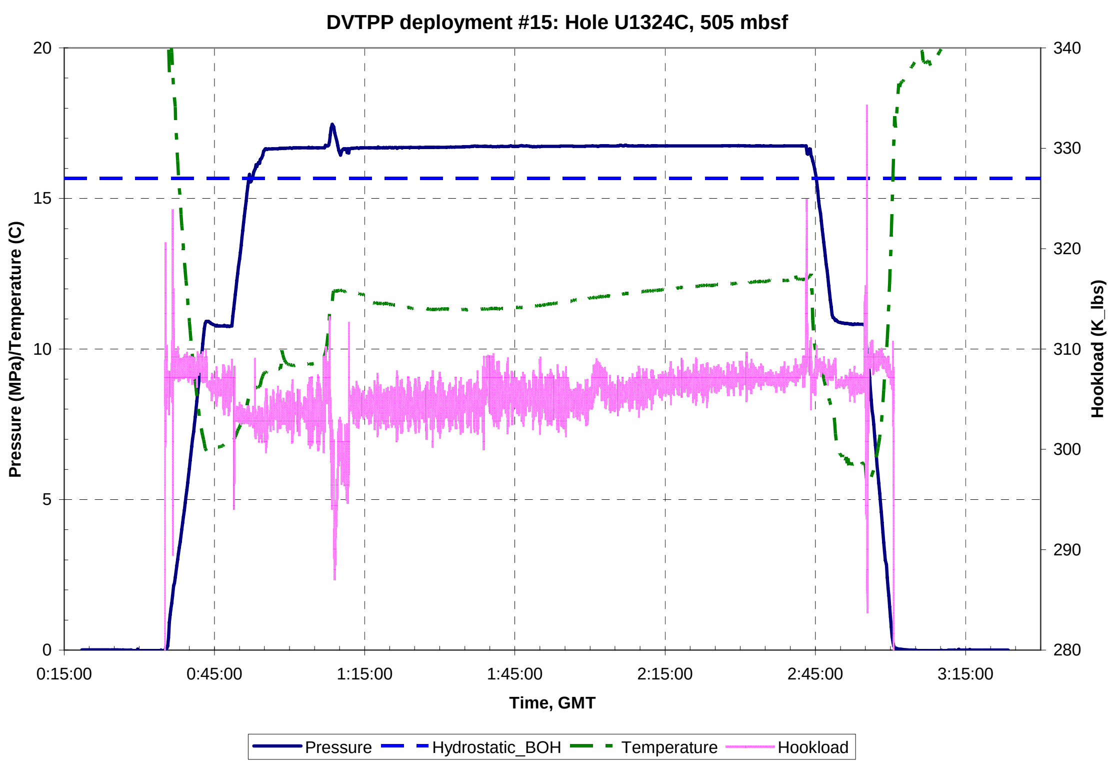

Figure A.A.14.f

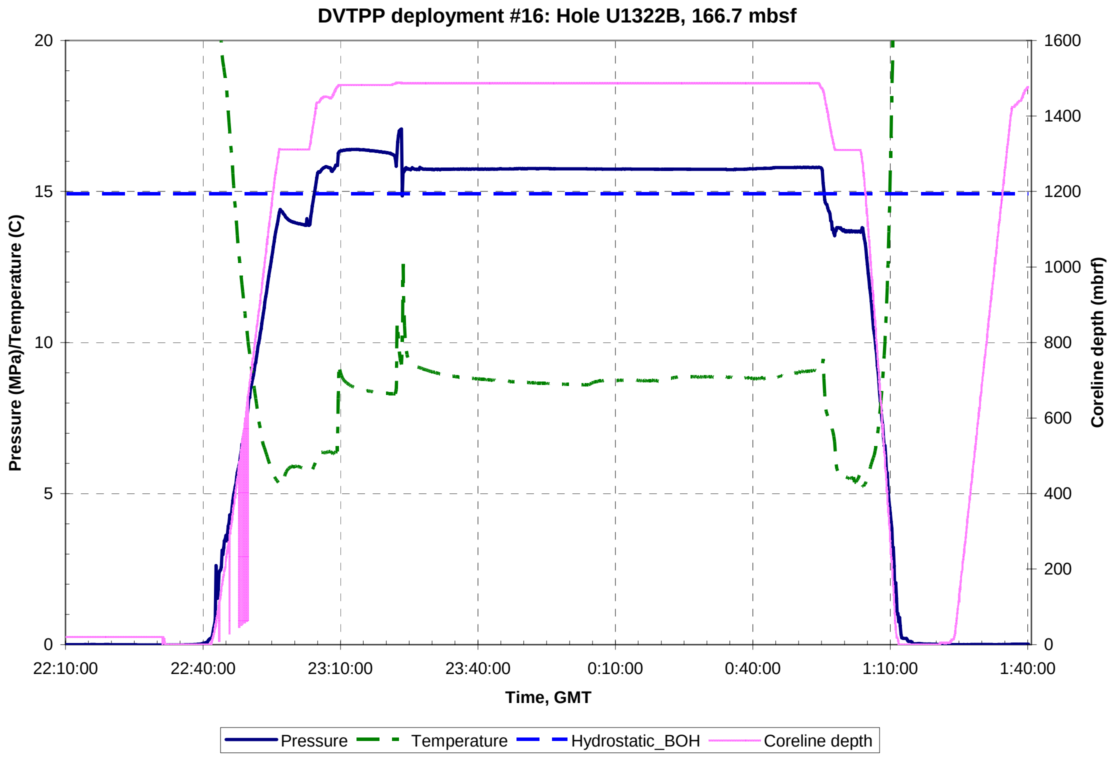

Figure A.A.15.a: Pressure, temperature and Truview data for DVTPP Deployment #16, Hole U1322B, 166.7 mbsf. GMT = Greenwich Mean Time, Hydrostatic_BOH is the hydrostatic pressure at the bottom of the hole.

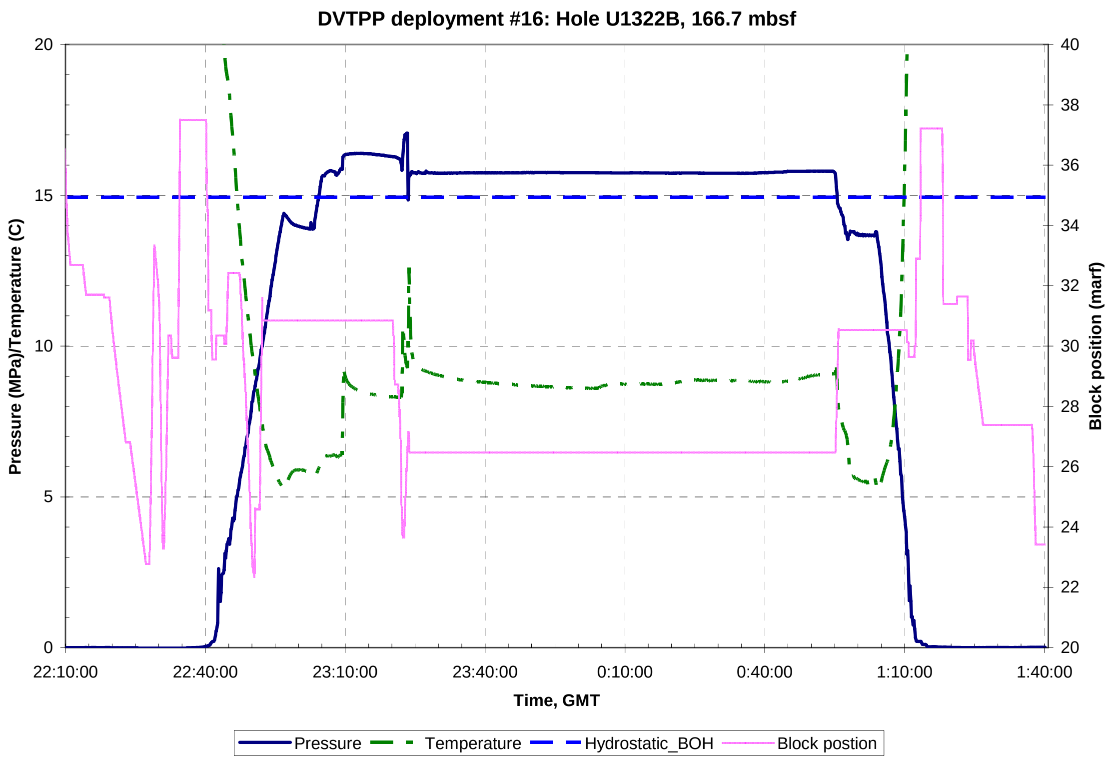

Figure A.A.15.b

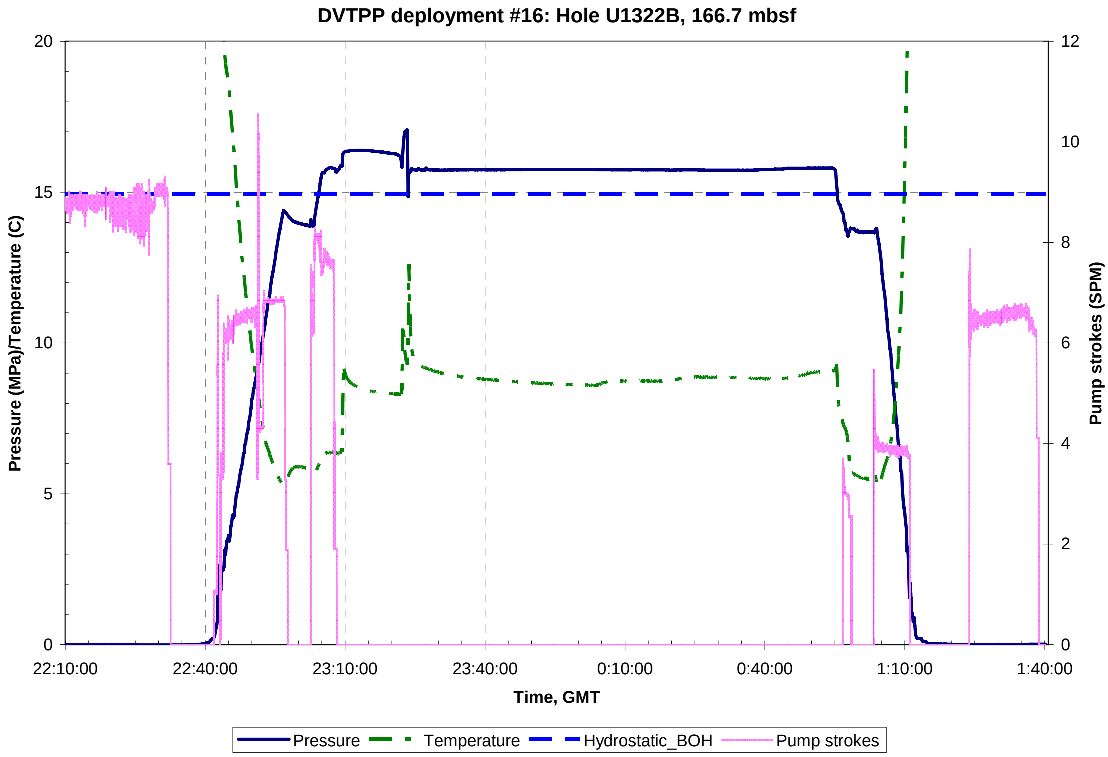

Figure A.A.15.c

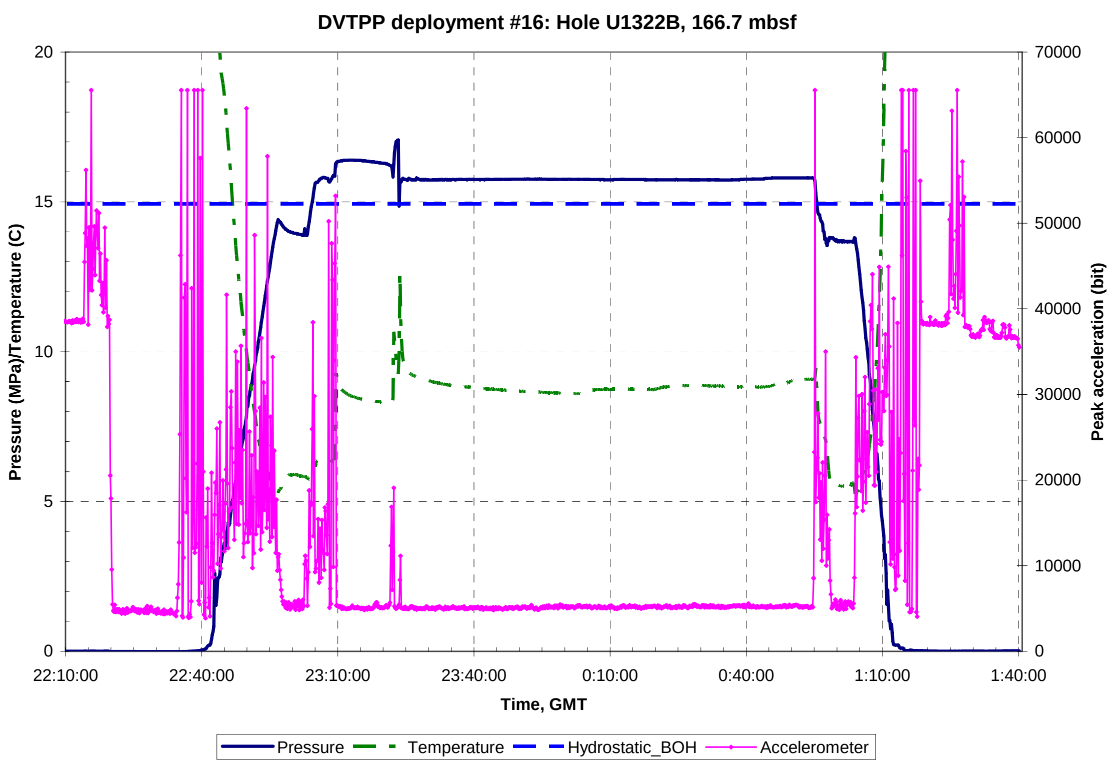

Figure A.A.15.d

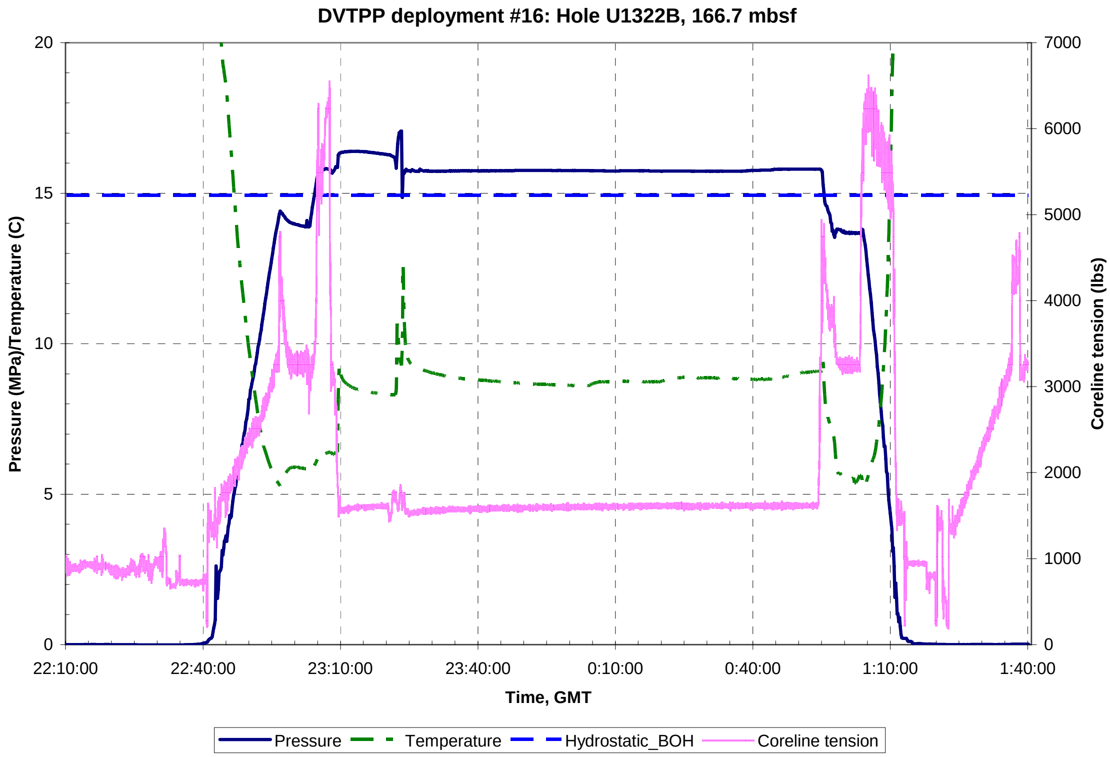

Figure A.A.15.e

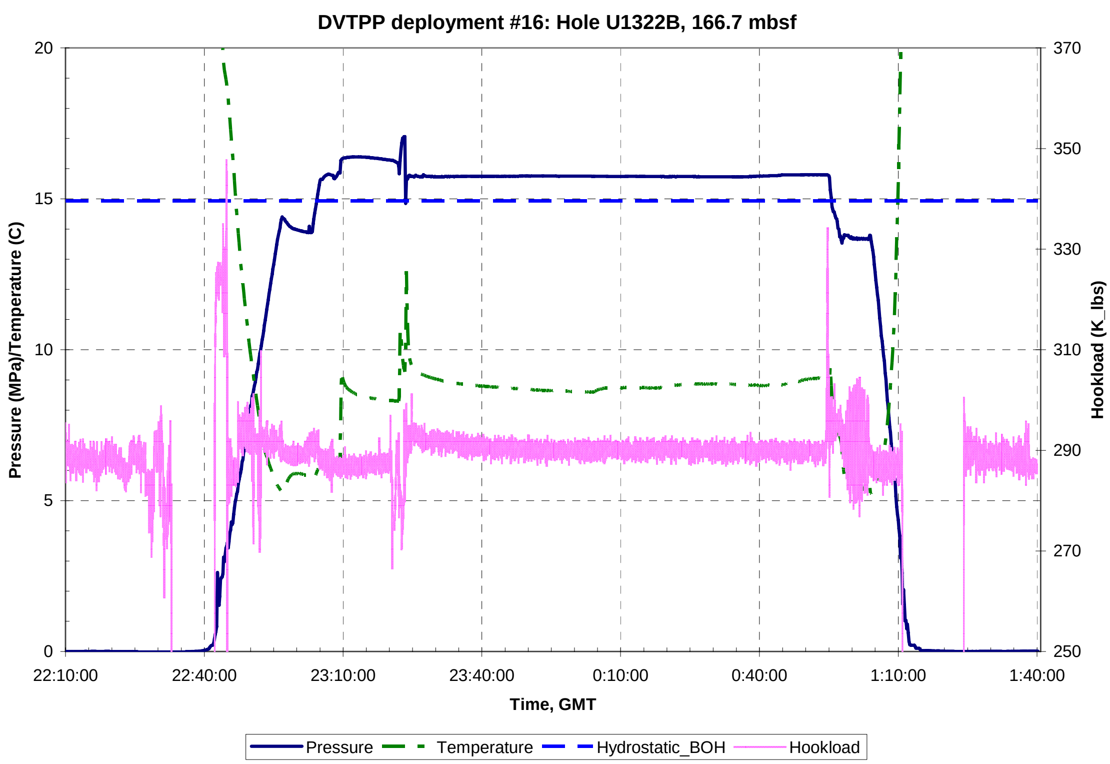

Figure A.A.15.f

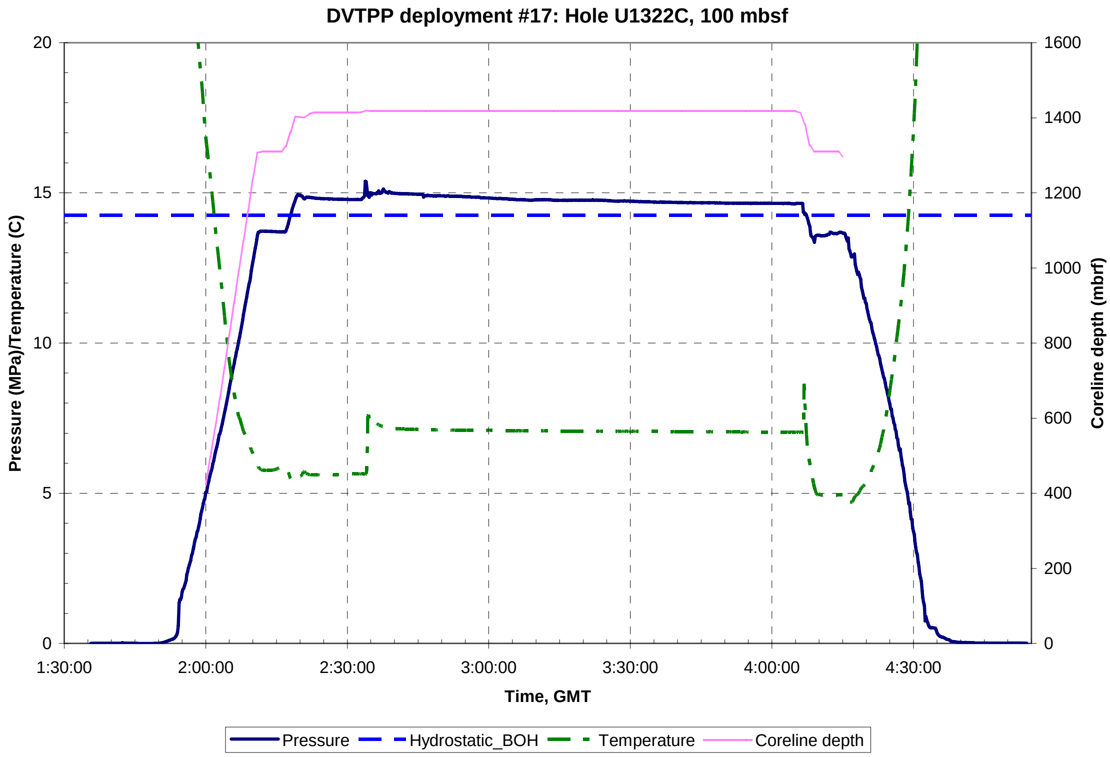

Figure A.A.16.a: Pressure, temperature and Truview data for DVTPP Deployment #17, Hole U1322C, 100 mbsf. GMT = Greenwich Mean Time, Hydrostatic_BOH is the hydrostatic pressure at the bottom of the hole.

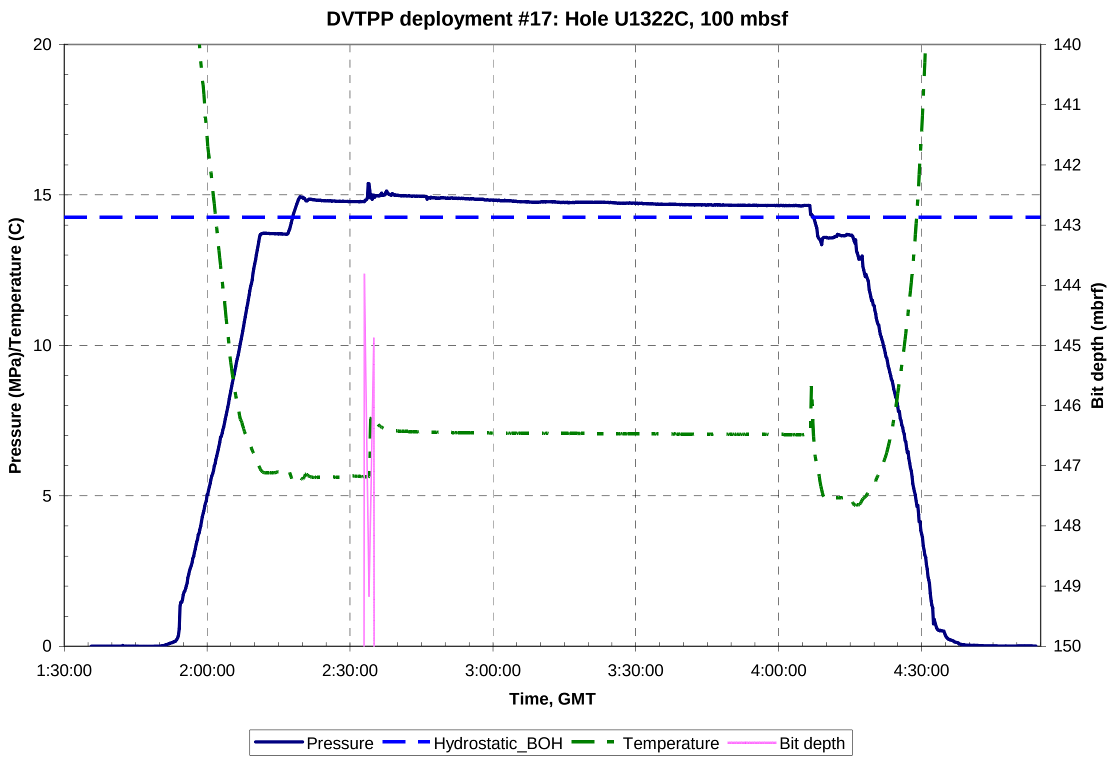

Figure A.A.16.b

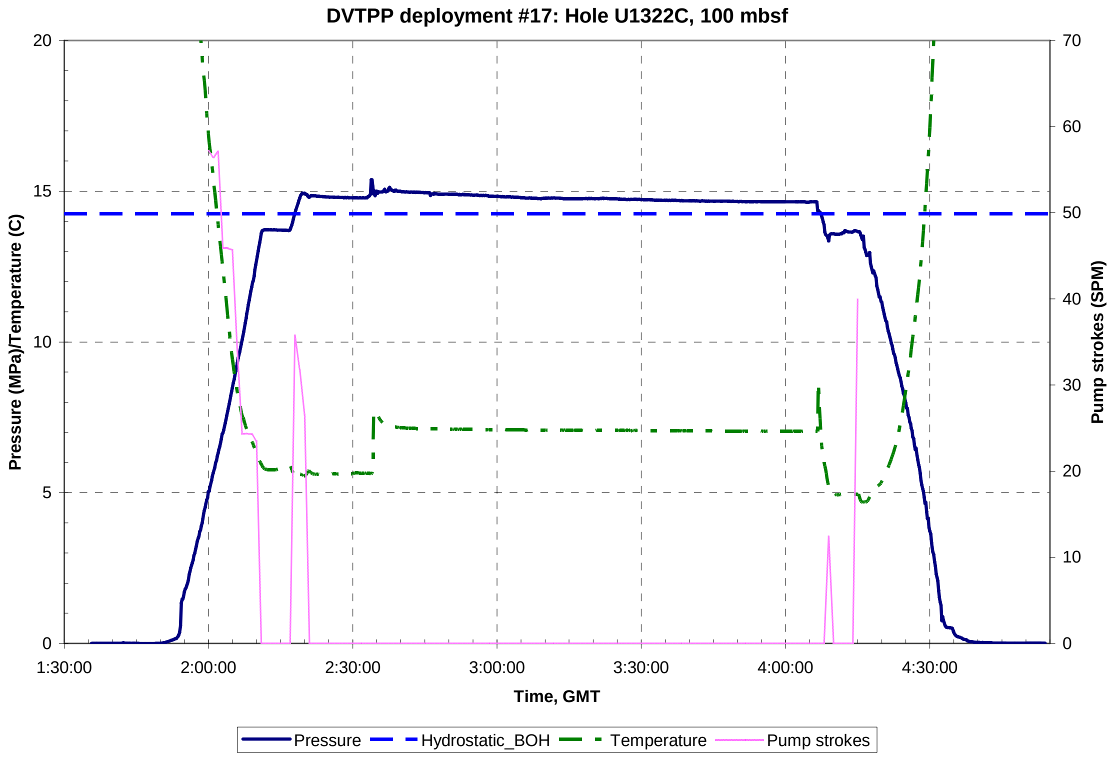

Figure A.A.16.c

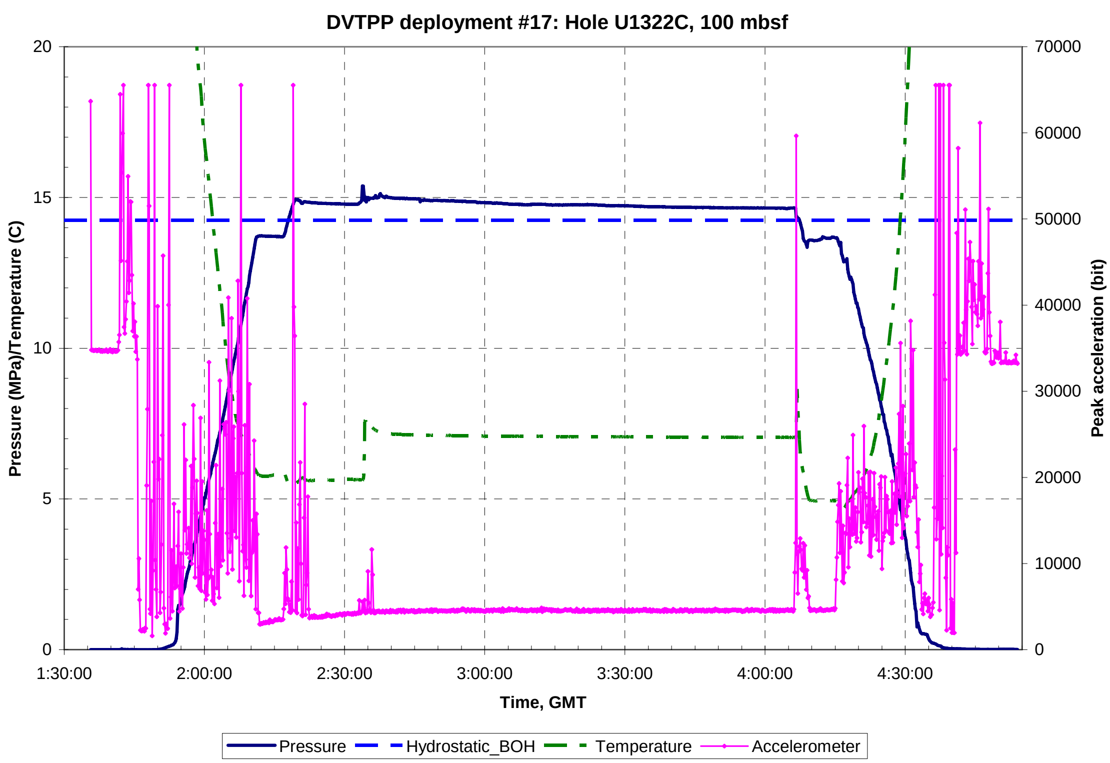

Figure A.A.16.d

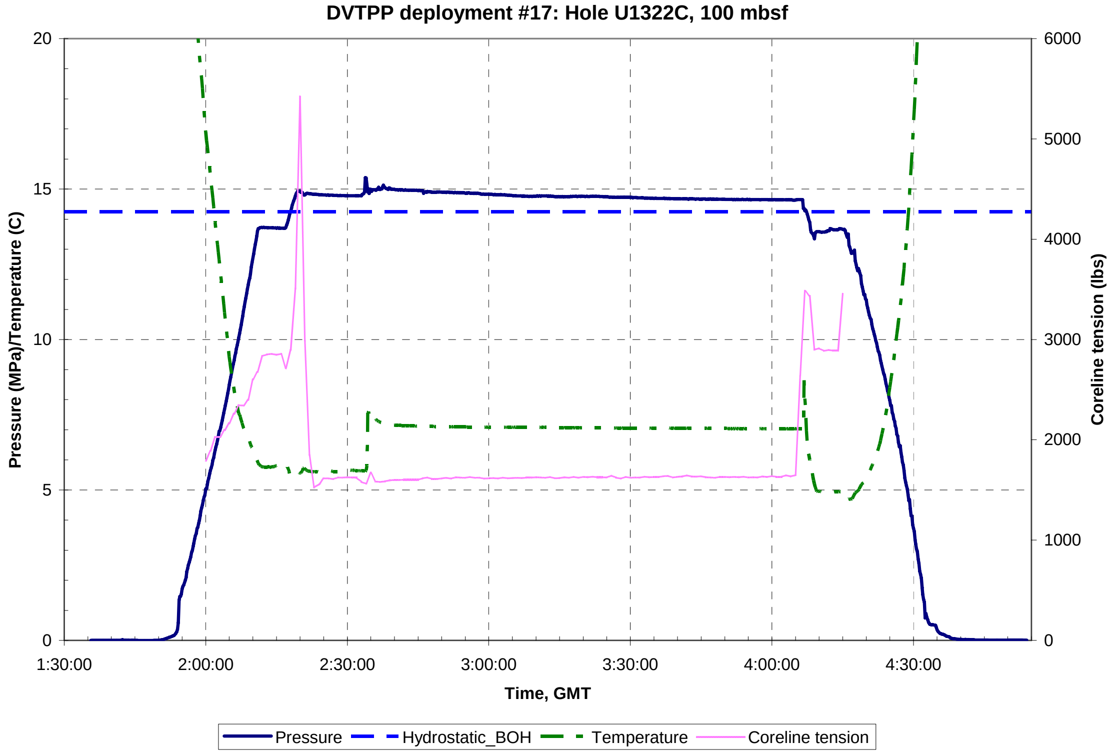

Figure A.A.16.e

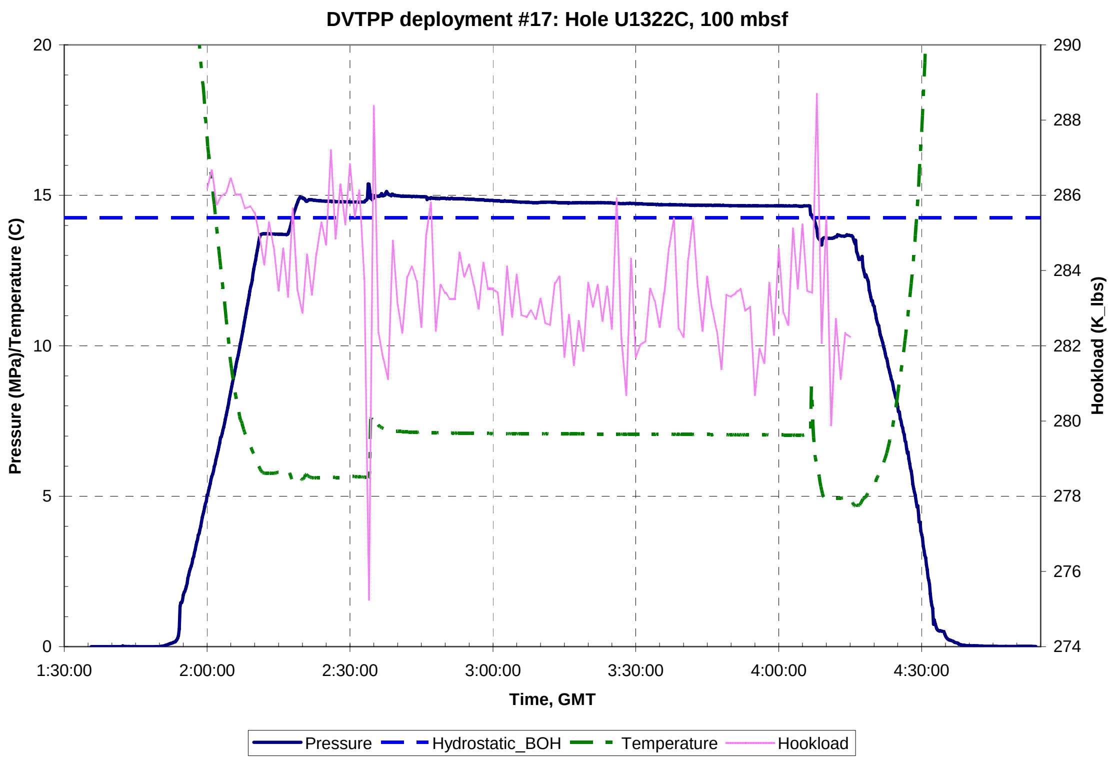

Figure A.A.16f

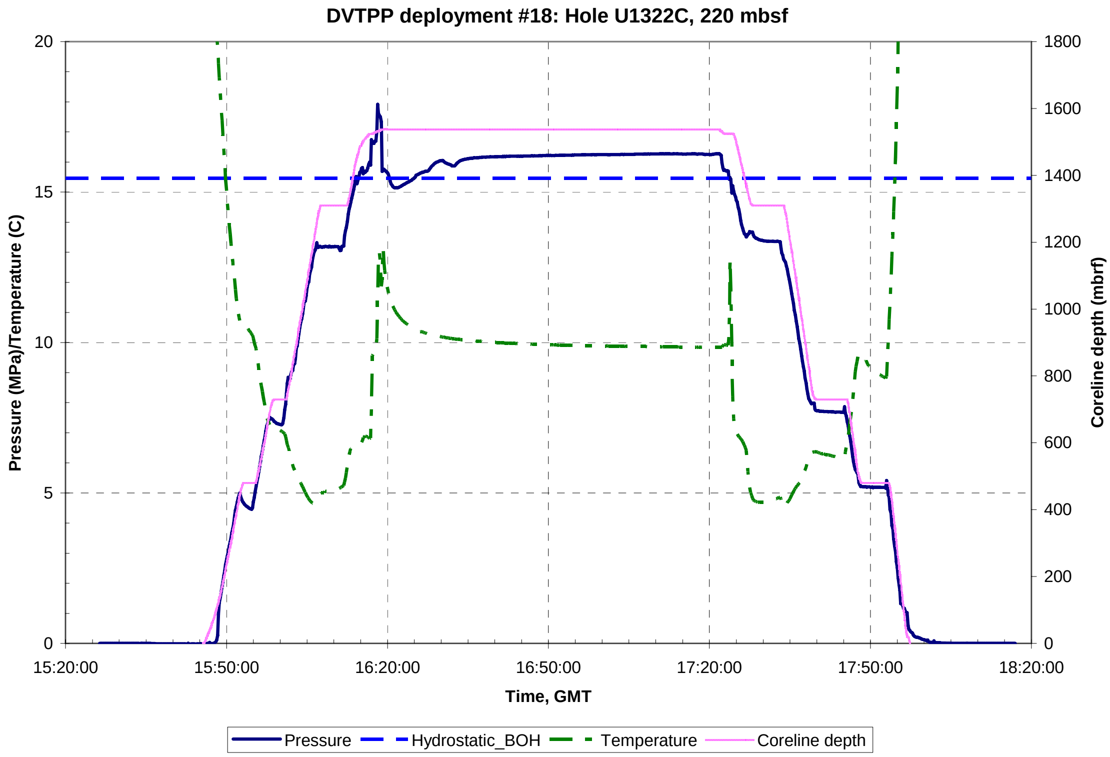

Figure A.A.17.a: Pressure, temperature and Truview data for DVTPP Deployment #18, Hole U1322C, 220 mbsf. GMT = Greenwich Mean Time, Hydrostatic_BOH is the hydrostatic pressure at the bottom of the hole.

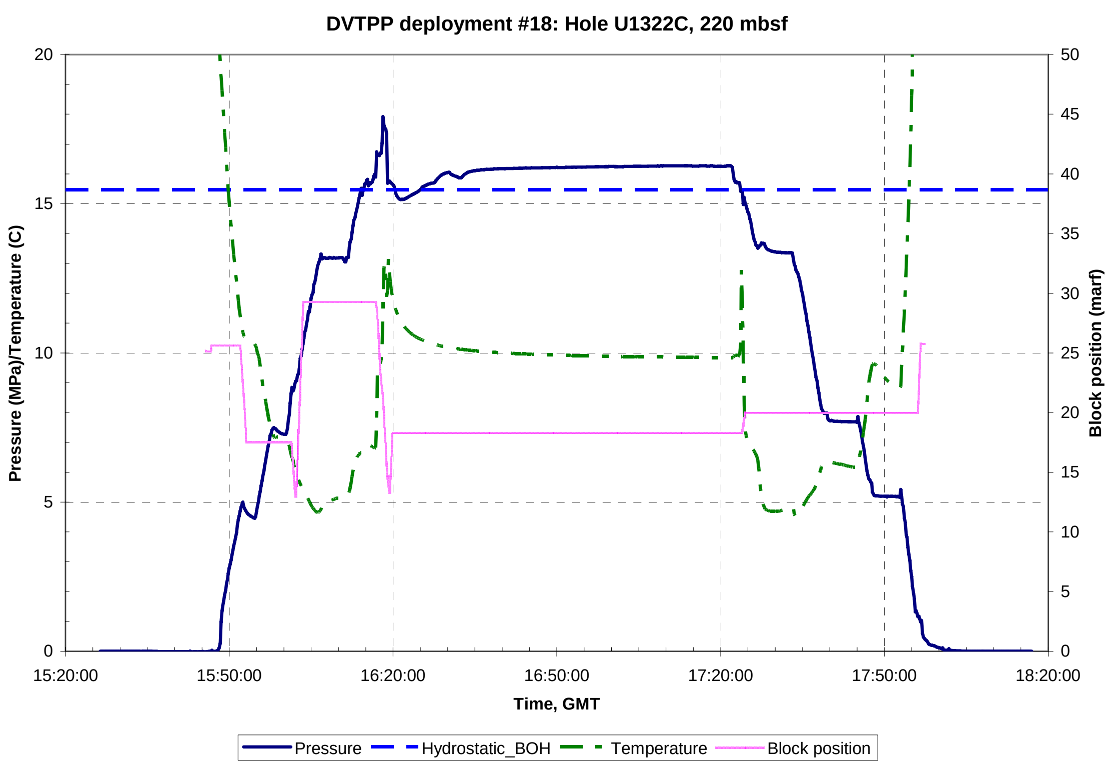

Figure A.A.17.b

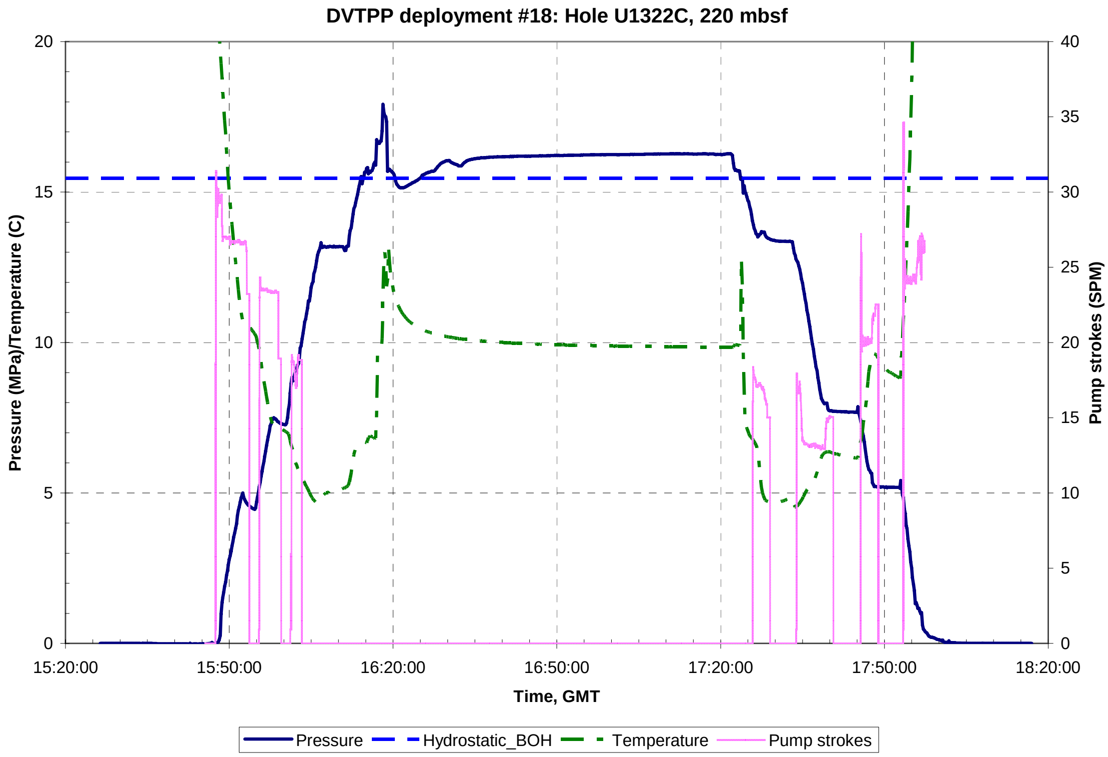

Figure A.A.17.c

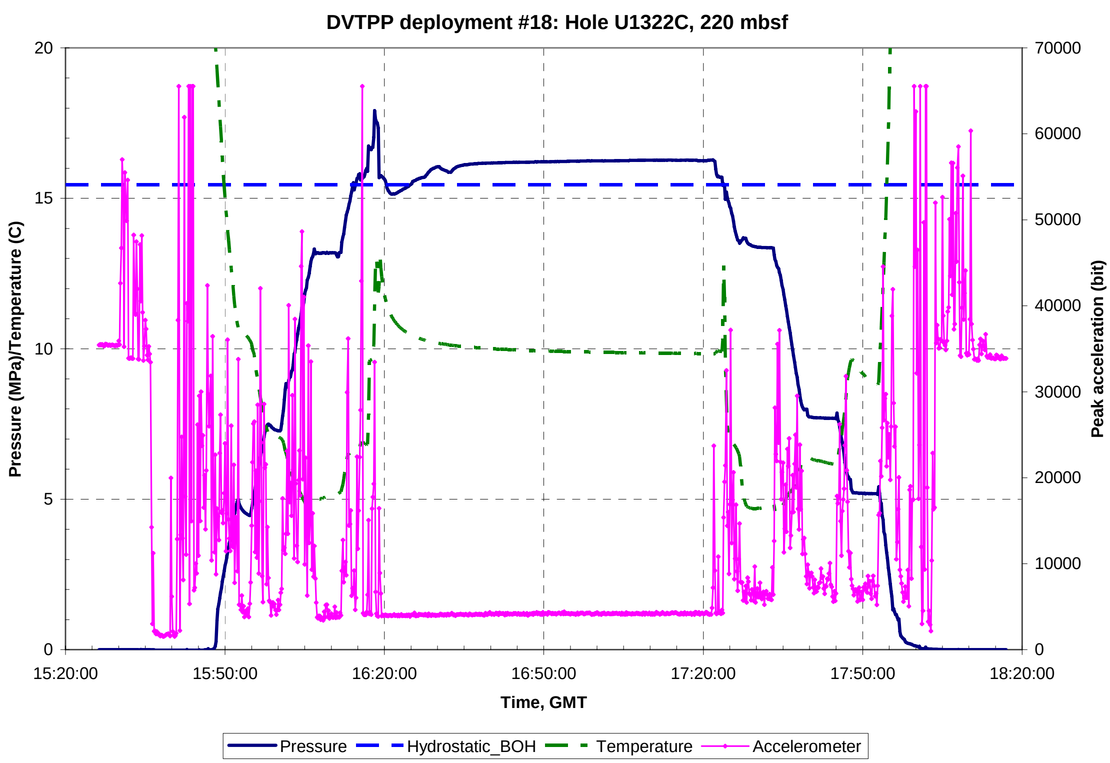

Figure A.A.17.d

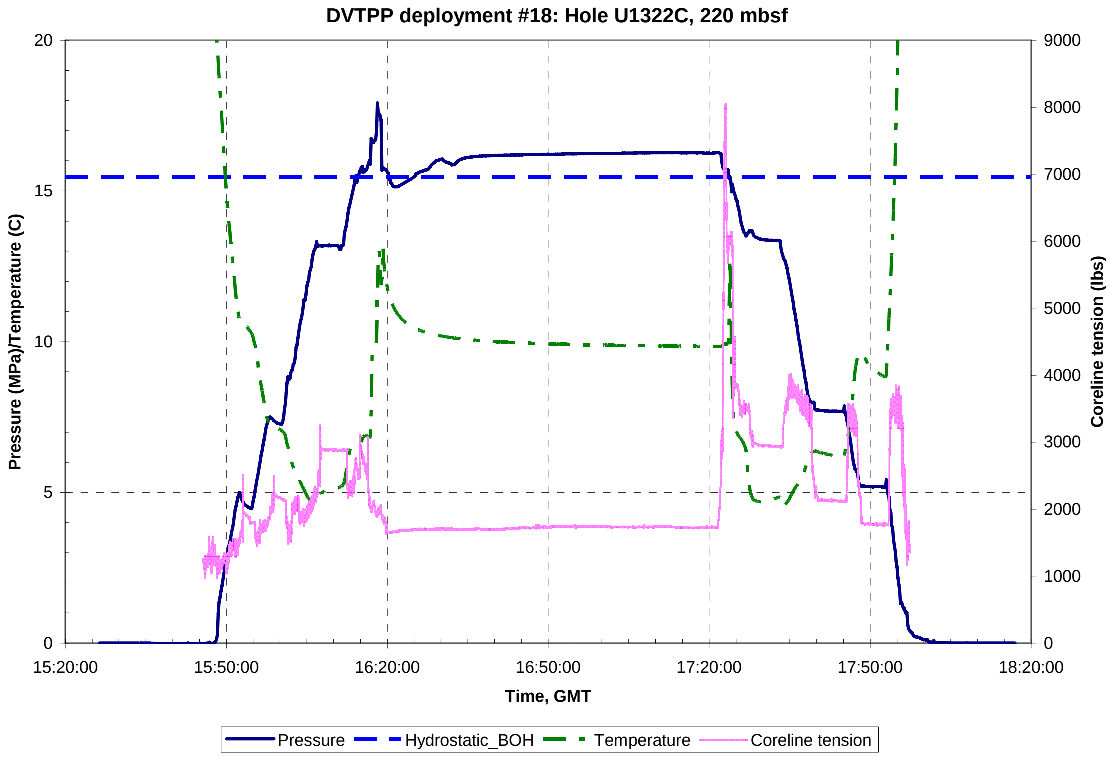

Figure A.A.17.e

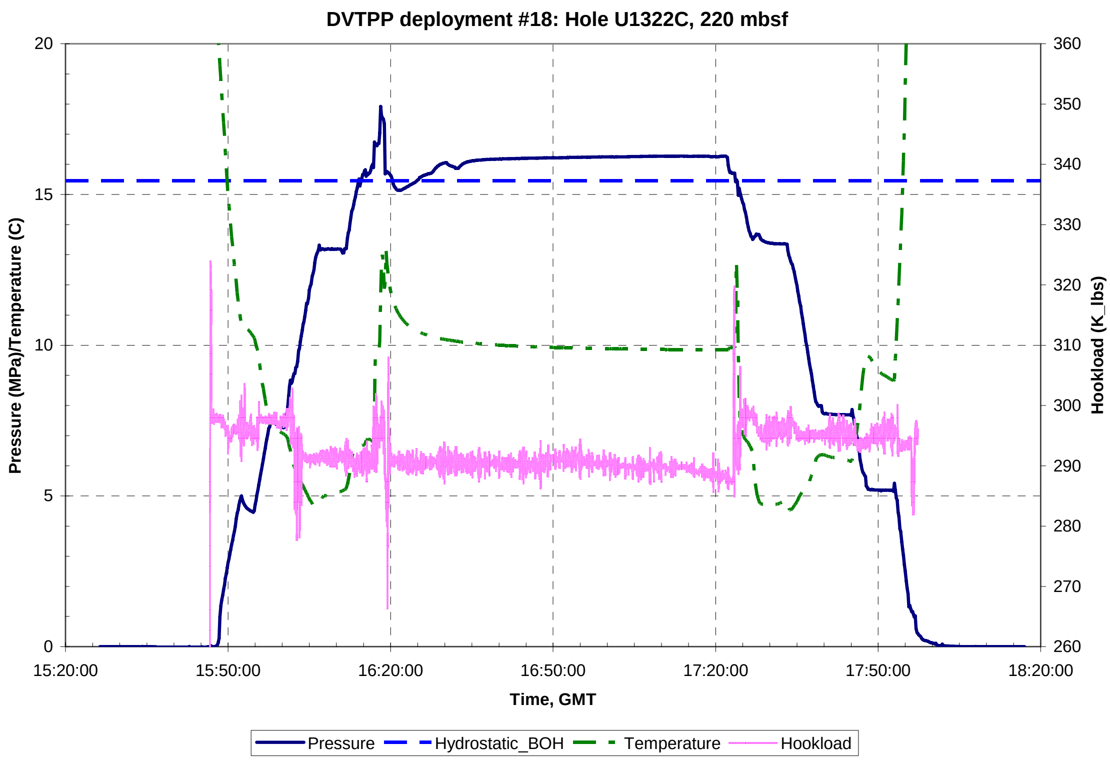

Figure A.A.17.f

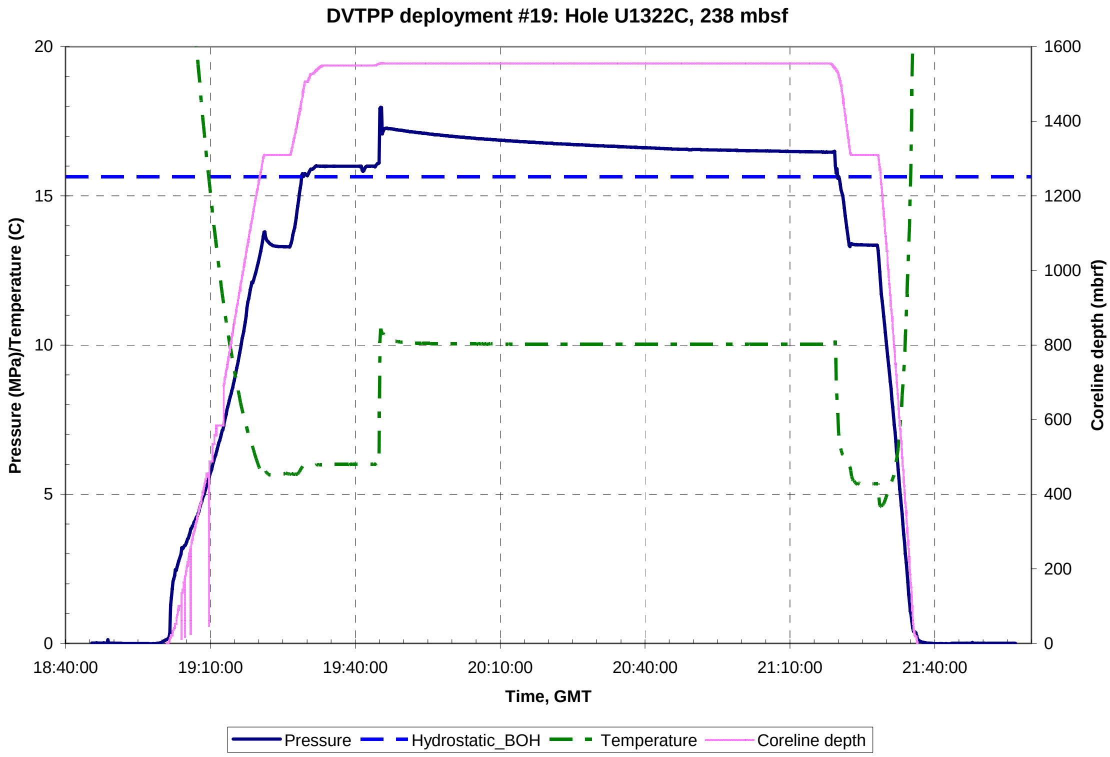

Figure A.A.18.a: Pressure, temperature and Truview data for DVTPP Deployment #19, Hole U1322C, 238 mbsf. GMT = Greenwich Mean Time, Hydrostatic_BOH is the hydrostatic pressure at the bottom of the hole.

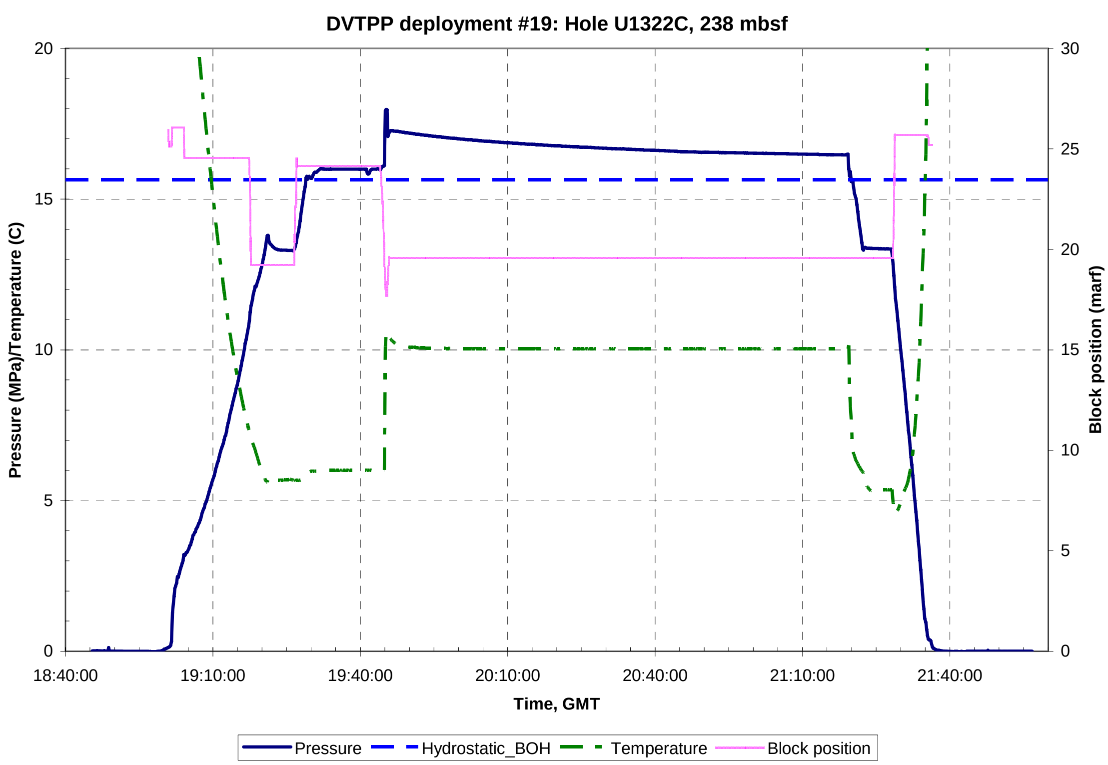

Figure A.A.18.b

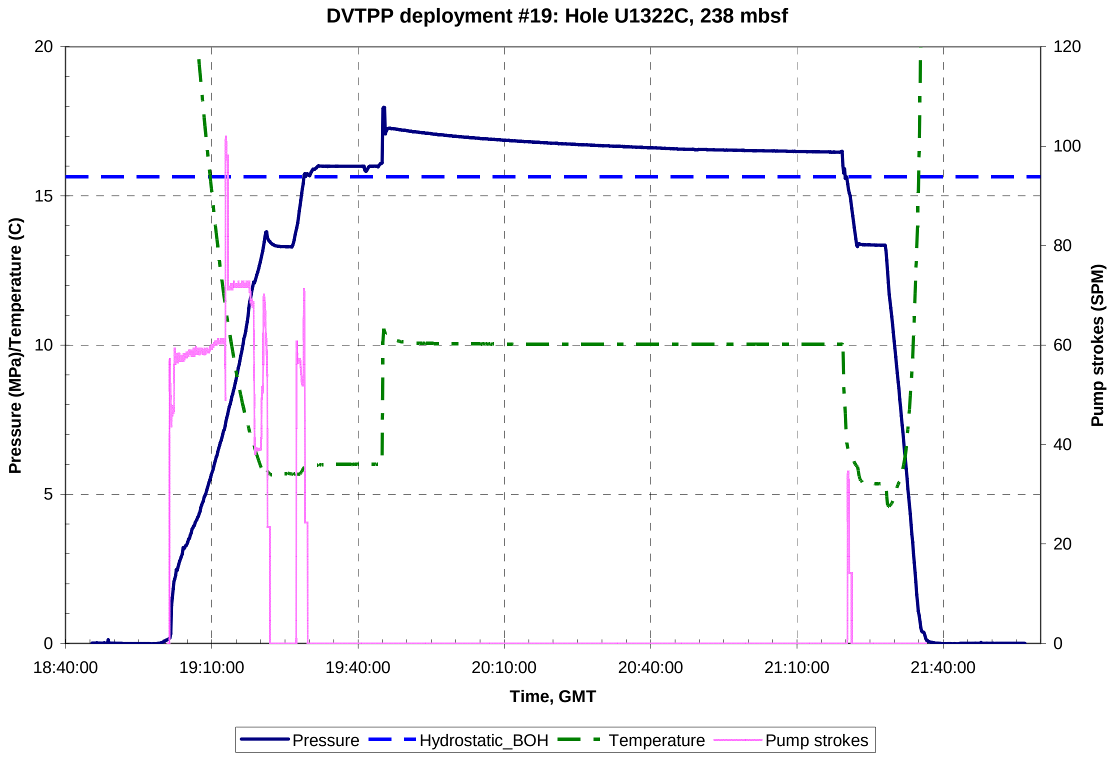

Figure A.A.18.c

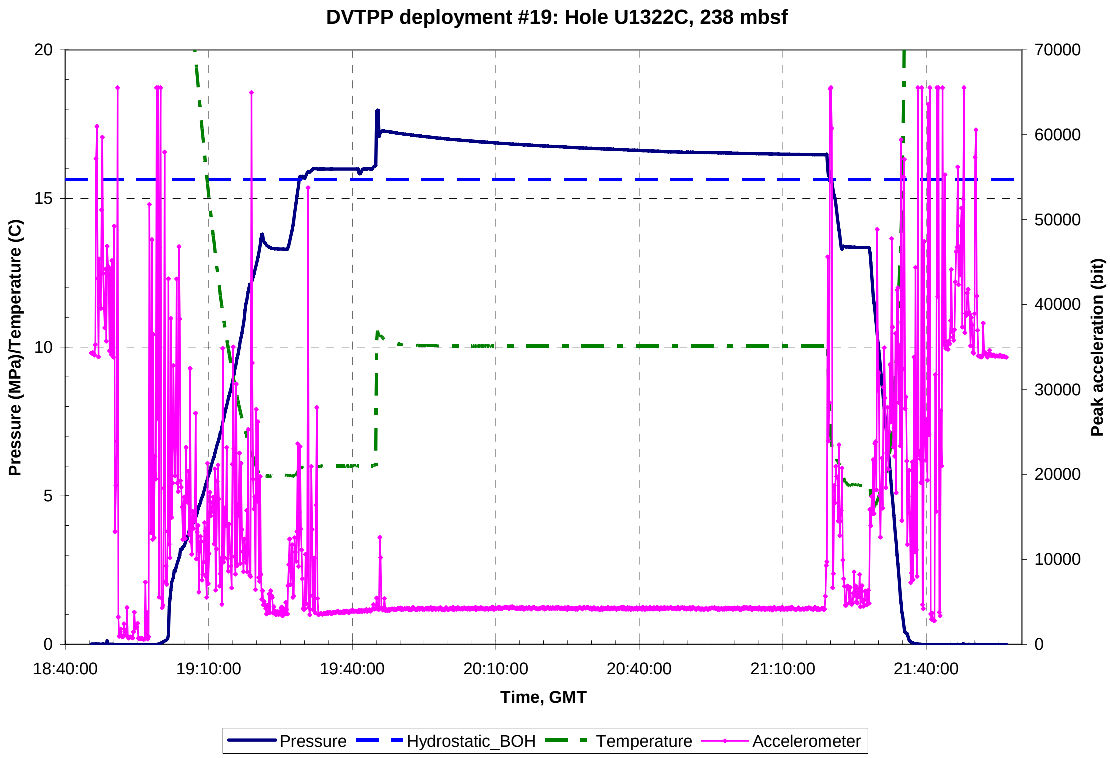

Figure A.A.18.d

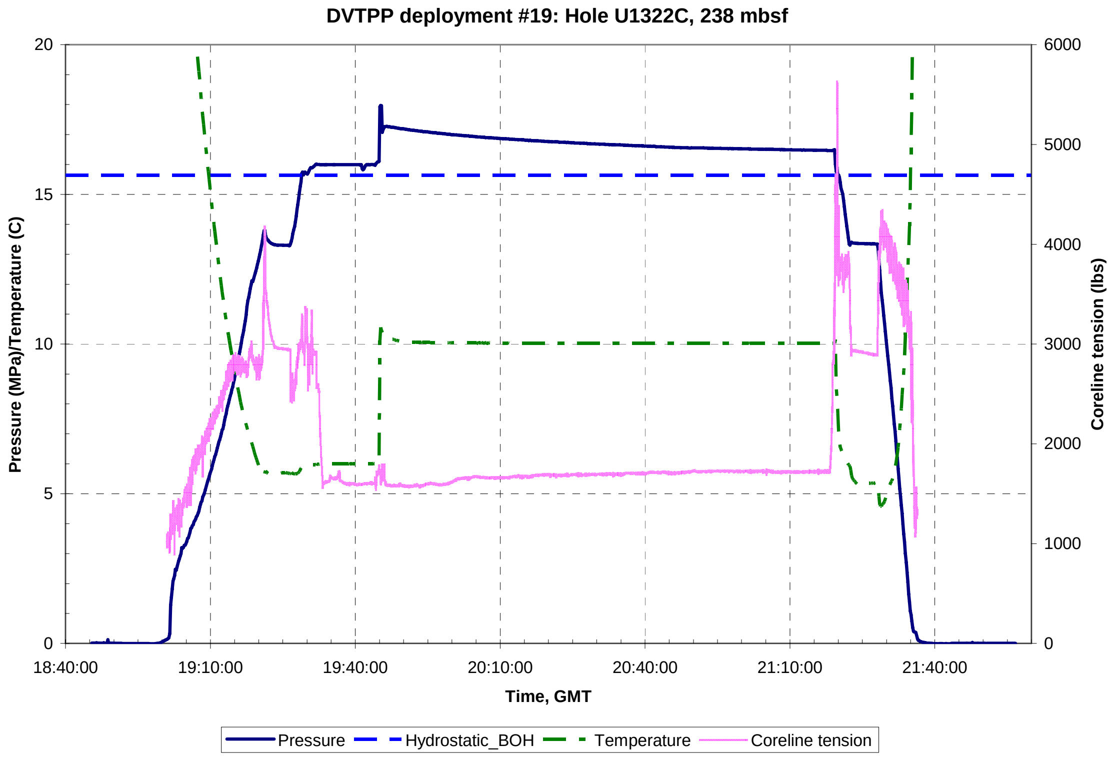

Figure A.A.18.e

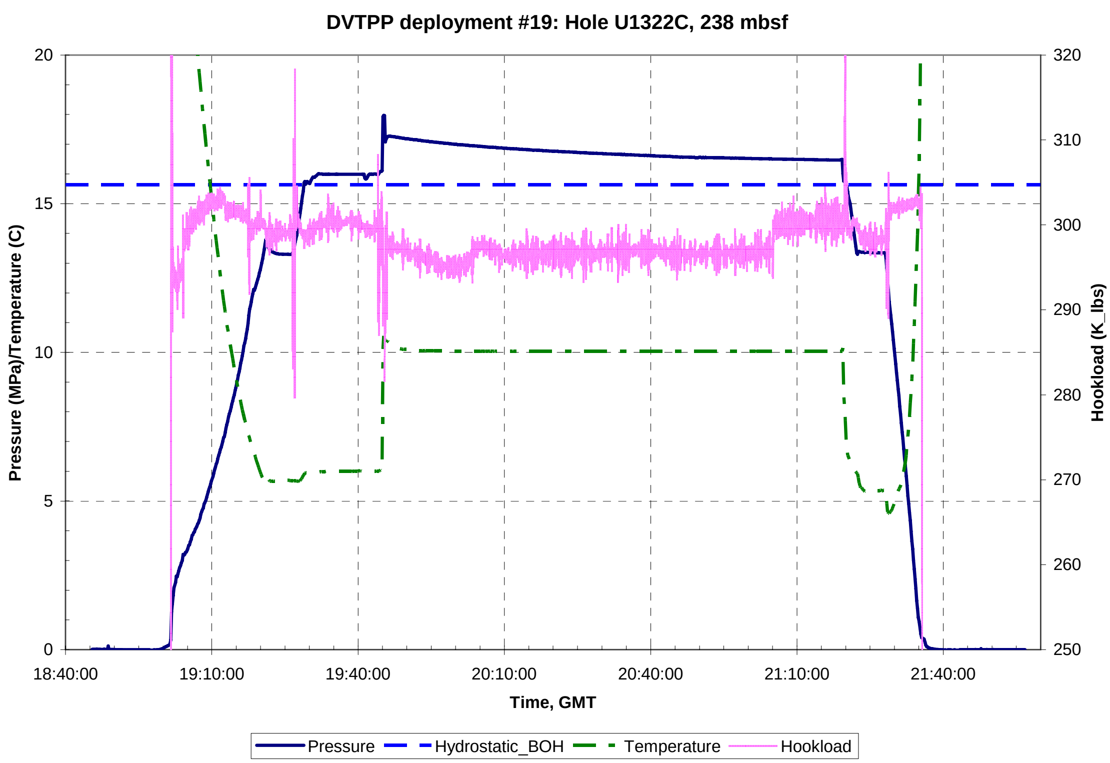

Figure A.A.18.f

Appendix A.B Temperature/Dual Pressure (T2P) Probe

A.B.1 Overview

In Appendix A.B, we present the T2P deployments during Expedition 308. It includes four parts: 1) the instruments that were used; 2) temperature calibration; 3) pressure calibration and 4) detailed description of each T2P deployment.

A.B.2 Instruments

During Expedition 308, two types of penetrometer tips (Figure A.4), two data loggers, six pressure transducers and five thermistors were used in combination to form the T2P probes that measured the formation pressure and temperature (Table A.1).

A.B.3 Temperature Calibration

Temperature calibrations were carried out on the data logger and thermistor separately. The data logger response to resistance was determined using a highly stable resistance box that simulates the resistance variation of the thermistor over its full temperature range. The calibration coefficients of the data logger were provided by the USIO prior to the cruise (Table A.B1a). Table A.B1b presents the commercial calibration of the thermistors prior to the cruise. Accuracy of the presented data is ±0.05 $^{\circ}$C between -40 and 125 $^{\circ}$C. The Steinhart-Hart relationship is used to describe the temperature as a function of the thermistor resistance (Table A.B1a) [*Davis*, 1997].

A.B.4 Pressure Calibration

The T2P measures pore pressure with steel pressure transducers. The force on the sensing element due to the pressure results in a deformation of the sensing element and a change in the output signal.

A.B.5 Onboard calibration

Five out of six pressure transducers were calibrated using a witness pressure transducer provided by the USIO and a high pressure oil pump in the downhole tool lab on the drill ship prior to deployments. We ran the pump pressure from atmosphere pressure up to 5000 psi and then stepped down to atmosphere pressure. The hysteresis was insignificant (Figure A.B1). The calibration curve is a straight line that can be characterized by its slope and its intersection on the y-axis (Figure A.B1 and Table A.B2).

A.B.6 Problems in the pressure calibration

All the transducers were flooded with seawater whenever the tip of the T2P was broken. The seawater that was leaked into the transducer weakened the insulation of the circuit inside the transducer. The transducers became unstable. Their reading at a constant pressure could randomly change significantly. Analysis of the pressure data also showed that they might perform differently on different channels and data loggers. This meant that the original pressure calibrations were no longer valid.

To remove the moisture and stabilize the pressure transducers, the transducers were oven dried on the drill ship at up to 60 $^{\circ}$C for up to 24 hours before re-use. After oven drying, the slope of the calibration curve showed no significant change but the intersection on the y-axis was subject to change (Table A.B2). On the drill ship, we did not recalibrate the transducers each time after being flooded. Therefore, we needed a systematic approach to correct any potential errors related to the change of the intersection due to oven drying.

Furthermore, analysis of pressure data calibrated according to the onboard calibrations showed that certain transducers were very sensitive to the operating temperature. For instance, Figure A.B7a shows the onboard pressure calibration of T2P Deployment #1 (a tool test in water column). The measurements were made at temperature ranges from 4 to 27 °C. The tip pressure was in good agreement with the hydrostatic pressure calculated by assuming an average fluid density of 1.024 g/cc. The shaft pressure matched the tip pressure closely around 20 °C at which the transducers were calibrated. However, at significantly colder temperature, there was discrepancy between the tip and shaft pressures. The discrepancy varied with water temperature and up to 0.6 MPa at ~ 5 °C. In this example, the shaft pressure transducer was much more sensitive to temperature than the tip transducer.

The "compensated temperature range" of the T2P pressure transducers is from 25 °C to 235 °C. Out of this range, the slope (*S*) and intersection (*I*) of the calibration curve are subject to change due to variation in temperature (Figure A.B2). The onboard calibrations were done at the room temperature of the downhole tool lab on the vessel. These calibrations are not sufficient to describe the behavior of the transducers over the operating temperature range of the tool. Therefore, the temperature influence on the calibration curve must be tested to achieve accurate pressure calibration.

A.B.7 Post-cruise calibration

Two pressure transducers were lost during post-cruise shipment between labs. We checked the performance of the four available transducers before the recalibration. They were not stable and performed differently on different channels and data loggers. This was similar to the behavior observed immediately after being flooded on the ship. We interpret this was caused by the salt left in the transducers when they were flooded during deployments.

To correct for this problem, the transducers were baked at 55 °C in an oven prior to recalibration to stabilize the transducers. Three of the four available transducers were very stable after oven drying.

In March 2007, we recalibrated the T2P pressure transducers using the same deadweight tester that was used to verify the calibrations of the DVTPP pressure transducers (Appendix A.A). Calibrations were conducted at controlled temperatures to explore the influence of temperature on the slope and intersection of the calibration curve.

We ran the deadweight tester pressure from atmosphere pressure up to 4015 psi and then stepped down to atmosphere pressure. The hysteresis was insignificant and the calibration curves were straight lines (Figure A.B3). No significant difference was observed between loggers Sn2 and Sn4, and between the tip pressure channel and the shaft pressure channel.

The results show that the slope and intersection of the calibration curve are linear functions of temperature (Figure A.B4, A.B5 and A.B6). These relationships allow us to confidently interpret the calibration coefficients (slope and intersection of the calibration curve) for any given temperature within the range.

A.B.8 Recalibration of the T2P pressure data

We present the T2P deployment in the water column (T2P #1) to illustrate how we recalibrated the T2P pressure data using the post-cruise calibrations (Figure A.B7). The two pressure transducers (S50-73 at the tip and Z59-72 at the shaft) were recalibrated under controlled temperatures. We take the temperature measured at the T2P tip thermistor to determine the calibration coefficients from the trendlines in Figures A.B4 and A.B5. We then apply the calibration coefficients to calculate the pressure from the transducer reading.

Both the calculated tip and shaft pressures do not match the hydrostatic pressures at the tool stops (Figure A.B7b). We interpret this is caused by changes of the intersection due to oven drying (Table A.B2). The offset from hydrostatic pressure is a constant value regardless of the operating temperature for both transducers (Figure A.B7b). This suggests that the change in the intersection due to oven drying is constant for any given deployment (e.g. a constant vertical shift of the *I-T* relationship presented in Figures A.B4b, A.B5b and A.B6b).

The offset was corrected by matching the tip and shaft pressure records to the hydrostatic pressure at tool stops (Figure A.B7c). After this correction, the tip pressure matches the shaft pressure very well. The hydrostatic pressures at tool stops are calculated from an assumed seawater density of 1.024 g/cc in which the atmosphere pressure is not accounted.

For the three pressure transducers not recalibrated under controlled temperatures, we apply the calibration coefficients obtained from the onboard calibration tests (Table A.B2). We then compare it to the pressure data of one of the recalibrated transducers (S50-73, S50-75 and Z59-72). We take the difference between the tip and the shaft pressures as a function of the temperature measured at the probe tip (Figure A.B8 for T2P Deployment #9 presented in Figure A.B16). The temperature influence and the shift of the intersection (a constant value) are then compensated by applying this function (Figure A.B16).

A.B.9 T2P Deployment Procedure

The deployment procedure of T2P is similar to that of the DVTPP (Appendix A.A). We integrate the TruView data, the shipboard ‘T2P Deployment Log Sheet’, and the pressure and temperature records to define the operation events, and to understand the field measurements.

A.B.10 T2P Deployments during IODP 308

A.B.10.1 T2P Deployment #1: Hole 1319A, tool test in water column

Deployment #1, completed in the water column prior to drilling, was the first sea deployment of the T2P probe. The deployment was intended to pressure test the T2P probe, to check the pressure transducer calibrations and to confirm that the T2P probe could successfully pass through the lockable flapper valve (LFV) of the BHA.

The time-event log for T2P Deployment #1 is illustrated in Table A.B3, and a graphical representation of the pressure and temperature records are illustrated in Figure A.B7. The T2P was lowered until the tip was at 511 meters below sea level (mbsl) where a hydrostatic reference was recorded for two minutes. The tool was then lowered until the tip was at 1011 mbsl for another two-minute reference. The T2P probe was then lowered through the LFV. The T2P probe tip reached a maximum depth of 1387.5 mbsl (42.1 m above seafloor) where a seven-minute reference was recorded. References were also taken during retrieval of the T2P probe when the tip was at 1010 mbsl and at 511 mbsl. No drilling fluid was circulated during the deployment.

The tool test was successful. The tool recorded pressure and temperature for the entire deployment (Figure A.B7) and successfully passed through the LFV. The temperature record showed a downhole decrease in temperature to 4.58 $^{\circ}$C at 1387.5 mbsl.

A.B.10.2 T2P Deployment #2: Hole U1319A, 80.5 mbsf

Table A.B4 and Figure A.B9 present the sequence of the operations and the tool response to particular events for T2P Deployment #2. Traveling block position data are not available for this deployment. The bit depth data has dramatic shift during this deployment (Figure A.B9b). Drilling fluid circulation was stopped when taking hydrostatic reference, when pushing the probe into the sediment, and for the first 12 minutes the T2P probe was in the sediment (Figure A.B9c). The fluid circulation was resumed 12 minutes after the penetration at 14 strokes per minute (SPM) (Figure A.B9c). Corresponds to the onset of fluid circulation, both the tip and shaft pressures had a very slight pressure increase (less than 0.01 MPa).

The temperature and pressure records increased when the CDS was latching into position (Table A.B4 and Figure A.B9d). This response suggests the tool entered the formation while positioning the CDS to the retracted position. When the drill bit was lowered down to insert the tool, it recorded a second temperature and pressure increase (Figure A.B9b). Pressure and temperature records varied during the penetration process. We believe these variations were due to variations of the soil properties. After 35 minutes in the formation, the pressure at the tip was 15.71 MPa whereas the shaft recorded 16.35 MPa. Extrapolation of the pressure records may provide an estimate of the in situ pressure. The temperature record provides an in situ formation temperature of 7.23 ºC at the end of the deployment.

When the T2P probe was recovered on the rig floor, the shroud was not covering the tip. The tip of the tool was damaged and the thermistor was missing. The drive tube was bent slightly. We interpret that the shroud never re-seated over the tip during retrieval of the tool. Damage of the tip was interpreted to result from bending of the tip during penetration followed by a straightening of the tip when the T2P probe was pulled through the LFV in the BHA. Most likely, the T2P probe and drive tube were damaged because the T2P probe did not enter the sediment vertically. To achieve vertical penetration, future deployments occurred with the drill bit less than 2 m off the BOH instead of 12 m.

A.B.10.3 T2P Deployment #3: Hole U1320A, 126.3 mbsf

Contrast to Deployment #2, this deployment used the tapered needle probe and was initiated with the drill bit ~1m off the BOH. These modifications were done to decrease the chance for bending or breaking the needle probe. The quality of the bit depth data is poor. Its absolute bit depth value is not reliable (Figure A.B10b). To explore the bit movement during the deployment, the bit depth data have to be used together with Table A.B5.

The T2P recorded temperature and pressure at the tip whereas the shaft transducer did not record any data during the deployment (Figure A.B10). The temperature and pressure records increased while positioning the CDS to retracted position (Table A.B5 and Figure A.B10d). When the drill bit was lowered down to insert the tool, it recorded a second temperature and pressure increase (Figure A.B10b). The tip pressure decreased abruptly when the drill bit was lifted. The fluid circulation was resumed to 10 SPM 5 minutes after the penetration. No significant pressure and temperature responses were observed due to the onset of fluid circulation (Figure A.B10c). Pressure dissipation was recorded at the tip until the probe was pulled out of the formation. The last recorded pressure was 16.27 MPa. Extrapolation of the pressure records will provide an estimate of the in situ pressure. The temperature decay was continuous and provided an in situ formation temperature of 6.99 ºC.

A.B.10.4 T2P Deployment #4: Hole U1320A, 213.0 mbsf

Deployment #4 used the straight needle probe. Operation procedures were similar to Deployment #3 except we did not use the drill string to push the T2P into the formation. We used the weight of the tool to push the tool into the formation. The tip pressure and temperature recorded spikes during penetration by the tool weight whereas the shaft pressure did not record any penetration response (Table A.B6 and Figure A.B11). This indicates that the shaft pressure port did not go into the formation throughout the deployment. Fluid circulation was resumed 6 minutes after the insertion spike, which caused slight increase in both pressure and temperature. The final tip pressure was 17.19 MPa that was same as the shaft pressure. This suggests that the borehole fluid have communication with the tip pressure due to the short penetration distance (<0.25 m). The temperature reached an equilibrium value of 8.99 ºC. The temperature measurement may be subject to the influence of the borehole fluid.

A.B.10.5 T2P Deployment #5: Hole U1324B, 51.3 mbsf

The bit depth data has dramatic shift whereas the bit movement directions match the bit movements recorded in the T2P log sheet (Figure A.B12b and Table A.B7). To explore the bit position during the deployment, the bit depth data should be used together with Table A.B7.

The BHA was positioned to 0.5 m off the BOH before the CDS latch in (Table A.B7). The temperature and pressure records increased while positioning the CDS to the retracted position (Table A.B7 and Figure A.B12d). According to the tool dimensions, the T2P tip went into the formation by approximately 0.6 m at the latch-in position. The drill bit was lowered down to 0.25 m off the BOH at the end of penetration (Table A.B7). The tool only recorded slight temperature and pressure increase (Figure A.B12b) due to the 0.25 m further insertion. The fluid circulation was resumed 10 minutes after the penetration at 9 SPM (Figure A.B12c). Corresponding to the onset of fluid circulation, both the tip and shaft pressures had a slight pressure increase (less than 0.05 MPa). The tip and shaft pressures were more or less constant during the dissipation phase. The tip had a final pressure of 11.37 MPa and the shaft had a final pressure of 11.65 MPa. The temperature record continuously decayed to an equilibrium temperature of 5.78 $^{\circ}$C.

Upon pulling the tool out of the formation, all sensor readings were lost. At the rig floor, it was noted that the tip was bent and the thermistor and bottom porous stone were missing from the tool. We believed the tool may have been bent during penetration and then broken during the pullout when all sensor readings were lost. The pressure and temperature measurements should be viewed cautiously because of the damage incurred during the deployment.

A.B.10.6 T2P Deployment #6: Hole U1324B, 89.3 mbsf

The pressure and temperature records showed three strikes (Table A.B8 and Figure A.B13). The first spike occurred when the tool landed in the BHA; the second pulse occurred when the tool was pushed into the formation; and the third pulse occurred when circulation began while the tool was in the sediment. The shaft had a continuous dissipation curve to its end value of 12.09 MPa. The tip pressure was not smooth and went close to or below the hydrostatic pressure after each pulse. We interpreted that there was an internal hydraulic leak at the tip. The temperature record was reasonable after the first two pulses whereas it showed a rapid decrease after the third pulse. The last temperature reading was 5.74 °C, which was even lower than the borehole fluid temperature (5.98 °C) that was recorded prior to the first spike. We use the temperature data after the second spike to constrain the in situ temperature.

A.B.10.7 T2P Deployment #7: Hole U1324B, 117.8 mbsf

Similar to Deployment #6, the pressure and temperature records all showed responses to latching of the tool in the BHA, pushing into to the formation, and turning on circulation while in the formation (Table A.B9 and Figure A.B14). The internal leak at the tip pressure was not identified and repaired in Deployment #7. The shaft had a continuous dissipation curve to its end value of 12.84 MPa after the third spike. The temperature record exhibited a type decay curve and provided an in situ temperature of 7.00 °C.

A.B.10.8 T2P Deployment #8: Hole U1324B, 136.3 mbsf

Table A.B10 and Figure A.B15 present the sequence of the operations and the tool response to particular events for Deployment #8. The shaft pressure was not stable during this deployment with multiple abrupt increases and decreases in pressure that were not associated with deployment events. The tip pressure and temperature records showed responses to latching of the tool in the BHA, pushing into to the formation, and backing-off the drill bit after penetration. The hydraulic leak at the tip pressure resulted in erratic dissipation curve. The temperature decay was smooth and provided an in situ temperature of 7.35 $^{\circ}$C. The tool was disassembled and reassembled after this deployment because of the poor pressure readings on both transducers.

A.B.10.9 T2P Deployment #9: Hole U1324B, 368 mbsf

This deployment recorded large pressure and temperature increases with the landing of the tool in the BHA (Table A.B11 and Figure A.B16). After a short period of decay, the tool was pulled out of the formation by pulling the wireline up (Figure A.B16d). The pressure abruptly dropped to the borehole fluid pressure. The temperature increased abruptly first and then decreased to the borehole fluid temperature. The pressure and temperature had similar responses when pushing the tool into the formation (Figure A.B16). The abrupt pressure decrease was caused by backing off the drill bit. The pressure and temperature records suggest that the tool was measuring the pressure and temperature of the borehole fluid. No in situ conditions can be ascertained from this deployment.

A.B.10.10 T2P Deployment #10: Hole U1324B, 394.5 mbsf

The connection between the sensors and the data acquisition system had poor contact. This precluded collection of any data.

A.B.10.11 T2P Deployment #11: Hole U1324B, 593.2 mbsf

All connections were cleaned and the tool was reassembled because of the communication problem in Deployment #10. Deployment #11 was a test of the sensors and data acquisition system and did not involve pushing the probe into the sediment (Table A.B12 and Figure A.B17). The coreline depth and hook load data were not reliable during this deployment.

The tip pressure showed excellent agreement with the shaft pressures. Two pressure decreases occurred in the tip pressure (Figure A.B17). These may have been caused by the tip being partly embedded in the sediment, whereas the shaft has not penetrated the formation. Overall this deployment confirmed that the electronic failure had been fixed.

A.B.10.12 T2P Deployment #12: Hole U1324C, 50 mbsf

The bit depth data had dramatic shift and was not reliable (Figure A.B18b). To explore the bit movement during the deployment, the bit depth data should be used together with Table A.B13. The temperature and pressure records increased while positioning the CDS to the retracted position (Table A.B13 and Figure A.B18d). When the drill bit was lowered down to insert the tool, it recorded further temperature and pressure responses (Figure A.B18b). Pressure and temperature records varied during the penetration process. These variations were due to variations of the soil properties. The tip and shaft pressures had a decrease when the BHA was lifted whereas the magnitude of the decreases was small (< 0.1 MPa). At the same time, the thermistor recorded a rapid increase. The fluid circulation was resumed 8 minutes after the penetration at 10 SPM (Figure A.B18c). Corresponding to the onset of fluid circulation, both the tip and shaft pressures had a slight pressure increase. Then all sensors recorded a gradual dissipation. The tip had an end value of 11.21 MPa. The shaft had an end value of 11.56 MPa. Extrapolation of the pressure records will provide an estimate of the in situ pressure. The temperature decayed to an equilibrium temperature of 5.66 $^{\circ}$C.

A.B.10.13 T2P Deployment #13: Hole U1324C, 100 mbsf

All sensors had significant increase associated with pushing the tool into the sediment (Table A.B14 and Figure A.B19). The tip and shaft pressures decreased when the BHA was lifted whereas the magnitude of the decrease was much larger at the tip. As the same time, the thermistor recorded a small increase. All sensors recorded a gradual dissipation. The tip had an end value of 11.93 MPa. The shaft had an end value of 12.39 MPa. Extrapolation of the pressure records will provide an estimate of the in situ pressure. The temperature decayed to an equilibrium temperature of 6.65 °C.

A.B.10.14 T2P Deployment #14: Hole U1324C, 150 mbsf

Similar to deployment #13, pressure and temperature increased with insertion into the formation, which were followed by dissipation curves (Table A.B15 and Figure A.B20). All sensors recorded two perturbations while in the formation that could not be associated with any deployment event (Table A.B15 and Figure A.B20). After the last perturbation, the shaft pressure continued along a normal dissipation curves. Whereas, the tip showed a larger pressure decrease followed by a pressure increase. The tip had an end value of 12.69 MPa. The shaft had an end value of 13.10 MPa. The pressure records likely can be used to evaluate the in situ pressure. The temperature (7.57 °C) appeared to be in equilibrium with the formation prior to pulling the tool out of the BOH.

A.B.10.15 T2P Deployment #15: Hole U1324C, 200 mbsf

The temperature and pressure records increased while positioning the CDS to the retracted position (Table A.B16 and Figure A.B21d). When the drill bit was lowered down to insert the tool, it recorded further temperature and pressure responses. The tip and shaft pressures had a rapid decrease when the BHA was backing-off the BOH. At the same time, the thermistor recorded a rapid increase. The shaft then continued along a normal dissipation curves. Whereas, the tip showed a pressure rebound followed by a gradual dissipation. The tip had an end value of 14.09 MPa. The shaft had an end value of 14.44 MPa. The pressure records can be used to evaluate the in situ pressure. The temperature decayed to an equilibrium temperature of 8.58 °C.

All sensors lost communication with the data acquisition unit during retrieval of the tool from the formation. When the tool reached the rig floor, the tip was bent and the drive tube was loose. The loose drive tube most likely caused the failure to record data during the retrieval as the sensor cables were routed through the drive tube where they were connected with the data acquisition unit.

A.B.10.16 T2P Deployment #16: Hole U1324C, 300 mbsf

The temperature and tip pressure records increased while positioning the CDS to the retracted position (Table A.B17 and Figure A.B22). When the drill bit was lowered down to insert the tool, it recorded further temperature and pressure responses. Pressure and temperature records varied during the penetration process. These variations were due to variations of the soil properties and penetration rate. The pressure and temperature sensors recorded continuous dissipation curves. The end temperature of 10.29 $^{\circ}$C was equilibrated with the formation. The end shaft pressure was 15.2 MPa, and the end tip pressure was 14.42 MPa. Extrapolation of the pressure records will provide an estimate of the in situ pressure.

A.B.10.17 T2P Deployment #17: Hole U1322B, 42 mbsf

When the drill bit was lowered down to insert the tool, it recorded temperature and pressure responses (Figure A.B23 and Table A.B18). However, the pressure signals decreased significantly when backing-off the drill bit. The pressures were constant during the dissipation phase and were equal to the pressure recorded prior to the tool insertion. The temperature record showed a second spike when backing-off the drill bit, and then decayed to a temperature that was close to the borehole fluid temperature. These observations suggest that the tool was communicating with the borehole fluid. Therefore this deployment did not provide any constraint on in situ conditions.

A.B.10.19 T2P Deployment #19: Hole U1322B, 134.3 mbsf

The temperature and pressure records increased while positioning the CDS to the retracted position (Table A.B19 and Figure A.B24). When the drill bit was lowered down to insert the tool, it recorded further temperature and pressure responses. Pressure and temperature records varied during the penetration process. These variations were due to variations of the soil properties. The tip and shaft pressures had an abrupt decrease when the BHA was backing-off the BOH. At the same time, the thermistor recorded a rapid increase. After this perturbation, the tip and shaft pressure rapidly rebounded to nearly constant values. The end shaft pressure was 15.22 MPa, and the end tip pressure was 15.08 MPa. The temperature decayed to an equilibrium temperature of 7.89 $^{\circ}$C.

A.B.10.20 T2P Deployment #20: Hole U1322B, 157.8 mbsf

The temperature and pressure records increased during the first landing attempt with the bit 12 m off the BOH, then the tool was pulled back up to re-land it with the bit 3 m off the BOH (Table A.B20 and Figure A.B25). Fluids were circulated during landing of the tool in the BHA. When the drill bit was lowered down to insert the tool, it recorded further temperature and pressure responses. The tip and shaft pressures had an abrupt decrease when the BHA was backing-off the BOH. At the same time, the thermistor recorded a rapid increase. After this perturbation, the tip pressure rapidly rebounded to a value and then was slowly building up to an end pressure of 15.41 MPa. The shaft pressure rapidly rebounded to a nearly constant value of 15.60 MPa. The end pressures may provide a rough estimate of the in situ pressure. The temperature decayed to an equilibrium temperature of 8.47 $^{\circ}$C.

A.B.10.21 T2P Deployment #21: Hole U1322C, 50 mbsf

A data acquisition error resulted in only three minutes of recorded data. Inspection of the data acquisition unit after recovering the probe led to the discovery that the memory card had come ajar and thus data could not be recorded. The memory card was replaced and the quick release button for the card was removed. This modification made it harder for the memory card to be accidentally ejected.

A.B.10.22 T2P Deployment #22: Hole U1322C, 75 mbsf

This deployment suffered from a hydraulic leak that flooded the electronics connecting the pressure transducers and the thermistor to the data acquisition unit. The flooding shorted all circuits and thus no pressure and temperature data were recorded. All electrical components were cleaned and dried after the deployment.

A.B.10.23 T2P Deployment #23: Hole U1322C, 150 mbsf

Truview data are only available for the dissipation phase. Temperature and pressure signals increased with landing of the tool in the BHA and again with penetration into the formation (Table A.B21 and Figure A.B26). The tip had a decrease in pressure when the bit was pulled up and then slowly rebounded to a final pressure of 15.29 MPa. The shaft had a pressure decrease when the bit was lifted and then continuously decayed to an end pressure of 15.99 MPa. The temperature decayed to an equilibrium value of 8.26 $^{\circ}$C.

A.B.10.24 T2P Deployment #24: Hole U1322C, 200 mbsf

The tip pressure and temperature records increased while positioning the CDS to the retracted position (Table A.B22 and Figure A.B27). A second increase recorded by all sensors occurred when the tool was pushed into the formation. Pressure and temperature records then smoothly dissipated while the tool was in the formation. The tip decayed to a final pressure of

16.34 MPa and the shaft dissipated to a final pressure of 17.16 MPa. Extrapolation of the pressure records will provide good estimate of the in situ pressure. The temperature decayed to an equilibrium value of 9.28 $^{\circ}$C.

A.B.10.25 T2P Deployment #25: Hole U1322D, 40 mbsf

The TruView data are missing for this deployment. Key deployment events are derived from the shipboard 'T2P log Sheet' [*Flemings*, 2006b]. Pressure and temperature pulses were recorded when the probe was pushed into the formation but the pressure dropped rapidly when the drill bit was lifted off the BOH (Table A.B23; Figure A.B28). The tip and shaft then increased to a nearly constant pressure of 13.78 MPa, which was equal to the fluid pressure at the BOH. The temperature decreased rapidly upon pulling up of the bit and then was nearly constant and close to the temperature of the borehole fluid. The pressure and temperature records suggest that the measurement was influenced by communication with the borehole fluid. Thus this deployment did not provide any constraint on in situ conditions.

A.B.10.26 T2P Deployment #26: Hole U1322D, 70 mbsf

Table A.B24 and Figure A.B29 present the sequence of the operations and the tool response to particular events for Deployment #26. Similar to Deployment #25, the seal around the probe was weakened when the bit was lifted off the BOH. The pressure and temperature measurements were subject to influence of the borehole fluid. This deployment did not provide any constraint on in situ conditions.

A.B.10.27 T2P Deployment #27: Hole U1322D, 100 mbsf

The pressure and temperature records increased while positioning the CDS to the retracted position and pushing the tool into the formation (Table A.B25 and Figure A.B30). The tip and shaft pressures rapidly decreased while backing-off the bit. The tip pressure rebounded to a near-constant value of 14.69 MPa. The shaft pressure dissipated to a final value of 15.11 MPa. This dissipation curve can extrapolated to evaluate the in situ pressure. Smooth temperature decay was measured. The final temperature of 7.11 $^{\circ}$C was equilibrated with the formation.

A.B.10.28 T2P Deployment #28: Hole U1322D, 134 mbsf

The pressure and temperature records increased while positioning the CDS to the retracted position and pushing the tool into the formation (Table A.B26 and Figure A.B31). The tip and shaft pressures rapidly decreased while backing-off the bit. Pressures at the shaft and tip were near-constant during the dissipation phase. The temperature increased while backing-off the bit and then rapidly decayed to a final temperature of 7.31 $^{\circ}$C. The pressure and temperature measurements were subject to influence of the borehole fluid. This deployment did not provide any constraint on in situ conditions.

All sensor data records were lost during recovery of the probe. At the rig floor, it was noted that the tip had broken and the drive tube had bent during the deployment. Damage to the probe likely occurred while pushing into the formation and then the tip was broken when pulling out of the formation.

Table A.B1. Temperature calibration of T2P. a) Calibration coefficients for data loggers and thermistors. b) Actual thermistor calibration data.

a)

Temperature channel calibration

The formula for counts to ohms:

Rt'= R1*(5/(x/65535*3.5/24900)-24900) + R2

x = Counts

Rt' = the resistance in ohms of the thermistor.

Logger Sn #2	
R1=	1.000729
R2=	176.136606

Logger Sn #4	
R1=	0.990307767
R2=	-72.74909712

Thermistor calibration

The formula for ohms to Kelvin

(Steinhart & Hart):

1/T = A+B*Ln(Rt')+C*Ln(Rt')^3

ºC = K - 273.15

T = Temperature in Kelvin

Rt' = the resistance in ohms of the thermistor.

Thermistor 0509-1	
A=	4.63276461E-04
B=	2.10947147E-04
C=	6.19690000E-08

0.000209203

Thermistor 0509-2	
A=	5.43051013E-04
B=	1.99981837E-04
C=	8.35910000E-08

Thermistor 0509-3	
A=	4.75887900E-04
B=	2.08557612E-04
C=	6.34430000E-08

Thermistor 0509-4	
A=	4.82495572E-04
B=	2.09282474E-04
C=	6.20870000E-08

Thermistor 0509-5	
A=	4.82688206E-04
B=	2.08833095E-04
C=	6.40080000E-08

Thermistor 0509-6	
A=	4.71824656E-04
B=	2.09263995E-04
C=	6.27480000E-08

b)

ºC vs. Ohms				
Serial #	**0.000ºC**	**30.000ºC**	**60.000ºC**	**100.000ºC**
0509-1	1795000	406620	116210	28980
0509-2	1720000	389890	114500	27795
0509-3	1740000	394200	112590	28035
0509-4	1651000	373340	106560	26535
0509-5	1655000	375720	107480	26810
0509-6	1712000	388430	111130	27740

Table A.B2. Onboard pressure calibration of T2P, June 2005.

Transducer #	Slope (psi/bit)	Intersection (psi)	R^2
S50-73	0.11768162	64.28686942	0.99999094
S50-74[1]	0.12469840	209.49786126	0.99995831
S50-74[2]	0.12473479	161.99347791	0.99999663
S50-75	0.13043403	221.74997847	0.99999299
Z59-72[1]	0.11819436	26.92982866	0.99997830
Z59-72[2]	0.11816986	-490.20091995	0.99997433
Y67-16	0.11944345	99.71216680	0.99999905

[1]- pressure calibration before being flooded
[2]- pressure calibration after oven drying

Table A.B3. T2P deployment #1, Hole 1319A, tool test in water column, 07-June-2005.

Event #	Time (GMT)	Event Description
1	23:31:00	Data logger started at 1 Hz
2	1:46:00	T2P on rig floor
3	2:10:00	T2P raised vertically
4	2:10:20	Pressure response chamber removed from T2P tip
5	2:10:20	Shroud in place over T2P tip
6	2:11:19	T2P placed in drill pipe
7	2:13:00	T2P connected to spacer
8	2:16:16	CDS connected to spacer
9	2:16:43	CDS in extedended position
10	2:20:05	Start lowering T2P downhole
11	2:32:35	Stop at 511 mbsl
12	2:35:00	Start lowering probe
13	2:41:27	Stop at 1011 mbsl
14	2:44:00	Start lowering probe
15	2:55:33	Stop at 1388 mbsl
16	3:01:30	Start pulling T2P uphole
17	3:16:59	Stop at 1010 mbsl
18	3:19:02	Continue pulling T2P uphole
19	3:23:05	Stop at 511 mbsl
20	3:25:09	Continue pulling T2P uphole
21	3:41:40	T2P on rig floor
22	3:41:52	T2P tip in pressure response chamber
23	3:46:46	Pressure response test
24	3:58:00	Data downloaded from data logger
25	4:40:00	Battery removed from T2P

Table A.B4. Event summary of T2P deployment #2, Hole U1319A, 80.5 mbsf, 07-June-2005.

Event #	Time (GMT)	Event Description
1	6:07:50	Data logger started at 1 Hz
2	13:13:28	T2P on rig floor
3	13:15:48	T2P raised vertically
4	13:16:10	Pressure response chamber removed from T2P tip
5	13:16:10	Shroud in place over T2P tip
6	13:19:38	T2P placed in drill pipe
7	13:20:11	T2P connected to spacer
8	13:23:54	CDS connected to spacer
9	13:25:15	CDS in extedended position
10	13:26:52	Start lowering T2P downhole, pumps on
11	13:35:03	Stop at 511 mbsl, pumps off
12	13:37:20	Start lowering probe, pumps on
13	13:44:25	Stop at 1012 mbsl, pumps off
14	13:46:30	Start lowering probe, pumps on
15	13:52:39	Stop at 1431 mbsl, pumps off
16	13:55:05	Start lowering probe
17	13:58:20	T2P passes through LFV
18	14:05:45	CDS lands in BHA
19	14:08:52	Start penetration of T2P into sediment
20	14:15:29	End of T2P penetration
21	14:27:03	Pumps on at 10 strokes per minute (SPM)
22	14:47:30	Start pulling T2P uphole
23	14:48:50	Stop pulling at 1509 mbsl
24	14:49:30	Pulling/relasing winch to free CDS from BHA
25	14:52:20	Start pulling T2P uphole
26	15:09:04	Stop at 511 mbsl, pumps off
27	15:11:30	Start pulling T2P uphole
28	15:20:59	CDS detatched from wireline
29	15:27:50	CDS detatched from spacer
30	15:30:16	Spacer detached from T2P
31	15:30:50	T2P on rig floor
32	15:31:16	T2P tip in pressure response chamber
33	15:39:00	T2P in workroom
34	15:49:00	Battery removed from T2P
35	16:04:38	T2P connected to DC power
36	16:05	Data downloaded from data logger

Table A.B5. Event summary of T2P deployment #3, Hole U1320A, 126.3 mbsf, 08-June-2005 to 09-June-2005.

Event #	**Time (GMT)**	**Event Description**
1		Data logger started at 1 Hz
2	23:08	T2P on rig floor
3	23:14	Pressure response chamber removed from T2P tip
4	23:14	Shroud in place over T2P tip
5	23:15	T2P connected to spacer
6	23:17	CDS connected to spacer
7	23:22	CDS in connected to wireline
8	23:23	Start lowering T2P downhole, pumps on
9	23:30	Stop at 511 mbsl, pumps off
10	23:33	Start lowering probe, pumps on
11	23:40	Stop at 1011 mbsl, pumps off
12	23:43	Start lowering probe, pumps on
13	23:44	Pumping at 13 SPM
14	23:50	Stop at 1490 mbsl, pumps off
15	23:53	Start lowering probe, pumps on at 13 SPM
16	23:57	Pumps off
17	0:00	CDS lands in BHA
18	0:00	Raising BHA to 2 m off BOH
19	0:02	Start penetration of T2P into sediment, 2m advance of BHA
20	0:03	End of T2P penetration
21	0:04	Raising BHA 3m off BOH
22	0:07	Pumping at 10 SPM
23	0:55	Pulling T2P uphole slowly 10 m
24	0:59	10 m pull completed
25	0:59	Start pulling T2P uphole, pumping at 10 SPM
26	1:05	Stop at 511 mbsl, pumps off
27	1:09	Start pulling T2P uphole, pumps on
28	1:13	CDS detatched from wireline
29	1:16	CDS detatched from spacer
30	1:18	Spacer detached from T2P
31	1:18	T2P on rig floor
32	1:18	T2P tip in pressure response chamber
33	1:26	T2P in workroom
34	1:46	Battery removed from T2P
35	1:46	T2P connected to DC power
		Data downloaded from data logger

Table A.B6. Event summary of T2P deployment #4, Hole U1320A, 213.0 mbsf, 09-June-2005.

Event #	Time (GMT)	Event Description
1		Data logger started at 1 Hz
2	11:24	T2P on rig floor
3	11:29	Pressure response chamber removed from T2P tip
4	11:29	Shroud in place over T2P tip
5	11:31	T2P in drill pipe
6	11:32	T2P connected to spacer
7	11:34	CDS connected to spacer
8	11:37	CDS in connected to wireline
9	11:39	Start lowering T2P downhole, pumps on
10	11:44	Stop at 511 mbsl, pumps off
11	11:46	Start lowering probe, pumps on
12	11:52	Stop at 1011 mbsl, pumps off
13	11:54	Start lowering probe, pumps on
14	12:00	Stop at 1471 mbsl, pumps off
15	12:03	Drill bit positioned 0.5-0.75m off BOH
16	12:12	CDS lands in BHA, probe in formation
17	12:12	Raising BHA 2.5m
18	12:17	Pumping at 10 SPM
19	12:36	Pulling T2P uphole to disengage CDS
20	12:37	Pulling T2P uphole
21	12:51	T2P tip at 372 mbsl
22	12:54	T2P lowered to 511 mbsl, pumps off
23	12:56	Pulling T2P uphole
24	13:05	CDS lowered to retracted position
25	13:08	CDS detatched from spacer
26	13:09	T2P detatched from spacer
27	13:09	T2P tip in pressure response chamber
28	13:16	T2P in workroom
29		Battery removed from T2P
30		T2P connected to DC power
31		Data downloaded from data logger

Table A.B7. Event summary of T2P deployment #5, Hole U1324B, 51.3 mbsf, 21-June-2005.

Event #	Time (GMT)	Event Description
1		Data logger started at 1 Hz
2	11:40	T2P on rig floor
3	11:47	Pressure response chamber removed from T2P tip
4	11:47	Shroud in place over T2P tip
5	11:48	T2P connected to spacer
6	11:50	CDS connected to spacer
7	11:55	Start lowering T2P downhole, pumps on
8	12:04	Stop at 515 mbsl, pumps off
9	12:08	Start lowering probe, pumps on
10	12:12	Stop at 768 mbsl, pumps off
11	12:14	Start lowering probe, pumps on
12	12:19	Stop at 1066 mbsl, pumps off
13	12:22	Start lowering probe, pumps on at 18 SPM
14	12:23	Bit is 0.5m off BOH
15	12:24	Start lowering probe to land in BHA
16	12:25	CDS lands in BHA ; pumps off
17	12:25	Raising BHA to 2 m off BOH
18	12:26	Start penetration of T2P into sediment, 2m advance of BHA
19	12:27	End of T2P penetration; bit 0.25 m off BOH
20	12:27	Raising BHA 2m off BOH
21	12:32	Pumping at 11 SPM
22	12:57	Pulling T2P uphole slowly with wireline
23	12:58	CDS clear of BHA
24	13:00	Stop at 1067 mbsl, pumps off
25	13:04	Pulling T2P uphole slowly with wireline
26	13:09	Stop at 767 mbsl, pumps off
27	13:11	Pulling T2P uphole slowly with wireline
28	13:15	Stop at 516 mbsl, pumps off
29	13:17	Pulling T2P uphole slowly with wireline
30	13:25	Wireline disconnected from CDS
31	13:25	CDS extended
32	13:28	CDS disconnected from spacer
33	13:28	Spacer disconnected from CDS
34	13:30	T2P disconnected from spacer
35	13:33	T2P out of pipe
36		Data downloaded from data logger

Table A.B8. Event summary of T2P deployment #6, Hole U1324B, 89.3 mbsf, 21-June-2005.

Event #	Time (GMT)	Event Description
1	14:17:00	Data logger started at 1 Hz
2	16:15:19	T2P on rig floor
3	16:47:09	Start lowering T2P downhole, pumps on
4	16:56:03	Stop at 511 mbsl, pumps off
5	16:57:57	Start lowering probe, pumps on
6	17:03:05	Stop at 761 mbsl, pumps off
7	17:04:57	Start lowering probe, pumps on
8	17:10:14	Stop at 1058 mbsl, pumps off
9	17:16:30	Start lowering probe
10	17:18:50	Stop at 1135 mbsl, pumps off
11	17:20:54	Start lowering probe to land in BHA
12	17:22:56	CDS lands in BHA ; pumps off
13	17:31:02	Start penetration of T2P into sediment
14	17:33:43	End of T2P penetration; bit 1 m off BOH
15	17:36:02	Raising BHA 2m off BOH
16	17:42:09	Pumping at 11 SPM
17	18:08:17	Pulling T2P uphole slowly with wireline
18	18:11:30	CDS clear of BHA
19	18:13:40	Stop at 1058 mbsl, pumps off
20	18:15:47	Pulling T2P uphole slowly with wireline
21	18:18:55	Stop at 760 mbsl, pumps off
22	18:20:52	Pulling T2P uphole slowly with wireline
23	18:23:50	Stop at 511 mbsl, pumps off
24	18:25:46	Pulling T2P uphole slowly with wireline
25	18:31:24	Wireline disconnected from CDS
26	18:32:30	CDS retracted
27	18:35:22	CDS disconnected from spacer
28	18:37:31	Spacer disconnected from CDS
29	18:38:23	T2P out of pipe
30	18:50:30	Data downloaded from data logger

Table A.B9. Event summary of T2P deployment #7, Hole U1324B, 117.8 mbsf, 21-June-2005.

Event #	Time (GMT)	Event Description
1	20:18:00	Data logger started at 1 Hz
2	20:56:13	T2P on rig floor
3	21:07:34	Start lowering T2P downhole, pumps on
4	21:15:37	Stop at 511 mbsl, pumps off
5	21:17:21	Start lowering probe, pumps on
6	21:20:55	Stop at 761 mbsl, pumps off
7	21:22:48	Start lowering probe, pumps on
8	21:26:40	Stop at 1058 mbsl, pumps off
9	21:30:00	Start lowering probe
10	21:33:23	Stop at 1164 mbsl, pumps off
11	21:40:04	Start lowering probe to land in BHA
12	21:44:27	CDS lands in BHA ; pumps off
13	21:47:23	Start penetration of T2P into sediment
14	21:48:41	End of T2P penetration; bit 1 m off BOH
15	21:52:24	Raising BHA 2m off BOH
16	21:58:15	Pumping at 14 SPM
17	22:28:50	Pulling T2P uphole slowly with wireline
18	22:33:15	CDS clear of BHA
19	22:34:00	Stop at 1058 mbsl, pumps off
20	22:36:23	Pulling T2P uphole slowly with wireline
21	22:40:42	Stop at 760 mbsl, pumps off
22	22:42:49	Pulling T2P uphole slowly with wireline
23	22:46:02	Stop at 511 mbsl, pumps off
24	22:48:12	Pulling T2P uphole slowly with wireline
25	22:55:35	Wireline disconnected from CDS
26	22:56:39	CDS retracted
27	22:58:10	CDS disconnected from spacer
28	22:59:55	Spacer disconnected from CDS
29	23:01:00	T2P out of pipe
30	23:08:18	Data downloaded from data logger

Table A.B10. Event summary of T2P deployment #8, Hole U1324B, 136.3 mbsf, 22-June-2005.

Event #	Time (GMT)	Event Description
1	0:28:15	Data logger started at 1 Hz
2	1:45:41	T2P on rig floor
3	1:58:19	Start lowering T2P downhole, pumps on
4	2:08:05	Stop at 511 mbsl, pumps off
5	2:10:10	Start lowering probe, pumps on
6	2:14:29	Stop at 761 mbsl, pumps off
7	2:17:00	Start lowering probe, pumps on
8	2:21:21	Stop at 1058 mbsl, pumps off
9	2:23:35	Start lowering probe
10	2:27:07	Stop at 1151 mbsl, pumps off
11	2:32:50	Start lowering probe
12	2:34:35	Stop at 1181 mbsl, pumps off
13	2:38:25	Start lowering probe
14	2:43:12	CDS lands in BHA ; pumps off
15	2:43:58	Start penetration of T2P into sediment
16	2:44:49	End of T2P penetration; bit at BOH
17	2:45:21	Raising BHA 1.5m off BOH
18	3:16:41	Pulling T2P uphole slowly with wireline
19	3:18:30	CDS clear of BHA
20	3:20:50	Stop at 1058 mbsl, pumps off
21	3:23:50	Pulling T2P uphole slowly with wireline
22	3:27:26	Stop at 761 mbsl, pumps off
23	3:30:25	Pulling T2P uphole slowly with wireline
24	3:33:40	Stop at 511 mbsl, pumps off
25	3:36:00	Pulling T2P uphole slowly with wireline
26	3:42:35	Wireline disconnected from CDS
27	3:45:08	CDS disconnected from spacer
28	3:46:30	Spacer disconnected from CDS
29	3:47:15	T2P out of pipe
30	4:11:00	Data downloaded from data logger

Table A.B11. Event summary of T2P deployment #9, Hole U1324B, 368.0 mbsf, 23-June-2005.

Event #	Time (GMT)	Event Description
1	13:28:29	Data logger started at 1 Hz
2	14:57:35	T2P on rig floor
3	15:11:43	Start lowering T2P downhole, pumps on
4	15:28:24	Stop at 1058 mbsl, pumps off
5	15:33:36	Start lowering probe
6	15:45:14	Stop at 1432 mbsl, pumps off
7	15:49:43	Start lowering probe
8	15:53:27	CDS lands in BHA ; pumps off
9	15:54:10	Start penetration of T2P into sediment
10	15:58:39	End of T2P penetration; bit at BOH
11	15:59:31	Raising BHA 2m off BOH
12	16:40:15	Pulling T2P uphole slowly with wireline
13	16:48:13	Stop at 1058 mbsl, pumps off
14	16:51:35	Pulling T2P uphole slowly with wireline
15	17:01:39	Wireline disconnected from CDS
16	17:04:35	CDS disconnected from spacer
17	17:06:10	Spacer disconnected from CDS
18	17:08:23	T2P out of pipe
19	17:30:00	Data downloaded from data logger

Table A.B12. Event summary of T2P deployment #11, Hole U1324B, 593.2 mbsf, 25-June-2005.

Event #	Time (GMT)	Event Description
1	18:02:00	Data logger started at 1 Hz
2	18:18:13	T2P on rig floor
3	18:31:55	Start lowering T2P downhole, pumps on
4	18:42:00	Stop at 1068 mbsl, pumps off
5	18:45:46	Start lowering probe
6	18:50:23	Stop at 1510 mbsl, pumps off
7	18:56:38	Start lowering probe
8	18:58:11	CDS lands in BHA ; pumps off
9	19:14:02	Pulling T2P uphole slowly with wireline
10	19:25:02	Stop at 1067 mbsl, pumps off
11	19:28:02	Pulling T2P uphole slowly with wireline
12	19:34:27	Wireline disconnected from CDS
13	19:38:21	CDS disconnected from spacer
14	19:40:15	Spacer disconnected from CDS
15	19:46:40	T2P out of pipe
16	20:10:36	Data downloaded from data logger

Table A.B13. Event summary of T2P deployment #12, Hole U1324C, 50.0 mbsf, 26-June-2005.

Event #	Time (GMT)	Event Description
1		Data logger started at 1 Hz
2	10:44:26	T2P on rig floor
3	10:52:56	Start lowering T2P downhole, pumps on
4	11:09:00	Stop at 491 mbsl, pumps off
5	11:11:37	Start lowering probe
6	11:14:13	Stop at 741 mbsl, pumps off
7	11:19:00	Stop at 1057 mbsl, pumps off
8	11:22:09	Stop at 1095 mbsl, pumps off
9	11:28:08	Start lowering probe
10	11:29:20	CDS lands in BHA ; pumps off
11	11:32:50	Start penetration of T2P into sediment
12	11:40:35	End of T2P penetration; bit on BOH
13	11:40:36	Raising BHA 4.5m off BOH
14	12:41:05	Pulling T2P uphole slowly with wireline
15	12:44:52	Stop at 1057 mbsl, pumps off
16	12:48:00	Pulling T2P uphole slowly with wireline
17	12:54:09	Stop at 741 mbsl, pumps off
18	12:56:09	Pulling T2P uphole slowly with wireline
19	13:00:57	Stop at 491 mbsl, pumps off
20	13:02:57	Pulling T2P uphole slowly with wireline
21		Data downloaded from data logger

Table A.B14. Event summary of T2P deployment #13, Hole U1324C, 100.0 mbsf, 26-June-2005.

Event #	Time (GMT)	Event Description
1	14:42:47	Data logger started at 1 Hz
2	16:18:30	T2P on rig floor
3	16:28:42	Start lowering T2P downhole, pumps on
4	16:44:22	Stop at 741 mbsl, pumps off
5	16:46:30	Start lowering probe
6	16:52:33	Stop at 1057 mbsl, pumps off
7	16:54:39	Start lowering probe
8	17:03:38	CDS lands in BHA ; pumps off
9	17:04:34	Start penetration of T2P into sediment
10	17:05:22	End of T2P penetration; bit 1 m off BOH
11	17:06:00	Raising BHA 2m off BOH
12	18:08:10	Pulling T2P uphole slowly with wireline
13	18:11:22	Stop at 1057 mbsl, pumps off
14	18:13:30	Pulling T2P uphole slowly with wireline
15	18:17:18	Stop at 741 mbsl, pumps off
16	18:19:36	Pulling T2P uphole slowly with wireline
17	18:22:53	Stop at 491 mbsl, pumps off
18	18:24:29	Pulling T2P uphole slowly with wireline
19	18:30:32	Wireline disconnected from CDS
20	18:34:39	CDS disconnected from spacer
21	18:36:28	Spacer disconnected from CDS
22	18:36:28	T2P out of pipe
23		Data downloaded from data logger

Table A.B15. Event summary of T2P deployment #14, Hole U1324C, 150.0 mbsf, 26-June-2005.

Event #	Time (GMT)	Event Description
1		Data logger started at 1 Hz
2	21:28:16	Stop at 491 mbsl, pumps off
3	21:30:16	Start lowering probe
4	21:35:17	Stop at 741 mbsl, pumps off
5	21:37:29	Start lowering probe
6	21:43:36	Stop at 1057 mbsl, pumps off
7	21:45:49	Start lowering probe
8	21:49:31	Stop at 1195 mbsl, pumps off
9	21:52:07	Start lowering probe
10	21:55:00	CDS lands in BHA ; pumps off
11	21:56:30	Start penetration of T2P into sediment
12	21:57:25	End of T2P penetration; bit on BOH
13	21:57:44	Raising BHA 2.5m off BOH
14	23:02:47	Pulling T2P uphole slowly with wireline
15	23:09:44	Stop at 1057 mbsl, pumps off
16	23:14:53	Pulling T2P uphole slowly with wireline
17	23:18:53	Stop at 741 mbsl, pumps off
18	23:21:27	Pulling T2P uphole slowly with wireline
19	23:24:07	Stop at 491 mbsl, pumps off
20	23:26:07	Pulling T2P uphole slowly with wireline
21		Data downloaded from data logger

Table A.B16. Event summary of T2P deployment #15, Hole U1324C, 200.0 mbsf, 27-June-2005.

Event #	Time (GMT)	Event Description
1	0:49:19	Data logger started at 1 Hz
2	1:56:31	T2P on rig floor
3	2:09:04	Start lowering T2P downhole, pumps on
4	2:17:40	Stop at 491 mbsl, pumps off
5	2:19:52	Start lowering probe
6	2:24:36	Stop at 741 mbsl, pumps off
7	2:26:51	Start lowering probe
8	2:32:55	Stop at 1057 mbsl, pumps off
9	2:35:34	Start lowering probe
10	2:40:23	Stop at 1245 mbsl, pumps off
11	2:43:42	Start lowering probe
12	2:47:37	CDS lands in BHA ; pumps off
13	2:48:02	Start penetration of T2P into sediment
14	2:49:28	End of T2P penetration; bit 1 m off BOH
15	2:52:20	Raising BHA 4.5m off BOH
16	3:53:17	Pulling T2P uphole slowly with wireline
17	3:56:56	Stop at 1057 mbsl, pumps off
18	3:59:23	Pulling T2P uphole slowly with wireline
19	4:02:52	Stop at 741 mbsl, pumps off
20	4:05:07	Pulling T2P uphole slowly with wireline
21	4:07:56	Stop at 491 mbsl, pumps off
22	4:10:05	Pulling T2P uphole slowly with wireline
23	4:15:55	Wireline disconnected from CDS
24	4:17:54	CDS disconnected from spacer
25	4:19:43	Spacer disconnected from CDS
26	4:21:51	T2P out of pipe
27		Data downloaded from data logger

Table A.B17. Event summary of T2P deployment #16, Hole U1324C, 300.0 mbsf, 27-June-2005.

Event #	Time (GMT)	Event Description
1		Data logger started at 1 Hz
2	11:18:00	Start lowering T2P downhole, pumps on
3	11:37:22	Stop at 491 mbsl, pumps off
4	11:39:35	Start lowering probe
5	11:43:21	Stop at 741 mbsl, pumps off
6	11:45:21	Start lowering probe
7	11:49:33	Stop at 1057 mbsl, pumps off
8	11:52:30	Start lowering probe
9	11:57:30	Stop at 1345 mbsl, pumps off
10	11:59:30	Start lowering probe
11	12:05:15	Start penetration of T2P into sediment
12	12:17:12	End of T2P penetration; bit on BOH
13	12:22:15	Raising BHA 4m off BOH
14	13:47:24	Pulling T2P uphole slowly with wireline
15	13:54:09	Stop at 1057 mbsl, pumps off
16	13:57:00	Pulling T2P uphole slowly with wireline
17	14:02:33	Stop at 741 mbsl, pumps off
18	14:04:30	Pulling T2P uphole slowly with wireline
19	14:09:10	Stop at 491 mbsl, pumps off
20	14:11:10	Pulling T2P uphole slowly with wireline
21		Data downloaded from data logger

Table A.B18. Event summary of T2P deployment #17, Hole U1322B, 42.0 mbsf, 28-June-2005.

Event #	Time (GMT)	Event Description
1	18:39:55	Data logger started at 1 Hz
2	20:10:31	T2P on rig floor
3	20:22:12	Start lowering T2P downhole, pumps on
4	20:29:54	Stop at 491 mbsl, pumps off
5	20:31:58	Start lowering probe
6	20:35:04	Stop at 741 mbsl, pumps off
7	20:37:04	Start lowering probe
8	20:43:20	Stop at 1321 mbsl, pumps off
9	20:46:30	Start lowering probe
10	20:48:58	Stop at 1351 mbsl, pumps off
11	20:50:55	Start lowering probe
12	20:57:30	CDS lands in BHA ; pumps off
13	20:57:49	Start penetration of T2P into sediment
14	21:00:31	End of T2P penetration; bit on BOH
15	21:00:37	Raising BHA 4.0m off BOH
16	22:07:42	Pulling T2P uphole slowly with wireline
17	22:10:32	Stop at 1321 mbsl, pumps off
18	22:13:27	Pulling T2P uphole slowly with wireline
19	22:19:47	Stop at 741 mbsl, pumps off
20	22:21:57	Pulling T2P uphole slowly with wireline
21	22:26:12	Stop at 491 mbsl, pumps off
22	22:28:28	Pulling T2P uphole slowly with wireline
23	22:32:54	Wireline disconnected from CDS
24	22:35:38	CDS disconnected from spacer
25	22:37:15	Spacer disconnected from CDS
26	22:38:00	T2P out of pipe
27		Data downloaded from data logger

Table A.B19. Event summary of T2P deployment #19, Hole U1322B, 134.3 mbsf, 29-June-2005.

Event #	Time (GMT)	Event Description
1		Data logger started at 1 Hz
2	12:30:53	Start lowering T2P downhole, pumps on
3	12:36:29	Stop at 491 mbsl, pumps off
4	12:38:38	Start lowering probe
5	12:44:32	Stop at 741 mbsl, pumps off
6	12:46:30	Start lowering probe
7	13:03:56	Stop at 1321 mbsl, pumps off
8	13:07:17	Start lowering probe
9	13:34:36	Stop at 1443 mbsl, pumps off
10	13:36:23	Start lowering probe
11	13:41:16	CDS lands in BHA ; pumps off
12	13:52:56	Start penetration of T2P into sediment
13	13:54:18	End of T2P penetration; bit on BOH
14	13:54:18	Raising BHA 4.0m off BOH
15	14:25:47	Pulling T2P uphole slowly with wireline
16	14:29:38	Stop at 1321 mbsl, pumps off
17	14:31:25	Pulling T2P uphole slowly with wireline
18	14:40:06	Stop at 741 mbsl, pumps off
19	14:41:40	Pulling T2P uphole slowly with wireline
20	14:46:08	Stop at 491 mbsl, pumps off
21	14:47:40	Pulling T2P uphole slowly with wireline
22		Data downloaded from data logger

Table A.B20. Event summary of T2P deployment #20, Hole U1322B, 157.8 mbsf, 29-June-2005.

Event #	Time (GMT)	Event Description
1		Data logger started at 1 Hz
2	18:15:52	T2P on rig floor
3	18:38:28	Start lowering T2P downhole, pumps on
4	18:46:30	Stop at 491 mbsl, pumps off
5	18:49:40	Start lowering probe
6	18:54:04	Stop at 741 mbsl, pumps off
7	18:57:00	Start lowering probe
8	19:05:42	Stop at 1321 mbsl, pumps off
9	19:08:33	Start lowering probe
10	19:13:48	Stop at 1467 mbsl, pumps off
11	19:19:02	Start lowering probe
12	19:36:51	CDS lands in BHA ; pumps off
13	19:36:52	Start penetration of T2P into sediment
14	19:37:39	End of T2P penetration; bit on BOH
15	19:37:50	Raising BHA 4.0m off BOH
16	20:43:13	Pulling T2P uphole slowly with wireline
17	21:10:30	Wireline disconnected from CDS
18	21:13:15	CDS disconnected from spacer
19	21:14:30	Spacer disconnected from CDS
20	22:15:00	T2P out of pipe
21		Data downloaded from data logger

Table A.B21. Event summary of T2P deployment #23, Hole U1322C, 150.0 mbsf, 01-July-2005.

Event #	Time (GMT)	Event Description
1		Data logger started at 1 Hz
2	6:51:00	T2P on rig floor
3	7:01:01	Start lowering T2P downhole, pumps on
4	7:09:59	Stop at 491 mbsl, pumps off
5	7:12:10	Start lowering probe
6	7:17:10	Stop at 741 mbsl, pumps off
7	7:19:30	Start lowering probe
8	7:29:29	Stop at 1321 mbsl, pumps off
9	7:43:31	Start lowering probe
10	7:52:12	Stop at 1459 mbsl, pumps off
11	7:54:02	Start lowering probe
12	7:58:21	CDS lands in BHA ; pumps off
13	7:58:31	Start penetration of T2P into sediment
14	8:02:56	End of T2P penetration; bit 1m off BOH
15	8:03:30	Raising BHA 4.0m off BOH
16	9:05:35	Pulling T2P uphole slowly with wireline
17	9:12:44	Stop at 1321 mbsl, pumps off
18	9:14:59	Pulling T2P uphole slowly with wireline
19	9:24:45	Stop at 741 mbsl, pumps off
20	9:26:45	Pulling T2P uphole slowly with wireline
21	9:32:17	Stop at 491 mbsl, pumps off
22	9:34:17	Pulling T2P uphole slowly with wireline
23		Data downloaded from data logger

Table A.B22. Event summary of T2P deployment #24, Hole U1322C, 200.0 mbsf, 01-July-2005.

Event #	Time (GMT)	Event Description
1	12:01:05	Stop at 491 mbsl for 2 minutes
2	12:08:10	Stop at 741 mbsl for 2.5 minutes
3	12:22:19	Stop at 1321 mbsl for 3 minutes
4	12:26:50	Stop at 1367 mbsl for 7 minutes
5	12:39:36	Stop at 1509 mbsl, pumps off
6	12:12:23	Start lowering probe
7	12:48:14	CDS lands in BHA
8	12:49:52	Lowering BHA; start penetration
9	12:51:15	End of T2P penetration; bit 1m off BOH
10	12:51:44	Raising BHA 5m off BOH
11	13:51:30	Pulling T2P uphole slowly with wireline
12	13:57:55	Stop at 1321 mbsl for 2.5 minutes, pumps off
13	14:09:04	Stop at 741 mbsl for 2 minutes, pumps off
14	14:14:50	Stop at 491 mbsl for 3 minutes, pumps off
15	14:16:37	Pulling T2P uphole slowly with wireline

Table A.B23. Event summary of T2P deployment #25, Hole U1322D, 40.0 mbsf, 02-July-2005.

Event #	Time (GMT)	Event Description
1		Data logger started at 1 Hz
2	2:06:25	Start lowering T2P downhole, pumps on
3	2:14:56	Stop at 491 mbsl, pumps off
4	2:21:58	Stop at 741 mbsl, pumps off
5	2:32:58	Stop at 1321 mbsl, pumps off
6	2:38:36	Stop at 1349 mbsl, pumps off
7	2:40:40	Start lowering probe
8	2:45:08	CDS lands in BHA ; pumps off
9	2:46:36	Start penetration of T2P into sediment
10	2:46:51	End of T2P penetration; bit 0.8m off BOH
11	2:46:56	Raising BHA 4.0m off BOH
12	3:49:19	Pulling T2P uphole slowly with wireline
13	3:52:54	Stop at 1321 mbsl, pumps off
14	3:55:26	Pulling T2P uphole slowly with wireline
15	4:02:38	Stop at 741 mbsl, pumps off
16	4:04:48	Pulling T2P uphole slowly with wireline
17	4:08:33	Stop at 491 mbsl, pumps off
18	4:10:41	Pulling T2P uphole slowly with wireline
19		Data downloaded from data logger

Table A.B24. Event summary of T2P deployment #26, Hole U1322D, 70.0 mbsf, 02-July-2005.

Event #	Time (GMT)	Event Description
1		Data logger started at 1 Hz
2	6:32:00	T2P on rig floor
3	6:56:53	Stop at 741 mbsl, pumps off
4	7:07:51	Stop at 1321 mbsl, pumps off
5	7:18:15	Stop at 1386 mbsl, pumps off
6	7:20:27	Start lowering probe
7	7:24:50	CDS lands in BHA ; pumps off
8	7:26:47	Start penetration of T2P into sediment
9	7:27:48	End of T2P penetration; bit 0.8m off BOH
10	7:27:54	Raising BHA 4.0m off BOH
11	8:14:30	Pulling T2P uphole slowly with wireline
12	8:16:29	Stop at 1321 mbsl, pumps off
13	8:26:26	Stop at 741 mbsl, pumps off
14	8:32:09	Stop at 491 mbsl, pumps off
15		Data downloaded from data logger

Table A.B25. Event summary of T2P deployment #27, Hole U1322D, 100.0 mbsf, 02-July-2005.

Event #	Time (GMT)	Event Description
1		Data logger started at 1 Hz
2	11:04:50	Stop at 491 mbsl, pumps off
3	11:15:50	Stop at 741 mbsl, pumps off
4	11:15:56	Stop at 1321 mbsl, pumps off
5	11:24:06	Stop at 1409 mbsl, pumps off
6	11:26:27	Start lowering probe
7	11:29:25	CDS lands in BHA ; pumps off
8	11:29:26	Start penetration of T2P into sediment
9	11:30:20	End of T2P penetration; bit 0.8m off BOH
10	11:30:25	Raising BHA 4.0m off BOH
11	12:16:01	Pulling T2P uphole slowly with wireline
12	12:19:11	Stop at 1321 mbsl, pumps off
13	12:28:55	Stop at 741 mbsl, pumps off
14	12:35:10	Stop at 491 mbsl, pumps off
15		Data downloaded from data logger

Table A.B26. Event summary of T2P deployment #28, Hole U1322D, 134.0 mbsf, 02-July-2005.

Event #	Time (GMT)	Event Description
1		Data logger started at 1 Hz
2	14:52:35	T2P on rig floor
3	15:10:03	Stop at 491 mbsl, pumps off
4	15:12:03	Start lowering probe
5	15:15:00	Stop at 741 mbsl, pumps off
6	15:16:15	Start lowering probe
7		Data downloaded from data logger

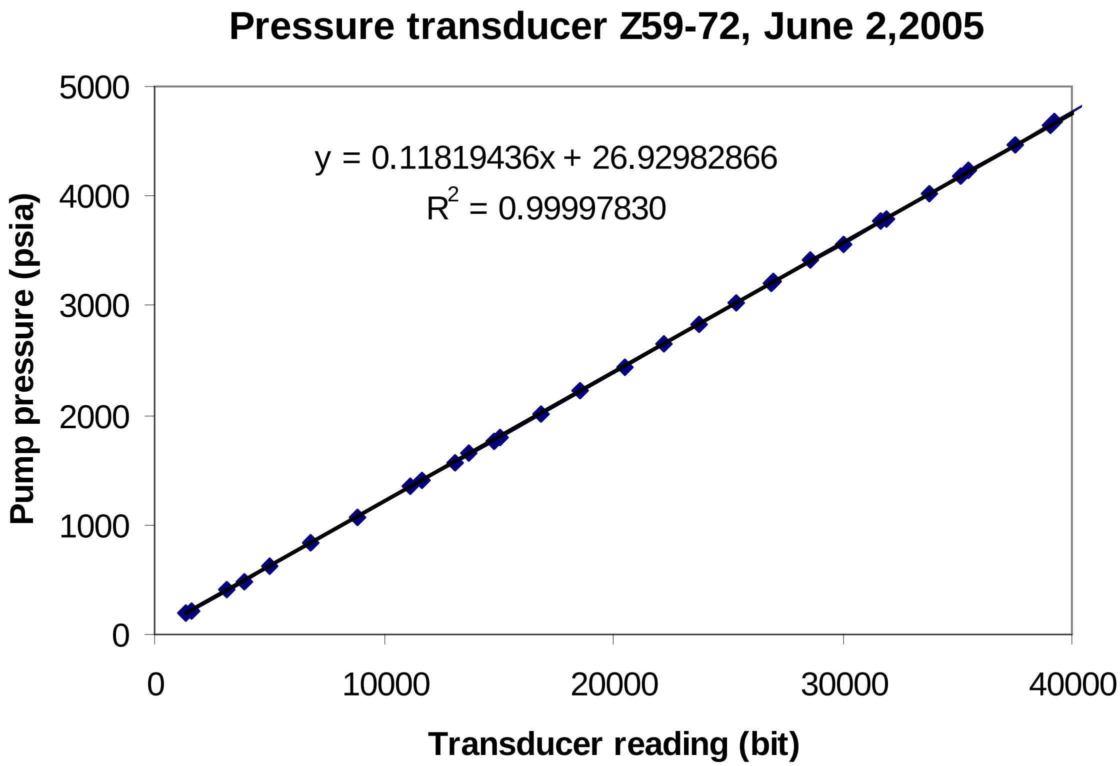

Figure A.B.1: Onboard pressure calibration of transducer Z59-72. The pump pressure run up to 4000 psi from atmosphere pressure and then stepped down to atmosphere pressure.

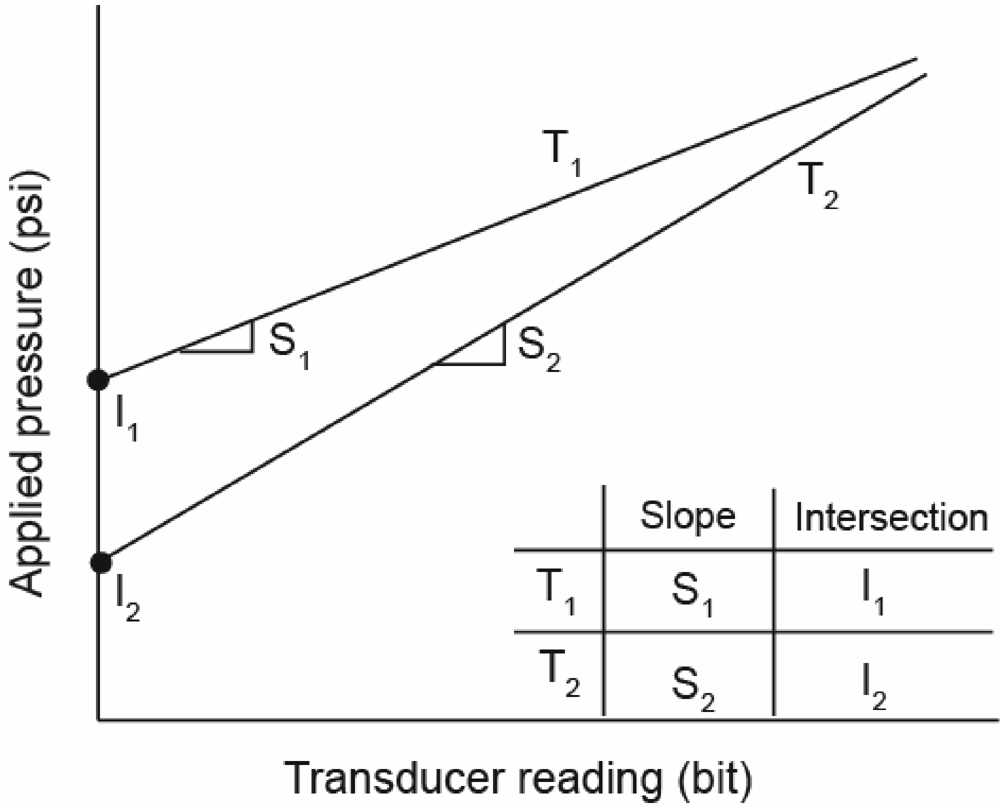

	Slope	Intersection
T_1	S_1	I_1
T_2	S_2	I_2

Figure A.B.2: Influence of temperature on T2P pressure transducers. The slope and intersection of the calibration curve can change with temperature.

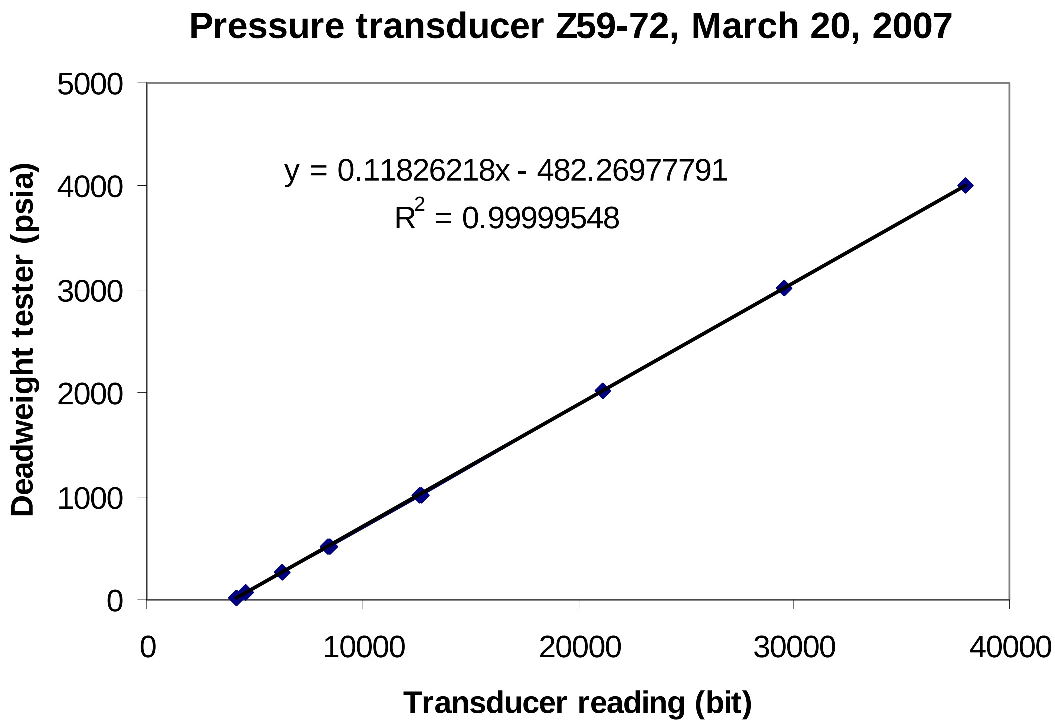

Figure A.B.3: Post-cruise pressure calibration of transducer Z59-72. The calibration was done at 19.976 °C in a temperature bath. The deadweight tester run up to 4015 psi from atmosphere pressure and then stepped down to atmosphere pressure.

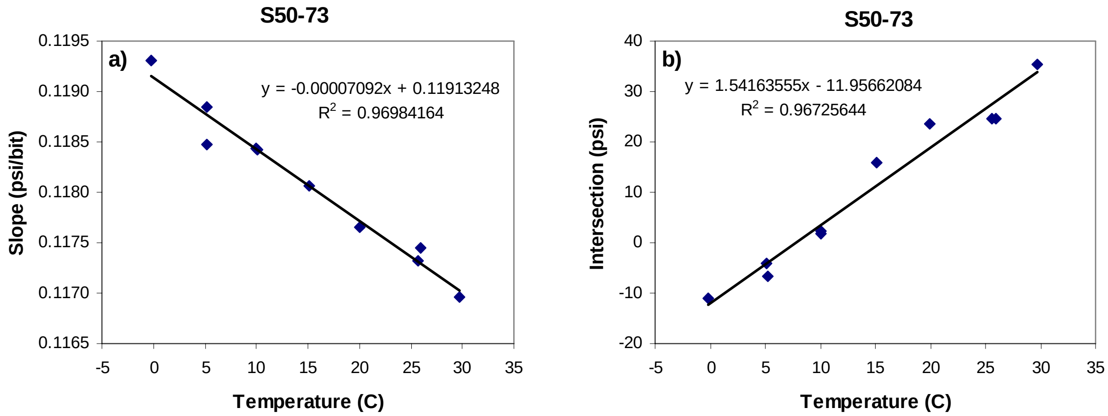

Figure A.B.4: Calibration coefficients of transducer S50-73 vs. temperature. A) The slope of the calibration curve vs. temperature. B) The intersection on y-axis of the calibration curve vs. temperature.

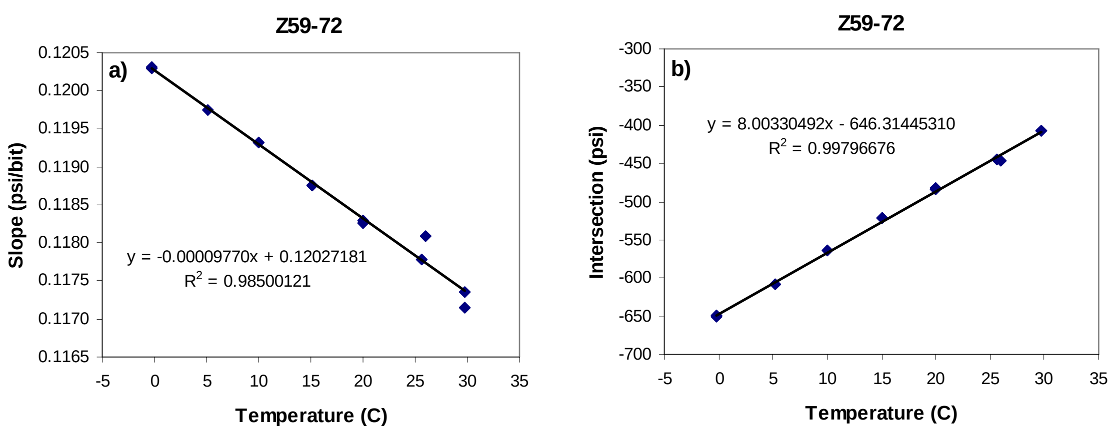

Figure A.B.5: Calibration coefficients of transducer Z59-72 vs. temperature. A) The slope of the calibration curve vs. temperature. b) The intersection on y-axis of the calibration curve vs. temperature.

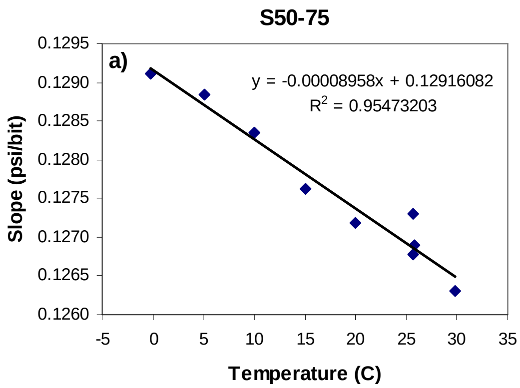

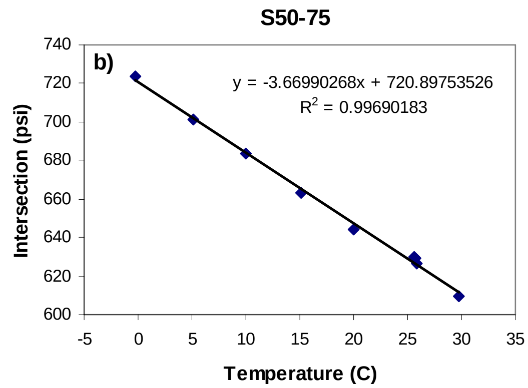

Figure A.B.6 : Calibration coefficients of transducer S50-75 vs. temperature. a) The slope of the calibration curve vs. temperature. b) The intersection on y-axis of the calibration curve vs. temperature.

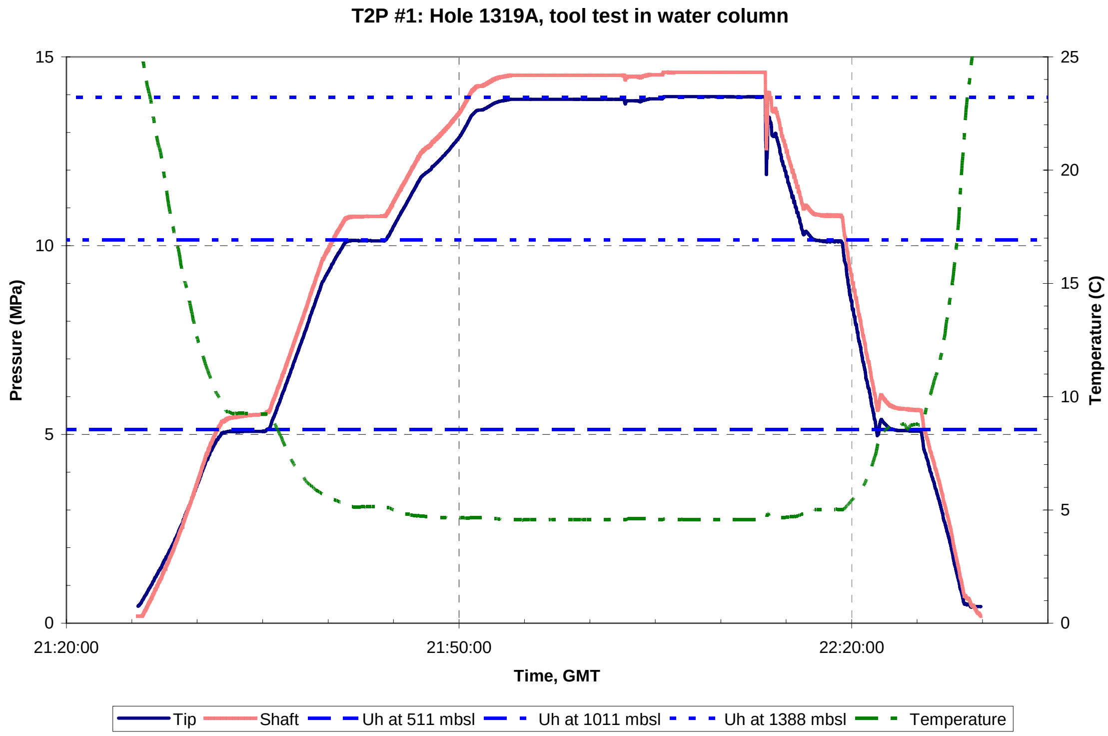

Figure A.B.7.a: T2P deployment #1: pressure test in water column. Transducer S50-73 measures the tip pressure. Transducer Z59-72 measures the shaft pressure. GMT = Greenwich Mean Time. a) pressure data calculated using the calibration coefficients from the onboard pressure calibration (Table A.B.2). b) pressure data calculated using the calibration coefficients interpreted from the post-cruise pressure calibration (Figure A.B.4 and A.B.5). c) Correction of shift of the intersection on y-axis due to oven drying: the tip pressure (Figure A.B.7.b) was added 0.25 MPa and the shaft pressure (Figure A.B.7.b) was added 3.57 MPa to match the hydrostatic pressure at the tool stops.

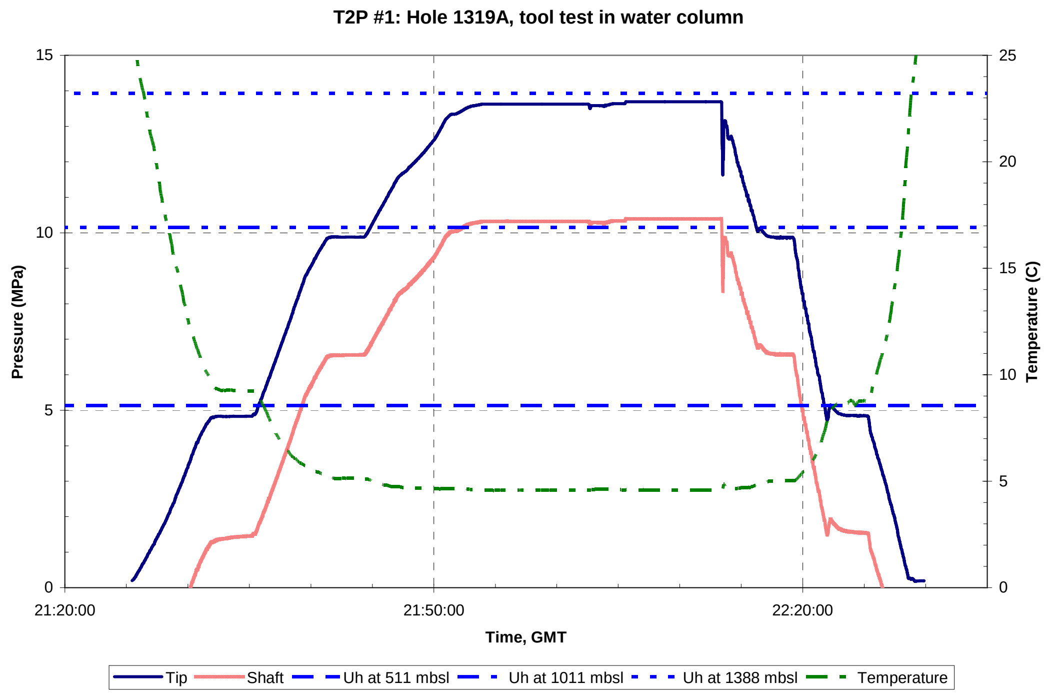

Figure A.B.7.b

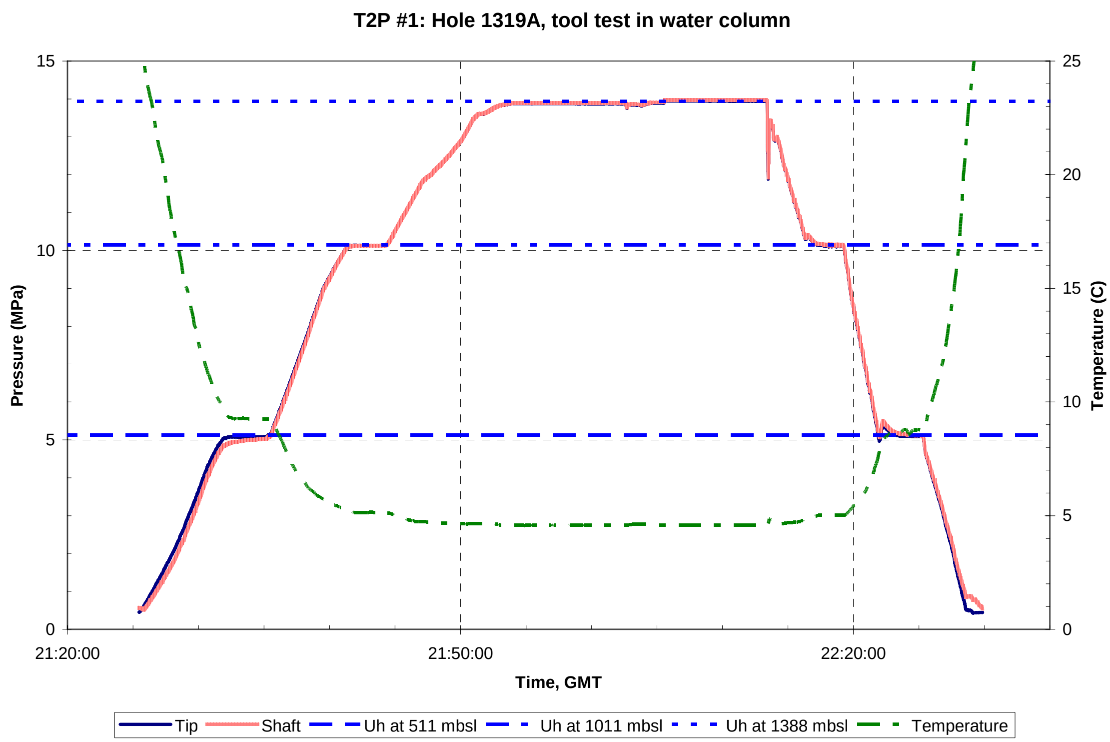

Figure A.B.7.c

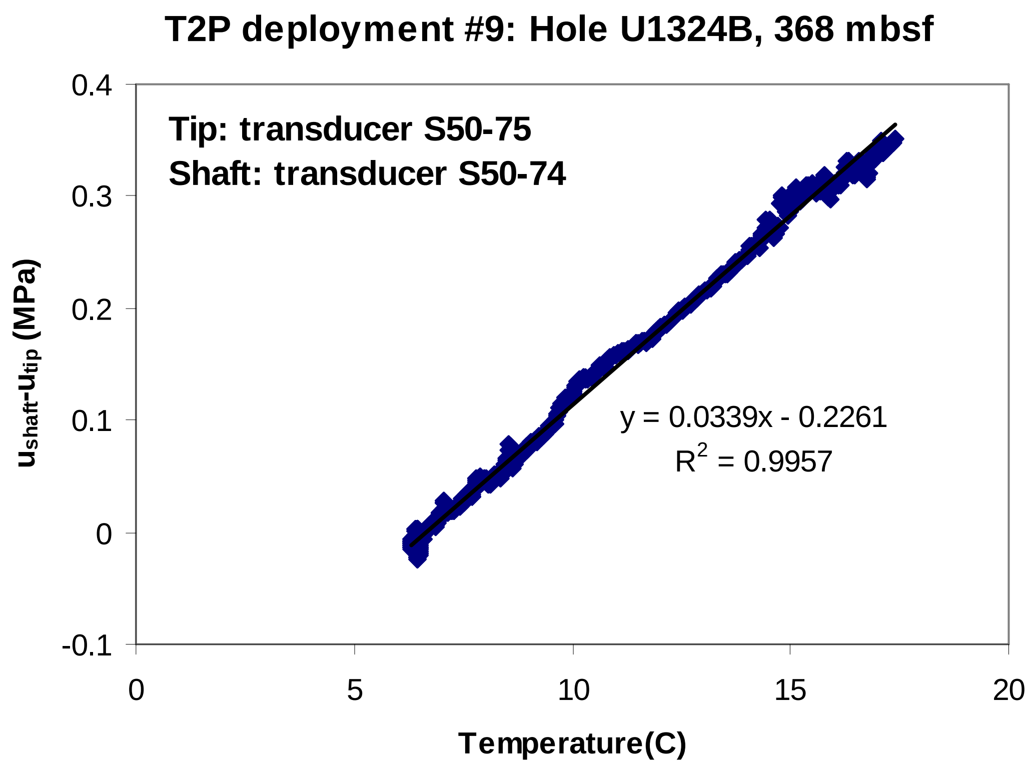

Figure A.B.8: Pressure difference between the tip pressure and shaft pressure for T2P Deployment #9, Hole U1324B, 368 mbsf. The tip pressure was calibrated using the post-cruise calibration data of transducer S50-75. The shaft pressure was calibrated using the onboard calibration factors of transducer S50-74. The tip and shaft pressures prior to penetration were used.

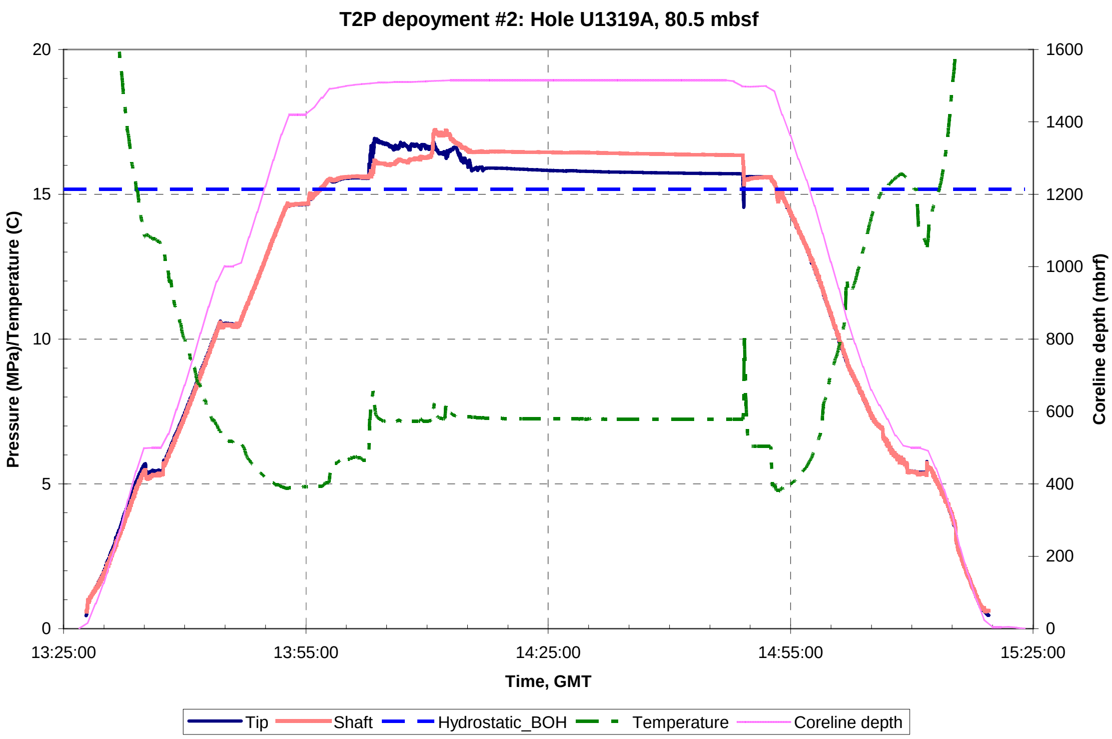

Figure A.B.9.a: Pressure, temperature and Truview data for T2P deployment #2, Hole U1319A, 80.5 mbsf. GMT = Greenwich Mean Time, Hydrostatic_BOH is the hydrostatic pressure at the bottom of the hole.

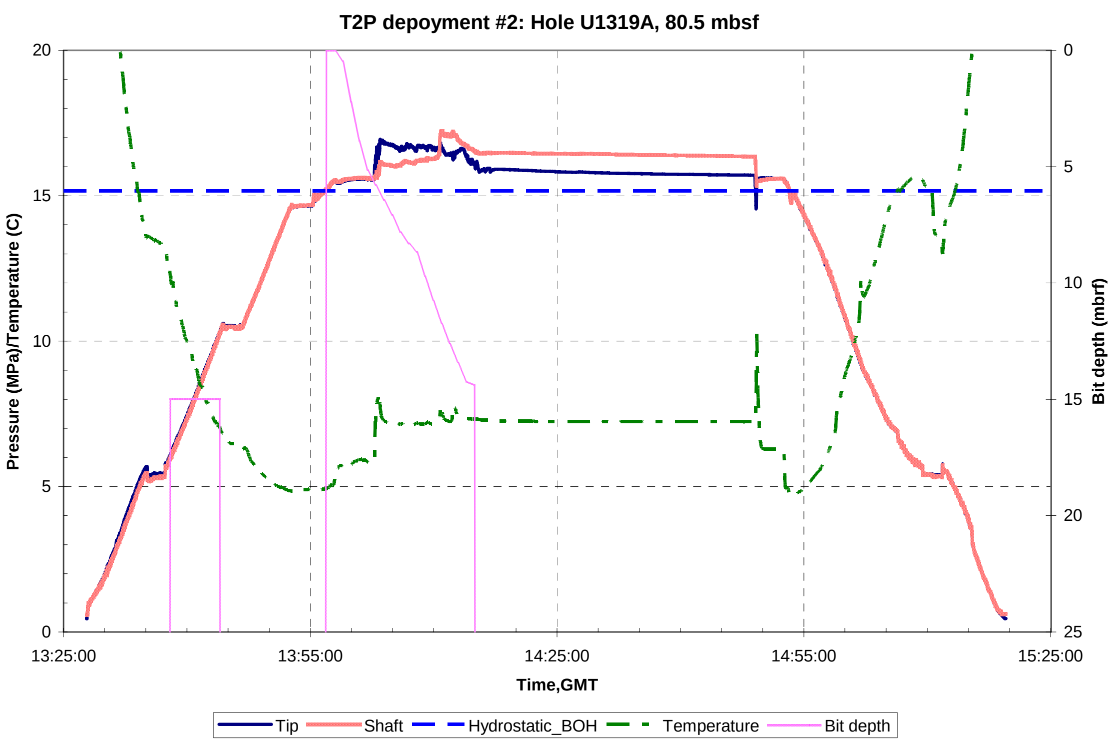

Figure A.B.9.b

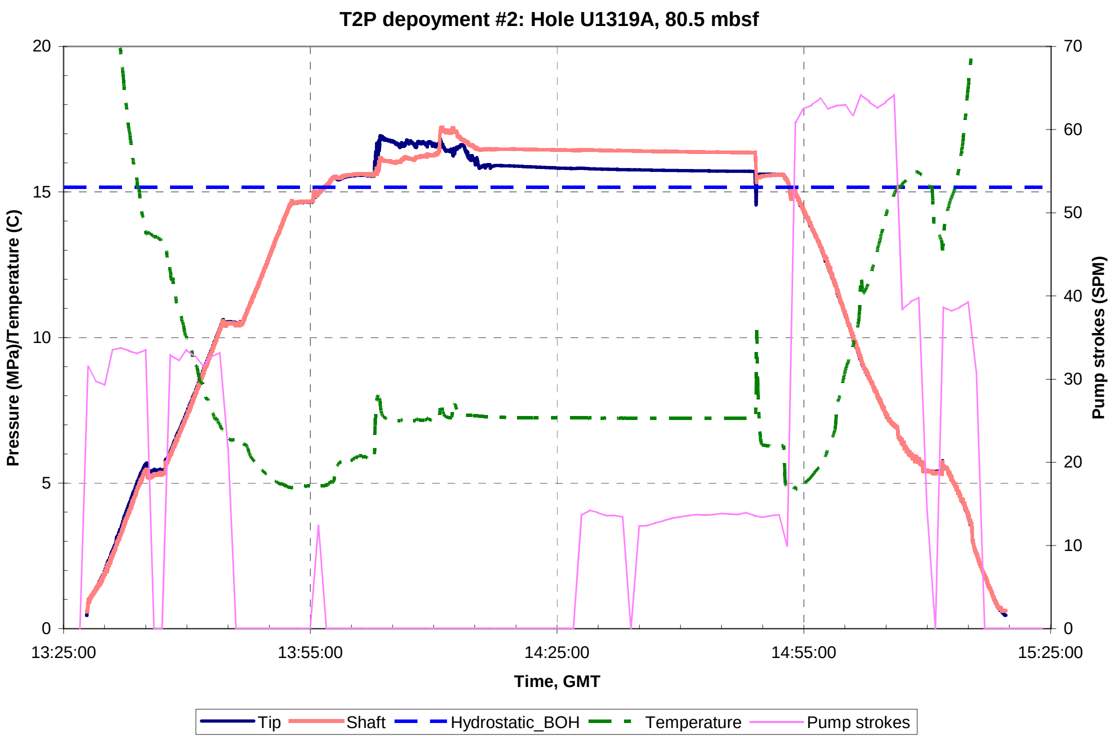

Figure A.B.9.c

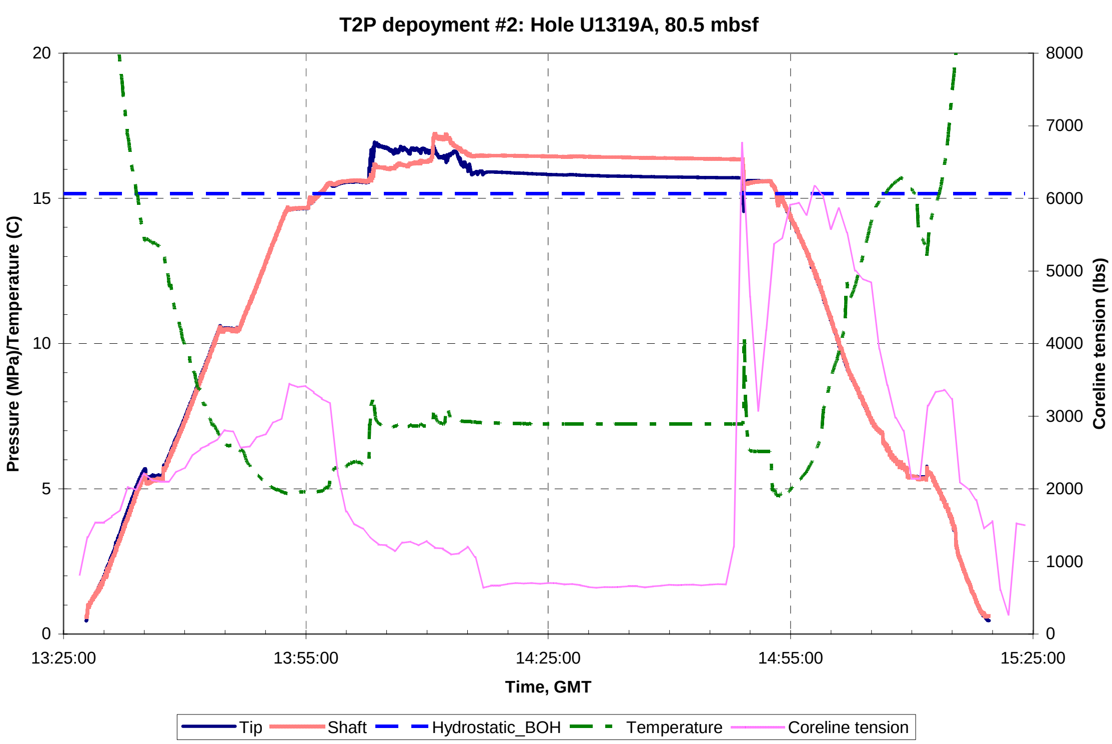

Figure A.B.9.d

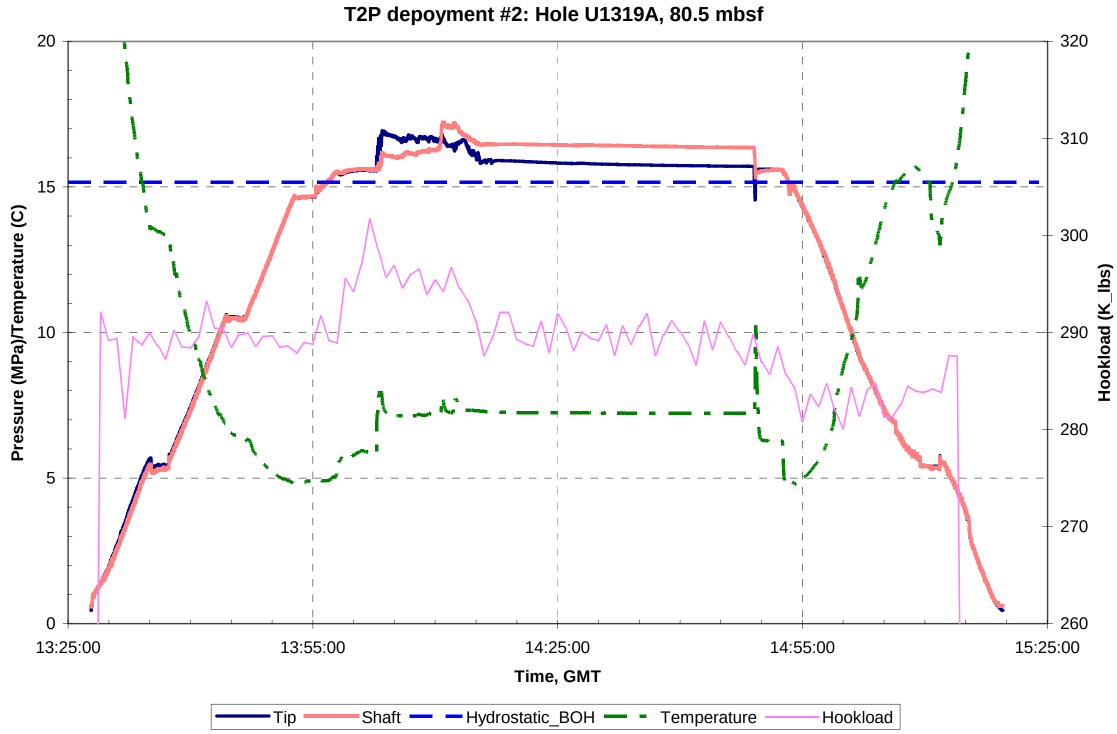

Figure A.B.9.e

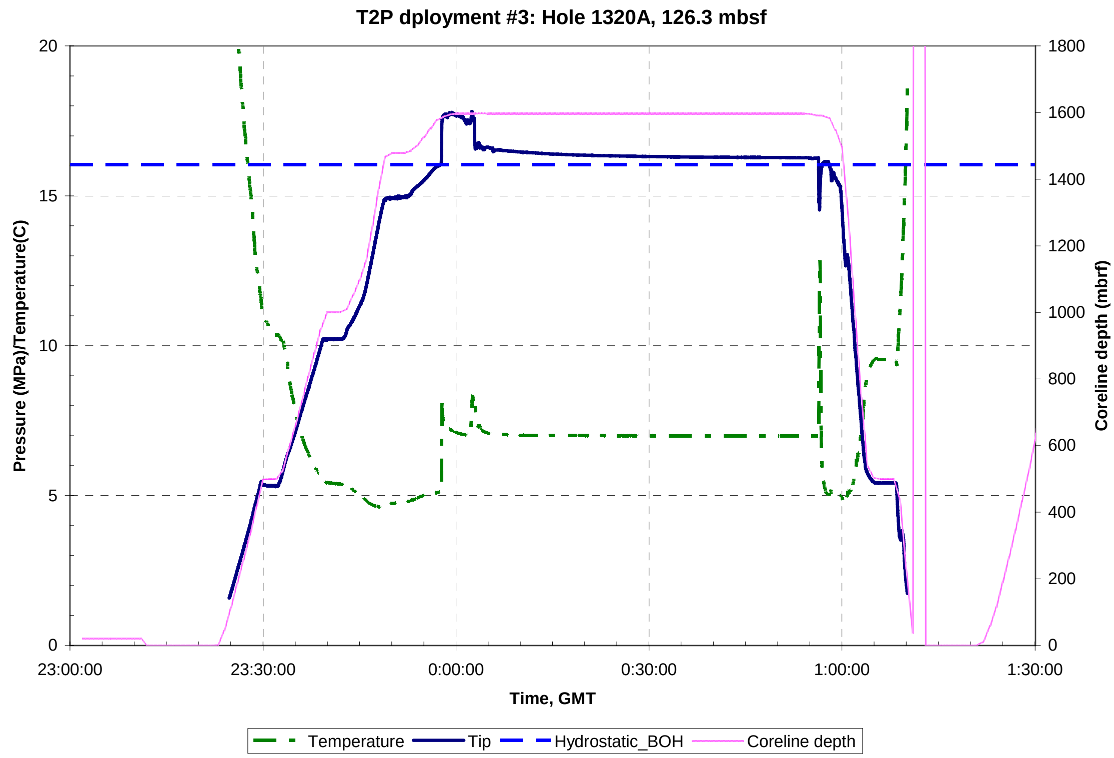

Figure A.B.10.a: Pressure, temperature and Truview data for T2P deployment #3, Hole U1320A, 126.3 mbsf. GMT = Greenwich Mean Time, Hydrostatic_BOH is the hydrostatic pressure at the bottom of the hole.

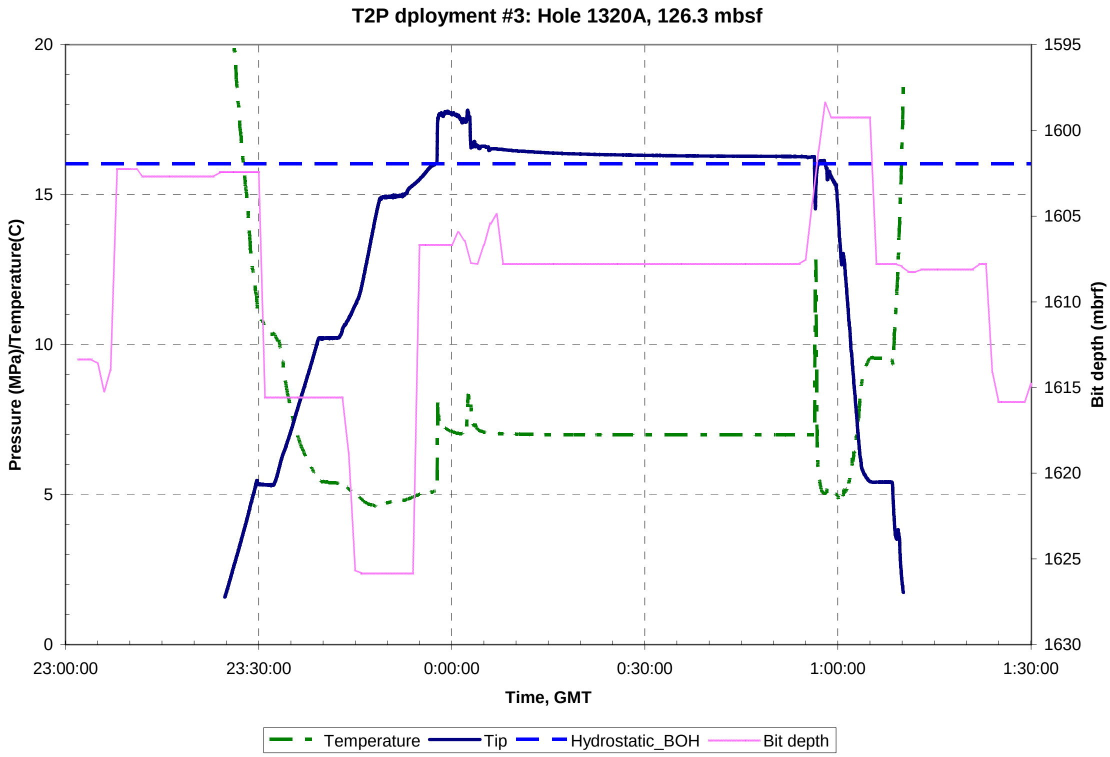

Figure A.B.10.b

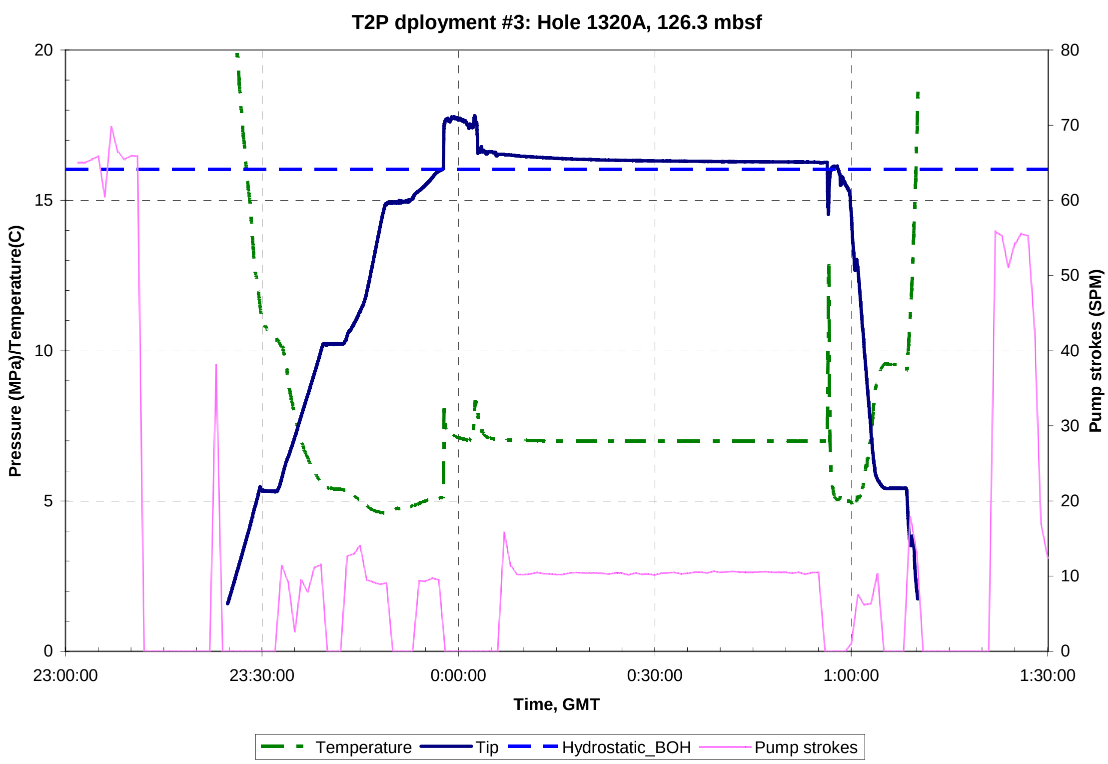

Figure A.B.10.c

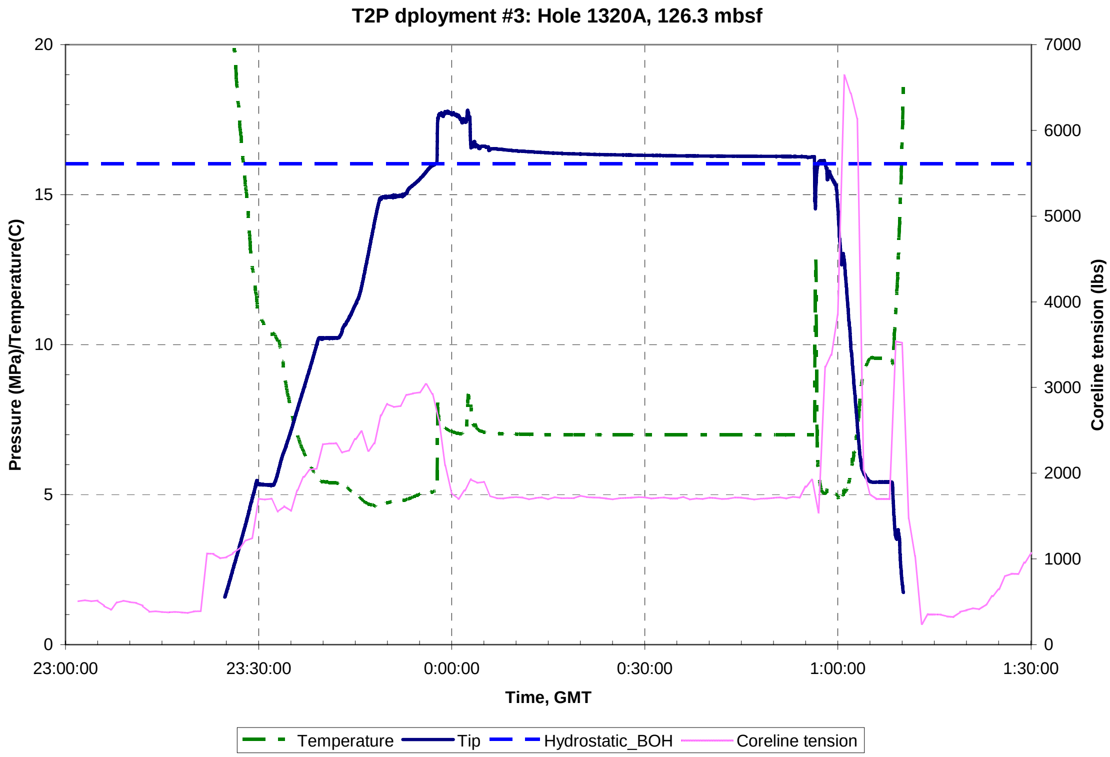

Figure A.B.10.d

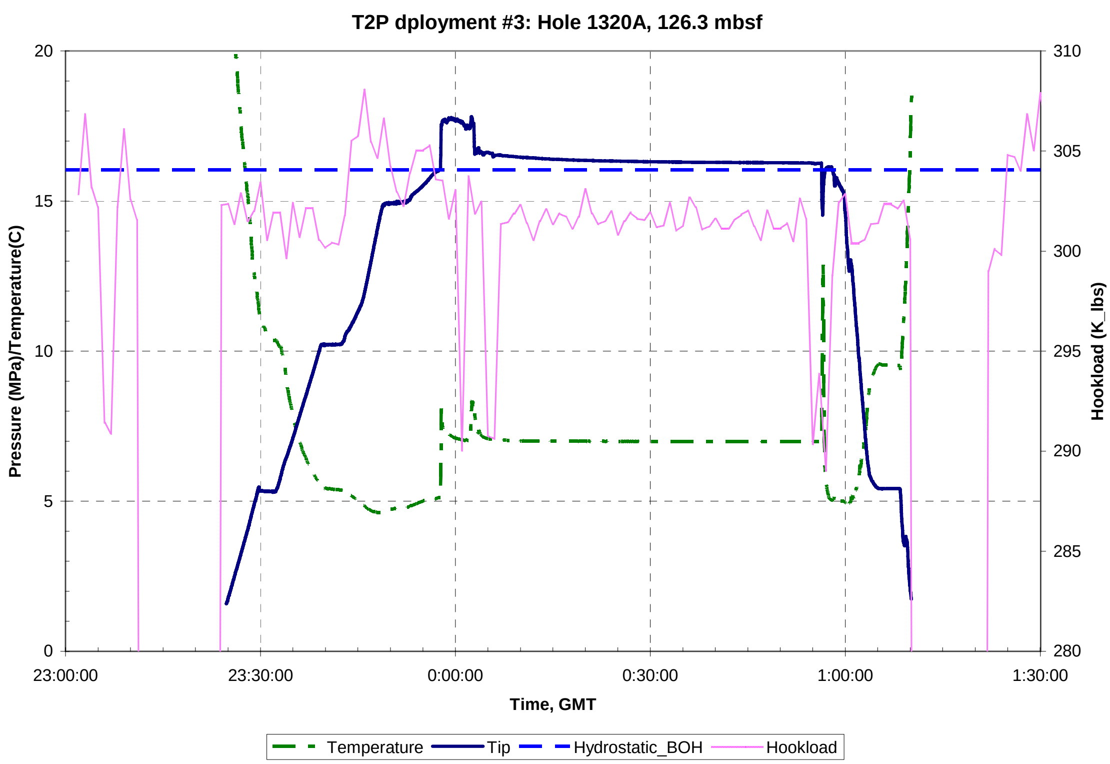

Figure A.B.10.e

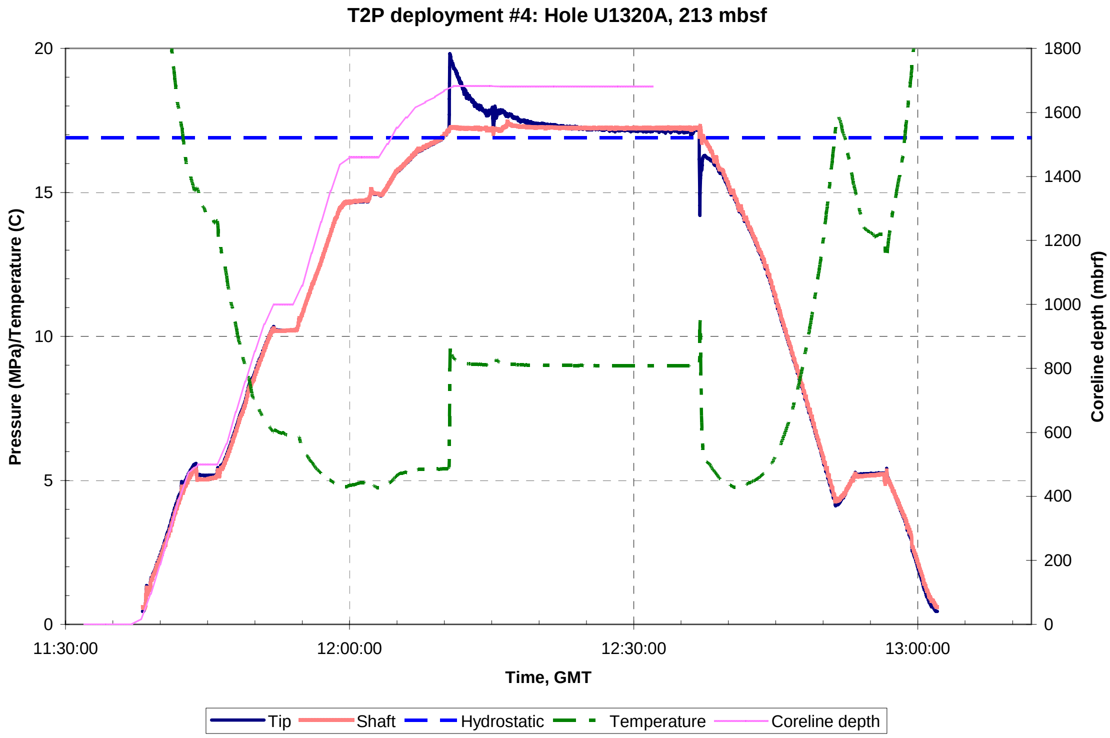

Figure A.B.11.a: Pressure, temperature and Truview data for T2P deployment #4, Hole U1320A, 213 mbsf. GMT = Greenwich Mean Time, Hydrostatic_BOH is the hydrostatic pressure at the bottom of the hole.

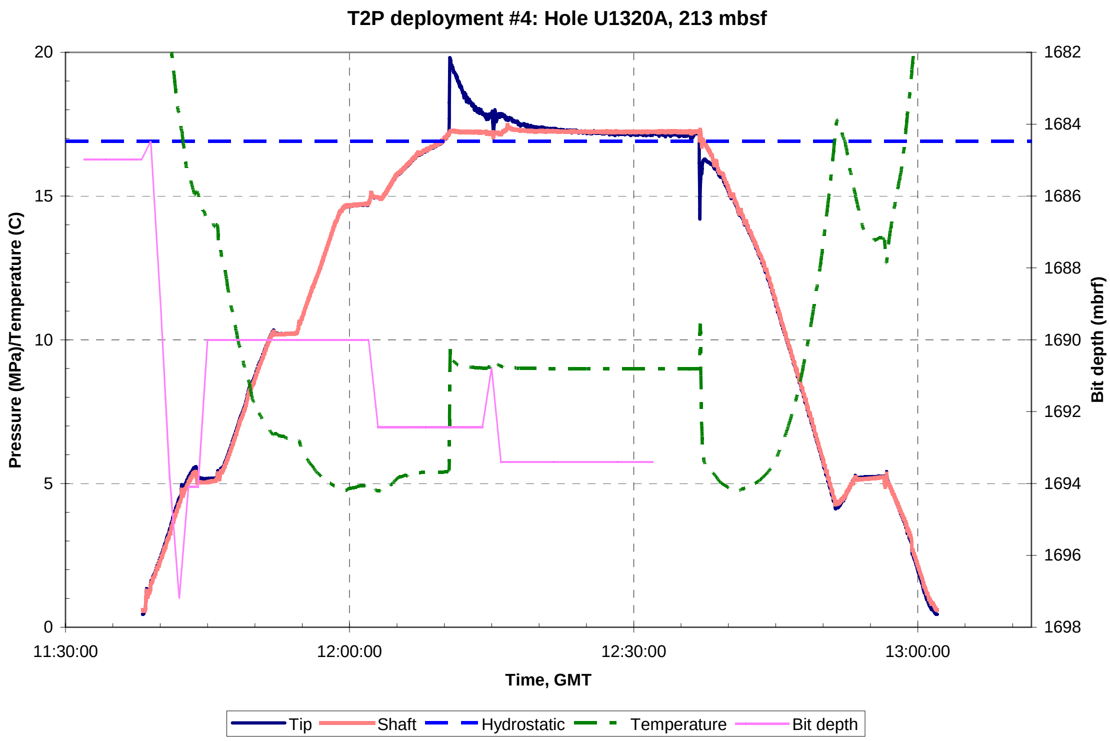

Figure A.B.11.b

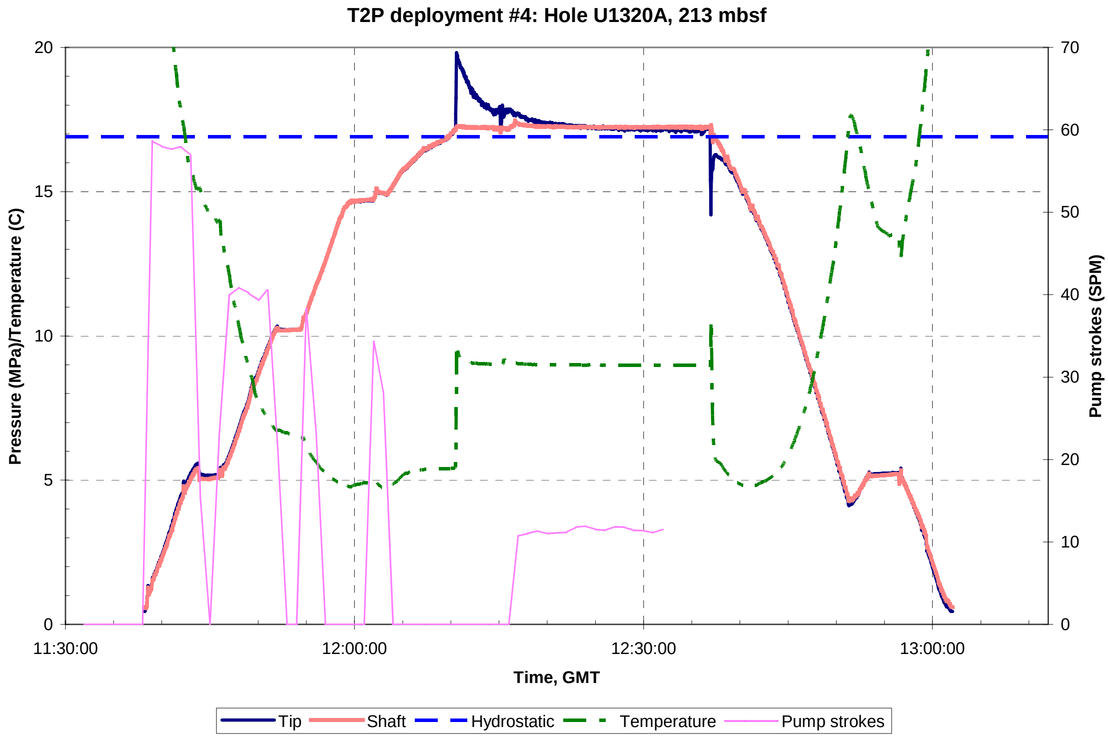

Figure A.B.11.c

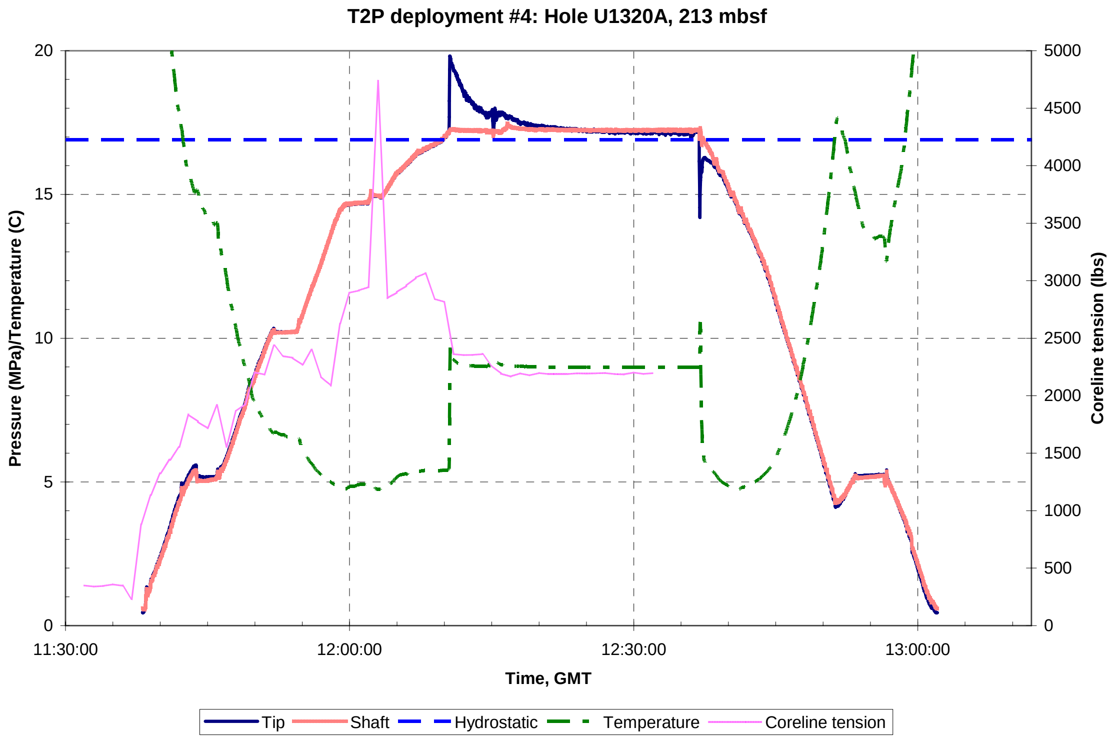

Figure A.B.11.d

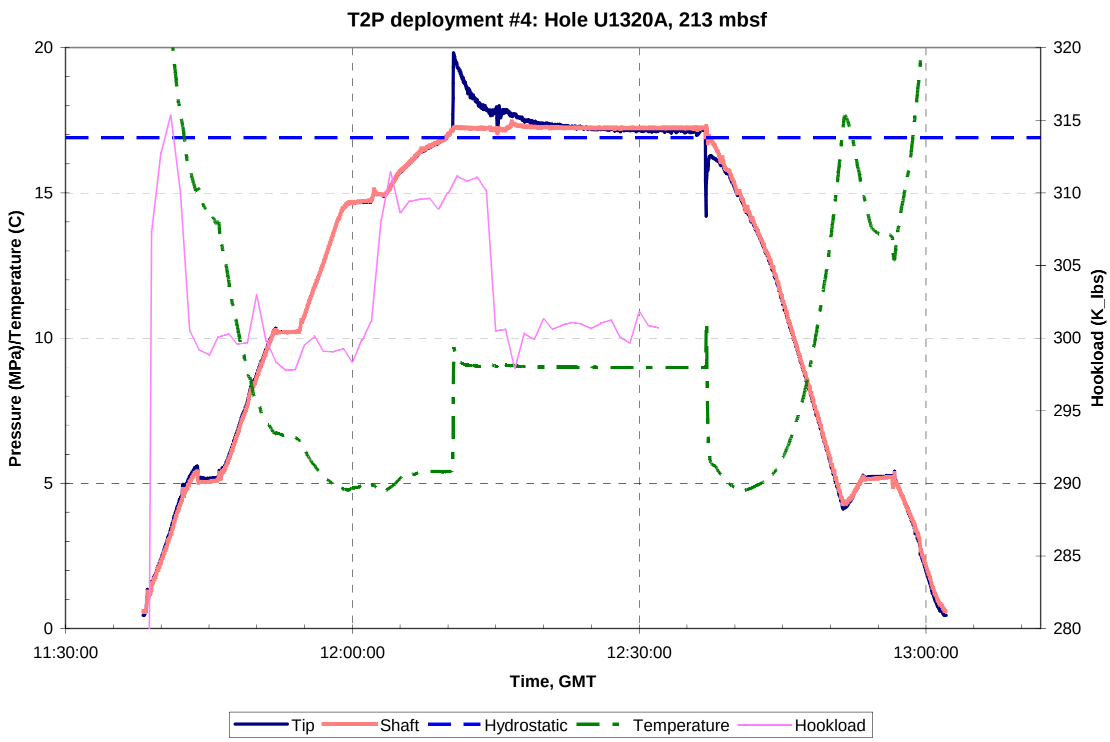

Figure A.B.11.e

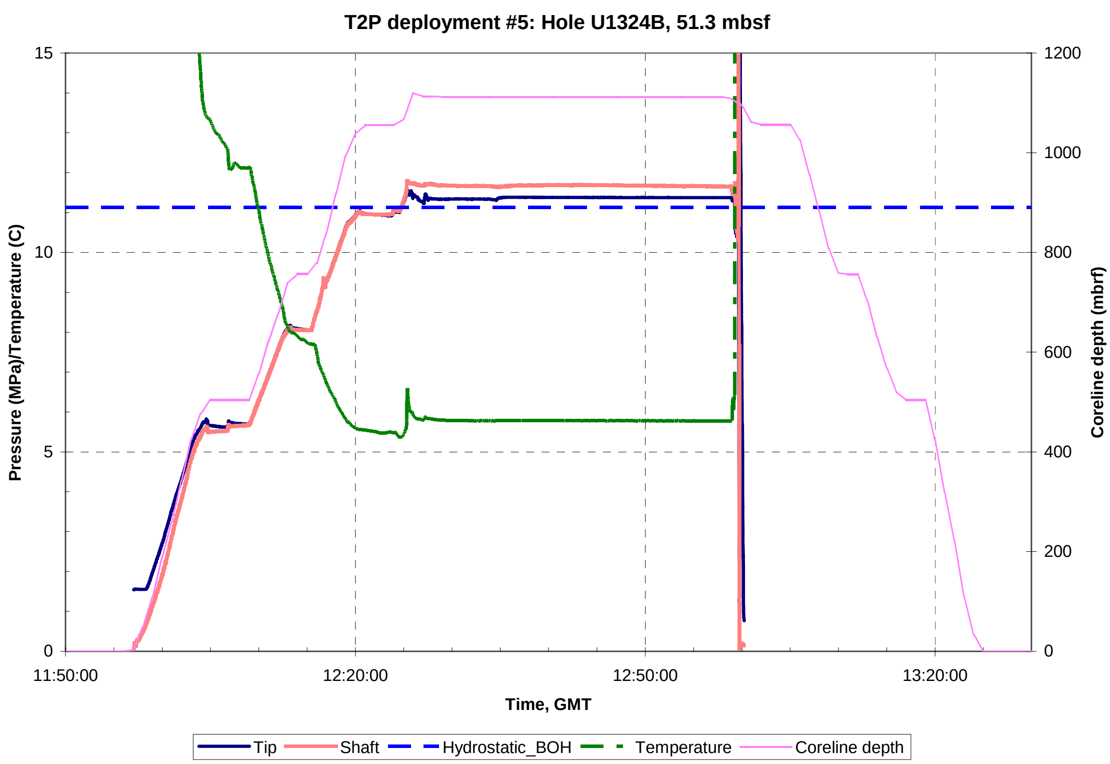

Figure A.B.12.a: Pressure, temperature and Truview data for T2P deployment #5, Hole U1324B, 51.3 mbsf. GMT = Greenwich Mean Time, Hydrostatic_BOH is the hydrostatic pressure at the bottom of the hole.

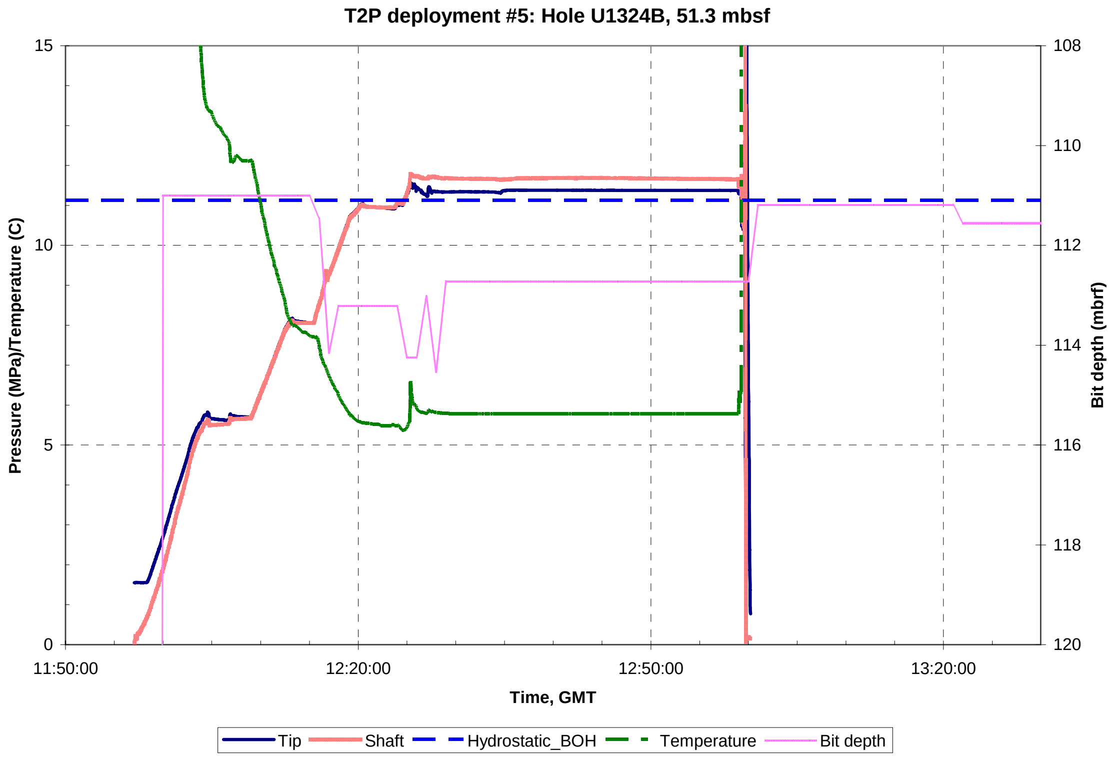

Figure A.B.12.b

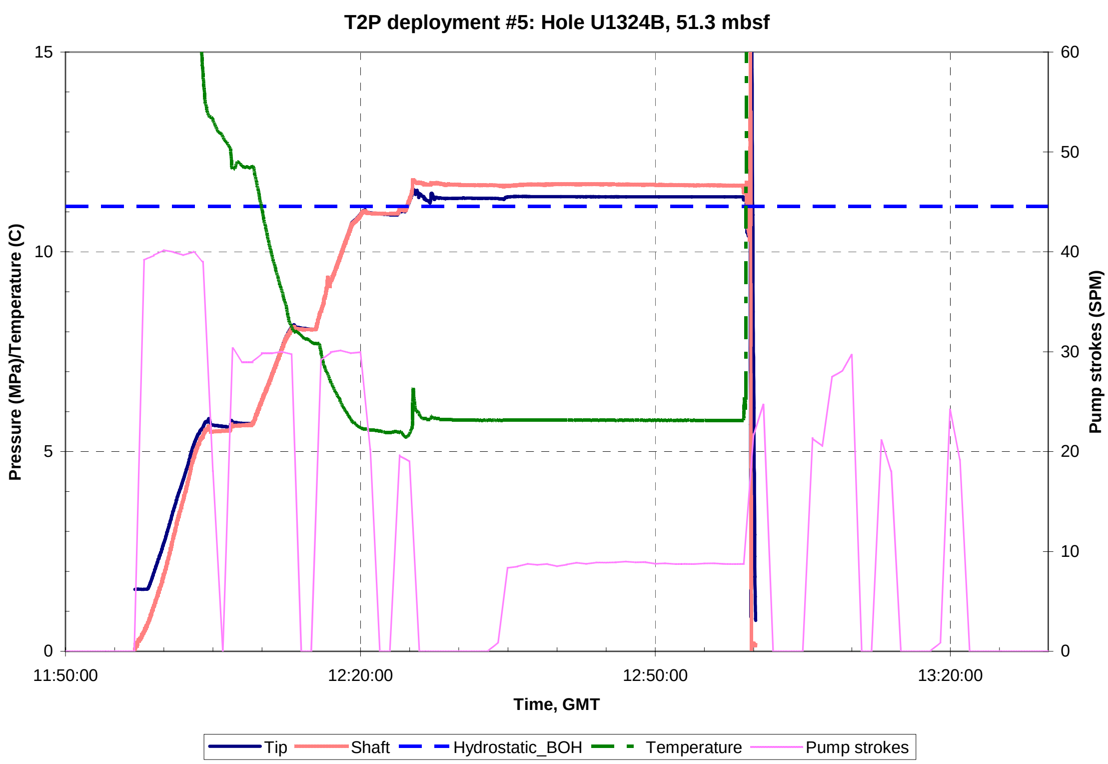

Figure A.B.12.c

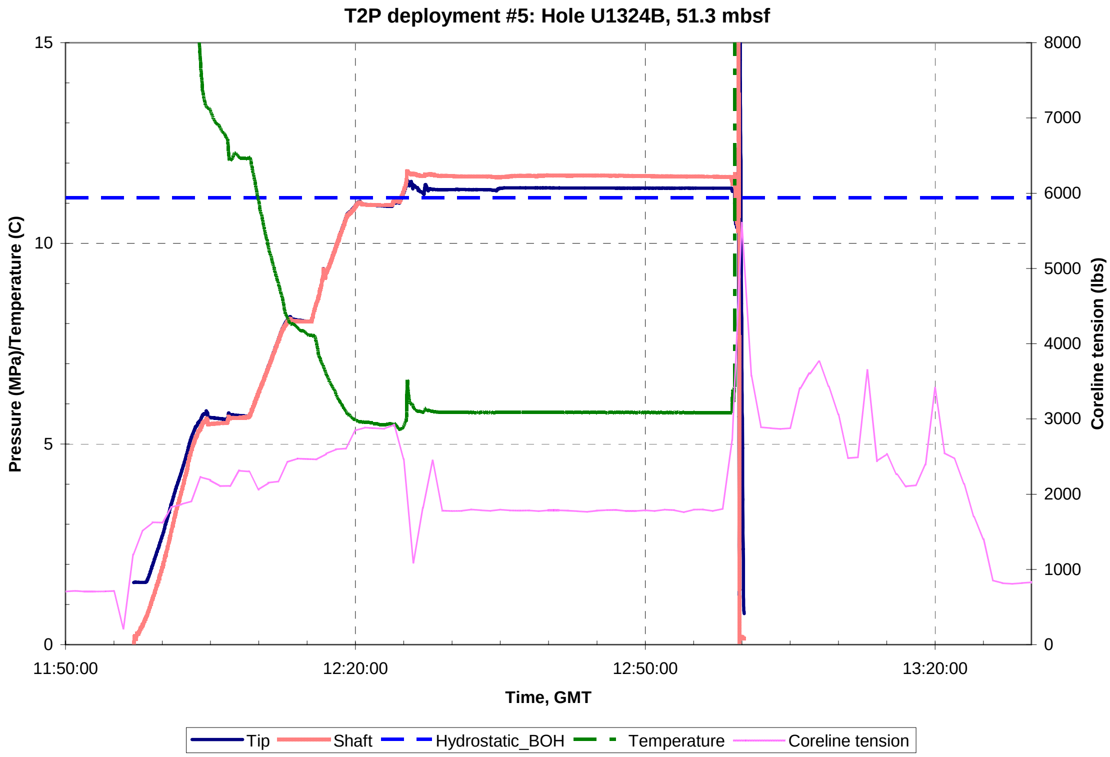

Figure A.B.12.d

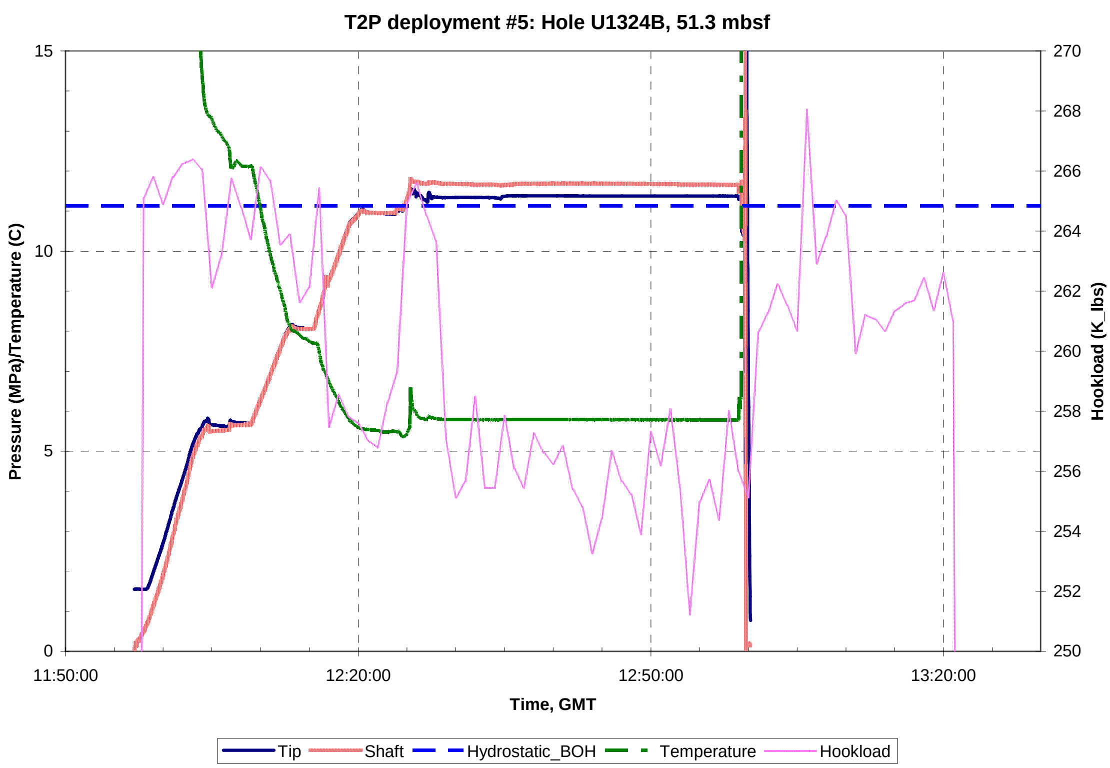

Figure A.B.12.e

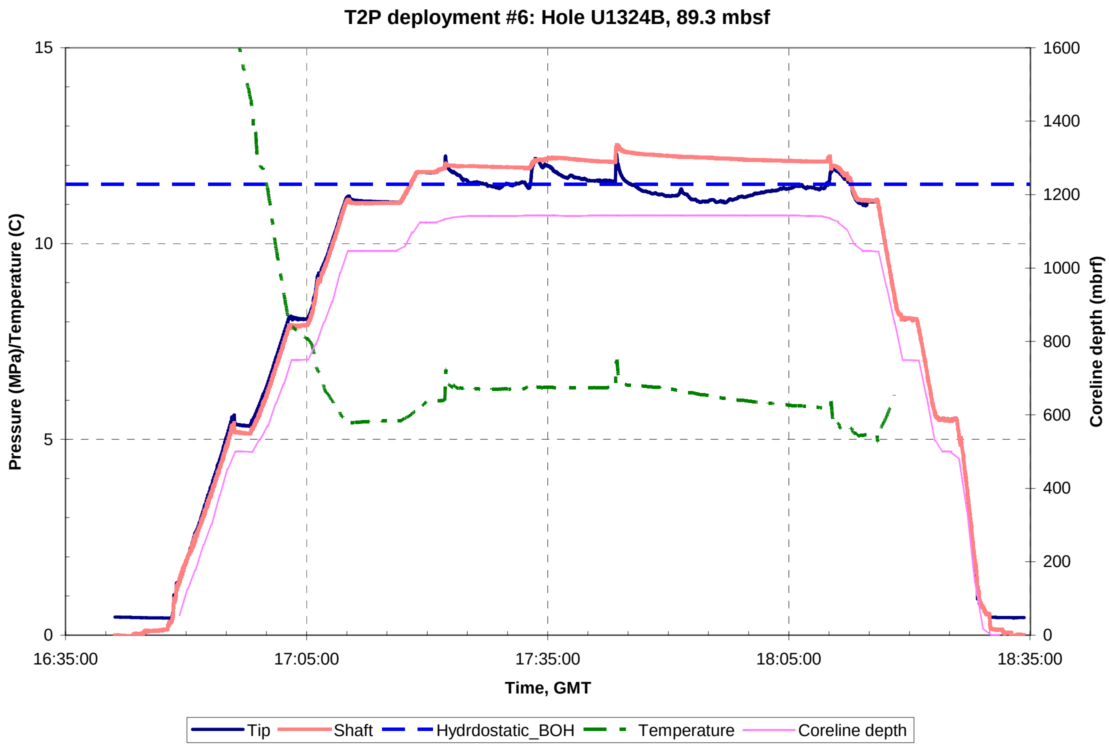

Figure A.B.13.a: Pressure, temperature and Truview data for T2P deployment #6, Hole U1324B, 89.3 mbsf. GMT = Greenwich Mean Time, Hydrostatic_BOH is the hydrostatic pressure at the bottom of the hole.

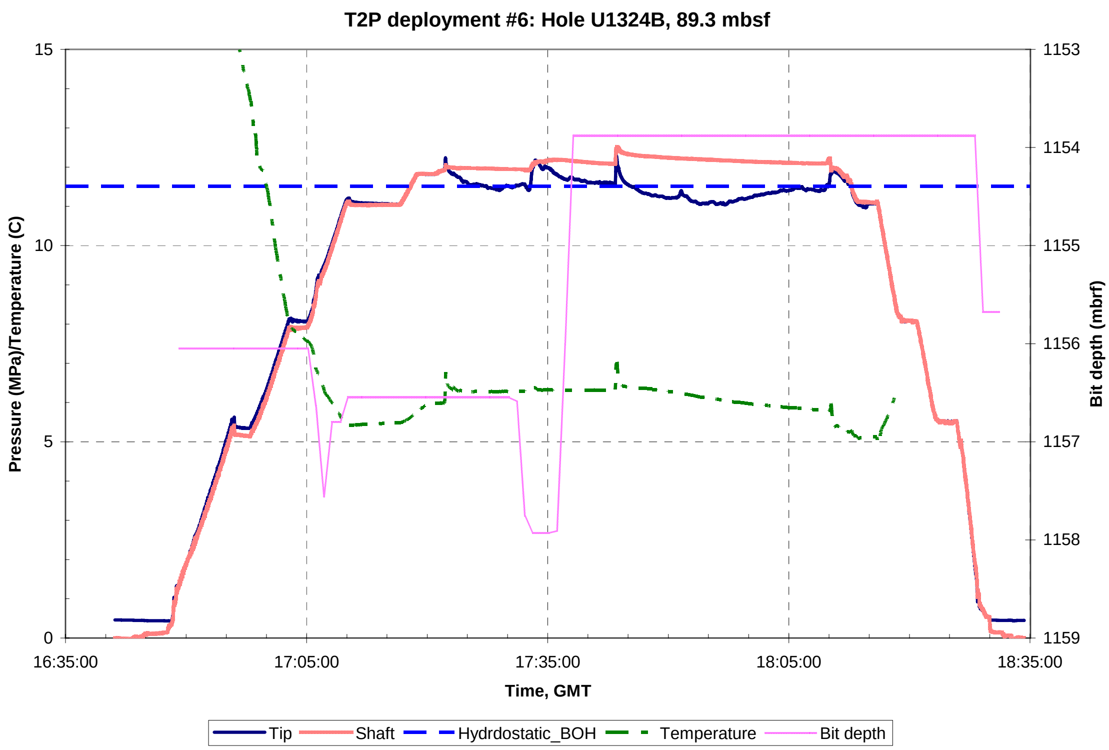

Figure A.B.13.b

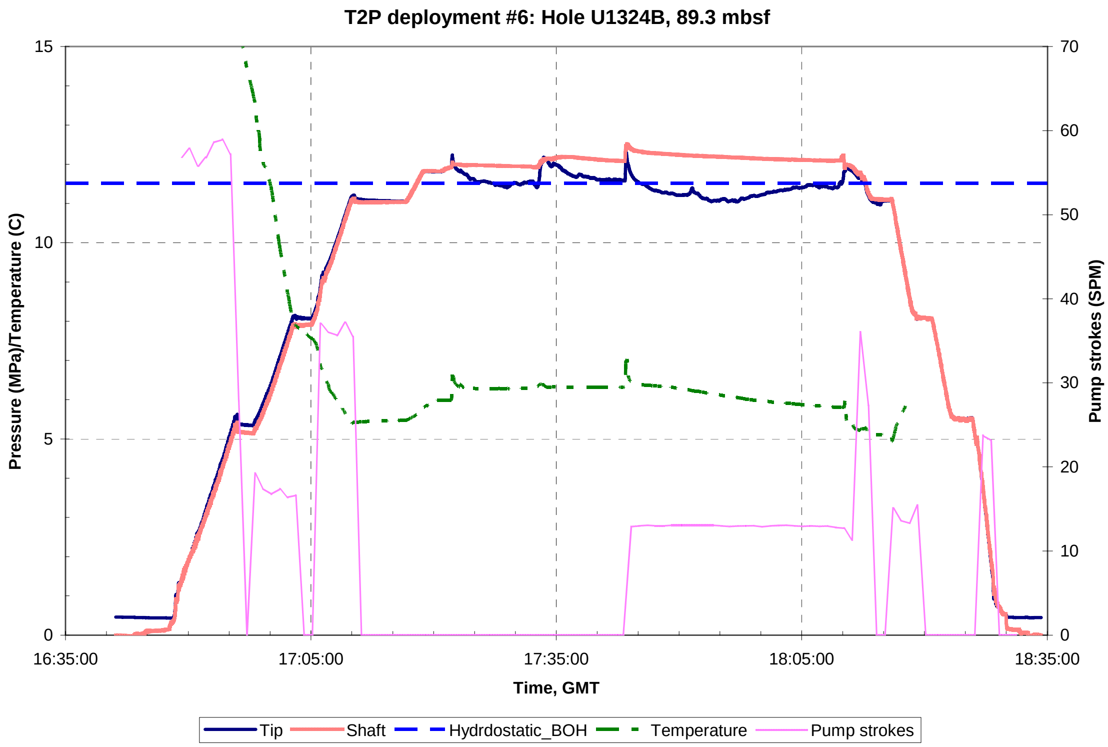

Figure A.B.13.c

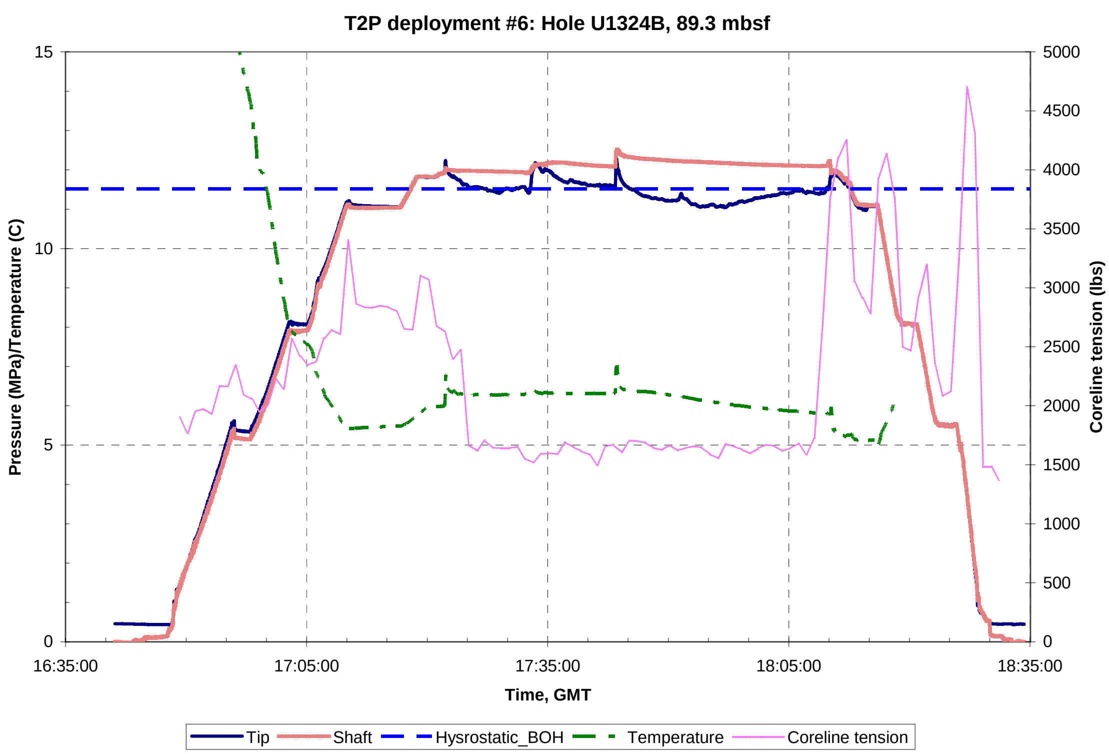

Figure A.B.13.d

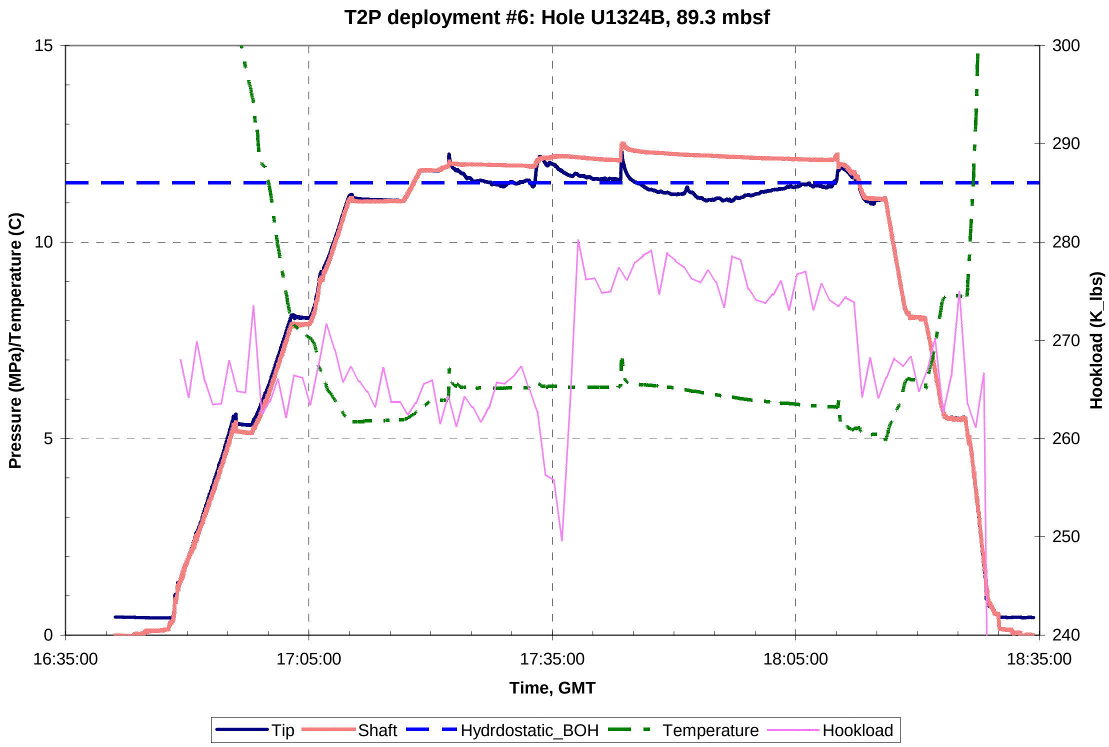

Figure A.B.13.e

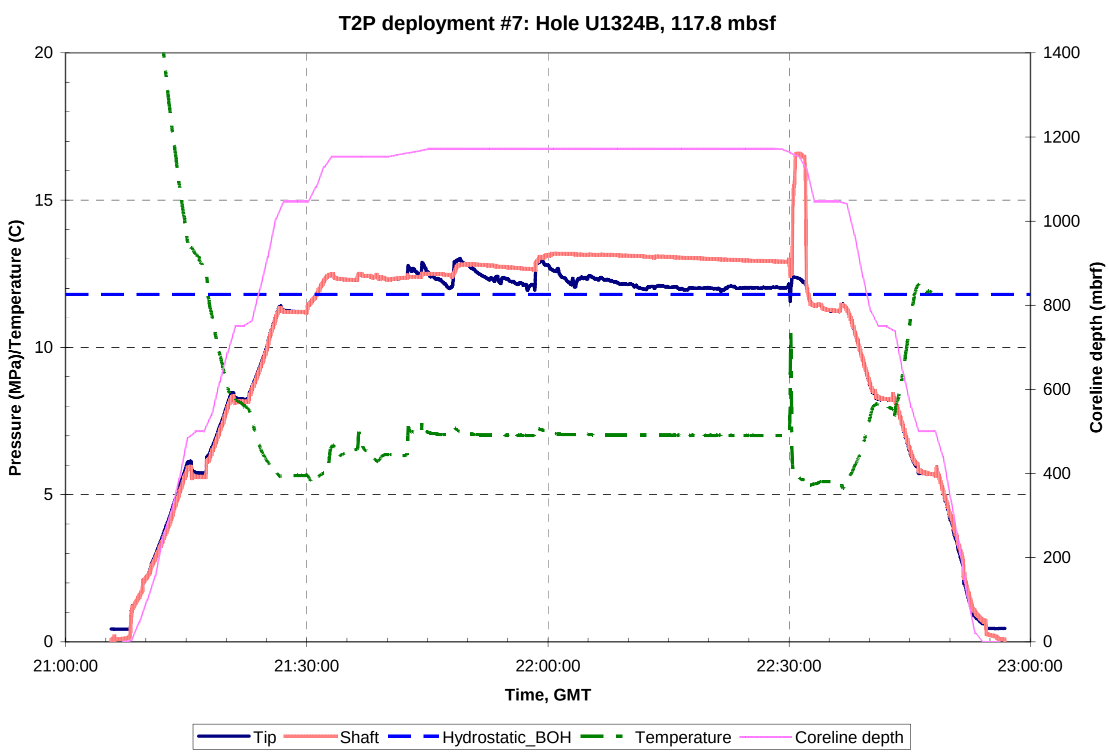

Figure A.B.14.a: Pressure, temperature and Truview data for T2P deployment #7, Hole U1324B, 117.8 mbsf. GMT = Greenwich Mean Time, Hydrostatic_BOH is the hydrostatic pressure at the bottom of the hole.

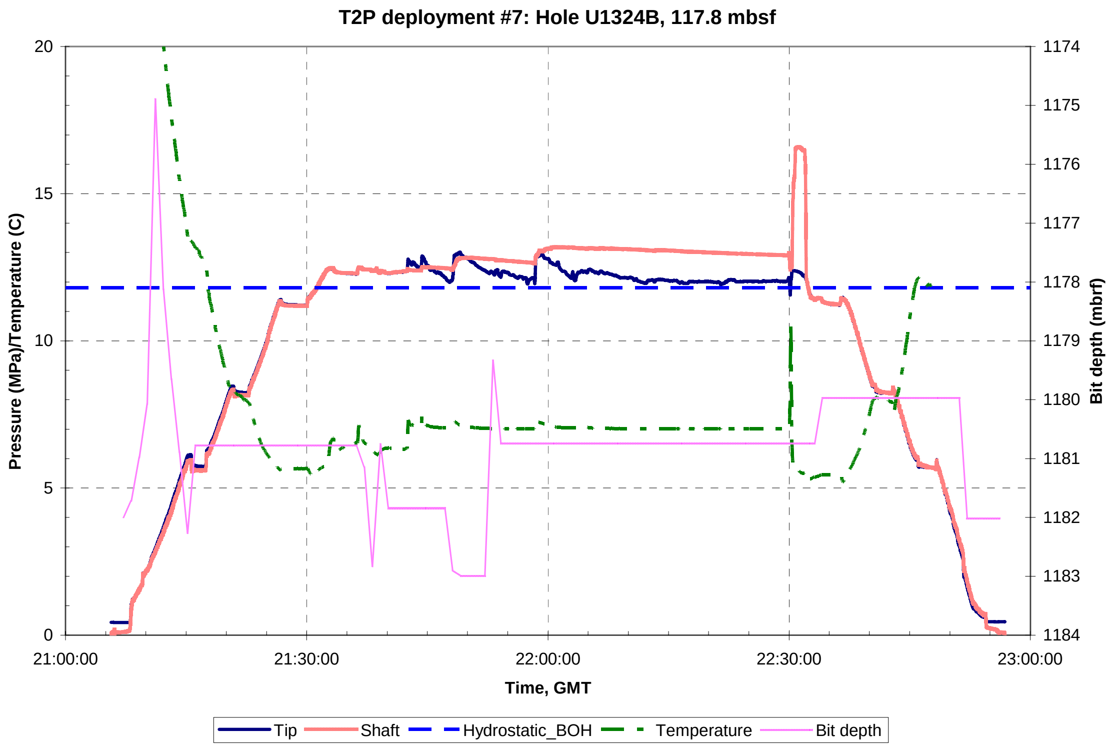

Figure A.B.14.b: Pressure, temperature and Truview data for T2P deployment #7, Hole U1324B, 117.8 mbsf. GMT = Greenwich Mean Time, Hydrostatic_BOH is the hydrostatic pressure at the bottom of the hole

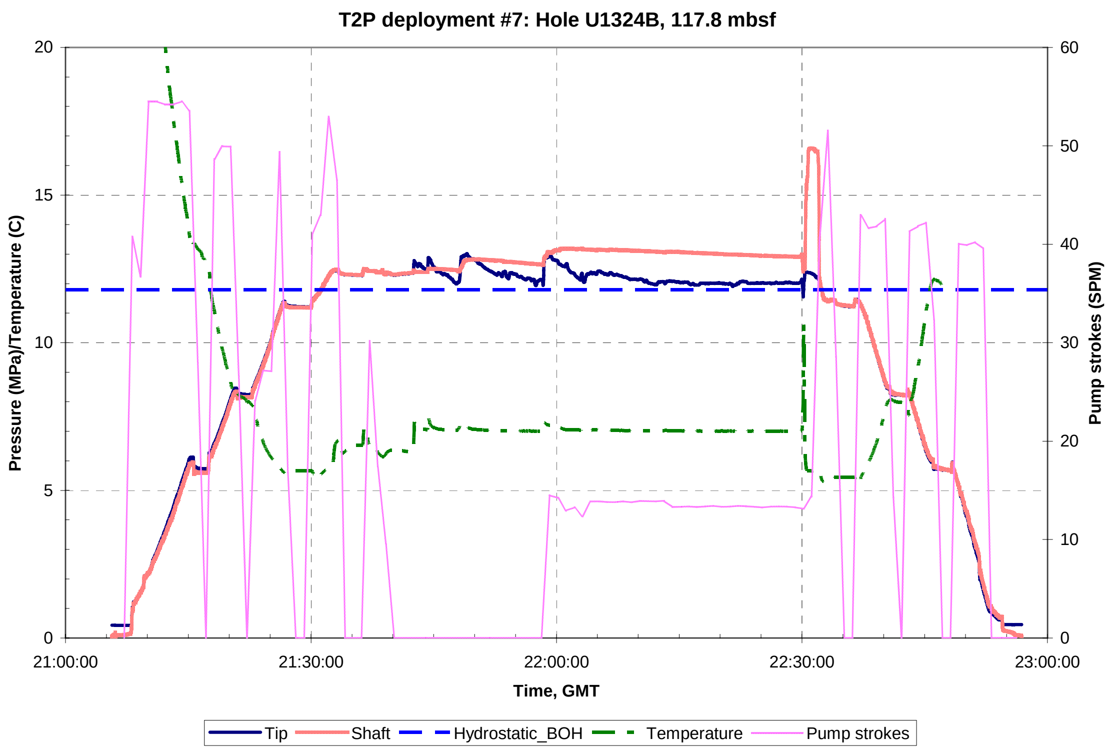

Figure A.B.14.c

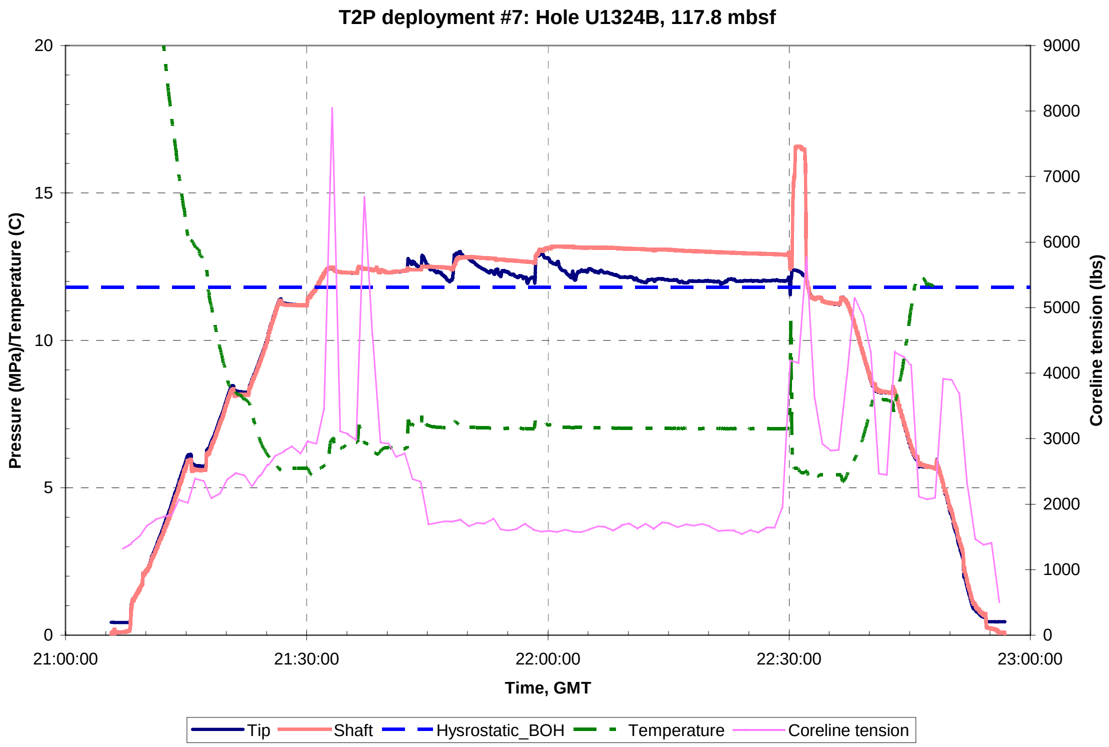

Figure A.B.14.d

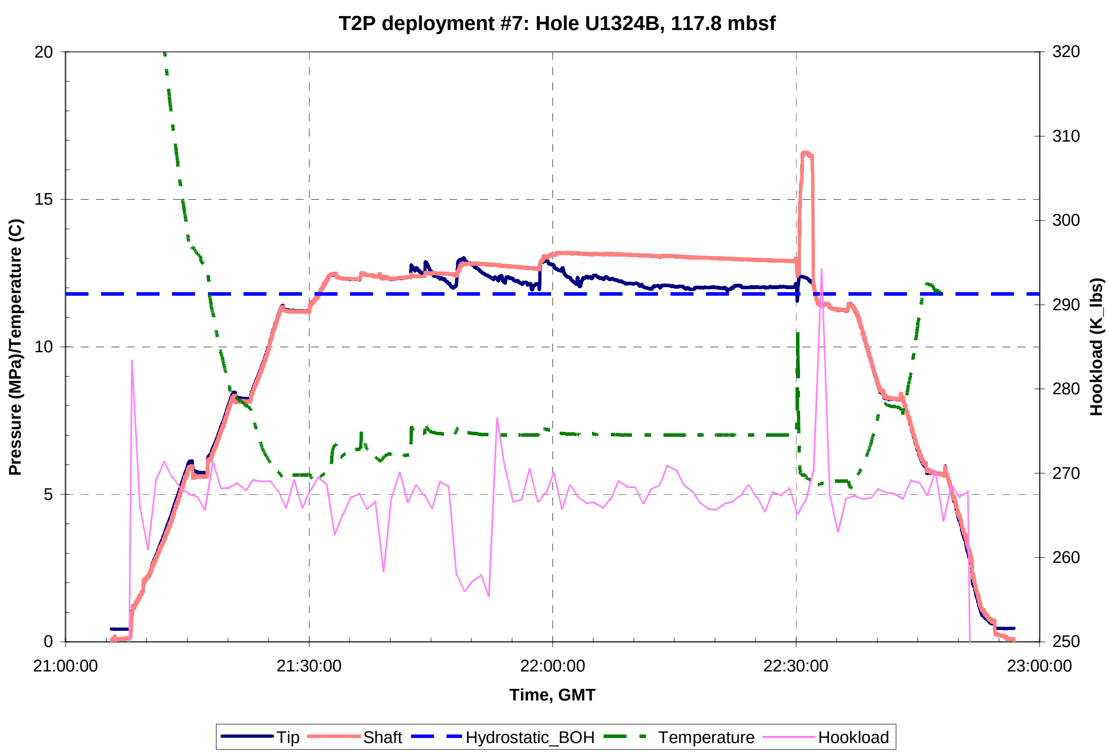

Figure A.B.14.e

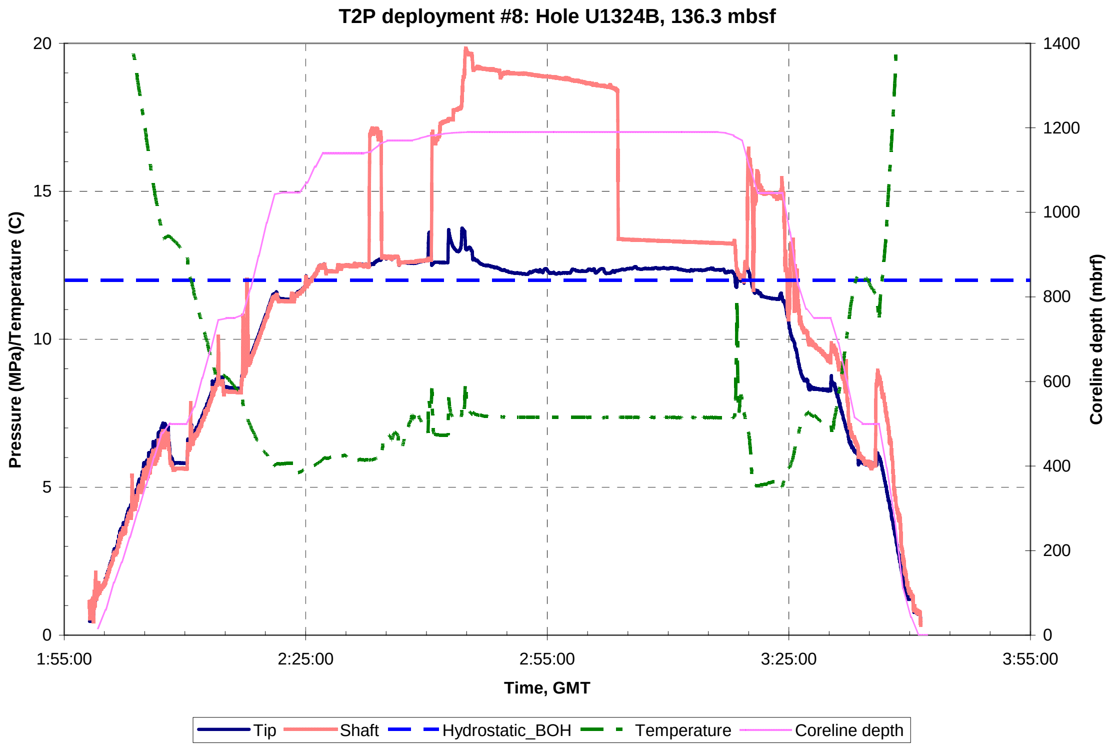

Figure A.B.15.a: Pressure, temperature and Truview data for T2P deployment #8, Hole U1324B, 136.3 mbsf. GMT = Greenwich Mean Time, Hydrostatic_BOH is the hydrostatic pressure at the bottom of the hole.

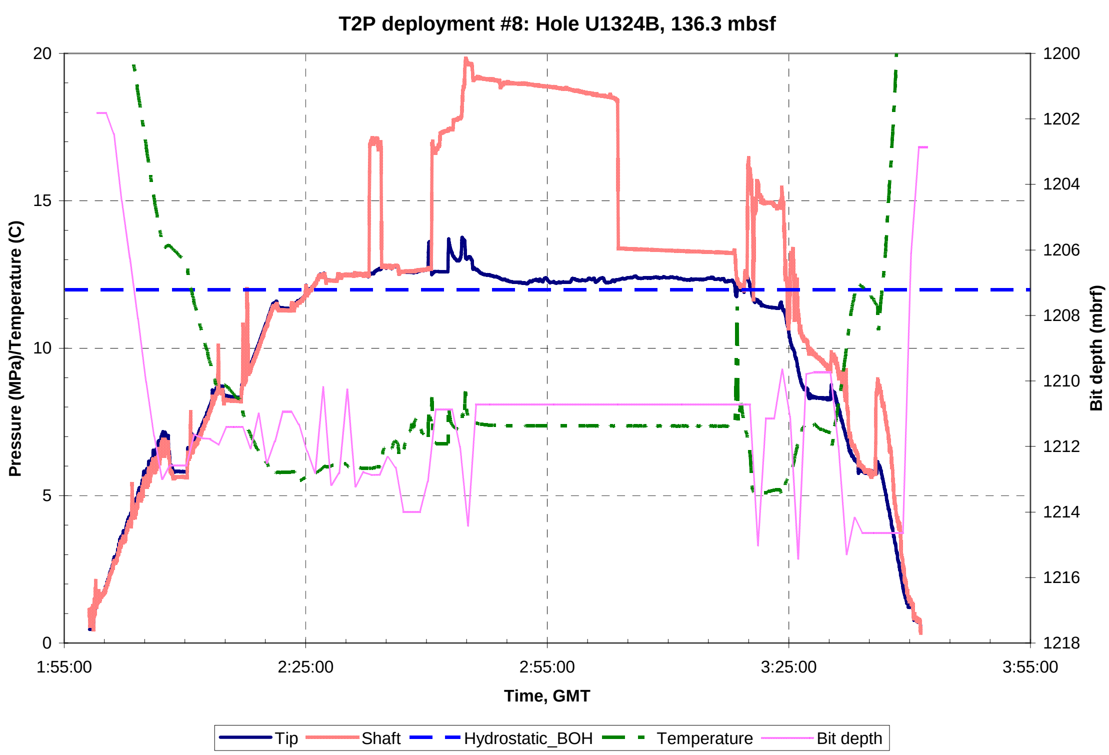

Figure A.B.15.b

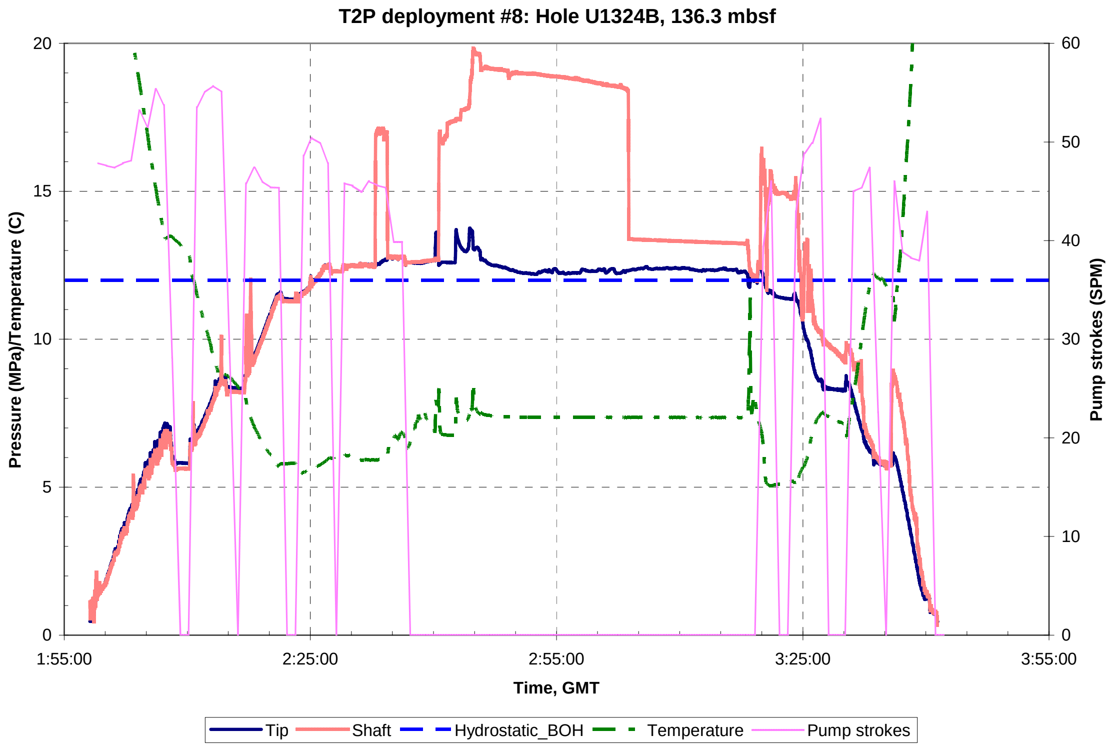

Figure A.B.15.c

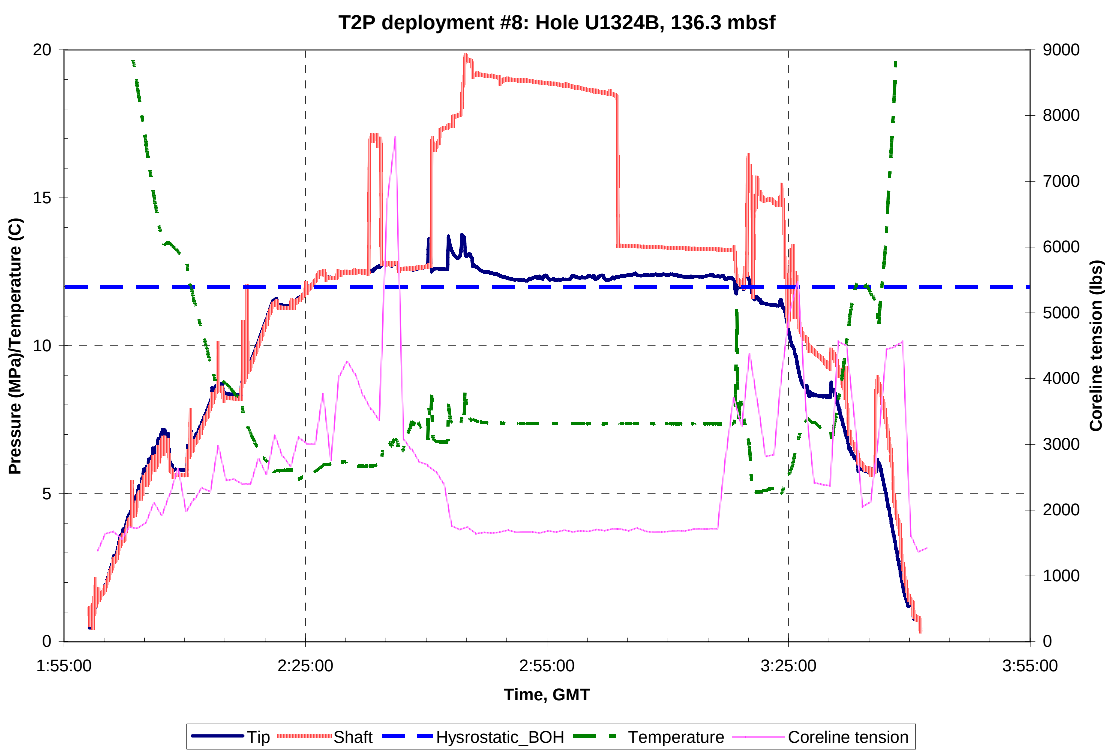

Figure A.B.15.d

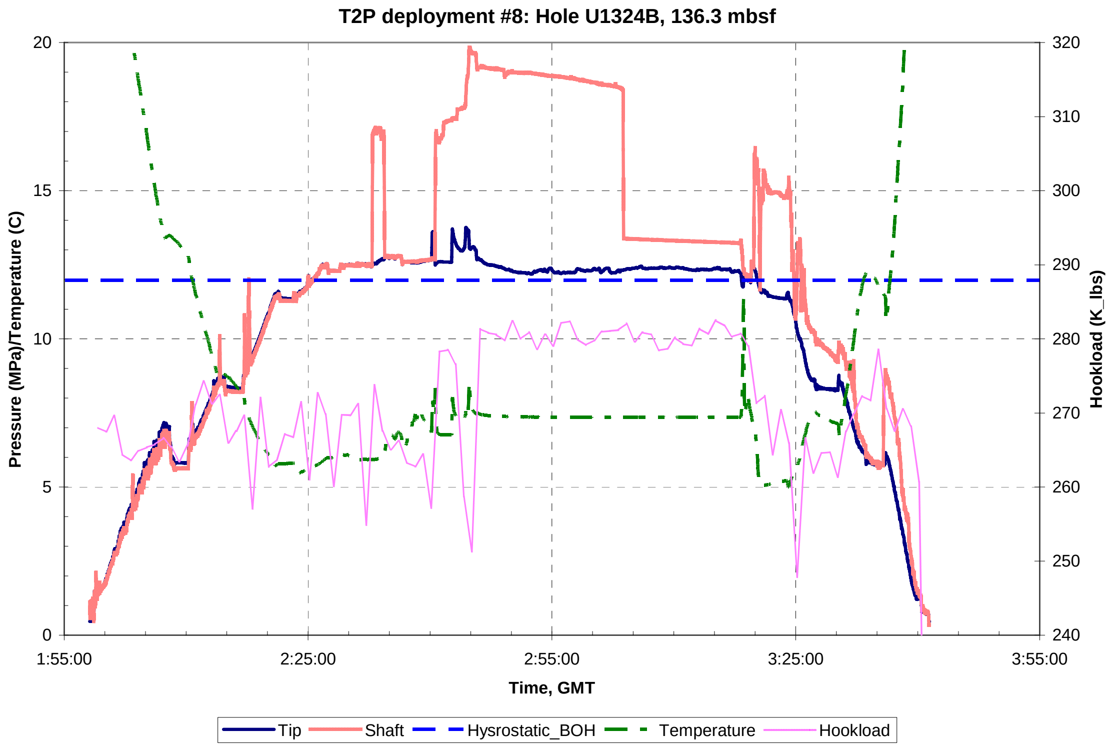

Figure A.B.15.e

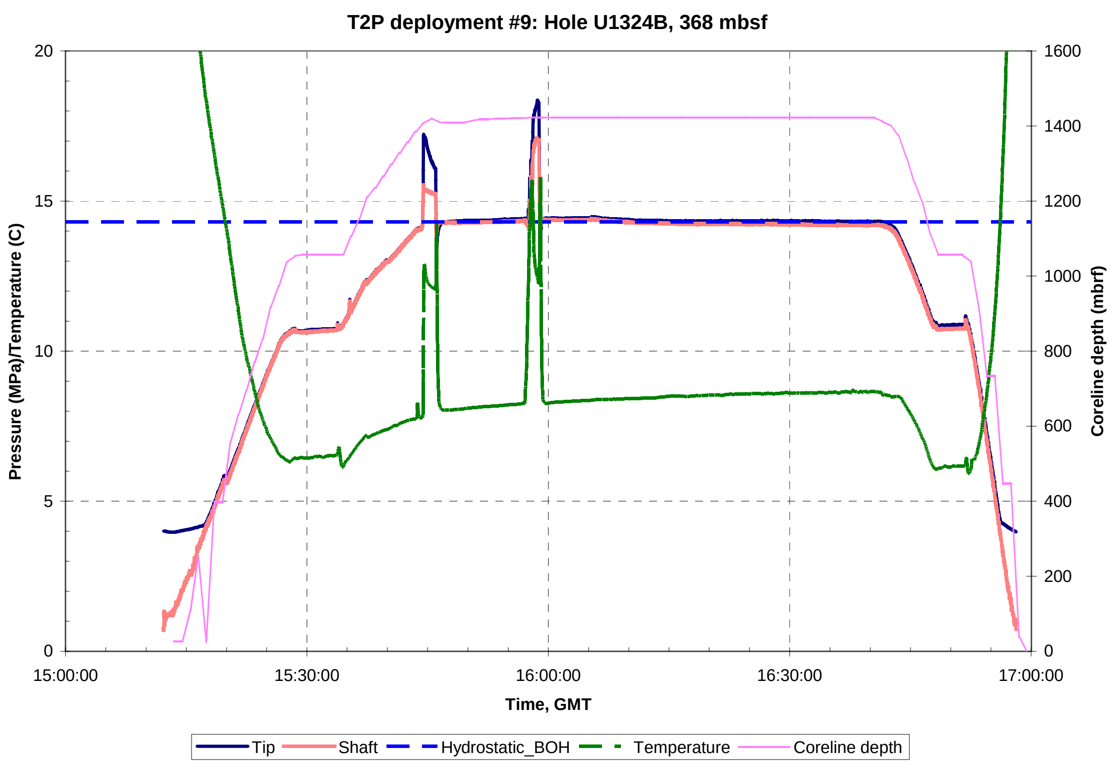

Figure A.B.16.a: Pressure, temperature and Truview data for T2P deployment #9, Hole U1324B, 368 mbsf. GMT = Greenwich Mean Time, Hydrostatic_BOH is the hydrostatic pressure at the bottom of the hole.

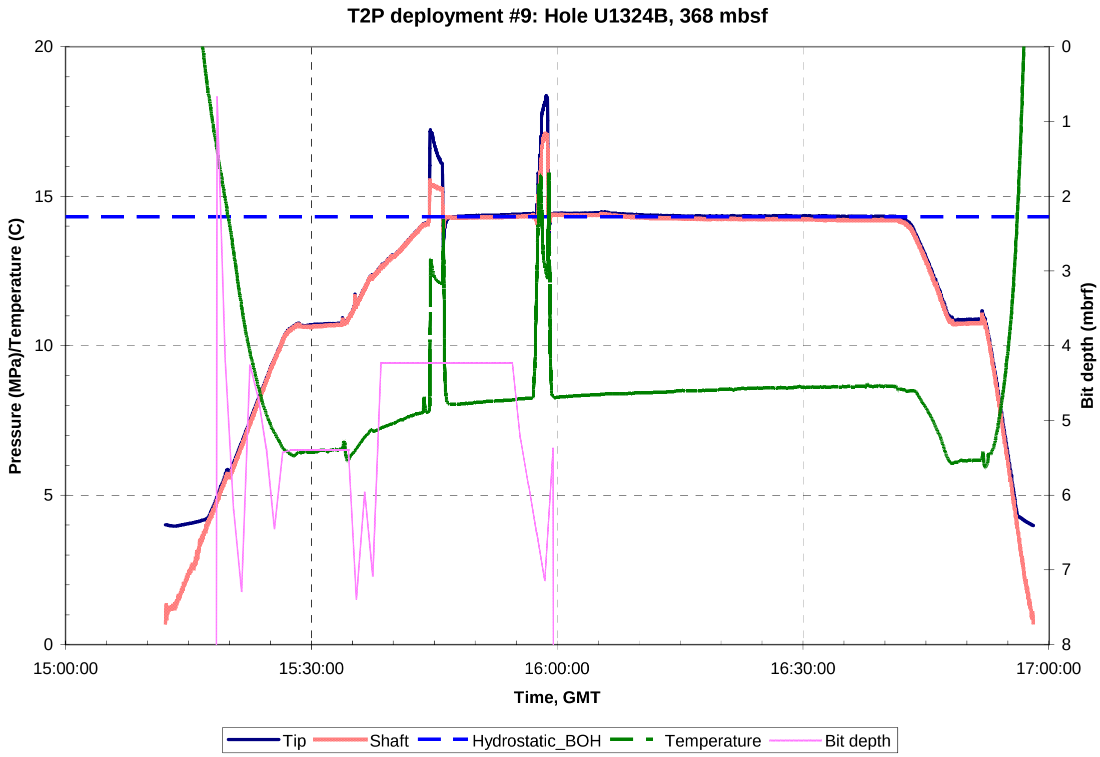

Figure A.B.16.b

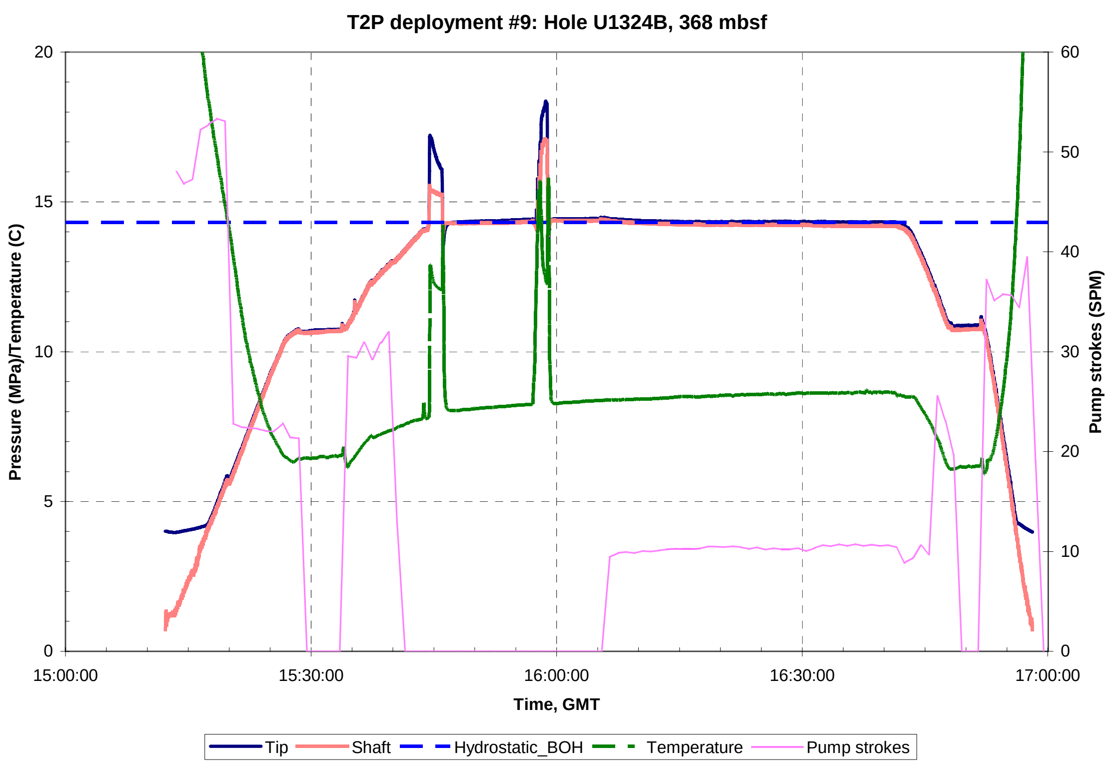

Figure A.B.16.c

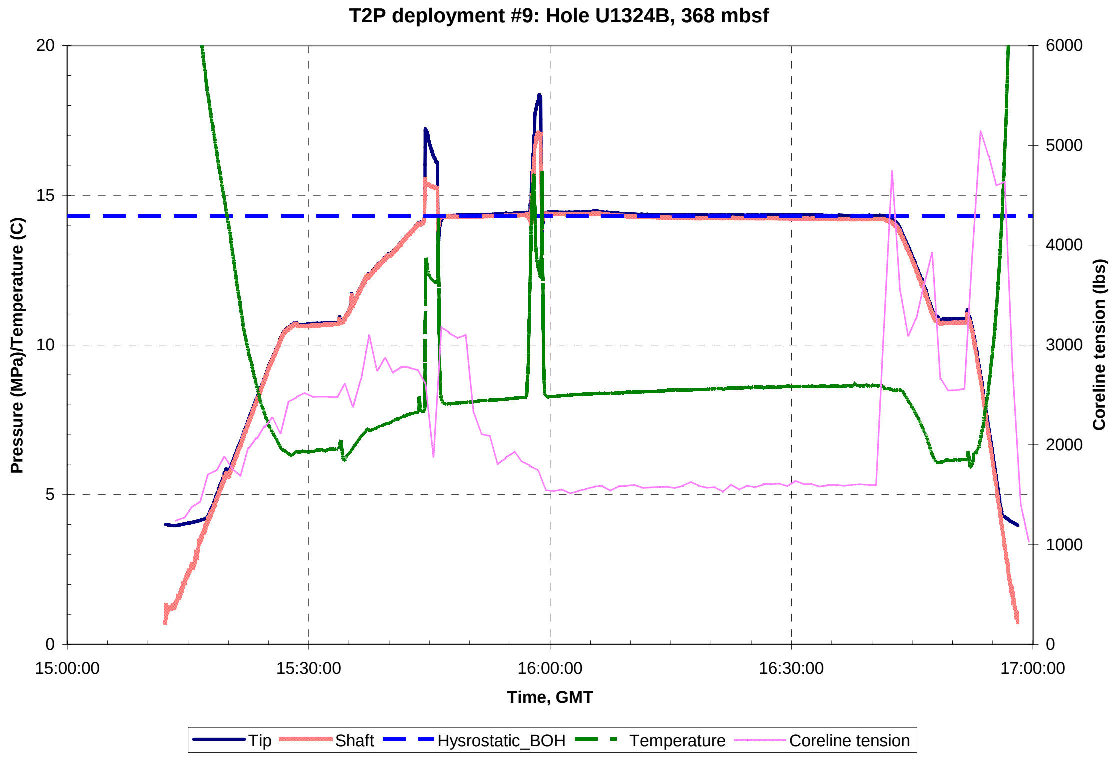

Figure A.B.16.d

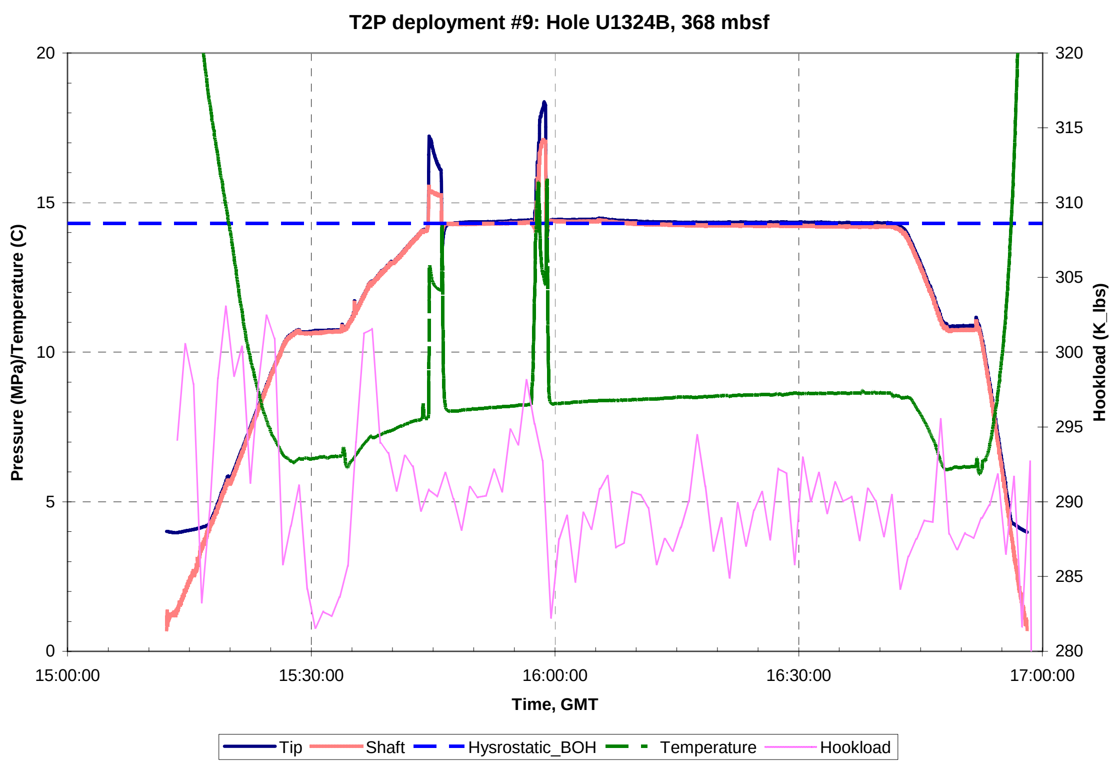

Figure A.B.16.e

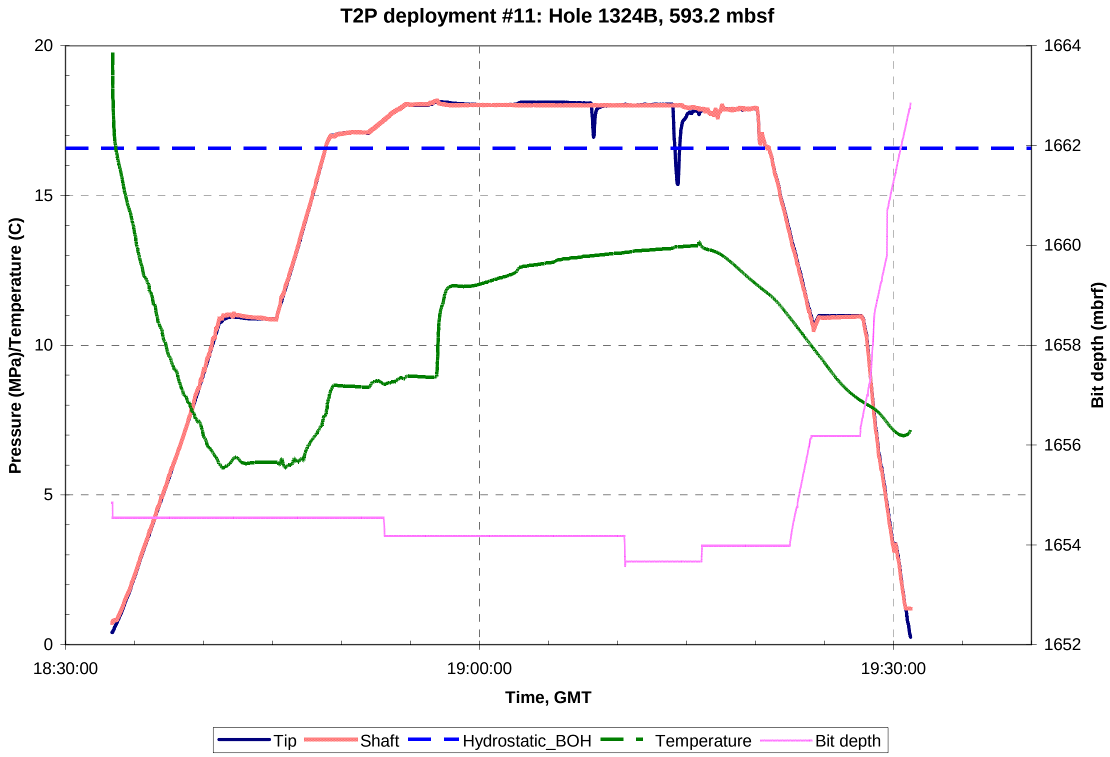

Figure A.B.17.a: Pressure, temperature and Truview data for T2P deployment #11, Hole U1324B, 593.2 mbsf. GMT = Greenwich Mean Time, Hydrostatic_BOH is the hydrostatic pressure at the bottom of the hole.

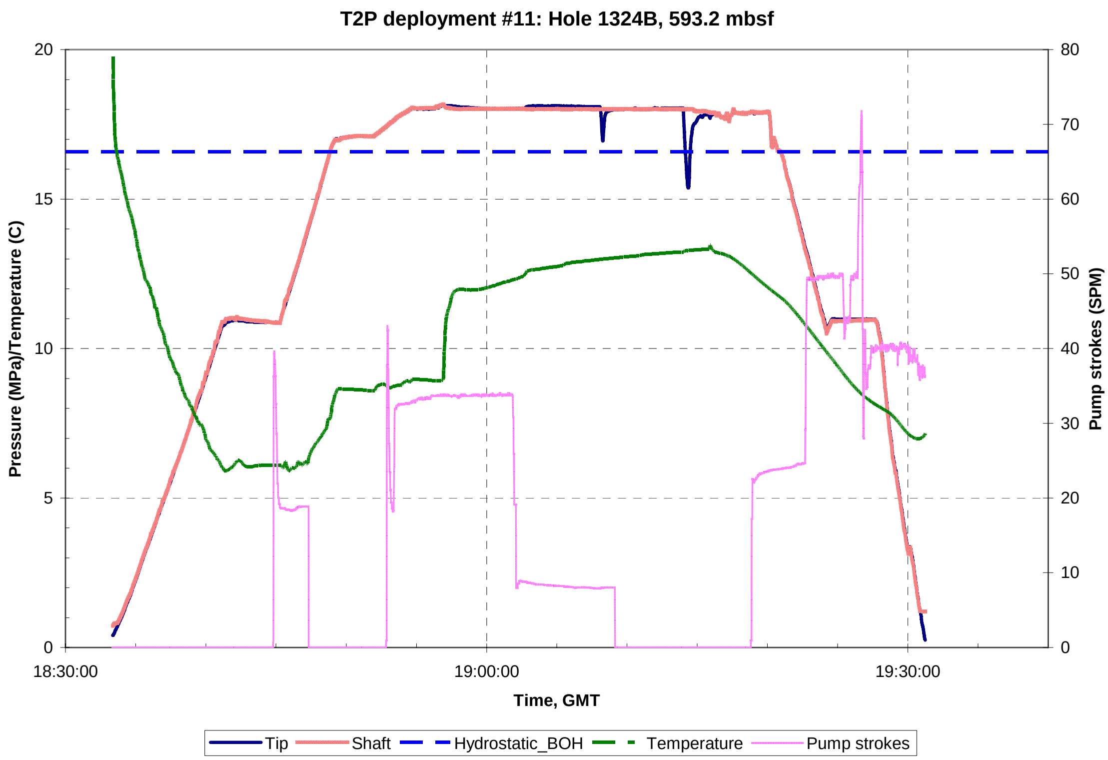

Figure A.B.17.b

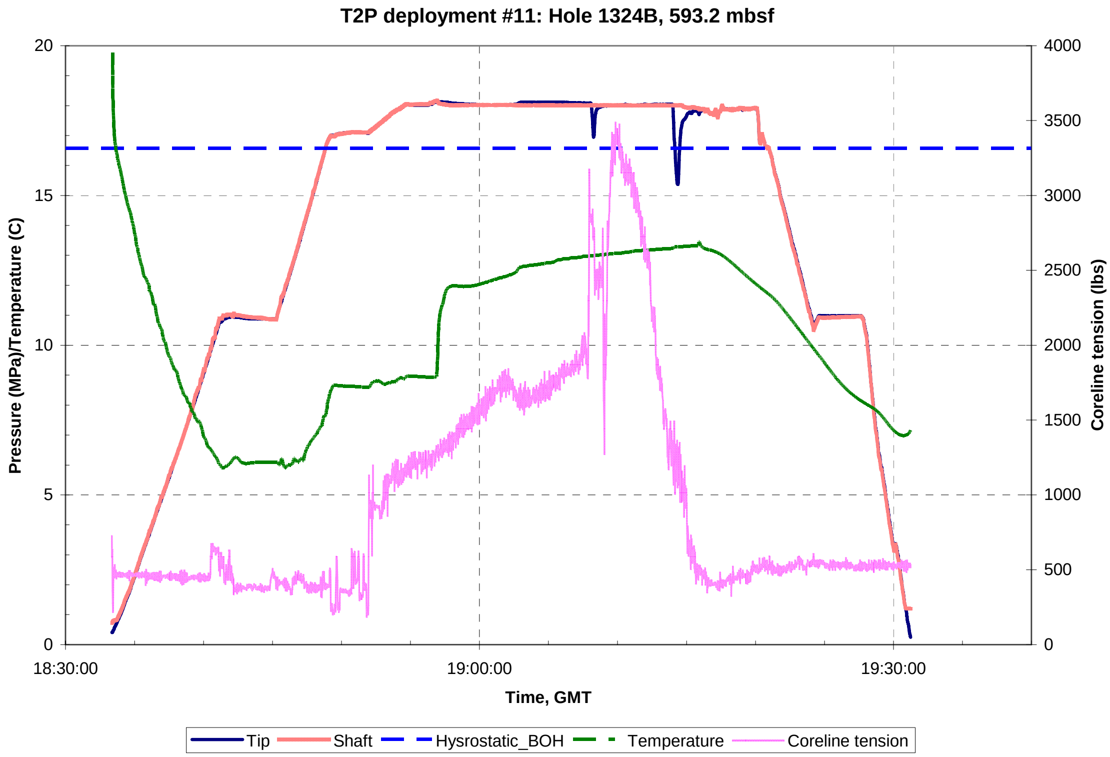

Figure A.B.17.c

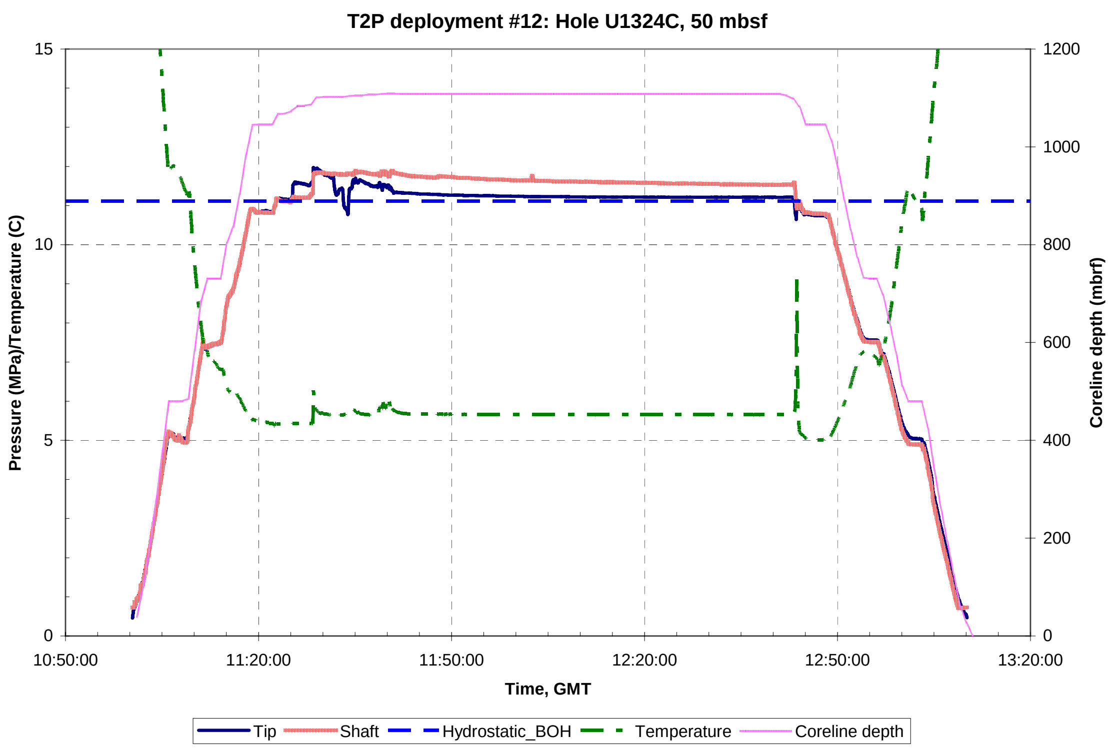

Figure A.B.18.a: Pressure, temperature and Truview data for T2P deployment #12, Hole U1324C, 50 mbsf. GMT = Greenwich Mean Time, Hydrostatic_BOH is the hydrostatic pressure at the bottom of the hole.

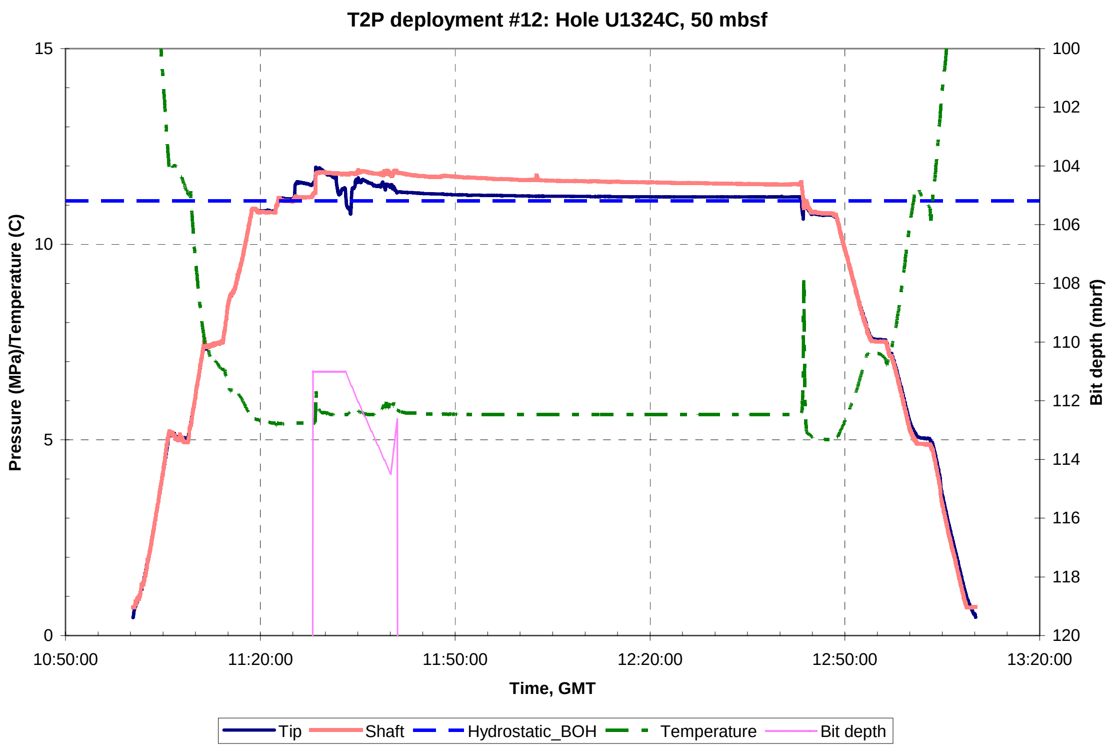

Figure A.B.18.b

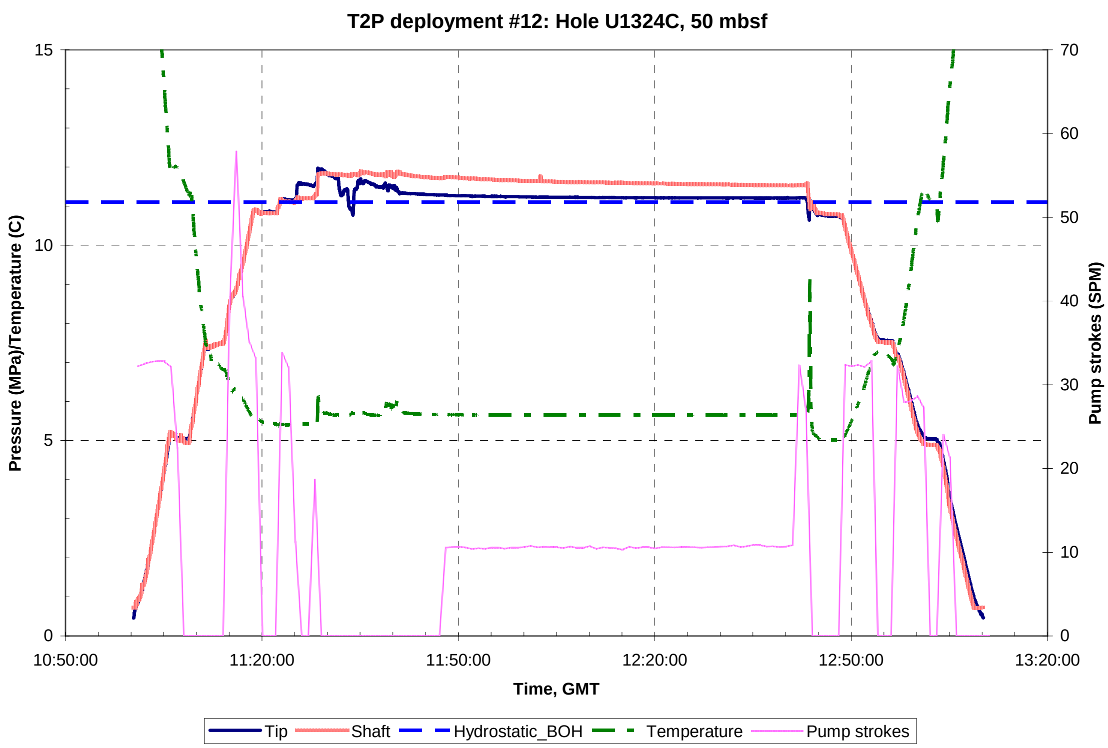

Figure A.B.18.c

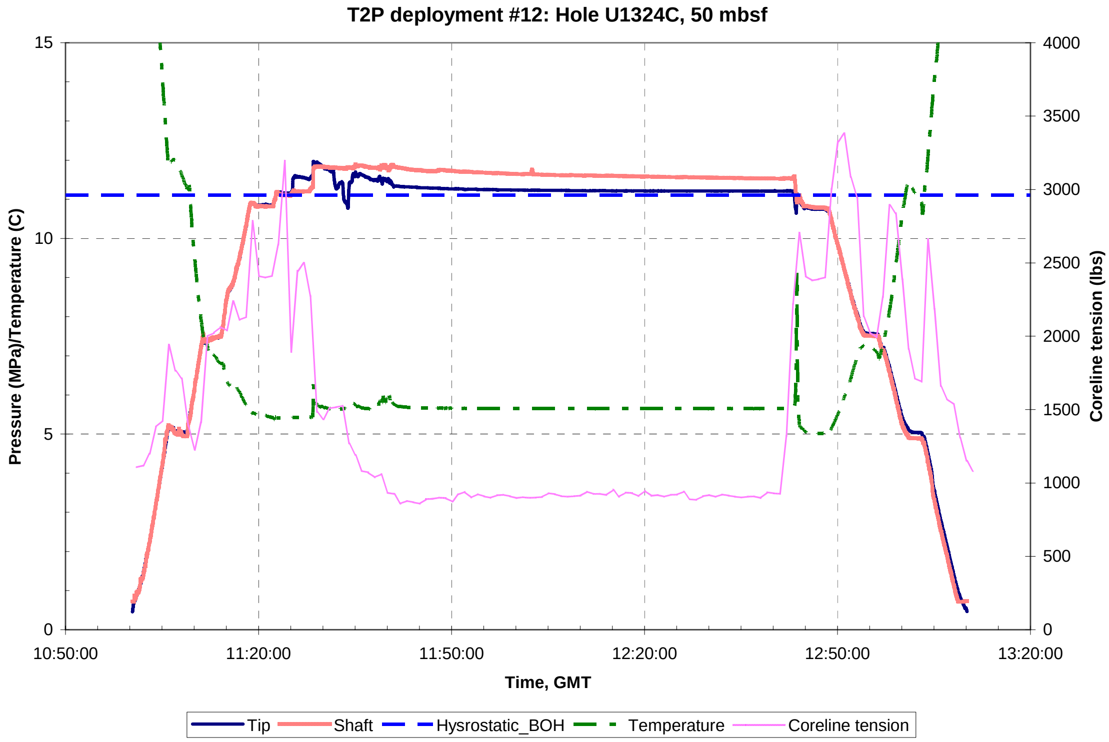

Figure A.B.18.d

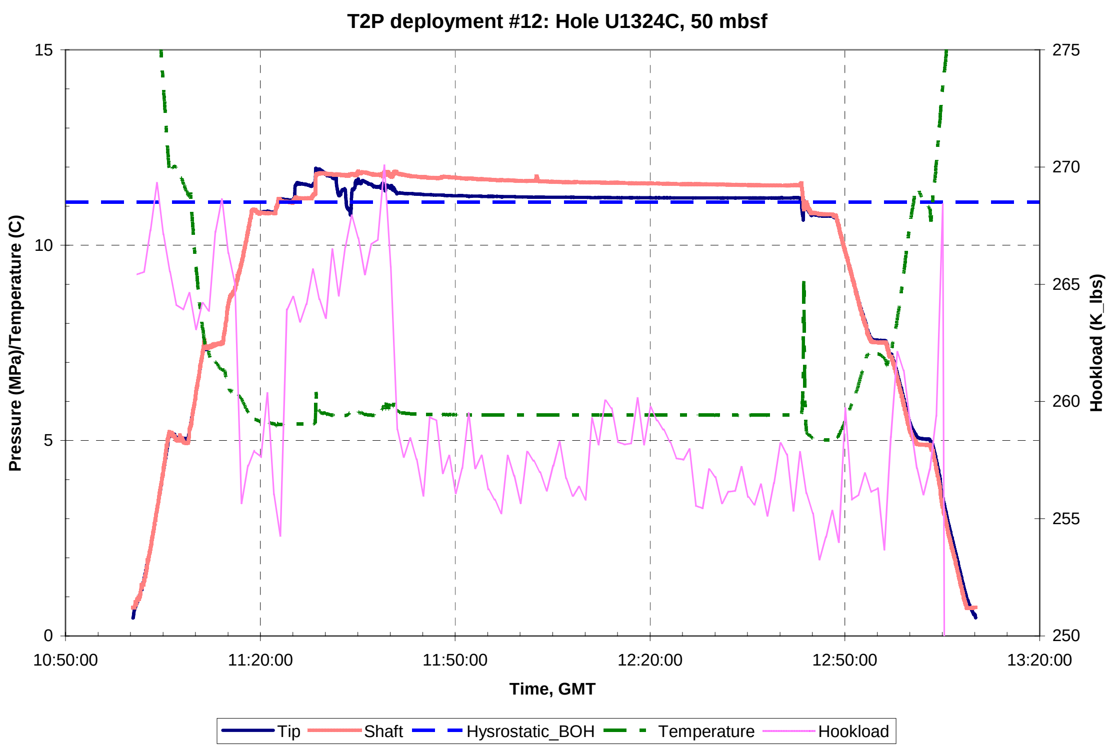

Figure A.B.18.e

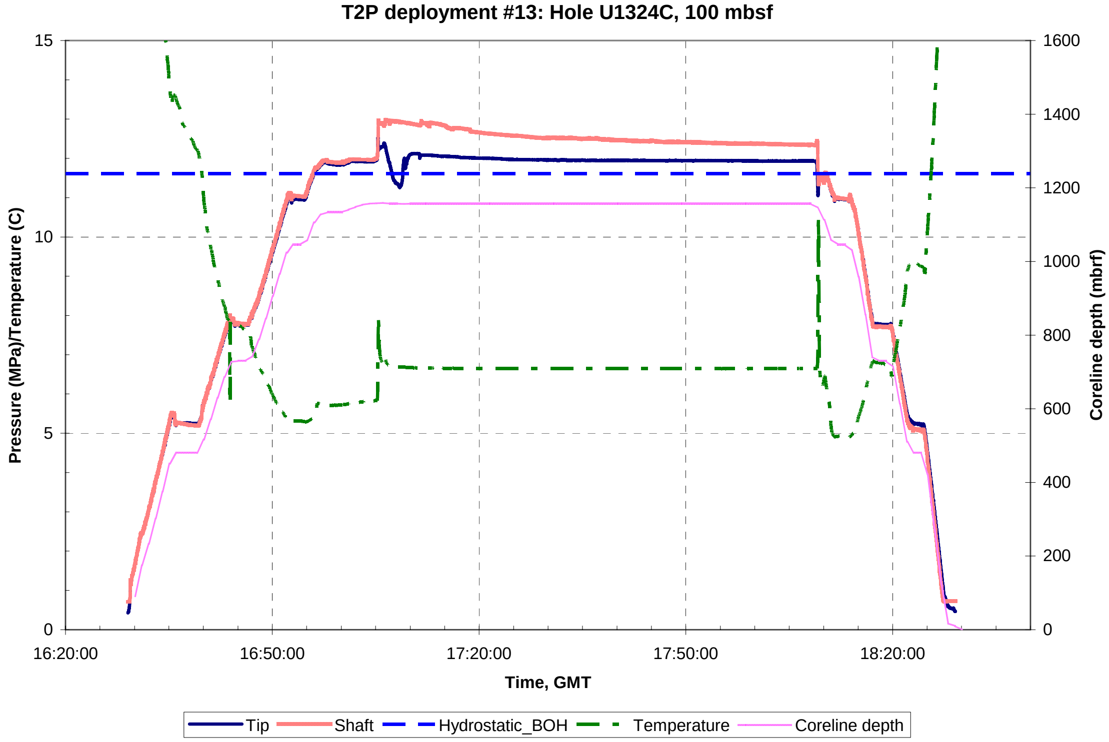

Figure A.B.19.a: Pressure, temperature and Truview data for T2P deployment #13, Hole U1324C, 100 mbsf. GMT = Greenwich Mean Time, Hydrostatic_BOH is the hydrostatic pressure at the bottom of the hole.

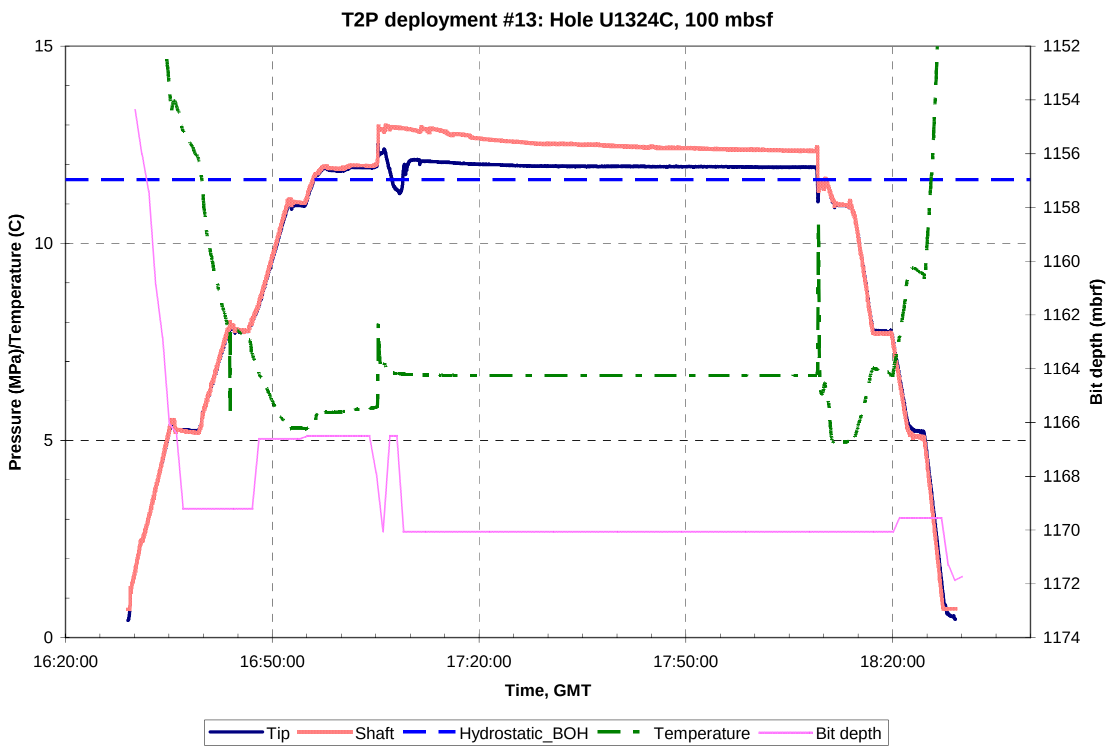

Figure A.B.19.b

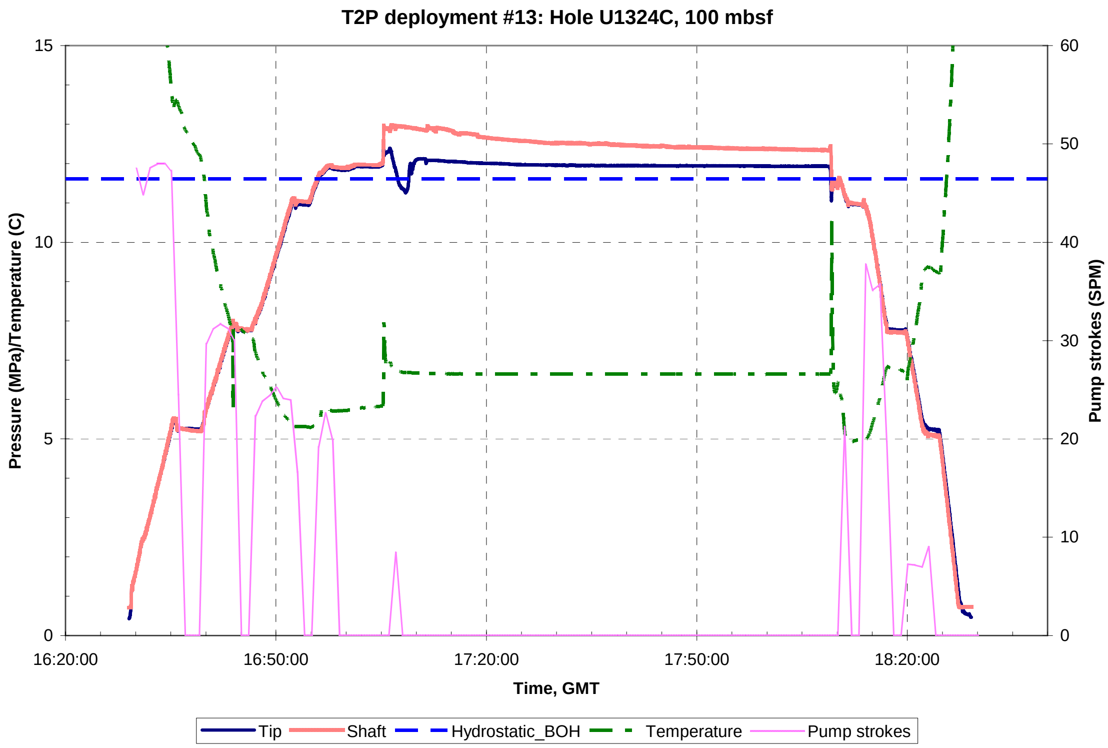

Figure A.B.19.c

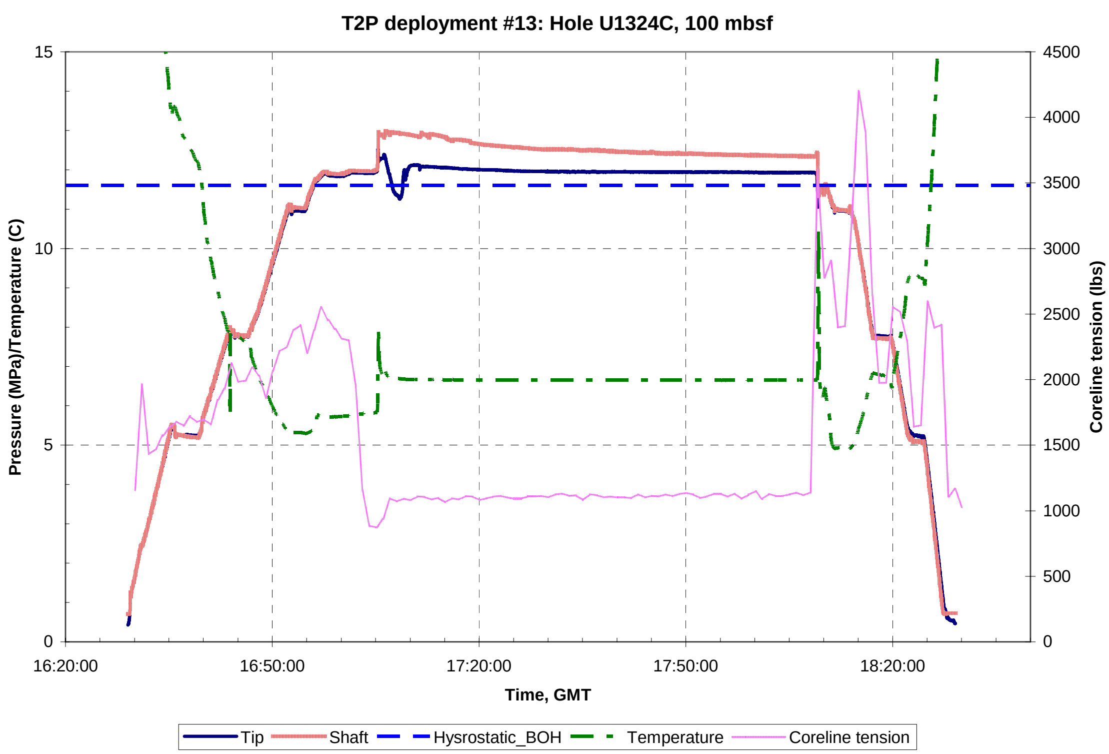

Figure A.B.19.d

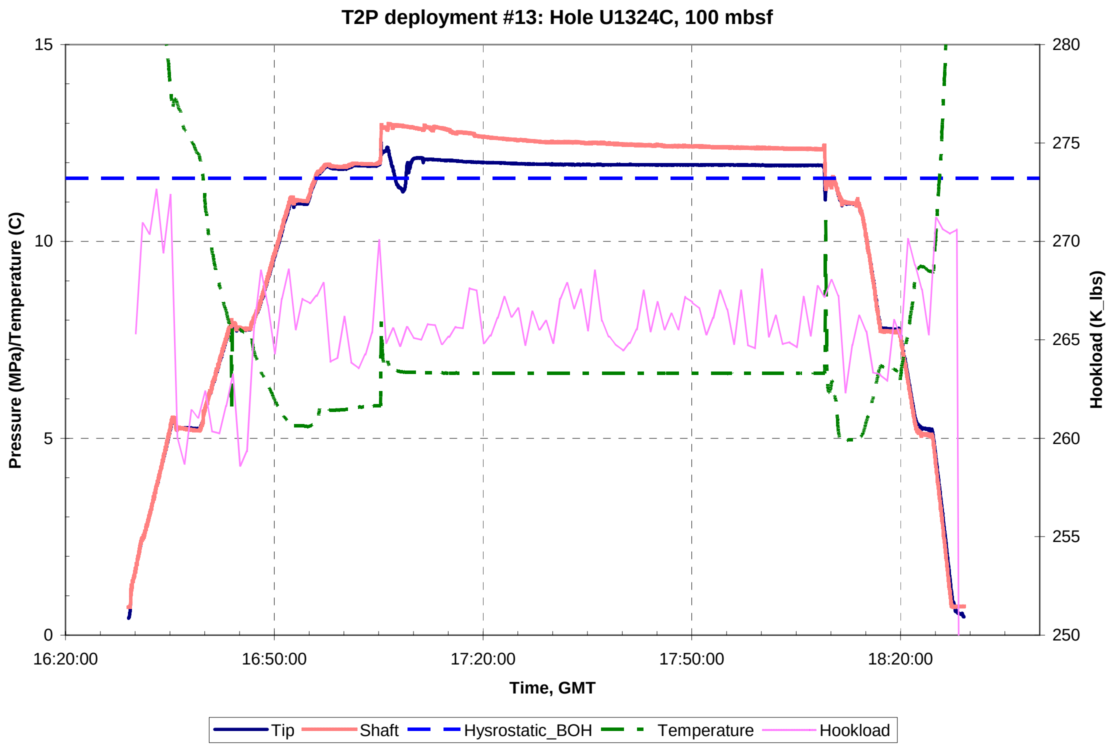

Figure A.B.19.e

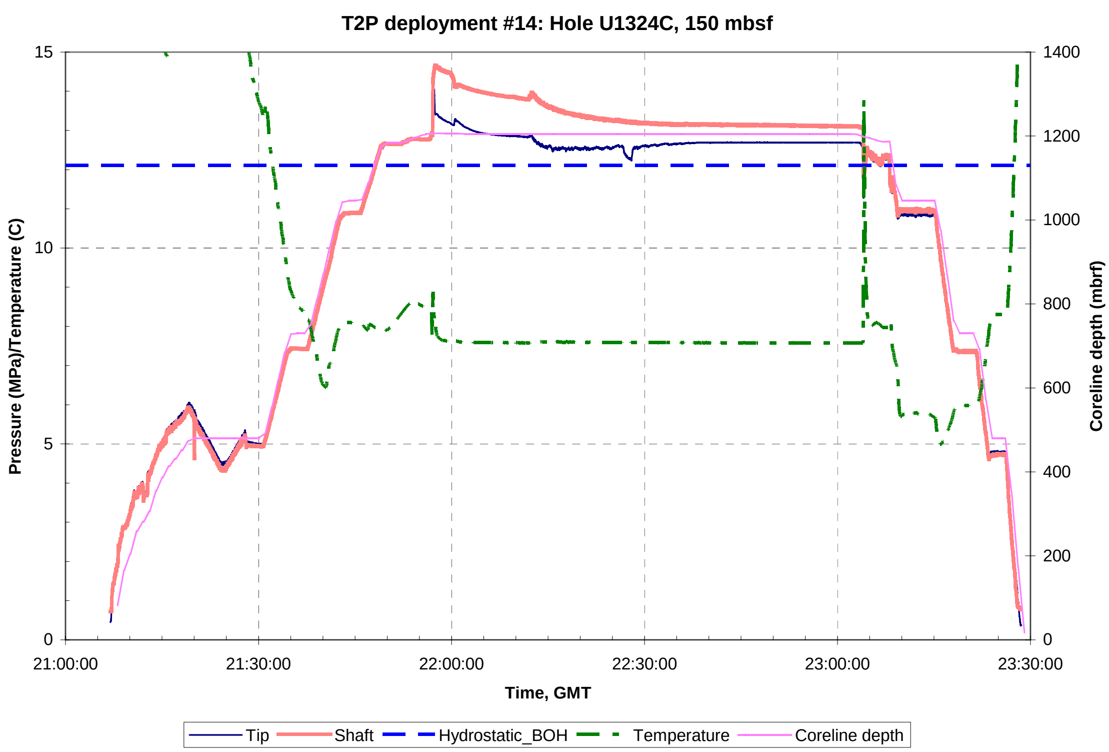

Figure A.B.20.a: Pressure, temperature and Truview data for T2P deployment #14, Hole U1324C, 150 mbsf. GMT = Greenwich Mean Time, Hydrostatic_BOH is the hydrostatic pressure at the bottom of the hole.

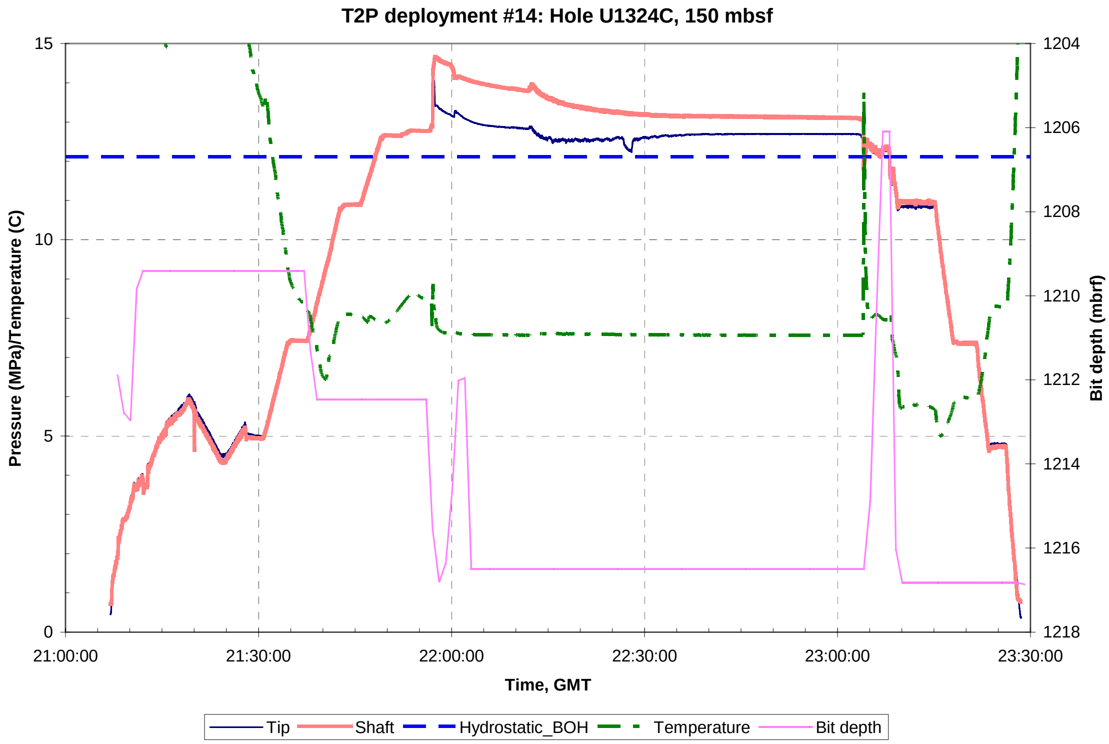

Figure A.B.20.b

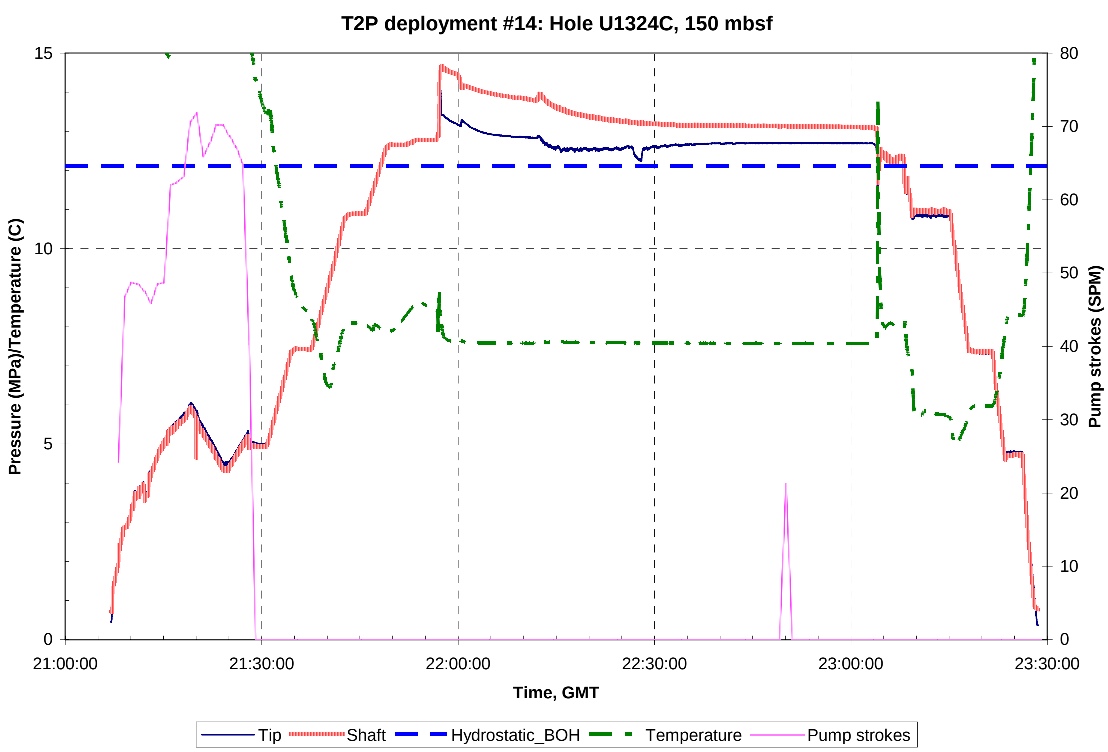

Figure A.B.20.c

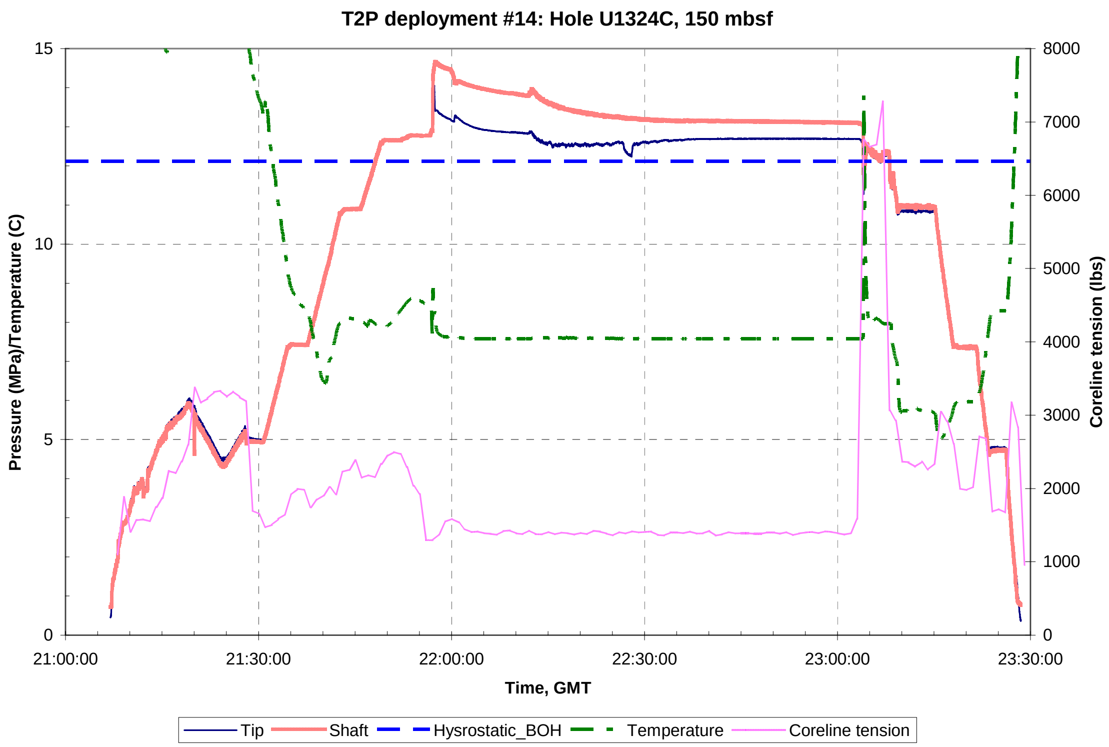

Figure A.B.20.d

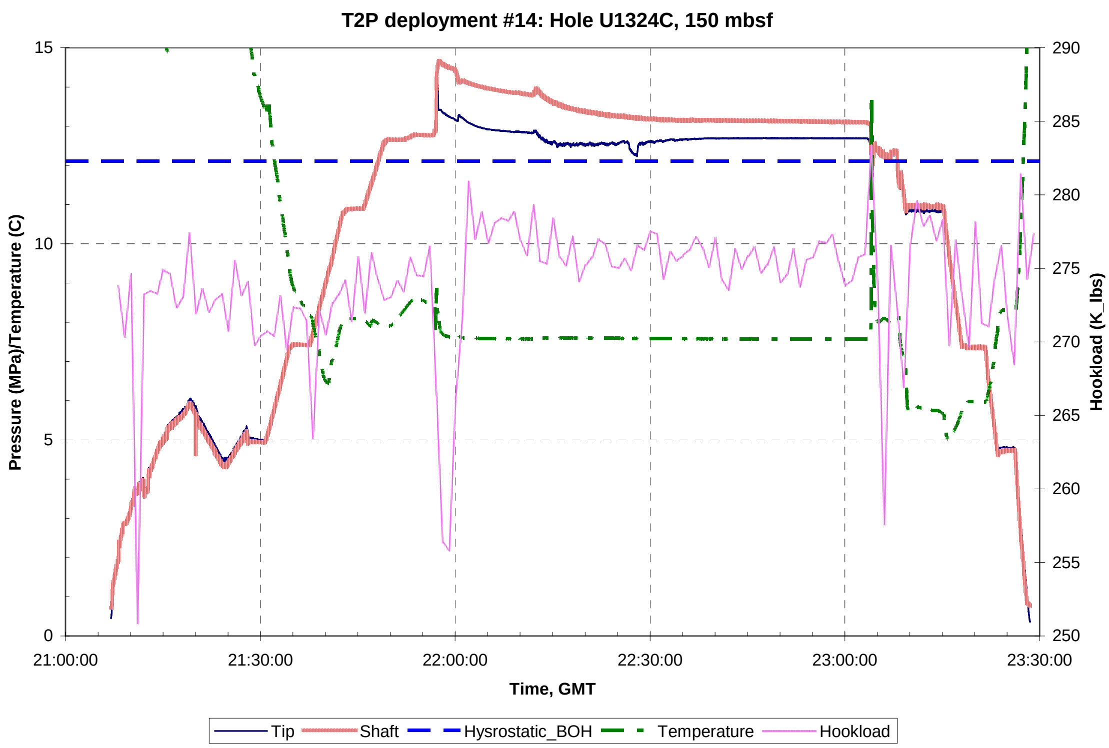

Figure A.B.20.e

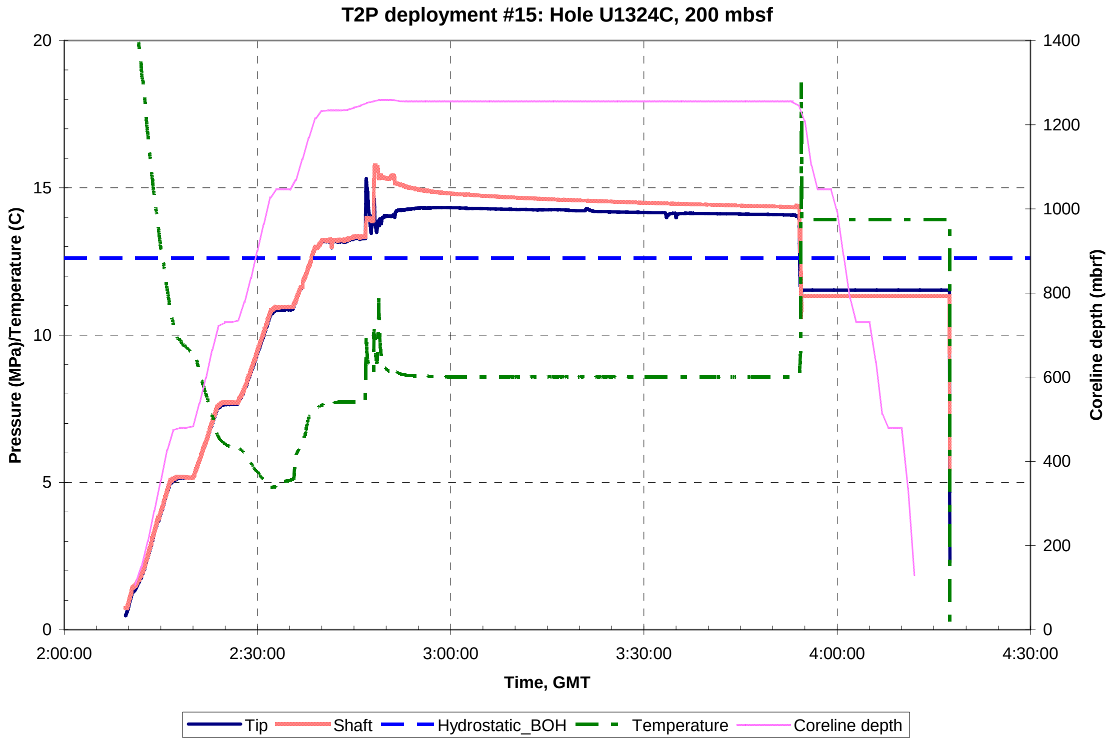

Figure A.B.21.a: Pressure, temperature and Truview data for T2P deployment #15, Hole U1324C, 200 mbsf. GMT = Greenwich Mean Time, Hydrostatic_BOH is the hydrostatic pressure at the bottom of the hole.

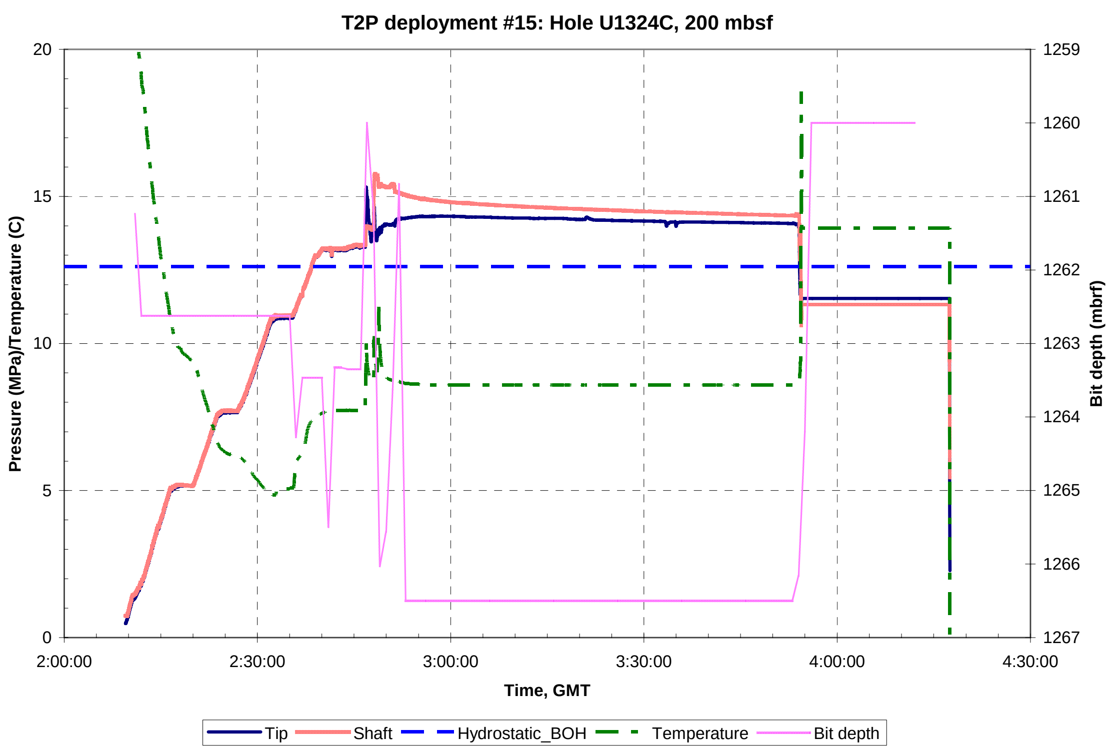

Figure A.B.21.b

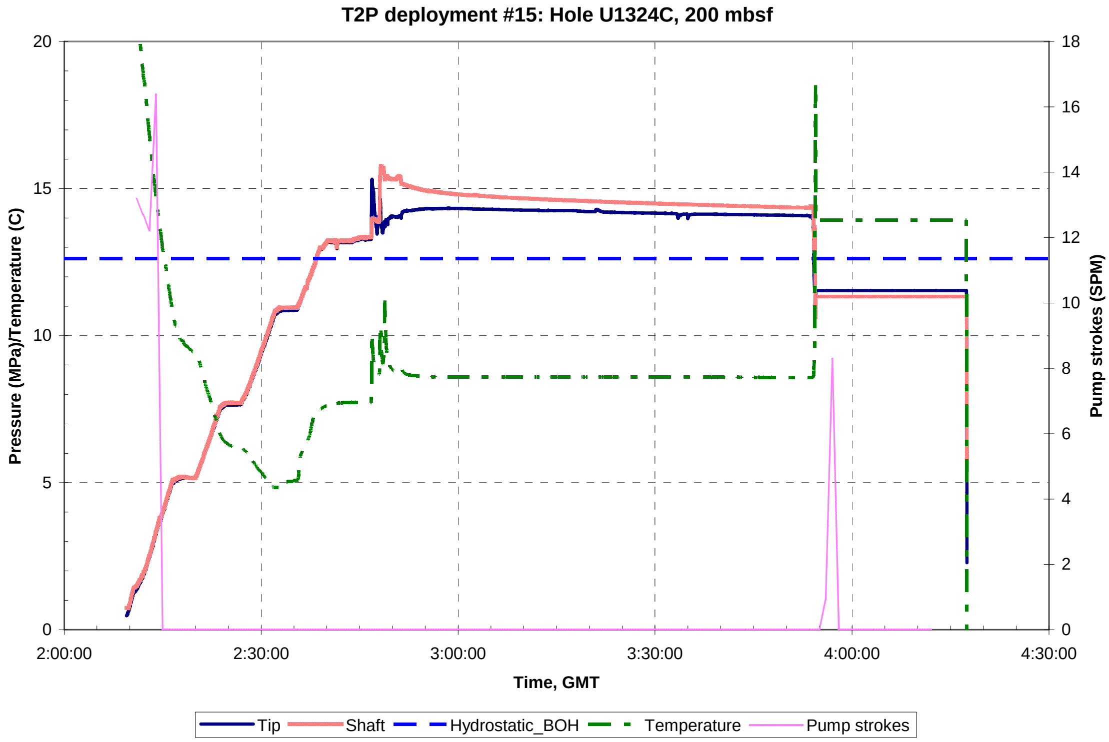

Figure A.B.21.c

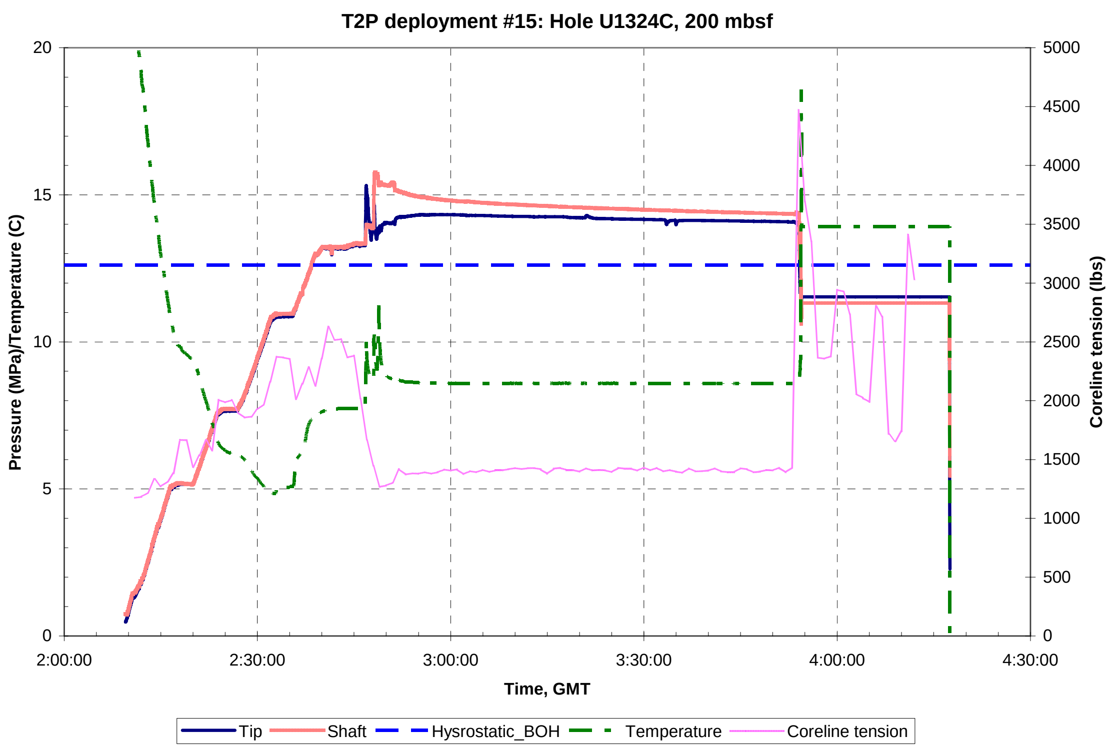

Figure A.B.21.d

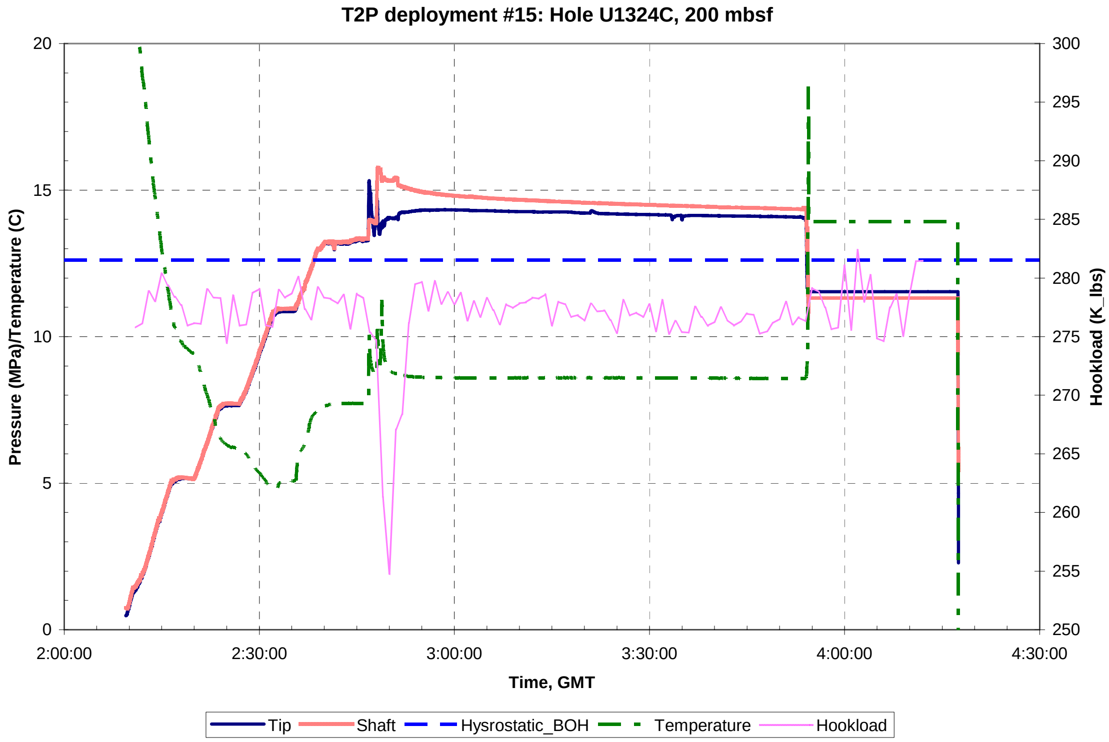

Figure A.B.21.e

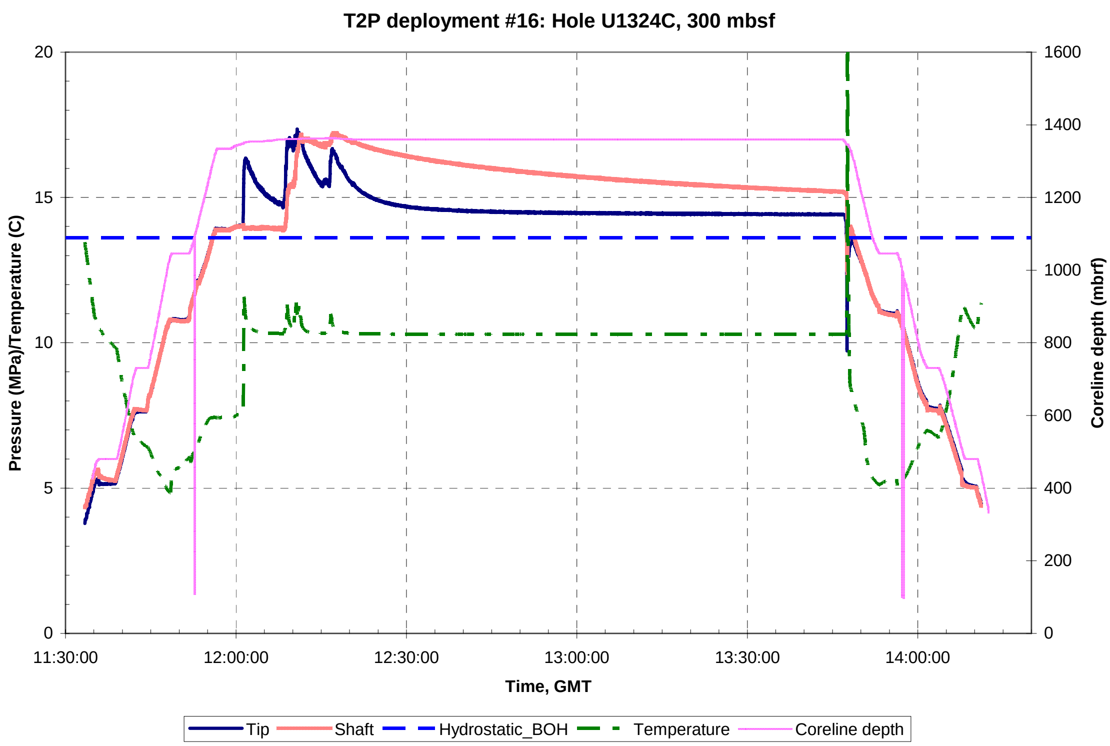

Figure A.B.22.a: Pressure, temperature and Truview data for T2P deployment #16, Hole U1324C, 300 mbsf. GMT = Greenwich Mean Time, Hydrostatic_BOH is the hydrostatic pressure at the bottom of the hole.

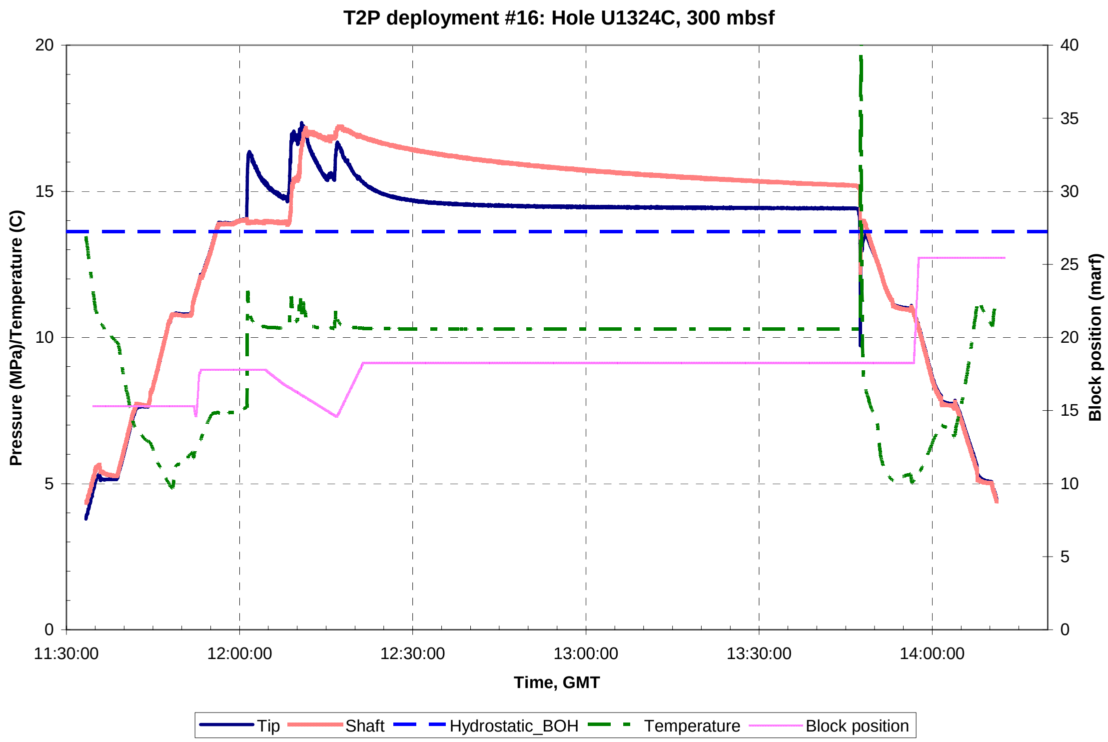

Figure A.B.22.b

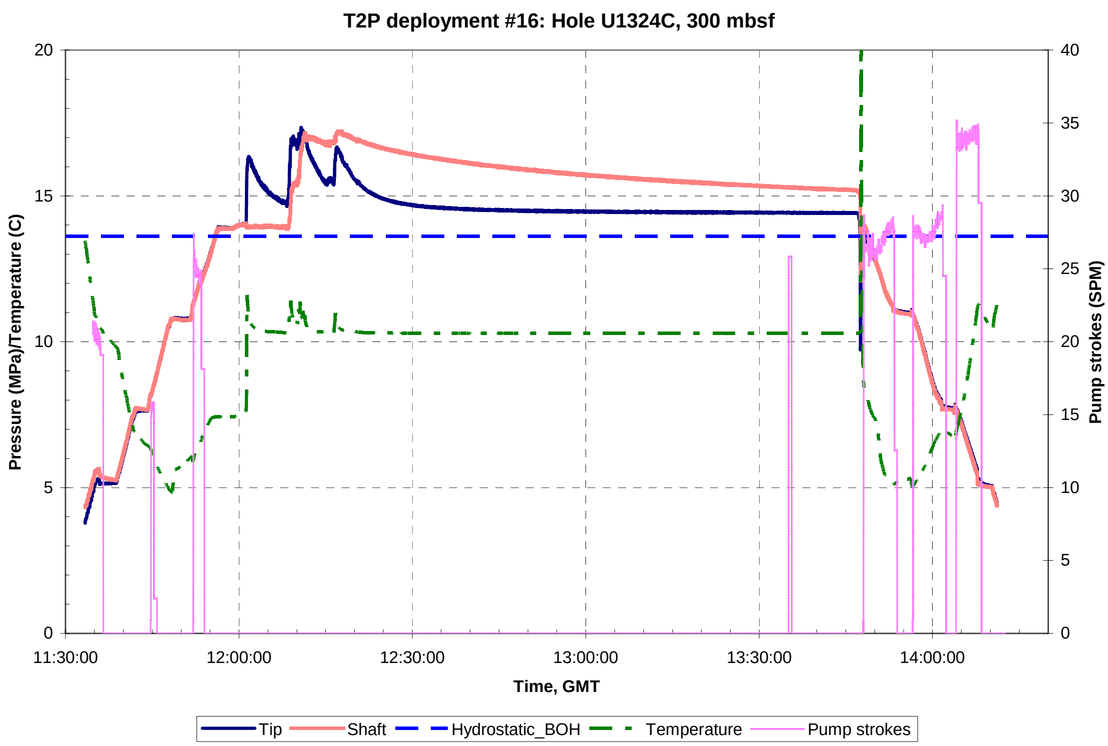

Figure A.B.22.c

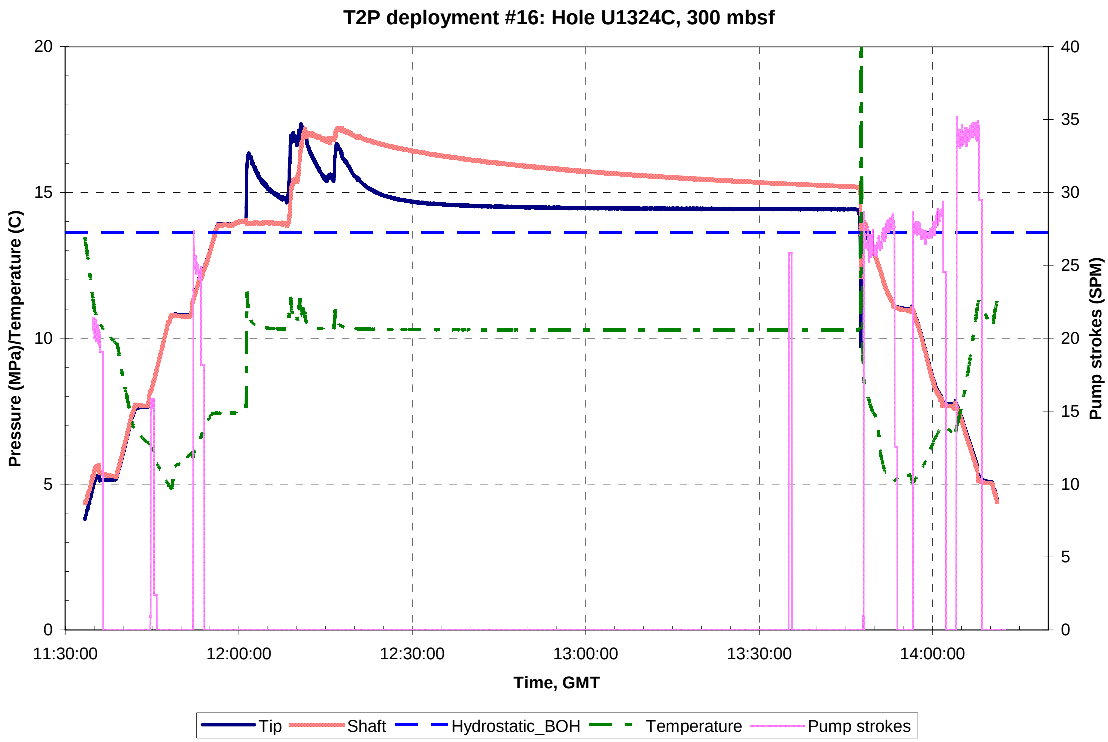

Figure A.B.22.d

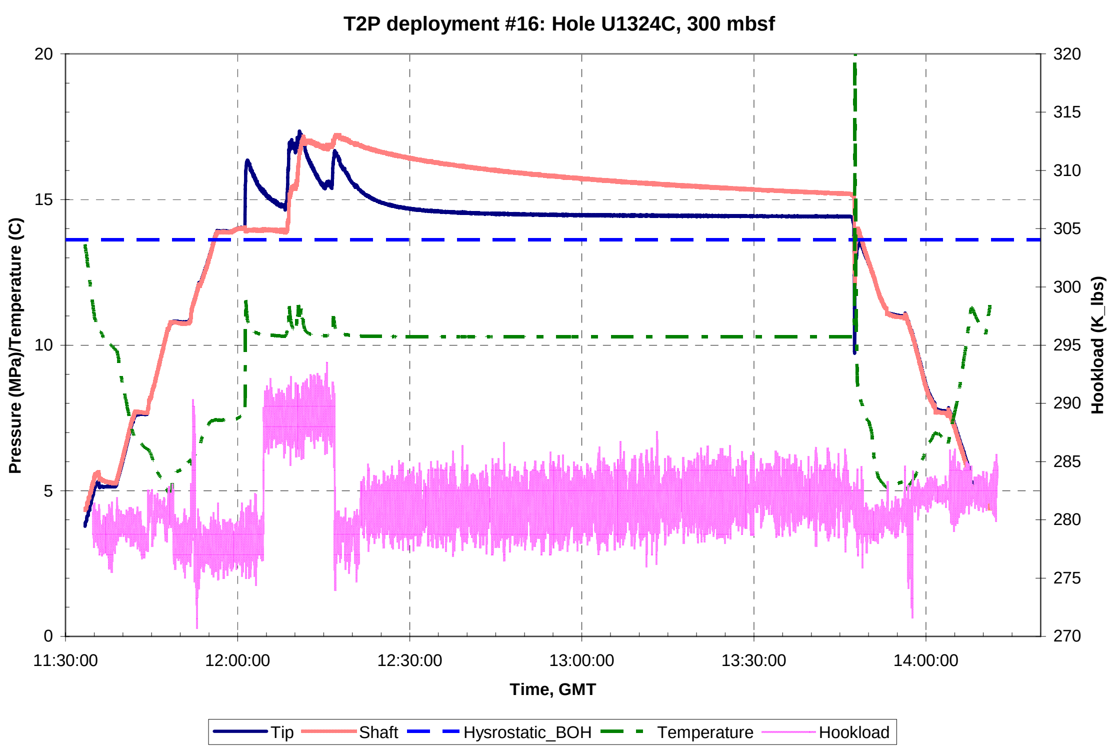

Figure A.B.22.e

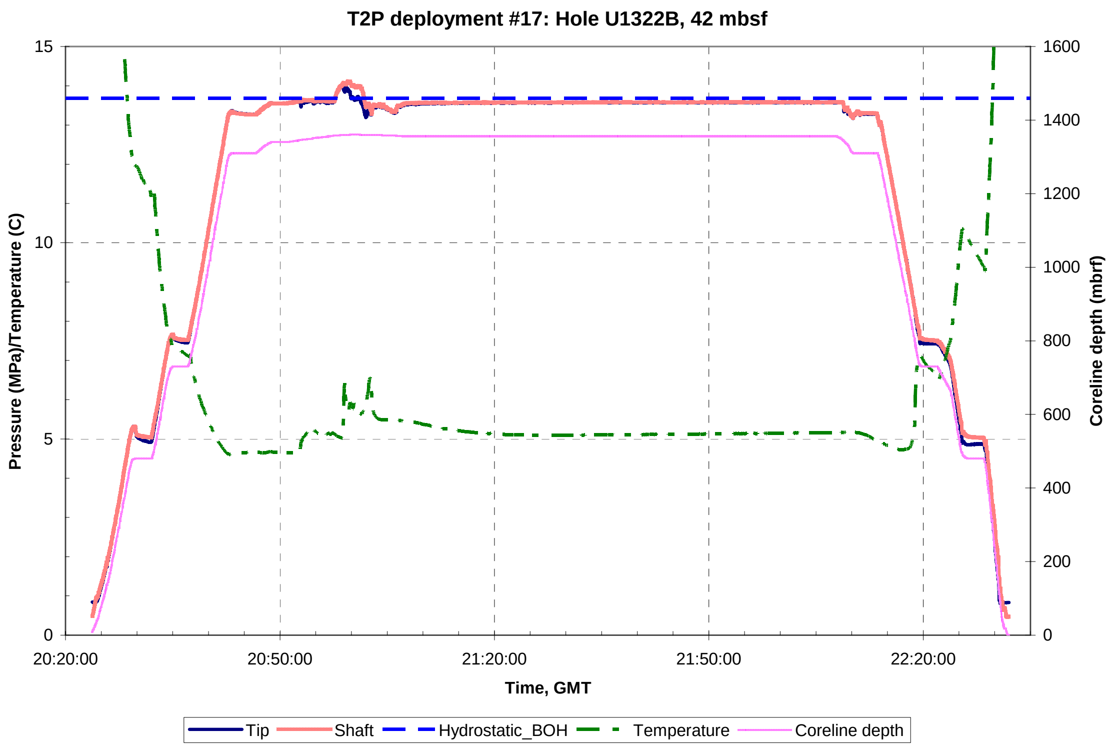

Figure A.B.23.a: Pressure, temperature and Truview data for T2P deployment #17, Hole U1322B, 42 mbsf. GMT = Greenwich Mean Time, Hydrostatic_BOH is the hydrostatic pressure at the bottom of the hole.

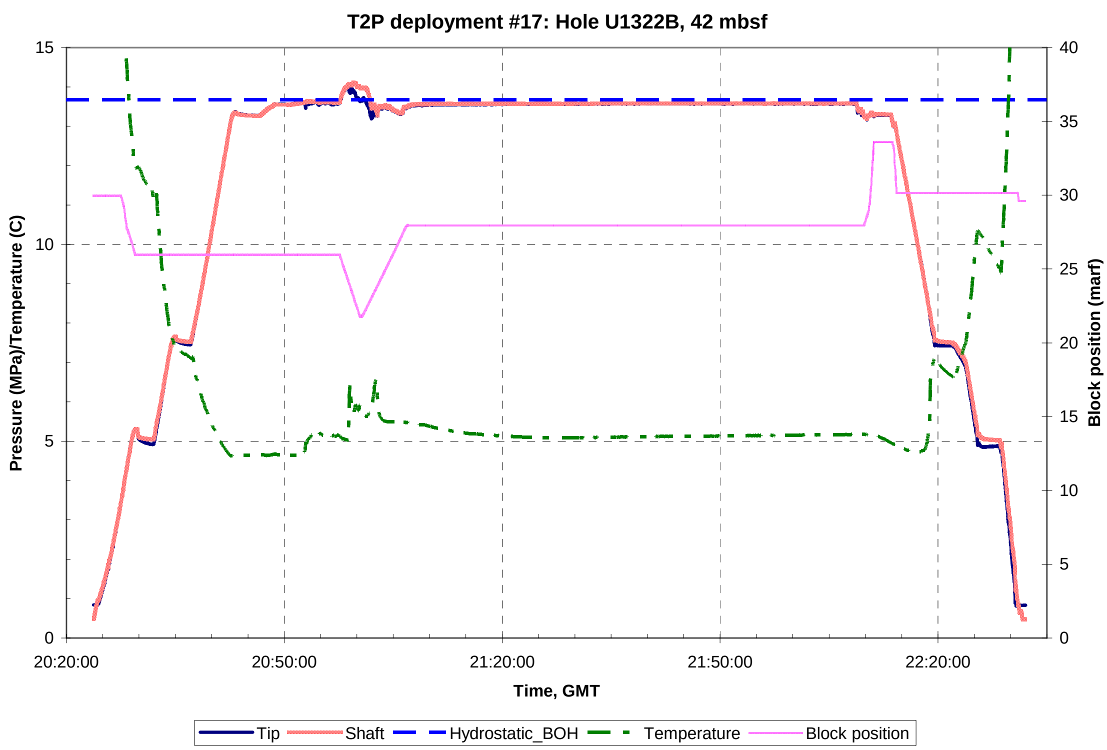

Figure A.B.23.b

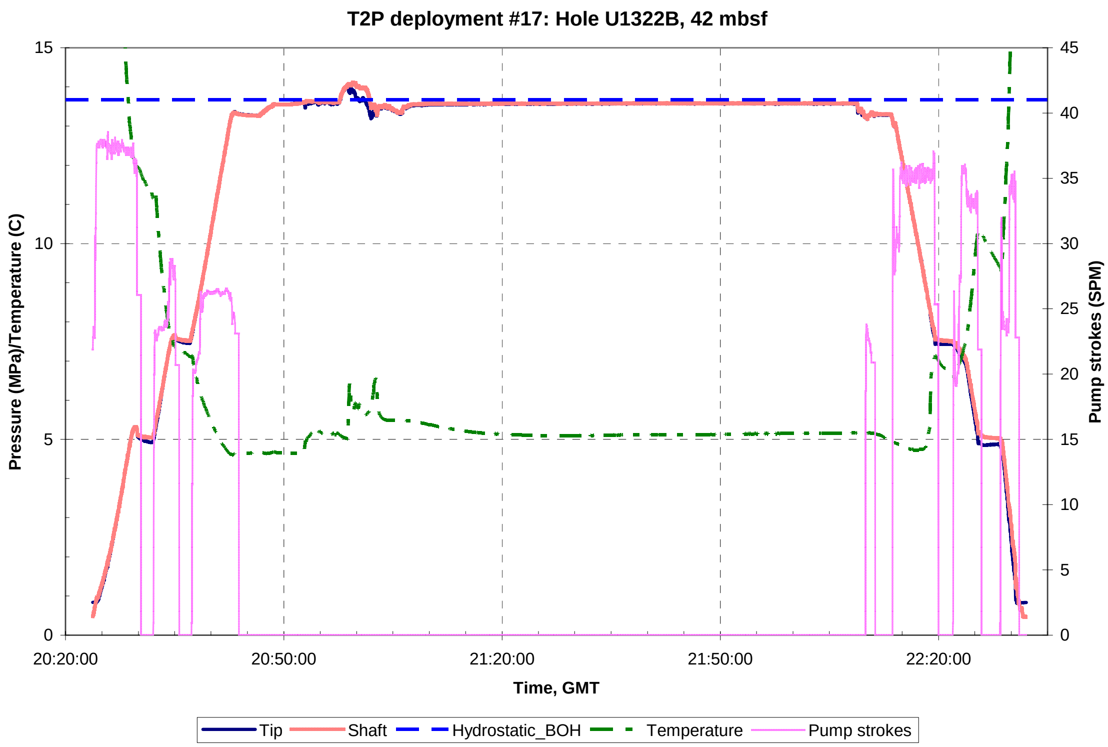

Figure A.B.23.c

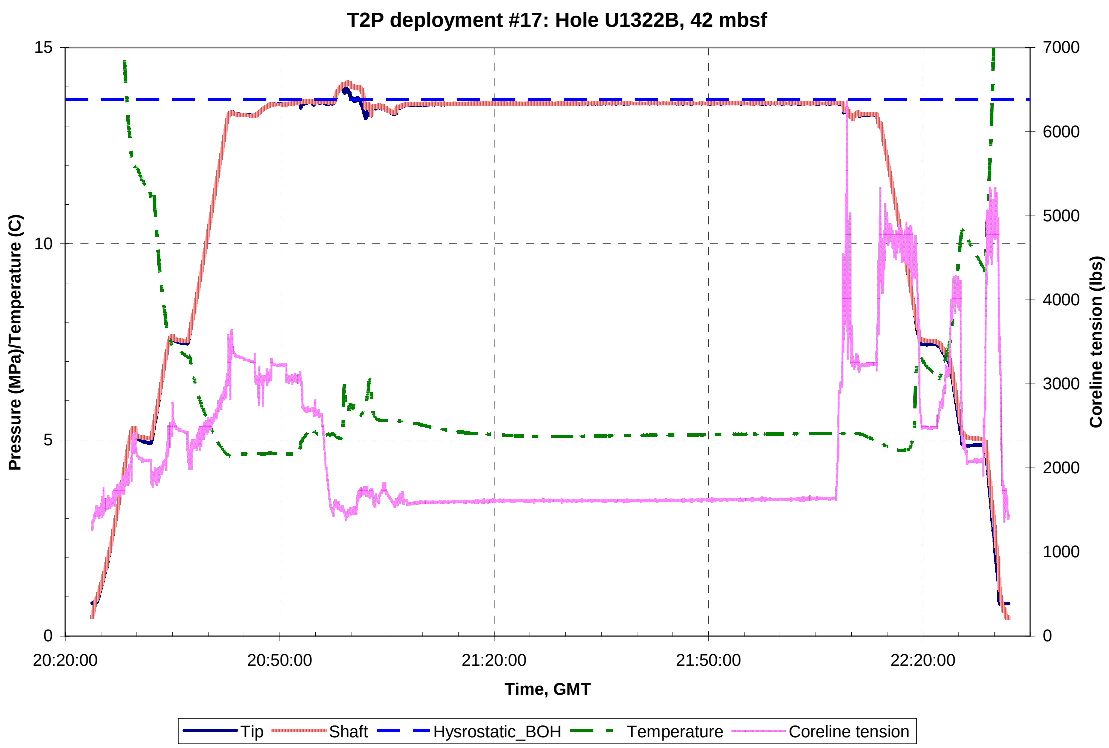

Figure A.B.23.d

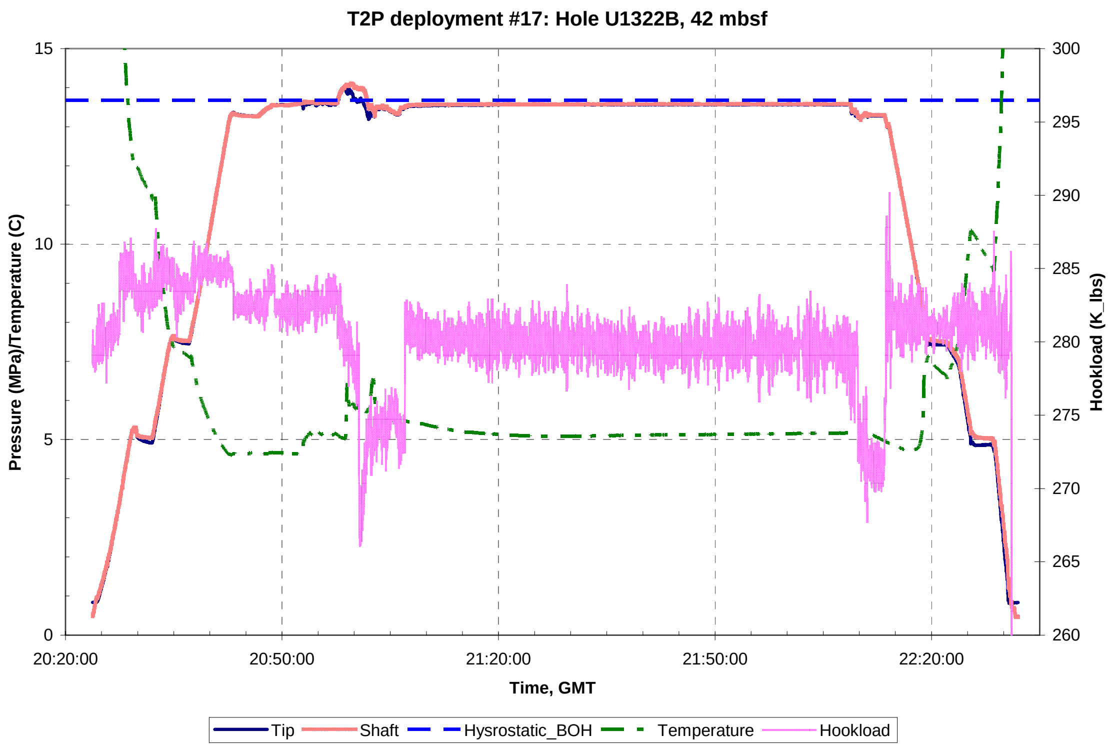

Figure A.B.23.e

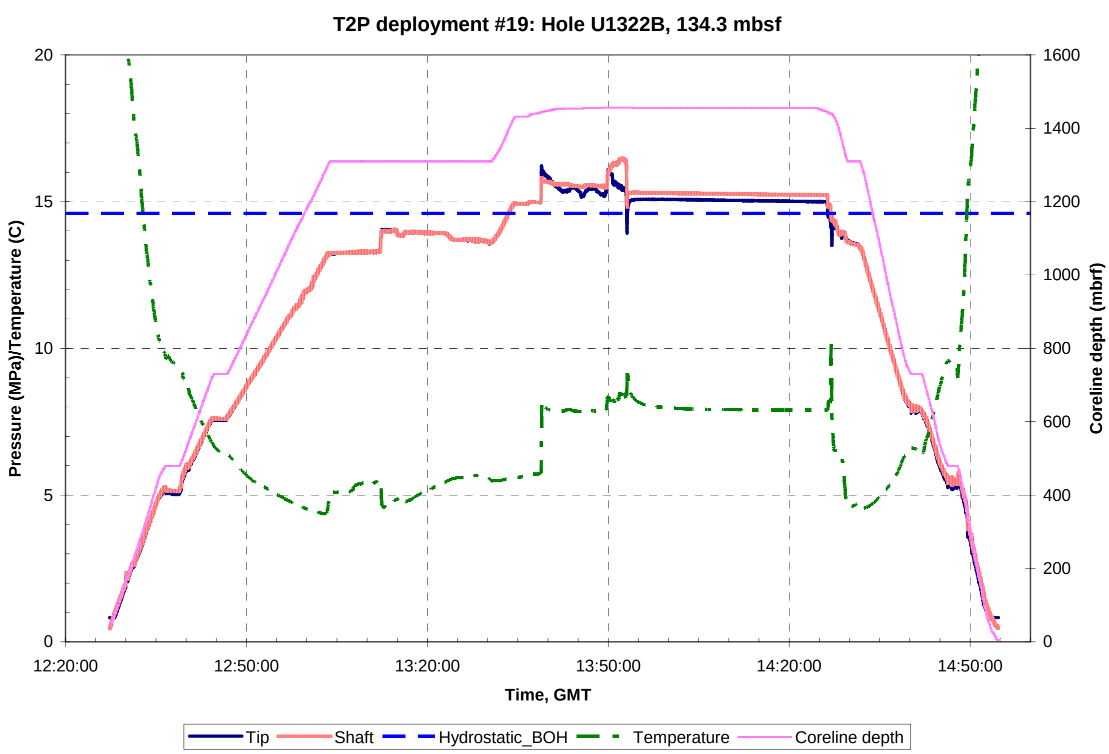

Figure A.B.24.a: Pressure, temperature and Truview data for T2P deployment #19, Hole U1322B, 134.3 mbsf. GMT = Greenwich Mean Time, Hydrostatic_BOH is the hydrostatic pressure at the bottom of the hole.

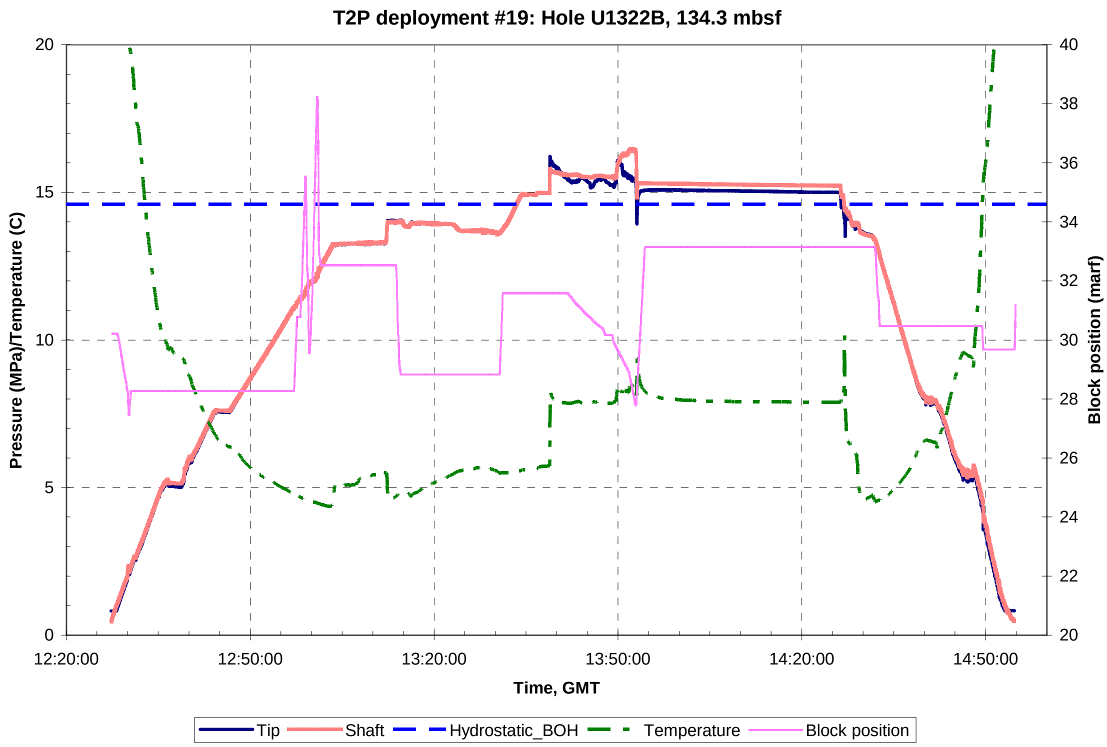

Figure A.B.24.b

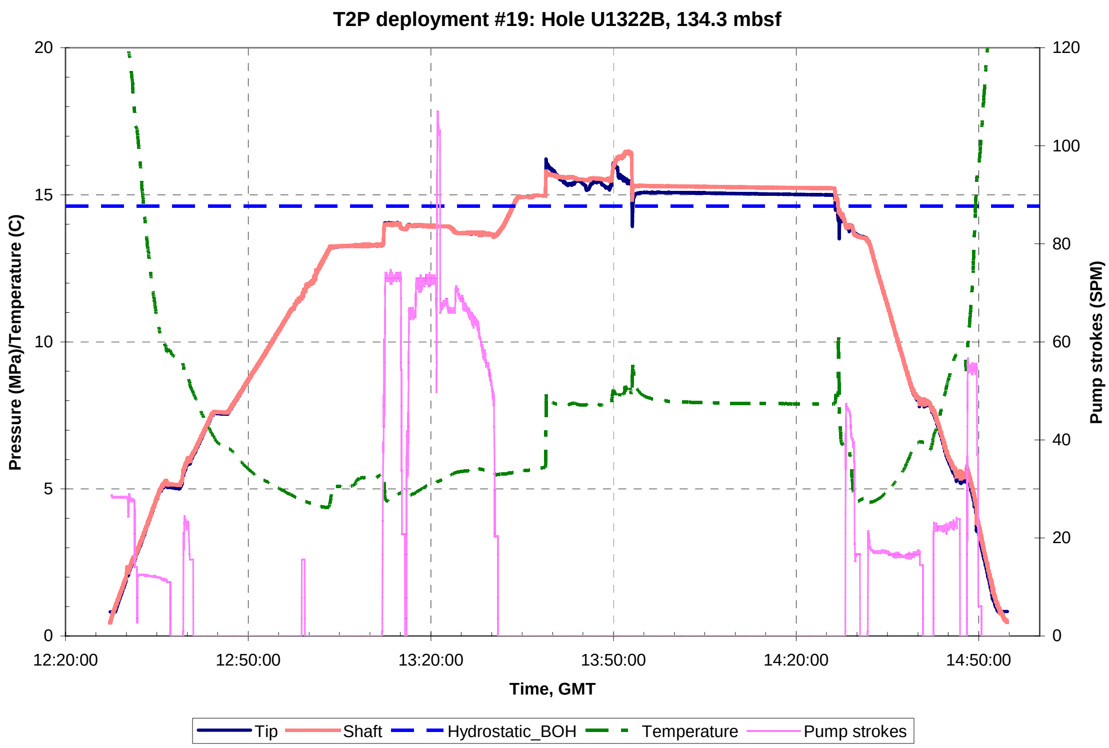

Figure A.B.24.c

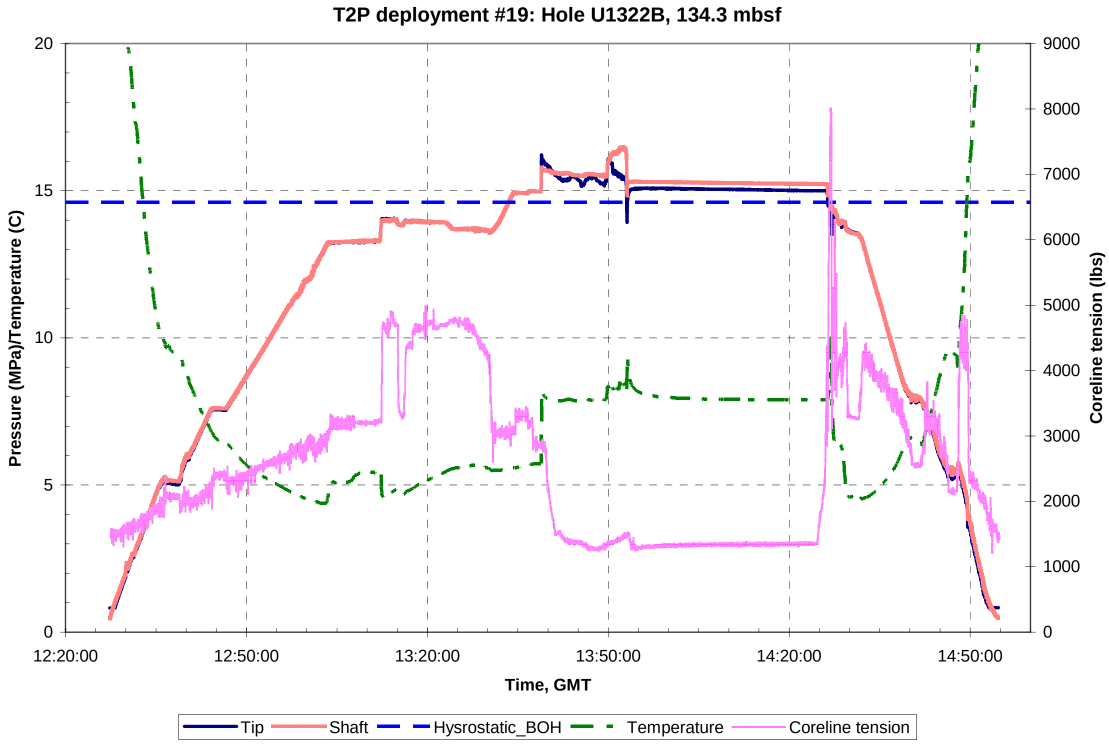

Figure A.B.24.d

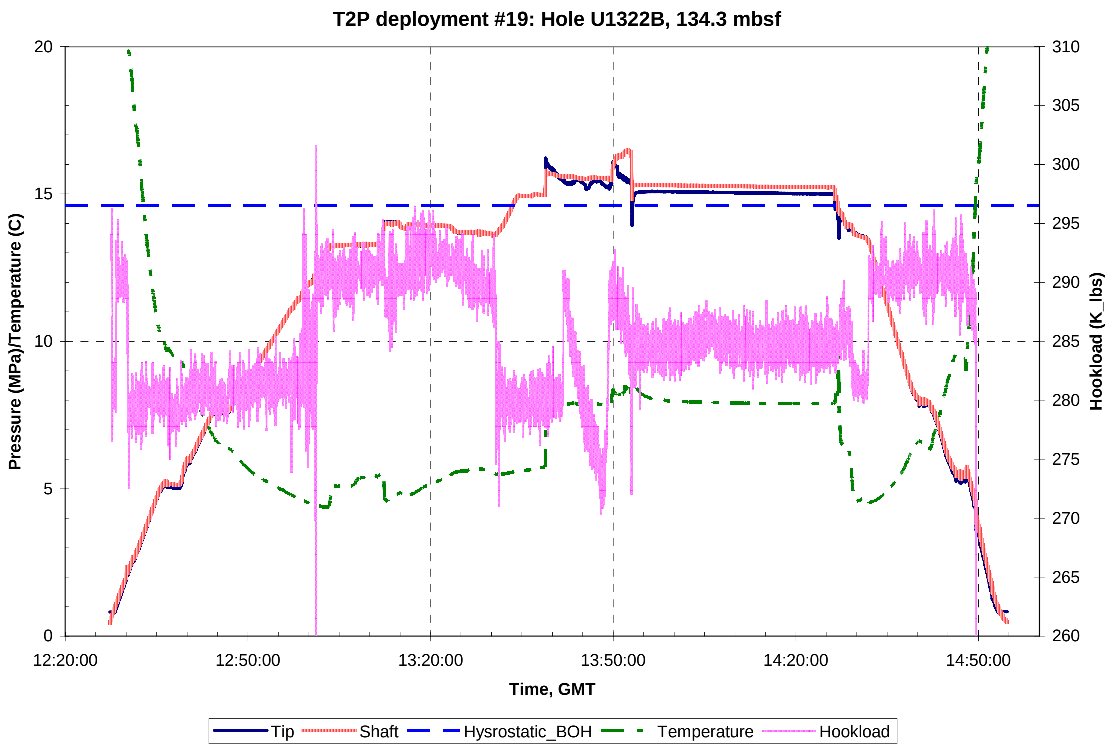

Figure A.B.24.e

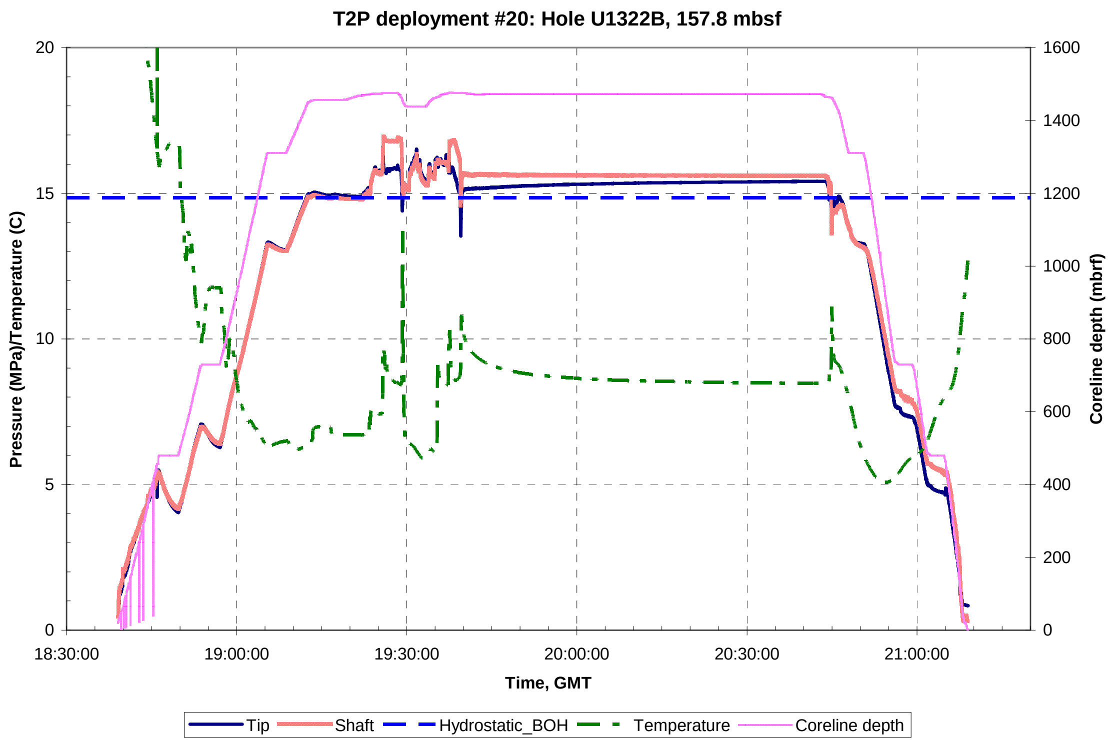

Figure A.B.25.a: Pressure, temperature and Truview data for T2P deployment #20, Hole U1322B, 157.8 mbsf. GMT = Greenwich Mean Time, Hydrostatic_BOH is the hydrostatic pressure at the bottom of the hole.

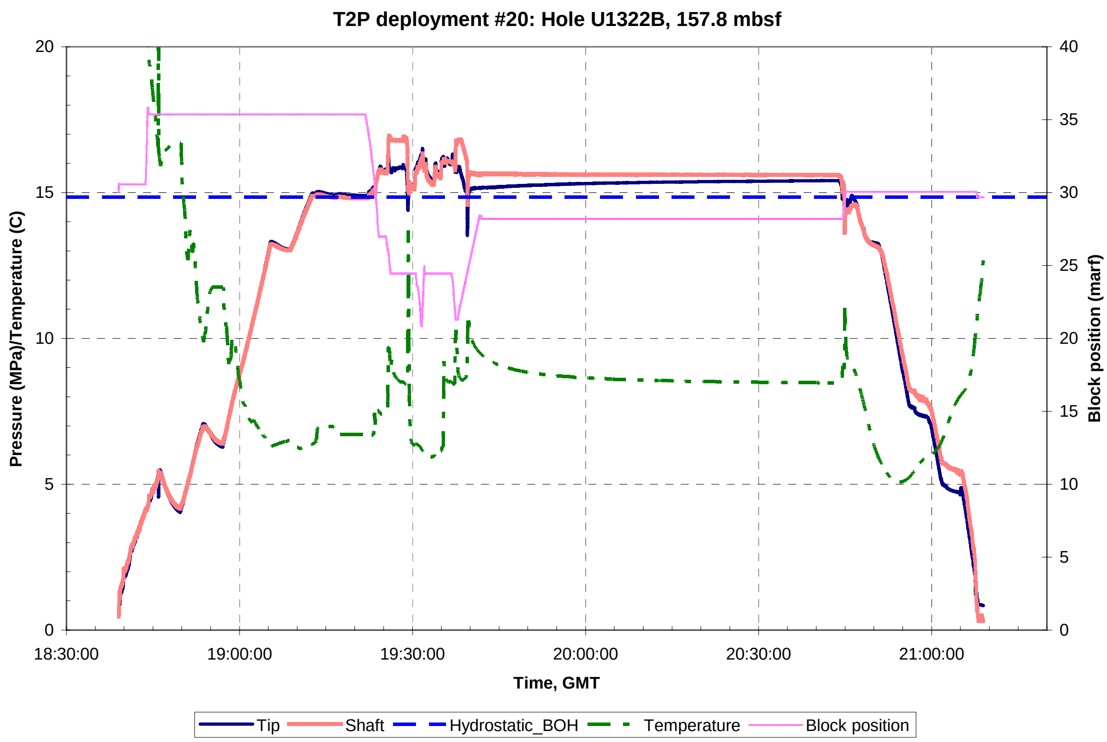

Figure A.B.25.b

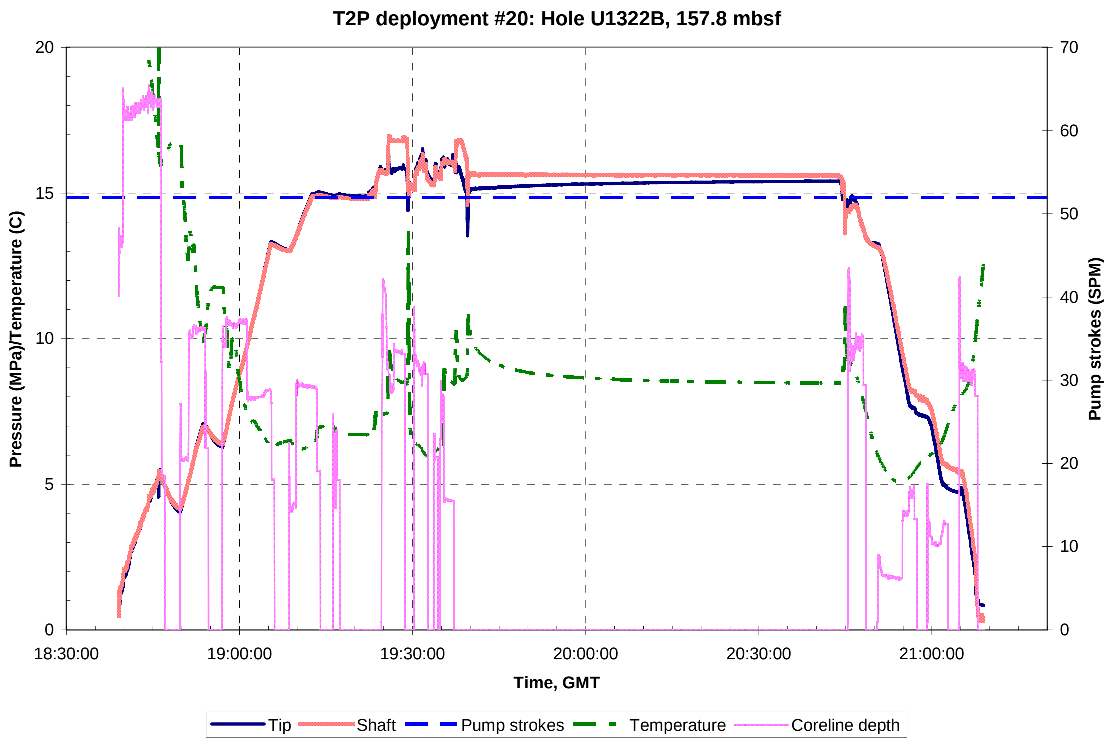

Figure A.B.25.c

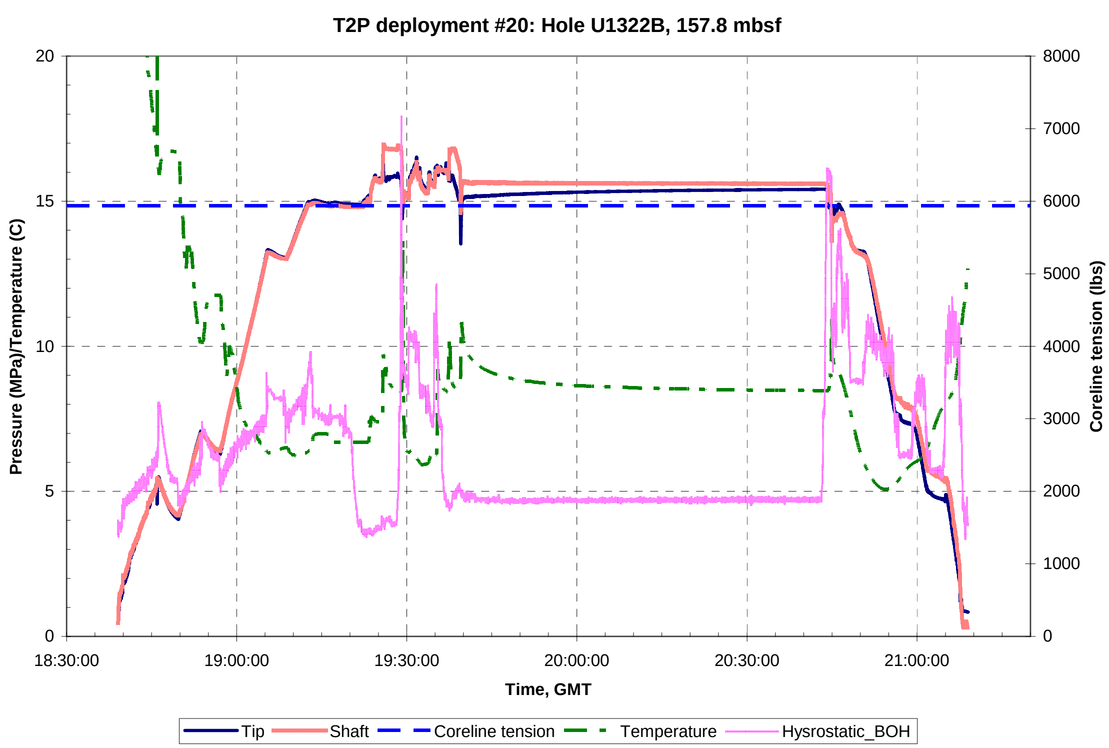

Figure A.B.25.d

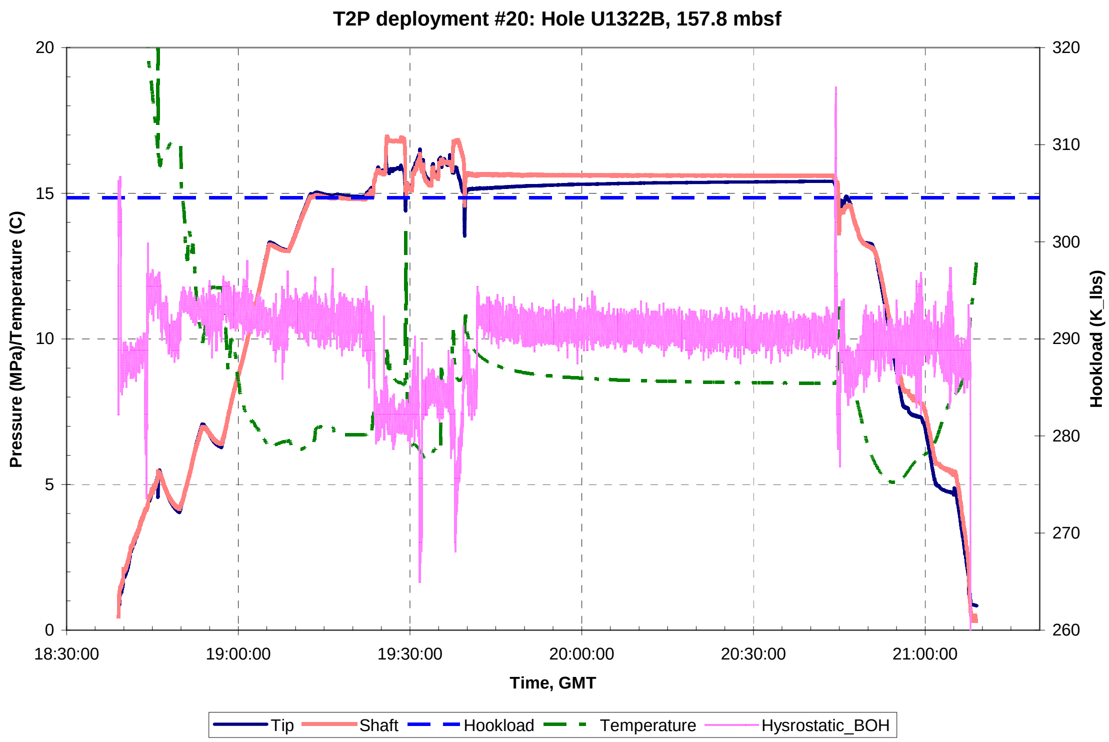

Figure A.B.25.e

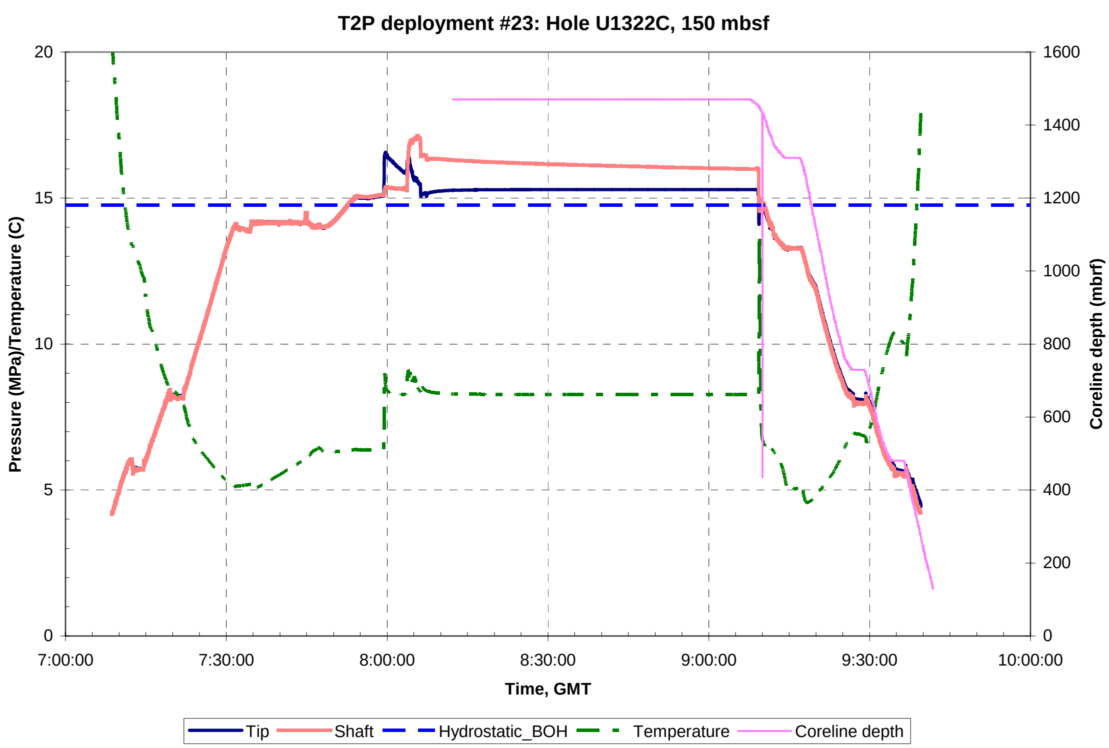

Figure A.B.26.a: Pressure, temperature and Truview data for T2P deployment #23, Hole U1322C, 150 mbsf. GMT = Greenwich Mean Time, Hydrostatic_BOH is the hydrostatic pressure at the bottom of the hole.

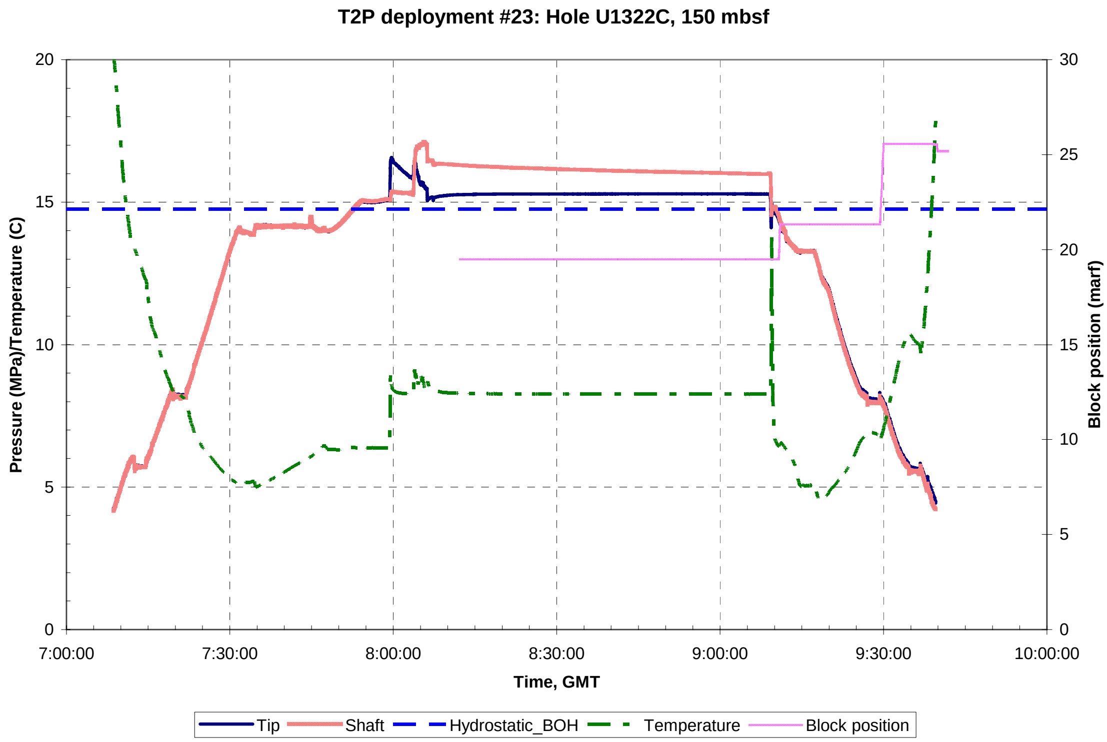

Figure A.B.26.b

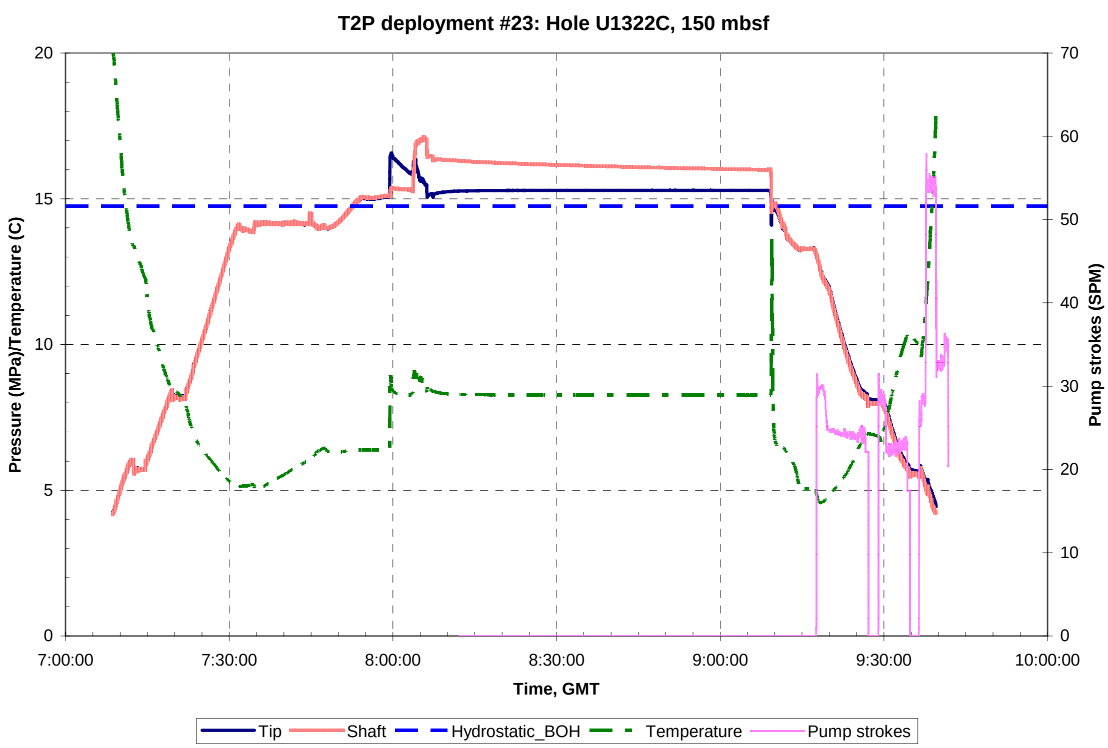

Figure A.B.26.c

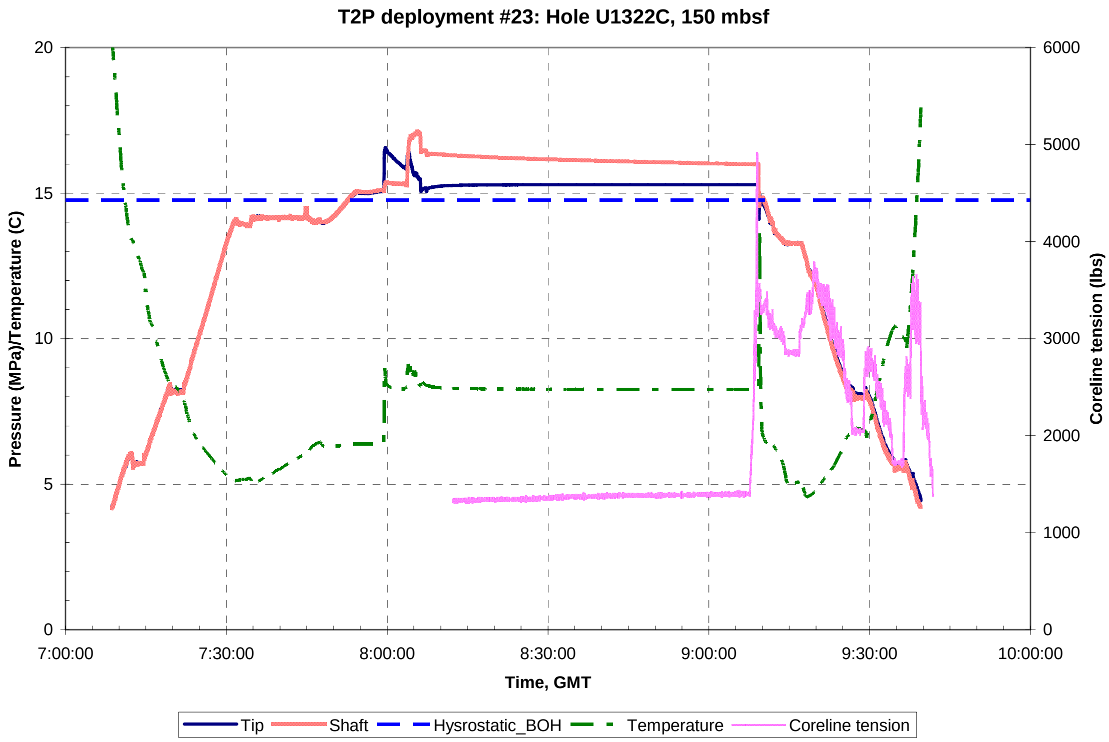

Figure A.B.26.d

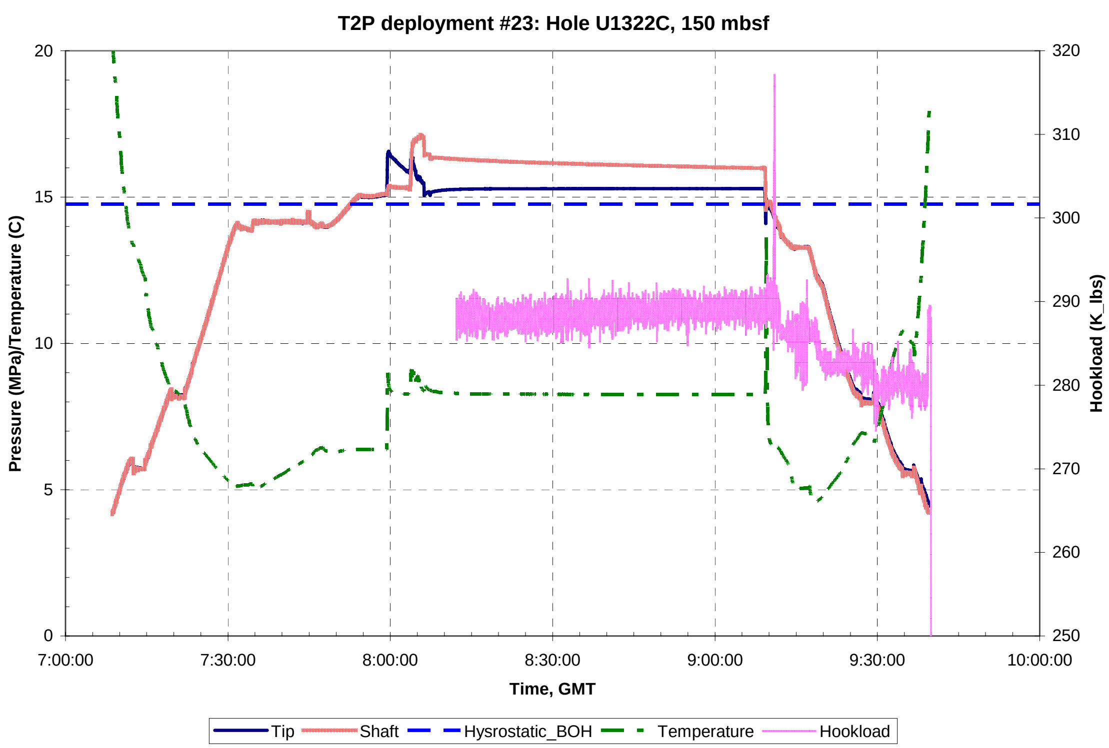

Figure A.B.26.e

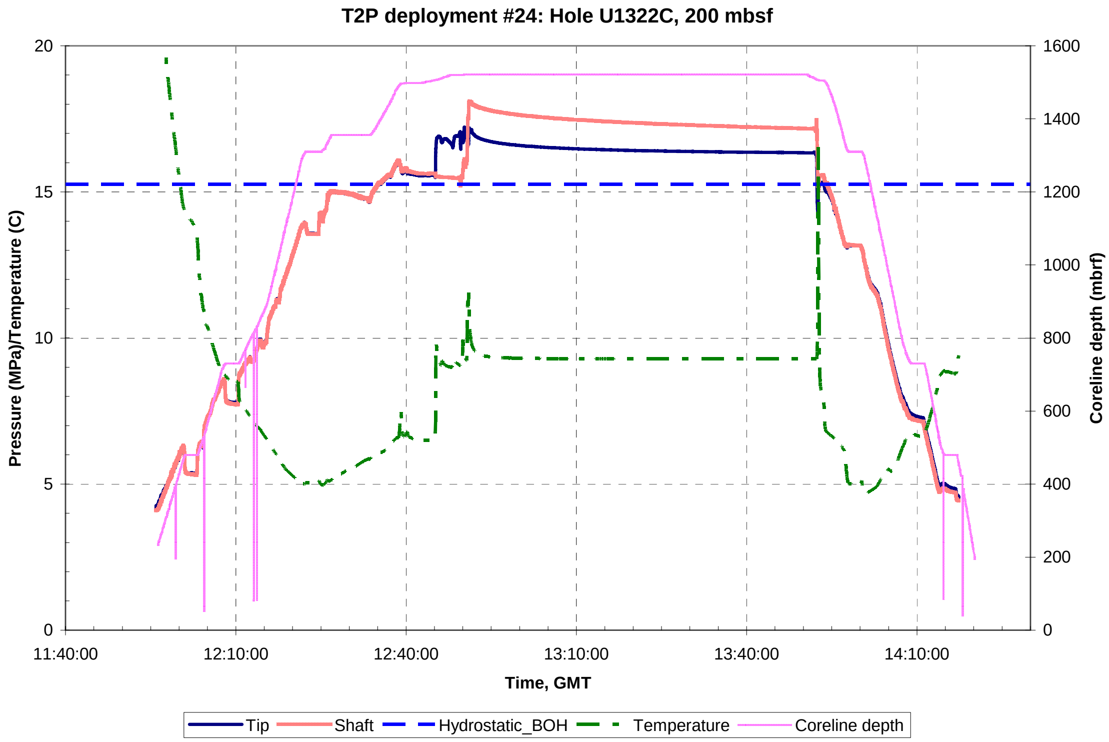

Figure A.B.27.a: Pressure, temperature and Truview data for T2P deployment #24, Hole U1322C, 200 mbsf. GMT = Greenwich Mean Time, Hydrostatic_BOH is the hydrostatic pressure at the bottom of the hole.

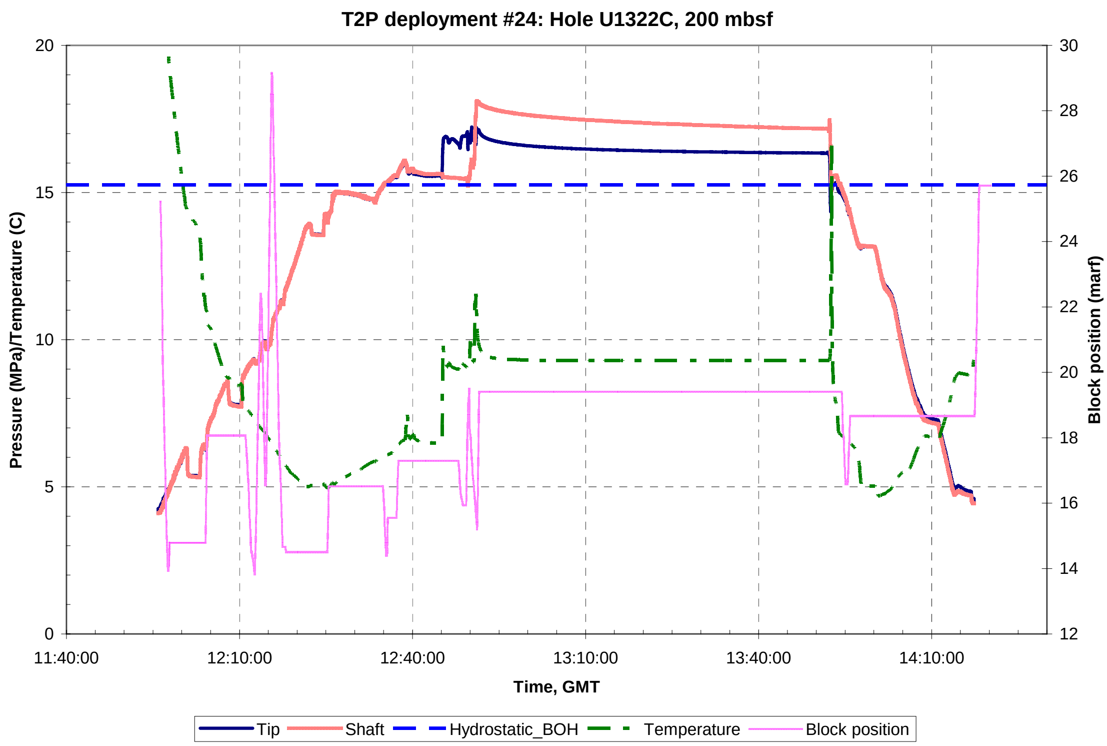

Figure A.B.27.b

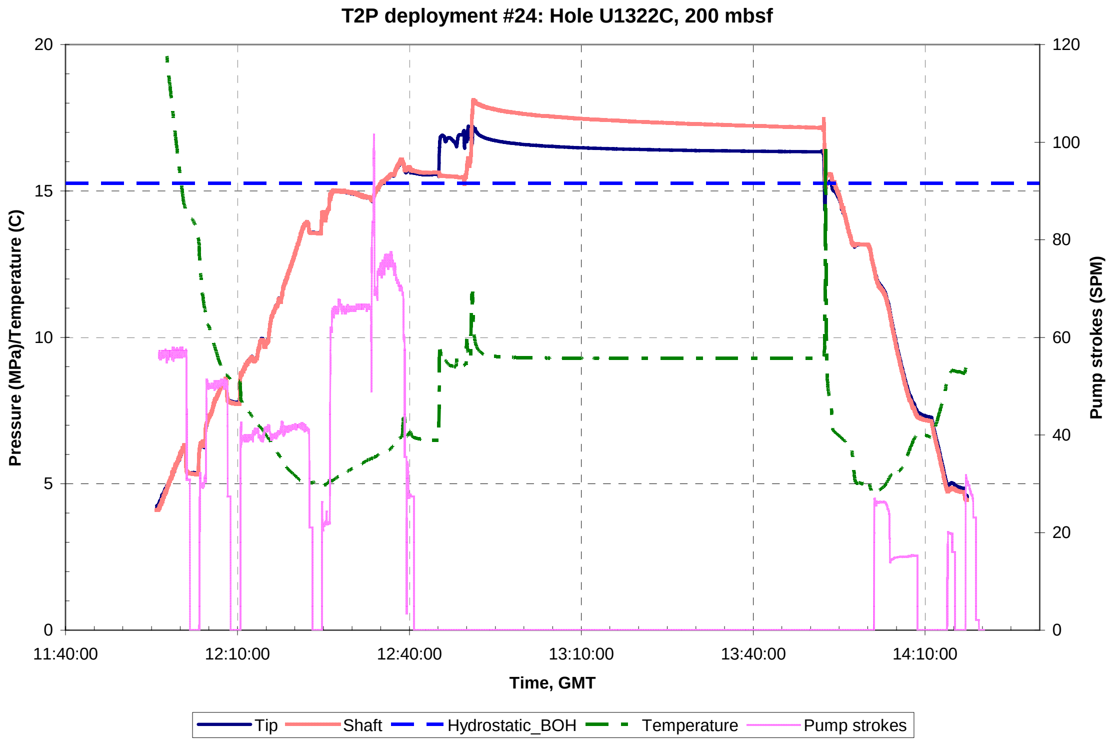

Figure A.B.27.c

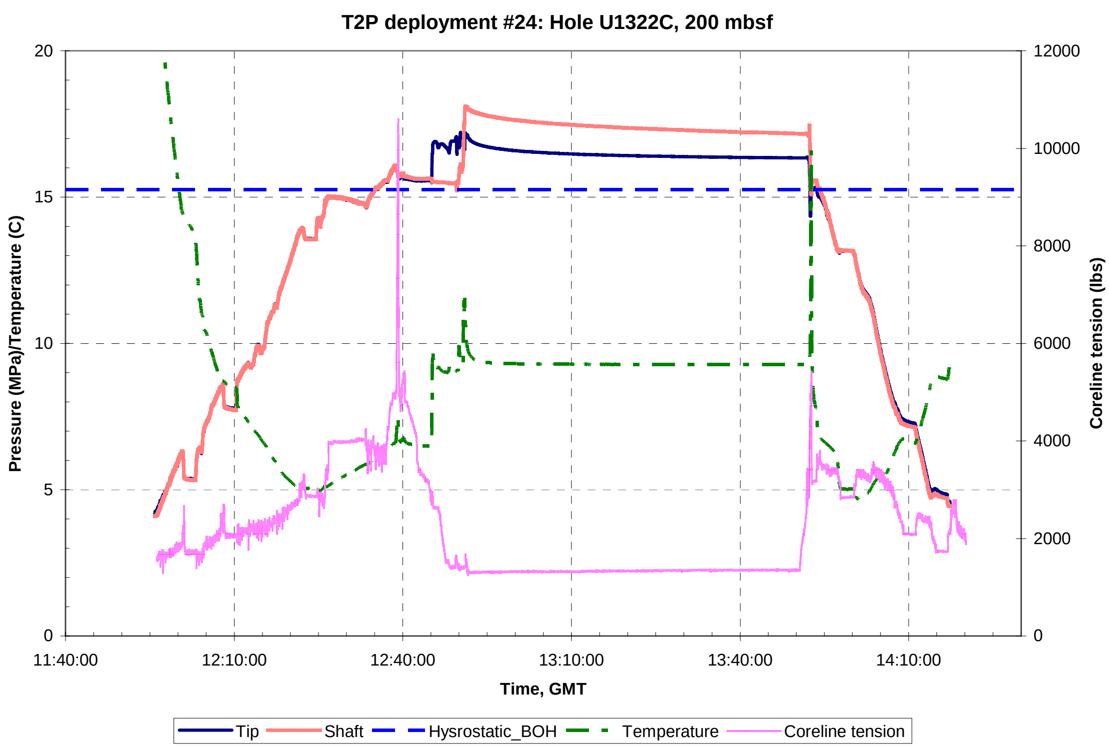

Figure A.B.27.d

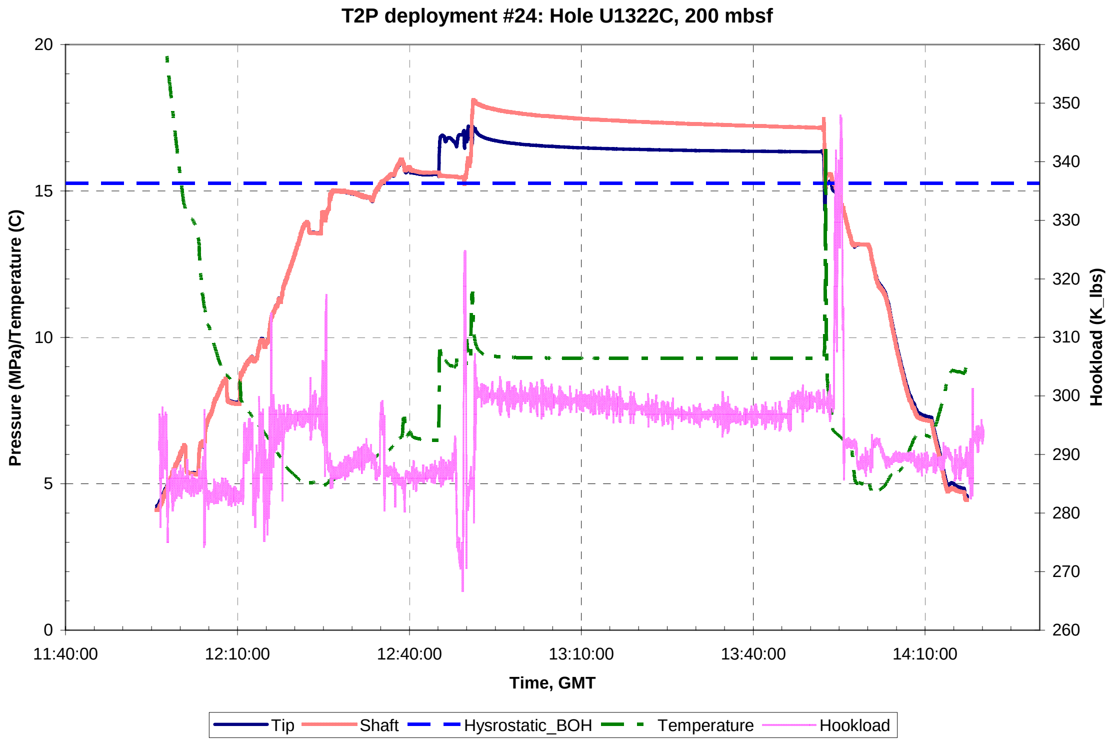

Figure A.B.27.e

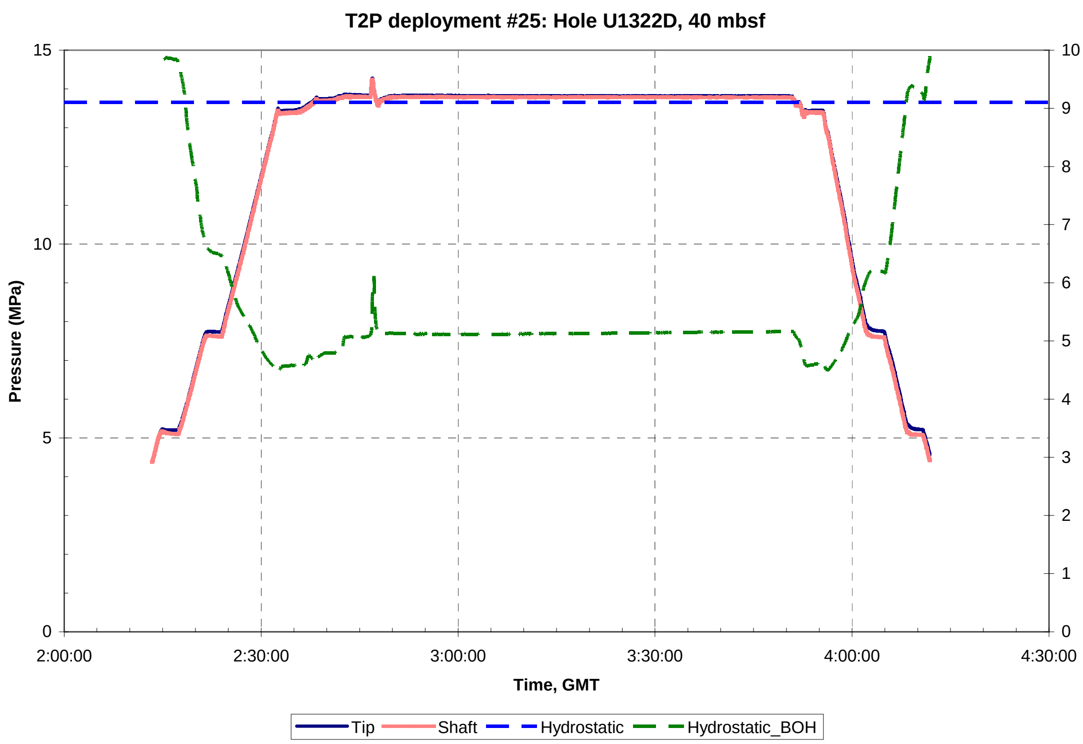

Figure A.B.28: Pressure and temperature data for T2P deployment #25, Hole U1322D, 40 mbsf. GMT = Greenwich Mean Time, Hydrostatic_BOH is the hydrostatic pressure at the bottom of the hole.

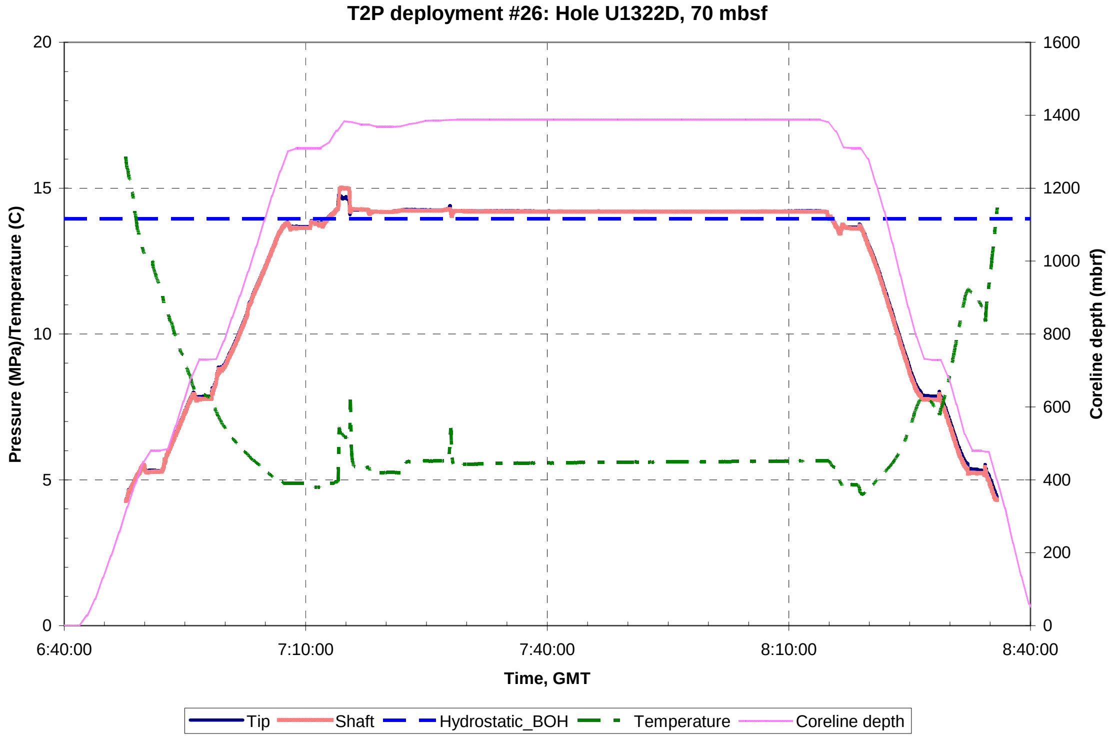

Figure A.B.29.a: Pressure, temperature and Truview data for T2P deployment #26, Hole U1322D, 70 mbsf. GMT = Greenwich Mean Time, Hydrostatic_BOH is the hydrostatic pressure at the bottom of the hole.

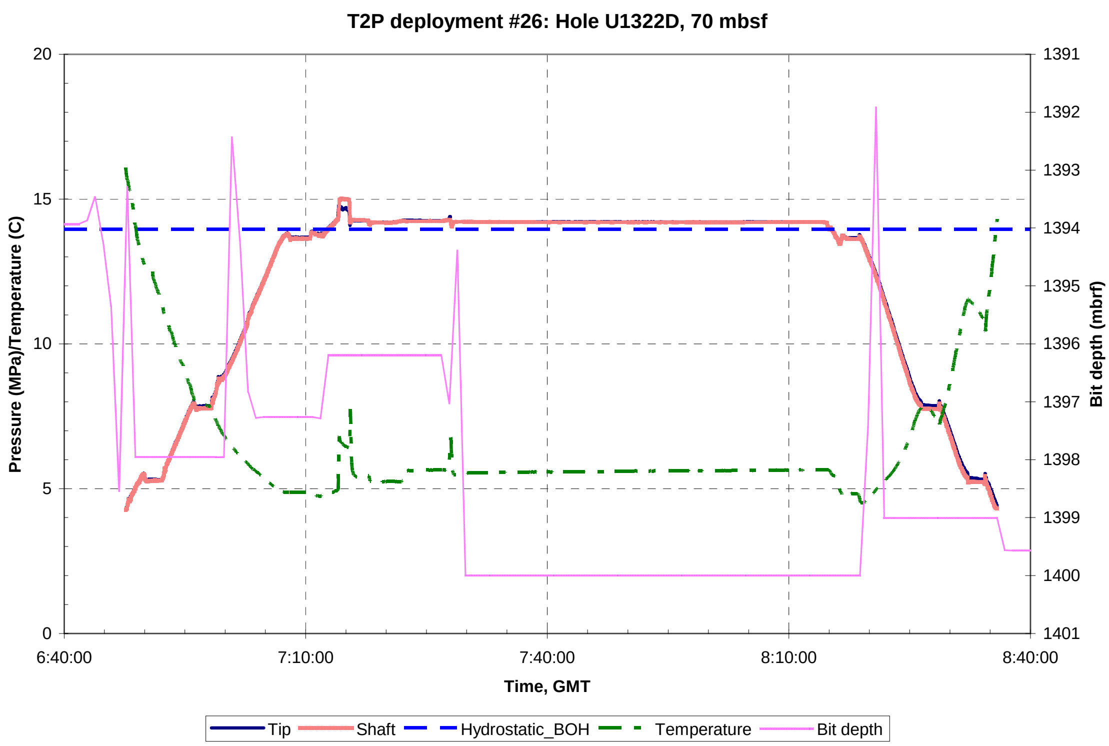

Figure A.B.29.b

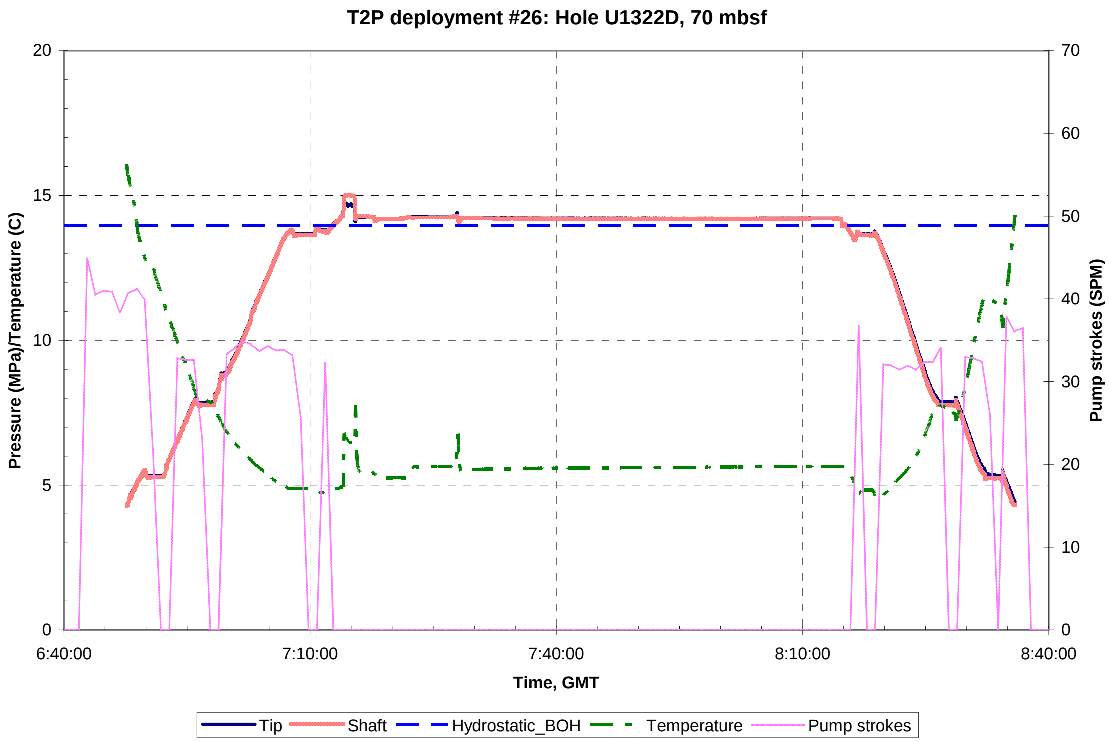

Figure A.B.29.c

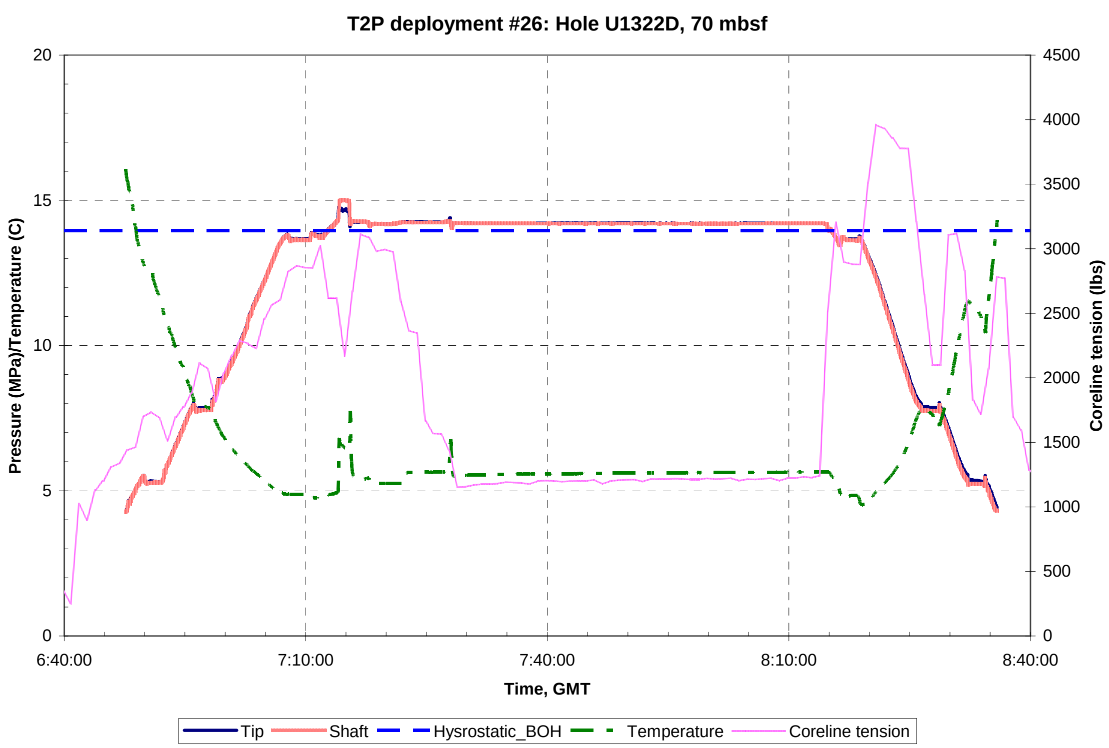

Figure A.B.29.d

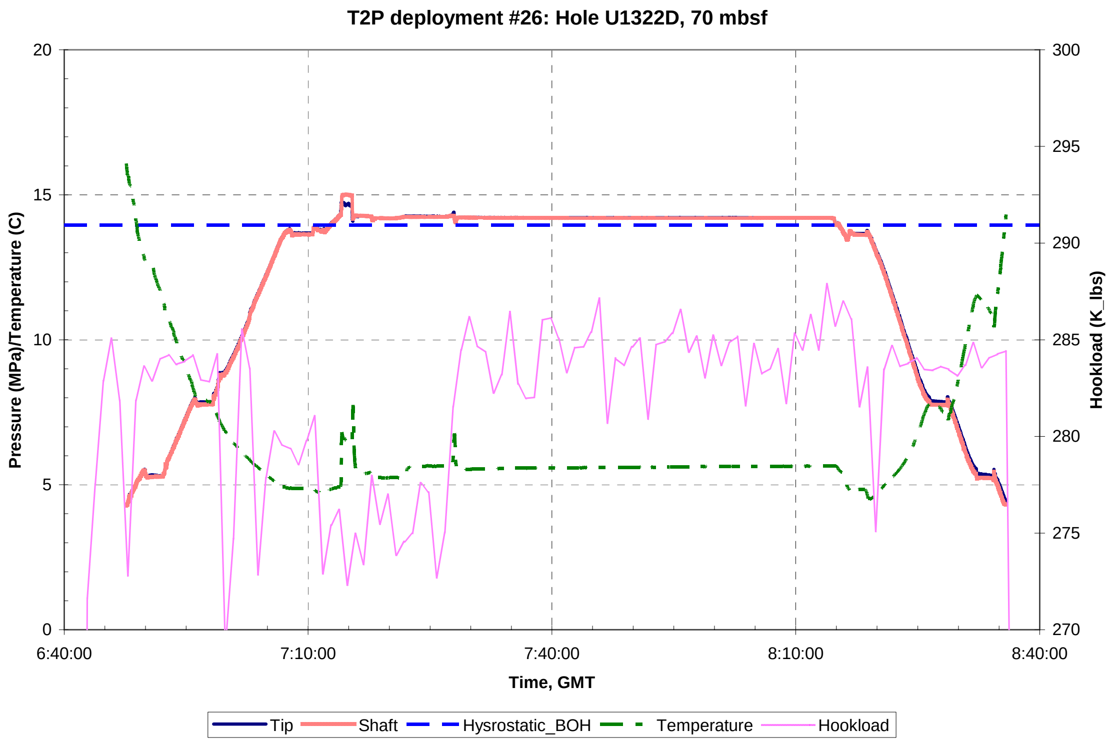

Figure A.B.29.e

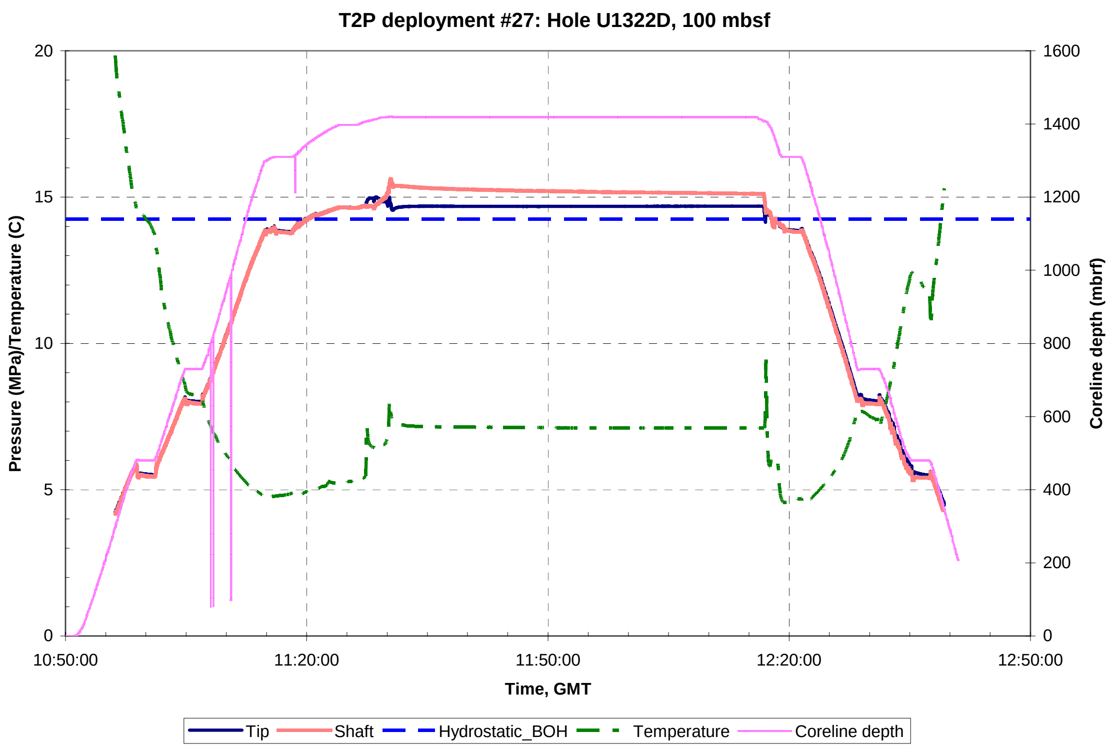

Figure A.B.30.a: Pressure, temperature and Truview data for T2P deployment #27, Hole U1322D, 100 mbsf. GMT = Greenwich Mean Time, Hydrostatic_BOH is the hydrostatic pressure at the bottom of the hole.

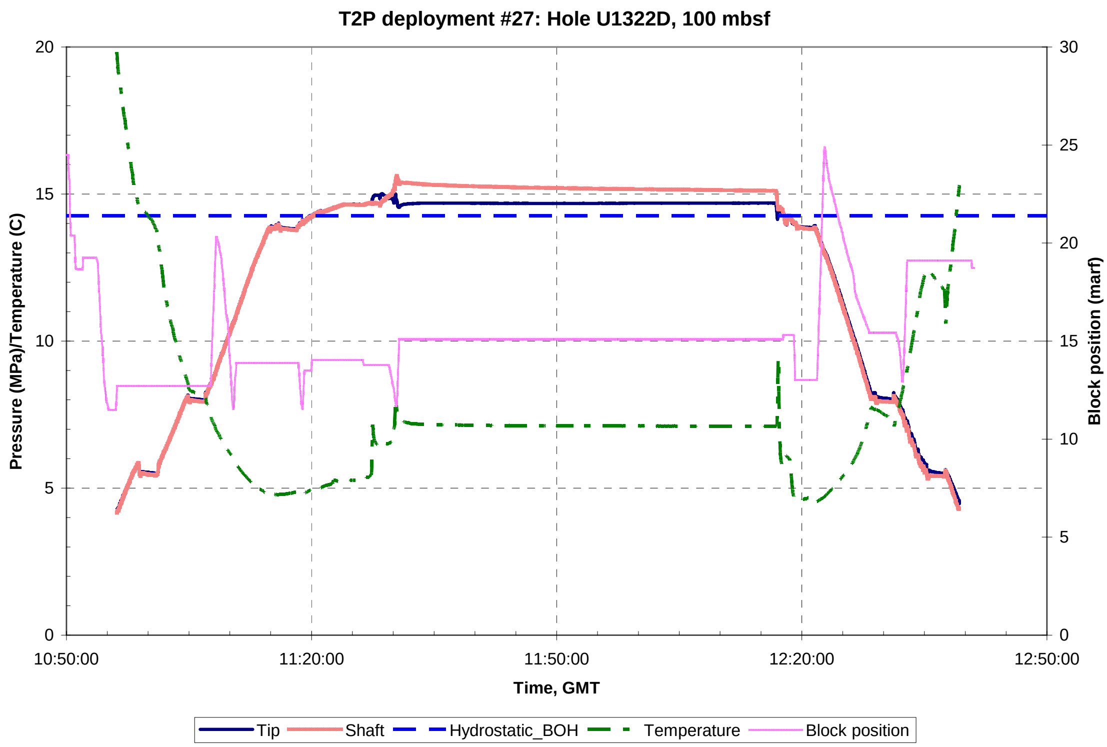

Figure A.B.30.b

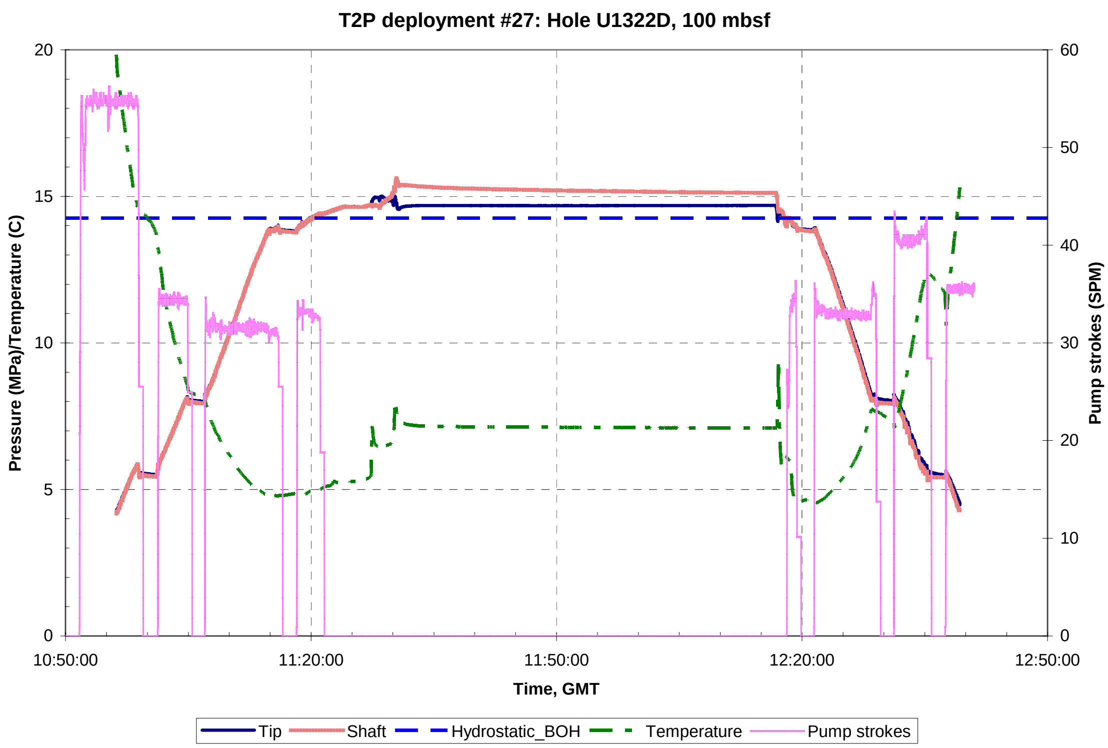

Figure A.B.30.c

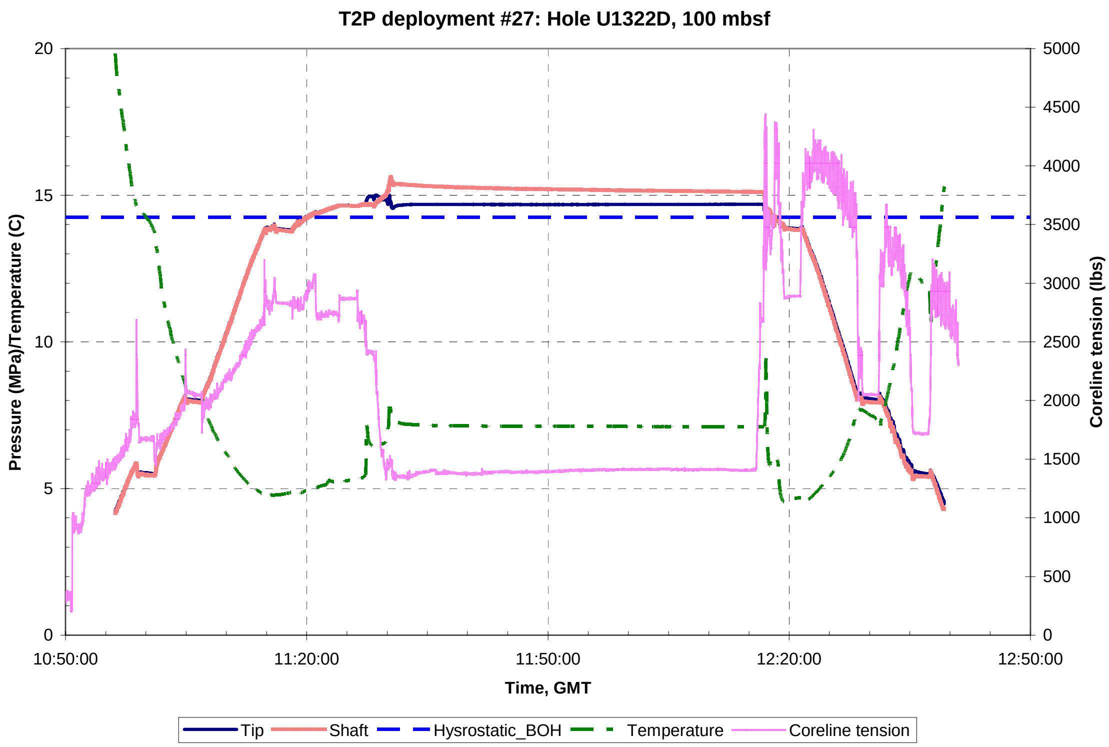

Figure A.B.30.d

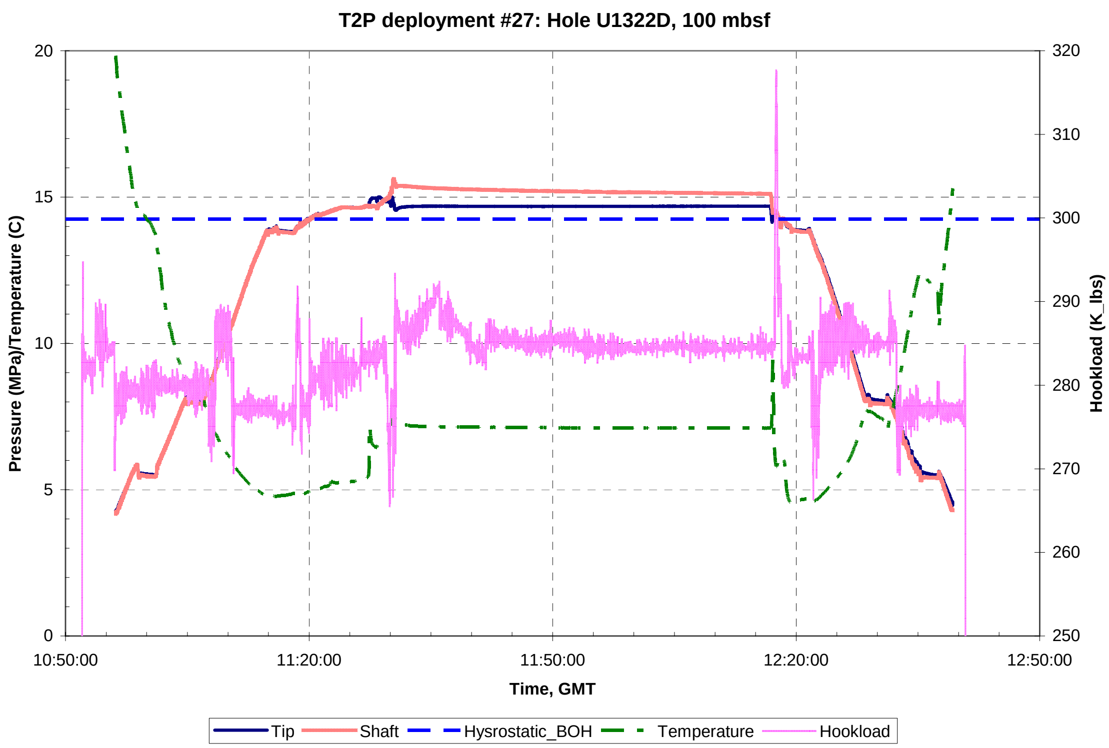

Figure A.B.30.e

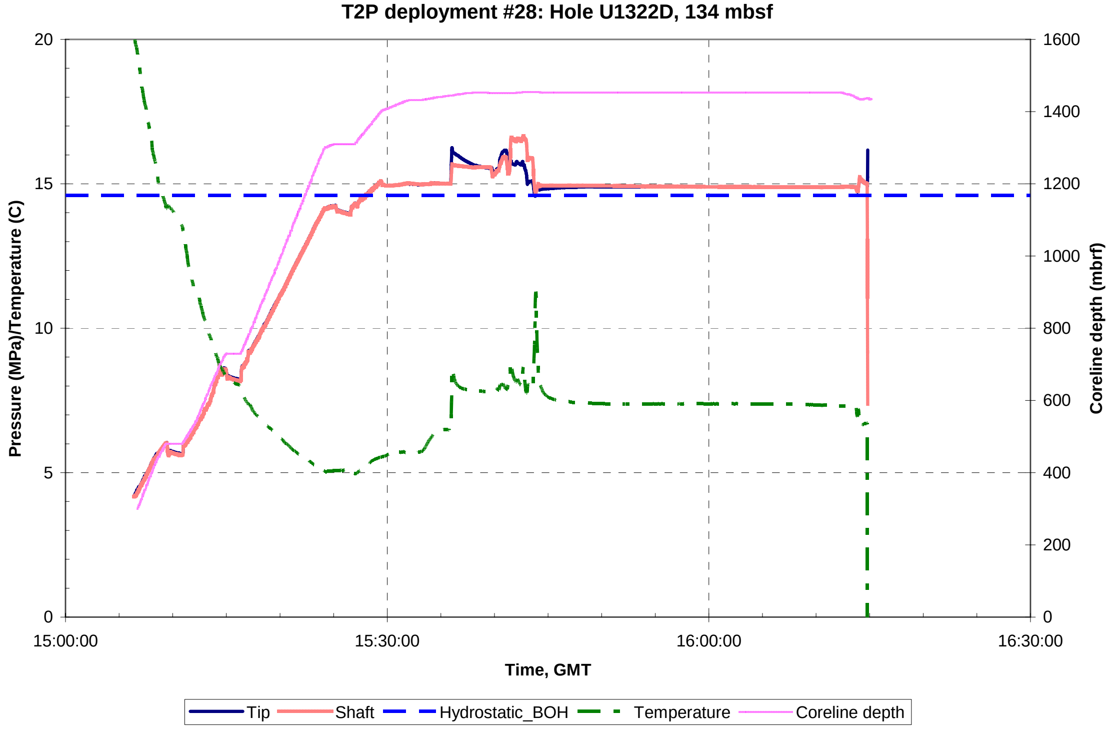

Figure A.B.31.a: Pressure, temperature and Truview data for T2P deployment #28, Hole U1322D, 134 mbsf. GMT = Greenwich Mean Time, Hydrostatic_BOH is the hydrostatic pressure at the bottom of the hole.

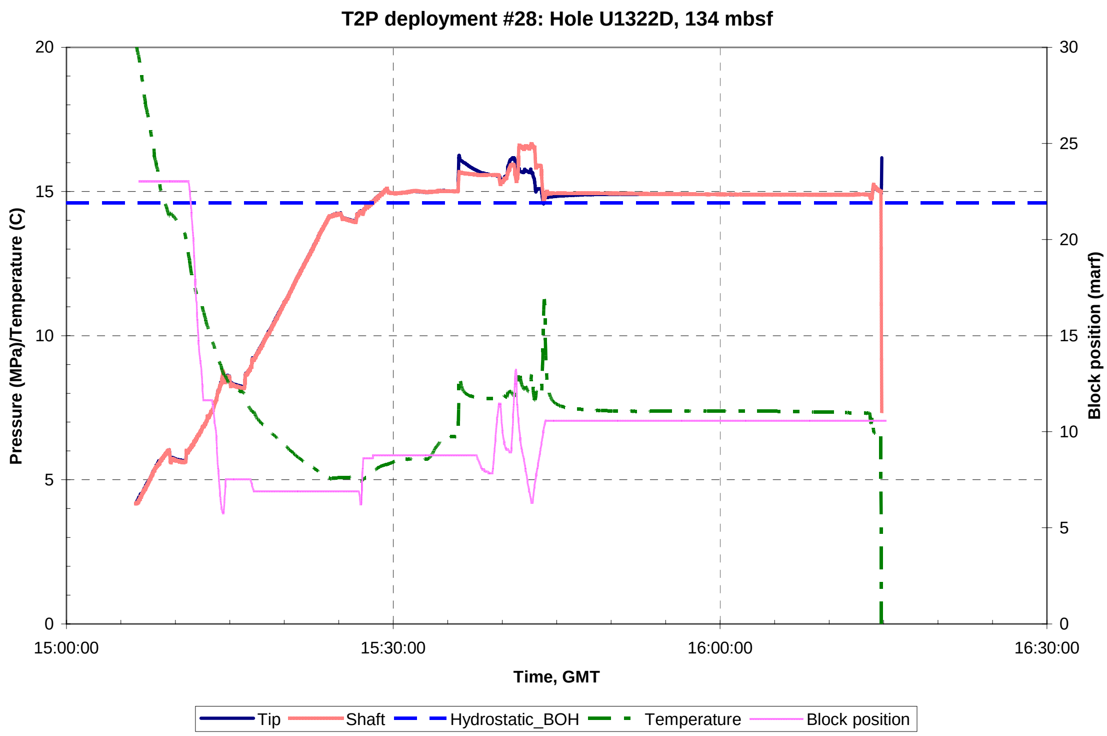

Figure A.B.31.b

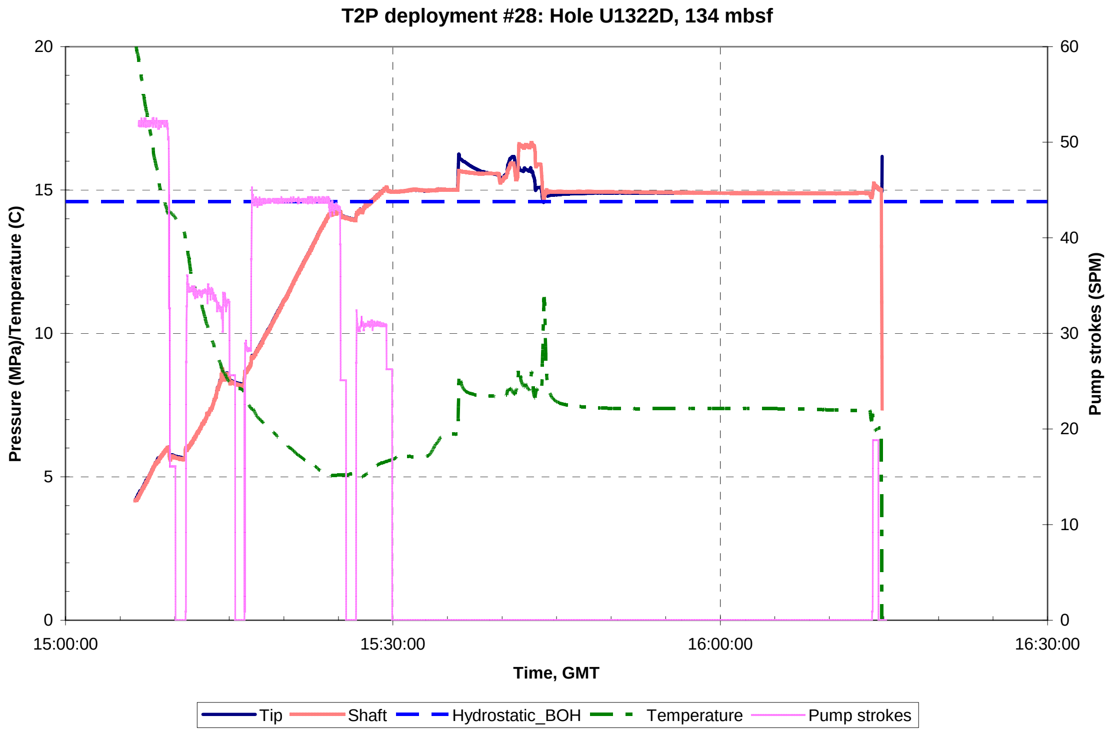

Figure A.B.31.c

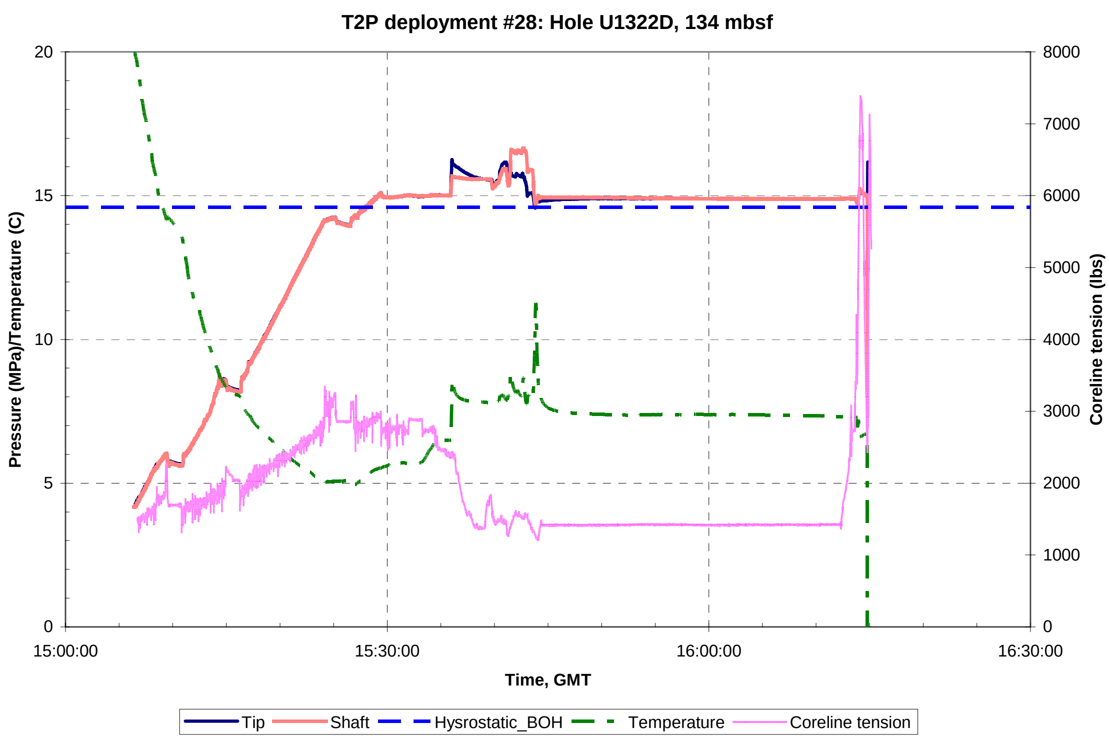

Figure A.B.31.d

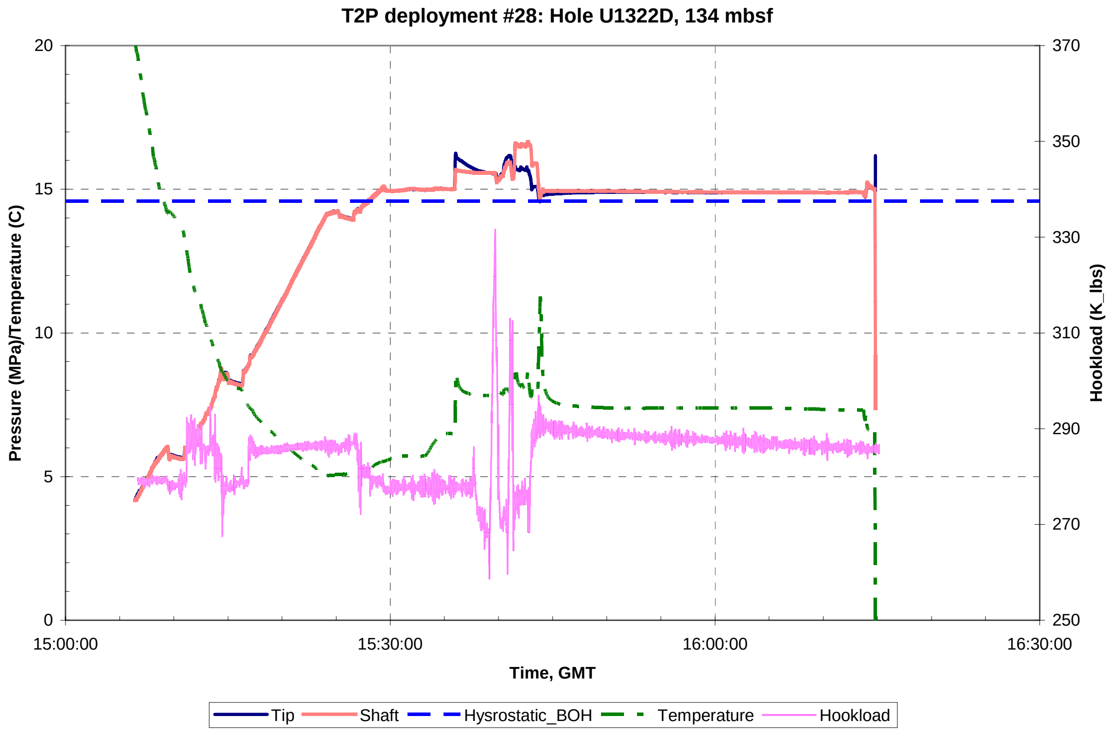

Figure A.B.31.e: Pressure, temperature and Truview data for T2P deployment #28, Hole U1322D, 134 mbsf. GMT = Greenwich Mean Time, Hydrostatic_BOH is the hydrostatic pressure at the bottom of the hole.

Appendix A.C. Fluid pressure within the drilling pipe

To check the tool performance and the pressure calibration, we made multiple 2 to 10 minute tool stops to take the fluid pressure in the drill-pipe prior to and after the tool penetration. We stopped fluid circulation during the tool stop to remove the effect of pump pressure on the measured pressure. Here, we present a discussion of the pressure state within the drill-pipe based on the DVTPP pressure measurements.

Figure A.C1 presents the fluid pressure taken at or above the seafloor. The measured fluid pressure is generally not equal to the calculated hydrostatic pressure. The tool pressure is either close to or higher than hydrostatic pressure for deployments with no drilling mud involved. However, the tool pressure can be either significantly higher or lower than hydrostatic pressure if drilling mud was used. In addition, the range of the offset values is larger than the no mud cases. Thus, the tool-stop technique can not effectively check the pressure calibration.

Figure A.C2 presents the fluid pressure taken at the bottom of the hole (BOH) prior to tool penetration. The fluid pressure at the BOH is either close to or higher than the hydrostatic pressure for deployments with no drilling mud involved. The tool pressure is significantly higher than hydrostatic pressure if drilling mud was used. It shows a general trend where the pressure offset at the BOH increases with the depth of the borehole.

To understand the fluid pressure in the drill-pipe, we present two ideal scenarios of the fluid conditions within the drill-pipe and outside the drill-pipe (Figure A.C3): a) No drilling mud was used and the seawater was not contaminant with the drilling cuttings. In this case, the fluid in the pipe is static and the pressure is equal to hydrostatic pressure everywhere (Figure A.C3a). b) Drilling mud was used and the mud elevations inside and outside the pipe are at the seafloor. The fluid in the drill-pipe is static and has hydrostatic pressure above the mud elevation (e.g.

stops 1 & 2 in Figure A.C3b). The fluid pressure below the mud elevation (e.g. stop 3 in Figure A.C3b) is higher than hydrostatic pressure, follows the static pressure gradient of the drilling mud, and can be calculated using

$$P = \rho_w g H_w + \rho_m g(z - H_w) \tag{A.C1}$$

Where g is the acceleration of gravity, ρ_w is density of seawater, ρ_m is density of drilling mud, z is the target depth, and H_w is the depth of water at the location of the hole.

For almost all deployments, the tool pressure during tool stop reached a steady pressure within 1 minute (Appendices A.A and A.B). This suggests that fluid in the dill-pipe was static during most of the time of the tool stop. It is reasonable to assume that the fluid pressure within the drill-pipe was equal to the fluid pressure inside the annulus at the BOH.

Figure A.C4 presents three possible scenarios that could be encountered at tool stops.

Case a): No drilling mud was used: the elevation of fluid with cuttings inside the pipe is lower than that outside the pipe. The fluid elevation in the drill-pipe must be above sea level to reach the static condition. ΔH can be calculated by

$$\Delta H = \frac{(\rho_c - \rho_w)H_1}{\rho_w} \tag{A.C2}$$

Once ΔH is determined, the fluid pressure in the drill-pipe can be calculated everywhere. The offset from hydrostatic pressure is constant above the interface of seawater and the fluid with cuttings (e.g. stops 1 & 2). Below the interface, fluid pressure follows the pressure gradient of the fluid with drilling cuttings (Figure A.C4a).

Case b): Drilling mud was used to stabilize the borehole and the mud elevation within the pipe is lower than that outside the pipe. The fluid elevation in the drill-pipe has to be above sea level to equilibrate with the fluid pressure at BOH. ΔH can be calculated by

$$\Delta H = \frac{(\rho_c - \rho_w)H_1 + (\rho_m - \rho_w)H_2}{\rho_w} \quad \text{(A.C3)}$$

The pressure within the pipe is higher than hydrostatic pressure everywhere. The offset from hydrostatic pressure is constant above the interface of seawater and the drilling mud (e.g. stops 1 & 2). Below the interface, fluid pressure follows the pressure gradient of the drilling mud (Figure A.C4b)

Case c): Drilling mud was used to stabilize the borehole and the mud elevation within the pipe is higher than the mud elevation outside the pipe. The fluid elevation in the drill-pipe will be lower than sea level to equilibrate with the fluid pressure at the BOH. *ΔH* can be calculated by

$$\Delta H = \frac{(\rho_w - \rho_m)H_1 + (\rho_c - \rho_m)H_2}{\rho_w} \quad \text{(A.C4)}$$

The pressure within the pipe could be either lower (e.g. stops 1 & 2) or higher than hydrostatic pressure (e.g. stop 3) depending on where the tool stop is (Figure A.C4c).

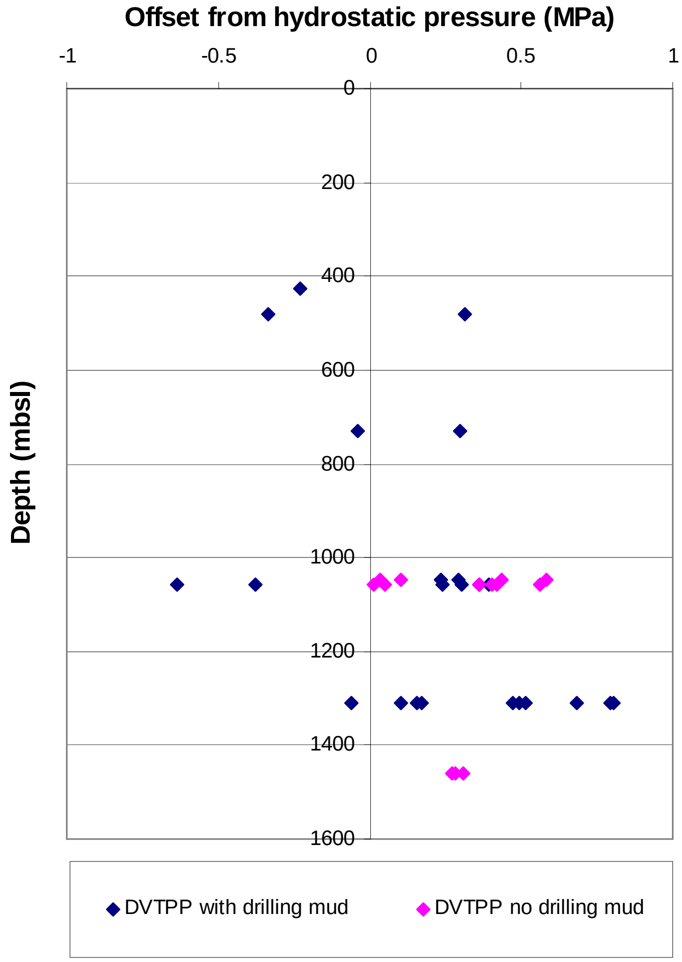

Figure A.C.1 : Offset between the tool pressure and the hydrostatic pressure for tool stops at or above the seafloor. The hydrostatic pressure was calculated assuming a seawater density of 1.024 g/cc.

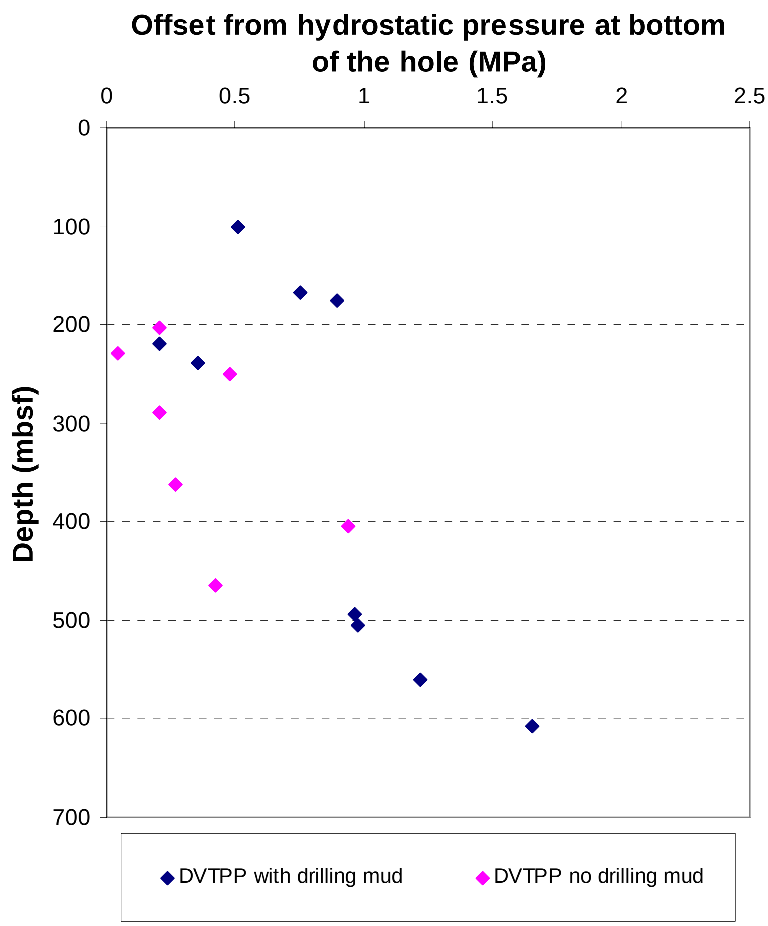

Figure A.C.2 : Offset between the tool pressure and the hydrostatic pressure at the bottom of the hole. The hydrostatic pressure was calculated assuming a seawater density of 1.024 g/cc.

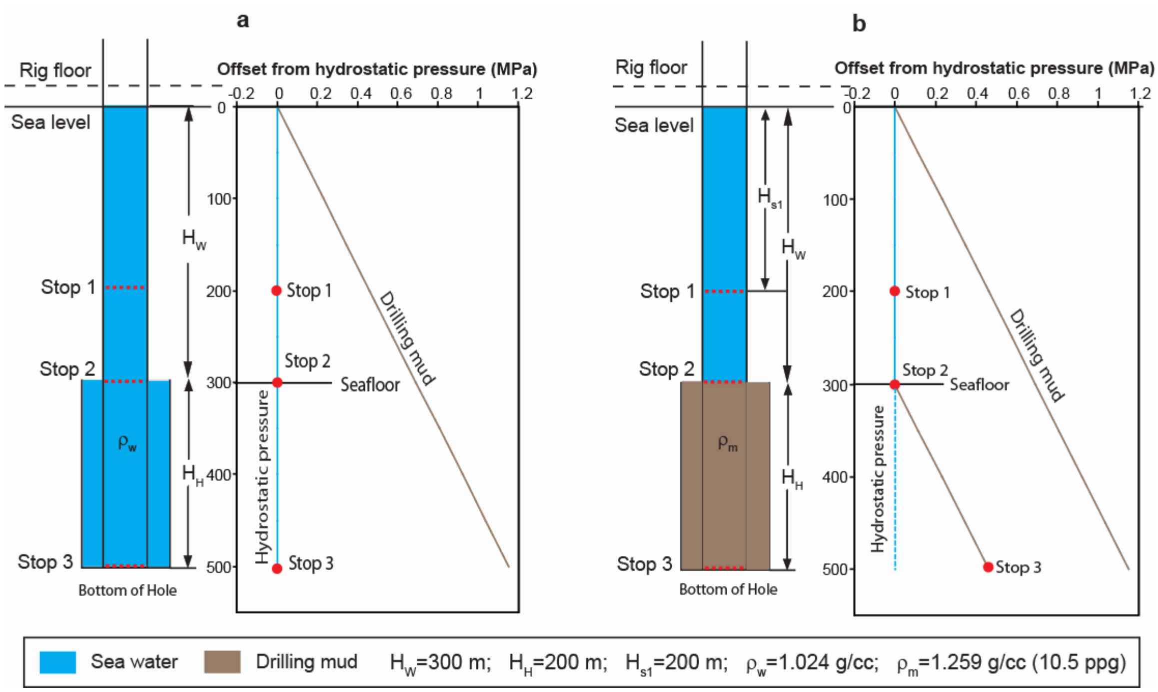

Figure A.C.3 : Two ideal scenarios of fluid condition in drill-pipe. The solid brown line represents the predicted static pressure by assuming the borehole was filled with a 10.5 ppg drilling mud. a) Predicted fluid pressure profile for cases with no drilling mud was used and the seawater was not contaminant with the drilling cuttings. b) Predicted fluid pressure profile for cases with drilling mud was used and the mud elevations inside and outside the pipe are at seafloor.

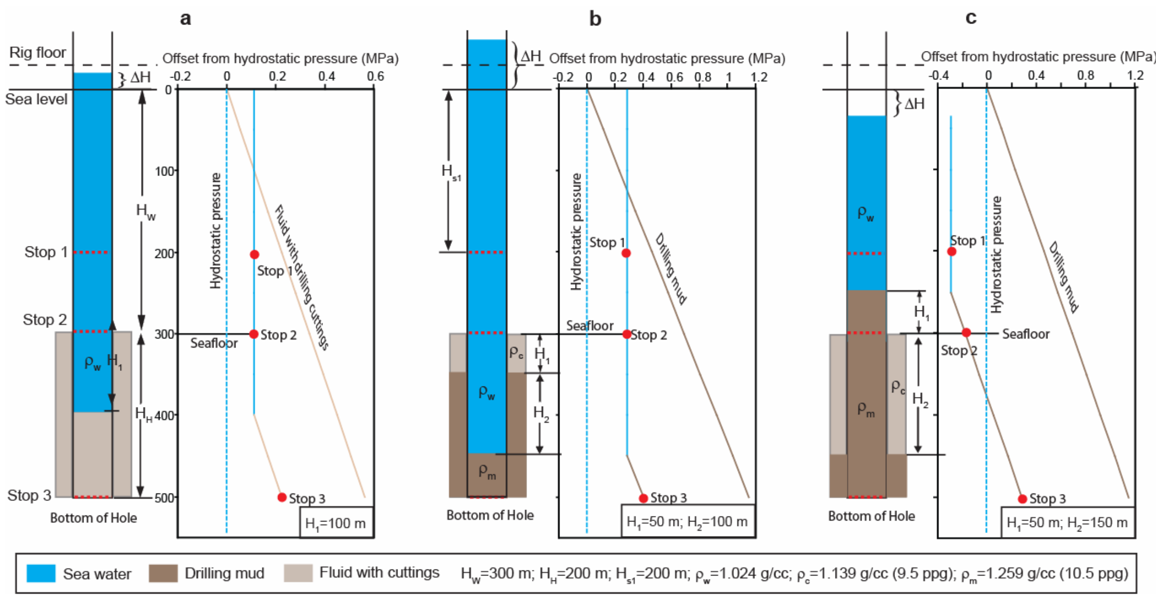

Figure A.C.4: Three possible scenarios that could be encountered at tool stops. The drill-pipe above the rig floor was assumed to be sufficiently long, and three fluids with different density do not mix. The solid brown line represents the predicted static pressure by assuming the borehole was filled with a 10.5 ppg drilling mud. a) Predicted fluid pressure profile for cases with no drilling mud was used whereas fluid in the borehole was contaminated with drilling cuttings. b) Predicted fluid pressure profile for cases with drilling mud was used to stabilize the borehole and the mud elevation within the pipe is lower than the mud elevation outside the pipe. c) Predicted fluid pressure profile for cases with drilling mud was used to stabilize the borehole and the mud elevation within the pipe is higher than the mud elevation outside the pipe.

References

Baligh, M. M., and J. N. Levadoux (1986), Consolidation after undrained piezocone penetration II: interpretation, *Journal of Geotechnical Engineering, ASCE*, *112*, 447-461.

D'Hondt, S. L., Jørgensen, B.B., Miller, D.J., et al., (2003), *Proc. ODP, Init. Repts., 201 [CD-ROM]*, Available from: Ocean Drilling Program, Texas A&M University, College Station TX 77845-9547, USA.

Davis, D., J. Suppe, and F.A. Dahlen (1983), Mechanics of fold-and-thrust belts and accretionarywedges, *J. Geophys. Res.*, *88*, 1153-1172.

Davis, E. E., H. Villinger, R. D. Macdonald, R. D. Meldrum and J. Grigel (1997), A robust rapid-response probe for measuring bottom-hole temperatures in deep-ocean boreholes, *Marine Geophys. Res.*, *19*, 267-281.

Davis, E. E., R. D. Macdonald, H. Villinger, R. H. Bennett, and H. Li (1991), Pore pressures and permeabilities measured in marine sediments with a tethered probe, *J. Geophys. Res.*, *96*, 5975-5984.

Dugan, B., and P.B. Flemings (2002), Fluid flow and stability of the US continental slope offshore New Jersey from the Pleistocene to the present, *Geofluids*, *2*, 137-146.

Flemings, P. B., Behrmann, J., John, C., and Shipboard Scientists IODP Expedition 308 (2005), Overpressure and fluid flow processes in the deepwater Gulf of Mexico: slope stability, seeps, and shallow-water flow, paper presented at in IODP Prel. Rept, Integrated Ocean Drilling Program, College Station, TX.

Flemings, P. B., Behrmann, J., John, C., and Shipboard Scientists IODP Expedition 308 (2006a), Proceedings of the Integrated Ocean Drilling Program, DOI: doi:10.2204/iodp.proc.308.2006.

Flemings, P. B., Behrmann, J., John, C., and Shipboard Scientists IODP Expedition 308 (2006b), Supplementary material, in. Proceeding of the integrated ocean drilling program, vol, 308, [Online]. Available from World Wide Web: <http://iodp.tamu.edu/publications/exp308/308toc.htm#Supplementary%20material>.

Flemings, P. B., Germaine, J., Long, H., Dugan, B., Sawyer, D., Behrmann, J.H., John, C., Shipboard Scientific Party, IODP Expedition 308 (2006c), Measuring Temperature and Pressure with the Temperature Two Pressure (T2P) Probe in the Ursa Basin, Gulf of Mexico: Development of a New Pressure and Temperature Probe for the IODP, *Proceedings of the Offshore Technology Conference, Houston, Texas, May 1-4, 2006, OTC Paper #17957*.

Graber, K. K., Pollard, E., Jonasson, B., and Schulte, E. (Eds.), (2002), Overview of Ocean Drilling Program engineering tools and hardware. ODP Tech. Note, 31 [Online]. Available from World Wide Web: <http://www-odp.tamu.edu/publications/tnotes/tn31/INDEX.HTM>.

Gupta, R. C., and J.L. Davidson (1986), Piezoprobe Determined Coefficient of Consolidation, *Soil and Foundations*, *26*, 12-22.

Lim, B. S., M.T. Tumay, and D.D. Seo (2006), Status of Consolidation from Incomplete Piezocone Dissipation Tests, *In: Site and Geomaterial Characterization (GSP 149), Proceedings of Sessions of GeoShanghai. Shanghai, China.*

Long, H., P. B. Flemings, and J. T. Germaine (2007a), Interpreting in situ pressure and hydraulic properties with borehole penetrometers in ocean drilling: DVTPP and Piezoprobe deployments at southern Hydrate Ridge, offshore Oregon, *J. Geophys. Res.*, *112*, B04101, doi:04110.01029/02005JB004165.

Long, H., P.B. Flemings, J. Germaine, B. Dugan, D. Sawyer, and Shipboard Scientific Party, IODP Expedition 308 (2007b), In Situ Pore Pressure at IODP Site U1324, Ursa Basin, Gulf of Mexico, *Proceedings of the Offshore Technology Conference, Houston, Texas*, *OTC Paper #18772*.

Moore, G. F., Taira, A., Klaus, A., et al. (2001), Proc. ODP, Init. Repts., v. 190 [CD-ROM]. Available from: Ocean Drilling Program, Texas A&M University, College Station TX 77845-9547, USA.

Ostermeier, R. M., Pelletier, J.H., Winker, C.D. and Nicholson, J.W. (2001), Trends in Shallow Sediment Pore Pressures - Deepwater Gulf of Mexico, paper presented at Society of Petroleum Engineers, SPE/IADC 67772.

Sawyer, D., Flemings, P.B., Dugan, B., Shipboard Scientific Party, IODP Expedition 308 (2007), Lateral Variations in Core, Log, and Seismic Attributes of a Mass Transport Complex in the Ursa Region, IODP Expedition 308, Northern Gulf of Mexico, paper presented at Proceedings of the Offshore Technology Conference, Houston, Texas, April 30-May 3.

Tréhu, A. M. (2007), Personal communication.

Tréhu, A. M., Bohrmann, G., Rack, F.R., Torres, M.E., et al., (2003), *Proc. ODP, Init. Repts., v. 204 [CD-ROM]*, Available from: Ocean Drilling Program, Texas A&M University, College Station TX 77845-9547, USA.

Villinger, H., and E. E. Davis (1987), A new reduction algorithm for marine heat flow measurements, *J. Geophys. Res.*, *92*, 1557-1563.

Whittle, A. J., T. Sutabutr, J. T. Germaine and A. Varney (2001), Prediction and interpretation of pore pressure dissipation for a tapered piezoprobe, *Geotechnique*, *51*, 601-617.

Appendix B: Consolidation Characteristics of Sediments from IODP Expedition 308, Ursa Basin, Gulf Of Mexico

Abstract

We conducted Constant Rate of Strain Consolidation (CRSC) tests on 7 samples from Site U1322 and 17 samples from Site U1324 in two laboratories (MIT and PSU) to obtain the consolidation properties of the soil, as well as determine the stress history of the site. The sediments above 200 mbsf at both Sites have similar consolidation properties. The compression index (C_c) ranges from 0.1508 to 0.5052. Cc decreases with void ratio at both Sites. The expansion index (C_e) ranges from 0.0153 to 0.1144, and decreases with void ratio at both Sites. The in situ hydraulic conductivity (K_i) ranges from 2.18 x10^{-11} to 6.38x10^{-10} m/s. K_i decreases with depth. The e-log(K_i) relation has different slopes for sediments above and below 300 mbsf at Site U1324. The coefficient of consolidation (c_v) ranges from 1.5 x10^{-8} and 4.2x10^{-7} m^2/s. c_v increases with depth for the sediments above 200 mbsf at both Sites and shows no clear trend for the sediments below 200 mbsf at Site U1324.The pre-consolidation pressure (P'_c) is significantly less than the hydrostatic vertical effective stress (σ'_{vh}) at both Sites, which suggests that Ursa sediments are overpressured.

B.1 Introduction

Understanding overpressure, fluid flow and sediment compression behavior is critical for evaluating the stability of continental slopes. IODP Expedition 308 was aimed at testing a multi-dimensional flow model by examining how physical properties, pressure, temperature, and pore fluid composition vary within low permeability mudstones that overlie a permeable and overpressured aquifer [*Flemings*, 2006a]. We drilled, logged, cored and made in situ measurements in a region of very rapid Pleistocene sedimentation: the Ursa Basin (Figure B.1).

We took substantial whole core geotechnical samples for shore-based consolidation tests (Table B.1). Consolidation tests describe how porosity evolves with effective stress under one-dimensional gravitational compaction due to sedimentation (passive margin). The transition from recompression to virgin compression behavior provides an estimate of maximum in situ effective stress [*Becker*, 1987; *Casagrande*, 1936]. The deformation behavior provides insight into how permeability evolves with burial and compression.

Consolidation properties were determined from results of constant rate of strain consolidation (CRSC) tests on intact samples.

B.2 Laboratory Testing Methodology

B.2.1 Sample Handling and Preparation

The coring techniques include the advanced piston corer (APC) and the extended core barrel (XCB) systems (Table B.1). These standard coring systems and their characteristics are summarized in the technical note of the Ocean Drilling Program [*Graber*, 2002]. The soil was not extruded from the core liner onboard the drilling ship. Whole core samples were capped and sealed in wax to maintain natural saturation during refrigerated storage prior to the experiments. For the experiments, each sample was removed from the wax-sealed liner and sub-sampled with a sharp cutting shoe (PSU) or a trimming jig (MIT).

B.2.2 Sample Descriptions

Most of the samples were X-rayed at MIT's radiography facility in order to select undisturbed portions of the core for experiments, and to assess presence of inclusions, and variation in soil fabric. The core X-rays can be found in the IODP data report prepared by Nelson et al. [*Nelson*]. Quality of samples generally decreases with depth.

All tested samples are silty clays that contain 50 to 70% clay except U1324C-7H-1WR (405 mbsf) which is clayey silt with 30% clay [*Jacoby*, in preparation]. The mineralogy composition of the silty clay samples is similar. The dominated clay mineral is smectite (>80%).

B.2.3 Index Properties

Two water contents were measured in the consolidation test: w_c and w_n. w_c is the water content measured on the leftover trimmings during sample preparation. w_n is the water content measured on the test specimen itself. We measured the water content by oven-drying the samples. Water content is calculated by taking the difference in the weight of a soil before and after oven-drying, and dividing this difference by the oven-dried weight.

B.2.4 CRSC Testing

The CRSC tests were conducted in two laboratories (MIT and PSU) in general accordance with ASTM D4186 guidelines [*International*, 2003]. The dimensions of the specimen are slightly different between the two laboratories. MIT specimens were 5.95 to 6.35 cm in diameter with an initial height of 2.35 cm. PSU specimens were 5 cm in diameter with an initial height of 2.0 cm.

Specimens were laterally confined with a steel ring. Prior to testing, specimens were saturated with de-aired water and backpressured to approximately 300 kPa for 24 hours to drive any gases present into solution. We applied a constant rate of strain using a computer-controlled load frame, with the sample base undrained and the sample top open to the backpressure. We continuously monitored sample height (H, in mm), applied vertical stress (σ_v, in kPa), and basal pore pressure (u, in kPa).

The vertical effective stress (σ'_v), hydraulic conductivity (K), compressibility (m_v), coefficient of consolidation (c_v) and strain energy density (SED) were calculated using the following equations [*Tan*, 2006]:

$$\sigma'_v = \sigma_v - \frac{2}{3} \cdot \Delta u \tag{B.1}$$

$$K = \frac{\dot{\varepsilon} \cdot H_0 \cdot H \cdot \gamma_w}{2 \cdot \Delta u} \tag{B.2}$$

$$m_v = \frac{\Delta \varepsilon}{\Delta \sigma'_v} \tag{B.3}$$

$$c_v = \frac{K}{m_v \cdot \gamma_w} \tag{B.4}$$

$$SED = \frac{\sigma'_{vi-1} + \sigma'_{vi}}{2} \cdot Ln\left(\frac{1-\varepsilon_{i-1}}{1-\varepsilon_i}\right) \tag{B.5}$$

All variables are presented in Table B.2.

B.3 Laboratory Testing Results

We conducted CRSC test on 7 samples from Site U1322 and 17 samples from Site U1324 in two laboratories (MIT and PSU). Table B.3 gives a summary of the details of each CRSC test. Figures B.2 to Figure B.25 show the consolidation curves in both e-log (σ'_v) and ε-log (σ'_v), normalized excess pore pressure, coefficient of consolidation (c_v), strain energy density, and hydraulic conductivity (K) for each CRSC test. The CRSC data sheet can be found online in excel format under the "**Supplementary material**" section, which includes 12 columns (Table B.4).

The compression index (C_c) refers to the slope of the normally consolidated portion of the compression curve in e-log (σ'_v) space. The compression behavior of the samples is similar at

Sites U1322 and U1324 (Figure B.26A). The measured values of C_c range from 0.1508 to 0.5052. Cc decreases with void ratio at both Sites (Figure B.26A). The expansion index (C_e) refers to the slope of the unloading portion of the compression curve in the e-log (σ'_v) space. It ranges from 0.0153 to 0.1144 and also decreases with void ratio (Figure B.26B). It must be noted that the expansion index varies with the amount of unloading that occurs. As such, the quoted expansion indexes are for unloading to an over consolidation ratio (OCR) of 10.

The in situ hydraulic conductivity (K_i) is obtained by extrapolating the linear portion of the e-log(K) relation to the in situ void ratio. Values of K_i range from 2.18 x10^{-11} to 6.38x10^{-10} m/s. K_i decreases with depth (Figure B.27A). The e_i-log(K_i) relations for sediments above and below 300 mbsf have different slopes (Figure B.27B). K_i of the clayey silt sample (405.81 mbsf) is significantly higher than those of the silty clay samples and stands out on the e_i-log(K_i) plot (Figure B.27), which reflects the lithology difference.

The coefficient of consolidation, c_v, ranges from 1.5 x10^{-8} and 4.2x10^{-7} m^2/s (Figure B.28). c_v increases with depth for the sediments above 200 mbsf at both Sites and shows no clear trend for the sediments below 200 mbsf. c_v of the clayey silt sample (405.81 mbsf) is significantly higher than those of the silty clay samples, which reflects the lithology difference.

The pre-consolidation pressure, P'_c, is determined using the work-stress method proposed by Becker et al., [*Becker*]. P'_c is significantly less than the hydrostatic vertical effective stress (σ'_{vh}) at both Sites (Figure B.29), which suggests that Ursa sediments are overpressured.

Table B.1. Summary table of tests conducted on Ursa sediments

Hole-Core-Section	Depth (mbsf)	Interval (cm)	Cutting shoe	Index tests		X-ray	CRSC	
				WC	PSA		MIT	PSU
1322B-15H-1WR	125.8	100-150	IODP-APC	1	1	1	1	
1322B-18H-6WR	156.9	0-40	Fugro	1	1	1	1	
1322B-21H-3WR	178.62	112-132	IODP-APC	1	1	1	1	
1322B-25H-6WR	209.5	97-147	IODP-APC	1	1	1	1	
1322B-4H-3WR	27.17	117-137	Fugro	1	1	1	1	
1322D-2H-2WR	72	50-150	Fugro	2	2	1	2	
1324B-10H-7WR	88.8	0-45	IODP-APC	1	1	1	1	
1324B-13H-7WR	117.24	15-35	Fugro	1	1			1
1324B-15H-5WR	134.2	90-150	IODP-APCT	1	1	1	1	
1324B-16H-5WR	142.13	90-150	IODP-APC	1	1	1	1	
1324B-23H-5WR	199.8	0-22	Fugro	1	1	1	1	
1324B-4H-7WR	31.86	56-116	Fugro	1	1	1	1	
1324B-60X-2WR	476.7	130-150	IODP-XCB	1	1			1
1324B-70X-6WR	577.67	40-90	IODP-XCB	1	1			1
1324B-7H-7WR	60.31	0-63	Fugro	1	1	1	1	
1324C-1H-1WR	51.1	110-140	IODP-APC	4	4	1	2	2
1324C-2H-4WR	104.5	0-100	Fugro	1	1	1	1	
1324C-6H-3WR	303	0-106	Fugro	2	2			2
1324C-7H-1WR	405.5	50-150	IODP-APC	1	1			1

Notes:

Hole-Core-Section: numbering of sites, holes, cores, and sections follows the standard IODP procedure

Depth: depth of the top of the whole core sample in mbsf

Interval: the top and bottom of the whole core sample within the core section

Cutting shoe: These standard coring systems and their characteristics are summarized in the technical note of the Ocean Drilling Program [*Graber*, 2002]

WC: Water Content Measurements

PSA: Particle Size Analysis can be found in IODP data report [*Jacoby*, in preparation]

X-ray: images can be found in IODP data report [*Nelson*, in preparation]

CRSC: Constant Rate of Strain Consolidation

MIT: Massachusetts Institute of Technology

PSU: The Pennsylvania State University

Table B.2. Nomenclature

Variable	Definition	Dimensions	SI Units
C_c	Compression index	Dimensionless	--
C_e	Expansion index	Dimensionless	--
G_s	Grain density	M/L^3	g/cc
H	Height of specimen	L	mm
H_0	Initial height of specimen	L	mm
K	Hydraulic conductivity	L/T	m/s
K_i	In-situ hydraulic conductivity	L/T	m/s
OCR	Over consolidation ratio	Dimensionless	--
P'_c	Preconsolidation pressure	M/LT^2	kPa
SED	Strain energy density	M/LT^2	KJ/m^3
S_i	Initial saturation	Dimensionless	--
c_v	Coefficient of consolidation	L^2/T	m^2/s
e	Void ratio	Dimensionless	--
ei	Initial void ratio measured on specimen	Dimensionless	--
k_i	In-situ permeability	L^2	m^2
m_v	Frame compressibility	LT^2/M	1/kPa
u	Basal pore pressure	M/LT^2	kPa
u_b	Back pressure	M/LT^2	kPa
w_c	Water content measured on trimmings	Dimensionless	--
w_n	Water content measured on specimen	Dimensionless	--
Δu	Excess pore pressure	M/LT^2	kPa
$\Delta u/\sigma_v$	Normalized excess pore pressure	Dimensionless	--
$\delta\varepsilon/\delta t$	Strain rate	1/T	%/hr
ε	Axial strain	Dimensionless	%
ε_i	Axial strain prior to compression	Dimensionless	%
ρ_b	Bulk density	M/L^3	g/cc
γ_w	Unit weight of water	M/L^2T^2	kN/m^3
σ_v	Applied vertical stress	M/LT^2	kPa
σ'_v	Vertical effective stress	M/LT^2	kPa
σ'_{iv}	Vertical effective stress prior to compression	M/LT^2	kPa
σ'_{vh}	Hydrostatic vertical effective stress	M/LT^2	kPa
σ'_{vm}	Maximum vertical effective stress during consolidation	M/LT^2	kPa

Table B.3. CRSC test conditions and consolidation properties

Spec. Location		Index	Specimen		Test Conditions		Consolidation	
Test #	Depth	w_c	w_n	e_i	u_b	ε_i (%)	C_c	c_v
Hole	Location	SD		S_i (%)	σ'_{iv}	$\delta\varepsilon/\delta t$	C_e	K_i (m/s)
Core-section	Depth	# obs	ρ_b	G_s		$\Delta u/\sigma_v$	P'$_c$	k_i (m^2)
CRS796	72	46.3	47.25	1.281	384	0.05	0.4675	1.7e-8
1322D	0.78	0.8		102.6	2	0.25	0.1114	1.46e-10
2H-2WR	72.78	2	1.795	2.78		13.5	280	1.46e-17
CRS797	51.1	42.0	55.69	1.500	385	-0.06	0.4887	1.5e-8
1324C	0.17	12.6		103.2	4	0.27	0.1144	1.54e-10
1H-01WR	51.27	2	1.731	2.78		12.0	160	1.54e-17
CRS798	72	44.9	44.30	1.193	383	0.06	0.3762	3.7e-8
1322D	0.83	2.9		103.2	3	0.30	--	2.29e-10
2H-2WR	72.83	2	1.829	2.78		6.0	200	2.29e-17
CRS799	51.1	51.2	54.18	1.462	374	0.03	0.4736	1.5e-8
1324C	0.21	1.3		103.0	6	0.27	--	1.82e-10
1H-1WR	51.31	2	1.741	2.78		13.0	224	1.82e-17
CRS800	31.86	47.6	46.20	1.255	357	0.06	0.3846	5.0e-8
1324B	--	6.7		102.4	3	0.30	0.0717	2.62e-10
4H-7WR	--	2	1.803	2.78		4.8	180	2.62e-17
CRS801	142.13	33.3	33.77	0.925	379	0.00	0.2564	7.0e-8
1324B	--	0.5		101.5	3	0.26	--	1.60e-10
16H-5WR	--	2	1.932	2.78		3.0	435	1.59e-17
CRS802	60.31	44.6	44.42	1.228	349	0.04	0.4196	2.1e-8
1324B	--	1.8		100.6	3	0.31	--	1.64e-10
7H-7WR	--	2	1.802	2.78		11.0	283	1.64e-17
CRS803	134.2	31.8	34.99	0.943	378	-0.07	0.2517	8.0e-8
1324B	--	0.0		103.2	10	0.26	0.0524	1.56e-10
15H-5WR	--	2	1.932	2.78		2.6	422	1.56e-17
CRS807	104.5	37.3	35.89	1.018	410	-1.25	0.3204	3.8e-8
1324C	0.98	0.1		98.0	16	0.21	--	1.23e-10
2H-4WR	105.48	2	1.872	2.78		4.5	448	1.23e-17
CRS808	125.8	34.1	37.39	1.080	396	-0.07	03123	8.6e-8
1322B	0.48	1.2		96.3	5	0.20	0.0500	2.44e-10
15H-1WR	126.28	2	1.837	2.78		1.7	516	2.44e-17
CRS810	157.3	32.5	34.48	1.088	423	-0.15	0.2848	8.0e-8
1322B	0.12	0.1		88.1	12	0.21	0.0359	4.52e-10
18H-6WR	157.42	2	1.790	2.78		2.2	480	4.52e-17
CRS812	199.8	30.9	32.01	0.911	425	-0.23	0.2717	5.2e-8
1324B	0.2	0.6		97.7	13	0.20	0.0470	1.10e-10

23H-5WR	200	2	1.920	2.78		3.5	700	1.10e-17
CRS813	88.8	37.8	38.12	1.078	424	-0.09	0.3175	3.1e-8
1324B	0.42	3.3		98.3	18	0.21	0.0725	1.79e-10
10H-7WR	89.22	2	1.848	2.78		5.6	400	1.79e-17
CRS815	27.17	55.1	58.42	1.606	424	-0.16	0.5052	2.0e-8
1322B	0.04	2.9		101.1	5	0.18	--	3.67e-10
4H-3WR	27.21	2	1.690	2.78		7.0	135	3.67e-17
CRS824	209.5	32.8	34.50	1.150	384	-1.53	0.3544	3.6e-8
1322B	0.31	0.6		83.4	5	0.21	--	2.45e-10
25H-6WR	209.81	3	1.739	2.78		5.5	450	2.45e-17
CRS825	178.62	28.3	30.39	0.924	403	-0.09	0.2627	9.2e-8
1322B	0.08	0.5		91.5	9	0.16	--	4.27e-10
21H-3WR	178.7	3	1.884	2.78		1.8	580	4.27e-17
CRS001	303	31	--	0.84*	300	-0.03	0.3037	7.0e-8
1324C	1.02	0.20			112	0.42	0.0421	1.41e-10
6H-3WR	304.02	4	--	2.74		2.5	1124	1.41e-17
CRS002	303	32	--	0.85*	300	-0.14	0.2694	5.0e-8
1324C	0.94	1.40			112	0.60	0.0442	1.01e-10
6H-3WR	303.94	3	--	2.74		4.0	1020	1.01e-17
CRS003	51.1	50	--	1.33*	300	-1.59	0.4126	2.5e-8
1324C	0.11	1.80			7	0.15	0.0365	5.08e-10
1H-1WR	51.21	3	--	2.74		4.0	197	5.08e-17
CRS004	51.1	50	--	1.33*	299	-0.41	0.4393	2.0e-8
1324C	0.04	2.90			8	0.27	0.0674	1.46e-10
1H-1WR	51.14	3	--	2.74		8.0	232	1.46e-17
CRS005	117.24	40	39.700	1.05	300	0.69	0.3613	4.0e-8
1324B	0.16	1.40		101.60	80	0.27	0.0734	1.86e-10
13H-7WR	117.4	3	1.867	2.74		3.0	500	1.86e-17
CRS006	577.67	26	28.000	0.74	320	-0.38	0.2478	1.5e-8
1324B	0.46	0.60		102.10	50	0.45	--	2.18e-11
70X-6WR	578.13	2	2.018	2.74		11.0	1829	2.18e-18
CRS007	476.7	30	30.600	0.84	320	-0.66	0.2791	1.5e-8
1324B	0.16	0.70		98.00	50	0.36	0.0624	3.60e-11
60X-2WR	476.86	3	1.946	2.74		11.0	1050	3.60e-18
CRS008	405.5	23	19.900	0.61	300	0.84	0.1508	4.2e-8
1324C	0.31	0.60		87.90	40	0.60	0.0153	6.38e-10
7H-1WR	405.81	3	2.040	2.74		1.0	1502	6.38e-17

Notes: 1) See Table B.2 for variables that were used in headings. 2) In column 2, "Depth" in the first row gives depth of the top of the whole core sample in mbsf (see Table B.1, column 2). "Location" provides the specimen location in meters relative to the top of the whole core sample. "Depth" in the third row provides depth of the tested specimen in mbsf. 3) In column 3, "# obs" refers to the numbers of measurements; "SD" refers to the standard deviation. 4) * No water content was measured on the specimen. e_i is calculated from w_c assuming a grain density of 2.74 g/cc. For other tests, e_i is calculated from w_n assuming a grain density of 2.74 g/cc (PSU) and 2.78 g/cc (MIT).

Table B.4. Header of the consolidation data file

Time (sec)	ε (%)	σ_v (kPa)	u (kPa)	u_b (kPa)	σ'_v (kPa)	e	Δu (kPa)	K (m/s)	c_v (m^2/s)	$\Delta u/\sigma_v$	SED (KJ/m^3)
154750	-0.0302	120.169	281.752	299	120.001	0.8415	0.252	0.00E+00	0.00E+00	0.0021	0
155750	-0.0148	140.032	283.899	300	138.4327	0.8412	2.399	3.53E-10	1.29E-06	0.0171	0.0199
156740	0.0556	151.746	283.04	301	150.7193	0.8399	1.54	1.09E-09	1.40E-06	0.0101	0.1217
157750	0.1556	162.441	285.188	301	159.9823	0.8381	3.688	4.80E-10	5.22E-07	0.0227	0.2772
158740	0.2364	171.608	283.899	300	170.0087	0.8366	2.399	7.94E-10	7.49E-07	0.014	0.4107
159740	0.3493	181.794	287.335	301	177.904	0.8345	5.835	3.42E-10	2.49E-07	0.0321	0.6076
160750	0.4416	189.434	288.624	301	184.6847	0.8328	7.124	2.66E-10	1.71E-07	0.0376	0.7758
161740	0.5433	194.017	287.335	301	190.127	0.8309	5.835	3.23E-10	1.80E-07	0.0301	0.9671

Notes: See Table B.2 for variables that were used in headings.

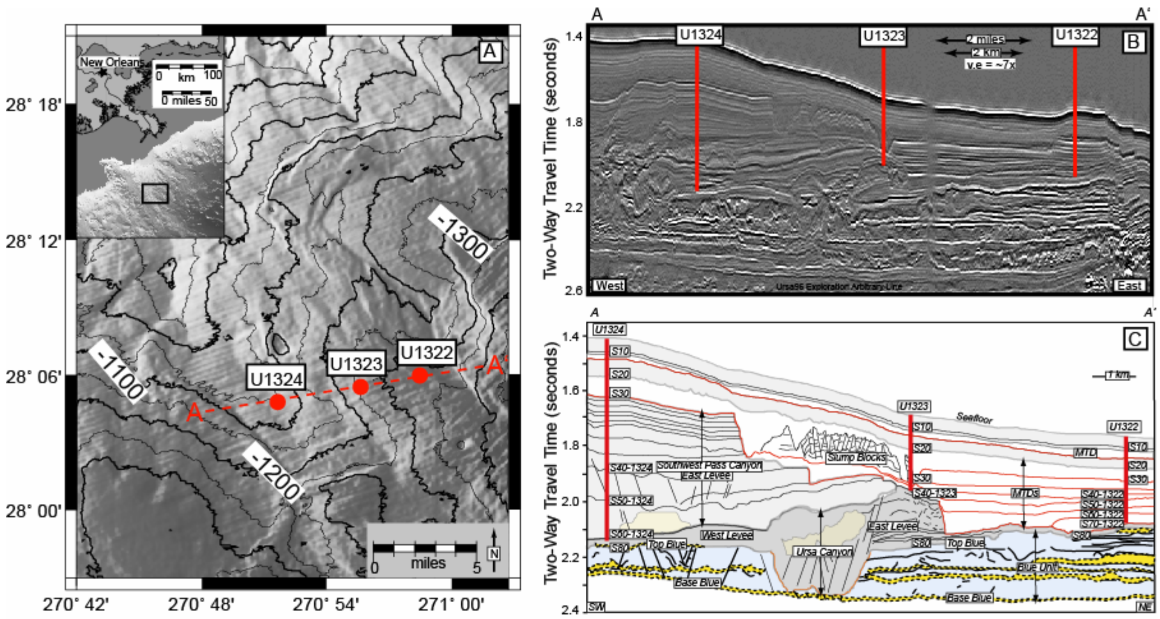

Figure B.1: A) IODP Expedition 308 Site locations, and bathymetry contours. The Ursa Basin is located 210 km SE of New Orleans, Louisiana, USA (inset map). Three drilled Sites are delineated with red dots. Contour interval is 100 m. (B) East-West seismic cross section A-A' (located in Figure 1A). (C) Interpreted cross section A-A'. Light and dark gray represent mud-rich levee, rotated channel-margin slides, and hemipelagic drape; yellow represents sand-rich channel fill. The Blue Unit (light blue) is composed of sand and mud. Mass transport deposits have occurred in the mud-rich levee deposits above the Blue Unit. Detachment surfaces are colored red.

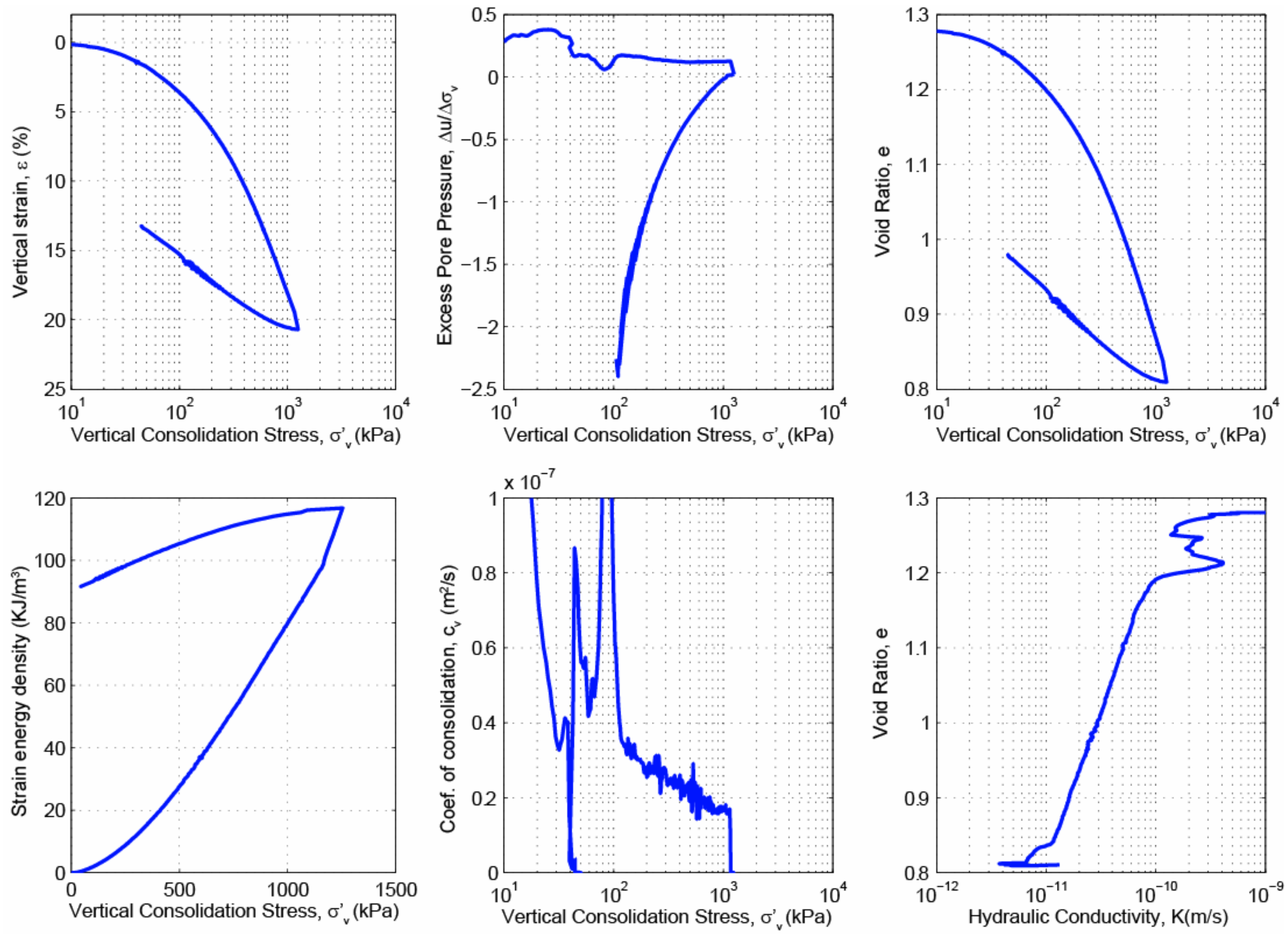

Figure B.2: CRS796 consolidation data for Sample U1322D-2H-2WR, 72.78 mbsf.

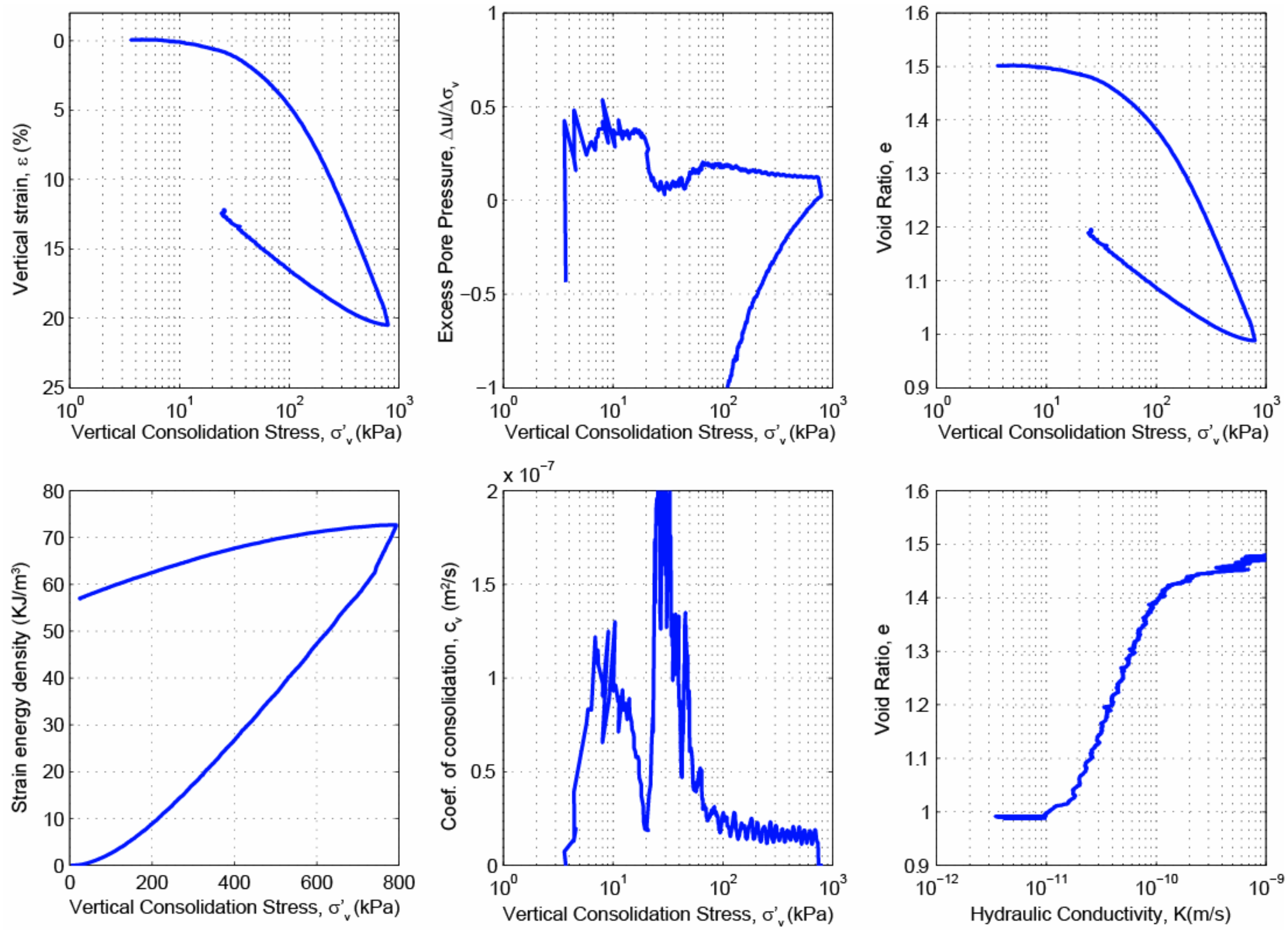

Figure B.3: CRS797 consolidation data for Sample U1324C-1H-1WR, 51.27 mbsf.

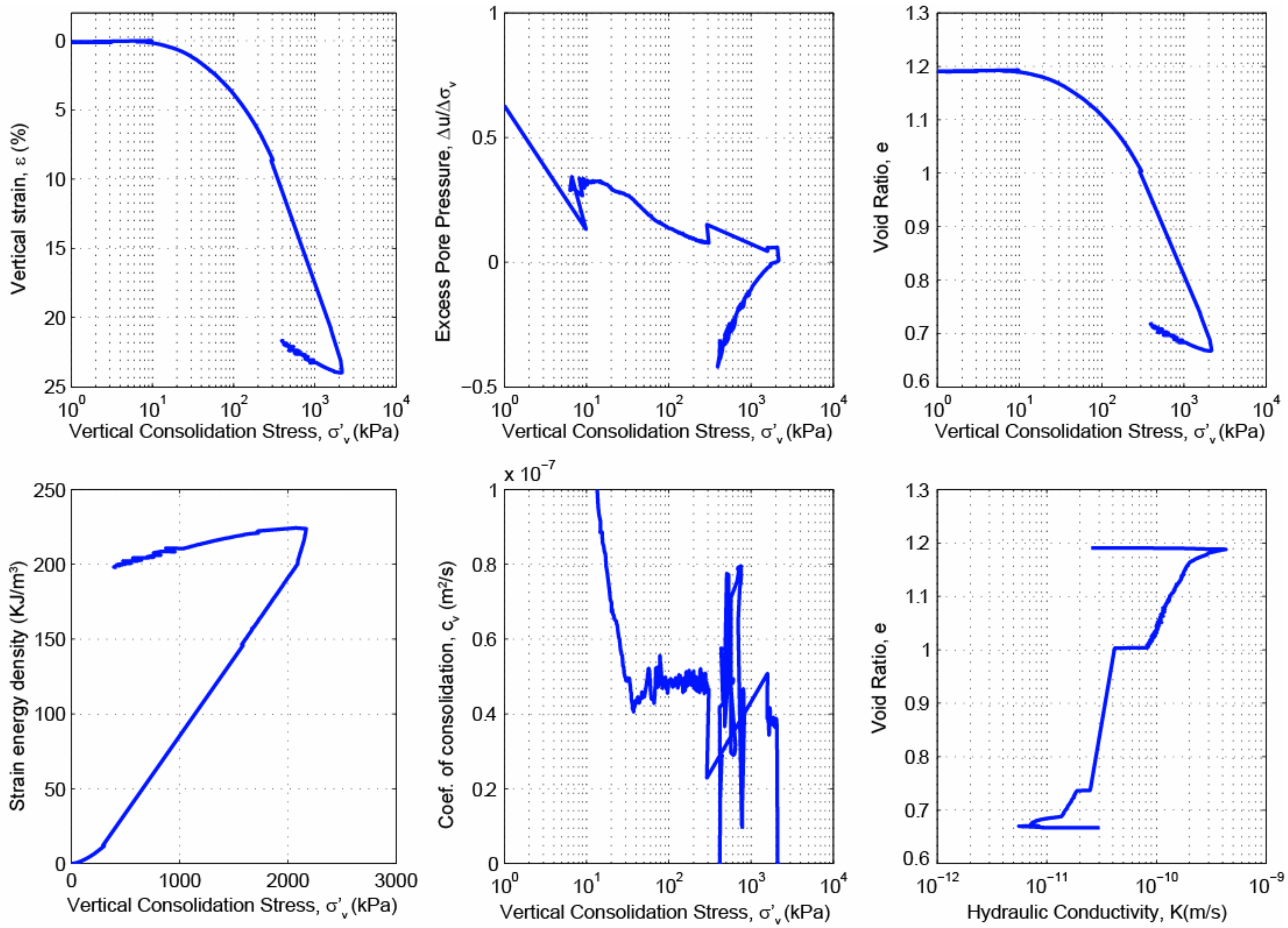

Figure B.4: CRS798 consolidation data for Sample U1322D-2H-2WR, 72.83 mbsf.

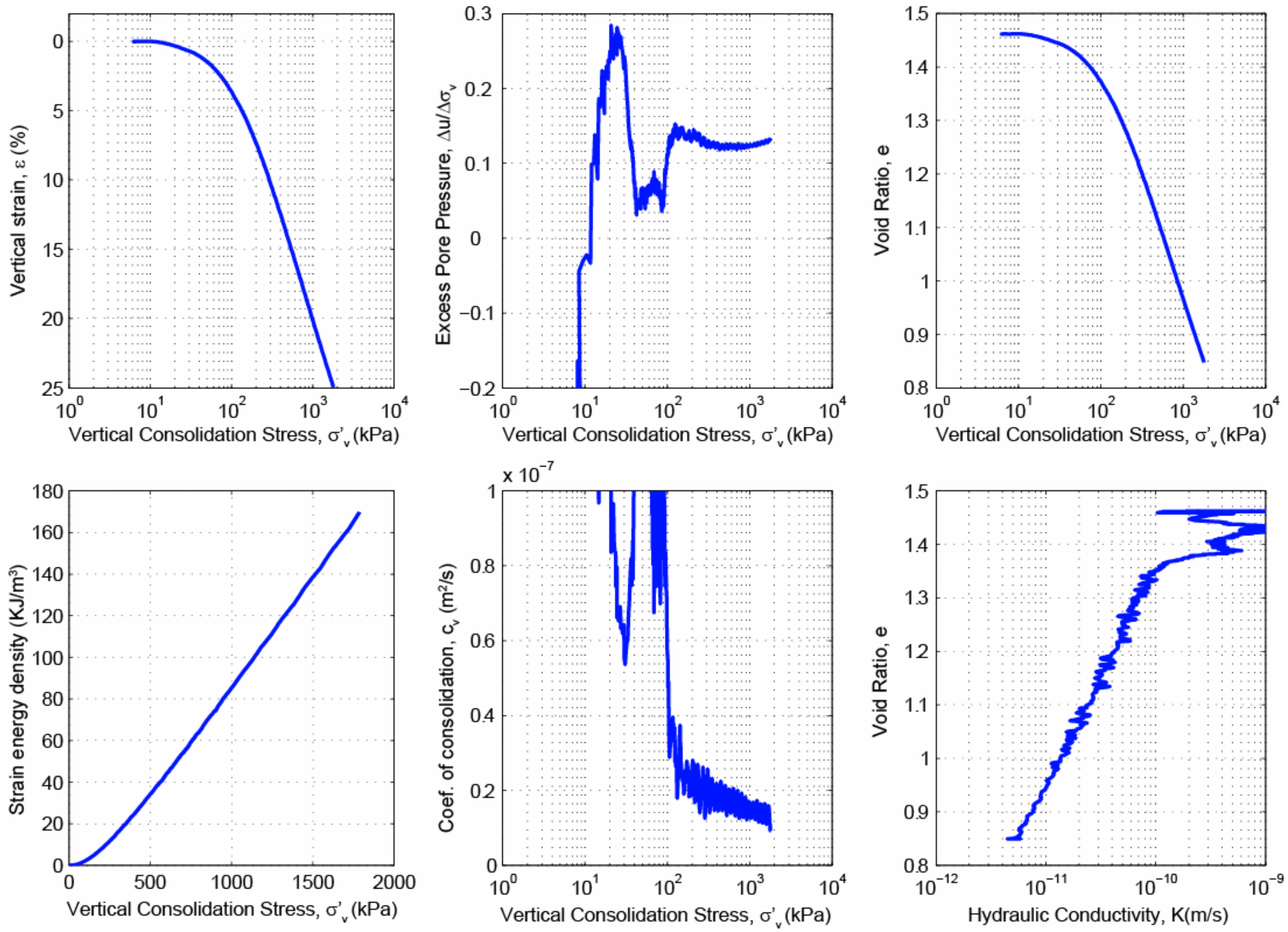

Figure B.5: CRS799 consolidation data for Sample U1324C-1H-1WR, 51.31 mbsf.

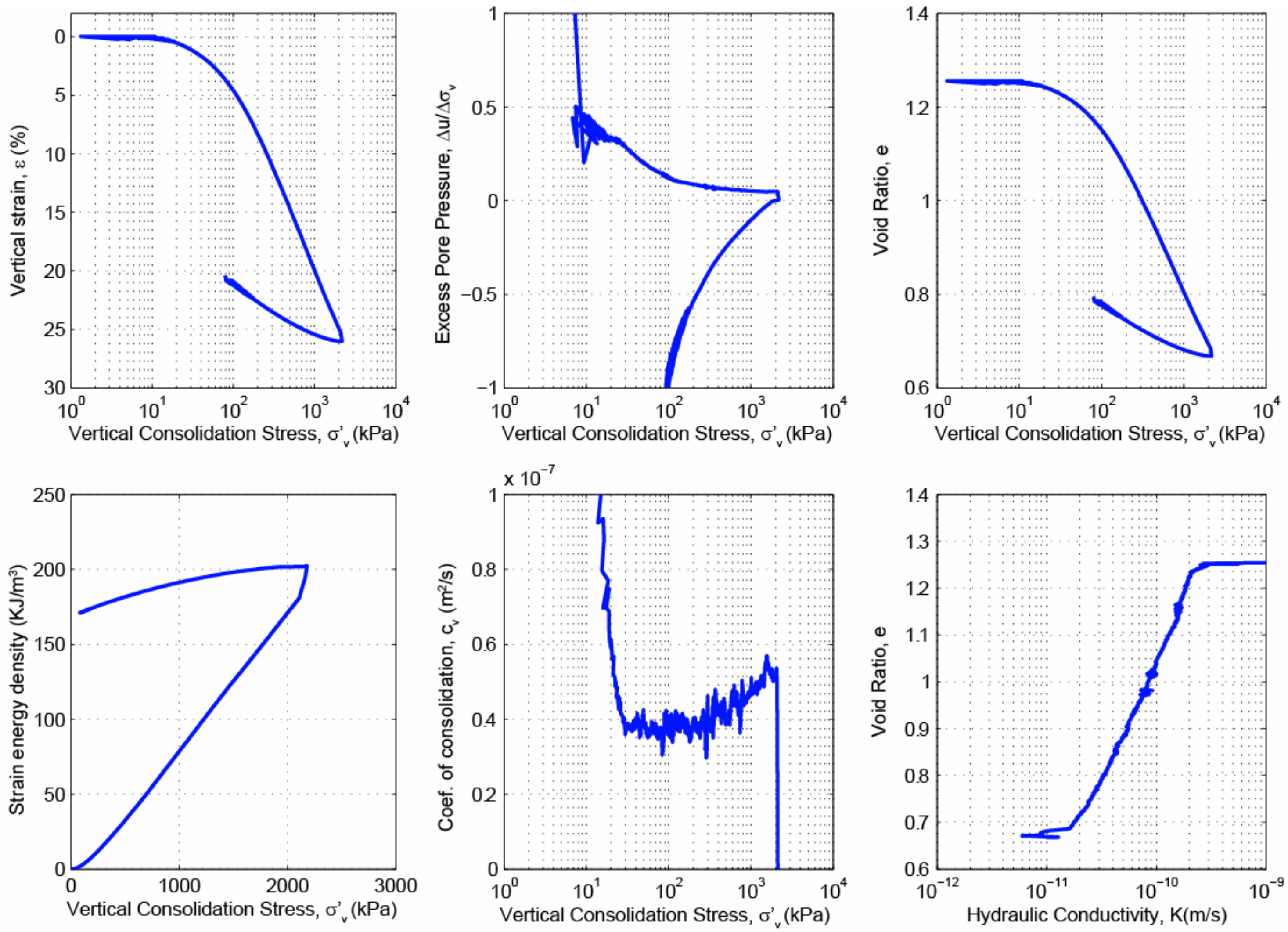

Figure B.6: CRS800 consolidation data for Sample U1324B-4H-7WR, 31.86 mbsf.

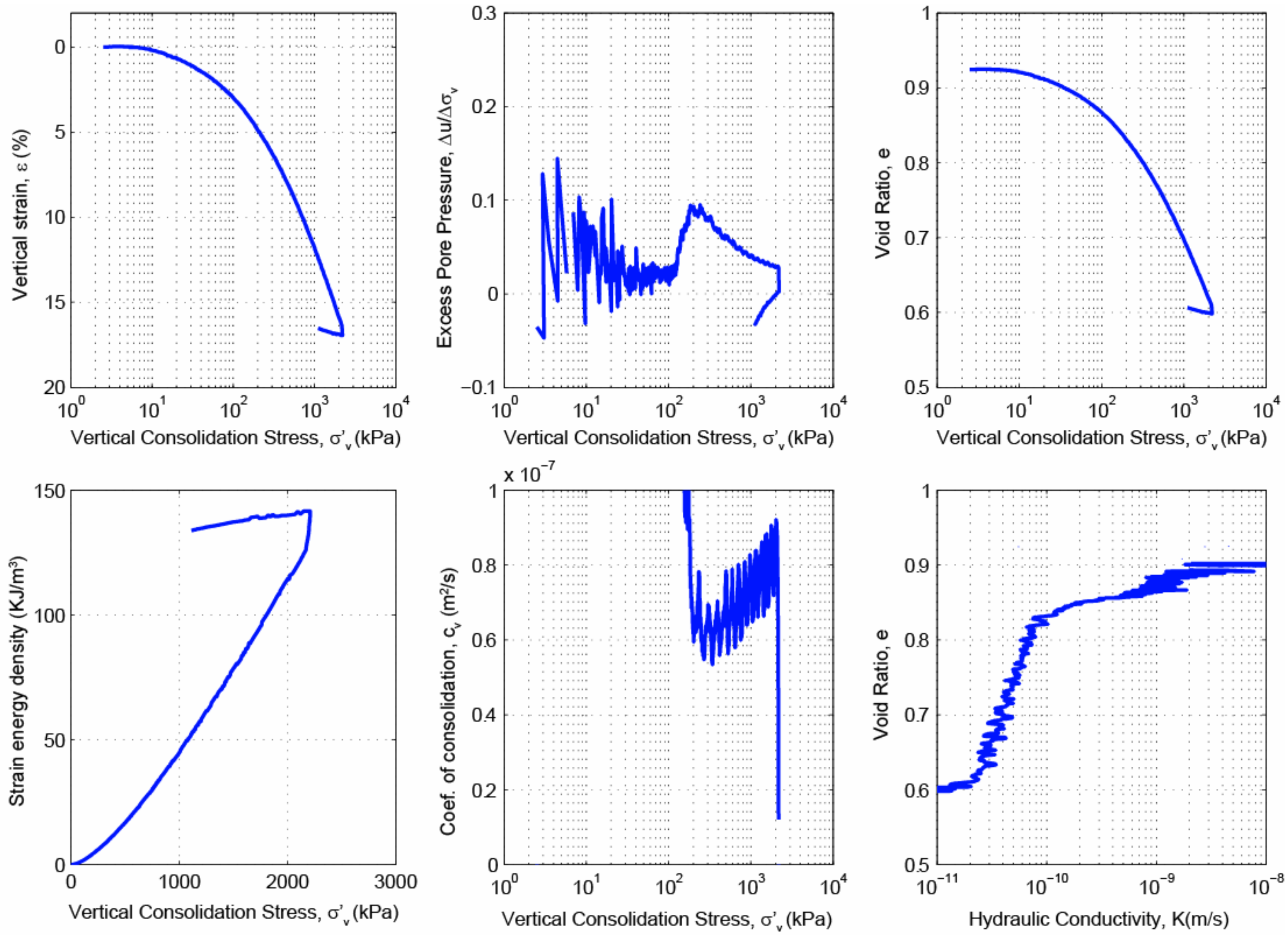

Figure B.7: CRS801 consolidation data for Sample U1324B-16H-5WR, 142.13 mbsf.

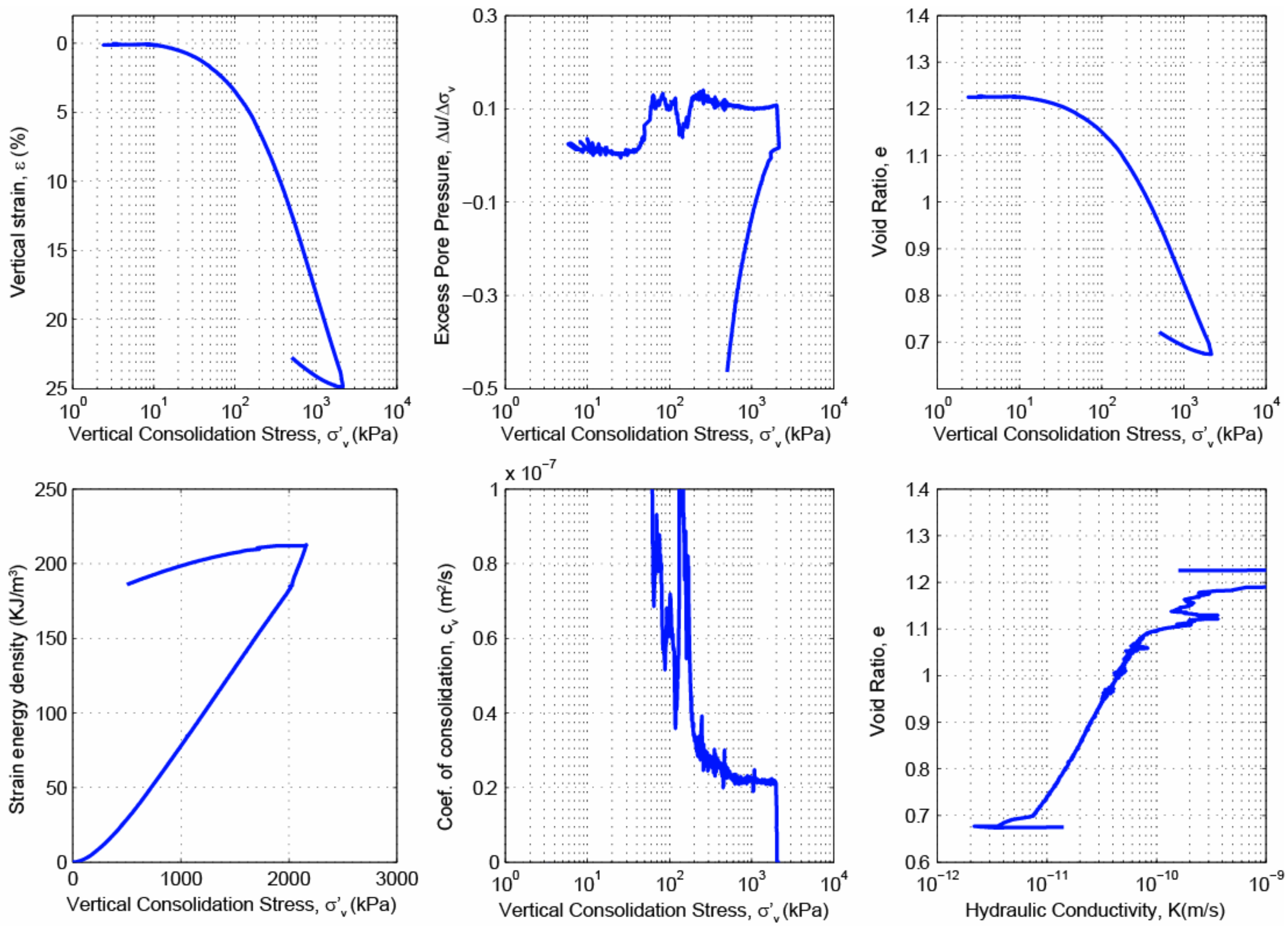

Figure B.8: CRS802 consolidation data for Sample U1324B-7H-7WR, 60.31 mbsf.

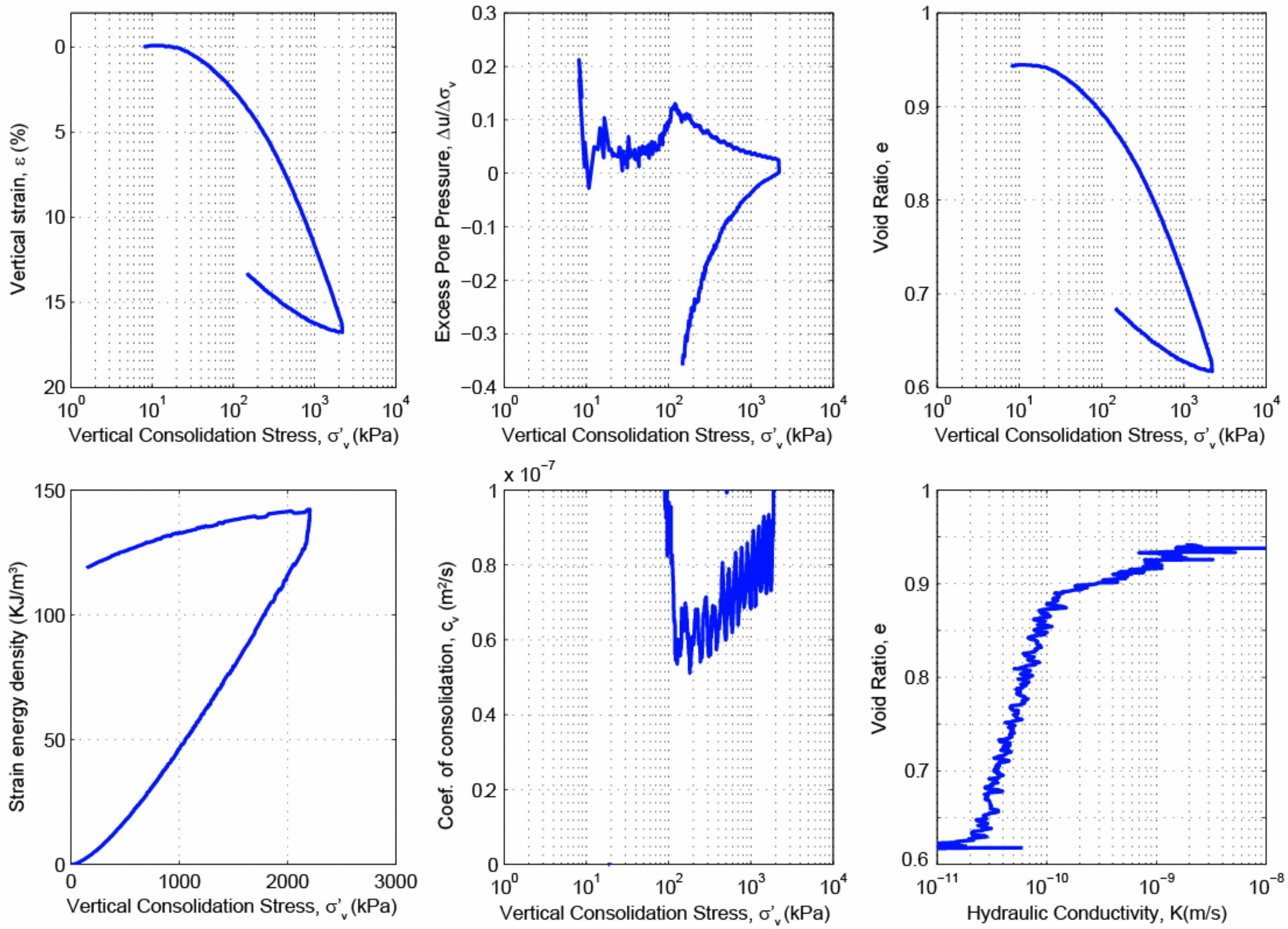

Figure B.9: CRS803 consolidation data for Sample U1324B-15H-5WR, 134.2 mbsf.

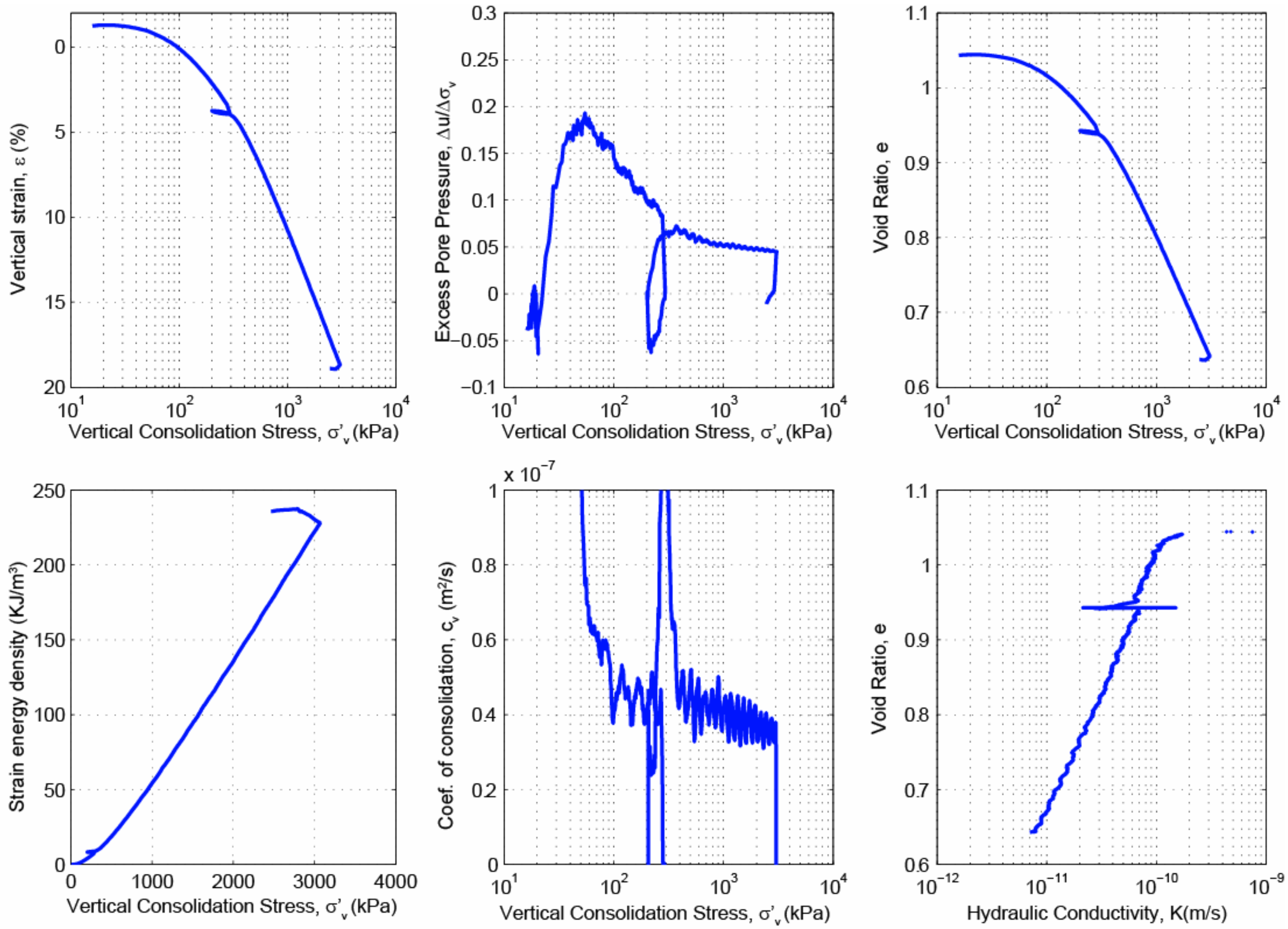

Figure B.10: CRS807 consolidation data for Sample U1324C-2H-4WR, 105.48 mbsf.

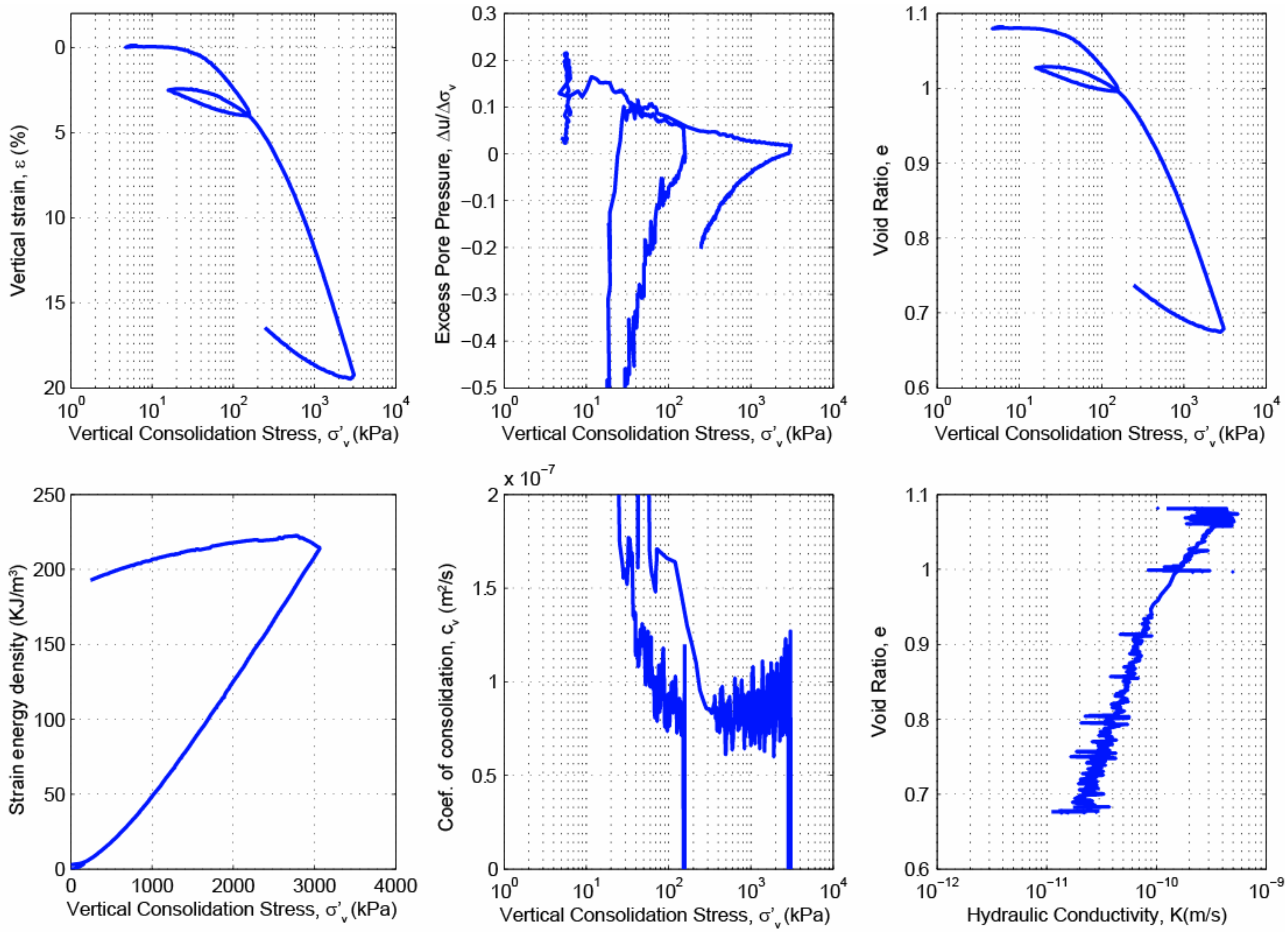

Figure B.11: CRS808 consolidation data for Sample U1322B-15H-1WR, 126.28 mbsf.

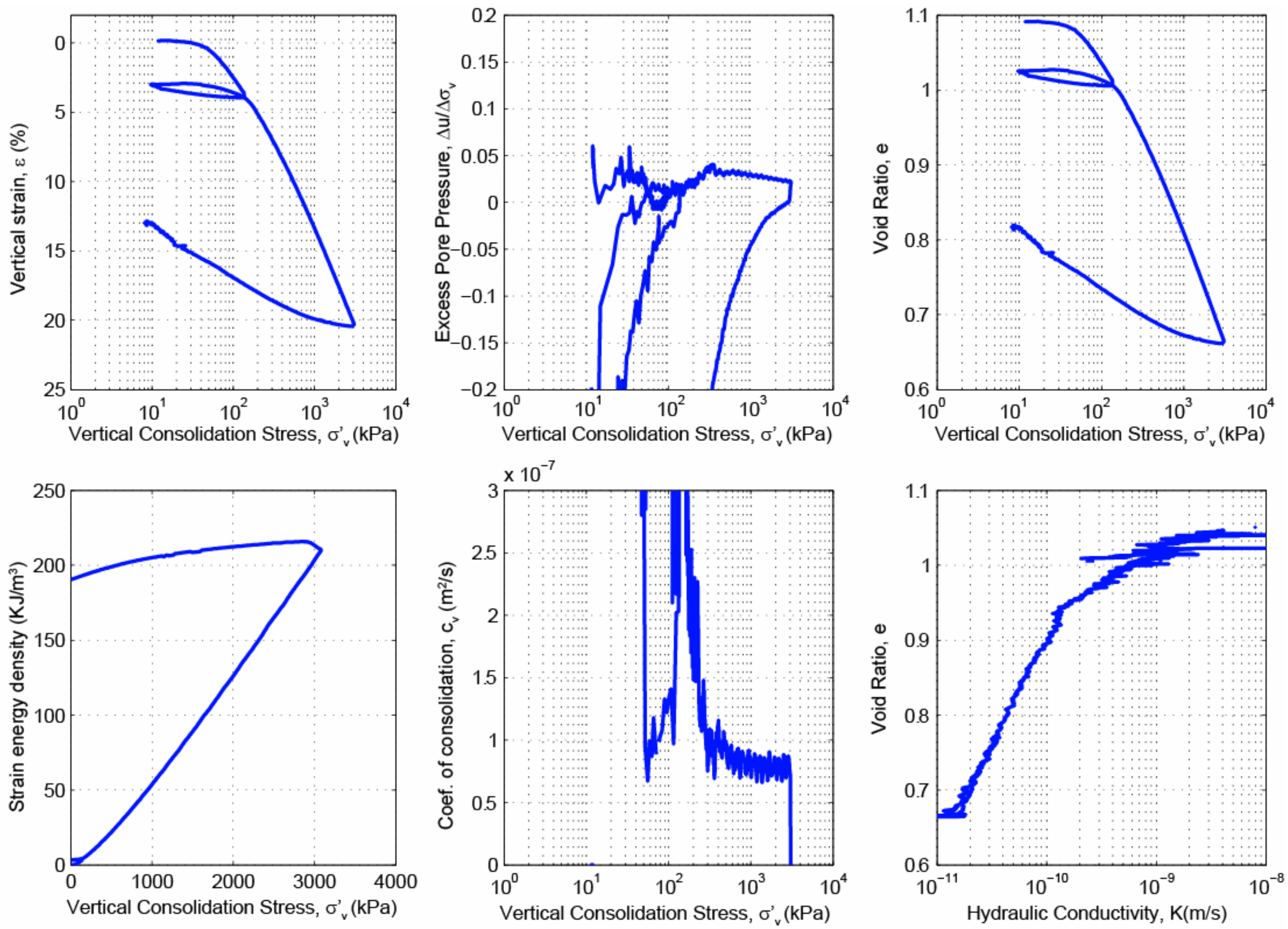

Figure B.12: CRS810 consolidation data for Sample U1322B-18H-6WR, 157.42 mbsf.

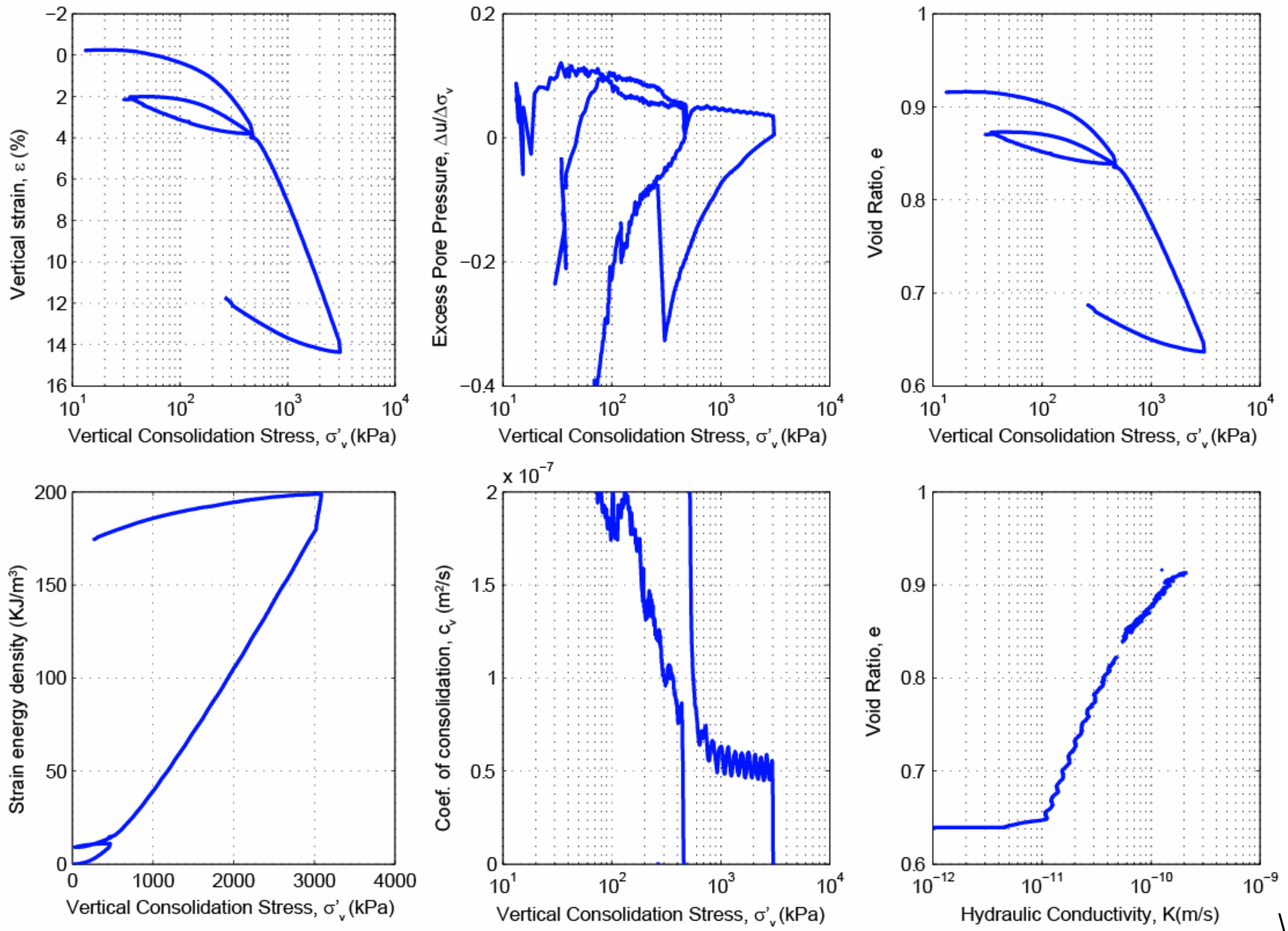

Figure B.13: CRS812 consolidation data for Sample U1324B-23H-5WR, 200 mbsf.

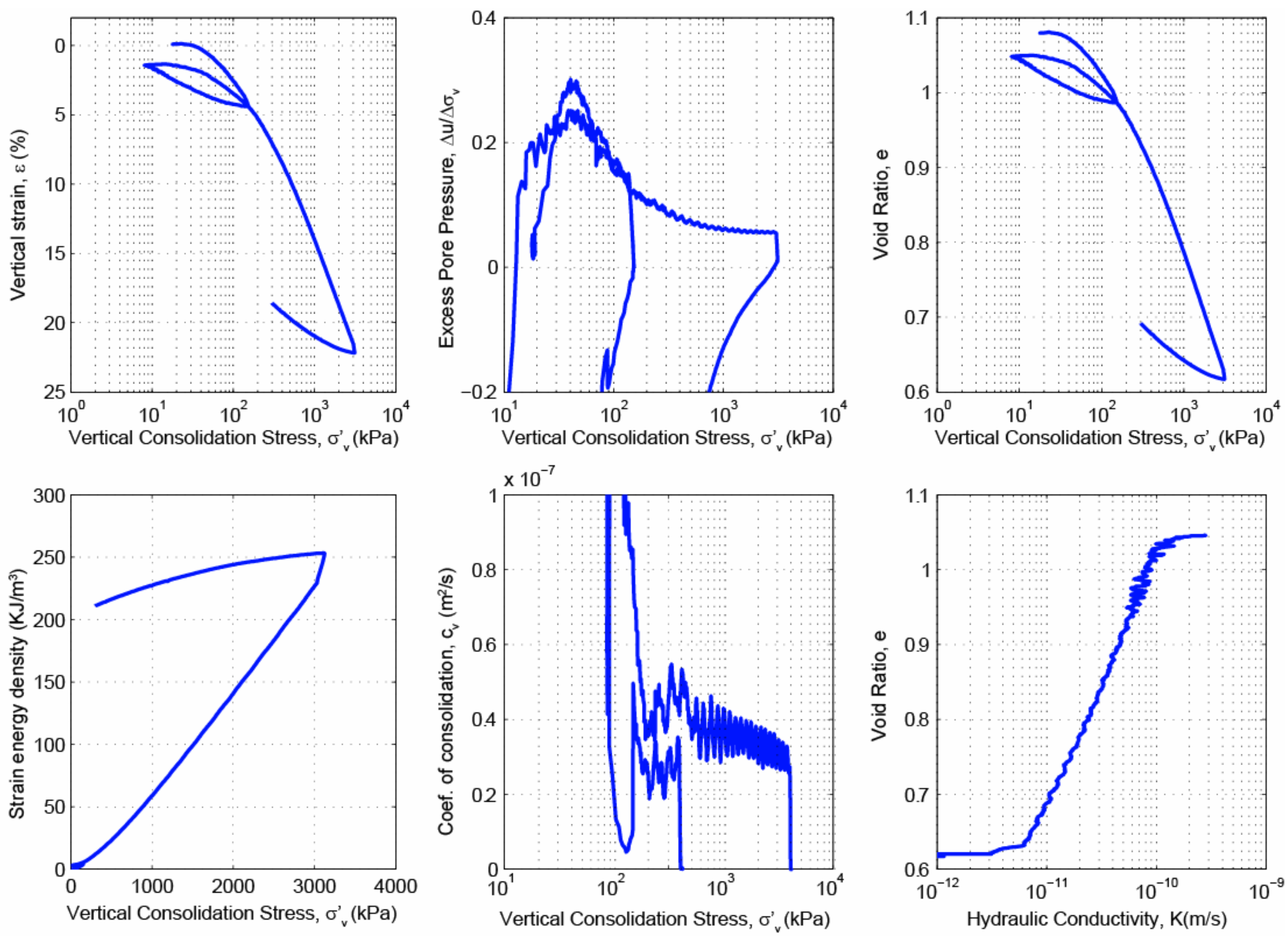

Figure B.14: CRS813 consolidation data for Sample U1324B-10H-7WR, 89.22 mbsf.

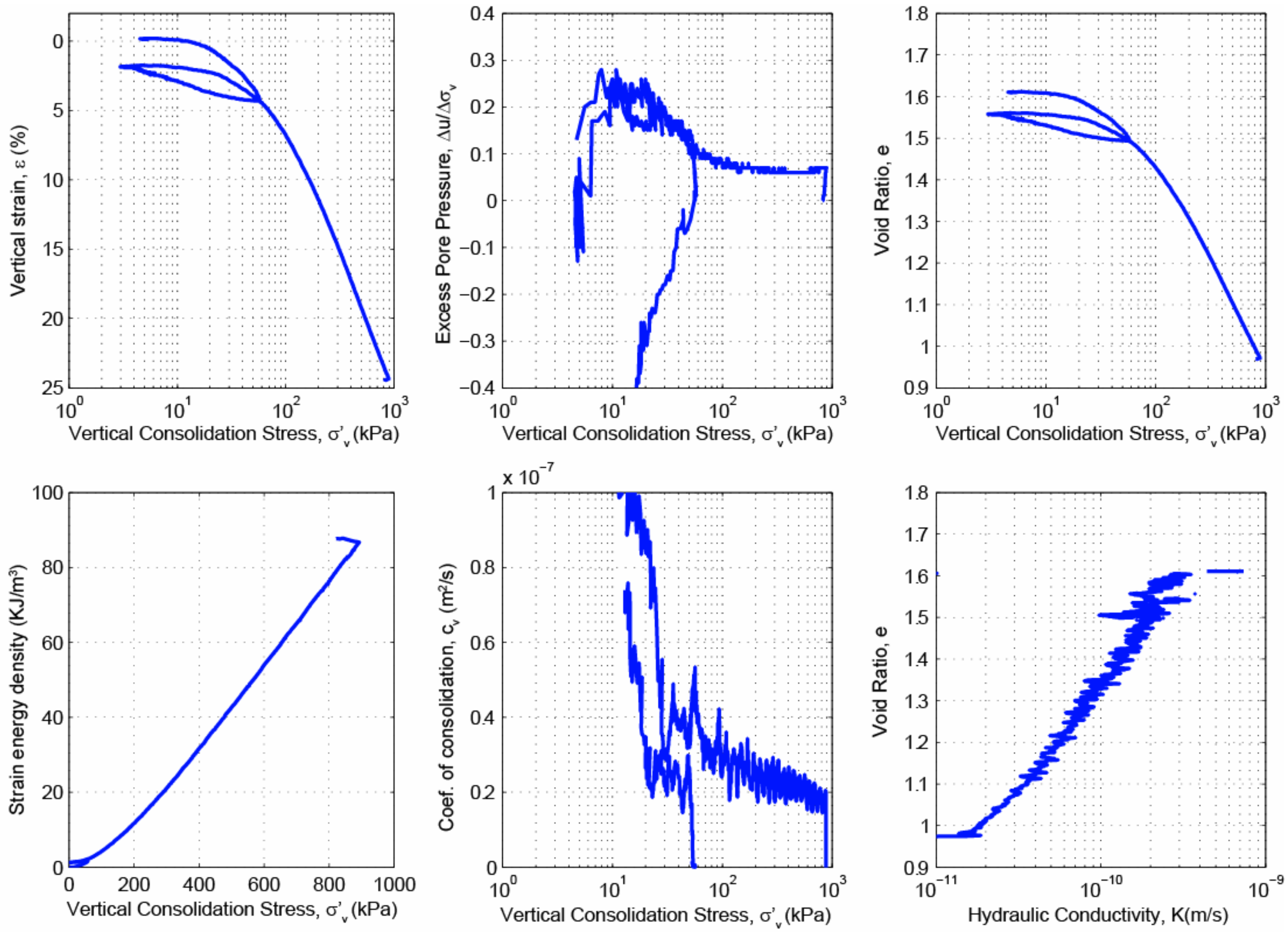

Figure B.15: CRS815 consolidation data for Sample U1322B-4H-3WR, 27.21 mbsf.

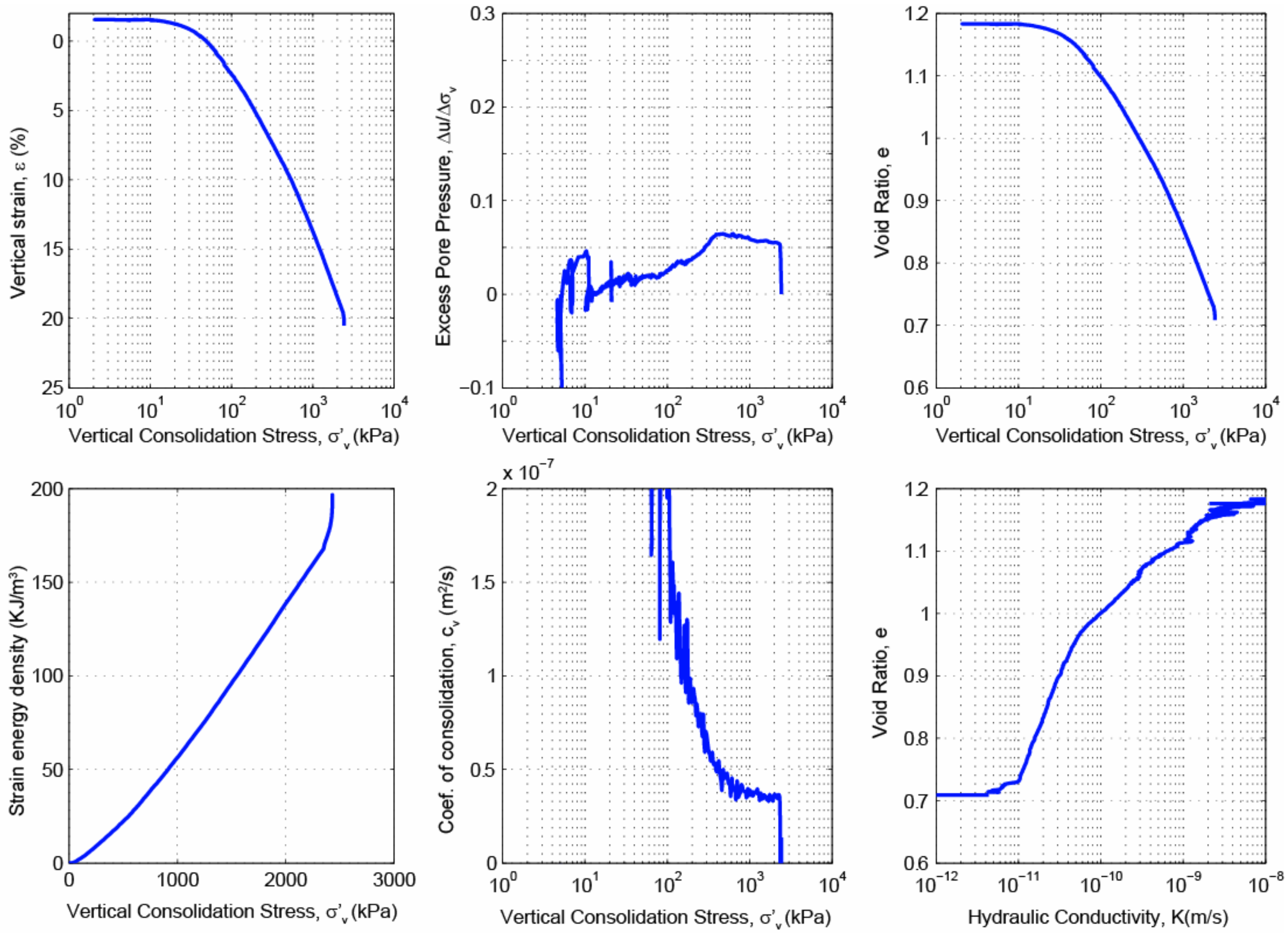

Figure B.16: CRS824 consolidation data for Sample U1322B-25H-6WR, 209.81 mbsf.

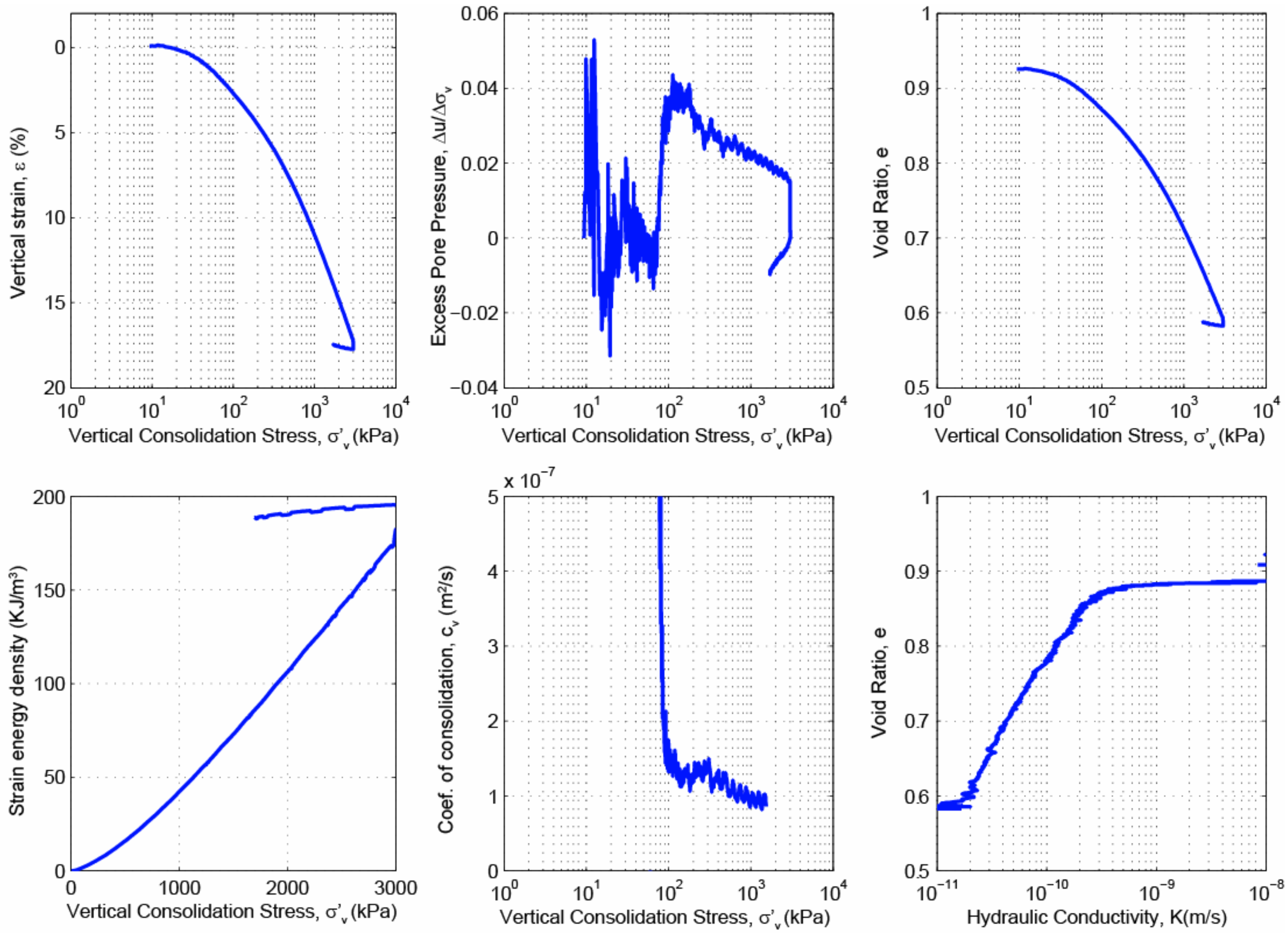

Figure B.17: CRS825 consolidation data for Sample U1322B-21H-3WR, 178.7 mbsf.

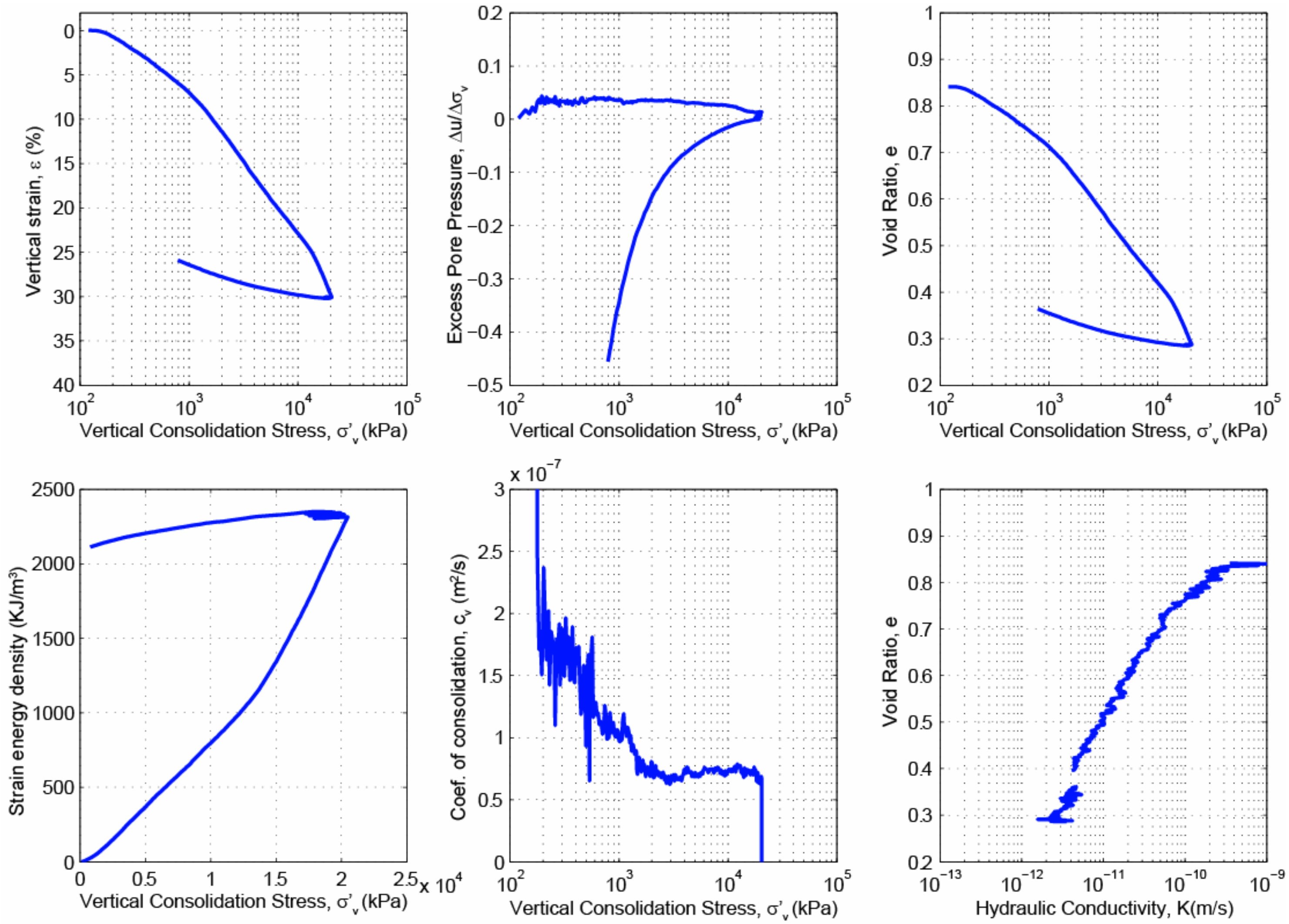

Figure B.18: CRS001 consolidation data for Sample U1324C-6H-3WR, 304.02 mbsf.

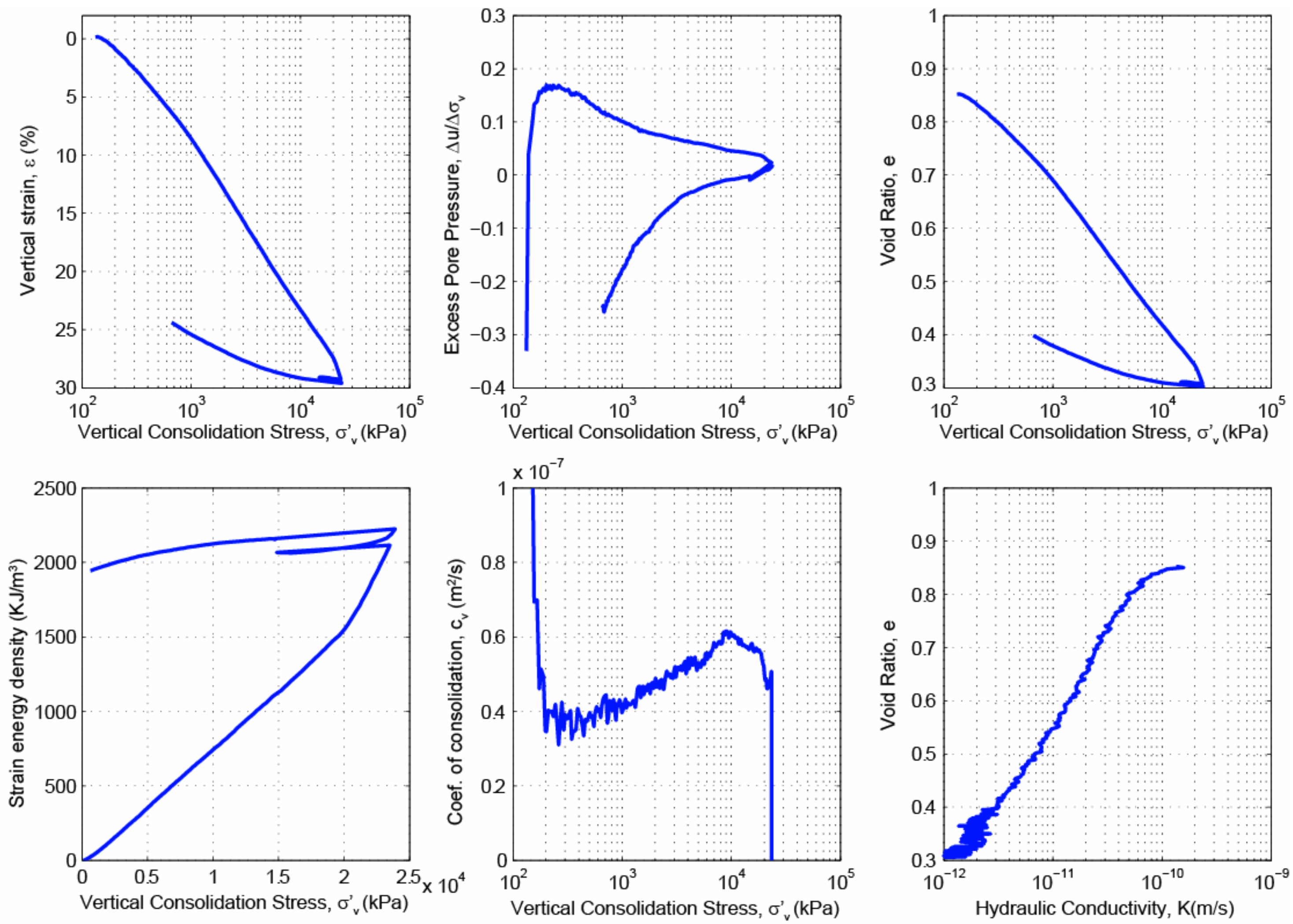

Figure B.19: CRS002 consolidation data for Sample U1324C-6H-3WR, 303.94 mbsf.

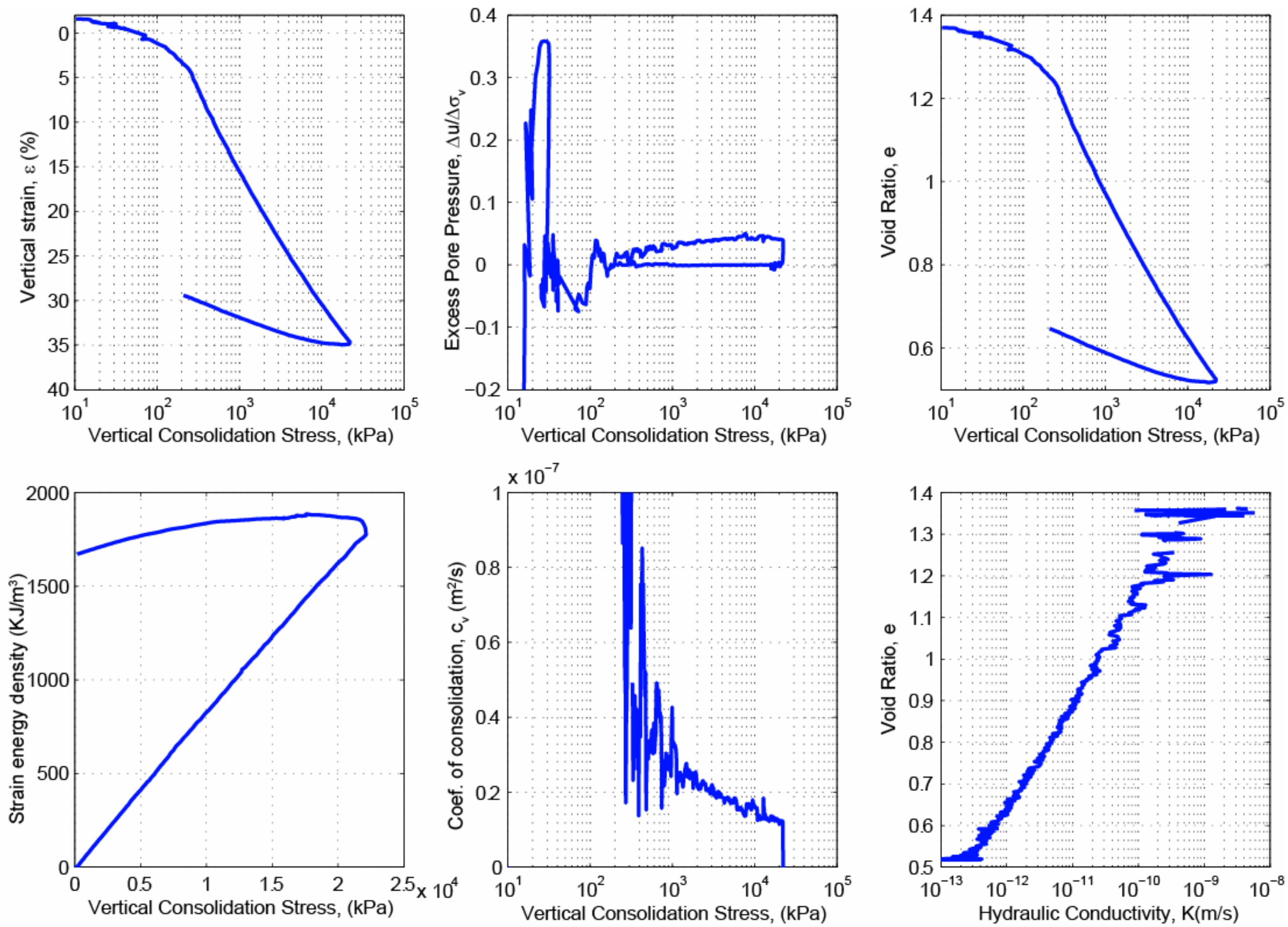

Figure B.20: CRS003 consolidation data for Sample U1324C-1H-1WR, 51.21 mbsf.

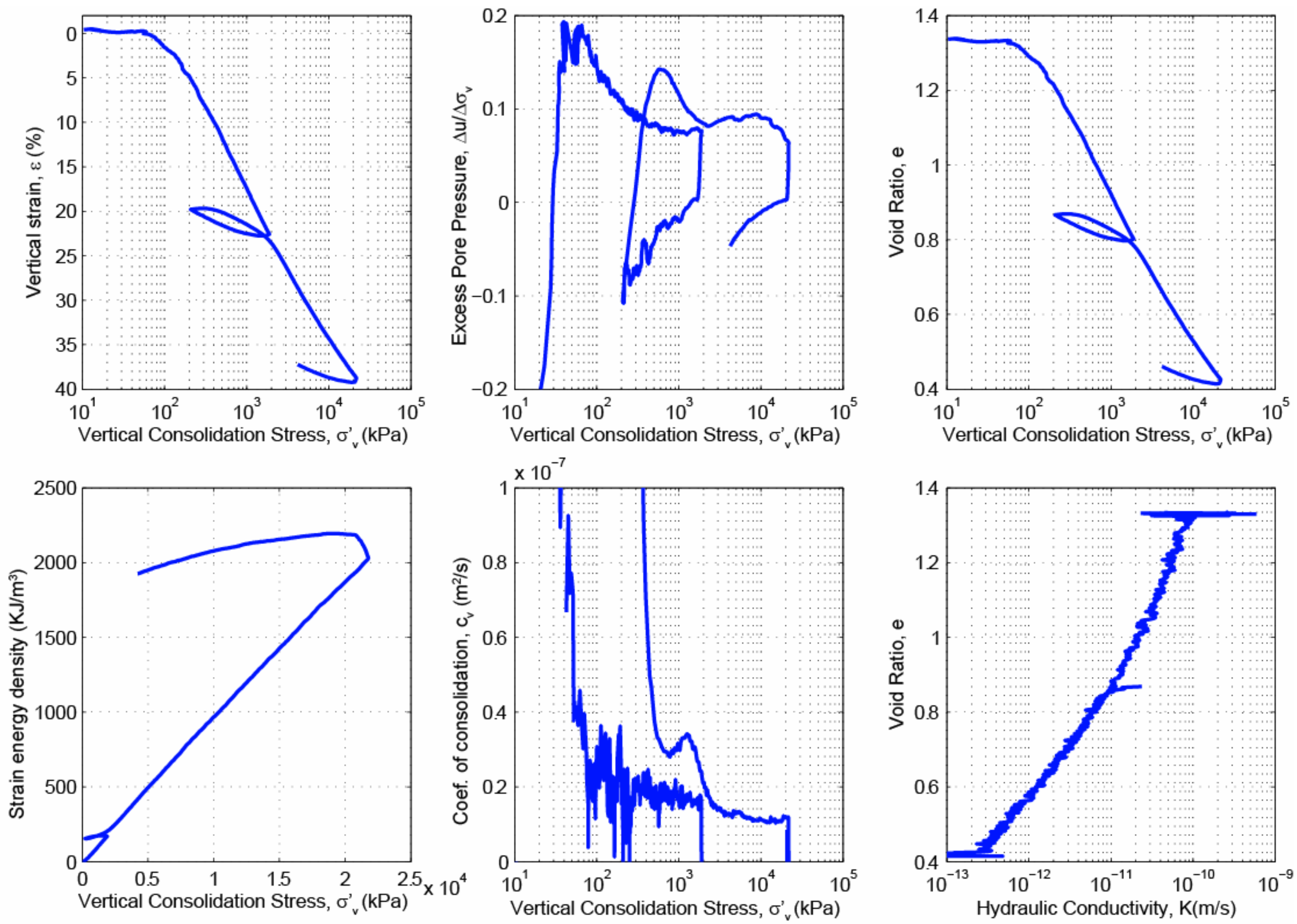

Figure B.21: CRS004 consolidation data for Sample U1324C-1H-1WR, 51.14 mbsf.

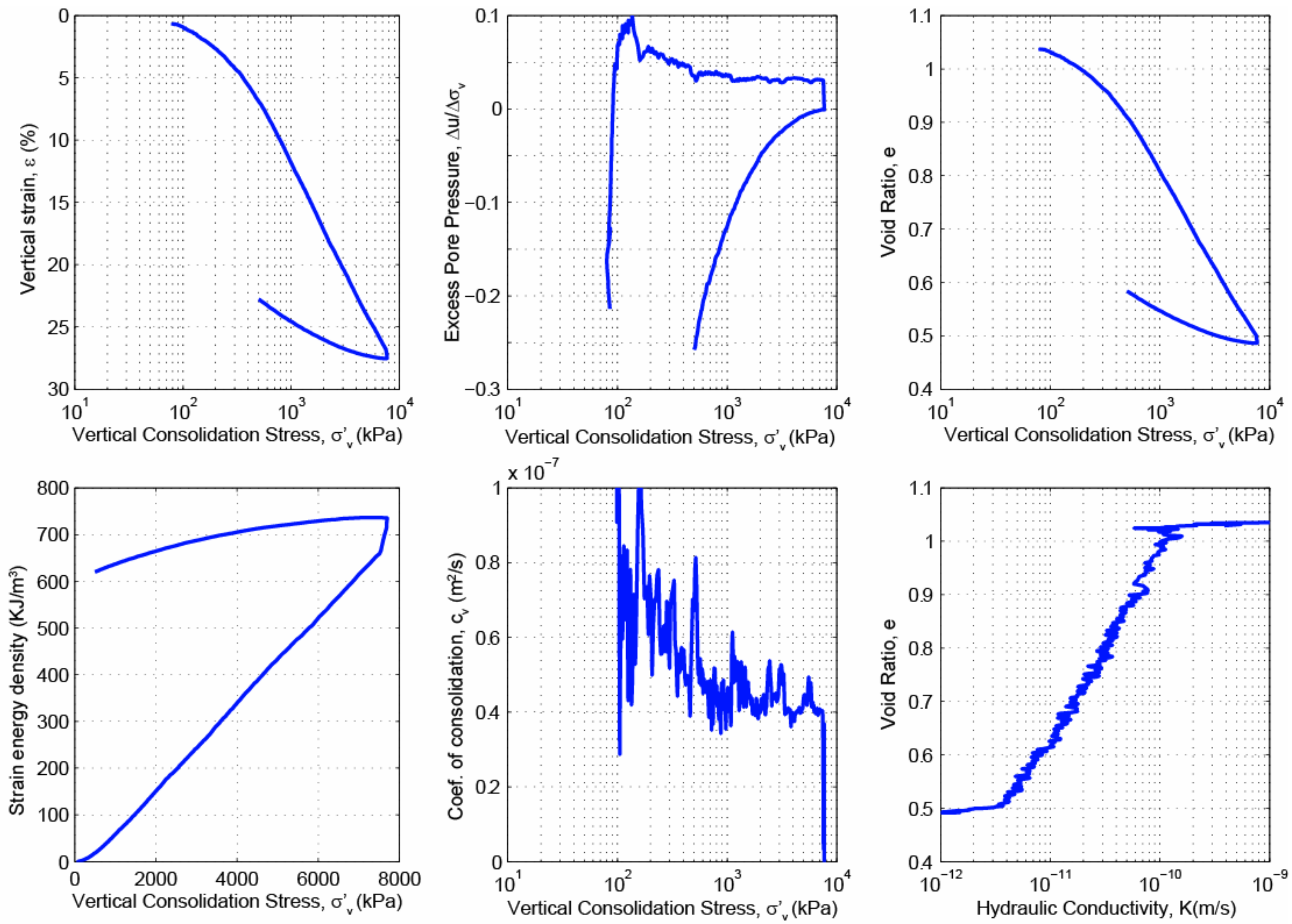

Figure B.22: CRS005 consolidation data for Sample U1324B-13H-7WR, 117.4 mbsf.

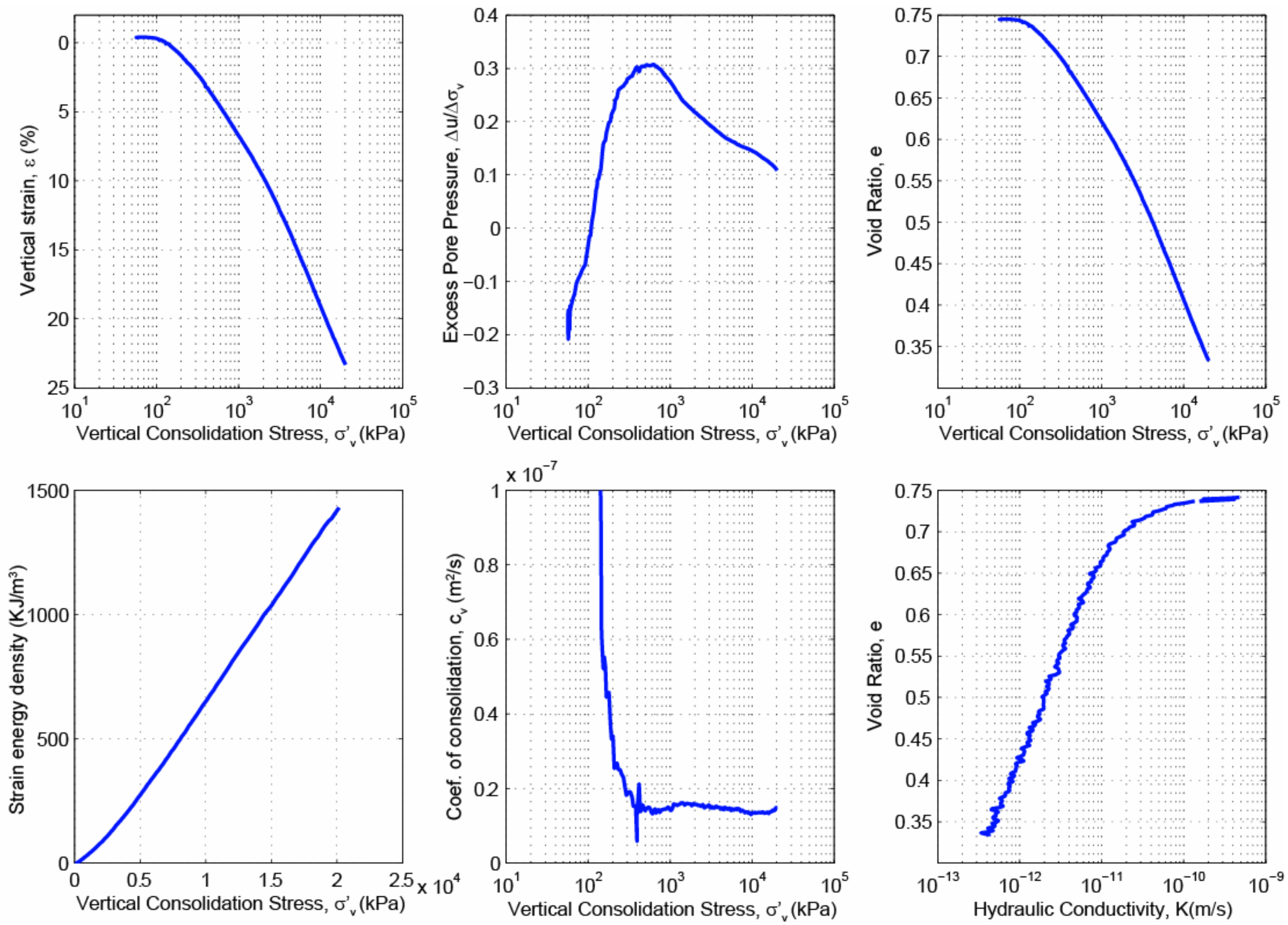

Figure B.23: CRS006 consolidation data for Sample U1324B-70X-6WR, 578.13 mbsf.

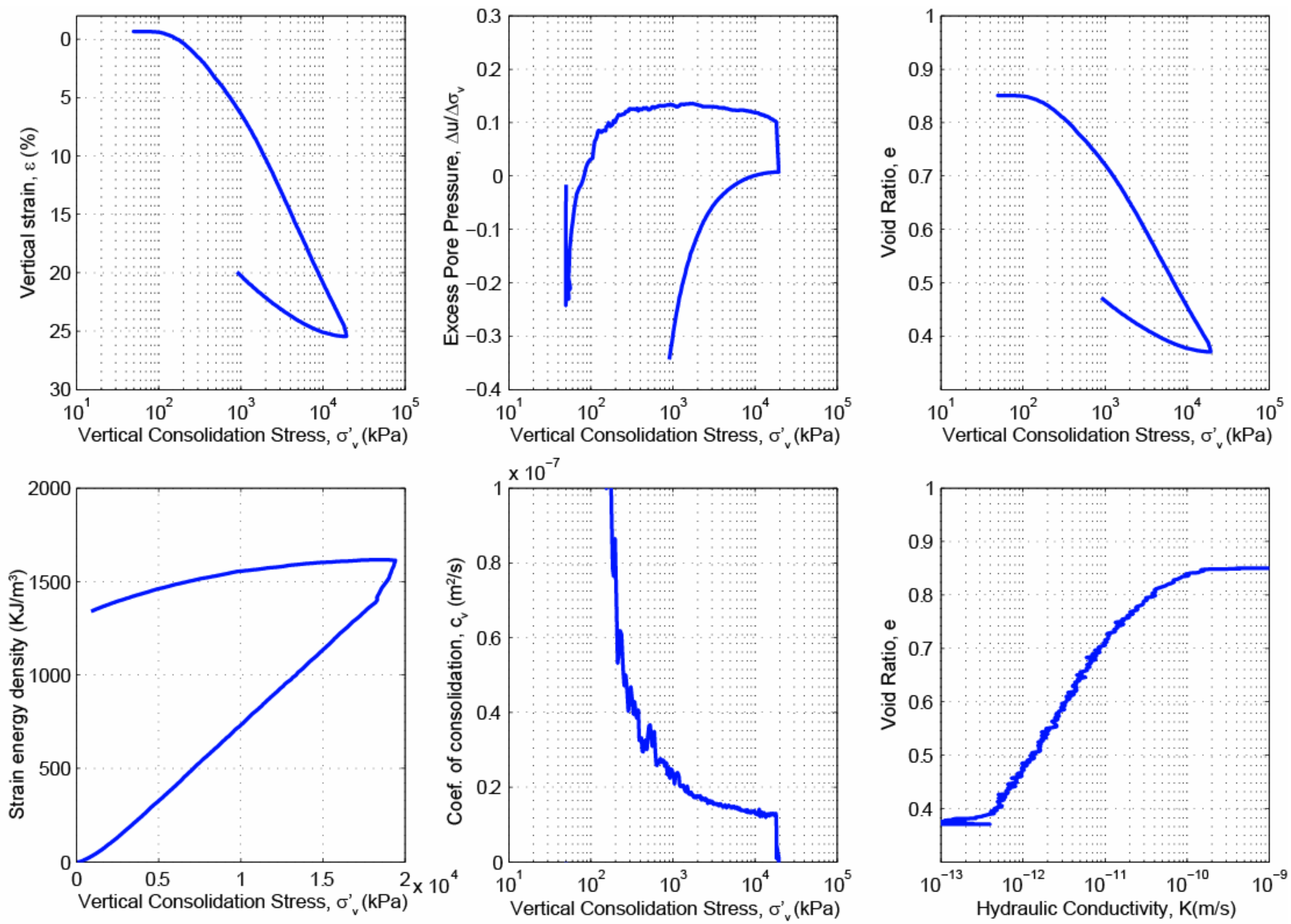

Figure B.24: CRS007 consolidation data for Sample U1324B-60X-2WR, 476.86 mbsf.

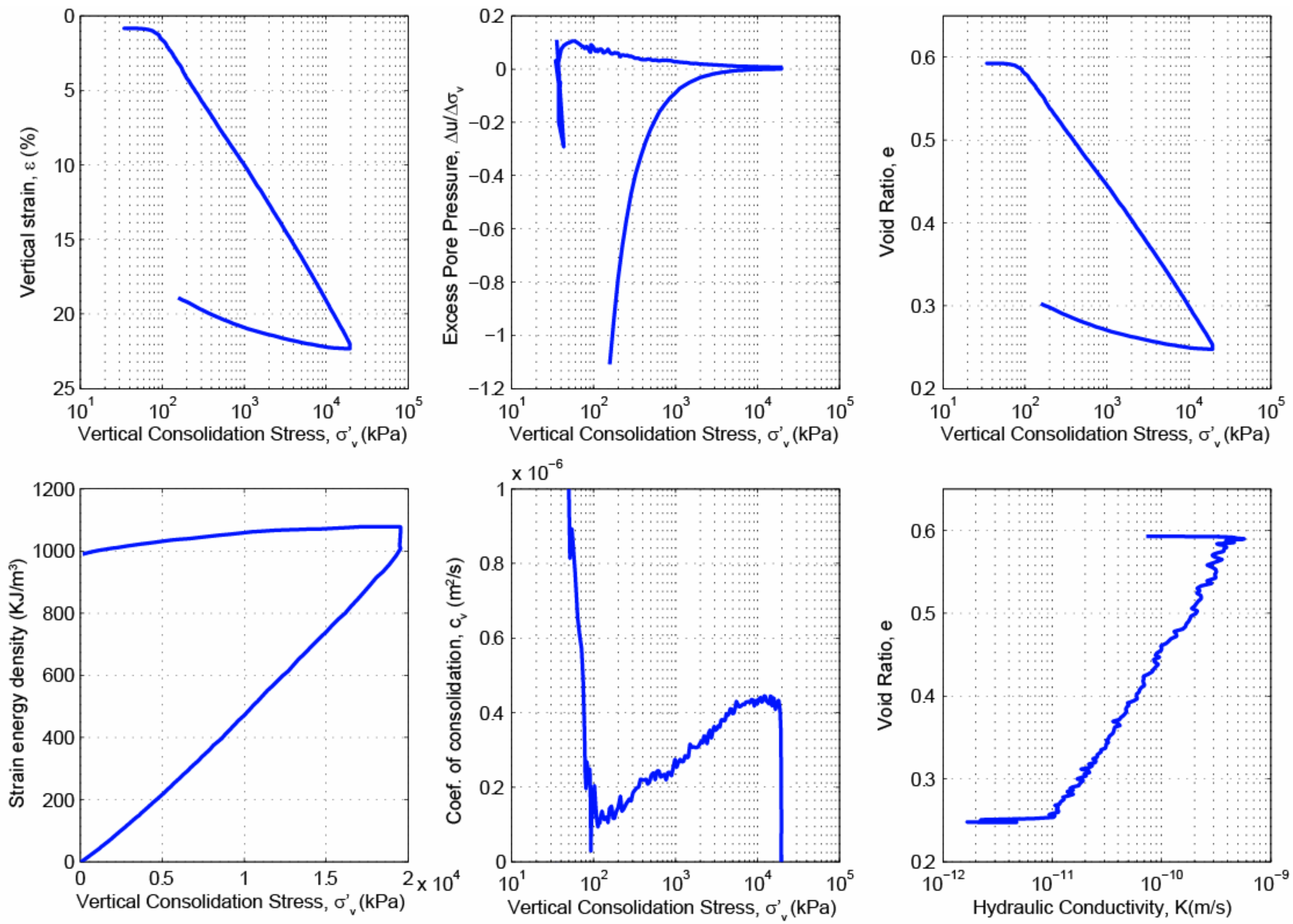

Figure B.25: CRS008 consolidation data for Sample U1324C-7H-1WR, 405.81 mbsf.

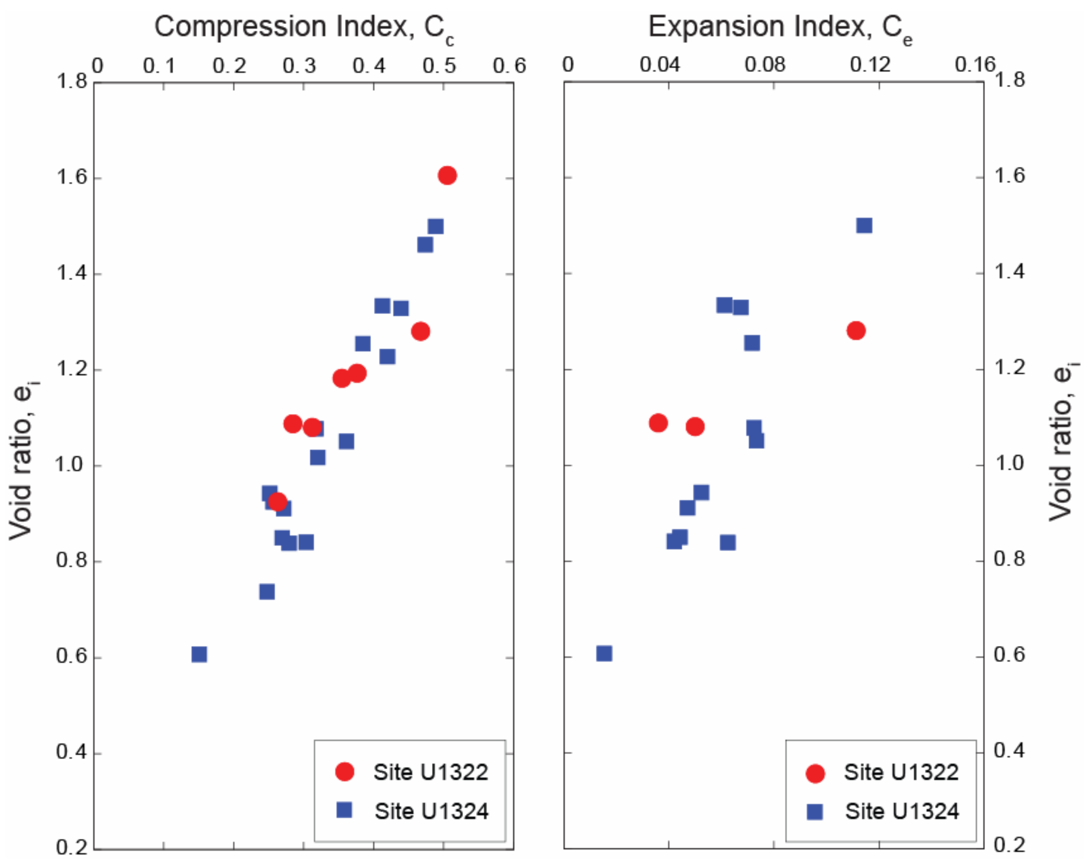

Figure B.26: Compression and expansion indices for Ursa sediments (Table B.3, columns 3 and 8).

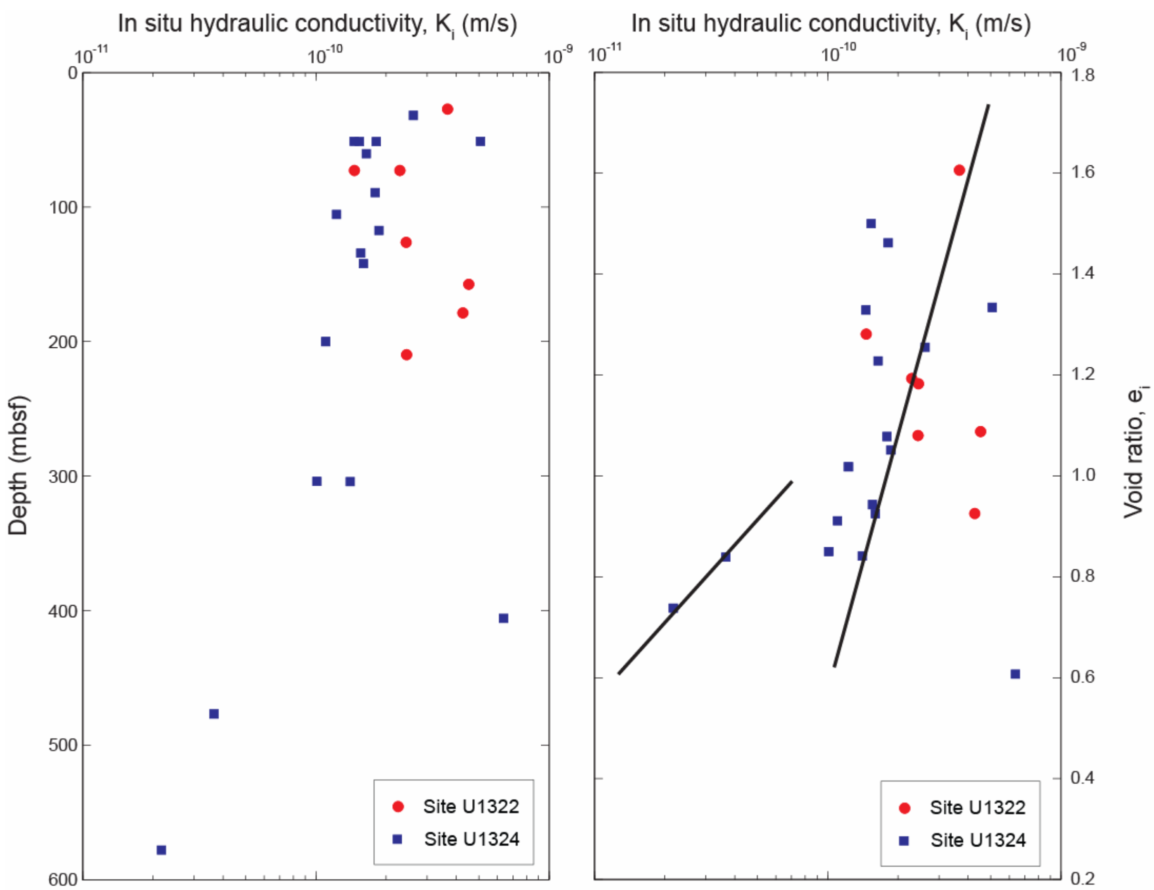

Figure B.27: In situ hydraulic conductivity for Ursa sediments (Table B.3, columns 2, 3 and 9).

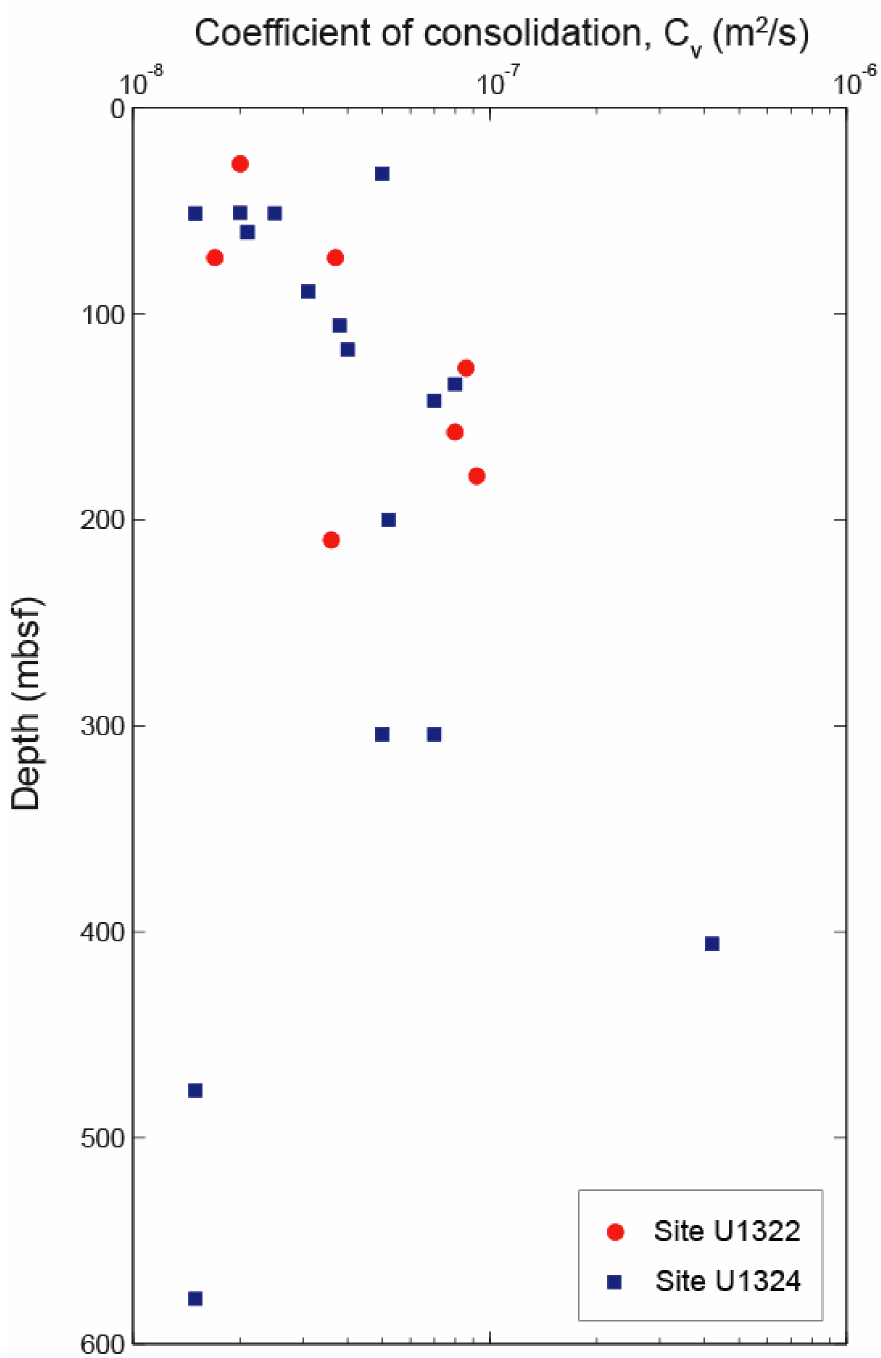

Figure B.28: Coefficient of consolidation for Ursa sediments (Table B.3, columns 2 and 9).

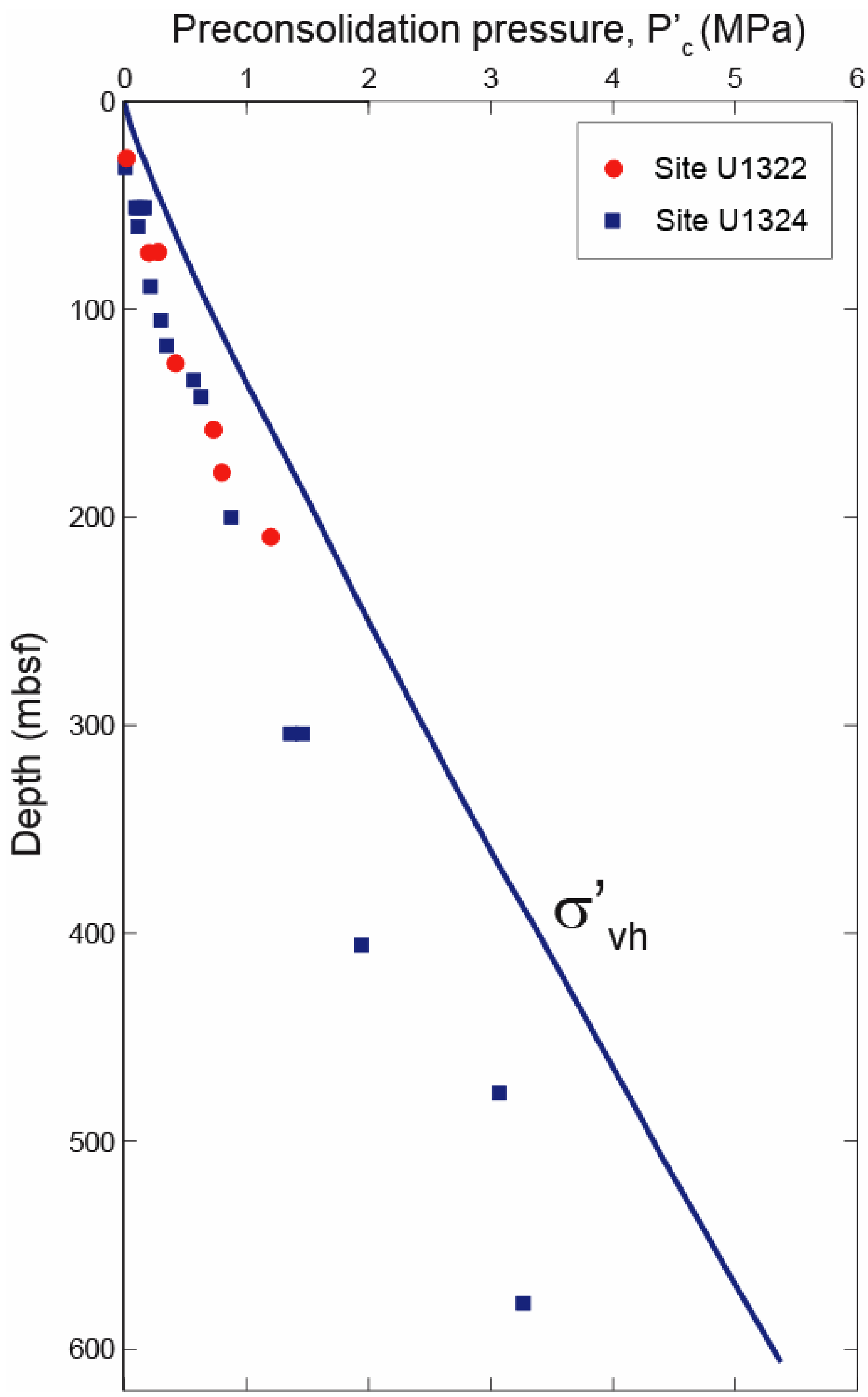

Figure B.29: Pre-consolidation pressure for Ursa sediments (Table B.3, columns 2 and 8). The pre-consolidation stress is determined using the work-stress method proposed by Becker, (1987). The hydrostatic vertical effective stress is calculated using the shipboard bulk density data assuming a seawater density of 1.024 g/cc.

Acknowledgements

This research used samples provided by the Integrated Ocean Drilling Program (IODP). Funding for this research was provided by the U.S. Science Support Program for IODP that is administered by Joint Oceanographic Institutions. In addition, the NSF Grants 0447235 and 0351085 supported this research.

References

ASTM International (2003), Standard test method for one-dimensional consolidation properties of soils using controlled-strain loading (Standard D4186), *In Annual Book of ASTM Standards*, *Vol. 04.08*, Soil and Rock (I): West Conshohocken, PA (Am. Soc. Testing and Mater.), 530–535.

Becker, D. E., J.H.A. Crooks, K. Been and M.G. Jefferies (1987), Work as a criterion for determing in situ and yield stresses in clays, *Can. Geotch. J.*, *24*, 549-564.

Casagrande, A. (1936), The determination of the pre-consolidation load and its practical significance, *1st International Conference on Soil Mechanics*, 60-64.

Flemings, P. B., Behrmann, J., John, C., and Shipboard Scientists IODP Expedition 308 (2006), Proceedings of the Integrated Ocean Drilling Program, DOI: doi:10.2204/iodp.proc.308.2006.

Graber, K. K., Pollard, E., Jonasson, B., and Schulte, E. (Eds.), (2002), Overview of Ocean Drilling Program engineering tools and hardware. ODP Tech. Note, 31 [Online]. Available from World Wide Web: <http://www-odp.tamu.edu/publications/tnotes/tn31/INDEX.HTM>.

Jacoby, R., Sawyer, D., Flemings, P.B., and Germain, J.T. (in preparation), Particle size distribution analysis, IODP Leg 308 Sites 1322 and 1324 in the Ursa Region on the continental slope of the Northern Gulf of Mexico, *in. Proceeding of the integrated ocean drilling program, vol, 308*.

Nelson, H., J. Germaine, H. Long, and P.B. Flemings (in preparation), X-ray radiography and C.T. scan of whole cores from IODP Expedition 308, *in. Proceeding of the integrated ocean drilling program, vol, 308*.

Tan, B., Germaine, J.T., and Flemings, P.B., (2006), Consolidation and strength characteristics of sediments from ODP Site 1244, Hydrate Ridge, Cascadia continental margin, paper presented at Proc. ODP, Sci. Results, 204.

Hui Long

Education:

2002-2007	Ph.D., Energy & Geo-Environmental Engineering, Penn State University Thesis: Interpreting Pore Fluid Pressure from Marine Mudstones with Pore Pressure Penetrometers, In Situ Data, and Laboratory Measurements
2001-2002	M.S., Energy & Geo-Environmental Engineering, Penn State University Thesis: Transports Properties of Seafloor Sediments Inferred from Pore Pressure Response to Penetration Tests
1998-2001	M.S., Engineering Geology, Institute of Geology and Geophysics, Chinese Academy of Sciences Thesis: A Nonlinear Model of Rainfall Triggered Landslides and Chaotic Effect in Slope Evolution
1994-1998	B.S., Geology, Northwest University Thesis: Application of Fuzzy Judgment in Evaluation of Reservoir

Research Experience:

2001-2007	Graduate Assistant, Penn State University
June-Aug 2006	Intern, ExxonMobil Upstream Research Company
June-July 2005	Physical Properties/Downhole Tools Specialist, IODP Expedition 308

Selected Publications:

Long, H., P.B. Flemings, J.T. Germaine, and D.M. Saffer (in review), Consolidation characteristics, effective stress and pore fluid pressure of Ursa sediments, Gulf of Mexico, *Earth and Planetary Science Letter*.

Long, H., Flemings, P.B., Germaine, J.T., and Elsworth, D. (in review), Analysis and Interpretation of Pore Pressure Measurement by a New Penetrometer: Temperature-Two-Pressure (T2P) Probe, *Journal of Geophysical Research*.

Long, H., P. B. Flemings, J. T. Germaine, and D. M. Saffer (in review), Consolidation characteristics of sediments from IODP Expedition 308, Ursa Basin, Gulf of Mexico, *in. Proc. IODP, Sci. Results, vol, 308*.

Long, H., P. B. Flemings, J. T. Germaine, B. Dugan, D. Ferrell, and Expedition 308 Scientists (in review), Penetrometer Measurements of In Situ Temperature and Pressure on IODP Expedition 308, *in. Proc. IODP, Sci. Results, vol, 308*.

Long, H., P.B. Flemings, J. Germaine, B. Dugan, D. Sawyer, and Shipboard Scientific Party, IODP Expedition 308 (2007), In Situ Pore Pressure at IODP Site U1324, Ursa Basin, Gulf of Mexico, *Proceedings of the Offshore Technology Conference, Houston, Texas, OTC Paper #18772*.

Long, H., P. B. Flemings, and J. T. Germaine (2007), Interpreting in situ pressure and hydraulic properties with borehole penetrometers in ocean drilling: DVTPP and Piezoprobe deployments at southern Hydrate Ridge, offshore Oregon, *J. Geophys. Res.*, *112*, B04101, doi:04110.01029/02005JB004165.

Professional Affiliations:

AGU, SPE, ASTM